

SPECTROSCOPIC STUDIES OF NANOMATERIALS WITH A  
LIQUID-HELIUM-FREE HIGH-STABILITY CRYOGENIC  
SCANNING TUNNELING MICROSCOPE

by

DMITRY ANATOLEVICH KISLITSYN

A DISSERTATION

Presented to the Department of Chemistry and Biochemistry  
and the Graduate School of the University of Oregon  
in partial fulfillment of the requirements  
for the degree of  
Doctor of Philosophy

December 2016

## DISSERTATION APPROVAL PAGE

Student: Dmitry Anatolevich Kislitsyn

Title: Spectroscopic Studies of Nanomaterials with a Liquid-Helium-Free High-Stability Cryogenic Scanning Tunneling Microscope

This dissertation has been accepted and approved in partial fulfillment of the requirements for the Doctor of Philosophy degree in the Department of Chemistry and Biochemistry by:

Andrew H. Marcus	Chairperson
George V. Nazin	Advisor
Mark C. Lonergan	Core Member
Shannon W. Boettcher	Core Member
Eric I. Corwin	Institutional Representative

and

Scott L. Pratt	Dean of the Graduate School
----------------	-----------------------------

Original approval signatures are on file with the University of Oregon Graduate School.

Degree awarded December 2016

© 2016 Dmitry Kislitsyn

## DISSERTATION ABSTRACT

Dmitry Anatolevich Kislitsyn

Doctor of Philosophy

Department of Chemistry and Biochemistry

December 2016

Title: Spectroscopic Studies of Nanomaterials with a Liquid-Helium-Free High-Stability Cryogenic Scanning Tunneling Microscope

This dissertation presents results of a project bringing Scanning Tunneling Microscope (STM) into a regime of unlimited operational time at cryogenic conditions. Freedom from liquid helium consumption was achieved and technical characteristics of the instrument are reported, including record low noise for a scanning probe instrument coupled to a close-cycle cryostat, which allows for atomically resolved imaging, and record low thermal drift. Subsequent studies showed that the new STM opened new prospects in nanoscience research by enabling Scanning Tunneling Spectroscopic (STS) spatial mapping to reveal details of the electronic structure in real space for molecules and low-dimensional nanomaterials, for which this depth of investigation was previously prohibitively expensive.

Quantum-confined electronic states were studied in single-walled carbon nanotubes (SWCNTs) deposited on the Au(111) surface. Localization on the nanometer-scale was discovered to produce a local vibronic manifold resulting from the localization-enhanced electron-vibrational coupling. STS showed the vibrational overtones, identified as D-band Kekulé vibrational modes and K-point transverse out-of plane phonons. This study experimentally connected the properties of well-defined localized electronic states

to the properties of associated vibronic states.

Electronic structures of alkyl-substituted oligothiophenes with different backbone lengths were studied and correlated with torsional conformations assumed on the Au(111) surface. The molecules adopted distinct planar conformations with alkyl ligands forming cis- or trans- mutual orientations and at higher coverage self-assembled into ordered structures, binding to each other via interdigitated alkyl ligands. STS maps visualized, in real space, particle-in-a-box-like molecular orbitals. Shorter quaterthiophenes have substantially varying orbital energies because of local variations in surface reactivity. Different conformers of longer oligothiophenes with significant geometrical distortions of the oligothiophene backbones surprisingly exhibited similar electronic structures, indicating insensitivity of interaction with the surface to molecular conformation.

Electronic states for annealed ligand-free lead sulfide nanocrystals were investigated, as well as hydrogen-passivated silicon nanocrystals, supported on the Au(111) surface. Delocalized quantum-confined states and localized defect-related states were identified, for the first time, via STS spatial mapping. Physical mechanisms, involving surface reconstruction or single-atom defects, were proposed for surface state formation to explain the observed spatial behavior of the electronic density of states.

This dissertation includes previously published co-authored material.

## CURRICULUM VITAE

NAME OF AUTHOR: Dmitry Anatolevich Kislitsyn

### GRADUATE AND UNDERGRADUATE SCHOOLS ATTENDED:

University of Oregon, Eugene, Oregon, USA  
Moscow Institute of Physics and Technology, Moscow, Russia

### DEGREES AWARDED:

Doctor of Philosophy, Chemistry, 2016, University of Oregon, USA  
Master of Science, Physics, 2006, Moscow Institute of Physics and Technology,  
Moscow, Russia  
Bachelor of Science, Physics, 2004, Moscow Institute of Physics and Technology,  
Moscow, Russia

### AREAS OF SPECIAL INTEREST:

Scanning Tunneling Microscopy  
Scanning Tunneling Spectroscopy

### PROFESSIONAL EXPERIENCE:

Graduate Research Assistant, Department of Chemistry and Biochemistry,  
University of Oregon, Eugene, OR, 2010-2016

Graduate Teaching Assistant, Department of Chemistry and Biochemistry,  
University of Oregon, Eugene, OR, 2012, 2013, 2016

### GRANTS, AWARDS, AND HONORS:

Marthe E. Smith Memorial Science Scholarship, College of Arts and Sciences,  
University of Oregon, 2013

### PUBLICATIONS:

Hackley, J. D.; Kislitsyn, D. A.; Beaman, D. K.; Ulrich, S.; Nazin, G. V. High-Stability Cryogenic Scanning Tunneling Microscope Based on a Closed-Cycle Cryostat. *Rev. Sci. Instrum.* **2014**, 85 (10), 103704.

Kislitsyn, D. A.; Hackley, J. D.; Nazin, G. V. Vibrational Excitation in Electron Transport through Carbon Nanotube Quantum Dots. *J. Phys. Chem. Lett.* **2014**, *5* (18), 3138–3143.

Kislitsyn, D. A.; Gervasi, C. F.; Allen, T.; Palomaki, P. K. B.; Hackley, J. D.; Maruyama, R.; Nazin, G. V. Spatial Mapping of Sub-Bandgap States Induced by Local Nonstoichiometry in Individual Lead Sulfide Nanocrystals. *J. Phys. Chem. Lett.* **2014**, *5* (21), 3701–3707.

Gervasi, C. F.; Kislitsyn, D. A.; Allen, T. L.; Hackley, J. D.; Maruyama, R.; Nazin, G. V. Diversity of Sub-Bandgap States in Lead-Sulfide Nanocrystals: Real-Space Spectroscopy and Mapping at the Atomic-Scale. *Nanoscale* **2015**, *7* (46), 19732–19742.

Taber, B. N.; Kislitsyn, D. A.; Gervasi, C. F.; Mannsfeld, S. C. B.; Zhang, L.; Briseno, A. L.; Nazin, G. V. Adsorption-Induced Conformational Isomerization of Alkyl-Substituted Thiophene Oligomers on Au(111): Impact on the Interfacial Electronic Structure. *ACS Appl. Mater. Interfaces* **2015**, *7* (28), 15138–15142.

Kislitsyn, D. A.; Taber, B. N.; Gervasi, C. F.; Mannsfeld, S. C. B.; Zhang, L.; Briseno, A. L.; Nazin, G. V. Coverage-Dependent Self-Assembly Regimes of Alkyl-Substituted Thiophene Oligomers on Au(111): Scanning Tunneling Microscopy and Spectroscopy. *J. Phys. Chem. C* **2015**, *119* (48), 26959–26967.

Kislitsyn, D. A.; Taber, B. N.; Gervasi, C. F.; Zhang, L.; Mannsfeld, S. C. B.; Prell, J. S.; Briseno, A. L.; Nazin, G. V. Oligothiophene Wires: Impact of Torsional Conformation on the Electronic Structure. *Phys. Chem. Chem. Phys.* **2016**, *18* (6), 4842–4849.

Taber, B. N.; Kislitsyn, D. A.; Gervasi, C. F.; Mills, J. M.; Rosenfield, A. E.; Zhang, L.; Mannsfeld, S. C. B.; Prell, J. S.; Briseno, A. L.; Nazin, G. V. Real-Space Visualization of Conformation-Independent Oligothiophene Electronic Structure. *J. Chem. Phys.* **2016**, *144* (19), 194703.

Kislitsyn, D. A.; Kocevski, V.; Mills, J. M.; Chiu, S.-K.; Gervasi, C. F.; Taber, B. N.; Rosenfield, A. E.; Eriksson, O.; Ruzs, J.; Goforth, A. M.; et al. Mapping of Defects in Individual Silicon Nanocrystals Using Real-Space Spectroscopy. *J. Phys. Chem. Lett.* **2016**, *7* (6), 1047–1054.

Kislitsyn, D. A.; Mills, J. M.; Kocevski, V.; Chiu, S.-K.; DeBenedetti, W. J. I.; Gervasi, C. F.; Taber, B. N.; Rosenfield, A. E.; Eriksson, O.; Ruzs, J.; et al. Communication: Visualization and Spectroscopy of Defects Induced by Dehydrogenation in Individual Silicon Nanocrystals. *J. Chem. Phys.* **2016**, *144* (24), 241102.

Taber, B. N.; Gervasi, C. F.; Mills, J. M.; Kislitsyn, D. A.; Darzi, E. R.; Crowley, W. G.; Jasti, R.; Nazin, G. V. Quantum Confinement of Surface Electrons by Molecular Nanohoop Corrals. *J. Phys. Chem. Lett.* **2016**, 3073–3077.

## ACKNOWLEDGMENTS

I would like to thank my adviser George Nazin for conceiving the project to create a new instrument and leading our group through its construction and subsequent research use. Serving as an example, he taught me the attitude, dedication, and work ethic that are necessary to succeed and achieve goals despite any circumstances and challenges. I also appreciate his encouragement and support in all aspects of life during the PhD years.

I would like to sincerely thank all members of the Nazin Group with whom I was fortunate to meet and work: Jason Hackley, Sheila Hurley, Daniel Beaman, Yinghao Liu, Christian Gervasi, Ben Taber, Jon Mills, and Hank Seeley. I consider myself lucky for being part of an outstanding team. I also thank all of the undergraduate students, whose help is much appreciated. I also thank graduate students from other groups, as well as CAMCOR employees, who helped me and the group in our projects. I am grateful to the professors, administrators, and all employees of the University of Oregon for creating a great environment to learn and flourish.

I would like to thank Jeffrey Garman, Kris Johnson, John Boosinger and David Sankovich of the University of Oregon Machine Shop for their expert machining and invaluable help in the construction process, and Cliff Dax of the UO Electronics Shop for his expert advising on making custom electronics and fixing broken ones. I thank Ryan Murdick and Stefan Ulrich from RHK Technology for their contribution to the construction of the STM scanner. I thank Advanced Research Systems for their help during the troubleshooting stage of the project. I thank Jeffery Cina and Shannon Boettcher for their comments on journal manuscripts.



I would like to thank my collaborators Motoaki Honda and Ryuichiro Maruyama from Sony Corporation; Thomas Allen and Peter Palomaki from VoxtelNano; Lei Zhang and Alejandro Briseno from University of Massachusetts Amherst; Stefan Mannsfeld from Technische Universität Dresden; Sheng-Kuei Chiu, William DeBenedetti, and Andrea Goforth from Portland State University; Vancho Kocevski, Olle Eriksson, and Ján Rusz from Uppsala University; Svetlana Kilina from North Dakota State University.

Instrument construction was supported by the U.S. National Science Foundation under Grant DMR-0960211 and the Oregon Nanoscience and Microtechnologies Institute under Grant 16716. The works presented in this dissertation were supported in part by the U.S. National Science Foundation (Grant CHE-1454036), SONY Corporation, the American Chemical Society Petroleum Research Fund (Grant 52732-DNI6) and the NSF Center for Sustainable Materials Chemistry (Grant CHE-1102637).

To my family and my teachers, especially Oleg Petrovich Polikarpov, who left us,  
but will always remain in my mind and heart.

## TABLE OF CONTENTS

Chapter	Page
I. INTRODUCTION .....	1
1.1. Background .....	1
1.2. Advantages of STM-UO for STS Spatial Mapping .....	5
1.3. Application of STM-UO to Materials With Special Requirements .....	11
II. HIGH-STABILITY CRYOGENIC SCANNING TUNNELING MICROSCOPE BASED ON A CLOSED-CYCLE CRYOSTAT .....	17
2.1. Introduction .....	17
2.2. Background .....	18
2.3. System design .....	20
2.4. Performance .....	28
2.5. Conclusions .....	35
2.6. Bridge to Chapter III .....	36
III. VIBRATIONAL EXCITATION IN ELECTRON TRANSPORT THROUGH CARBON NANOTUBE QUANTUM DOTS .....	37
3.1. Introduction .....	37
3.2. Background .....	38
3.3. Experimental details .....	39
3.4. Results and discussion .....	39
3.5. Conclusions .....	52
3.6. Bridge to Chapter IV .....	52

Chapter	Page
IV. ADSORPTION-INDUCED CONFORMATIONAL ISOMERIZATION OF	
ALKYL-SUBSTITUTED THIOPHENE OLIGOMERS ON AU(111): IMPACT	
ON THE INTERFACIAL ELECTRONIC STRUCTURE.....	53
4.1. Introduction.....	53
4.2. Background.....	54
4.3. Experimental details.....	55
4.4. Results and discussion.....	56
4.5. Conclusions.....	66
4.6. Bridge to Chapter V.....	67
V. COVERAGE-DEPENDENT SELF-ASSEMBLY REGIMES OF ALKYL-	
SUBSTITUTED THIOPHENE OLIGOMERS ON AU(111): SCANNING	
TUNNELING MICROSCOPY AND SPECTROSCOPY.....	68
5.1. Introduction.....	68
5.2. Background.....	69
5.3. Experimental details.....	72
5.4. Results and discussion.....	73
5.5. Conclusions.....	91
5.6. Bridge to Chapter VI.....	91
VI. OLIGOTHIOPHENE WIRES: IMPACT OF TORSIONAL CONFORMATION	
ON THE ELECTRONIC STRUCTURE.....	93
6.1. Introduction.....	93

Chapter	Page
6.2. Background.....	94
6.3. Experimental details.....	97
6.4. Results and discussion .....	97
6.5. Conclusions.....	111
6.6. Bridge to Chapter VII .....	112
VII. REAL-SPACE VISUALIZATION OF CONFORMATION-INDEPENDENT OLIGOTHIOPHENE ELECTRONIC STRUCTURE .....	113
7.1. Introduction.....	113
7.2. Background .....	114
7.3. Experimental details.....	116
7.4. Results and discussion .....	118
7.5. Conclusions.....	129
7.6. Bridge to Chapter VIII.....	130
VIII. SPATIAL MAPPING OF SUB-BANDGAP STATES INDUCED BY LOCAL NON-STOICHIOMETRY IN INDIVIDUAL LEAD-SULFIDE NANOCRYSTALS.....	132
8.1. Introduction.....	132
8.2. Background .....	133
8.3. Experimental details.....	134
8.4. Results and discussion .....	135
8.5. Conclusions.....	147

Chapter	Page
8.6. Bridge to Chapter IX.....	148
<b>IX. DIVERSITY OF SUB-BANDGAP STATES IN LEAD-SULFIDE</b>	
<b>NANOCRYSTALS: REAL-SPACE SPECTROSCOPY AND MAPPING AT</b>	
<b>THE ATOMIC-SCALE .....</b>	
	149
9.1. Introduction.....	149
9.2. Background.....	150
9.3. Experimental details.....	154
9.4. Results and discussion .....	155
9.5. Conclusions.....	176
9.6. Bridge to Chapter X.....	177
<b>X. MAPPING OF DEFECTS IN INDIVIDUAL SILICON NANOCRYSTALS</b>	
<b>USING REAL-SPACE SPECTROSCOPY .....</b>	
	178
10.1. Introduction.....	178
10.2. Background .....	179
10.3. Experimental details.....	180
10.4. Results and discussion .....	182
10.5. Conclusions.....	196
10.6. Bridge to Chapter XI.....	197
<b>XI. VISUALIZATION AND SPECTROSCOPY OF DEFECTS INDUCED BY</b>	
<b>DEHYDROGENATION IN INDIVIDUAL SILICON NANOCRYSTALS.....</b>	
	198
11.1. Introduction.....	198

Chapter	Page
11.2. Background.....	199
11.3. Experimental details.....	200
11.4. Results and discussion .....	202
11.5. Conclusions.....	211
XII. CONCLUSIONS AND PROSPECTS .....	213
12.1. Conclusions.....	213
12.2. Prospects for future research.....	217
12.3. Combined Scanning Tunneling an Optical Probe Microscopy and Spectroscopy in application to SWNT research .....	221
APPENDICES .....	230
A. SUPPORTING INFORMATION TO CHAPTER III .....	230
B. SUPPORTING INFORMATION TO CHAPTER IV .....	237
C. SUPPORTING INFORMATION TO CHAPTER V.....	243
D. SUPPORTING INFORMATION TO CHAPTER VI .....	250
E. SUPPORTING INFORMATION TO CHAPTER VII .....	258
F. SUPPORTING INFORMATION TO CHAPTER VIII.....	262
G. SUPPORTING INFORMATION TO CHAPTER IX .....	267
H. SUPPORTING INFORMATION TO CHAPTER X.....	274
I. SUPPORTING INFORMATION TO CHAPTER XI.....	305
REFERENCES CITED.....	311
References Cited for Chapter I .....	311

Chapter	Page
References Cited for Chapter II .....	316
References Cited for Chapter III.....	317
References Cited for Chapter IV.....	321
References Cited for Chapter V .....	324
References Cited for Chapter VI.....	331
References Cited for Chapter VII .....	336
References Cited for Chapter VIII.....	342
References Cited for Chapter IX.....	347
References Cited for Chapter X.....	353
References Cited for Chapter XI.....	359
References Cited for Chapter XII .....	363
References Cited for Appendices.....	369



## LIST OF FIGURES

Figure	Page
<p>2.1. STM scanner suspended inside the thermal radiation shields. Left: front view of STM in shields with front-facing shields removed. Right: side view of STM in shields with side-facing shields removed. The inner radiation shield is mounted directly to the cold tip, which is the second cooling stage of the cold finger. The outer radiation shields mount directly to the first cooling stage of the cold finger (not shown). Springs extend approximately four inches above the area shown .....</p>	21
<p>2.2. Overview of the vacuum and cooling systems. (a) Thermal connection between the Cryocooler and Cold Finger is realized via He-filled volume confined by a rubber bellows. (b) View of the UHV system. The cryostat is mounted above the UHV system to the cryostat support structure. The cryostat support structure has no contact with the UHV system .....</p>	24
<p>2.3. View of the main chamber interior looking through the view port. Both the outer and inner radiation shield doors are open, affording a view of the STM .....</p>	25
<p>2.4. (a) Typical cool down curves showing temperatures measured at the STM and at the Cold Finger. The two curves in the upper right corner show the variation of the temperatures after unclamping of the STM (seen as a spike in the top curve). (b) Histogram showing typical variations of the STM temperature when the temperature stabilization feedback mechanism is engaged. Each count corresponds to an individual reading of the temperature by the controller electronics.....</p>	29
<p>2.5. Atomic-resolution images acquired with the new STM. (a) Topography scan showing atomic resolution of a reconstructed Au(111) surface [set point: 1.00 V, 100 pA]. The bright peaks represent the Au atoms. (b) Topography scan of monolayer of NaCl(100) thermally evaporated on the Au(111) surface [set point: 1.50 V, 10.0 pA]. The bright peaks represent the Cl atoms. (c) Cross-section of topography from (a) taken along the black line shown in (a). (d) cross-section of topography from (b) taken along the black line shown in (b). (e) Atomically resolved surface of single-wall carbon nanotube [set point: 1.50 V, 5.0 pA] .....</p>	30
<p>2.6. Quantification of the CCC-induced noise in the tunneling current. (a) Tunneling current as a function of time. (b) Fourier transform of the tunneling current showing the overtones of the CCC fundamental frequency (~2.4 Hz) at 4.76, 7.16, 9.56 and 16.73 Hz. (c) Exponential</p>	

	dependence of the tunneling current on $Z$ . Tunneling set point used: 1 V, 410 pA.....	31
2.7.	STS spectroscopy of a single-wall carbon nanotube. (a) STM image of the nanotube. (b) Two STS spectra measured in one sweep from -1.5 V to 1.5 V (red curve) and back to -1.5 V (blue curve). The spectra were measured in the location shown by an asterisk in (a). The peaks observed in (b) are identified as Van Hove singularities associated with the valence (peak $H_1$ ) and conduction (peak $E_1$ ) bands. Higher order bands $H_2$ and $E_2$ are also observed. The STS spectra were obtained by measuring differential conductance, $dI/dV$ , using the lockin-technique with a modulation of 20 mV. Tunneling set point: 1.5 V, 0.1 nA. Acquisition time: 2 minutes per spectrum.....	34
2.8.	X-Y spatial drift as a function of time. The drift was calculated by comparing STM images of the same area.....	35
3.1.	Geometry of a SWCNT adsorbed across a gap between two atomic steps on the Au(111) surface. (a) A schematic representation of the system under study (not to scale). (b) STM topography of the nanotube. Au(111) step edges are marked as $g_1$ and $g_2$ . To the left of point $n_1$ and to the right of point $n_2$ the nanotube contains defects, which manifest themselves as protrusions in the topographical image. Tunneling set point: 1.5 V, 10 pA. (c) Height profiles taken along lines $L_1$ and $L_2$ in (b). $L_1$ corresponds to the nanotube top, and $L_2$ to the gold substrate near the nanotube. The profile of the nanotube shows point $L$ is 2.34 Å, a number identical to the Au(111) step height (2.34 Å), lower than point $n_2$ , which suggests that the nanotube touches the bottom of the Au trench at point $L$ . The nanotube profile between points $L$ and $R$ is relatively straight, which suggests that part of the nanotube is suspended above the substrate between these points.....	41
3.2.	STS signal (obtained by measuring differential conductance, $dI/dV$ , using the lockin-technique) as a function of the $x$ coordinate [identical to that in Figure 3.1c] and sample bias voltage. (STS signal serves as a measure of the local density of electronic states.) The spatial range corresponds to the part of line $L_1$ contained between points $n_1$ and $n_2$ in Figure 3.1b and Figure 3.1c. Positive voltages correspond to unoccupied electronic states, while negative voltages correspond to occupied states. Vertical dashed lines at $x = 4.4 \text{ nm}$ and $13.3 \text{ nm}$ (corresponding to points $L$ and $R$ in Figure 3.1) indicate positions of the nanotube contact with the Au substrate where the nanotube electronic bands are bent due to the charge transfer between the nanotube and Au. [The charge transfer is caused by a workfunction mismatch.] These points of contact reveal themselves	

- through the appearance of shifted electronic levels  $E_n^L$  (and  $H_n^L$ ) and  $E_n^R$  (and  $H_n^R$ ), as compared to the bands in the region between points  $L$  and  $R$ . The region in between points  $L$  and  $R$  ( $x = 4.4 \text{ nm}$  and  $13.3 \text{ nm}$ ) forms a quantum dot (QD) with three sets of particle-in-a-box states  $E_{1,n}$ ,  $E_{2,n}$  and  $E_{3,n}$  ( $n=1, 2$ ). All QD energy levels are marked with horizontal dashed lines. Electronic levels  $E_1^*$  and  $H_n^*$  to the left of point  $L$ , as well as levels  $E_n^{**}$  and  $H_1^{**}$  to the right of point  $R$  are shifted further up. All data were measured along the nanotube centerline. Tunneling set point: 1.5 V, 0.1 nA..... 43
- 3.3. Cross-sections of the data from Figure 3.2 along the horizontal dashed lines showing the spatial behavior of  $E_{m,n}$  states of the QD from Figure 3.2. Spatial distributions of states  $E_{1,1}$ ,  $E_{2,1}$  and  $E_{3,1}$  show single maxima in the QD center, whereas states  $E_{1,2}$ ,  $E_{2,2}$  and  $E_{3,2}$  each show a node in the QD center. States  $H_1^L$  and  $H_2^R$  are more strongly localized as compared to the QD states  $E_{m,n}$ . Individual cross-sections are offset for clarity..... 45
- 3.4. Cross-sections of the data from Figure 3.2 taken along the vertical dashed lines in Figure 3.2, showing DOS as functions of the sample bias voltage (the corresponding x-coordinates of these cross-sections are also shown). Individual cross-sections are offset for clarity. All spectra were measured along the nanotube centerline except the top curve in (b). (a) Occupied states that correspond to several distinct locations where the nanotube makes contact with the Au substrate. The onset of each spectrum shows a peak accompanied by two overtones (seen either as peaks or shoulders). For all spectra, the lower energy overtone is  $\sim 72 \text{ mV}$  below the main peak, whereas the higher energy overtone is  $\sim 108 \text{ mV}$  above the main peak. (b) Unoccupied states. In addition to three spectra measured roughly on top of the nanotube, a spectrum measured at  $x = 9 \text{ nm}$  slightly away from the nanotube centerline is also shown (top curve, all features contained in this curve are upshifted due to the larger fraction of the bias voltage dropped across the nanotube diameter). The manifold of  $E_{m,n}$  states is seen at positive voltages as peaks. Similarly to the occupied states in (a), states  $E_{1,1}$  and  $E_{2,1}$  contain fine structure, which is most clearly seen for the two spectra measured at  $x = 9 \text{ nm}$ : the top curve shows overtones at  $\sim 72 \text{ mV}$  below the corresponding  $E_{1,1}$  and  $E_{2,1}$  peaks; for the spectrum measured along the nanotube centerline (second from top) the main  $E_{1,1}$  and  $E_{2,1}$  peaks are accompanied by a side-peak and a shoulder correspondingly, both  $\sim 108 \text{ mV}$  higher than the corresponding main peaks ..... 47
- 4.1. Adsorption configuration of DDQT molecules on Au(111). (a) STM image of two DDQT molecules in cis-conformation forming a dimer, with

- overlaid molecular structures. (b) And (c) STM images of DDQT molecules in trans-conformation, with overlaid molecular structures. (d) Same as (b) and (c) for an individual cis-molecule. (e)-(h) Models of DDQT backbone matched to the Au(111) surface lattice for adsorption configurations from (a)-(d), respectively. (i) STS of the LUMO state corresponding to the two molecules from (a) – curves A1 and A2, and molecules from (b), (c) and (d) – curves B, C, and D respectively. STM imaging was carried out at bias voltages of 100 mV and tunneling current of 5-50 pA..... 58
- 4.2. Registry of DDQT molecules with the underlying Au(111) surface. (a)-(c) STM images of DDQT molecules on Au(111) substrate. (d)-(f) Same as (a)-(c) but showing the molecular orientations and Au(111) crystallographic directions. The quaterthiophene backbones of DDQT molecules aligned along one of three  $\langle 110 \rangle$  directions of the Au(111) surface, perpendicular to Au(111) surface reconstruction ridges aligned primarily along the  $\langle 112 \rangle$  directions, as shown. STM imaging was carried out at bias voltages 0.1-1.0 V and tunneling currents 1-5 pA..... 60
- 4.3. Correlation of DDQT adsorption location with LUMO peak energy. (a)-(c) STM topographies. Black dashed lines show the Au(111) reconstruction ridges. (d) STS spectra showing LUMO peaks for molecules in (a)-(c). Each numbered spectrum corresponds to a molecule appearing with the same number in (a)-(c). Molecules with black numbers in (a)-(c) are located closer to the reconstruction ridges than their neighbors. STS spectra of these molecules [black curves 2, 4, 8 and 10] in (d) show LUMO peaks downshifted by  $\sim 100$  mV in their respective groups of molecules (a), (b) and (c). Proximity of DDQT backbone to reconstruction ridges thus reduces the LUMO energy. STM imaging was carried out at bias voltages of 0.3-1.0 V and tunneling current of 5 pA..... 65
- 5.1. Molecular structures of didodecylquaterthiophene (DDQT) in both trans and cis conformations ..... 72
- 5.2. Adsorption of *cis*-DDQT molecules on Au(111) in the low coverage regime. (a) STM image [set point 100 mV, 1 pA] of a large area featuring reconstruction ridges of the Au(111) surface with sparingly absorbed DDQT molecules. Most of the molecules prefer the cis conformation, forming dimers. Dotted frame indicates enlarged area shown in (c). (b) STM image from (a) with indicated molecular orientations, Au(111) crystallographic directions, and highlighted reconstruction ridges. The quaterthiophene backbones of DDQT molecules aligned along one of three  $\langle 110 \rangle$  directions of the Au(111) surface, perpendicular to the  $\langle 112 \rangle$

- directions revealed by straight sections of surface reconstruction ridges. (c) STM image [set point 50 mV, 50 pA] with overlaid molecular structures of two DDQT molecules forming a dimer. (d) Model of DDQT backbones from (c) matched to the Au(111) surface lattice. Au(111) crystallographic directions are indicated. DDQT backbones are aligned along the  $\langle 110 \rangle$  direction and are positioned in a way that minimizes the terminal S to Au top-site distance ..... 74
- 5.3. Adsorption of *trans*-DDQT molecules on Au(111) in the low coverage regime. (a) STM image [set point 100 mV, 50 pA] of a *trans*-DDQT molecule with one alkyl ligand adjacent to another molecule's ligand. Au(111) crystallographic directions are deduced from the surface reconstruction ridges found in vicinity of the molecules. (b) Model of *trans*-DDQT molecule from (a) matched to the Au(111) surface lattice. The oligothiophene backbone is positioned on the lattice in a way that maximizes proximity of sulfur atoms to Au top-sites. The adsorption geometry of alkyl ligands is different for the free ligand (angles to  $\langle 110 \rangle$  and  $\langle 112 \rangle$  directions are indicated) and ligand bound via van der Waals forces to another molecule (aligned along  $\langle 112 \rangle$ ). (c) STM image [set point 100 mV, 5 pA] of *trans*-DDQT molecule with both alkyl ligands freely positioned on gold surface. (d) Model of *trans*-DDQT molecule from (c) matched to the Au(111) surface lattice. The adsorption configuration allows for more optimal positioning of the oligothiophene's sulfur atoms on the gold lattice as compared to (b). Both alkyl ligands are positioned symmetrically,  $9.2^\circ$  offset to the  $\langle 112 \rangle$  direction ..... 75
- 5.4. Adsorption of DDQT molecules on Au(111) in the intermediate coverage regime. (a) STM image [set point 100 mV, 5 pA] of a large area featuring a finite-sized 2D crystal of DDQT with individual DDQT dimers in the vicinity. Dotted frame indicates enlarged area shown in (c). (b) STM image from (a) with indicated molecular orientations, Au(111) crystallographic directions, and highlighted reconstruction ridges (the three  $\langle 112 \rangle$  directions of Au(111) surface correspond to straight sections of surface reconstruction ridges). The quaterthiophene backbones of DDQT molecules not included in the crystal are aligned along one of three  $\langle 110 \rangle$  directions of the Au(111) surface, whereas the backbones of DDQT forming the crystal are aligned along the  $\langle 112 \rangle$  direction perpendicular to  $\langle 110 \rangle$ . (c) STM image [set point 100 mV, 20 pA] with overlaid molecular structures of the part of the crystal indicated in (a). (d) Models of DDQT backbones matched to the Au(111) surface lattice for the crystal section shown in (c). Au(111) crystallographic directions are indicated. DDQT backbones are aligned with the  $\langle 112 \rangle$  direction and are positioned in a

- way that minimizes the distances from sulfur atoms of terminal thiophene rings to the corresponding Au top-sites ..... 79
- 5.5. Adsorption of DDQT molecules on Au(111) in the high coverage regime. (a) STM image [set point 200 mV, 5 pA] of a large area featuring extended 2D crystals of DDQT molecules and DDQT dimer agglomerations. Dotted frames indicate enlarged areas shown in (b) and (c). (b) Part of STM image from (a) with indicated molecular orientations and Au(111) crystallographic directions. The quaterthiophene backbones of DDQT molecules are all aligned along one of three  $\langle 110 \rangle$  directions of the Au(111) [which are perpendicular to  $\langle 112 \rangle$  directions], regardless of whether or not they are in an ordered crystal. DDQT prefers adsorbing in fcc regions of the Au(111) reconstruction, while hcp regions are avoided and mostly empty. (c) STM topography image [set point 200 mV, 5 pA] with overlaid molecular structures of part of the crystal indicated in (a). (d) Models of DDQT backbones matched to the Au(111) surface lattice for the crystal section shown in (c). Au(111) crystallographic directions are indicated. DDQT backbones are found to be aligned with  $\langle 110 \rangle$  direction and are positioned in a way that minimizes the distances from sulfur atoms of terminal thiophene rings to the corresponding Au top-sites..... 83
- 5.6. Spatial mapping of DDQT orbitals. (a) STS spectrum measured on the quaterthiophene backbone of the molecule in the bottom right corner (curve DDQT), and STS spectrum of the gold substrate near the dimers [curve Au(111)]. Portions of both spectra are magnified to show fine structure. (b) STM image of a group of DDQT dimers. (c) STM image from (b) processed to “sharpen” the topographic features. (d) Density of states (DOS) for the LUMO orbital [2.1 V, see curve DDQT in (a)] overlaid on image from (c). Mapped area is confined within the dashed lines. Low DOS intensity (near-background) areas were rendered transparent to show registry with topography. (e) Same as (d) for the HOMO orbital [-0.9 V, see curve DDQT in (a)]..... 85
- 5.7. LUMO molecular orbital of the DDQT crystal of the type formed in the intermediate molecular coverage regime. (a) STM image [set point 100 mV, 5 pA] of part of the crystal with overlaid DDQT models of backbone (ellipse) with attached alkyl chains (lines). Shown are three regular rows of *trans*-DDQT comprising the crystal and three additional DDQT molecules attached to a crystal with perpendicular backbones (two *trans* and one *cis* conformer). (b) dI/dV spectroscopy scans [set point 1.0 V, 1.0 pA] of the LUMO orbitals taken on top of every backbone indicated with A-L in (a). Dashed line at 2.1 V is the most common LUMO peak energy in this crystal, but deviations from 2.1 V in both directions are observed. (c) STM

- image from (a) processed to “sharpen” the topographic features. (d) LUMO DOS map at 2.1 V superimposed on enhanced topography showing LUMO localization. The DOS maps are superimposed on the enhanced topography from (c), with areas of low DOS [Au(111) background] rendered transparent in order to reveal registry with the topography ..... 87
- 5.8. LUMO of a DDQT crystal of the type formed in the high molecular coverage regime. (a) STM image [set point 200 mV, 5 pA] of part of the crystal with overlaid DDQT models of backbone (ellipse) with attached alkyl chains (lines). Regular chain of the crystal consisting of five DDQT molecules is shown. (b) dI/dV spectroscopy scans [set point 1.8 V, 2.0 pA] of the LUMO orbitals taken on top of every backbone indicated with A-E in (a). (c) STM image from (a) processed to “sharpen” the topographic features. (d)-(g) LUMO DOS maps for voltages corresponding to specific LUMO peaks in (b). The DOS maps are superimposed on the enhanced topography from (c), with areas of low DOS [Au(111) background] rendered transparent in order to reveal registry with the topography ..... 89
- 6.1. Adsorption of 8T molecules on Au(111). (a) STM image [set point 100 mV, 5 pA] of an aggregate of oligothiophene molecules absorbed on the Au(111) surface. (b) Close-up STM topography of the region confined by the dotted rectangle in (a). Atomic models of 8T molecules are overlaid on the STM image. The atomic models show that molecules are attached to each other via alkyl substituents. The thiophene rings comprising the DDQT backbones are nearly flat on the Au(111) surface, as determined by STM topographies. (c) STM image from (a) with indicated molecular orientations and Au(111) crystallographic directions and highlighted surface-reconstruction ridges. The oligothiophene backbones of 8T molecules are aligned along the  $\langle 110 \rangle$  directions of the Au(111) surface, perpendicular to the straight sections of surface-reconstruction ridges which run parallel to the  $\langle 112 \rangle$  directions. (d) Model of 8T molecules from (b) matched to the Au(111) surface lattice. Au(111) crystallographic directions are indicated. Dashed circles indicate the van der Waals radii of the hydrogen atoms ..... 98
- 6.2. Spatial (STS) DOS mapping across for a CCC conformer of 8T molecules. (a) STM image with an overlaid atomic model of the CCC-8T molecule. (b) STM image from (a) showing the path of mapping (dashed line). (c) DOS as a function of the bias voltage and position  $x$  along the path shown in (b). (d) LUMO, LUMO+1 and LUMO+2 DOS along the path shown in (b), obtained at voltages corresponding to the vertical dashed lines in (c). These voltages were chosen to maximize the contributions of the corresponding individual orbitals. Curves are shifted and normalized

	for clarity. (e) Backbone profile (z height vs. x coordinate) along the dashed line from (b). (f) Individual STS spectra from (c) measured at x=2.1 and 2.7 nm as indicated by horizontal lines in (c). Spectra are shifted for clarity. The LUMO state manifests itself as a peak at 1.85 V in the spectrum measured at x=2.7 nm, while LUMO+1 is observed as a peak at 2.3 V in the spectrum measured at x=2.1 nm. Only a shoulder of the LUMO+2 states is observed at 2.6 V (x=2.7 nm).....	104
6.3.	Same as Figure 6.2 for a TTT conformer of 8T molecules. The molecule is situated in the center of the molecular aggregate, with alkyl chains on both sides (see Figure D1d) .....	105
6.4.	Same as Figure 6.2 for a CTT conformer of 8T molecules .....	105
6.5.	Calculated electronic DOS for a CCC conformer of 8T molecules. (a) DOS (compare to Figure 6.2c) as a function of the bias voltage and position x along the path similar to that shown in Figure 6.2b. (b) LUMO, LUMO+1 and LUMO+2 DOS (compare to Figure 6.2d) along the same path as in (a), obtained at voltages corresponding to the vertical dashed lines in (a). These voltages were chosen to maximize the contributions of the corresponding individual orbitals. Curves are shifted and normalized for clarity. (c) Three-dimensional representations of DOS for LUMO, LUMO+1 and LUMO+2 showing nodal patterns (along the molecular backbone) characteristic of the particle-in-a-box nature of these states (no nodes for LUMO, one node for LUMO+1 and two nodes for LUMO+2). (d) Individual DOS spectra from (a) measured at spatial locations indicated by horizontal lines in (a). Spectra are shifted for clarity. The LUMO state manifests itself as a peak at 1.86 V (top curve), while LUMO+1 is observed as a peak at 2.32 V (bottom curve). Electronic structure calculations were performed with density functional theory (DFT) calculations using B3LYP/6-31G* .....	107
6.6.	Same as Figure 6.5 for a TTT conformer of 8T molecules .....	108
6.7.	Same as Figure 6.6 for a CTT conformer of 8T molecules .....	108
7.1.	Adsorption of oligothiophene molecules on Au(111). (a-c) STM images [set point 100 mV, 5 pA] of aggregates of oligothiophene molecules absorbed on the Au(111) surface. (d-f) STM images from (a-c) with indicated molecular orientations, Au(111) crystallographic directions, and highlighted surface-reconstruction ridges (white dashed lines). The oligothiophene backbones are aligned along the $\langle 110 \rangle$ directions of the Au(111) surface, perpendicular to the straight sections of surface-	



	reconstruction ridges, which run parallel to the $\langle 112 \rangle$ directions. Dashed boxes in (a-c) correspond to STM images in Fig. 7.2.....	117
7.2.	Model of 8T molecules from Fig. 7.1 matched to the Au(111) surface lattice. (a-d) STM images [set point 100 mV, 5 pA] of sub-areas from Figs. 7.1a-c. (e-h) Models of oligothiophene molecules from (a-d) overlaid on the Au(111) lattice. Crystallographic directions are indicated. Dashed circles indicate the van der Waals radii of the hydrogen atoms .....	119
7.3.	Molecular orbitals for a straight 8T conformer. (a) DOS spectra measured on the straight 8T molecule in the locations indicated in (d-e) and DOS spectrum of the gold substrate. (b) STM image of the molecule. (c) STM image from (b) processed to “sharpen” the topographic features. (d) DOS for the LUMO orbital overlaid on image from (c). Mapped area is confined within the dashed lines. Areas with low DOS intensity (near-background) were rendered transparent to show registry with topography. (e) Same as (d) for the LUMO+1 orbital. (f) Individual DOS spectra calculated at spatial locations A, B, and C in (i) and (j). Spectra are shifted for clarity. (g-h) Theoretically calculated wavefunctions of LUMO and LUMO+1 showing the particle-in-a-box nature of these states (no nodes for LUMO, one node for LUMO+1). (i-j) Theoretically calculated DOS maps of LUMO and LUMO+1, exhibiting similar behavior to (d) and (e), respectively. For details of theoretical calculations see text.....	122
7.4.	Molecular orbitals for a kinked 8T conformer. Data arrangement and markings are identical to those used in Fig. 7.3.....	126
7.5.	Molecular orbitals for a curved 8T conformer. Data arrangement and markings are identical to those used in Fig. 7.3.....	127
7.6.	LUMO energies for all measured and calculated 8T and 7T conformations. The data were obtained from Figs. 7.3f, 4f, 5f and Figs. E1f, E2f, E3f of the supplementary material <sup>42</sup> . Gray triangles are theoretical LUMO energies, and black circles are measured LUMO energies (experimental error ~50 mV) .....	129
8.1.	Representative dI/dV spectra for five PbS NCs (set point voltages and currents range from 1.2 V to 2.5 V, and 10 pA to 30 pA for the spectra shown). The bias voltage effectively serves as the energy scale (see, however, discussion associated with Figure F2 for a more complete description of the relationship between the bias voltage and energy). Occupied and unoccupied states are indicated by arrows and marked with	

- an 'H' and 'E' for electrons and holes respectively. The apparent band gaps for each of the NCs are marked with double sided arrows ..... 137
- 8.2. STM/STS characterization of a representative nanocrystal NC<sub>1</sub>. (a) STM topography image of NC<sub>1</sub> [set point 1.0 V, 1.0 pA]. (b) Topographical features attributable to step edges oriented along specific crystallographic directions. The majority of features indicate 120° angles, which suggests that the top facet of NC<sub>1</sub> corresponds to a {111} plane. (c) A cross-section of the topography [path indicated by the arrow in (a)] showing that the top facet of NC<sub>1</sub> is at a small angle with respect to the Au(111) surface. Individual steps are marked with dashed lines, with the step height (0.342 nm) corresponding to the distance between the sulfur {111} planes. (d) A representative STS spectrum [set point 2.0 V, 15 pA] measured at the location marked by the star in (a). Prominent occupied and unoccupied states are marked with an 'H' and 'E' respectively..... 139
- 8.3. Spatial DOS (STS) mapping across nanocrystal NC<sub>1</sub>. (a) Topographic image [set point 1.0 V, 1 pA] showing the path of mapping (points P<sub>1</sub> through P<sub>5</sub>). (b) Density of states [set point 2.0 V, 10 pA] as a function of bias voltage and position x along the path shown in (a). (c) Individual STS spectra from (b) measured at points P<sub>2</sub> through P<sub>5</sub>. Occupied and unoccupied states are marked 'H' and 'E' respectively in both (b) and (c). Spectral feature H<sup>\*\*</sup> corresponds to “reverse” tunneling<sup>35,36</sup> through a localized occupied state outside of the mapping path..... 141
- 8.4. (a) Topographic images of NC<sub>1</sub> [set point 1.0 V, 1 pA]. Bottom image is marked to indicate step edges with 120° angles oriented along <110> directions, the same set of marks is used in the bottom images of (b) and (c) for reference. (b) DOS maps for unoccupied states of NC<sub>1</sub> [set point 2.0 V, 15 pA] measured at the indicated bias voltages. Parallel dashed red lines indicate the apparent orientation of stripe-like features associated with states E<sub>1,n</sub>. (c) DOS maps for occupied states of NC<sub>1</sub> [set point 2.0 V, 15 pA] measured at the indicated bias voltages. High intensity signals in the top left and top right of the H<sub>2</sub> map in (c) are attributed to spectral features of nearby NCs. The spatial extent of maps in (b) and (c) corresponds to the yellow rectangle shown in (a). Numbered markers in the bottom images of (b) and (c) [identical for both sets of maps] indicate locations of high DOS intensity for states E<sub>1,n</sub> (1-9) and E<sub>2</sub> (10-15). Location 16 marks a region with a localized higher energy state [ ~1.9 V, map not shown], likely corresponding to a smaller NC (with a different crystallographic orientation) that is in the process of merging with NC<sub>1</sub>..... 142

- 9.1. STM topographies of ligand-covered (a)-(c) and ligand-free (d)-(f) PbS NCs. Figures (g)-(i) highlight topographical features observed in (d)-(f). The crystallographic directions and NC boundaries are identified with the aid of STS DOS mapping. All STM topographies measured with set-point 2.0 V bias, 1-2 pA tunneling current..... 156
- 9.2. (a) DOS spectra for six representative PbS NCs (individual spectra shifted for clarity). Occupied (unoccupied) states denoted by Hn (En) respectively. All dI/dV curves measured with set-point 1.6-2.6 V bias, 15-30 pA tunneling current. Histogram (bottom) of energetic locations and distributions for discernible states E1,1, E2, and H1 for 13 NCs, bin size 0.2 eV (b) Bandgaps vs. height for measured NCs overlaid on data for two limiting cases: spherical NCs and 2D PbS quantum wells. Open symbols correspond to the E1,1 - H1 energy differences, whereas closed symbols correspond to values obtained from PIAB orbitals differences of many measured DOS spectra in Figure 9.2a are considerably lower than those (as determined from DOS mapping). The curve for spherical PbS NCs, and gray shaded region corresponding to 2D PbS quantum wells, were obtained from Moreels et al.<sup>65</sup> and Lee et al.,<sup>66</sup> respectively..... 158
- 9.3. (a) STM topographic image of a PbS NC. (b) DOS "cross-section" mapping along the path of the dotted line in (a). (c) Individual DOS spectra measured at locations marked in (a). STS measurements in (b) and (c) were taken with a set-point of 1.9 V bias and 30 pA tunneling current. Variations in the energies of electronic states across the NC roughly follow the NC topography, which is a result of the location-specific variation of the bias voltage drop inside the NC.<sup>56</sup> ..... 161
- 9.4. (a) STM topographic image of NC1. (b) DOS mapping of NC1 along the path of the dotted line in (a). (c) Individual DOS spectra for locations marked in (a). STS measurements in (b) and (c) were taken with set-point 1.6 V bias, 30 pA tunneling current..... 162
- 9.5. 2D DOS maps of unoccupied (a-c) and occupied (d, e) states for NC1. DOS state representations show (from left to right) combination topography/DOS map overlay (yellow outline indicates area of DOS mapping), DOS map only, and DOS map with black lines showing DOS features that are in registry with NC1 crystallographic features from Figure 9.1g. Parameter  $\alpha$  is distance between two neighboring {211} planes, as shown in the model in Figures 9.6a and b. STS measurements taken with set-point 1.6 V bias, 30 pA tunneling current. STM topography image measured with set-point 2.0 V bias, 2 pA tunneling current ..... 164

- 9.6. Model representations of relevant PbS fcc crystallographic facets with idealized reconstruction features. (a, c) (111)-plane views showing rows of Pb adatoms oriented along  $\langle 110 \rangle$  and  $\langle 211 \rangle$  directions respectively, with indicated inter-atomic-row distances in integer multiples of distances  $\alpha$  and  $\beta$  respectively. (b, d) (110)-, and (211)-plane side-views of same structures as in (a) and (c) showing vertical atomic steps responsible for appearance of varied distances between the bright DOS “stripes” in Figure 9.5 and Figure 9.8 ..... 167
- 9.7. DOS spectra for NC2 measured at locations P1-3 shown in the inset STM topography. Sections of spectra P1 and P2 containing relevant states have been magnified by designated amount for clarity. STS measurements were taken with set-points of 1.5-2.2 V bias, 10-20 pA tunneling current. STM topography image measured with set-point 2.0 V bias, 1 pA tunneling current ..... 172
- 9.8. Same as Figure 9.5 for NC2. Parameters  $\alpha$  and  $\beta$  are the distances between two neighboring  $\{211\}$  and  $\{110\}$  planes respectively, as shown in the model in Figures 9.6. STM topography image measured with set-point 2.0 V bias, 1 pA tunneling current. STS maps measured with set-point 1.5 V bias, 20 pA tunneling current ..... 173
- 10.1. Spatial mapping of LDOS for NC<sub>1</sub>. (a) STM topographic image. (b) LDOS (measured as  $dI/dV$ ) as a function of the bias voltage and position  $x$  along the path shown in (a). R<sub>1</sub>-R<sub>3</sub> indicate regions with specific patterns of LDOS spectra. In (b), the individual unoccupied and occupied LDOS spectra were normalized separately, for clarity. (c) Individual LDOS spectra from (b) measured at points P<sub>1</sub> through P<sub>4</sub>. Spectra are offset for clarity. Identical spectra for P<sub>1</sub> and P<sub>2</sub> scaled by  $\times 0.2$  are also shown. Occupied and unoccupied states are marked “H” and “E” respectively in both (b) and (c). Individual LDOS peaks are observed at slightly different voltages across the NC due to the finite location-dependent voltage drop inside the NC. (d) Topography from (a) overlaid with its contour plot. Contours correspond to vertical separation of 0.68 Å (half of one Si(100) atomic step). (e-j) 2D LDOS maps for voltages corresponding to the peaks indicated in (c). Upper row shows the LDOS maps overlaid with contour lines from (d). Lower row of LDOS maps shows Si(100) lattice directions identified in the spatial LDOS intensity distributions. Solid lines are  $\langle 100 \rangle$  and  $\langle 010 \rangle$  directions (perpendicular to each other), dashed lines are  $\langle 110 \rangle$  and  $\langle \bar{1}10 \rangle$ , dotted lines are  $\langle 210 \rangle$  and  $\langle \bar{1}20 \rangle$ , dash-dotted lines are  $\langle 120 \rangle$  and  $\langle \bar{2}10 \rangle$ . [Assignment of the primary directions  $\langle 100 \rangle$  and  $\langle 010 \rangle$  is made using the predominant orientation of linear features in the LDOS patterns.] Measure of localization  $\zeta$  is calculated for every 2D map, as explained in

- the main text. (k) Calculated representation of NC<sub>1</sub> shape (see Supporting Information in Appendix H for details) with its contour plot overlaid. Black and white lines on top of the contours correspond to Si(100) directions..... 183
- 10.2. Theoretical LDOS for a model near-spherical (diameter ~3.5 nm) SiNC (with composition H<sub>412</sub>Si<sub>1087</sub>). (a) NC geometry. (b) Calculated 1D LDOS map as a function of the bias voltage and position *x* along the path shown in (a). (c) Individual LDOS spectra from (b) measured at points P<sub>1</sub> through P<sub>3</sub>. Spectra are offset for clarity. The number of discrete states in each peak is indicated. (d) NC geometry rotated by 90° around the vertical axis and exposing facets mapped in (b) as well as in (e-j). (e-j) 2D maps of LDOS for selected states near the electronic bandgap. LDOS intensities were calculated on a 3D surface equidistantly offset from the NC surface by 3 Å, similarly to the path shown in (a). In order to more closely reproduce experimental conditions, all spectra were normalized to give the same total current at 1.35 V (see Methods for details). Measure of localization  $\zeta$  is calculated for every 2D map, as explained in the main text ..... 187
- 10.3. Spatial mapping of LDOS for NC<sub>2</sub>. Data arrangement and markings are the same as in Figure 10.1. In (b), the individual unoccupied and occupied LDOS spectra were normalized separately, for clarity. Peak E<sub>2</sub> is measured at three voltages E<sub>2</sub><sup>n</sup> ..... 190
- 10.4. Theoretical LDOS for a model near-spherical (diameter ~2 nm) SiNC with a bridged oxygen (Si–O–Si) impurity, and composition H<sub>114</sub>Si<sub>175</sub>O. Data arrangement and markings are the same as in Figure 10.2. In (c), P<sub>1</sub> corresponds to the maximum of orbital E\* LDOS, P<sub>2</sub> corresponds to the defect location, and P<sub>3</sub> is positioned on the opposite side of NC with respect to P<sub>2</sub>. The top and bottom rows in (d-j) show two opposite sides of the NC, respectively. To more closely reproduce experimental conditions, all spectra were normalized to give the same total current at 1.7 V ..... 193
- 11.1. STM/STS characterization and theoretical modeling of SiNCs. (a) Topography of an area showing several SiNCs. (b) Enlarged topography corresponding to the dashed square in (a). (c) STS spectra measured at locations A and B marked in (b). Curves A<sub>1</sub> through A<sub>7</sub> show transformations of the LDOS spectra in location A with successive application of bias voltage pulses (see text for details). States marked 'H' and 'E' correspond to occupied and unoccupied states, respectively, except for features caused by “reverse” tunneling, as described in the text. Spectra are offset for clarity. (d) Model of fully hydrogen-passivated SiNC (composition H<sub>172</sub>Si<sub>239</sub>). (e) Theoretical LDOS spectra averaged over the entire NC surface. Spectra FH and R correspond to the fully hydrogen-

- passivated SiNC in (d), and to the completely reconstructed SiNC in (f), respectively. Spectrum PR corresponds to a partially reconstructed version of SiNC from (d), with 33% of dihydrides converted to monohydride dimers.  $DB^0$ ,  $DB^+$ , and  $DB^-$  are spectra of the completely reconstructed model with an additional DB and charges 0,  $+e$ , and  $-e$ , correspondingly. Spectrum  $SDB^-$  illustrates the effect of “bipolar” tunneling on STS of electronic states with LDOS described by curve  $DB^-$ . Spectra were Gaussian-broadened by 100 mV, with onsets corresponding to the discrete energy levels obtained from DFT calculations. All spectra were modeled assuming a finite bias voltage drop inside the SiNC (see text). (f) Model of a monohydride-passivated SiNC (composition  $H_{100}Si_{239}$ ) with  $2\times 1:H$  surface reconstruction, and silicon core identical to that of (d). Location of the DB is also indicated. .... 203
- 11.2. Spatial mapping of LDOS for the SiNC from Fig. 11.1(b) after (partial) dehydrogenation, but before DBs were generated. (a) Topography of the SiNC. (b) LDOS as a function of the bias voltage and position  $x$  along the path (solid line) shown in (a) ..... 207
- 11.3. Spatial mapping of LDOS for the SiNC from Fig. 11.1(b) after DBs were generated. (a,c) STM topographic images of the SiNC. (b) LDOS as a function of the bias voltage and position  $x$  along the path (solid line) shown in (a,c). (d,e) 2-D LDOS maps for voltages corresponding to  $H_D$ ,  $E_D$  LDOS peaks marked in (b). Mapping area corresponds to the dotted squares in (a,c). Dashed lines are topographic contours from (c)..... 209
- A1. Representative STM images of several CNTs deposited on the Au(111) surface using the “dry contact transfer” method. Nanotubes constituted ~70% of the SWNT-containing powder obtained from Sigma-Aldrich, which explains the presence of small clusters around the nanotubes in the majority of the STM images ..... 230
- A2. (a) STM topography of a SWNT, different from that of Figure 3.1b of the main text. (b) STS signal as a function of the  $x$  coordinate [as shown in (a)] and sample bias voltage. (STS signal serves as a measure of the local density of electronic states.) The spatial range corresponds to the dashed line between points  $n_1$  and  $n_2$  in (a). Positive voltages correspond to unoccupied electronic states, while negative voltages correspond to occupied states. All data were measured along the nanotube centerline. The spectra show Van Hove singularities, with the most visible states being  $H_1$ -type (derived from the valence band),  $E_1$ -type (derived from the conduction band), and  $E_2$ -type (derived from the band immediately above the conduction band). Some bandgap variation is observed in the STS map

	shown in Figure A2b, with levels $E_n^*$ and $H_1^*$ on the left side of the map, and levels $E_n^{**}$ and $H_1^{**}$ on the right side. The observed bandgap variation is likely a result of the non-uniform environment of the nanotube: the vicinity of point $n_2$ shows a higher density of impurities located around the nanotube.....	231
A3.	STS spectra showing fine spectral structures. (a) Spectra for the nanotube shown in Figure A2a, the bottom three spectra measured outside of the region contained between points $n_1$ and $n_2$ . (b) Additional spectra from localized states in other nanotubes.....	232
A4.	Zoomed-out view of the SWNT from Figure 3.1b showing the geometry of the Au trench straddled by the nanotube.....	233
A5.	Voltage drop in a biased STM junction with a SWNT under the STM tip .....	234
A6.	Spatial dependence of STS peaks corresponding to states $E_{1,1}$ [shown in (a)] and $H_1^*$ [shown in (b)] from Figure 3.2. The spatial coordinate $x$ is identical to that used in Figure 3.2. The STS signal has been renormalized so as to give constant integral DOS within the ranges shown .....	235
A7.	Spatial dependence of STS peaks corresponding to bipolar transport through state $E_d$ that originates from a defect located on the same nanotube as that shown in Figure 3.2. See text for definitions of band onsets $V_E^+$ and $V_E^-$ .....	236
B1.	Possible adsorption configurations for DDQT conformers in the main text. S atoms at Au top-sites are highlighted by green circles. (a) <i>cis</i> -DDQT conformer with S atoms at Au top-sites as observed in Chapter IV along with other possible orientations with (b) both exterior S atoms at Au top-sites and (c)-(g) one exterior and one interior S atom at Au top-sites. (h) <i>trans</i> -DDQT conformer with exterior S atoms at Au top-sites as observed in Chapter IV along with other possible orientations with (i) both exterior S atoms at Au top-sites, (j) adjacent interior and exterior S atom in Au top-sites (this is the only possibility for <i>trans</i> -DDQT having neighboring S atoms located at Au top-sites), and (k) and (l) non-adjacent interior and exterior S atoms at Au top-sites .....	237
B2.	Manipulation of <i>cis</i> -DDQT monomer and alkyl side chains with STM tip. After the initial topography (a), the DDQT monomer rotated by $60^\circ$ on the substrate (b). Subsequent STS measurements of this <i>cis</i> -conformer resulted in the alkyl chains folding over themselves (c) and the DDQT backbone (d)-(e). Topographies acquired at 1.0 V bias, 5.0 pA set point.....	238

- B3. Examples of scission observed during STS at higher (~2.5-3.0 V) bias. Topographies (a) before STS, and (b) after. This susceptibility of DDQTs to scission limited the lifetime of individual DDQT *cis*-conformers and inhibited detailed study of unoccupied states beyond the LUMO. In addition to the scission of DDQT backbones, alkyl side chains could also dislocate from the stable dimer position (b). STM topographies were acquired at 100 mV bias, 5.0 pA set point..... 238
- B4. Density Functional Theory gas-phase electronic structure calculations of (a) *trans* DDQT and (b) *cis* DDQT. (c) and (d) LUMOs and their energies for *trans* and *cis* conformers, correspondingly. (e) and (f) HOMOs and their energies for *trans* and *cis* conformers, correspondingly. The dipole moment of the *trans* (*cis*) conformation is 0.06 Debye (2.32 Debye). Computations were performed with Gaussian09<sup>4</sup> using B3LYP/6-31G\* and visualized with Avogadro<sup>5</sup> ..... 239
- B5. Registry of DDQT molecules with the underlying Au(111) surface as in Figure 4.2 of the main text, with surface reconstruction ridges highlighted by white dashed lines delineating face-centered-cubic (fcc) and hexagonal-close-packed (hcp) regions of the Au(111) surface (d)-(f). (a)-(c) STM images of DDQT molecules on Au(111) substrate. DDQT molecules primarily adsorbed in the fcc regions, with the quaterthiophene backbones aligned along one of three  $\langle 110 \rangle$  directions of the Au(111) surface, perpendicular to Au(111) surface reconstruction ridges aligned primarily along the  $\langle 112 \rangle$  directions, as shown in Figure 4.2 (main text). STM imaging was carried out at bias voltages 0.1-1.0 V and tunneling currents 1-5 pA ..... 241
- B6. Distributions of LUMO energies for 50 *cis* and 18 *trans*-conformers, as measured by STS ..... 242
- C1. DDQT crystals agnostic to Au(111) surface features. (a) STM image [set point 100 mV, 10 pA] of a crystal formed over a single-atom step. The crystal order on both sides of the step are identical, and the DDQT molecules on higher terrace are connected to the molecules below in a regular manner. Note that the hcp areas of the Au(111) reconstruction are avoided. (b) Image from (a) with marked molecular orientations and Au(111) crystallographic directions. Oligothiophene backbones are oriented along the  $\langle 112 \rangle$  directions and the alkyl ligands are positioned 16° from the  $\langle 110 \rangle$  direction, as evident from the edges of the crystal formation. (c) STM image [set point 100 mV, 5 pA] of a crystal formed over a Au(111) surface reconstruction ridge, resulting in occupation of the energetically unfavorable hcp region. The crystallographic order of the



	DDQT crystal and DDQT backbone orientation are not modified as compared to a regular case of crystal formed in fcc area. (d) Image from (c) with marked molecular orientations and Au(111) crystallographic directions. Oligothiophene backbones are oriented along the $\langle 112 \rangle$ directions and the alkyl ligands are positioned $16^\circ$ from the $\langle 110 \rangle$ direction .....	243
C2.	Spatial mapping of DDQT LUMO. (a) STS spectra measured on the quaterthiophene backbone of the molecules A and B indicated in (b) [curves DDQT], and STS spectrum of the gold substrate near the dimers [curve Au(111)]. Spectrum for molecule A is shifted for clarity as indicated by 0 of the signal on the right vertical axis. (b) STM image of a DDQT dimer. (c) STM image from (b) processed to “sharpen” the topographic features. (d) Density of states (DOS) for the LUMO orbital [2.1 V, see curve DDQT in (a)] overlaid on image from (c). Mapped area is confined within the dashed lines. Low DOS intensity (near-background) areas were rendered transparent to show registry with topography.....	245
C3.	Distribution of LUMO orbital energies of DDQT backbones in cis and trans conformations. Trans-1 refers to trans conformers observed at low and intermediate coverage, and trans-2 refers to tans conformers observed in the high coverage regime .....	246
C4.	STS dI/dV scans of the DDQT crystal in Figure 5.8 of the main text, demonstrating that LUMO peak voltages were not sensitive to the precise location of the tip on the measured molecules. (a)-(d) Density of states maps obtained by overlaying spatially mapped STS dI/dV signal [set point 1.8 V, 2.0 pA, lock-in modulation 100 meV] on the enhanced topography to show LUMO orbital localization. Low dI/dV signal of the map (background) was rendered transparent in order to reveal alignment with the topography. (e) dI/dV spectroscopy scans [set point 1.8 V, 2.0 pA, lock-in modulation 100 meV] taken at indicated locations on top of backbones A-E in (a)-(d) .....	247
C5.	Expansion of the DOS maps shown in Figure 5.8 in the main text. (a) STM image [set point 200 mV, 5 pA] of part of the crystal with overlaid DDQT models of backbone (ellipse) with attached alkyl chains (lines). Regular chain of the crystal consisting of five DDQT molecules is shown. (b) dI/dV spectroscopy scans [set point 1.8 V, 2.0 pA, lock-in modulation 100 meV] taken on top of every backbone indicated with A-E in (a). (c) STM image from (a) processed to “sharpen” the topographic features. (d)- (p) DOS mapping from 1.85-2.50 V in 50 mV increments.....	248

- C6. LUMO DOS maps of a DDQT crystal of the type formed in the high molecular coverage regime. (a) STM image [set point 200 mV, 5 pA] of part of the crystal with overlaid DDQT models of backbones (ellipses) with attached alkyl chains (lines). Regular chain of the crystal consisting of three DDQT molecules is shown. (b) STM image from (a) processed to “sharpen” the topographic features. (c)-(j) Density of states maps from 1.8-2.5 V in 100 mV increments obtained by overlaying spatially mapped STS dI/dV signal [set point 1.8 V, 2.0 pA, lock-in modulation 100 meV at 570 Hz] on the enhanced topography to show LUMO orbital localization. Low dI/dV signal of the map (background) was rendered transparent in order to reveal alignment with the topography. (k) dI/dV spectra [set point 1.8 V, 2.0 pA, lock-in modulation 100 meV at 570 Hz] taken on top of every backbone indicated with A-C in (a) ..... 249
- D1. Sample characterization using nanoelectrospray ionization (nano-ESI) mass spectrometry [solution in THF, ESI voltage 1.4 kV]: (a) part of the spectra corresponding to alkyl-substituted 7T (calculated for  $C_{64}H_{88}S_7$  1080.49, found 1080.45), (b) part of the spectra corresponding to alkyl-substituted 8T (calculated for  $C_{80}H_{114}S_8$  1330.66, found 1330.58). The progression of peaks beyond the main m/z peak is the isotope series for each conformational isomer ..... 250
- D2. Adsorption of 7T molecules on Au(111). (a) STM image [set point 100 mV, 5 pA] of an aggregate of 7T molecules absorbed on the Au(111) surface. (b) Close-up STM topography of the region confined by the dotted rectangle in (a) with overlaid atomic models of 7T molecules showing that molecules attach to each other via alkyl substituents. The molecular models show that the thiophene rings comprising the DDQT backbones are nearly flat on the Au(111) surface, as determined from STM topography. (c) STM image from (a) with indicated molecular orientations and Au(111) crystallographic directions and highlighted surface reconstruction ridges. The oligothiophene backbones of 7T molecules are aligned along the  $\langle 110 \rangle$  directions of the Au(111) surface, perpendicular to the straight sections of surface-reconstruction ridges, which run parallel to the  $\langle 112 \rangle$  directions. (d) Model of 7T molecules from (b) matched to the Au(111) surface lattice. Au(111) crystallographic directions are indicated. 7T backbones are roughly aligned along the  $\langle 110 \rangle$  direction. Dashed circles indicate the van der Waals radii of the hydrogen atoms ..... 251
- D3. 7T molecular aggregates on Au(111). (a) STM image [set point 100 mV, 5 pA] of an aggregate of 7T molecules absorbed on the Au(111) surface. (b) STM image in (a) with indicated molecular orientations and Au(111) crystallographic directions and highlighted surface-reconstruction ridges.

	The oligothiophene backbones of 7T molecules are preferentially adsorbed in fcc regions of the Au(111) surface reconstruction and aligned along the $\langle 110 \rangle$ directions of the Au(111) surface, perpendicular to the straight sections of surface reconstruction ridges, which run parallel to the $\langle 112 \rangle$ directions. (c) and (d) close-up STM topographies of molecular chains indicated in (a) showing chains extending over a Au(111) step.....	252
D4.	Distribution of LUMO and LUMO+1 energies of 7T and 8T acquired by STS. 5 8T molecules (2 CCC, 1 each of TTT, CCT and CTT) and 50 7T molecules (23 TC, 16 TT, 9 CC and 2 CT) were measured. Standard deviations for the 7T conformations are 0.031 eV (TC), 0.038 eV (TT), 0.051 eV (CC) and 0.117 eV (CT). DFT results are presented for comparison.....	253
D5.	Same as Figure 6.3 for a CC conformer of 7T molecules. (a) STM image with an overlaid atomic model of the CCC-7T molecule. (b) STM image from (a) showing the path of mapping (dashed line). (c) DOS as a function of the bias voltage and position $x$ along the path shown in (b). (d) LUMO, LUMO+1 and LUMO+2 DOS along the path shown in (b), obtained at voltages corresponding to the vertical dashed lines in (c). These voltages were chosen to maximize the contributions of the corresponding individual orbitals. Curves are shifted and normalized for clarity. (e) Backbone profile ( $z$ height vs. $x$ coordinate) along the dashed line from (b). (f) Individual STS spectra from (c) measured at $x=2.1$ and $2.7$ nm as indicated by horizontal lines in (c). Spectra are shifted for clarity. The LUMO state manifests itself as a peak at 1.85 V in the spectrum measured at $x=2.7$ nm, while LUMO+1 is observed as a peak at 2.3 V in the spectrum measured at $x=2.1$ nm. Only a shoulder of the LUMO+2 state is observed.....	254
D6.	Same as Figure 6.3 for a TT conformer of 7T molecules.....	255
D7.	Same as Figure 6.3 for a TC conformer of 7T molecules.....	255
D8.	Calculated electronic DOS for a CC conformer of 7T molecules. (a) DOS (compare to Figure D3c) as a function of the bias voltage and position $x$ along the path similar to that shown in Figure D3b. (b) LUMO, LUMO+1 and LUMO+2 DOS (compare to Figure D3d) along the same path as in (a), obtained at voltages corresponding to the vertical dashed lines in (a). These voltages were chosen to maximize the contributions of the corresponding individual orbitals. Curves are shifted and normalized for clarity. (c) Three-dimensional representations of DOS for LUMO, LUMO+1 and LUMO+2 showing the particle-in-a-box nature of these states. (d) Individual DOS spectra from (a) measured at spatial locations indicated by horizontal lines	

Figure	Page
in (a). Spectra are shifted for clarity. The LUMO state manifests itself as a peak at 1.9 V (top curve), while LUMO+1 is observed as a peak at 2.3 V (bottom curve). Electronic structure calculations were performed with density functional theory (DFT) calculations using B3LYP/6-31G* .....	256
D9. Same as Figure D8 for a TT conformer of 7T molecules .....	257
D10. Same as Figure D8 for a TC conformer of 7T molecules .....	257
E1. Molecular orbitals for a straight 7T conformer. (a) DOS spectra measured on the straight 7T molecule in the locations indicated in (d-e) and DOS spectrum of the gold substrate. (b) STM image of the molecule. (c) STM image from (b) processed to “sharpen” the topographic features. (d) DOS for the LUMO orbital overlaid on image from (c). Mapped area is confined within the dashed lines. Areas with low DOS intensity (near-background) were rendered transparent to show registry with topography. (e) Same as (d) for the LUMO+1 orbital. (f) Individual DOS spectra calculated at spatial locations A, B, and C in (i) and (j). Spectra are shifted for clarity. (g-h) Theoretically calculated wavefunctions of LUMO and LUMO+1 showing the particle-in-a-box nature of these states (no nodes for LUMO, one node for LUMO+1). (i-j) Theoretically calculated DOS maps of LUMO and LUMO+1, exhibiting similar behavior to (d) and (e), respectively. For details of theoretical calculations, see Expanded Experimental Details above .....	258
E2. Molecular orbitals for a kinked 7T conformer. Data arrangement and makings are identical to those used in Figure E1 .....	260
E3. Molecular orbitals for an L-shaped 7T conformer. Data arrangement and makings are identical to those used in Figure E1 .....	261
F1. STM topographic images showing crystallographic features for three PbS NCs. (a), (b), (c) Topographies for three representative NCs. (d), (e), (f) NC topographies, [same as in (a), (b), and (c) respectively] with lines and relative angles indicating orientations of crystallographic features for each NC. The observed angles suggest that the top NC facets corresponds to crystal planes (111), (100), and (100) respectively. (g), (h), (i) Enhanced topographic images [for the same NCs] with same crystallographic markings as in (d), (e) and (f) .....	262
F2. Voltage drop in a biased STM junction with a NC under the STM tip .....	263

Figure	Page
F3. Plot of the energy difference between the $E_2$ and $E_{1,1}$ states vs. the energy difference between the $E_{1,1}$ and $H_1$ states for 10 measured NCs. During this experiment, many of the measured NCs did not exhibit clearly-defined $H_1$ or $E_2$ states, and thus were not included here.....	264
F4. Absorbance and PL spectra of PbS NCs following thiol-ligand exchange. The emission peak at 977 nm (1.27 eV) corresponds to an approximate diameter of 3.2 nm PbS NC .....	266
G1. Figure shows the prominent unoccupied states for NC1. Subfigures (a-f) include (from left to right) a combination of topography(grayscale), and DOS map(color) overlay (where the yellow outline encloses the area of DOS mapping), DOS map only, and DOS map with black lines showing DOS features that are in registry with NC1 crystallographic features from Figure 9.1g in the main text. Parameter $\alpha$ is defined as the distance between two neighboring $\{211\}$ planes, as shown in the model in Figures 9.6a and b in the main text. STS measurements taken with set-point 1.6 V bias, 30 pA tunnelling current. STM topography image measured with set-point 2.0 V bias, 2 pA tunneling current.....	267
G2. Figure shows the prominent occupied states for NC1. Same area and representation as Figure G1 for the occupied states of NC1. Parameter $\beta$ is defined as the distance between two neighboring $\{110\}$ planes, as shown in the model in Figures 9.6c and d in the main text. Set-points of STM topography image and STS maps same as in Figure G1 .....	269
G3. Figure shows the prominent unoccupied states of NC2. Same representation as in Figure G1 for NC1. Parameter $\beta$ is defined as before for figure G2, and as shown in the model in Figures 9.6c and d in the main text. STM topography measured with set-point 2.0 V bias, 1 pA tunneling current. STS maps measured with set-point 1.5 V bias, 20 pA tunneling current .....	270
G4. Figure shows the prominent occupied states of NC2. Same representation as in Figure G3 for NC2. Parameter $\alpha$ is defined as the distance between two neighboring $\{211\}$ planes, as shown in the model in Figures 9.6a and b in the main text. Set-points of STM topography image and STS maps same as in Figure G3.....	271
G5. Figure shows examples of PbS NCs displaying localized defect-related states in their DOS. Unoccupied $E_{1,n}$ and occupied $H_1$ states show marked intensity differences depending on location, and are associated with the reconstruction of polar PbS (111) surfaces or regions of marked	

- non-stoichiometry in which excess S (Pb) atoms at the surface lead to sub-bandgap states broken off from the valence(conduction) bands. These observations are in keeping with and further support conclusions made with regard to the sub-bandgap states observed for NCs discussed in the main journal article ..... 272
- G6. DOS maps for  $H_{1,n}$  and  $E_{1,n}$  states of NC2 showing anti-correlation in their spatial distributions. White circles (black x's) mark locations of local high intensity for states  $E_{1,n}$  ( $H_{1,n}$ )DOS intensity maps for the sub-bandgap states of NC2 (Figure G6), show that the locations of high intensity for states  $H_{1,n}$  in general correspond (on the atomic scale) to locations of low intensity for states  $E_{1,n}$ , and vice-versa suggesting that  $H_{1,n}$  and  $E_{1,n}$  patterns are carried by atoms corresponding to different elements. Theoretical calculations predict that  $H_{1,n}$  and  $E_{1,n}$  patterns result from non-stoichiometric surface S and Pb atoms respectively.<sup>14</sup> ..... 273
- H1. Scanning Tunneling Spectroscopy of SiNCs. (a) Representative DOS spectra for five different SiNCs (Set point voltages and currents range from 1.0 V to 1.5 V, and 5 pA to 10 pA for the spectra shown). (b) Calculated DOS for a model with size comparable to a NC featuring spectrum  $S_5$  from (a). Occupied and unoccupied states are indicated by arrows and marked with an 'H' and 'E' for holes and electrons respectively ..... 274
- H2. STM/STS characterization of NC<sub>1</sub>. (a) STM topography image of NC<sub>1</sub> [set point 1.2 V, 5.0 pA]. (b) STS spectra [set point 1.2 V, 10 pA] measured at the locations A-I marked in (a). Spectra are offset for clarity. Prominent occupied and unoccupied states are marked with an 'H' and 'E' respectively. Individual DOS peaks are observed at slightly different voltages across the NC due to the location-dependent voltage drop inside the NC. (c-d) Close-up of spectra from B, C and H locations showing finer structure (spectra marked "\*" were acquired with better signal-to-noise ratio by using longer acquisition times) ..... 275
- H3. Reconstruction of the NC shape from STM topography. (a) Trajectory of a STM tip over a three-dimensional object when scanned in the "constant tunneling current" regime typically used for STM topography. Apparent object shape is enlarged and sharp features are rounded due to the finite tip-sample distance and the possibility to tunnel sideways. Additional broadening occurs, in a similar fashion, due to the finite dimensions of the tip apex. Both effects can be accounted for (in the first approximation) by assuming that the tunneling current only depends on the distance (defined in three dimensions) between the tip apex and object of interest. This is equivalent to assuming that the tip wavefunctions have an approximately

s-orbital nature at the tip apex, a common approximation in theoretical calculations of STM images. If the tip-object separation  $R$  is known [see (a)], then a model of the actual object shape can be calculated by constructing a 3D surface that consists of points located at identical minimal distances  $R$  from the experimental topographical surface [see (a)]. The calculation can also be reversed and a model of the STM topography can be recalculated from the calculated NC shape. The difference between the experimental STM topography and recalculated STM topography can be used as a measure of the accuracy of such a representation. The accuracy is affected by the noise in STM topography, and the value chosen as  $R$ . For example, if  $R$  is smaller than the characteristic dimensions of all features in the STM topography, the error is zero. If features with dimensions smaller than  $R$  are present in the STM topography, then they may not contribute to the model of real NC shape, and may be lost in the recalculated STM topography, thus adding to the error. This means that when  $R$  is smaller than the actual gap (usually on the scale of several angstroms), the error is mostly dominated by the topographic noise and atomic-scale features. However, once  $R$  exceeds the real tunneling gap (the latter defines the curvature of the features in STM topography), an additional component of the error, caused by the mismatch between the true and calculated NC shapes, becomes non-zero. It is easy to show that the dependence of this error component on  $R$  is quadratic. In order to find the best fit to the real effective gap, we calculated the described error using different values of  $R$ , and found that at small values of  $R$  (where noise dominates) the dependence is linear [see (b)]. By subtracting this component from the error and plotting its square root as a function of  $R$ , we found that at higher  $R$  the dependence is linear, in accordance with the geometric considerations. A linear fit to this function allows us to find the best approximation to true  $R$ , as shown in figure (b).

(c) Experimental STM topography of  $\text{NC}_1$  with its contour lines overlaid. (d) Calculated shape of the  $\text{NC}_1$  using  $R=0.8$  nm. Top facet of  $\text{NC}_1$  was found to be flat and almost horizontal. (e) Model of  $\text{NC}_1$  digitally processed to “sharpen” the features (pseudo-3D rendering). (f-h) Same as (c-e) for the  $\text{NC}_2$ ..... 276

- H4. Volume distribution of theoretical DOS for a model near-spherical (composition  $\text{H}_{412}\text{Si}_{1087}$ , diameter  $\sim 3.5$  nm) SiNC without impurities. (a) NC geometry. (b-g) DOS for the peaks from Figure 10.2c.  $N$  is the number of individual states comprising the peak. First row represents the normalized DOS maps on the surface (identical to Figure 10.2e-j). Second, third, and fourth rows show bulk unnormalized DOS distributions across the main coordinate planes going through the center of the SiNC. Each

	displayed DOS datapoint was averaged over a 3.6 Å-long segment orthogonal to, and bisected by the corresponding plane.....	278
H5.	Bulk cross-sections for individual orbitals of a model near-spherical (composition $H_{412}Si_{1087}$ , diameter ~3.5 nm) SiNC without impurities. Section planes and view angles are the same as in Figure H4. Each displayed DOS datapoint was averaged over a 3.6 Å-long segment orthogonal to, and bisected by the corresponding plane. (a) Highest occupied molecular orbitals (HOMO). (b) Lowest unoccupied molecular orbitals (LUMO) .....	278
H6.	STM/STS characterization of $NC_2$ . (a) STM topography image of $NC_2$ [set point 2.2 V, 5.0 pA]. (b) DOS spectra [set point 2.0 V, 20 pA] measured at the locations A-I marked in (a). Spectra are offset for clarity. Prominent occupied and unoccupied states are marked with an 'H' and 'E' respectively. (c-d) Close-up of spectra from C, G and J locations.....	280
H7.	Theoretical DOS for a model near-spherical (composition $H_{114}Si_{175}O$ , diameter ~2 nm) SiNC with a Si=O impurity. Data arrangement and markings are the same as in Figure 10.2. In (c), $P_2$ corresponds to the defect location. Locations $P_1$ and $P_3$ correspond to locations $P_2$ and $P_3$ in Figures 10.4, H8 and H9. The top and bottom rows in (d-j) show opposite sides of the NC. To more closely reproduce experimental conditions, all spectra were normalized to give the same total current at 1.7 V .....	281
H8.	Theoretical DOS for a model near-spherical (composition $H_{116}Si_{175}$ , diameter ~2 nm) SiNC without impurities. Data arrangement and markings are the same as in Figure 10.2. In (c), locations $P_1$ , $P_2$ and $P_3$ are the same as in Figures 10.4 and H9. The top and bottom rows in (d-i) show opposite sides of the NC. To more closely reproduce experimental conditions, all spectra were normalized to give the same total current at 1.7 V .....	283
H9.	Theoretical DOS for a model near-spherical (composition $H_{116}Si_{175}O$ , diameter ~2 nm) SiNC with a Si-OH impurity. Data arrangement and markings are the same as in Figure 10.2. In (c), $P_1$ is the same location as in Figure 10.4. Location $P_2$ corresponds to the defect location. Location $P_3$ is positioned on the opposite side of NC with respect to $P_2$ . The top and bottom rows in (d-i) show opposite sides of the NC. To more closely reproduce experimental conditions, all spectra were normalized to give the same total current at 1.7 V .....	285
H10.	Volume distribution of theoretical DOS for a model near-spherical (composition $H_{114}Si_{175}O$ , diameter ~2 nm) SiNC with a Si=O impurity.	



	(a) NC geometry. (b-g) DOS for the peaks from Figure H7c. N is the number of individual states comprising the peak. First row represents the normalized DOS maps on the surface (identical to Figure H7e-j). Second and third rows show bulk unnormalized DOS distributions across the main coordinate planes containing the oxygen atom. Each displayed DOS datapoint was averaged over a 3.6 Å-long segment orthogonal to, and bisected by the corresponding plane .....	287
H11.	Bulk cross-sections for individual orbitals of a model near-spherical (composition $H_{114}Si_{175}O$ , diameter ~2 nm) SiNC with a Si=O impurity. Section planes and view angles are the same as in Figure H10. Each displayed DOS datapoint was averaged over a 3.6 Å-long segment orthogonal to, and bisected by the corresponding plane. (a) Highest occupied molecular orbitals (HOMO). (b) Lowest unoccupied molecular orbitals (LUMO) .....	289
H12.	Volume distribution of theoretical DOS for a model near-spherical (composition $H_{114}Si_{175}O$ , diameter ~2 nm) SiNC with a Si-O-Si impurity. (a) NC geometry. (b-g) DOS for the peaks from Figure 10.4c. N is the number of individual states comprising the peak. First row represents the normalized DOS maps on the surface (identical to Figure 10.4e-j). Second and third rows show bulk unnormalized DOS distributions across the main coordinate planes containing the oxygen atom. Each displayed DOS datapoint was averaged over a 3.6 Å-long segment orthogonal to, and bisected by the corresponding plane .....	291
H13.	Bulk cross-sections for individual orbitals of a model near-spherical (composition $H_{114}Si_{175}O$ , diameter ~2 nm) SiNC with a Si-O-Si impurity. Section planes and view angles are the same as in Figure H12. Each displayed DOS datapoint was averaged over a 3.6 Å-long segment orthogonal to, and bisected by the corresponding plane. (a) Highest occupied molecular orbitals (HOMO). (b) Lowest unoccupied molecular orbitals (LUMO) .....	293
H14.	Volume distribution of theoretical DOS for a model near-spherical (composition $H_{116}Si_{175}O$ , diameter ~2 nm) SiNC with a Si-OH impurity. (a) NC geometry. (b-f) DOS for the peaks from Figure H9c. N is the number of individual states comprising the peak. First row represents the normalized DOS maps on the surface (identical to Figure H9e-i). Second and third rows show bulk unnormalized DOS distributions across the main coordinate planes containing the oxygen atom. Each displayed DOS datapoint was averaged over a 3.6 Å-long segment orthogonal to, and bisected by the corresponding plane .....	295

- H15. Bulk cross-sections for individual orbitals of a model near-spherical (composition  $H_{116}Si_{175}O$ , diameter  $\sim 2$  nm) SiNC with a Si–OH impurity. Section planes and view angles are the same as in Figure H14. Each displayed DOS datapoint was averaged over a  $3.6 \text{ \AA}$ -long segment orthogonal to, and bisected by the corresponding plane. (a) Highest occupied molecular orbitals (HOMO). (b) Lowest unoccupied molecular orbitals (LUMO) ..... 297
- H16. Volume distribution of theoretical DOS for a model near-spherical (composition  $H_{116}Si_{175}$ , diameter  $\sim 2$  nm) SiNC without impurities. (a) NC geometry. (b-f) DOS for the peaks from Figure H8c.  $N$  is the number of individual states comprising the peak. First row represents the normalized DOS maps on the surface (identical to Figure H8e-i). Second and third rows show bulk unnormalized DOS distributions across the main coordinate planes containing the oxygen atom. Each displayed DOS datapoint was averaged over a  $3.6 \text{ \AA}$ -long segment orthogonal to, and bisected by the corresponding plane ..... 299
- H17. Bulk cross-sections for individual orbitals of a model near-spherical (composition  $H_{116}Si_{175}$ , diameter  $\sim 2$  nm) SiNC without impurities. Section planes and view angles are the same as in Figure H16. Each displayed DOS datapoint was averaged over a  $3.6 \text{ \AA}$ -long segment orthogonal to, and bisected by the corresponding plane. (a) Highest occupied molecular orbitals (HOMO). (b) Lowest unoccupied molecular orbitals (LUMO) ..... 301
- H18. Comparison of theoretical DOS for model near-spherical (diameter  $\sim 3.5$  nm) SiNCs with and without impurities. (a) Geometry of a NC with a Si=O impurity and composition  $H_{410}Si_{1087}O$ . (b) Calculated 1D DOS map as a function of bias voltage and position  $x$  along the path shown in (a). (c) Individual DOS spectra from (b) measured at points P1 through P3. Spectra are offset for clarity. (d-f) Same as (a-c) for a NC with a Si–O–Si impurity and composition  $H_{410}Si_{1087}O$ . (g-i) Same as (a-c) for a NC with a Si–OH impurity and composition  $H_{412}Si_{1087}O$ . (j-l) Same as (a-c) for a NC without impurities, and composition  $H_{412}Si_{1087}$ . To more closely reproduce experimental conditions, all spectra were normalized to give the same total current at  $1.35 \text{ V}$  ..... 302
- II. Impact of the finite bias voltage drop inside a SiNC on the STS spectra. (a) “Direct” tunnelling through an occupied electronic state with energy  $E_S$  below the Fermi level ( $E_F$ ) of the Au(111) substrate (corresponding states shown in blue). In a biased tunnel junction involving a SiNC (corresponding states shown in red), a finite voltage drop occurs across the SiNC volume changing the energy of all electronic states by  $\alpha eV_B$ , where

$V_B$  is the bias voltage, and  $\alpha < 1$  is a function of the SiNC dimensions and dielectric susceptibility. Tunnelling into the state thus occurs when the Fermi level of the tip is aligned with the electronic state, which happens when  $E_S = (1 - \alpha)eV_B$  (here, and everywhere in Fig. 11, we assume that all quantities are positive). The onset tunnelling voltage can thus be calculated as  $E_S/(1 - \alpha)$ .<sup>3, 11</sup> (b) “Reverse” tunneling through an occupied state. In contrast to “direct” tunnelling, “reverse” tunneling is initiated when the Fermi level of the *Au(111) substrate* is aligned with the electronic state, which happens at opposite polarity to that of (a), when  $E_S = \alpha eV_B$ . This gives the onset tunnelling voltage of  $E_S/\alpha$ .<sup>3, 11</sup> ..... 305

- I2. Spatial mapping of LDOS for a representative SiNC showing spectral peaks corresponding to “direct” and “reverse” tunneling. (a) STM topographic profile [z height vs. x coordinate along the path shown in (b)]. (b) STM topographic image. Solid line is a trajectory for 1D STS mapping in (c). (c)  $dI/dV$  as a function of the bias voltage and position x along the path shown in (a). (d) Individual LDOS spectrum from (c) measured in the center of the path. Peaks originating from occupied (unoccupied) states produced by “direct” tunneling are marked 'H' ('E'), while peaks originating from “reverse” tunneling are marked 'H\*' ('E\*'). Horizontal error bars indicate the uncertainty in identification of the peak onsets. At the center of the SiNC, the ratio of the onsets for peaks  $E_1$  and  $E_1^*$  gives  $\alpha = 0.18 \pm 0.02$ , and  $\alpha = 0.20 \pm 0.02$  for peaks  $H_1$  and  $H_1^*$ . (In the main text, we use  $\alpha = 0.2$  as a representative value for SiNCs, to estimate the energy-voltage relationships for STS features corresponding to “direct” and “reverse” tunneling.) Voltage onsets for both “direct” and “reverse” tunnelling (at opposite bias polarities) vary with tip position on the NC surface. This is particularly noticeable for “reverse” tunneling peaks  $E_1^*$  and  $H_1^*$ , while the onsets of “direct” tunneling peaks  $E_1$  and  $H_1$  are relatively insensitive to the position along the SiNC. These onset variations are explained by the sensitivity of  $\alpha$  to the geometry of the junction.<sup>3</sup> Indeed, both the tip position with respect to the SiNC, and the relative tip height z, which can both be expected to affect  $\alpha$ , vary considerably across the scan range shown in the topography profiles (a) and (b). The larger sensitivity of peaks  $E_1^*$  and  $H_1^*$  to spatial location is explained by the fact that the onsets for these are inversely proportional to  $\alpha$  (changes significantly), while the onsets for peaks  $E_1$  and  $H_1$  are inversely proportional to  $1 - \alpha$  (changes relatively insignificantly due to the small value of  $\alpha$ ) ..... 306
- I3. Spatial mapping of LDOS for the SiNC from Fig. 11.1(b) after partial dehydrogenation, but before DBs were generated. (a) Topography of the SiNC. (b) LDOS as a function of the bias voltage and position x along the path (solid line) shown in (a). (c) Individual LDOS spectra from (b)

- measured at points 1 and 2. Spectra are offset for clarity. Occupied and unoccupied states are marked 'H' and 'E' respectively ..... 308
- I4. FT-IR spectra of as-prepared hydrogen-terminated SiNCs dispersed in a hexane solution as described elsewhere.<sup>16</sup> (a) Low frequency region. Broad peak at 600-700  $\text{cm}^{-1}$  includes: 1) the Si-H bending modes and Si-H<sub>2</sub> rocking mode of Si(100),<sup>17</sup> 2) the Si-H bending mode of Si(111)-(1 $\times$ 1),<sup>18</sup> and 3) the Si-H bending modes and Si-H<sub>2</sub> wagging mode originating from step-edges of vicinal H/Si(111) surfaces.<sup>19</sup> The peak at 904  $\text{cm}^{-1}$ , on the other hand, has no contribution from Si-H: it contains the Si-H<sub>2</sub> scissoring bending mode,<sup>17, 20</sup> as well as the Si-H<sub>3</sub> degenerate deformation mode<sup>21</sup> (note that Si-H<sub>3</sub> population is expected to be significantly lower due to 2 times higher oxidation rate while exposed to the air during the measurement).<sup>22</sup> Intensity of both peaks are comparable, which suggests a significant presence of Si-H<sub>2</sub> on the {100}Times facets of measured SiNCs. For comparison, for the Si(100)-(3 $\times$ 1) surface, where  $\sim$ 1/3 of the surface Si atoms are terminated with dihydrides (and the rest are terminated with monohydrides), the relative intensity of the  $\sim$ 900  $\text{cm}^{-1}$  region is an order of magnitude smaller than that of the  $\sim$ 600  $\text{cm}^{-1}$ .<sup>17</sup> (b) High-frequency spectral region associated with silicon-hydride stretching modes. While the peak at 2100  $\text{cm}^{-1}$  may be associated with both Si-H and Si-H<sub>2</sub>, the shoulder observed at 2120-2140  $\text{cm}^{-1}$  is indicative of Si-H<sub>2</sub>.<sup>17</sup> ..... 309
- I5. STS characterization of additional SiNCs of different sizes. (a-d) STS spectra before (“pristine” state) and after application of ESD pulses causing reconstruction (narrowing of the bandgap) and the creation of localized DB states deep in the bandgap. The observed charge state of the DB is neutral (DB<sup>0</sup>) in (a, b), switching from positive (DB<sup>+</sup>) to neutral (DB<sup>0</sup>) in (c), and switching from negative (DB<sup>-</sup>) to neutral (DB<sup>0</sup>) in (d). Note that “reverse” tunneling features (marked with “\*”) are observed in (a) and (d) with different values of  $\alpha$  ..... 310

## LIST OF TABLES

Table	Page
B1. Frontier orbital energies and dipole moments from DFT calculations using the B3YLP <sup>6,7</sup> — a non-local (hybrid) functional — and PBE <sup>8</sup> and PW91 <sup>9</sup> — semi-local exchange-correlation functionals. The calculated dipole moments of <i>cis</i> -DDQT (2.3-2.5 Debye) were significantly greater than that of <i>trans</i> -DDQT (0.06 Debye), leading to the enhanced interaction of the <i>cis</i> -conformer with image charges at the metal surface. In all three calculations, the <i>cis</i> -LUMO was found to be higher (by ~30 meV) than the <i>trans</i> -LUMO. All DFT computations used the 6-31G* basis set .....	240

# CHAPTER I

## INTRODUCTION

### 1.1. Background

Scanning tunneling microscopy (STM) was the very first technique to utilize scanning of a sample surface with a sharp probe (tip), without a direct contact, to achieve atomic resolution of surface features.<sup>1-3</sup> Despite the development of a very wide range of other approaches, which constitute the more general field of Scanning Probe Microscopy (SPM),<sup>4-6</sup> STM still remains one of the most important and popular SPM techniques.<sup>7-9</sup> It continues to inspire development of innovative instruments and novel experimental methods. Prominent recent breakthroughs in STM technology include development of Inelastic Electron Tunneling Spectroscopy (STM-IETS),<sup>10,11</sup> which allows chemical fingerprinting of molecules with a single-bond sensitivity; Scanning Tunneling Hydrogen Microscopy (STHM)<sup>12-14</sup> and Scanning Tunneling Microscopy With Single Molecule (CO) Inelastic Tunneling Probe (STM-itProbe),<sup>15</sup> both of which utilize decoration of the microscope tip with a molecule (tip fictionalization) to achieve sub-molecular resolution; and Scanning Tunneling Luminescence (STL),<sup>16-19</sup> which combines STM with a photon collection system to enable optical studies with sub-diffractive spatial resolution. There is also an ongoing project to bring STM into the domain of industrial application (metrology) by combining nanometer measuring precision with the ability to scan over an extremely large area (the goal is to scan up to  $50 \text{ mm}^2$ , which is an enormous length comparing to  $\sim 10 \text{ }\mu\text{m}^2$  of a maximum scan area for a typical STM).<sup>20</sup> In addition, STM is not only flourishing and evolving on its own, but also can be combined with other SPM

techniques in a single tool,<sup>21-23</sup> providing versatility of measurements and unique experiments, such as simultaneous operation as an Atomic Force Microscope (AFM) and a STM.<sup>24</sup>

The impact and longevity of STM are due to its unique use of the quantum tunneling phenomenon. When a sharp conductive tip and conducting surface are brought within sub-nanometer proximity, a tunneling current can be detected between them, which is extremely sensitive to the local electronic structure of both a tip and a sample. Moreover, it is very sensitive to the voltage bias applied between the sample and the tip (usually referred to as the sample bias, because the tip is grounded in the standard configuration), because it defines which states participate in forming tunneling current and which are not.<sup>8</sup> This allows a STM to extract selective information about different electronic states by controlling the sample bias. One prominent example is the use of topographic scanning at different biases which under certain conditions provides a direct visualization of molecular orbitals of an individual molecule adsorbed on the surface.<sup>25-27</sup> Sample bias defines which orbital(s) dominates tunneling current, hence determining the complete geometry of a topographic image.<sup>28,29</sup>

Another important ramification of bias control is the spectroscopic capabilities of the STM-based instrument.<sup>30</sup> Scanning tunneling spectroscopy (STS) is a technique that employs recording of the tunneling current, or its derivative, after freezing the tip position (opening the feedback loop) and then ramping the bias voltage in a selected range. Thus obtained curves as a function of bias are called  $I(V)$  or  $dI/dV$  STS spectra. The later is especially important because it directly corresponds to the local density of states (LDOS) as a function of energy. In studies of molecules adsorbed on the surface,

the availability of  $dI/dV$  spectroscopy is the main advantage of STM over other SPM methods, because it enables the identification of energies of electronic states, such as the highest occupied molecular orbital (HOMO) and the lowest unoccupied molecular orbital (LUMO), thus giving a direct measurement of the electronic bandgap, which defines optical properties of the molecule under study. While  $dI/dV$  spectra can in principle be obtained by numerically differentiating  $I(V)$ , the resulting signal-to-noise ratio is usually low, so hardware-based techniques of measuring  $dI/dV$  signal are the preferred approach.

Two described techniques complement each other and often provide very convincing direct measurement of the electronic structure of a molecule, with experimental values, like the electronic state energies and orbital symmetry and shape, in good agreement to the ones obtained from theoretical calculations.<sup>25</sup> Nevertheless, both of these methods have limitations. Topographic orbital imaging was only achieved for several planar molecules in environments where they were sufficiently decoupled from the electronic states of the conductive substrate (for example, with the help of thin insulating films).<sup>25</sup> If degenerate or closely spaced electronic states are present, then the topography will reflect a mixture of contributions from all orbitals that significantly contribute to tunneling at a given sample bias. Special treatment of the tip, such as fictionalization or a particular geometry of the dangling state at the end of the tip, might be required and could make reproducibility of results very difficult.<sup>28</sup> STS, on the other hand, is essentially a single-point technique and its simplest form does not provide information about the spatial distribution of electronic states. It is natural, however, to extend the STS technique into the one-dimensional (1-D) and the two-dimensional (2-D)



realm by performing the series of the single-point STS measurements over 1-D array or 2-D grid of points.<sup>31,32</sup> These techniques are called STS mapping or spectroscopic STM imaging.<sup>33</sup> 1-D STS mapping provides a cross-section of the electronic density of states in one spatial direction and is especially useful when a system has a uniform LDOS distribution, such as a symmetrical single-point impurity center,<sup>34</sup> or has a particular axis along which the evolution of the LDOS can provide interesting physical insight, such as two impurity centers interacting and changing the LDOS along the axis connecting them.<sup>35</sup> 2-D STS mapping, on the other hand, has a complete analogy with STM topographic mapping of orbitals in real space. One important difference (and a main advantage over topographic orbital mapping) is the ability to select specific energy for visualizing the LDOS. While topography at a particular bias  $V_{orb}$  is affected by all states between the Fermi level and  $V_{orb}$ , the  $dI/dV$  signal at selected voltage corresponds only to the LDOS of corresponding energy. STM topographic mapping is affected by the LDOS in a range of energies from the Fermi level up to the energy defined by a sample bias voltage. Therefore, it is able to image a single orbital only if the orbital makes a dominant contribution into the tunneling current. At energies, that are further away from the Fermi level than lowest unoccupied and highest occupied orbitals, this generally is not the case.<sup>8</sup> 2-D STS mapping, on the other hand, uses only a narrow range of energies for imaging (usually defined by a lock-in modulation). This results in ability to produce orbital images for more complex LDOS structures with number of orbitals, and the technique is also less demanding for molecular environment. It helped to image electronic states in situations, where the STM topographic imaging didn't work, for example, in systems which are strongly coupled to the electronic states of the metallic

substrate, like artificial atomic chains,<sup>36</sup> molecules<sup>37</sup> and a coupled system of a molecule and metal atom chains<sup>38</sup> (note that the latter system was also complicated by degeneracy of electronic states of the molecule, but orbital symmetries were still well-resolved).

Advantages of the 2-D STS mapping come with the steep price of a very long data acquisition time, which translates into strict requirements for the system stability and high cost of running of an experiment. Usually researchers can afford only very limited set of data, such as  $dI/dV$  at only one single bias voltage value.<sup>39,40</sup> The main motivation for a project of new STM instrument construction, described in this dissertation, was to make STS map acquisitions more affordable and less limited for the duration of single scan, as well as to increase overall experiment running time. This new system achieved unprecedented stability and an order of magnitude improvement in operation time, and thus is referred to as Scanning Tunneling Microscope with Unlimited Operation (STM-UO) in this dissertation. In addition, longer experimental time opens a possibility to investigate materials, that are considered difficult for SPM studies and therefore existing reports had limited information obtained on single-molecule (nanoparticle) scale. Combining these two research avenues, we acquired more complete and insightful physical pictures of materials that are challenging to investigate with STM, but interesting from a technological perspective. The next two sections describe in more detail the foundations of the research presented in this dissertation.

## **1.2. Advantages of STM-UO for STS Spatial Mapping**

STM instruments operate with the tunneling junction held in a wide range of environmental conditions, such as junction medium (vacuum, atmosphere, high-pressure, liquid), and temperature (cryogenic, room temperature, elevated temperatures), and

others (external magnetic field, illumination, etc.).<sup>41</sup> The most controlled state of environment is achieved using ultra-high vacuum (UHV) and cryogenic technology.<sup>42</sup> UHV allows preparation of atomically well-defined sample:<sup>43</sup> a typical sample is a substrate with wide, atomically flat terraces, single-atom steps between terraces and a monolayer or sub-monolayer of deposited molecules of interest, but with minimal amount of extraneous adsorbate molecules (e.g. physisorbed or chemisorbed gas molecules that are unavoidable in ambient conditions). Low temperatures freeze the motion of molecules, reduce the noise in the tunneling current, improve stability of the tunneling junction and lower the thermal broadening of electronic states in spectroscopy. The instrument capable of state-of-the-art STS and sub-molecular resolution has to incorporate UHV and cryogenic environments, so these were the first requirements for the design of our new microscope.

The effect of these two requirements for the duration of the STM experiment is opposite. While UHV greatly increases the time available for investigating of the surface (by dramatically decreasing the rate at which surface is bombarded by gas molecules), cryogenic state requires constant supply of cryo-cooler to maintain the low temperature. Conventional way to operate cryogenic STM is to couple the scanner with continuous flow cryostat which supplies liquid nitrogen or helium as a coolant agent.<sup>44–46</sup> Liquid helium is a preferred medium because of the extremely low temperatures that can be achieved provide optimal STM conditions. However, the price of liquid helium supply limits the time available for a single experiment and significantly increases its cost. A new generation of closed-cycle cryostats (CCC) offers a solution to this problem, which dramatically increases the limit for one experiment time and decreases expenses.

Coupling of a STM with a CCC presents significant technological difficulties that were for the first time overcome in our group as described in Chapter II of this dissertation, which was previously published under the title “High-stability cryogenic scanning tunneling microscope based on a closed-cycle cryostat” in *Review of Scientific Instruments* and co-authored by Jason D. Hackley, Dmitry A. Kislitsyn, Daniel K. Beaman, Stefan Ulrich, and George V. Nazin.

There are three straightforward advantages that the extended operation regime of STM-UO offers to the STS technique. Most important is improvement in the quality of the STS data that can be achieved by extending the scanning time. Second is a reduction of thermal drift by better thermal stability of the scanning head. Third is the availability of more time for conditioning of the STM tip to make it appropriate for spectroscopy.

Improvement in quality stems from an increase in signal-to-noise and an opportunity to remove tunneling gap fluctuations.  $dI/dV$  spectroscopy with lock-in technique is the standard tool for quality of STS. One spectroscopic curve is obtained by measuring  $dI/dV$  signal for a set of sample bias voltages. The signal-to-noise ratio is directly affected by the time allocated for a single point measurement (fixed X, Y and V coordinates) and an amplitude of lock-in modulation. Higher modulation amplitude defines the low limit for energy resolution of spectroscopic features (electronic states and vibrational overtones) and its reduction is often desirable and can be compensated by increase of the sampling time of the lock-in signal. A compromise between the quality of the signal and the total time of acquisition has to always be made.

The STM-UO instrument significantly improves quality of data, especially if low tunneling current is required as described in the next section. The following example

illustrates trade-offs between data quality and acquisition time. For materials presented in this dissertation, typical sampling time 1000 ms was giving a good quality of  $dI/dV$  spectra (this is judged by reproducibility and stability of resolved features in the STS spectrum). If a voltage range of 2.0 to -2.0 V has to be covered with 10 mV resolution, then 400 points are to be acquired for a spectrum in every spatial pixel. Typical resolution for a 1-D STS mapping is 64 pixels to obtain sub-molecular spatial resolution (for example, if 1-D trajectory is 3 nm, then resolution is 0.5 Å). Total time required for one 1-D STS pass is then ~7 hours. This type of scan can be setup for overnight acquisition. It is often desirable to produce two passes of 1-D STS mapping over the same trajectory to check the reproducibility of the measurement, while keeping the total acquisition time below 10 hours (this is a typical time that can be extended for the highest quality up to 24 hours, which is a practical limit posed by the thermal drift as described below). In this case, in order to maintain quality, one needs to sacrifice the number of points for a single spectrum (e.g. use 20 mV spacing between the voltage points) or increase the modulation (thus reduce feature resolution) and reduce the single point sampling time. Limitations become increasingly severe when one goes from 1-D to 2-D STS spatial mapping. For example, if one would like to obtain 32x32 pixel map with the same parameters as above, it will take ~114 hours! Obviously, significant tradeoffs should be incorporated to make 2-D STS mapping feasible. The most widely used one is the reduction of the number of bias points for a single spectra for every pixel. For example, when we go to a 100 mV distance between points, the total acquisition time drops to 11 hours.

Fluctuations of the gap between the tip and the sample of STM can significantly affect the quality of STS mapping images. Ideally, constant-current STS mapping

consists of a set of spectroscopy curves obtained with a tunneling gap in every spatial point corresponding to given tunneling current and sample bias setpoint (this is current  $I_0$  and voltage  $V_0$  used by STM to move on the surface, before the tip Z position is frozen for every spectroscopic measurement). However, there is a slight stochastic deviation in the actual tunneling gap realized in every pixel. Since the tunneling signal depends exponentially on the tip-sample distance, even miniscule errors in this distance produce a noticeable increase or decrease of the measured  $dI/dV$  signal. The effect of this on single point STS is usually negligible because it is the relative intensity of the features in spectrum that give valuable information. However, spatial STS mapping is affected adversely by this phenomenon with the visual quality of produced images usually being unsatisfactory (appearing as image noise) unless a special filtering procedure is applied to the spectroscopic data. This is called “normalization” and consists of equalizing the surface of the area under the positive part of every curve:

$$\frac{d\tilde{I}}{dV}(x, y, V) = \frac{dI}{dV}(x, y) / I(x, y, V_0),$$

where  $V_0$  is a setpoint sample bias, which is usually the upper limit of the voltage range. The goal of the normalization is to get  $dI/dV$  data closer to

$$\int_0^{V_0} \frac{d\tilde{I}}{dV}(x, y, V) dV = \tilde{I}(x, y, V_0) = \text{const},$$

which would be the case in the absence of stochastic fluctuations in tunneling gap. In practice, this results in improvement of the image’s quality and reduction of noise, because the transition from a pixel to pixel becomes smoother at each particular voltage value. Numerically, normalization can be achieved in two ways. The first one is to use the  $dI/dV$  curve itself to approximate  $I(x, y, V_0)$  in every pixel:

$$\frac{d\tilde{I}}{dV}(x, y, V) = \frac{dI}{dV}(x, y) / \left( \int_0^{V_0} \frac{dI}{dV}(x, y) dV \right).$$

The second method is to use  $I(x, y, V_0)$  from the  $I(V)$  curve, which is always recorded for every pixel simultaneously with  $dI/dV$  during STS. The first method generally produces much better results, because it fixes not only the error in tunneling junction gap that originates from imperfection in  $Z$  position of the scanner at the *beginning moment* of disconnecting the feedback loop (the second method only does this), but also takes into account the  $Z$  position fluctuation *during* the spectroscopic measurement itself. It essentially calculates “average” or “effective”  $I_{eff}(x, y, V_0)$  for the whole duration of the voltage ramp. Therefore the first normalization technique is preferred, but it is only possible if enough data points is present in the spectroscopic  $dI/dV$  curve, because the accuracy of the normalizing integral depends on this number. As we have seen in the example above, 1-D STS mapping can easily achieve very high voltage resolution with STM-UO system. 2-D STS mapping, on the other hand, is always more limited in the number of data points for every curve and a researcher needs to decide whether the first or the second normalization method is justified for every particular case. For the 32x32 pixel map example with 20 points per positive side of the  $dI/dV$  curve, the first technique usually produces a good result without introducing any artifacts. For higher spatial resolutions with 64x64 pixel maps, where usually only one, two or three voltage points are used, only the second normalization technique is a viable option. STM-UO provides opportunity to use first type of normalization in cases where it would not be possible for a system with limited operation time.

A second major advantage of STM-UO is the ability to stabilize the temperature of the scanner head using the feedback control of a heater. As shown in Chapter II, this results in dramatic decrease of the spatial thermal drift and increase of acquisition time for 1-D and 2-D STS mapping up to 24 hours, without adverse spatial distortion. Nevertheless, the thermal drift has to be taken into account to calculate an actual trajectory of a STS map and determine the exact spatial relations between different STS maps and the topography of a nano-object of study. Another advantage of very low drift rates is possibility to account for a drift accurately using the approximation of unidirectional uniform drift velocity.

An additional advantage of STM-UO for STS is the possibility to spend longer time cleaning and checking the tip. Preparing an atomically sharp and adsorbate-free tip is critical for STS success, and it can be a tedious and time-consuming task. Furthermore, two standard tip preparation techniques, field emission by voltage pulse and controlled tip crush, require clean metallic substrate to be efficient. While some deposition methods, like in-vacuum sublimation, result in a well-controlled percentage of the surface area being a clean flat metallic surface, others, like dry-contact transfer and in-vacuum pulse valve deposition from solution, result in a scarcity of clean exposed metal and require special tip treatment techniques that are less predictable and hence require more time. Some materials need to be deposited by less perfect techniques as described in the next section.

### **1.3. Application of STM-UO to Materials With Special Requirements**

STM-UO system not only makes STS mapping very affordable and allows for routine operation, but it extends other experimental capabilities. An experiment can be



run continuously for as long as ~60 days and is only limited by the slow build-up of frozen atmosphere gases that leak into the helium-filled cryostat-scanner interface (see Chapter II). This allows for detailed studies of materials that present difficulties for conventional STM instruments. As mentioned before, an ideal STM sample has a clean well-defined surface. Additional preferences are for the molecule of study to be flat and have a very stable adsorption configuration. Flatness of the molecule reduces the probability that molecule will be disturbed while the tip is moving over it. It also minimizes the influence of the tip shape on imaging (every part of the molecule is interacting with the tip apex positioned directly over it, as compared to interaction with the side of the tip). Larger nanoparticles, like nanotubes and quantum dots, have a curved top shape and tall profile, thus requiring careful and prudent maneuvering on the surface, as well as recoverability of the tip in case of crashes and accidental object adsorption by the tip. By virtue of its longer operating times, STM-UO is uniquely able to address these challenges.

The stability of the molecule's adsorption configuration allows for the use of higher tunneling currents in a conventional STM setup. While typical tunneling currents used for high stability systems range from 0.5-4 nA, the currents needed to be used with gentle materials presented in this dissertations were below 30 pA, i.e. orders of magnitude lower. The magnitude of the tunneling current is inversely proportional to the signal-to-noise ratio. The only way to improve signal-to-noise is to use longer acquisitions times.

The scope of this dissertation is to utilize the full potential of the new STM-UO system in the forefront of research of three classes of materials. Two fundamental

challenges presented above define three regimes of STM-UO operation in the order of complexity. First, we explore the molecules that present challenges in terms of flatness and substrate cleanliness, but are very robust under STM probing. The second case is the opposite: molecules that can be deposited in conventional atomically clean fashion and have flat geometry, but do not survive high tunneling currents. And finally, the third material combines both challenges and thus provides an opportunity for an ultimate test of the capabilities of STM-UO for research of challenging materials.

The first type of system was realized by study of Single-Wall Carbon Nanotubes (SWCNT). These large molecules cannot be sublimated onto the surface, thus the dry-transfer contact technique was implemented which results in unavoidable mechanical damage to a substantial part of the substrate.<sup>47</sup> Use of STM-UO helped overcome difficulties with substrate imperfections, enabling STS spatial mapping to relate the properties of electronic states in a well-defined localization regime to the characteristics of associated vibrational modes. These results are described in Chapter III, which was previously published under the title “Vibrational Excitation in Electron Transport through Carbon Nanotube Quantum Dots” in *The Journal of Physical Chemistry Letters* and co-authored by Dmitry A. Kislitsyn, Jason D. Hackley, and George V. Nazin.

The second type of system is represented by studies of a class of organic molecules that are becoming increasingly important in various electronic applications: alkyl-substituted quaterthiophenes.<sup>48</sup> These molecules were discovered to not be able to withstand high tunneling currents,<sup>27</sup> and even with using lower values a certain probability to permanently damage a molecule remained. STM-UO allowed longer acquisition times as well as large number of attempts to obtain data if a molecules

became damaged. Successful implementation of standard STM imaging, as well as imaging of electronic orbitals using 2-D STS mapping, showed advantages of STM-UO in addressing the challenges presented by delicate molecules. The results are presented in Chapter IV, which was previously published under the title “Adsorption-Induced Conformational Isomerization of Alkyl-Substituted Thiophene Oligomers on Au(111): Impact on the Interfacial Electronic Structure” in *ACS Applied Materials & Interfaces*, co-authored by Benjamin N. Taber, Dmitry A. Kislitsyn, Christian F. Gervasi, Stefan C. B. Mannsfeld, Lei Zhang, Alejandro L. Briseno, and George V. Nazin; Chapter V, which was previously published under the title “Coverage-Dependent Self-Assembly Regimes of Alkyl-Substituted Thiophene Oligomers on Au(111): Scanning Tunneling Microscopy and Spectroscopy” in *The Journal of Physical Chemistry C*, co-authored by Dmitry A. Kislitsyn, Benjamin N. Taber, Christian F. Gervasi, Stefan C. B. Mannsfeld, Lei Zhang, Alejandro L. Briseno, and George V. Nazin; Chapter VI, which was previously published under the title “Oligothiophene wires: impact of torsional conformation on the electronic structure” in *Physical Chemistry Chemical Physics*, co-authored by Dmitry A. Kislitsyn, Benjamin N. Taber, Christian F. Gervasi, Lei Zhang, Stefan C. B. Mannsfeld, Jim S. Prell, Alejandro L. Briseno, and George V. Nazin; and Chapter VII, which was previously published under the title “Real-space visualization of conformation-independent oligothiophene electronic structure” in *The Journal of Chemical Physics*, co-authored by Benjamin N. Taber, Dmitry A. Kislitsyn, Christian F. Gervasi, Jon M. Mills, Ariel E. Rosenfield, Lei Zhang, Stefan C. B. Mannsfeld, James S. Prell, Alejandro L. Briseno, and George V. Nazin.

The third type of system, which presents the ultimate challenge for STM investigationa with combined issues of substrate cleanliness, complex three dimensional (3-D) shapes of large nano-objects and weak stability on the surface, was provided by colloidal nanocrystal quantum dots<sup>49</sup> deposited from solution using the in-vacuum pulse valve technique.<sup>50</sup> STM-UO is the very first system to implement STS spatial mapping studies of these challenging materials: first applied to PbS nanocrystals, for which we discovered that the ligand shell had to be removed in order to make STM studies feasible, and second to H-Si nanocrystals, which were investigated with the hydrogen passivation shell preserved intact (and then controllably damaged to create point defects). STM-UO achieved unprecedented imaging of electronic states of nanocrystals in real space and provided an important insight into the mechanisms that govern the behavior of individual surface defects and the surface reconstruction of nanocrystals' facets, and revealed physical and chemical processes related to the performance of colloidal nanocrystals in technical applications. These results are presented in Chapter VII, which was previously published under the title "Spatial Mapping of Sub-Bandgap States Induced by Local Nonstoichiometry in Individual Lead Sulfide Nanocrystals" in *The Journal of Physical Chemistry Letters*, co-authored by Dmitry A. Kislitsyn, Christian F. Gervasi, Thomas Allen, Peter K. B. Palomaki, Jason D. Hackley, Ryuichiro Maruyama, and George V. Nazin; Chapter IX, which was previously published under the title "Diversity of sub-bandgap states in lead-sulfide nanocrystals: real-space spectroscopy and mapping at the atomic-scale" in *Nanoscale*, co-authored by Christian F. Gervasi, Dmitry A. Kislitsyn, Thomas L. Allen, Jason D. Hackley, Ryuichiro Maruyama, and George V. Nazin; Chapter X, which was previously published under the title "Mapping of Defects in

Individual Silicon Nanocrystals Using Real-Space Spectroscopy” in *The Journal of Physical Chemistry Letters*, co-authored by Dmitry A. Kislitsyn, Vancho Kocevski, Jon M. Mills, Sheng-Kuei Chiu, Christian F. Gervasi, Benjamin N. Taber, Ariel E. Rosenfield, Olle Eriksson, Ján Ruzs, Andrea M. Goforth, and George V. Nazin; and Chapter XI, which was previously published under the title “Communication: Visualization and spectroscopy of defects induced by dehydrogenation in individual silicon nanocrystals” in *The Journal of Chemical Physics*, co-authored by Dmitry A. Kislitsyn, Jon M. Mills, Vancho Kocevski, Sheng-Kuei Chiu, William J. I. DeBenedetti, Christian F. Gervasi, Benjamin N. Taber, Ariel E. Rosenfield, Olle Eriksson, Ján Ruzs, Andrea M. Goforth, and George V. Nazin.

Chapter XII concludes the dissertation and describes future research directions to further utilize the unique advantages of STM-UO system in order to study a plethora of new materials and phenomena on the nanoscale.

# CHAPTER II

## HIGH-STABILITY CRYOGENIC SCANNING TUNNELING MICROSCOPE BASED ON A CLOSED-CYCLE CRYOSTAT

This chapter by Jason D. Hackley, Dmitry A. Kislitsyn, Daniel K. Beaman, Stefan Ulrich, and George V. Nazin has been previously published under the same title in *Review of Scientific Instruments* **85**, 103704 (2014). Copyright © 2014 AIP Publishing LLC.

### 2.1. Introduction

This chapter reports on the design and operation of a cryogenic ultra-high vacuum (UHV) scanning tunneling microscope (STM) coupled to a closed-cycle cryostat (CCC). The STM is thermally linked to the CCC through helium exchange gas confined inside a volume enclosed by highly flexible rubber bellows. The STM is thus mechanically decoupled from the CCC, which results in a significant reduction of the mechanical noise transferred from the CCC to the STM. Noise analysis of the tunneling current shows current fluctuations up to 4% of the total current, which translates into tip-sample distance variations of up to 2 picometers. This noise level is sufficiently low for atomic-resolution imaging of a wide variety of surfaces. To demonstrate this, atomic-resolution images of Au(111) and NaCl(100)/Au(111) surfaces, as well as of carbon nanotubes deposited on Au(111), were obtained. Thermal drift analysis showed that under

optimized conditions, the lateral stability of the STM scanner can be as low as 0.18 Å/hour. Scanning Tunneling Spectroscopy measurements based on the lock-in technique were also carried out, and showed no detectable presence of noise from the closed-cycle cryostat. Using this cooling approach, temperatures as low as 16 Kelvin at the STM scanner have been achieved, with the complete cool-down of the system typically taking up to twelve hours. These results demonstrate that the constructed CCC-coupled STM is a highly stable instrument capable of highly-detailed spectroscopic investigations of materials and surfaces at the atomic scale.

## **2.2. Background**

Now in its fourth decade of existence, scanning tunneling microscopy (STM)<sup>1</sup> has become an essential tool that has provided unique insights into the atomic structures of a wide variety of surfaces and nanoscale systems. Scanning Tunneling Spectroscopy (STS)<sup>1</sup> is one of the important capabilities of STM that provides atomic-resolution information about the electronic structures of sample surfaces. STM experiments probing the spatially-dependent spectroscopic properties of surfaces at the atomic scale typically require ultra high vacuum (UHV) conditions and cryogenic temperatures: UHV enables preparation and use of well-defined atomically clean surfaces, while low-temperatures greatly enhance the mechanical stability of the STM junction, freeze the motion of weakly-bound adsorbates, and improve the spectroscopic resolution of STM by reducing the thermal broadening of spectroscopic features. The majority of STM systems intended for high-performance STS experiments have so far been constructed coupled to a variety of different cryostats, such as continuous-flow<sup>2-4</sup> or bath-cryostats.<sup>5-7</sup> So far, operation of all of these cryostats relied on the use of cryogenes, with the best operating conditions

achievable with liquid helium. The dramatic increase of liquid helium costs over the past decade<sup>8</sup> has led to a situation where using liquid-helium for STM instruments is becoming prohibitively expensive. Near-future projections predict further price increases by up to 50%.<sup>8</sup> Development of a cryogen-free STM operating at near liquid-helium temperatures is thus important for sustaining the current level of activity of STS-based studies in a variety of research fields.

In this communication, we present a novel cryogenic UHV-STM instrument that, for the first time, achieves temperatures as low as 16 K by using a closed-cycle cryostat (CCC).<sup>9</sup> The cryostat is based on the Gifford-McMahon (GM) design, which uses recirculating helium-gas thus obviating the need for liquid helium. The use of a CCC for STM is counterintuitive due to the inherent noise of CCCs: GM cold-heads, in particular, incorporate moving parts located in close proximity of the cold finger where instrumentation is typically mounted. Another variation of CCC, pulse-tube based refrigerators also display significant mechanical vibrations.<sup>10</sup> By using a novel CCC, which is thermally linked to the STM system through helium exchange gas confined inside a volume confined by highly flexible rubber bellows, we have achieved a significant reduction of the mechanical noise transferred from the CCC to the STM.

The performance of the new STM is comparable to the established designs based on the continuous flow- or bath-cryostats. Noise analysis of the tunneling current shows current fluctuations up to 4% of the total current, which translates into tip-sample distance variations of up to 2 picometers. This noise level is sufficiently low to allow atomic-resolution imaging of most surfaces typically studied with STM, as demonstrated in this manuscript using Au(111) and NaCl(100)/ Au(111) surfaces, as well as carbon



nanotubes deposited on Au(111). With the need for conservation of liquid helium removed, we are able to actively stabilize the temperature of the scanner using a heater controlled by a feedback mechanism. This enables temperature stability on the scale of +/-1 milli-Kelvin, which leads to extremely low lateral and vertical (tip-sample distance) drift rates. Thermal drift analysis showed that under optimized conditions, the lateral stability of the STM scanner can be as low as 0.18 Å/hour. STS measurements (based on the lock-in technique) with the new STM show no detectable presence of noise from the closed-cycle cryostat.

### **2.3. System design**

#### **STM/Scan Head**

Despite the mechanical separation of the STM chamber from the CCC, residual mechanical noise appearing as spikes of up to 5 nanometers can still be present on the cryostat cold-finger mounted on the STM chamber side.<sup>11</sup> These vibrations have a low frequency of 2.4 Hz, which makes it imperative for the STM scanner assembly (including the sample and sample holder) to be as rigid as possible. The Pan-style design<sup>6</sup> was therefore chosen for the STM scanner, as it is one of the most rigid designs developed so far. The scan-head was designed in cooperation with RHK Technology, Inc., which has pioneered the commercial development of Pan-style STM scanners.<sup>12</sup>

The STM scanner, constructed by RHK Technology, incorporates a set of piezo-drive positioners, which, in addition to the coarse approach capability realized by a Pan-style Z-positioner, allow lateral coarse-positioning of the sample using a combined XY piezo-drive positioner.<sup>13</sup> The total range of all three positioners covers a volume of 8 mm x 4.5 mm x 4.5 mm. The positioners are assembled onto a rigid gold-coated

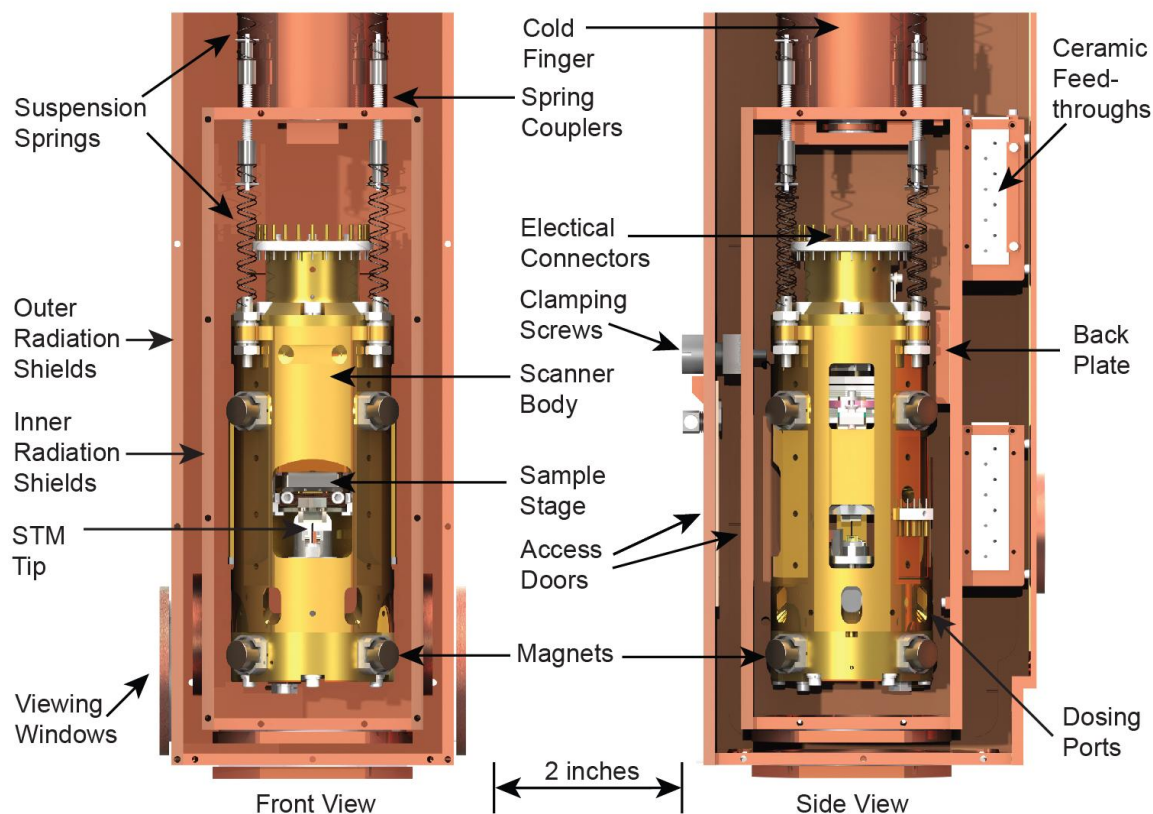


**FIG. 2.1.** STM scanner suspended inside the thermal radiation shields. Left: front view of STM in shields with front-facing shields removed. Right: side view of STM in shields with side-facing shields removed. The inner radiation shield is mounted directly to the cold tip, which is the second cooling stage of the cold finger. The outer radiation shields mount directly to the first cooling stage of the cold finger (not shown). Springs extend approximately four inches above the area shown.

molybdenum housing (Fig. 2.1). Molybdenum was chosen because in addition to high stiffness, it possesses good thermal conductivity and a low thermal expansion coefficient that is a good match for other components of the system. The body of the scanner was designed to accommodate an additional set of piezo motors for positioning of optics for Scanning Tunneling Luminescence experiments.<sup>14-17</sup> The constructed STM scanner is

highly immune to external vibrations and is capable of atomic-resolution imaging (of graphite surfaces) in ambient conditions with minimal vibrational isolation (for example, a rubber pad placed under the scanner was found to be sufficient). For optimal vibrational isolation, our STM is suspended on stainless steel springs, and is eddy-current damped by eight samarium-cobalt magnets attached to the STM body (Fig. 2.1). Each spring consists of two sections connected with a ceramic/stainless-steel coupler acting as an electrical and thermal break. The natural frequency of the hanging STM is 1.7 Hz, below the fundamental noise frequency generated by the CCC.

### **Radiation shields**

To achieve near-liquid helium temperatures, our design incorporates two nested thermal radiation shields constructed from gold-plated oxygen-free high-conductivity copper (Fig. 2.1).<sup>3</sup> The two radiation shields are mounted to two cooling stages of the CCC: the outer thermal shield is attached to the first cooling stage (not shown), which during experiment is at 25-35 K; and the inner radiation shield is attached to the second cooling stage (Cold Finger in Fig. 2.1), and is typically at ~15 K. The target temperature is typically maintained a fraction of a degree above the minimal attainable temperature using a heater wound on the cold finger. The heater is regulated using the feedback control loop of the temperature controller.

The STM body is cooled via a bundle of fine copper wires (0.005 in) connected to the top of the inner radiation shield via a sapphire piece (sapphire was chosen in order to avoid direct electrical contact). Additional cooling is provided by electrical connections (0.005 in copper wires) connected to electrical feedthrough panels mounted on the backside of the inner shield (Fig. 2.1). The feedthrough panels were made from

Shapal,<sup>18</sup> which has high thermal conductivity thus providing efficient thermal anchoring of electrical connections to the inner shield. Electrical connections from the inner shield feedthrough panels to the outside were made using stainless steel wires to minimize the thermal leak. To minimize the thermal load on the feedthrough panels, the stainless steel wires are thermally anchored at the outer thermal shield. During cool down, two spring-loaded screws mounted on the inner radiation shield are used to clamp the STM scanner to the back plate of the inner radiation shield (Fig. 2.1). The screws are released upon reaching the target temperature, so that the STM scanner hangs free, with the scanner temperature about 1.3 K higher than that of the inner radiation shield.

Each radiation shield incorporates a set of windows (sapphire for the inner shield and fused silica for the outer shield), which allow fine-scale observation of the STM junction and sample, as well as monitoring tip- or sample exchange. The radiation shields, as well as the STM scanner, were designed and constructed with line-of-site openings for in-situ evaporation/dosing directly into the STM junction by using thermal evaporators or gas sources mounted in the UHV system.

### **Cooling system**

To achieve cryogenic temperatures, we used a CCC manufactured by Advanced Research Systems, Inc.<sup>9</sup> The main components of the CCC are: 1) the GM cryocooler [DE202PF, Fig. 2.2(a)]; 2) a low-vibration interface (DMX-20) incorporating a UHV-compatible cold finger to which the STM radiation shields are mounted [Fig. 2.2(a)]; 3) a water-cooled compressor (ARS-2HW, not shown) that supplies compressed helium to the cryocooler. The cryocooler, the main source of the 2.4 Hz noise, is mounted on a separate support structure that is mechanically decoupled from the STM system

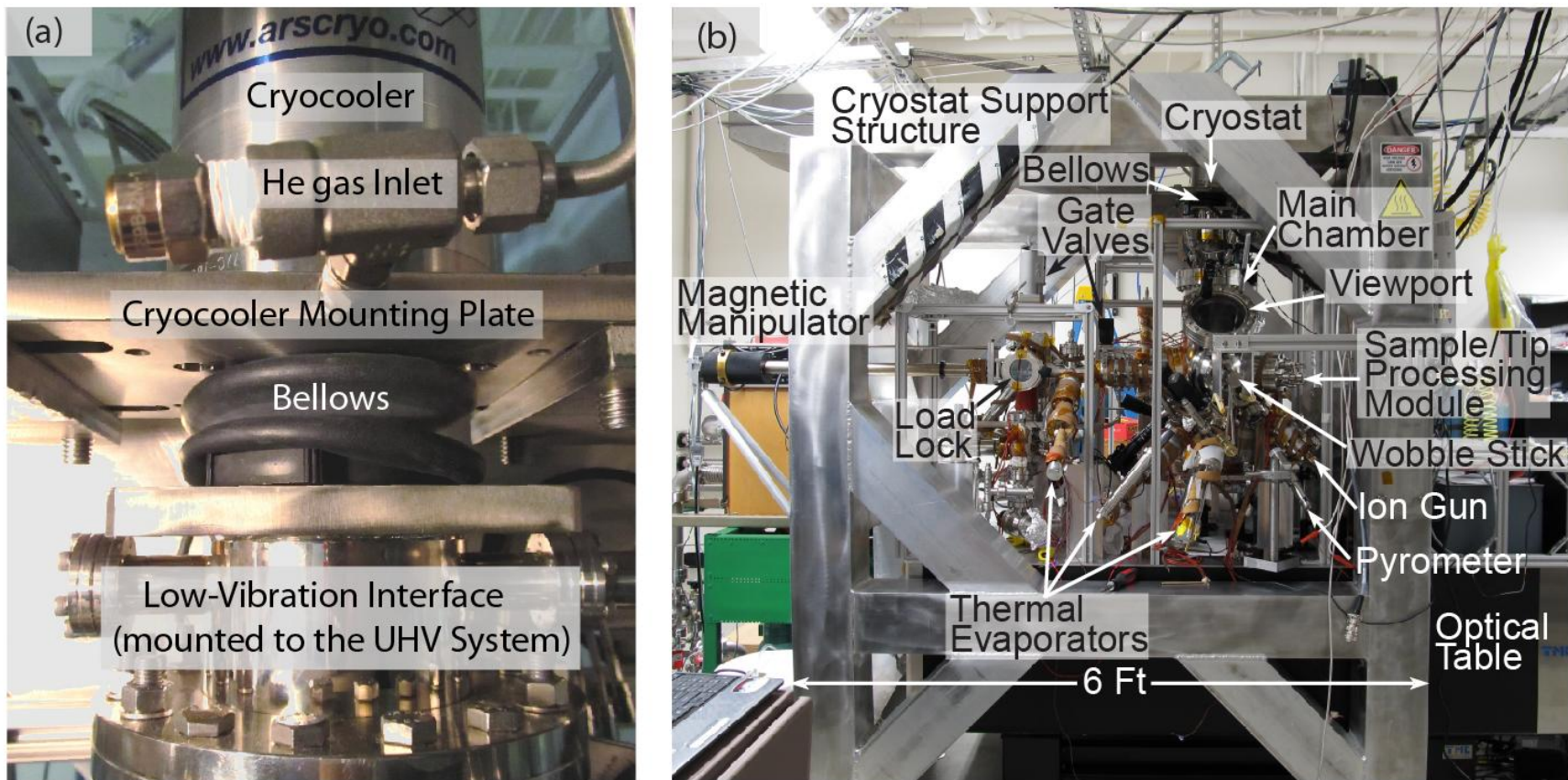


**FIG. 2.2.** Overview of the vacuum and cooling systems. (a) Thermal connection between the Cryocooler and Cold Finger is realized via He-filled volume confined by a rubber bellows. (b) View of the UHV system. The cryostat is mounted above the UHV system to the cryostat support structure. The cryostat support structure has no contact with the UHV system.

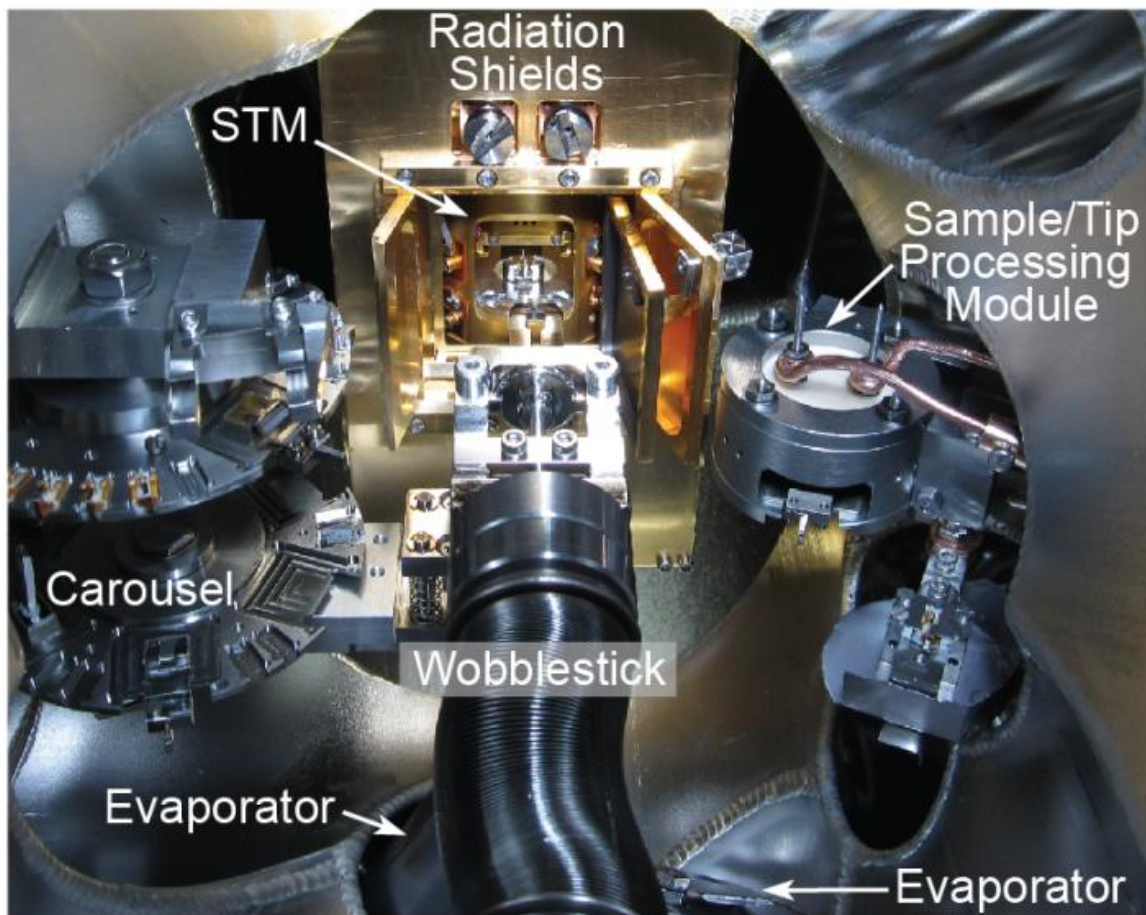


**FIG. 2.3.** View of the main chamber interior looking through the view port. Both the outer and inner radiation shield doors are open, affording a view of the STM.

[Fig. 2.2(b)], and is anchored directly to the floor surface that is in direct contact with the underlying bedrock below the laboratory space. The thermal link between the cooler and cold finger is realized using a heat exchange interface consisting partly of a rubber bellows filled with helium gas, with the rubber bellows being the only source of mechanical coupling between the cryocooler and the UHV system. While this does not completely eliminate vibrations, the residual vibrational noise typically registered at the cold finger end is within 5 nanometers, four orders of magnitude lower than the noise level at the cryocooler.<sup>11</sup>

## **UHV system design**

Several measures were taken to minimize the noise experienced by the STM system. The UHV STM system was assembled on the rigid concrete floor of the basement. The floor is anchored to the underlying bedrock via six reinforced concrete piers. The UHV chamber sits on an optical table with rigid mount legs without any additional vibrational isolation. The system is located in a “sound proof” room with low-noise ventilation baffles and dampers maintaining laminar air flow. The roughing pumps are located in an isolated pump room. The vacuum backing lines were attached to the chamber via stainless steel bellows, and are routed through sand-filled boxes to damp the mechanical vibrations generated by the backing pumps.

The vacuum system is composed of the main chamber, a load-lock chamber for quick tip and sample exchange, and a process gas manifold, each with a dedicated pumping line composed of a 75 L/s turbo pump and a dry scroll pump. In the case of the main chamber, the 75 L/s turbo pump serves as a backing pump for a 300 L/s magnetically-levitated turbo pump mounted directly on the chamber. In addition, the main chamber is pumped by a 300 L/s ion pump integrated with a combination of a titanium sublimation pump and cryogenically-cooled shroud. The baseline pressure in the main chamber is  $\sim 4 \times 10^{-11}$  torr, and at  $2 \times 10^{-11}$  torr during experiments at cryogenic temperatures, due to the cryo-pumping action of the radiation shields/cryostat.

## **Sample Preparation**

In addition to the STM, the main chamber houses the tip- and sample preparation and storage facilities. Samples (mounted on molybdenum sample holders) and tips are stored in a “carousel” module inside the main chamber (Fig. 2.3) with nine slots for

samples and thirty slots for tips. The samples and tips are exchanged between the load lock and the main UHV chamber by using a precision magnetic manipulator. Inside the main chamber, the samples and tips are manipulated using a wobble-stick allowing three-dimensional translation and rotation around the wobble-stick axis. Tips and samples are prepared in-situ via cycles of annealing and neon-ion-sputtering using a custom multifunctional processing module (Fig. 2.3). The module incorporates a current-carrying filament that can either be used for e-beam or radiation heating of individual samples and tips.<sup>3</sup> During the annealing process, the temperature of the sample is monitored by a pyrometer. An ion gun is used for sample sputtering, while tips are self-sputtered when biased to high voltage in neon pressure.

After an atomically clean sample surface is obtained, a wide variety of materials can be deposited on the surface using several facilities implemented in the system: 1) four different ports are available on the main chamber for mounting either gas/vapor sources or thermal evaporators [Fig. 2.2(b)], two of which are aligned into the STM junction. Thus, materials with appropriate vapor pressures can be evaporated in situ. All of these ports have dedicated gate valves, which allow exchange of gas/vapor sources or thermal evaporators without breaking vacuum in the main chamber; 2) a “dry contact transfer”<sup>19</sup> capability is available for deposition of nanoscale materials and molecular materials that do not have sufficient vapor pressures for evaporation, such as carbon nanotubes, graphene flakes, and polymers; 3) a facility for deposition of materials from solution using a pulsed valve<sup>20, 21</sup> is implemented in the load-lock, and has been successfully used for deposition of colloidal quantum dots.



## **2.4. Performance**

### **Cool-down and operation**

Full cool-down of the STM from room temperature to near-liquid helium temperatures takes approximately twelve hours [Fig. 2.4(a)], and is typically carried out overnight. During cool down, the STM is clamped to the back plate of the inner radiation shield. Upon reaching the target temperature the STM is unclamped and hangs free. After the cool-down, the cold-finger temperature is actively stabilized using a heater controlled by a feedback mechanism, such that the STM temperature remains stable for days within  $\pm 1$  mK [Fig. 2.4(b)]. The high temperature stability enables extremely low lateral and vertical tip-sample drift rates, as described below. So far, we have found no limitation on the duration of individual experiments: we have conducted experiments lasting several weeks without any major changes in operating conditions, except for the need to periodically (every several days) to increase the feedback set-point temperature. This is likely due to condensation of air/water vapor inside the volume filled with exchange He gas.

### **Atomic resolution**

The imaging capabilities of the new STM under cryogenic conditions were tested on several different samples with different surface structures. Fig. 2.5(a) shows a topography scan of a Au(111) surface (acquired at  $\sim 16$  K), which displays a clear hexagonal atomic pattern characteristic of the Au(111) surface,<sup>22</sup> with no identifiable features attributable to the CCC noise. Fig. 2.5(c), a cross-section of topography from Fig. 2.5(a), shows well-defined atomic corrugation of  $\sim 10$  pm. Another example of atomic-scale resolution, Fig. 2.5(b), shows a topography scan of a NaCl(100) monolayer

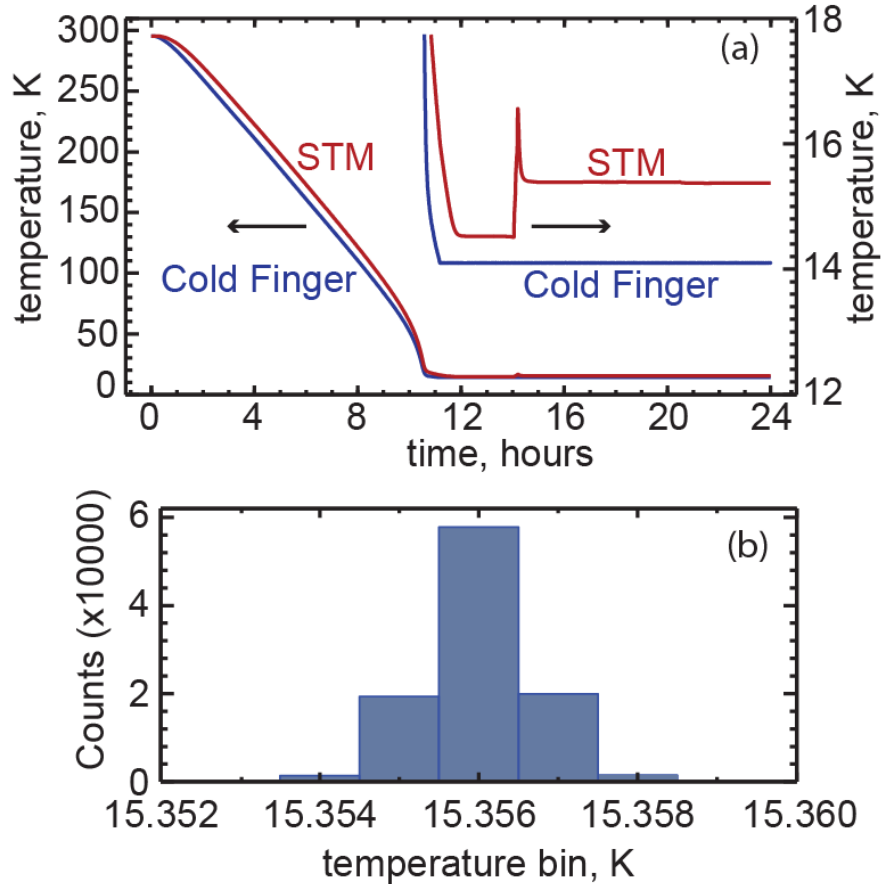


**FIG. 2.4.** (a) Typical cool down curves showing temperatures measured at the STM and at the Cold Finger. The two curves in the upper right corner show the variation of the temperatures after unclamping of the STM (seen as a spike in the top curve). (b) Histogram showing typical variations of the STM temperature when the temperature stabilization feedback mechanism is engaged. Each count corresponds to an individual reading of the temperature by the controller electronics.

film thermally deposited on the Au(111) surface (image acquired at  $\sim 16$  K). Fig. 2.5(b) shows a square lattice with a lattice constant of 0.39 nm, as expected for the NaCl(100) lattice. Similarly to Fig. 2.5(a), no identifiable features attributable to the CCC noise are present in the image. Fig. 2.5(d), a cross-section of topography from Fig. 2.5(b), shows well-defined atomic corrugation of  $\sim 10$  pm, suggesting that the CCC noise is significantly less than this number. Atomic-resolution images were also obtained on

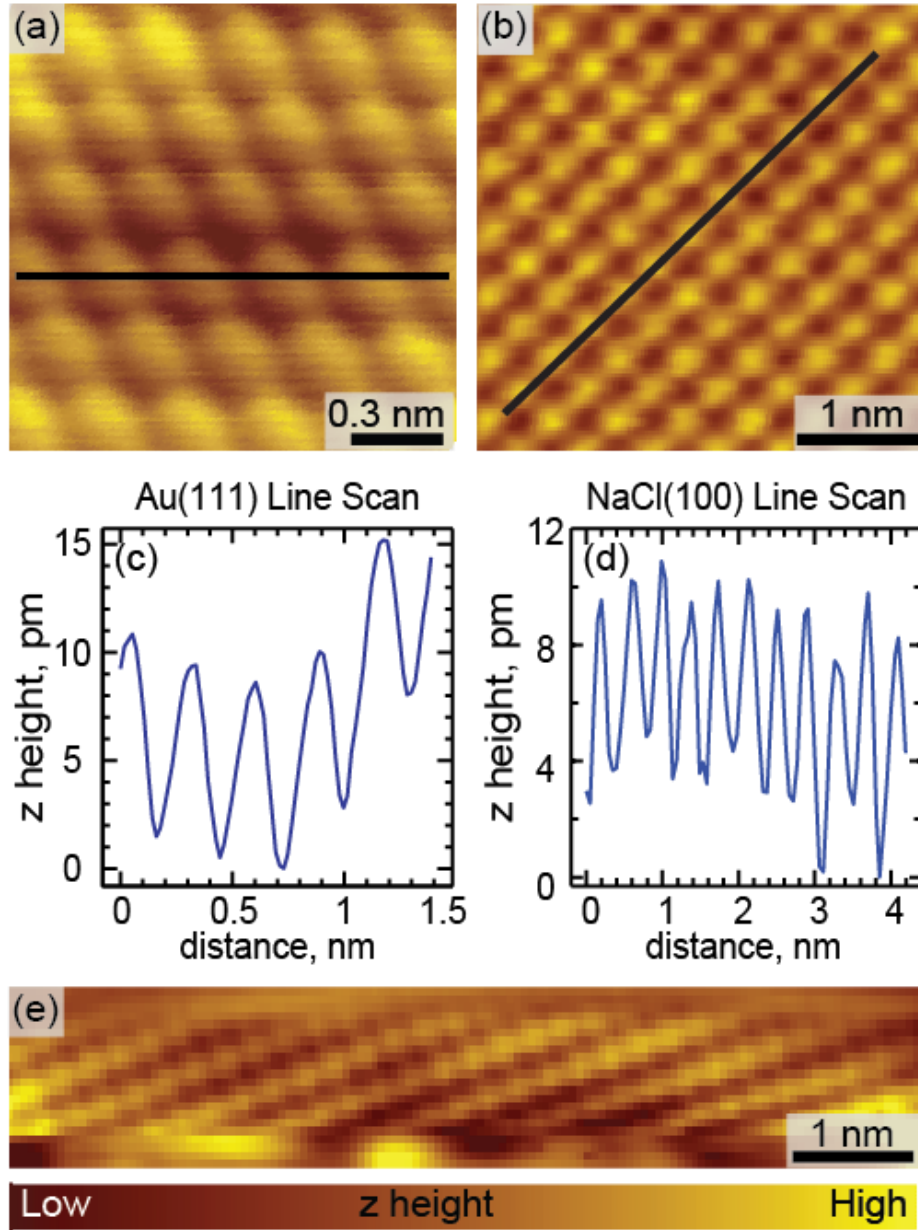


**FIG. 2.5.** Atomic-resolution images acquired with the new STM. (a) Topography scan showing atomic resolution of a reconstructed Au(111) surface [set point: 50 mV, 50 pA]. The bright peaks represent the Au atoms. (b) Topography scan of monolayer of NaCl(100) thermally evaporated on the Au(111) surface [set point: 1.50 V, 10.0 pA]. The bright peaks represent the Cl atoms. (c) Cross-section of topography from (a) taken along the black line shown in (a). (d) cross-section of topography from (b) taken along the black line shown in (b). (e) Atomically resolved surface of single-wall carbon nanotube [set point: 1.50 V, 5.0 pA].

single-walled carbon nanotubes deposited on the Au(111) surface, with one example shown in Fig. 2.5(e).

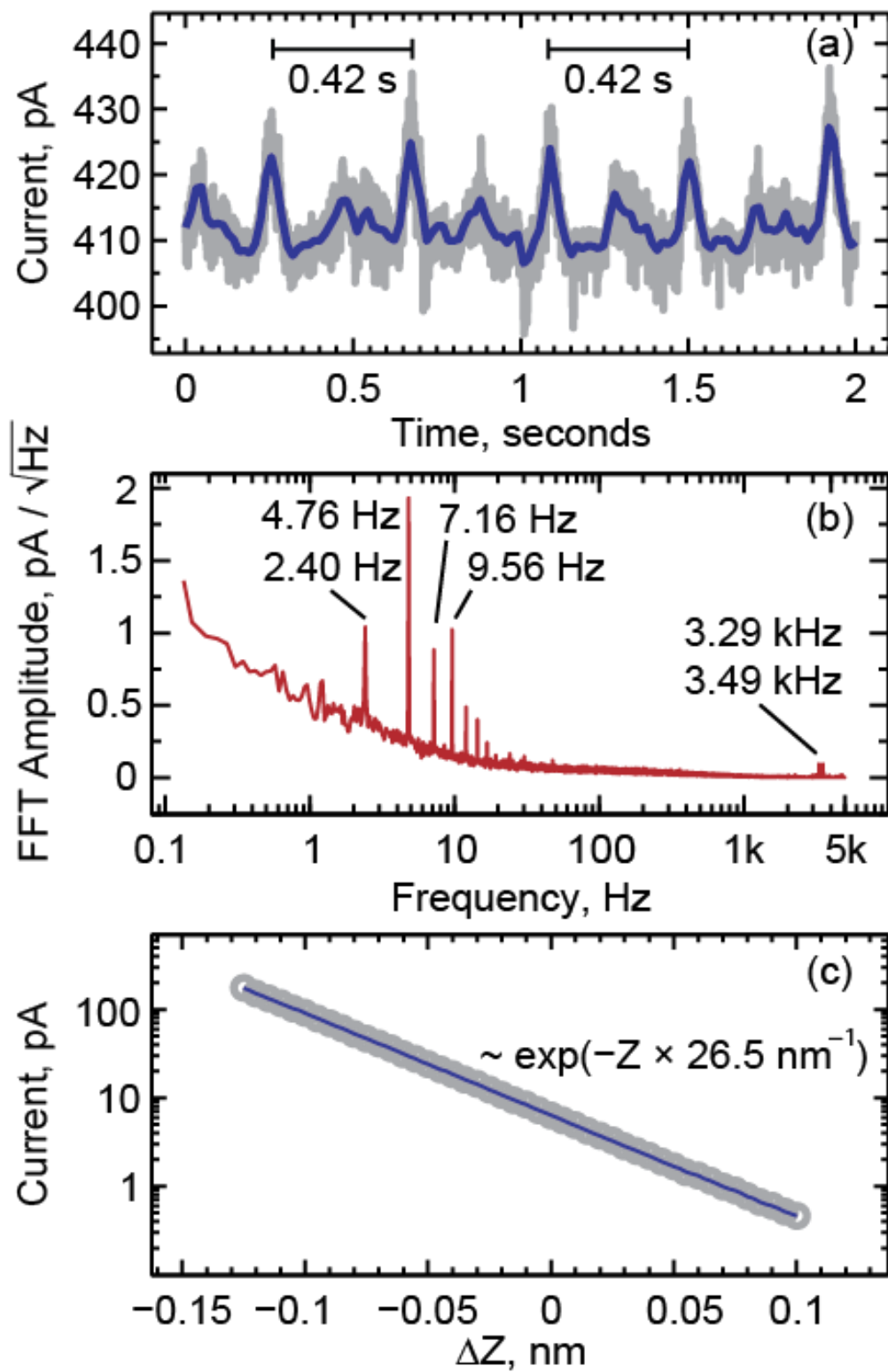
### Noise analysis

To quantify the noise generated by the CCC more directly, with the STM operating at 16 K, we measured the tunneling current as a function of time (Fig. 2.6) after turning off the z-piezo feedback, thus allowing the tip-sample distance  $z$  to be modulated by the external mechanical/acoustical noise. The tunneling current in Fig. 2.6 clearly shows periodic spikes with a period of  $\sim 0.42$  s, matching that expected for the fundamental frequency of the CCC (2.4 Hz). The typical amplitude of each spike is on the scale of  $\sim 16$  pA, a  $\sim 4\%$  correction to the total current. We estimate the corresponding noise-induced variation in  $Z$  by measuring the relationship between the tunneling current and  $Z$  at a fixed bias voltage (Fig. 2.6(c)). Using the found exponential relation, we find that a  $\sim 4\%$  variation in current should produce a 1.5 pm variation in  $Z$ .

---

**FIG. 2.6.** Quantification of the CCC-induced noise in the tunneling current.

(a) Tunneling current as a function of time (gray curve,  $z$ -feedback turned off), with the CCC operating at 15 K. To more clearly show the mechanical component of the CCC-noise, the current was measured with a low-pass filter with a corner frequency of 250 Hz. Despite the spike-like shape of the CCC-noise, only a limited number of higher harmonics with frequencies up to  $\sim 19$  Hz are distinguishable in the Fourier spectra of the tunneling current [Fig. 2.6(b)], which means that the CCC mechanical noise in Fig. 2.6(a) is not affected by the 250 Hz filter. The dark blue curve, obtained by numerical filtering of the tunneling current data, serves as a guide to the eye. (b) Fourier transform of the tunneling current showing the overtones of the CCC fundamental frequency ( $\sim 2.4$  Hz) at 4.76, 7.16, 9.56 and 16.73 Hz. (c) Exponential dependence of the tunneling current on  $Z$ . Tunneling set point used: 1 V, 410 pA.



This is a small number as compared to the atomic corrugations observed in Fig.5, explaining the lack of CCC-induced noise features in our STM images.

corrugations observed in Fig. 2.5, explaining the lack of CCC-induced noise features in our STM images.

### **Scanning Tunneling Spectroscopy**

STS measurements were carried out using the lock-in technique, with the modulation frequency typically in the range from 500 to 1000 Hz. With typical lock-in time constants being on the scale of at least a few hundred milliseconds, the lock-in signal is not expected to be very sensitive to the small current noise generated by the CCC, due to its low frequency of 2.4 Hz, even though higher harmonics (up to  $\sim 19$  Hz) are distinguishable in the Fourier spectra of the tunneling current (Fig.2.6(b)). This expectation is universally corroborated by the STS spectra measured for several nanoscale and molecular materials including: carbon nanotubes, PbS and CdSe quantum dots, and oligothiophene molecules. As a representative example of STS measurements, here we show a spectrum of a carbon nanotube deposited on the Au(111) surface (Fig.2.7). The STS spectrum of the nanotube clearly shows the first and second Van Hove singularities visible both in the valence and conduction bands, with the bandgap being  $\sim 1.3$  eV. Both forward and backward sweeps are presented showing reproducibility of the data.

### **Spatial drift analysis**

One of the critical specifications of a spectroscopic STM is its intrinsic rate of spatial drift: many types of STM-based spectroscopic measurements require extended data acquisition, which makes results sensitive to spatial drift on the atomic scale. Examples

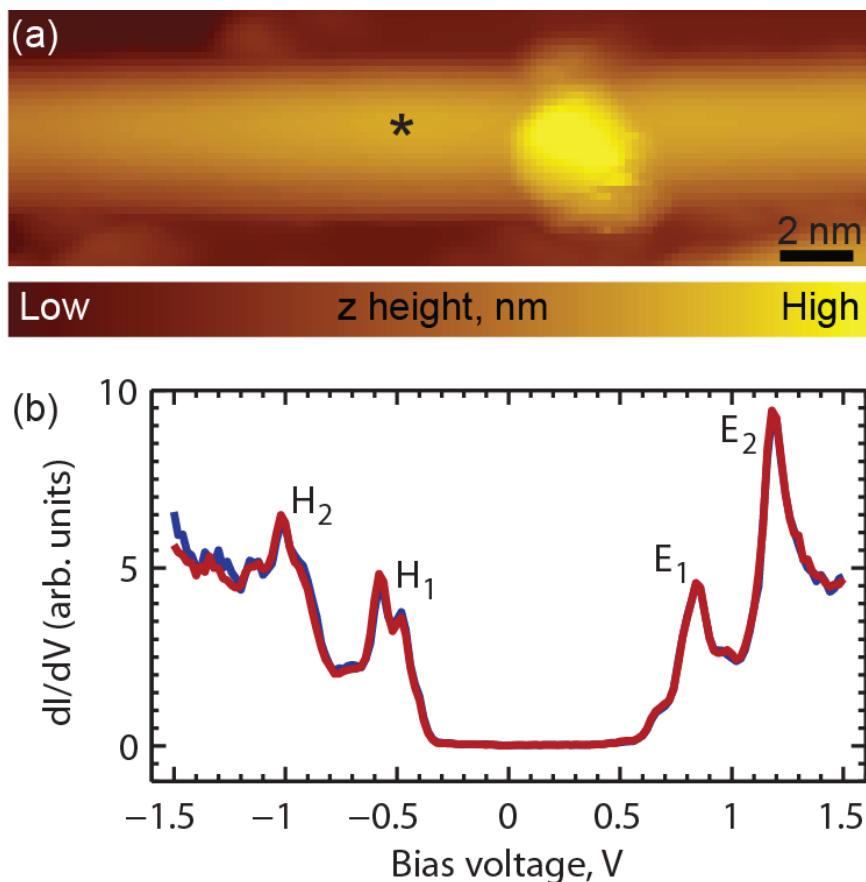


**FIG. 2.7.** STS spectroscopy of a single-wall carbon nanotube. (a) STM image of the nanotube. (b) Two STS spectra measured in one sweep from -1.5 V to 1.5 V (red curve) and back to -1.5 V (blue curve). The spectra were measured in the location shown by an asterisk in (a). The peaks observed in (b) are identified as Van Hove singularities associated with the valence (peak  $H_1$ ) and conduction (peak  $E_1$ ) bands. Higher order bands  $H_2$  and  $E_2$  are also observed. The STS spectra were obtained by measuring differential conductance,  $dI/dV$ , using the lockin-technique with a modulation of 20 mV. Tunneling set point: 1.5 V, 0.1 nA. Acquisition time: 2 minutes per spectrum.

of such spectroscopic measurements are the Inelastic Tunneling Spectroscopy,<sup>23</sup> Scanning Tunneling Luminescence,<sup>15</sup> or simply detailed mapping of STS spectra of individual molecules. To quantify the typical rates of spatial drift in our STM, we compared STM images taken over the course of 120 hours (images not shown).

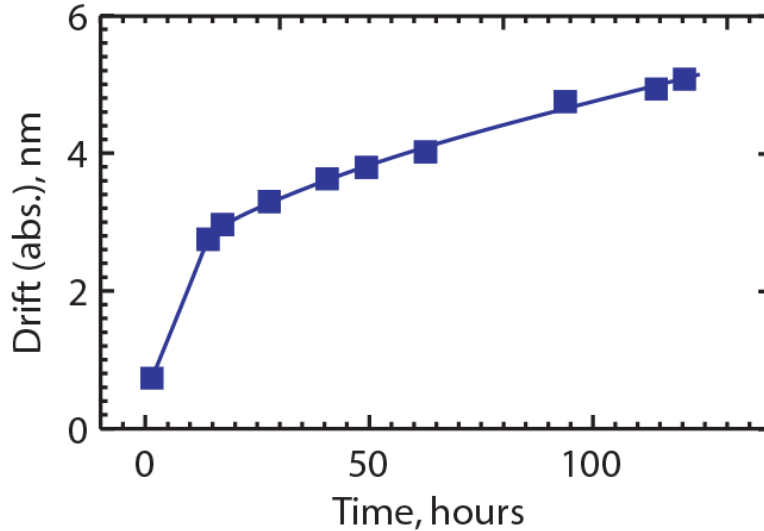


**FIG. 2.8.** X-Y spatial drift as a function of time. The drift was calculated by comparing STM images of the same area.

Fig. 2.8 shows that the lateral drift (caused primarily by the piezo creep after moving by 40 nm into a new area) slows down dramatically over the period of the first 15 hours, and reaches a small steady drift rate of 0.18 Å/hour after the first 30 hours.

## 2.5. Conclusions

The atomically-resolved data collected using the new STM demonstrate, for the first time, the feasibility of combining an ultra-high vacuum STM instrument with a closed-cycle cryostat for achieving near-liquid helium temperatures necessary for the optimal performance of the spectroscopic mode of STM, Scanning Tunneling Spectroscopy. The use of a closed-cycle cryostat eliminates costs associated with liquid-helium, and removes limitation on the durations of individual experiments. The quality of the collected data shows that the new STM is functionally equivalent to the existing high-performance cryogenic STM systems. Additionally, the STM spatial drift rate may be further reduced by using active stabilization of the scanner temperature with a feedback-



controlled heater. The combination of a virtually unlimited experiment duration and reduced spatial drift afforded by the new design will enable significantly more detailed spectroscopic investigations of samples that require extended characterization times. This, for example, includes a wide variety of samples important for nanoscale materials science, because nanoscale materials (quantum dots, carbon nanotubes, nanowires, thin films, etc) often exhibit pronounced structural or compositional inhomogeneities.

## **2.6. Bridge to Chapter III**

In following chapters the new instrument will be applied to study several classes of materials. The materials were chosen using two principles. First is to select materials that are difficult to research with conventional STM, and hence not enough studies in real space on single-particle scale had existed. Second is to choose materials promising for the development of future electronic devices, organic molecular electronics and nano-electronics. Unique characteristics of STM-UO allowed detailed investigations of local electronic structure using 1-D and 2-D STS spatial mapping and helped to reveal important microscopic mechanisms, that govern properties of these materials, therefore making progress towards better understanding of their physical and chemical properties, and future use in technological applications.

# CHAPTER III

## VIBRATIONAL EXCITATION IN ELECTRON TRANSPORT THROUGH CARBON NANOTUBE QUANTUM DOTS

This chapter by Dmitry A. Kislitsyn, Jason D. Hackley, and George V. Nazin has been previously published under the same title in *The Journal of Physical Chemistry Letters* **5**, 3138–3143 (2014). Copyright © 2014 American Chemical Society.

### 3.1. Introduction

Electron transport in single-walled carbon nanotubes (SWCNTs) is extremely sensitive to environmental effects. SWCNTs experiencing an inhomogeneous environment are effectively subjected to a disorder potential, which can lead to localized electronic states. An important element of the physical picture of such states localized on the nanometer-scale is the existence of a local vibronic manifold resulting from the localization-enhanced electron-vibrational coupling. In this report, Scanning Tunneling Spectroscopy (STS) is used to study the quantum-confined electronic states in SWCNTs deposited on the Au(111) surface. STS spectra show the vibrational overtones identified as D-band Kekulé vibrational modes and K-point transverse out-of plane phonons. The presence of these vibrational modes in the STS spectra suggests rippling distortion and dimerization of carbon atoms on the SWCNT surface. The present study thus, for the

first time, experimentally connects the properties of well-defined localized electronic states to the properties of their associated vibronic states.

### **3.2. Background**

Semiconducting single-walled carbon nanotubes (SWCNTs) are a promising material with unique photophysical<sup>1,2</sup> and electronic properties<sup>3,4</sup> which are, however, easily masked by interactions with the nanotube immediate environment. An important example of this environmental sensitivity is electron transport through SWCNTs, where environmental effects have been shown to be responsible for charge carrier scattering,<sup>5-7</sup> localization,<sup>8,9</sup> and random-telegraph-signal noise.<sup>10,11</sup> These effects have been attributed to the existence of charge traps localized in the nanotube vicinity, inferred from the marked spatial modulations of electrostatic potentials observed using scanning-gate microscopy<sup>12,13</sup> and scanning photovoltage microscopy.<sup>5</sup> Despite the insights obtained using these techniques, their spatial resolution is limited (10 nm for scanning probe techniques), which leaves the effects of shorter-scale disorder largely unexplored. Short-scale disorder is highly relevant to optoelectronic applications because optical excitation can produce photo-ionized charges transiently trapped in the SWCNT vicinity, a scenario suggested by blinking and spectral diffusion of SWCNT photoluminescence,<sup>14</sup> and by scanning photovoltage measurements.<sup>5</sup> Trapped charge would lead to the simultaneous creation of an effective potential barrier for one type of charge carriers (electrons or holes), and a potential well for the other type of charge carriers. While the influence of the former on charge transport is relatively well-understood,<sup>15</sup> the impact of a potential well is difficult to predict. Due to the electron-phonon coupling, the electronic states localized in the well can be expected to produce a manifold of local vibronic states

sensitive to the degree of localization. Such local vibronic states would have a direct impact on electron transport because they would mediate charge transfer across the localized electronic states.

### **3.3. Experimental details**

Experiments were carried out in a home-built ultra-high vacuum (UHV) cryogenic STM system. All imaging and spectroscopic measurements were carried out at a temperature of 15 Kelvin using electrochemically-etched silver tips. SWCNTs (obtained from Sigma-Aldrich) were deposited on Au(111)/mica substrates using the in-vacuum “dry contact transfer” (DCT) method, analogous to the approach demonstrated recently in other STM studies of carbon nanotubes.<sup>16,17</sup> Figure A1 (Supporting Information in Appendix A) shows representative STM images of several SWCNTs on a Au(111) surface.

### **3.4. Results and discussion**

We used Scanning Tunneling Spectroscopy<sup>18</sup> (STS) to study, for the first time, the electron-phonon coupling for electronic states localized in short segments of semiconducting SWCNTs. STM imaging of SWCNTs deposited on the Au(111) surface (see Experimental Methods) shows SWCNTs in a variety of environments. STS of SWCNTs adsorbed on Au(111) terraces (Figure A1) shows relatively spatially-uniform density of states (DOS) consistent with those reported in literature: the spectra are dominated by Van Hove singularities associated with the electronic band onsets.<sup>19,20</sup> Due to the presence of non-SWCNT material in the SWCNT-containing powder used for deposition, a significant fraction of SWCNTs in our experiments show unidentified

material in the nanotube vicinity. This material can locally prevent nanotubes from making extended contact with the surface resulting in height variations such as that shown in Figure A2a. The intermittent contact leads to spatially-modulated charge transfer interaction with the Au(111) substrate, capable of producing quantum-confined states.<sup>21</sup> In these conditions, the DOS-peaks found in the STS spectra of such SWCNTs (Figure A2b) contain fine structures with voltage-spacings reproducible for many different nanotubes (Figure A3). This suggests vibrational nature of these features, but to unequivocally establish their origin, it is useful to study examples of SWCNTs where electronic confinement is more pronounced, and the nanotube adsorption configuration is more well-defined. One such example corresponds to the situation where a SWCNT is suspended across an atomic step on the Au(111) surface, as schematically illustrated in Figure 3.1a. An STM image of a SWCNT adsorbed in this geometry is shown in Figure 3.1b. The topographic profiles of the nanotube and underlying surface (Figure 3.1c) show that the height change from point *L* to point *R* is identical to the height of an atomic step on the Au(111) surface. This allows us to conclude that the nanotube is in contact with the surface in points *L* and *R* assuming that the local electronic structures of the nanotube in these points are similar (this is corroborated by the STS measurements discussed below). The segment of the nanotube between these two points is relatively straight (as seen from Figure 3.1c), which suggests that at least a portion of this nanotube segment is not in direct contact with the substrate. As described in the following paragraph, the local electronic structure of this partially suspended nanotube shows the existence of strongly localized electronic states.

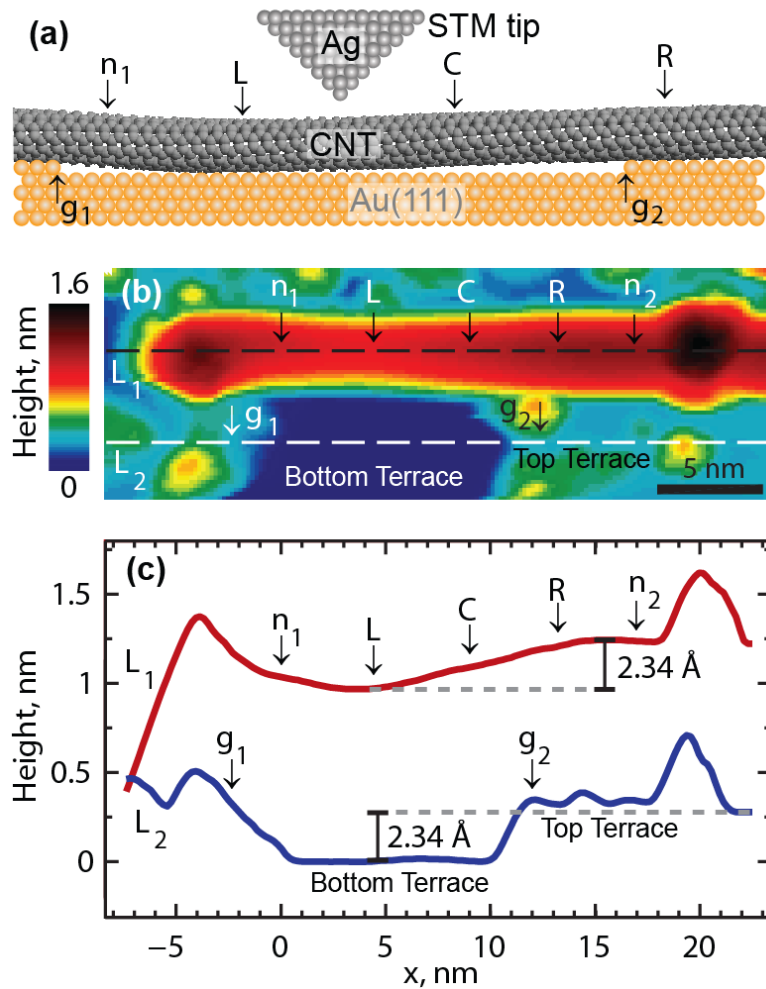


**Figure 3.1.** Geometry of a SWCNT adsorbed across a gap between two atomic steps on the Au(111) surface. **(a)** A schematic representation of the system under study (not to scale). **(b)** STM topography of the nanotube. Au(111) step edges are marked as  $g_1$  and  $g_2$ . To the left of point  $n_1$  and to the right of point  $n_2$  the nanotube contains defects, which manifest themselves as protrusions in the topographical image. Tunneling set point: 1.5 V, 10 pA. **(c)** Height profiles taken along lines  $L_1$  and  $L_2$  in (b).  $L_1$  corresponds to the nanotube top, and  $L_2$  to the gold substrate near the nanotube. The profile of the nanotube shows point  $L$  is  $2.34 \text{ \AA}$ , a number identical to the Au(111) step height ( $2.34 \text{ \AA}$ ), lower than point  $n_2$ , which suggests that the nanotube touches the bottom of the Au trench at point  $L$ . The nanotube profile between points  $L$  and  $R$  is relatively straight, which suggests that part of the nanotube is suspended above the substrate between these points.

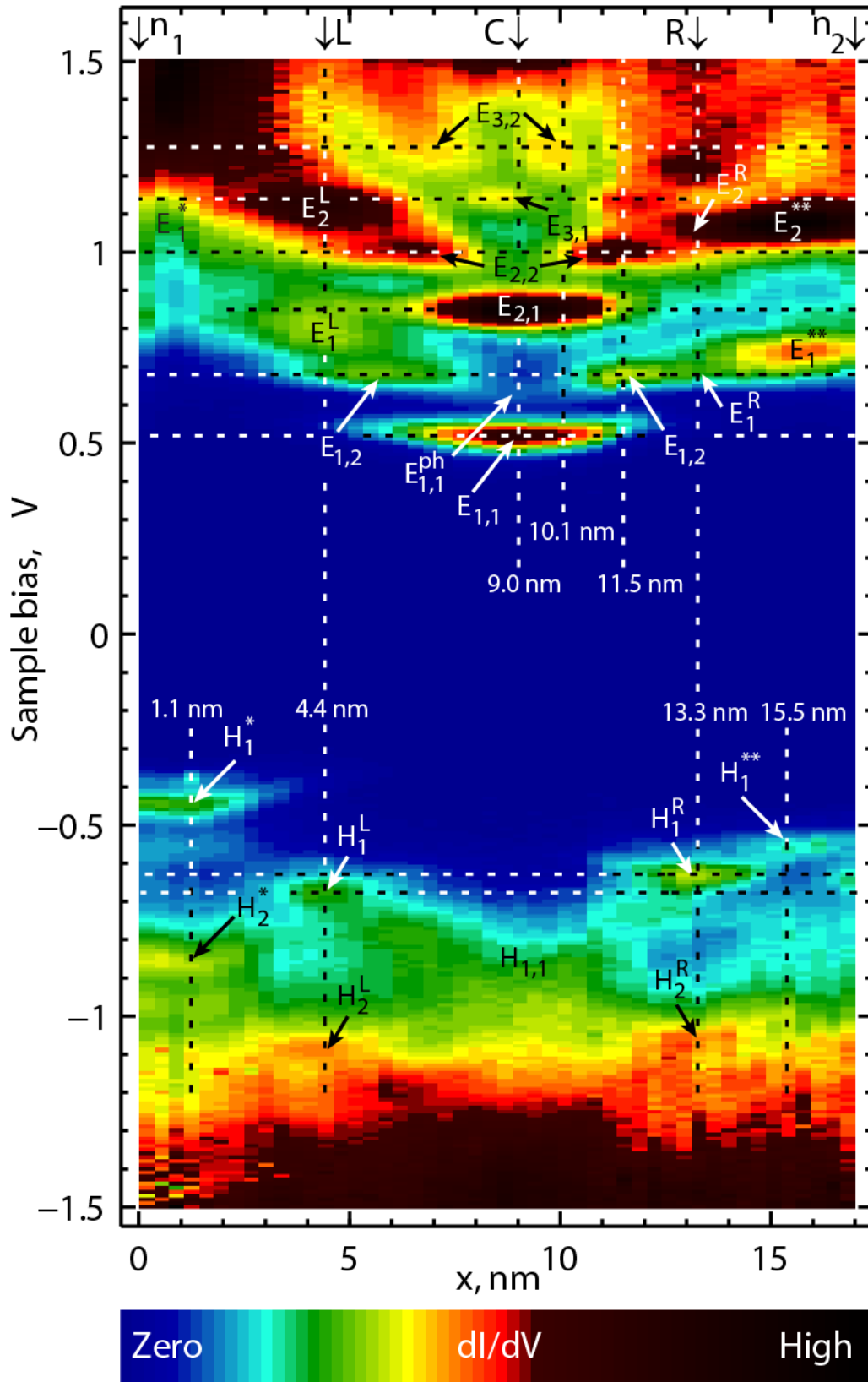
As shown in Figure 3.2, the voltage-dependent DOS of the nanotube from Figure 3.1b is considerably more structured than that of nanotubes on Au terraces (Figure A2b). However, for every spatial location mapped in Figure 3.2, the origins of the observed electronic states can be similarly traced to the same sequence of states, the most visible states being  $H_1$ -type (derived from the valence band),  $E_1$ -type (derived from the conduction band), and  $E_2$ -type (derived from the band immediately above the conduction band). For example, in the center section of the nanotube, these bands correspond to states  $H_{1,1}$ ,  $E_{1,1}$  and  $E_{2,1}$ . In points  $L$  and  $R$  (where the nanotube makes a contact with the Au surface), the electronic bands (levels  $E_n^L$  and  $E_n^R$  [these states coalesce with states  $E_n^{**}$  in Figure 3.2] together with their valence-band counterparts  $H_n^L$  and  $H_n^R$ ) are rigidly shifted up in energy by 200-250 meV, as compared to states  $H_{1,1}$ ,  $E_{1,1}$  and  $E_{2,1}$  in the center section of the nanotube. The band bending observed in points  $L$  and  $R$  is explained in a straightforward manner by the charge transfer<sup>22</sup> between the nanotube and Au substrate caused by the mismatch in their effective workfunctions.<sup>21</sup> This mismatch is clearly seen for the suspended section of the SWCNT, which is not subject to direct charge-transfer interaction with the Au surface. For the suspended section, the bias voltages corresponding to the onsets of conduction are asymmetric ( $\sim 0.5$  V for positive voltages and  $\sim -0.7$  V for negative voltages) suggesting that the SWCNT workfunction ( $4.8$  eV<sup>22</sup>) is  $\sim 100$  meV higher than the effective workfunction of the Au substrate. (This number is lower than the workfunction of the pristine Au(111) surface [ $5.3$  eV] apparently due to the direct proximity of a Au atomic step running along the SWCNT, as described in Figure A4 of Supporting Information in Appendix A).

The upshifts of electronic bands seen at points  $L$  and  $R$  are thus explained by partial electron transfer from the Au substrate to the nanotube, compensating somewhat for the mismatch of the workfunctions. Electronic levels  $E_1^*$  and  $H_n^*$  to the left of point  $L$ , as well as levels  $E_n^{**}$  and  $H_1^{**}$  to the right of point  $R$ , are shifted further up, as expected for a SWCNT section in a more extended contact with the Au surface. Overall, the bandgap of the nanotube does not change appreciably, and no new mid-gap states appear, suggesting that the spatially-dependent DOS in Figure 3.2 results primarily from band-bending.

---

**Figure 3.2.** STS signal (obtained by measuring differential conductance,  $dI/dV$ , using the lockin-technique) as a function of the  $x$  coordinate [identical to that in Figure 3.1c] and sample bias voltage. (STS signal serves as a measure of the local density of electronic states.) The spatial range corresponds to the part of line  $L_1$  contained between points  $n_1$  and  $n_2$  in Figure 3.1b and Figure 3.1c. Positive voltages correspond to unoccupied electronic states, while negative voltages correspond to occupied states. Vertical dashed lines at  $x = 4.4 \text{ nm}$  and  $13.3 \text{ nm}$  (corresponding to points  $L$  and  $R$  in Figure 3.1) indicate positions of the nanotube contact with the Au substrate where the nanotube electronic bands are bent due to the charge transfer between the nanotube and Au. [The charge transfer is caused by a workfunction mismatch.] These points of contact reveal themselves through the appearance of shifted electronic levels  $E_n^L$  (and  $H_n^L$ ) and  $E_n^R$  (and  $H_n^R$ ), as compared to the bands in the region between points  $L$  and  $R$ . The region in between points  $L$  and  $R$  ( $x = 4.4 \text{ nm}$  and  $13.3 \text{ nm}$ ) forms a quantum dot (QD) with three sets of particle-in-a-box states  $E_{1,n}$ ,  $E_{2,n}$  and  $E_{3,n}$  ( $n=1, 2$ ). All QD energy levels are marked with horizontal dashed lines. Electronic levels  $E_1^*$  and  $H_n^*$  to the left of point  $L$ , as well as levels  $E_n^{**}$  and  $H_1^{**}$  to the right of point  $R$  are shifted further up. All data were measured along the nanotube centerline. Tunneling set point: 1.5 V, 0.1 nA.





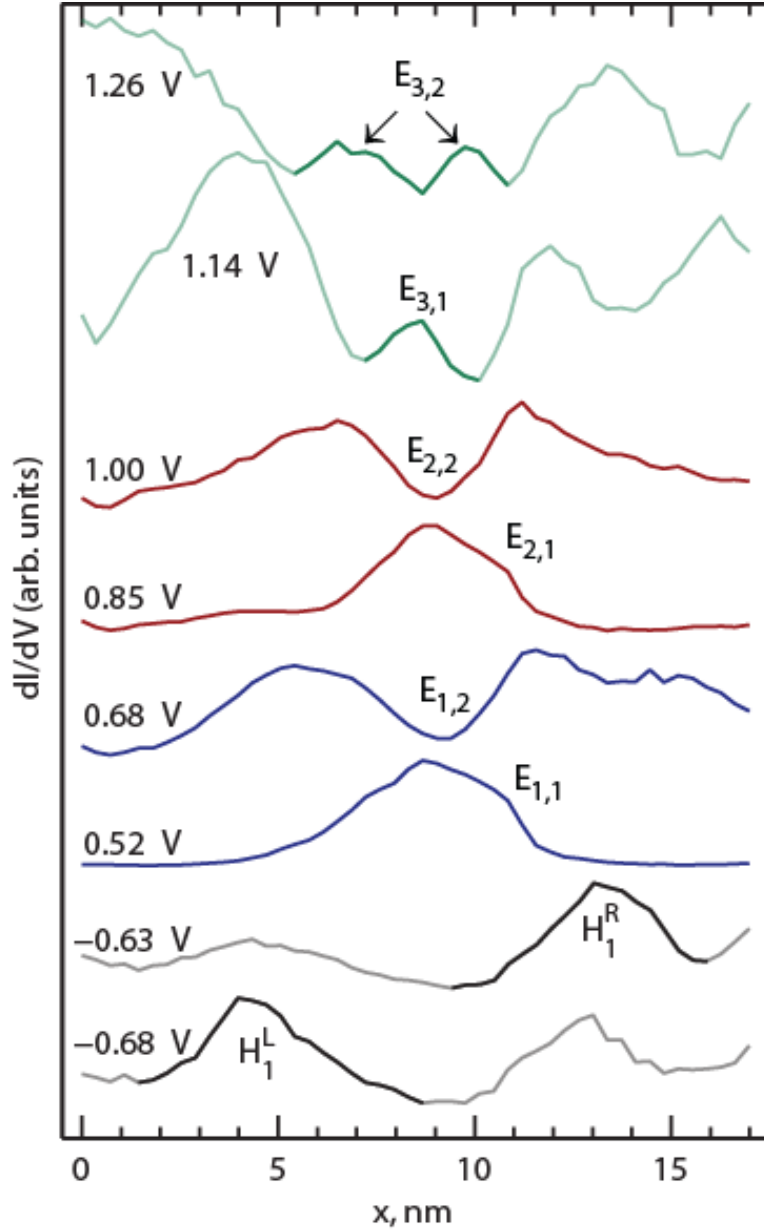


**Figure 3.3.** Cross-sections of the data from Figure 3.2 along the horizontal dashed lines showing the spatial behavior of  $E_{m,n}$  states of the QD from Figure 3.2. Spatial distributions of states  $E_{1,1}$ ,  $E_{2,1}$  and  $E_{3,1}$  show single maxima in the QD center, whereas states  $E_{1,2}$ ,  $E_{2,2}$  and  $E_{3,2}$  each show a node in the QD center. States  $H_1^L$  and  $H_2^R$  are more strongly localized as compared to the QD states  $E_{m,n}$ . Individual cross-sections are offset for clarity.

Electrons propagating along the suspended part of the nanotube are repelled by the potential-barriers caused by local band bending in points  $L$  and  $R$ , which results in electron confinement and formation of a quantum dot (QD) in the suspended section of the nanotube. The electron confinement is easily identifiable in Figure 3.2, with three sets of particle-in-a-box states  $E_{1,n}$ ,  $E_{2,n}$  and  $E_{3,n}$  ( $n=1, 2$ ) derived from three different electronic bands  $E_1$ ,  $E_2$  and  $E_3$  (states derived from band  $E_3$  are only visible in the suspended section of the nanotube, apparently due to the enhanced DOS produced by the confinement). The spatial behavior of these states is further clarified in Figure 3.3: spatial distributions of states  $E_{1,1}$ ,  $E_{2,1}$  and  $E_{3,1}$  show single maxima in the QD center, whereas states  $E_{1,2}$ ,  $E_{2,2}$  and  $E_{3,2}$  each show a node in the QD center. This spatial structure identifies states  $E_{1,1}$ ,  $E_{2,1}$  and  $E_{3,1}$  as ground electronic states of the three progressions, while states  $E_{1,2}$ ,  $E_{2,2}$  and  $E_{3,2}$  correspond to single-node excited states. Each of the three state progressions is truncated at  $n=2$ , because only these states lie lower in energy than the height of the confining potential ( $\sim 200$  meV, estimated from  $E_1^R - E_{1,1}$ ). States  $E_n^L$  and  $E_n^R$  as well as states  $H_n^L$  and  $H_n^R$  are more strongly localized than the QD states (the spatial extents of states  $H_1^L$  and  $H_1^R$ , somewhat exaggerated by the tip-convolution effects, are shown in Figure 3.3, bottom curves), which means that single-node excited states associated with states  $E_n^L$ ,  $E_n^R$ ,  $H_n^L$  and  $H_n^R$  cannot be observed because these states cannot be confined by the band bending observed in Figure 3.2. Indeed, due to their localized nature, such states would have to lie higher in energy than those of  $E_{1,n}$  and  $E_{2,n}$ , above the confining potential barrier.

Close inspection of spectroscopic peaks associated with individual electronic states reveals fine structure, which is particularly pronounced for the localized occupied

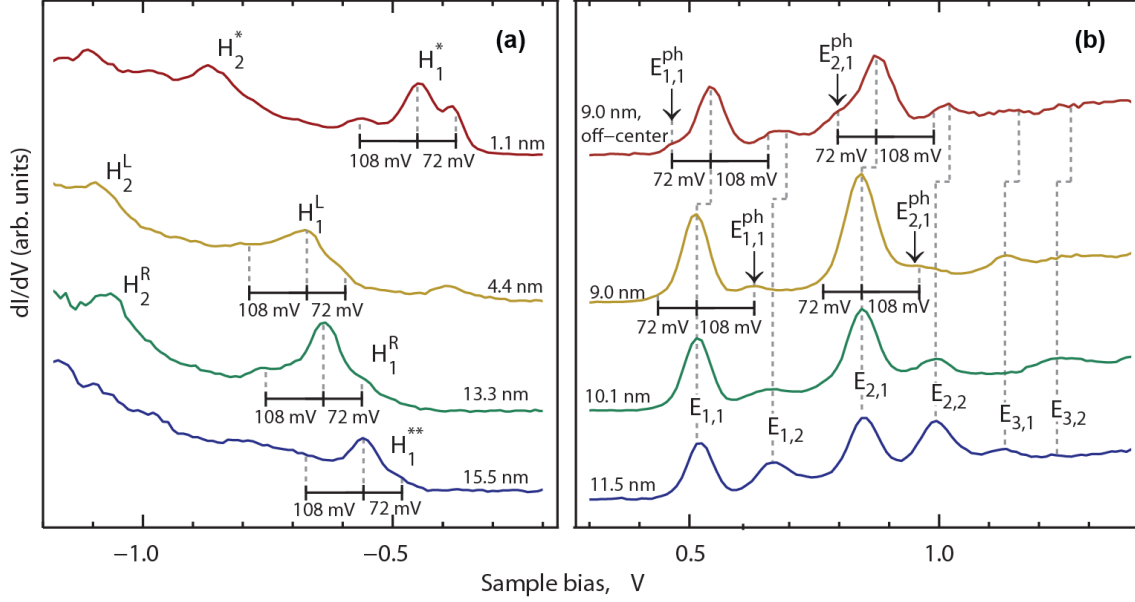


**Figure 3.4.** Cross-sections of the data from Figure 3.2 taken along the vertical dashed lines in Figure 3.2, showing DOS as functions of the sample bias voltage (the corresponding  $x$ -coordinates of these cross-sections are also shown). Individual cross-sections are offset for clarity. All spectra were measured along the nanotube centerline except the top curve in (b). **(a)** Occupied states that correspond to several distinct locations where the nanotube makes contact with the Au substrate. The onset of each spectrum shows a peak accompanied by two overtones (seen either as peaks or shoulders). For all spectra, the lower energy overtone is  $\sim 72$  mV below the main peak, whereas the higher energy overtone is  $\sim 108$  mV above the main peak. **(b)** Unoccupied states. In addition to three spectra measured roughly on top of the nanotube, a spectrum measured at  $x = 9$  nm slightly away from the nanotube centerline is also shown (top curve, all features contained in this curve are upshifted due to the larger fraction of the bias voltage dropped across the nanotube diameter). The manifold of  $E_{m,n}$  states is seen at positive voltages as peaks. Similarly to the occupied states in (a), states  $E_{1,1}$  and  $E_{2,1}$  contain fine structure, which is most clearly seen for the two spectra measured at  $x = 9$  nm: the top curve shows overtones at  $\sim 72$  mV below the corresponding  $E_{1,1}$  and  $E_{2,1}$  peaks; for the spectrum measured along the nanotube centerline (second from top) the main  $E_{1,1}$  and  $E_{2,1}$  peaks are accompanied by a side-peak and a shoulder correspondingly, both  $\sim 108$  mV higher than the corresponding main peaks.

states, as shown in Figure 3.4a (states  $H_1^*$ ,  $H_1^L$ ,  $H_1^R$  and  $H_1^{**}$ ). The onset of each spectrum shows a central peak accompanied by two overtones on either side of the peak (these are seen either as peaks or shoulders). For all spectra, the lower energy overtone is  $\sim 72$  mV below the main peak, whereas the higher energy overtone is  $\sim 108$  mV above the main peak. Similarly to the occupied states in Figure 3.4a, fine structures are also observed for states  $E_{1,1}$  and  $E_{2,1}$  (Figure 3.4b). The fine structures of the  $E_{1,1}$  and  $E_{2,1}$  states are less pronounced than those of the occupied states in Figure 3.4a, but similar overtone spacings are observed, the visibility of these features being somewhat location-dependent:  $108 \pm 4$  meV overtones (seen as a side-peak for  $E_{1,1}$  and a shoulder for  $E_{2,1}$ ) are clearly observed on top of the nanotube (Figure 3.4b, second curve from the top), while the  $\sim 72 \pm 4$  meV overtones are more pronounced slightly away from the nanotube centerline (Figure 3.4b, top curve). States other than  $E_{1,1}$  and  $E_{2,1}$  may also possess vibrational structures, which may be obscured by the complex DOS pattern in Figure 3.2.

The similarity in the spacings of the fine features observed at both positive and negative voltages in Figure 3.4 suggests that these fine features are not of electronic origin – in that scenario one would expect the fine structures to be different because of the different extents of localization observed for these states (states from Figure 3.4a as contrasted to states  $E_{1,1}$  and  $E_{2,1}$ ). Indeed, Figure 3.3 shows that states  $H_1^L$  and  $H_1^R$  are more strongly localized than the QD states  $E_{m,n}$ , and the different degree of localization would have produced different electronic splittings. The fine structures observed in Figure 3.4 must therefore be associated with vibrational excitation, analogous to the results reported for the STS spectroscopy of individual molecules.<sup>23-26</sup>

Vibrational patterns typically observed in STS spectroscopy on individual molecules are closely related to the changes in the molecular geometry caused by the transition to a transiently charged molecular state (anionic or cationic, depending on the bias polarity) that occurs during an electron tunneling event.<sup>27</sup> The precise patterns could either follow Frank-Condon patterns for displaced oscillators,<sup>28</sup> or have more complex structures when the transiently charged molecular state shows Jahn-Teller activity.<sup>29, 30</sup> Spectra shown in Figure 3.4 can be analyzed analogously, since the electron confinement observed in Figure 3.2 effectively creates localized molecular-sized electronic orbitals inside the SWCNT.

To identify the types of vibrations that can be excited in electron tunneling through the quantum-confined nanotube states, we thus need to identify the nature of structural distortions occurring in the presence of an extra localized charge in the nanotube. Importantly, neutral species of very short (a few nanometers) SWCNTs are predicted to show a variety of structural distortions, the exact structure being sensitive to the nanotube chirality,<sup>31</sup> length,<sup>32</sup> diameter,<sup>33</sup> and termination.<sup>33</sup> In particular, calculations for finite-length armchair nanotubes (possessing finite non-zero bandgaps) have shown structures combining Clar and/or Kekulé patterns.<sup>32, 34</sup> Chainlike distortions appearing as trans-poly-acetylene chains oriented roughly along the nanotube axis were predicted for infinite chiral nanotubes.<sup>31</sup> Similar bond alternations in polycyclic aromatic hydrocarbon molecules are argued to be related to the “distortivity” of  $\pi$ -electrons working against the stabilizing influence of  $\sigma$ -bonds,<sup>35</sup> which tends to result in Kekuléan distortions.<sup>36</sup> Such distortions can be generally expected to be more pronounced for more strongly localized states, with bond alternation on the scale of  $\sim 2$  picometers expected for

short achiral<sup>37</sup> and chiral<sup>38</sup> tubules (a few to several nanometers in length). In addition to the bond alternation, a short-range rippling-type of distortion of SWCNT surfaces was also found to occur in theoretical calculations.<sup>38</sup>

In contrast to neutral SWCNTs, calculations of anionic species for short tubules show significantly reduced bond alternation,<sup>37</sup> which can be interpreted in terms of the reduced “distortivity” of  $\pi$ -electrons in this state. Similar results were also obtained for the excitonic states in chiral nanotubes.<sup>38</sup> We therefore expect a similar behavior in the present case: a reduction of the overall local deformation of the nanotube for the charged state of the QD.

To identify the nature of vibrational modes contained in the spectra of Figure 3.4, we need to convert the voltage scale to the correct energy scale by taking into account the finite voltage drop inside the SWCNT. As shown in the discussion following Figure A5 (Supporting Information in Appendix A), the average potential inside the nanotube is  $\sim 10 \pm 1\%$  of the total bias voltage, so that the correct energy scale is calculated for the present system by multiplying the total applied voltage by a factor of  $0.9 \pm 0.01$ . This gives rescaled peak spacings of  $65 \pm 4$  meV and  $103 \pm 4$  meV for the two vibrational overtones. The first energy is equivalent to  $518 \pm 32$   $\text{cm}^{-1}$ , which can be explained by the presence of a rippling deformation of the QD-CNT surface, analogously to the short-range rippling deformation found in the calculated geometries of chiral SWCNTs.<sup>38</sup> Indeed, the found energy is close to the  $559$   $\text{cm}^{-1}$  energy of the transverse out-of-plane phonons in graphene at the K-point of the Brillouin zone (nominal optical and acoustical branches intersect at this point),<sup>39</sup> which could generate rippling with a spatial periodicity determined by the K-point wavevector.

To identify the phonon mode associated with the higher-energy sideband, we calculate the corresponding vibrational energy as  $65 + 97 \text{ meV} = 162 \pm 6 \text{ meV}$  (assuming that the onsets of conduction in our spectra correspond to zero-phonon peaks). This is equivalent to  $1296 \pm 48 \text{ cm}^{-1}$ , which is close to  $1378 \text{ cm}^{-1}$ , the energy of the D-band Kekulé modes<sup>33</sup> calculated for the present nanotube, which has a skeletal diameter of  $\sim 0.7 \text{ nm}$ , based on the measured topographic height of  $\sim 1.0 \text{ nm}$  (Figure 3.1c). Both of the found vibrational energies are red-shifted with respect to the corresponding expected values, which could be partially explained by the reduced bond order of the cationic and anionic states of the nanotube QD observed in the STS spectra of Figure 3.2 and Figure 3.4. The presence of Kekulé modes in our spectra suggests a Kekuléan in-plane dimerization of carbon atoms on the nanotube surface localized on and around the QD section of the nanotube.

In addition to the identified K-point-transverse out-of plane-phonons and Kekulé modes, other unresolved modes are likely present in the spectra of Figure 3.4. In particular, excitation of low energy modes are possible, including the radial breathing mode,<sup>40</sup> and center-of-mass motion perpendicular to the Au(111) surface,<sup>28</sup> which in the present case would involve bending of the nanotube. Excitation of these, as well as other low energy and/or weakly coupled modes, is likely the cause of the substantial widths of peaks in the spectra of Figure 3.4.<sup>25</sup> Further, the spectra may also be affected by non-adiabatic effects resulting from the vibronic inter-valley coupling, analogously to the Jahn-Teller activity identified recently in STS spectra of porphyrin molecules.<sup>29, 30</sup>



### **3.5. Conclusions**

The present work sheds light on one of the fundamental mechanisms determining the influence of local disorder on electron transport through SWCNTs: Figure 3.2 suggests that the energetically sparse progression of localized electronic states, created in a short SWCNT segment by a disorder potential, would be out of resonance with the conduction band (or valence band) states of the rest of the nanotube. This means that resonant electron transmission through such SWCNT segments would have to occur through the vibrational overtones of the localized electronic states (or, more generally, vibronic states). The precise structure of the manifold of such vibronic states also determines the rate of energy relaxation for charges traversing the SWCNT segments with localized electronic states, which determines the dynamics of charge trapping/de-trapping.

### **3.6. Bridge to Chapter IV**

In the next chapter we will continue studies of localized states in another model one-dimensional system and influence of environment on its electronic structure. Different physical realization of such system is pi-conjugated organic molecules. We will concentrate on alkyl-substituted oligothiophenes with variety of oligothiophene backbone lengths. This new class of molecules was never studied with STM before and is interesting from both fundamental and technical points of view. We will use the full potential of STM-UO to apply STS spatial mapping to visualization of electronic states in real space, despite the challenges associated with requirement of low tunneling currents for these gentle molecules.

# CHAPTER IV

## ADSORPTION-INDUCED CONFORMATIONAL ISOMERIZATION OF ALKYL-SUBSTITUTED THIOPHENE OLIGOMERS ON Au(111): IMPACT ON THE INTERFACIAL ELECTRONIC STRUCTURE

This chapter by Benjamin N. Taber, Dmitry A. Kislitsyn, Christian F. Gervasi, Stefan C. B. Mannsfeld, Lei Zhang, Alejandro L. Briseno, and George V. Nazin has been previously published under the same title in *ACS Appl. Mater. Interfaces* **7**, 15138–15142 (2015). Copyright © 2015 American Chemical Society.

### 4.1. Introduction

Alkyl-substituted quaterthiophenes on Au(111) form dimers linked by their alkyl substituents and, instead of adopting the trans-conformation found in bulk oligothiophene crystals, assume cis-conformations. Surprisingly, the impact of the conformation is not decisive in determining the LUMO energy. Scanning Tunneling Microscopy and Spectroscopy of the adsorption geometries and electronic structures of alkyl-substituted quaterthiophenes show that the orbital energies vary substantially due to the local variations in the Au(111) surface reactivity. These results demonstrate that interfacial oligothiophene conformations and electronic structures may differ substantially from those expected based on the band structures of bulk oligothiophene crystals.

## 4.2. Background

Operation of electronic devices based on organic semiconductors depends, to a great extent, on the properties of interfaces between the external electrical contacts and organic materials. The interface electronic structure is a particularly important element of the physical picture of electron transport, and is often a result of a substantial contact-induced rearrangement of the local electronic structures of the molecules and electrode surfaces.<sup>1,2</sup> The conformational flexibility of many classes of organic semiconductors composed of conjugated polymers and oligomers presents an additional level of complexity: the sensitivity of the molecule-surface interaction to the molecular conformation in the interfacial layer<sup>3,4</sup> can lead to pronounced inhomogeneities of electron transport properties across the interface. These interfacial conformations are difficult to study using surface-averaged experimental techniques, and also present an excessively large phase space of possible conformers for theoretical simulations.

An important example of organic semiconductors where interfacial conformational effects may be significant is the wide class of materials related to oligothiophenes. Recent work on alkyl-substituted oligothiophenes has demonstrated that judicious synthetic placement of alkyl substituents improves molecular packing in the solid state, which enables better electronic coupling between individual molecules resulting in charge carrier mobilities up to  $6 \text{ cm}^2 \text{ V}^{-1} \text{ s}^{-1}$ .<sup>5</sup> A potential complication that may impact oligothiophene-based applications is that the relative flexibility of oligothiophene backbones has been found to lead to conformational polymorphism<sup>6,7</sup> resulting in variations of electronic properties in the solid state.<sup>8,9</sup> Similarly, effects of conformational polymorphism specific to interfaces may be expected to affect charge

transport properties in oligothiophene-based devices. This expectation is supported by several Scanning Tunneling Microscopy (STM) studies, which demonstrated that substituted oligothiophenes can show conformational polymorphisms,<sup>10-12</sup> as well as diverse self-assembly regimes caused by the presence of substituent groups.<sup>13, 14</sup> However, while conformation-resolved Scanning Tunneling Spectroscopy (STS) studies of substituted oligothiophenes adsorbed on graphite have been reported,<sup>13</sup> the effects of conformational polymorphism on the interfacial electronic structure have not been investigated.

### **4.3. Experimental details**

Experiments were carried out in a home-built ultra-high vacuum (UHV) cryogenic (closed-cycle cryostat-based) STM system incorporating a STM scanner from RHK Technology.<sup>15</sup> A Au(111)/mica substrate was prepared in situ by using multiple sputter/anneal cycles. 3,3''-Didodecyl 2,2':5',2'':5'',2'''-quaterthiophene (DDQT) molecules were prepared by Briseno et al.<sup>16</sup> DDQT molecules were deposited at ultra-high vacuum via in situ sublimation on to a clean Au surface. Scale was determined by atomic resolution of Au(111) lattice.

In constant-current mode, a scanning tunneling microscope (STM) can image the topography of a sample by recording the changes in z-height necessary for maintaining a constant tunneling current as the tip rasters across the surface of the sample. For scanning tunneling spectroscopy (STS), the STM is used in constant-height mode, with the STM tip held in a constant position (x, y, and z) while the applied bias is varied. In this work, STS measurements were carried out using the lock-in technique, with a modulation frequency of 570 Hz. This allows for the direct measurement of the differential

conductance ( $dI/dV$ ) of the sample at that spatial location, giving a measurement of the local density of states.<sup>17</sup>

#### 4.4. Results and discussion

This chapter includes the first report of a STS study of the electronic structures of substituted oligothiophenes adsorbed in different conformations on a model metal [Au(111)] substrate showing atomic-scale chemical interaction with adsorbed oligothiophenes. In our study, we used alkyl-substituted quaterthiophene (didodecylquaterthiophene, or DDQT in the following) containing a conjugated backbone composed of four thiophene rings and two alkyl chains attached to the backbone (see Figure 4.1 for models of molecular structure). The relatively short thiophene backbone of DDQT allows us to isolate the effects of short-range disorder on the electronic structure, with the backbone still being long enough for the quantum-confined frontier orbitals to be sufficiently close to the Fermi level of the Au substrate, and accessible to STS.

We used a STM to image DDQT molecules on the Au(111) surface in the regime of sub-monolayer molecular surface coverage, which revealed that the majority of molecules were self-assembled into pairs. The molecules in each pair were found to bind to each other by interdigitating substituent alkyl chains (Figure 4.1a). In these dimer-like structures, the molecules assumed the *cis*-conformation, with both alkyl chains lying on the same side of the quaterthiophene backbone (Figure 4.1a). Individual molecules were observed less frequently, and were primarily found in the *trans*-conformation, with the alkyl chains lying on the opposite sides of the quaterthiophene backbone (Figures 1b and c). This *trans*-conformation morphology of the quaterthiophene backbone is close to that found in macroscopic crystals of unsubstituted quaterthiophenes,<sup>18</sup> and is also analogous

to that found in DDQT crystals, where the terminal thiophenes are rotated by  $\sim 12^\circ$  out of plane with the rest of the backbone.<sup>16</sup> The alkyl chains in the majority of DDQTs typically formed angles of  $\sim 90^\circ$  with respect to the quaterthiophene backbone (Figures 1a, b and c). More rarely, individual *cis*-conformers were also observed (Figure 4.1d), which showed varied angles between the substituent chains.

The observed tendency of DDQT molecules to form *cis*-dimers suggests that at room temperature, DDQT molecules are free to migrate on the Au(111) surface until encountering other molecules [or Au(111) step edges]. Since very few DDQT monomers were found, dimerization driven by the DDQT alkyl chains must provide additional stabilization beyond the Au-thiophene interaction. Indeed, a substantial intermolecular “binding energy” originating from interaction of alkyl chains can be expected based on the fact that interaction energy of a pair of dodecane molecules is calculated to be in the range of 0.4-0.5 eV.<sup>19</sup> The fact that dimers formed from *cis*-conformers were primarily observed, (very few *trans-cis* dimers and *trans-trans* dimers were observed), further suggests that in molecular aggregates, torsional transformation of molecules between the *cis* and *trans* conformations leading to minimization of the overall energy of molecular aggregates must readily occur at room temperature. This scenario is supported by the fact that the terminal rings of oligothiophenes have a low energy barrier for rotation.<sup>20</sup>

Additional stabilization of *cis*-conformers is provided by the enhanced electrostatic interaction of *cis*-conformers (as compared to *trans*-conformers) with the substrate. This enhanced interaction arises from the non-zero molecular dipole moments (2.32 Debye for the *cis*-conformer versus 0.06 Debye for the *trans*-conformer—see Table B1), which interact with image charges at the metal surface.<sup>21</sup>

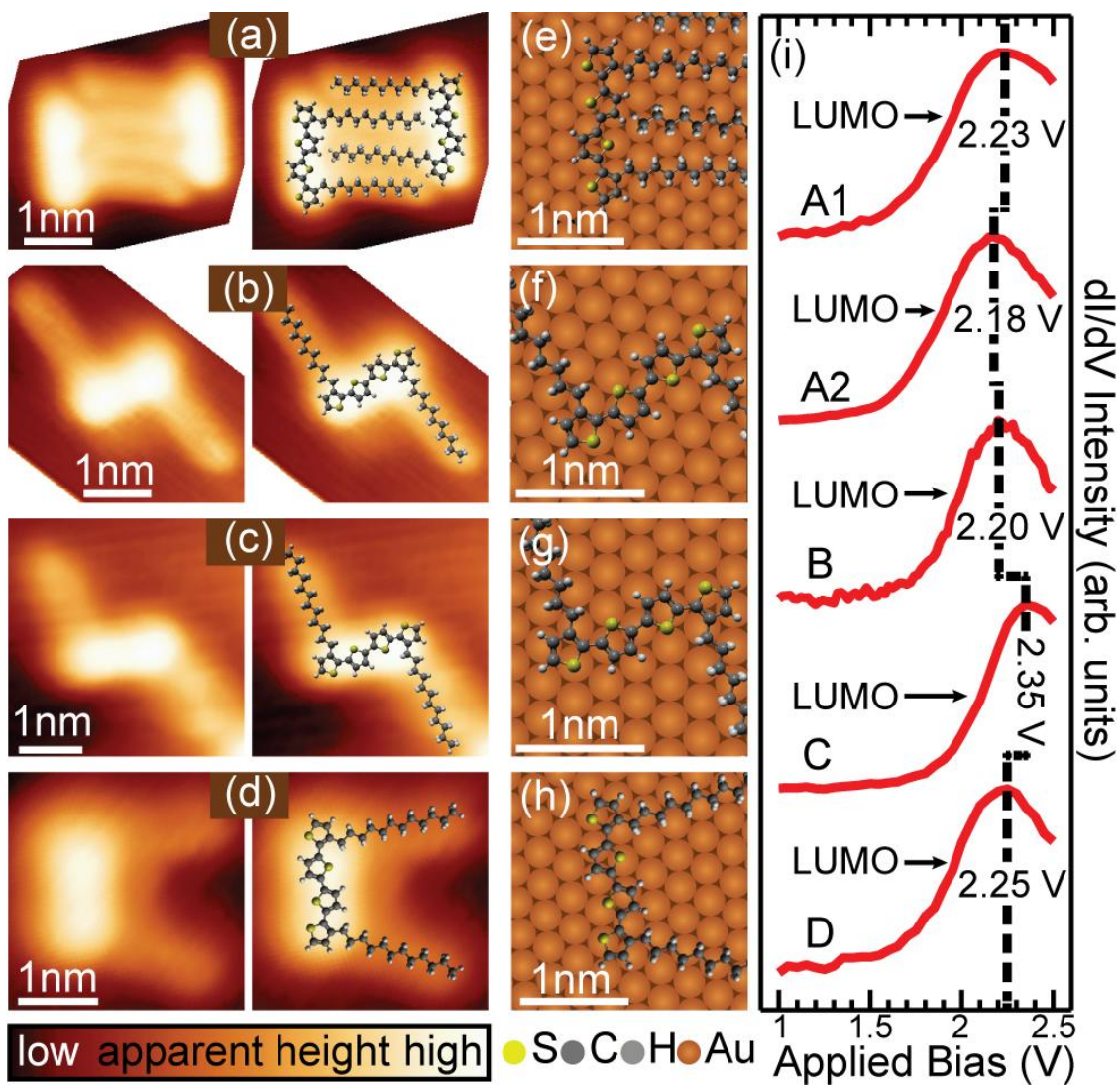


**Figure 4.1.** Adsorption configuration of DDQT molecules on Au(111). (a) STM image of two DDQT molecules in cis-conformation forming a dimer, with overlaid molecular structures. (b) And (c) STM images of DDQT molecules in trans-conformation, with overlaid molecular structures. (d) Same as (b) and (c) for an individual cis-molecule. (e)-(h) Models of DDQT backbone matched to the Au(111) surface lattice for adsorption configurations from (a)-(d), respectively. (i) STS of the LUMO state corresponding to the two molecules from (a) – curves A1 and A2, and molecules from (b), (c) and (d) – curves B, C, and D respectively. STM imaging was carried out at bias voltages of 100 mV and tunneling current of 5-50 pA.

Further inspection of STM images shows that thiophene backbones of the majority of observed molecules can assume three distinct orientations on the Au(111) surface (Figure 4.2). Specifically, in reference to the herringbone  $22 \times \sqrt{3}$  surface reconstruction features of Au(111), the backbones of all molecules were orthogonal to one of the three possible directions of the surface reconstruction herringbone ridges (these run along the three possible  $\langle 112 \rangle$  directions, see Figures 2d to f). The observed preferential orientations of the DDQT backbones can be rationalized by analyzing the oligomer-surface interaction in terms of the sum of interactions of individual thiophene units with the Au(111) surface. DFT calculations predict that binding of individual thiophene molecules to Au(111) results in adsorption configurations where the thiophene S atom binds directly on top of one of the surface Au atoms,<sup>22</sup> with other adsorption sites being up to 40 meV higher in energy.<sup>23</sup> The site-specific interaction is accompanied by a small charge transfer from Au surface to the S atom, which acquires an extra 0.08 e for the perpendicular (with respect to the surface plane) orientation of the thiophene ring, and 0.10 e for a nearly flat orientation forming a small angle with respect to the Au(111) surface.<sup>24</sup> These differences in the strength of interaction result in the nominally flat-lying orientation<sup>22</sup> being  $\sim 40$  meV more stable than the vertical orientation.<sup>23</sup> These predictions for individual thiophene molecules are consistent with STM imaging of DDQTs, which shows molecular profile heights of  $\sim 2$  Å, suggesting that the constituent thiophene rings are nearly flat on the Au(111) surface. [The flat adsorption geometry is also in accordance with previous results obtained for octithiophenes on Au(111) in the low-coverage regime.<sup>25</sup>]



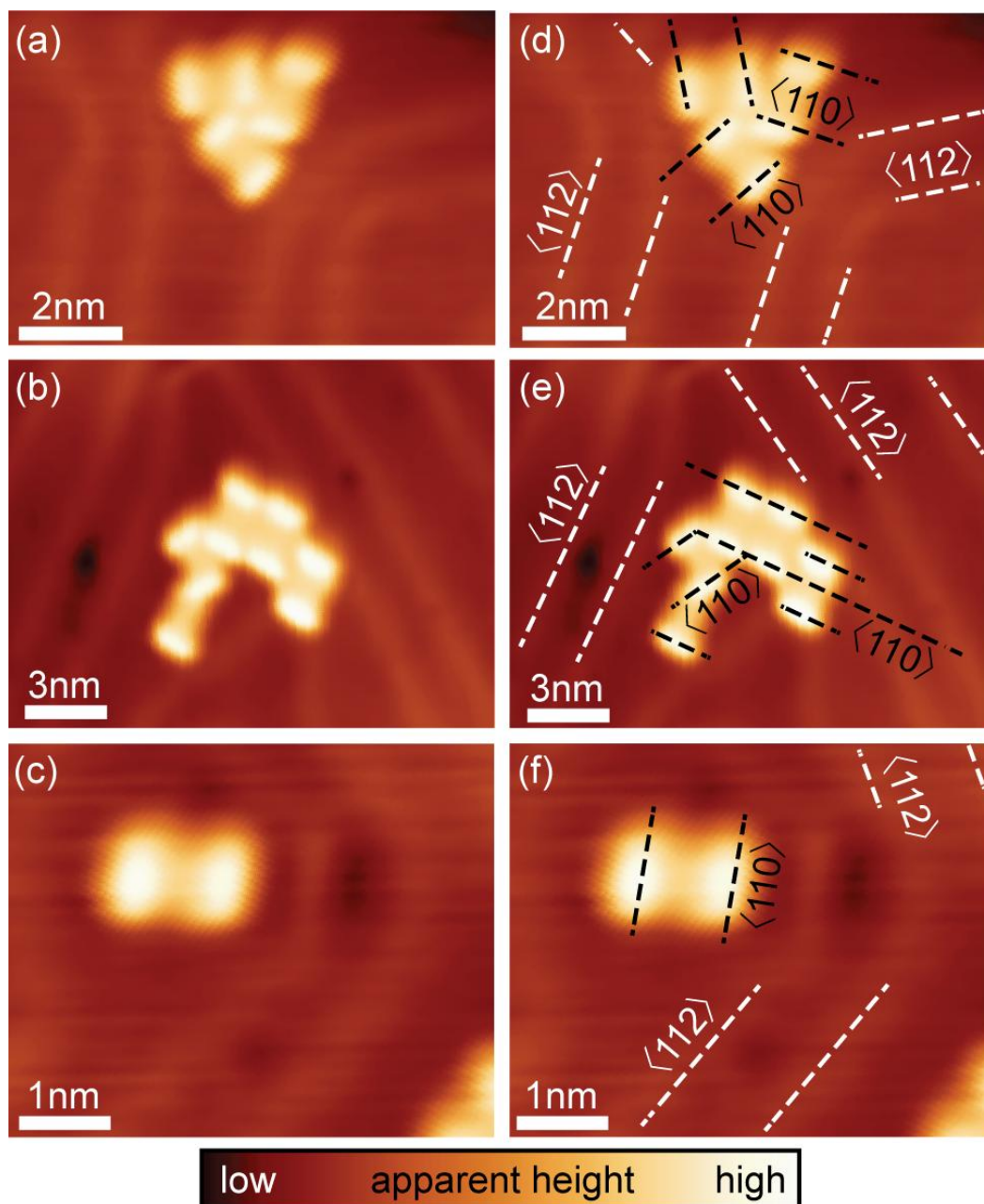


**Figure 4.2.** Registry of DDQT molecules with the underlying Au(111) surface. (a)-(c) STM images of DDQT molecules on Au(111) substrate. (d)-(f) Same as (a)-(c) but showing the molecular orientations and Au(111) crystallographic directions. The quaterthiophene backbones of DDQT molecules aligned along one of three  $\langle 110 \rangle$  directions of the Au(111) surface, perpendicular to Au(111) surface reconstruction ridges aligned primarily along the  $\langle 112 \rangle$  directions, as shown. STM imaging was carried out at bias voltages 0.1-1.0 V and tunneling currents 1-5 pA.

We expect that the site-specific interaction between the Au and S atoms described above should result in minimum-energy adsorption configurations of DDQT where the oligothiophene backbone is oriented as to allow the constituent S atoms to be in the direct vicinity of select Au atom top-sites. To qualitatively evaluate the possible DDQT/Au(111) adsorption configurations, we will thus focus on the placements of the S-atoms of the quaterthiophene backbone with respect to the Au(111) lattice. We first consider the two outermost S-atoms because this pair (as compared to other possible pairs of S-atoms) may be more easily matched to the Au(111) lattice (due to the larger separation between these S-atoms). In addition, the terminal thiophene rings are more torsionally flexible than the inner thiophene rings,<sup>20</sup> which may allow the terminal S-atoms to make better contact with the corresponding Au atoms. For the planar backbone structure of *cis*-quaterthiophene (*trans*-quaterthiophene) obtained using geometry optimization in the gas phase, the distance between the terminal S atoms is ~1.14 nm (1.19 nm), a very close match to 1.15 nm, which is equal to four Au lattice constants along the  $\langle 110 \rangle$  directions. Observation of molecular orientations parallel to the  $\langle 110 \rangle$  directions (Figure 4.2) is thus consistent with the expectation for the two terminal S atoms of every DDQT molecule to be located directly above individual Au atoms (Figures 1e to g). The question arises, however, if the geometries shown in Figures 1e to g are unique candidates for minimum-energy adsorption configurations based on our qualitative reasoning relying on the Au-S interaction. For example, by using the same reasoning, one can identify other backbone orientations where two of the four S-atoms are located at two different Au top-sites (Figure B1). As Figure B1 shows, such orientations are different from that of Figure 4.1e in that the latter orientation is the only

one where all four S-atoms are located in the direct vicinity of (different) Au top-sites, which means that this orientation should be the most stable. A similar distinction exists for the *trans*- versus *cis*-conformers aligned along the  $\langle 110 \rangle$  directions: the two inner S-atoms of *trans*-conformers are located near the Au three-fold hollow sites and bridge sites, which makes the *trans*-conformation less energetically favorable, consistent with the higher abundance of *cis*-conformers in STM images. The predominance of the *cis*-conformation may also be in part due to the better lattice-matching of the terminal S-atoms for the *cis*-conformation as compared to the *trans*-conformation (1.14 nm for *cis* versus 1.19 nm for *trans* matched to 1.15 nm corresponding to four Au lattice constants along the  $\langle 110 \rangle$  direction).

We note that despite the fact that intermolecular interaction via alkyl ligands is the main driving force for DDQT dimerization, this interaction does not noticeably affect the orientations of *cis*-conformers. This suggests that the interaction of alkyl ligands has a relatively weak dependence on orientation with respect to the Au(111) surface. This conclusion is supported by the fact that alkyl ligands in Figure 4.1 are aligned close to the  $\langle 112 \rangle$  directions rather than  $\langle 110 \rangle$  directions, as observed for alkanes self-assembled on Au(111).<sup>26</sup>

The presence of both *cis* and *trans* DDQT conformers in our STM images presents an opportunity to study the effects of torsional conformations on the oligothiophene electronic structure. To this end, we measured the local electronic structure of individual molecules by using Scanning Tunneling Spectroscopy (STS). In STS, the local electronic density of states (DOS) of individual molecules is quantified by measuring the derivative of the tunneling current  $dI/dV$  as a function of the bias voltage

that serves as the energy scale (see Supporting Information in Appendix B for further details).<sup>17</sup> STS spectra recorded on ~70 different DDQT conformers typically showed one well-resolved electronic state associated with the lowest unoccupied molecular orbital (LUMO) of DDQT, generally in the vicinity of 2.2 V (Figure 4.1i). Identification of molecular orbitals other than the LUMO is difficult due to the instability of DDQT ligands alkyl chains at higher voltages. This instability resulted in both motion and irreversible deformation of alkyl chains (Figure B2). At bias voltages comparable to that of the LUMO orbital, scission of the thiophene backbone was often observed (Figure B3), limiting molecular lifetime.

The obtained STS spectra (Figure 4.1i) allow us to make two unexpected observations. First, it is surprising that the LUMO energies for *trans* and *cis* conformations (measured using the same tip) can be very close (curves A2 and B in Figure 4.1i), despite the differences in their backbone structures. Indeed, density functional theory (DFT) calculations for planar quaterthiophenes predict the *cis*-LUMO to be ~30 meV higher than the *trans*-LUMO (Figure B4 and Table B1). Furthermore, molecules with nominally identical conformations (adsorption configurations) were found to have LUMO energies (measured using the same tip) differing by as much as 150 meV (for example, see curves A1 and A2 for the *cis* conformation, and curves B and C for *trans* conformation). These observations suggest that the energies of DDQT molecular orbitals are strongly affected by factors other than the apparent torsional conformation.

A possible explanation for the seemingly random variations of the observed LUMO energies is obtained through analysis of the locations of individual molecules on

the Au(111) surface. Indeed, the properties of the Au(111) surface are spatially modulated due to the presence of the herringbone  $22 \times \sqrt{3}$  surface reconstruction, which leads to variations in coordination of the surface Au atoms. For example, recent density-functional calculations of hydrogen and fluorine atoms adsorbed on Au(111) show that these atoms are more stable in the face-centered-cubic (fcc) areas, as compared to hexagonal-close-packed (hcp) areas.<sup>27</sup> In accordance with these predictions, we find that DDQTs adsorb primarily in the fcc regions of Au(111), rather than hcp areas (Figures 3a-c and B5). Further, similar preferential adsorption in the fcc areas was observed in STM studies of unsubstituted terthiophenes on Au(111).<sup>28</sup> In an analogous fashion, the spatially modulated coordination of the surface Au atoms can be expected to affect the Au-S interaction, and, consequently, the energies of DDQTs electronic orbitals. In line with these general expectations, we find that in our STS measurements, the LUMO energies of DDQT molecules are affected by proximity to hcp regions and reconstruction ridges. Specifically, as can be inferred from Figure 4.3, molecules located in the vicinity of the reconstruction ridges (molecules with black numbers in Figures 3a, b and c) exhibit LUMO peaks (black curves in Figure 4.3d) downshifted by up to ~100 mV as compared to molecules located further from the reconstruction ridges. A statistical analysis of LUMO energies determined from STS measurements for 68 molecules of both conformations (Figure B6) shows variations of the LUMO energies with a standard deviation of ~80 meV, which is considerable as compared to the ~30 meV energy difference between the *cis*- and *trans*-LUMOs obtained in DFT calculations (Table B1). Figure B6 shows that the average energy of *cis*-LUMOs is  $50 \pm 23$  meV higher than that of the *trans*-LUMO, consistent with the DFT calculations.

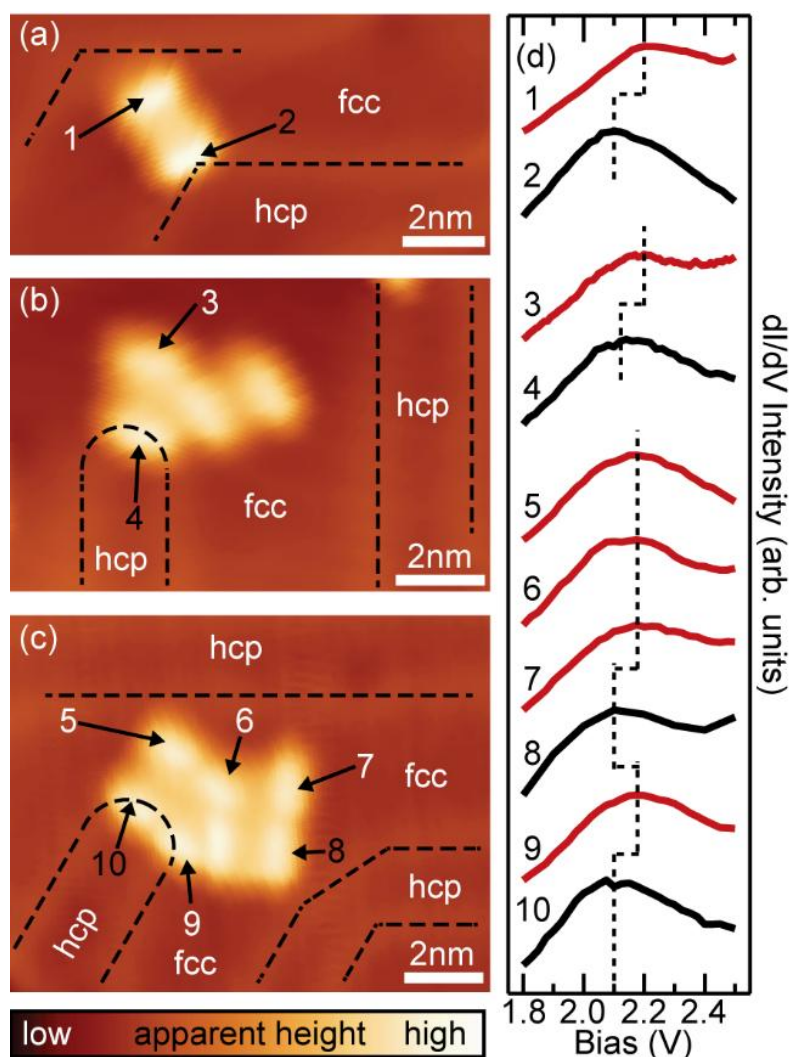


**Figure 4.3.** Correlation of DDQT adsorption location with LUMO peak energy. (a)-(c) STM topographies. Black dashed lines show the Au(111) reconstruction ridges. (d) STS spectra showing LUMO peaks for molecules in (a)-(c). Each numbered spectrum corresponds to a molecule appearing with the same number in (a)-(c). Molecules with black numbers in (a)-(c) are located closer to the reconstruction ridges than their neighbors. STS spectra of these molecules [black curves 2, 4, 8 and 10] in (d) show LUMO peaks downshifted by  $\sim 100$  mV in their respective groups of molecules (a), (b) and (c). Proximity of DDQT backbone to reconstruction ridges thus reduces the LUMO energy. STM imaging was carried out at bias voltages of 0.3-1.0 V and tunneling current of 5 pA.

While spatial variations in the surface reactivity clearly have a substantial effect on the LUMO energies, other, conformation-sensitive factors may also have significant contributions. Indeed, the varied matching of different conformers to the Au(111) lattice is likely to produce conformation-specific molecular structural relaxations and hybridization of molecular orbitals with the Au(111) states, which can both lead to conformation-specific orbital shifts.<sup>29</sup> For the same reasons, the overall Au-S interaction is likely to be different for *cis*- and *trans*-conformers resulting in different adsorption distances, which should, in addition to the factors noted above, affect the molecular orbital energies by altering the magnitude of image-potential screening.<sup>30</sup> Indeed, the adsorption distance of *cis*-conformers to the Au surface is likely smaller than that for the *trans*-conformers due to the better match to the Au(111) lattice (Figures 1a to c), and the much larger dipole (2.32 Debye for *cis* versus 0.06 Debye for *trans*, Table B1) interacting with its image in the Au surface.<sup>21</sup> The closer molecule-substrate distance, in turn, leads to a greater screening of the LUMO, which should result in a downshift of the orbital for *cis*-conformers.<sup>30</sup>

#### **4.5. Conclusions**

Our findings highlight the complexity of physical and chemical interactions at the interfaces of metals and organic semiconductors. The atomic lattice of the Au(111) predominately induces the *cis*-conformation of oligothiophene molecules that is very different from the *trans*-conformation found in bulk crystals. One can thus generally expect that in devices incorporating oligothiophene molecules and metal electrical contacts, the structure of the interfacial molecular layer may be entirely different from that of the molecular bulk of the device. The electronic structures of the molecules in the

interfacial layer can be expected to display differences caused by local atomic-scale variations of the surface reactivity, which may be caused by either surface reconstruction or the presence of polycrystalline facets at metal contacts. While the current chapter presents a direct visualization of this behavior, understanding the complex interplay between conformational variability and local reactivity, as well as their impact on the interfacial electronic structure, will require further studies.

#### **4.6. Bridge to Chapter V**

In the next chapter we will use STM to explore adsorption configurations of alkyl-substituted quaterthiophenes and the impact of surface coverage of molecules on their self-assembly, from diluted to high density concentration on the surface. This results in formation of ordered structure and drastic difference in molecular conformations, as compared to dilute molecular concentration. We will utilize STS spatial mapping to study electronic structure of the molecules in order to understand how it is affected by conformational diversity and differences in local molecular environments. It will be shown that molecules of identical apparent adsorption configurations can exhibit significant electronic differences. These results indicate the necessity for investigations of interface-induced transformations in the molecular electronic structure and its affect on charge transport in organic electronic devices.



# CHAPTER V

## COVERAGE-DEPENDENT SELF-ASSEMBLY REGIMES OF ALKYL-SUBSTITUTED THIOPHENE OLIGOMERS ON AU(111): SCANNING TUNNELING MICROSCOPY AND SPECTROSCOPY

This chapter by Dmitry A. Kislitsyn, Benjamin N. Taber, Christian F. Gervasi, Stefan C. B. Mannsfeld, Lei Zhang, Alejandro L. Briseno, and George V. Nazin has been previously published under the same title in *J. Phys. Chem. C* **119**, 26959–26967 (2015).  
Copyright © 2015 American Chemical Society.

### 5.1. Introduction

Charge transport in electronic applications involving molecular semiconductor materials strongly depends on the electronic properties of molecular-scale layers interfacing with external electrodes. In particular, local variations in molecular environments can have a significant impact on the interfacial electronic properties. In this study, we use Scanning Tunneling Microscopy and Spectroscopy to investigate the self-assembly regimes and resulting electronic structures of alkyl-substituted quaterthiophenes adsorbed on the Au(111) surface. We find that at dilute molecular concentrations, dimerized cis conformers were formed, while at higher concentrations corresponding to small fractions of a sub-monolayer the molecular conformation converted to trans, with the molecules self-assembled into ordered islands. At approximately half-monolayer

concentrations, the structure of the self-assembled islands transformed again showing a different type of the trans conformation and qualitatively different registry with the Au(111) lattice structure. Molecular distributions are observed to vary significantly due to variations in local molecular environments, as well as due to variations in the Au(111) surface reactivity. While the observed conformational diversity suggests the existence of local variations in the molecular electronic structure, significant electronic differences are found even with molecules of identical apparent adsorption configurations. Our results show that a significant degree of electronic disorder may be expected even in a relatively simple system composed of conformationally-flexible molecules adsorbed on a metal surface, even in structurally well-defined self-assembled molecular layers.

## **5.2. Background**

Over the last two decades, organic semiconductors have emerged as promising electronic materials for a wide range of applications including thin film transistors, light-emitting diodes, and photovoltaics.<sup>1-6</sup> Among other device-engineering aspects, the capability to control the properties of electrical contacts to organic materials in such devices is critical for efficient charge transport. To a large extent, the performance of electrical contacts is defined by the electronic structure at the interface of the electrodes and the organic material in question. Importantly, the interfacial electronic structure is difficult to predict a priori due to often substantial contact-induced rearrangement of the local electronic structures of both the organic material and electrode surfaces.<sup>7-10</sup> For organic materials composed of conformationally-flexible molecules and polymers, an additional level of complexity arises from the structural diversity resulting from conformation-sensitive molecular packing and molecule-metal interaction.<sup>11, 12</sup> The

resulting conformation-driven variations in electron transport properties are extremely difficult to understand using traditional sample-averaged experimental techniques that do not provide information about the local molecular conformational structure.

While problems described above are common for the majority of polymer- and oligomer based organic materials, oligothiophenes form a particularly important class of organic semiconductors where conformational effects are expected to be important. The well-defined structures of oligothiophenes allow growth of high-quality crystals with a low density of structural defects, which, in turn, enable charge carrier mobilities of up to  $6 \text{ cm}^2 \text{ V}^{-1} \text{ s}^{-1}$ .<sup>13</sup> Oligothiophenes have also been successfully used as hole-transport materials in organic photovoltaic devices,<sup>14, 15</sup> achieving power conversion efficiencies as high as 8.4%.<sup>16</sup> The structural flexibility of oligothiophenes has been shown to result in conformational polymorphism<sup>17, 18</sup> and variations in electronic properties in the solid state.<sup>19, 20</sup> Similar polymorphic effects can also be expected to play a role at molecule-metal interfaces, with potentially significant consequences for charge transport in oligothiophene-based devices.

Interest in oligothiophenes and poly-thiophenes as electronic materials has stimulated a number of studies of adsorption of oligothiophenes on a variety of conductive surfaces. Electronic structures of unsubstituted oligothiophenes have been studied using two-photon photoemission,<sup>21</sup> Scanning Tunneling Spectroscopy (STS),<sup>22-26</sup> high resolution electron energy loss spectroscopy,<sup>27</sup> and a combination of ultraviolet photoelectron spectroscopy and inverse photoelectron spectroscopy.<sup>28</sup> Studies combining complementary techniques are also available.<sup>29</sup>

In contrast to unsubstituted oligothiophenes, substituted oligothiophenes typically incorporate alkyl side chains to enhance solubility for processing, a functionality particularly important for large-area device applications. Scanning Tunneling Microscopy (STM) studies of adsorption of substituted oligo- and polythiophenes on a variety of surfaces show diverse self-assembly regimes caused by the presence of substituent groups.<sup>30-36</sup> Polymorphisms of oligothiophene backbone conformations have also been observed with STM.<sup>37-40</sup> However, the impact of the oligothiophene film morphology and associated conformational properties on the oligothiophene electronic structure has not been experimentally quantified. While investigations of the electronic structures of substituted oligothiophenes adsorbed on graphite have been reported,<sup>30, 31</sup> no structure-specific analysis has been presented. A conformationally-resolved STS study of the electronic structures of substituted oligothiophenes adsorbed on a Au(111) surface in the low molecular coverage regime was reported recently.<sup>41</sup> To obtain a more detailed picture of molecule-surface interaction and its impact on the molecular electronic structure, systematic studies targeting varied molecular structures in different surface coverage regimes are needed.

Here we present STM/STS studies of alkyl-substituted oligothiophenes (didodecylquaterthiophene, or DDQT in the following, see Figure 5.1 for molecular structure.) self-assembled on Au(111). These model studies focus on the coverage-dependent evolution of the properties of self-assembled oligothiophene structures. We observe dramatic transformations in the molecular adsorption configurations in transitioning from dilute to half-monolayer molecular surface coverage. We show that at higher coverage regimes, the molecules begin to self-assemble into well-ordered two-

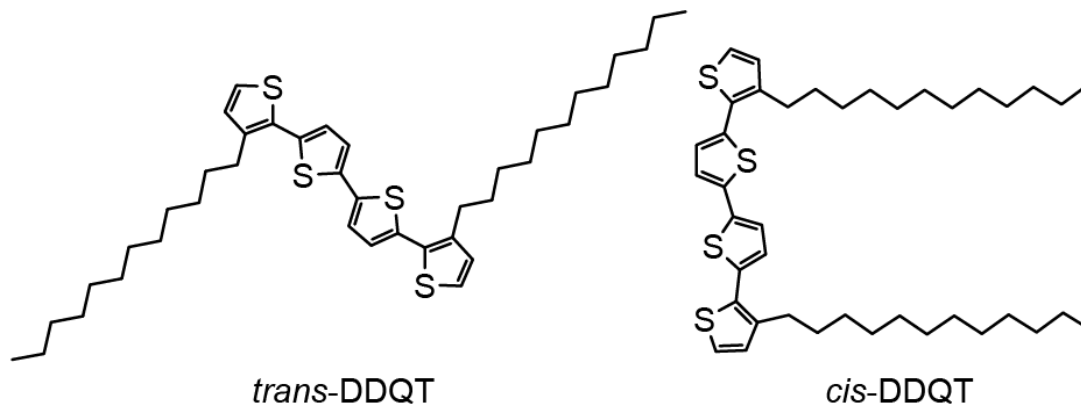


**Figure 5.1.** Molecular structures of didodecylquaterthiophene (DDQT) in both *trans* and *cis* conformations.

dimensional islands, with the internal structures of the islands varying dramatically depending on the molecular coverage. STS spectroscopy shows that for all coverages, substantial variations of the electronic orbital energies are observed. STS shows qualitative changes in the spatial maps of electronic orbitals of different molecular conformers.

### 5.3. Experimental details

Experiments were carried out in a home-built ultra-high vacuum (UHV) cryogenic (closed-cycle cryostat-based) STM system incorporating a STM scanner from RHK Technology.<sup>42</sup> A Au(111)/mica substrate was prepared *in situ* by multiple sputter/anneal cycles. 3,3''-Didodecyl 2,2':5',2'':5'',2'''-quaterthiophene (DDQT) molecules were prepared by Briseno *et al.*<sup>43</sup> DDQT molecules were deposited on to the Au surface (held at room temperature) via *in situ* sublimation in UHV conditions. All imaging and spectroscopic measurements were carried out at ~20K using electrochemically etched silver tips. All STS spectra were recorded using the lock-in

technique at ~600 Hz, and bias modulations varying from 10 mV (individual spectra, and one-dimensional spatial scans) to 50 mV (two-dimensional DOS maps).

#### 5.4. Results and discussion

STS measurements were conducted for three different coverage regimes: 0.013, 0.12 and 0.55 monolayer (ML). Before presenting results of STS measurements, we first discuss the variations in the molecular adsorption configurations for the three regimes, as described in the following.

##### **DDQT dimer formation at dilute (~0.013 ML) coverage.**

For dilute molecular coverage (much less than a monolayer), the majority of DDQT molecules were found to self-assemble into pairs (Figure 5.2a) bound by their interdigitating alkyl substituents (Figure 5.2b). In DDQT pairs, the molecules displayed the *cis* conformation, with both alkyl substituents located on the same side of the DDQT backbone (Figure 5.2b). The thiophene backbones of individual molecules were typically aligned along one of the three different  $\langle 110 \rangle$  directions of Au(111) [Figure 5.2b and c], as established from the geometry of the Au(111) surface-reconstruction herringbone ridges, which are preferentially aligned along the  $\langle 112 \rangle$  directions (Figure 5.2c).<sup>44</sup> While the majority of observed DDQT molecules were incorporated into *cis* dimers, isolated individual molecules were also sometimes observed. Individual molecules displayed primarily the *trans* conformation, with the alkyl substituents located on the opposite sides of the DDQT backbone (Figure 5.3). This *trans* conformation structure of DDQTs is similar to that found in three-dimensional DDQT crystals.<sup>43</sup> Similarly to *cis* conformers, the backbones of individual *trans*-DDQTs were found to be aligned along the  $\langle 110 \rangle$  directions.

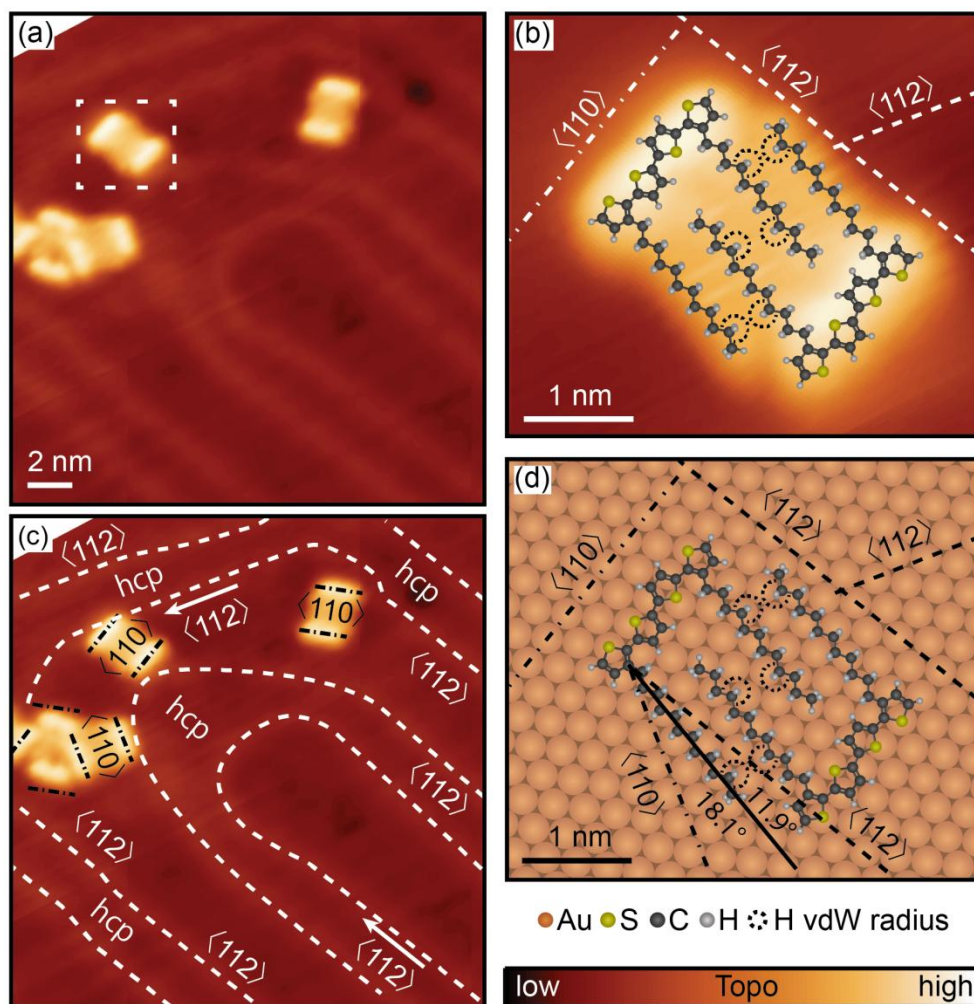


**Figure 5.2.** Adsorption of *cis*-DDQT molecules on Au(111) in the low coverage regime. (a) STM image [set point 100 mV, 1 pA] of a large area featuring reconstruction ridges of the Au(111) surface with sparsely adsorbed DDQT molecules. Most of the molecules prefer the *cis* conformation, forming dimers. Dotted frame indicates enlarged area shown in (c). (b) STM image from (a) with indicated molecular orientations, Au(111) crystallographic directions, and highlighted reconstruction ridges. The quaterthiophene backbones of DDQT molecules aligned along one of three  $\langle 110 \rangle$  directions of the Au(111) surface, perpendicular to the  $\langle 112 \rangle$  directions revealed by straight sections of surface reconstruction ridges. (c) STM image [set point 50 mV, 50 pA] with overlaid molecular structures of two DDQT molecules forming a dimer. (d) Model of DDQT backbones from (c) matched to the Au(111) surface lattice. Au(111) crystallographic directions are indicated. DDQT backbones are aligned along the  $\langle 110 \rangle$  direction and are positioned in a way that minimizes the terminal S to Au top-site distance.

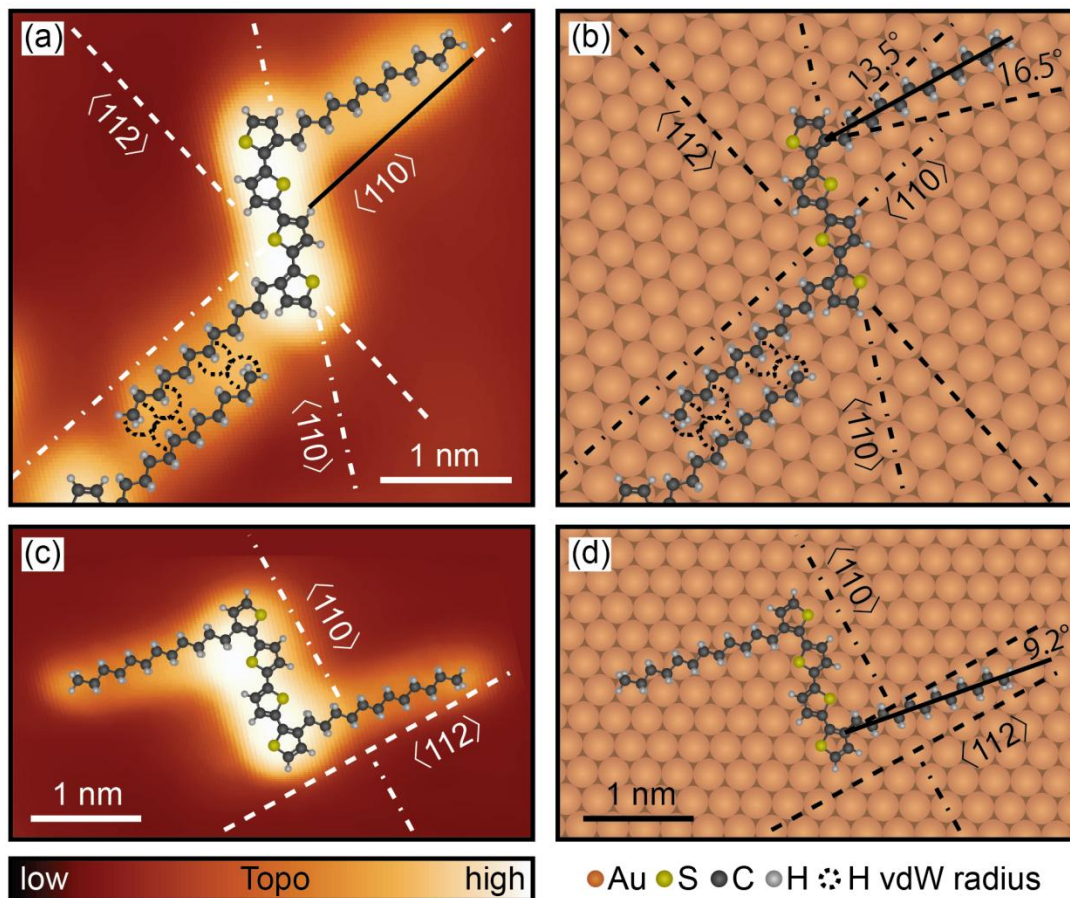


**Figure 5.3.** Adsorption of *trans*-DDQT molecules on Au(111) in the low coverage regime. (a) STM image [set point 100 mV, 50 pA] of a *trans*-DDQT molecule with one alkyl ligand adjacent to another molecule's ligand. Au(111) crystallographic directions are deduced from the surface reconstruction ridges found in vicinity of the molecules. (b) Model of *trans*-DDQT molecule from (a) matched to the Au(111) surface lattice. The oligothiophene backbone is positioned on the lattice in a way that maximizes proximity of sulfur atoms to Au top-sites. The adsorption geometry of alkyl ligands is different for the free ligand (angles to  $\langle 110 \rangle$  and  $\langle 112 \rangle$  directions are indicated) and ligand bound via van der Waals forces to another molecule (aligned along  $\langle 112 \rangle$ ). (c) STM image [set point 100 mV, 5 pA] of *trans*-DDQT molecule with both alkyl ligands freely positioned on gold surface. (d) Model of *trans*-DDQT molecule from (c) matched to the Au(111) surface lattice. The adsorption configuration allows for more optimal positioning of the oligothiophene's sulfur atoms on the gold lattice as compared to (b). Both alkyl ligands are positioned symmetrically,  $9.2^\circ$  offset to the  $\langle 112 \rangle$  direction.



The predominance of cis conformations and the existence of preferred DDQT orientations on the Au(111) surface can be understood by considering the nature of the molecule-surface interaction. This interaction contains several main contributions: 1) van der Waals interactions associated with thiophene backbones<sup>45</sup> as well as alkyl ligands,<sup>46</sup> 2) electrostatic interactions of the dipole moments of individual thiophene units with image charges at the metal surface,<sup>47</sup> and 3) charge-transfer interaction between the S-atoms in thiophene units and Au surface. The enhanced stability of the cis conformations can be explained, at least in part, by the substantial van der Waals interactions between the interdigitating alkyl ligands,<sup>46</sup> which for an isolated pair of dodecane molecules is predicted to be in the range of 0.4-0.5 eV.<sup>48</sup> The cis conformation is additionally stabilized by the enhanced image-charge interaction originating from the dipole moments of thiophene units for this conformation (as opposed to the all-trans-conformation with S-atoms in neighboring thiophene rings pointing in opposite directions, which is typically found for oligothiophene crystals).<sup>49</sup>

Further stabilization of all molecules is provided by the ligand-surface van der Waals interactions. For cis dimers DDQT alkyl ligands form an angle of  $\sim 18^\circ$  with respect to the  $\langle 110 \rangle$  directions of Au(111), an orientation intermediate between that of the free DDQT molecules, where the ligands are nearly orthogonal to the backbone, and the near-parallel orientation (to the  $\langle 110 \rangle$  directions) of self-assembled alkane molecules on Au(111), as established by STM-based studies.<sup>50, 51</sup> Similarly, theoretical simulations of the alkane adsorption geometry predict a small angle of  $\sim 7^\circ$ .<sup>52</sup> Trans molecules in Figure 5.3a and c show orientations with ligand- $\langle 110 \rangle$  angles of  $13.5^\circ$  and  $21^\circ$ , and varied ligand-backbone angles.

The departure of the alkane ligand orientation from optimal in Figure 5.2 and 5.3 suggests that the directionality in DDQT adsorption does not originate from van der Waals interactions associated with the alkyl ligands. Instead, this directionality can be attributed to the sensitivity of the Au-thiophene charge-transfer interaction and the precise matching of individual thiophene rings in the DDQT backbone with the atomic lattice of Au(111). Indeed, DFT calculations for thiophene molecules on Au(111) predict that in the lowest-energy binding configuration, the S atom is located at one of the top-sites on the Au(111) surface,<sup>53</sup> with the adsorption energy being up to 40 meV less favorable for other surface sites.<sup>54</sup> For cis conformers, among the possible adsorption configurations with the thiophene backbone oriented according to Figure 5.2c, only the configuration shown in Figure 5.2d corresponds to all four S-atoms being in direct proximity of four different Au top-sites.<sup>41</sup> Similarly to cis conformers, the backbones of individual trans conformers were aligned approximately along the  $\langle 110 \rangle$  directions allowing the S-atoms to be placed in the vicinity of Au top-sites, even though the exact geometry was slightly different for different trans conformers (Figure 5.3b). A similar scenario has been described in a computational study of adsorbed quaterthiophene molecules on the Cu(111) surface.<sup>45</sup> In this study, the lowest adsorption energies were found for quaterthiophene molecules (in trans conformations) aligned along the  $\langle 110 \rangle$  directions with S-atoms located directly on top of Cu top-sites, a direct consequence of the preferential adsorption of individual thiophene rings with their S-atoms at the Cu top-sites.

A nearly flat orientation of the thiophene ring is also predicted,<sup>55</sup> with its energy being ~40 meV lower than that of the vertical orientation.<sup>54</sup> STM images of DDQTs are

consistent with this prediction: observed molecular profiles typically have heights of approximately 2 Å, which suggests that the thiophene rings comprising DDQT backbones lie nearly flat on Au(111). It can therefore be expected that the lowest-energy DDQT adsorption configurations have the constituent thiophene rings oriented nearly parallel to the substrate, with S atoms being located close to a set of Au top-sites. Indeed, as shown in the atomic model of Figure 5.3b and d and analogous to the model of Figure 5.2d, S-atoms of the thiophene subunits are located close to Au top-sites. The consistency of the backbone orientations for different conformers thus provides additional support to the picture of Au-S interaction employed above.

#### **DDQT island formation at intermediate (~0.12 ML) coverage.**

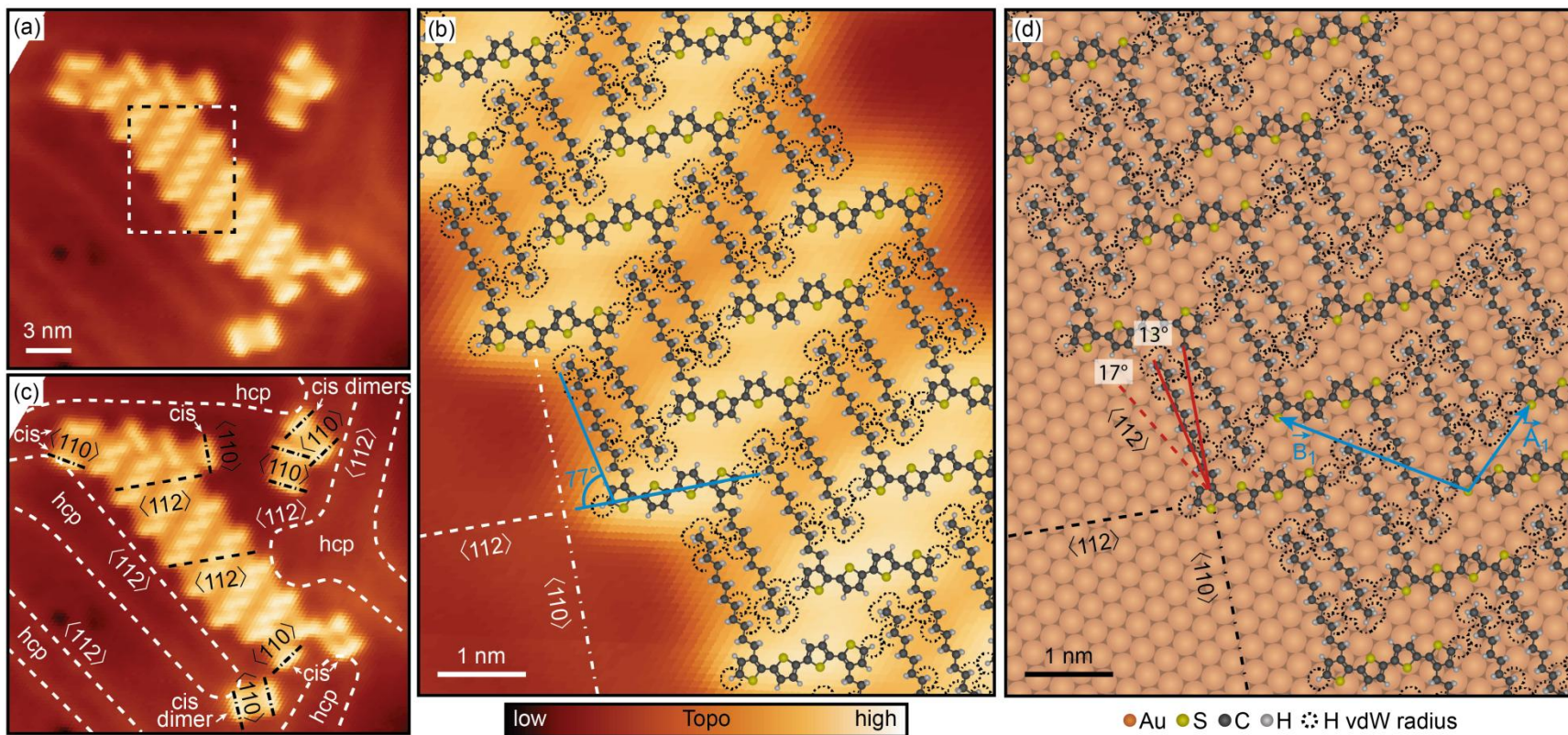
At higher (small fractions of a sub-monolayer) DDQT surface coverages, the predominant adsorption configurations of molecules were found to be dramatically different: most of the molecules self-assembled into regular-two-dimensional islands (Figure 5.4a), with the majority of molecules adopting a variation of the trans conformation (Figure 5.4c), even though some cis dimers similar to those displayed in Figure 5.2 were also observed (Figure 5.4b). In addition, islands composed of trans conformers were typically terminated with cis conformers, which allowed “passivation” of the trans ligands (Figure 5.4b as well as Figure C1a and c). Using the surface-reconstruction features as a reference (Figure 5.4c), we find that the trans conformers in two-dimensional “islands” are oriented roughly along the  $\langle 112 \rangle$  directions, rather than  $\langle 110 \rangle$  directions found for structures at lower coverage (Figure 5.2 and 3). For this backbone orientation it is impossible to place all four S-atoms of each DDQT molecule at Au top-sites. Moreover, the pattern observed in Figure 5.4b is incommensurate with the

Au(111) lattice in the direction corresponding to vector  $\vec{A}$  in Figure 5.4d, which suggests that the S atoms of each DDQT molecule in Figure 5.4b are not matched to an identical pattern of Au surface atoms underneath (Figure 5.4d), such that the Au-S interaction described above can be expected to be suboptimal.

The structure of the DDQT island in Figure 5.4b can instead be described as close-packed, leading to optimized van der Waals interactions and (apparently) a higher stabilization energy per molecule as compared to cis dimers. Some of this enhanced stability is likely afforded by the closer contact of the alkyl ligands of DDQT molecules in 2D islands (compare Figure 5.2d and Figure 5.4d). Additional stabilization of the 2D islands is provided by the van der Waals interaction originating from the proximity of

---

**Figure 5.4.** Adsorption of DDQT molecules on Au(111) in the intermediate coverage regime. (a) STM image [set point 100 mV, 5 pA] of a large area featuring a finite-sized 2D crystal of DDQT with individual DDQT dimers in the vicinity. Dotted frame indicates enlarged area shown in (c). (b) STM image from (a) with indicated molecular orientations, Au(111) crystallographic directions, and highlighted reconstruction ridges (the three  $\langle 112 \rangle$  directions of Au(111) surface correspond to straight sections of surface reconstruction ridges). The quaterthiophene backbones of DDQT molecules not included in the crystal are aligned along one of three  $\langle 110 \rangle$  directions of the Au(111) surface, whereas the backbones of DDQT forming the crystal are aligned along the  $\langle 112 \rangle$  direction perpendicular to  $\langle 110 \rangle$ . (c) STM image [set point 100 mV, 20 pA] with overlaid molecular structures of the part of the crystal indicated in (a). (d) Models of DDQT backbones matched to the Au(111) surface lattice for the crystal section shown in (c). Au(111) crystallographic directions are indicated. DDQT backbones are aligned with the  $\langle 112 \rangle$  direction and are positioned in a way that minimizes the distances from sulfur atoms of terminal thiophene rings to the corresponding Au top-sites.



alkyl ligands to terminal thiophene rings of neighboring DDQT molecules. Finally, the orientation of alkyl ligands of DDQT molecules comprising 2D-islands form an angle of  $\sim 13^\circ$  with one of the  $\langle 110 \rangle$  directions shown in Figure 5.4d, which is closer (as compared to cis dimers) to that of self-assembled alkane molecules on Au(111), and thus likely lower in energy.<sup>52</sup>

It is significant that while many 2D DDQT islands were observed (see also Figure C1a and c for additional examples), all of them showed nearly identical orientations of molecular backbones and ligands (Figure 5.4d as well as Figure C1b and d). Surprisingly, the internal structure of the islands was not affected by even substantial perturbations in the underlying surface structure such as observed for islands stretching across Au(111) step edges (Figure C1a). The robustness of the island structure suggests that Au-S interactions do play an important role in determining the orientation of DDQT molecules in islands. Indeed, by analyzing the adsorption pattern of molecules in 2D islands, we find that molecules can adsorb in a roughly commensurate fashion along vector  $\vec{B}$  in Figure 5.4d, even though deviations from this geometry are also observed. Therefore, the structure of DDQT islands such as shown in Figure 5.4 likely emerges from competition of several factors including the Au-S interaction, inter-ligand and ligand-thiophene van der Waals interactions, as well as potentials associated with deformation of DDQT molecules.

#### **DDQT island formation at high ( $\sim 0.55$ ML) coverage.**

Deposition of DDQT molecules at still higher ( $\sim$ half-monolayer) surface coverages resulted in further transformation of the molecular self-assembly regimes. Similar to the results obtained for lower surface coverages, the molecules predominantly

adsorbed in the face-centered cubic (fcc) regions of the surface, with the hexagonal close-packed (hcp) regions remaining almost completely free of molecules (Figure 5.5a).

Depending on the lateral dimensions of the fcc areas, different modes of self-assembly were observed: in sufficiently narrow fcc regions, the molecules typically formed cis dimers (top-right part of Figure 5.5b) or disordered islands (bottom right corner of Figure 5.5b). In wider fcc regions, ordered islands composed of *trans*-DDQT molecules were observed (left part of Figure 5.5b). The structure of these islands was found to be distinctly different from that of the island shown in Figure 5.4. Most notably, the DDQT backbones in Figure 5.5 were oriented approximately along the  $\langle 110 \rangle$  directions (Figure 5.5c), rather than  $\langle 112 \rangle$  directions as for molecules in Figure 5.4. Furthermore, the placement of the molecules is commensurate with the Au(111) surface, even though it is not entirely periodic (Figure 5.5d). Importantly, this allows for better matching of the S atoms to the Au(111) lattice. In addition, alkyl ligands in Figure 5.5d are nearly orthogonal to the corresponding DDQT backbones, unlike ligands in Figure 5.4d, which form a notably different angle ( $\sim 103^\circ$ ) even though the angles between ligands and the  $\langle 112 \rangle$  directions are nearly identical in both cases.

### **DDQT DOS.**

Figure 5.5a and b show that local molecular adsorption configurations can be very diverse, and both the molecular conformation (cis versus trans, or alkyl chain tilting) as well as the atomic structure of the underlying Au(111) surface can vary considerably (as can be seen by comparing Figure 5.2d, 5.4d and 5.5d). The diversity of molecular adsorption configurations likely leads to variations of the molecular orbital energies, either due to molecule-molecule effects or to varied molecule-surface interactions.

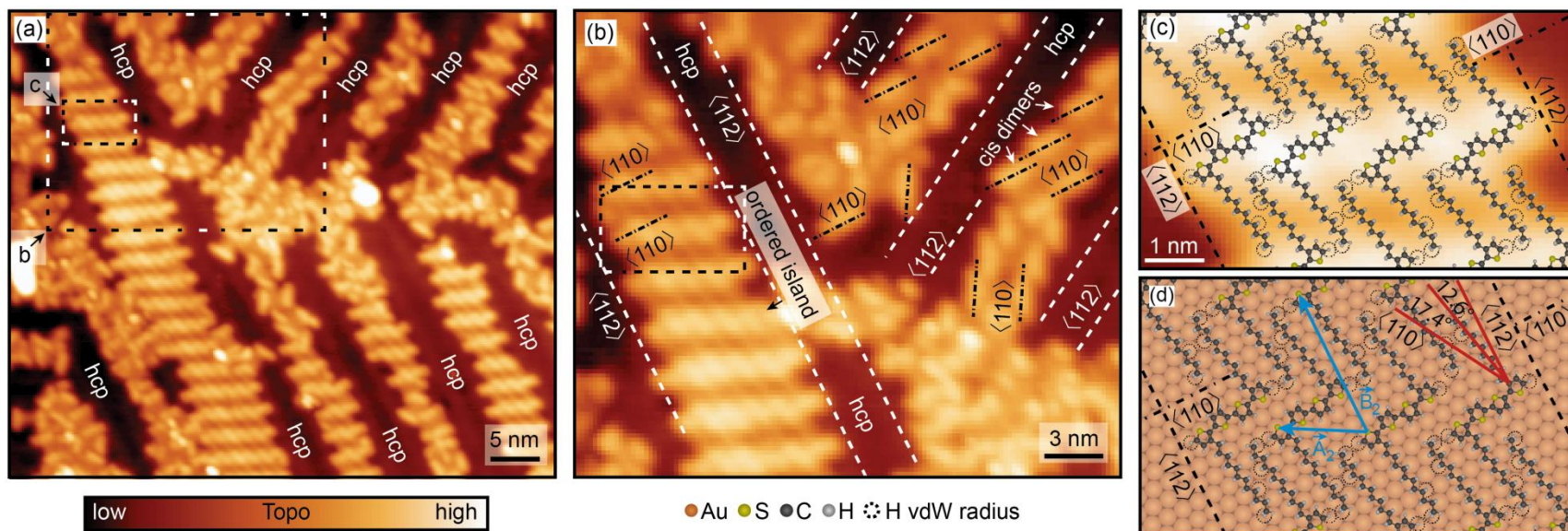


**Figure 5.5.** Adsorption of DDQT molecules on Au(111) in the high coverage regime. (a) STM image [set point 200 mV, 5 pA] of a large area featuring extended 2D crystals of DDQT molecules and DDQT dimer agglomerations. Dotted frames indicate enlarged areas shown in (b) and (c). (b) Part of STM image from (a) with indicated molecular orientations and Au(111) crystallographic directions. The quaterthiophene backbones of DDQT molecules are all aligned along one of three  $\langle 110 \rangle$  directions of the Au(111) [which are perpendicular to  $\langle 112 \rangle$  directions], regardless of whether or not they are in an ordered crystal. DDQT prefers adsorbing in fcc regions of the Au(111) reconstruction, while hcp regions are avoided and mostly empty. (c) STM topography image [set point 200 mV, 5 pA] with overlaid molecular structures of part of the crystal indicated in (a). (d) Models of DDQT backbones matched to the Au(111) surface lattice for the crystal section shown in (c). Au(111) crystallographic directions are indicated. DDQT backbones are found to be aligned with  $\langle 110 \rangle$  direction and are positioned in a way that minimizes the distances from sulfur atoms of terminal thiophene rings to the corresponding Au top-sites.



Quantifying the extent of such variations is important for the realization of electronic devices based on organic semiconductors, where local energetic inhomogeneities can effectively act as charge traps. To evaluate the extent of electronic disorder for DDQT on Au(111), we measured the local electronic structures of individual DDQT molecules in different self-assembled arrangements by using Scanning Tunneling Spectroscopy (STS, see Experimental Section for details). STS measurements were carried out by recording the derivative of the tunneling current,  $dI/dV$ , as a function of the bias voltage (see Experimental Section for further details).<sup>56</sup> The magnitude of the  $dI/dV$  signal serves as a measure of the local electronic density of states (DOS), while the bias voltage (multiplied by the electron charge) provides the energy scale.

DOS spectra measured on *cis* conformers typically show a peak at  $\sim 2.1$  V attributed to the lowest unoccupied molecular orbital (LUMO) of DDQT (Figure 5.6a, top two curves).<sup>41</sup> Spatial mapping of the electronic DOS associated with this peak shows that it is localized in the vicinity of the DDQT backbone (Figure 5.6d, see also Figure C2d), confirming the molecular origin of this state. The highest occupied molecular orbital (HOMO) was not clearly distinguishable in the DOS spectra due to the structured background associated with the Au d-bands (Figure 5.6a, bottom two curves). For this reason, in the following we focus on the LUMO orbitals when comparing the electronic structures of different molecules. The presence of the HOMO orbital, however, can be established with STS mapping at  $-0.9$  V (Figure 5.6e), which shows DOS localized in the vicinity of the DDQT backbone with enhanced intensities at the terminal thiophene rings. Based on the results of STS measurements, we roughly estimate the HOMO-LUMO

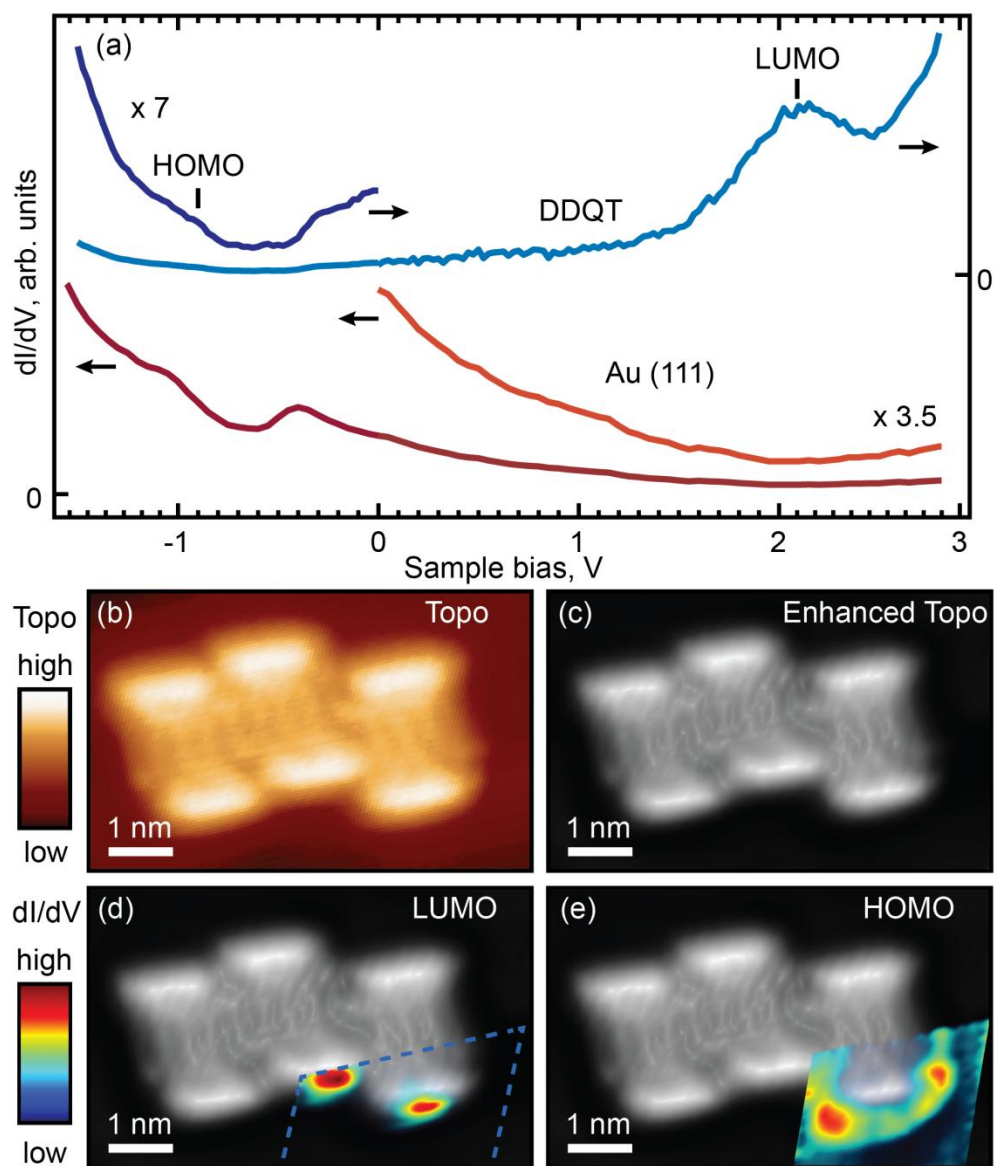


**Figure 5.6.** Spatial mapping of DDQT orbitals. (a) STS spectrum measured on the quaterthiophene backbone of the molecule in the bottom right corner (curve DDQT), and STS spectrum of the gold substrate near the dimers [curve Au(111)]. Portions of both spectra are magnified to show fine structure. (b) STM image of a group of DDQT dimers. (c) STM image from (b) processed to “sharpen” the topographic features. (d) Density of states (DOS) for the LUMO orbital [2.1 V, see curve DDQT in (a)] overlaid on image from (c). Mapped area is confined within the dashed lines. Low DOS intensity (near-background) areas were rendered transparent to show registry with topography. (e) Same as (d) for the HOMO orbital [-0.9 V, see curve DDQT in (a)].

energy difference to be in the range of  $\sim 3\text{eV}$ , in agreement with the expected band-gap of quaterthiophenes.<sup>57</sup>

Representative DOS data for molecules comprising the island from Figure 5.4 are presented in Figure 5.7a. The island is primarily comprised of trans molecules, but a few cis molecules are also present (these are marked as such in Figure 5.4b). The LUMO peaks for all molecules within the spatial range of Figure 5.7a are primarily clustered around 2.1 V (Figure 5.7b), commensurate with Figure 5.6 and slightly lower than the mean of cis conformers in Figure C3 and molecule C in Figure 5.7a (see curve C in Figure 5.7b). (Note that the LUMO peak voltages in all reported STS measurements were not sensitive to the precise location of the tip on the measured molecules. This is illustrated by the representative set of data shown in Figure C4. In addition, the variations in LUMO peak voltages for different molecules are not a result of changes in the tip structure, as was confirmed by repeated measurements of their spectra.) The most prominent outliers among the trans molecules in Figure 5.7b are molecules A, B, and G, which are clearly subjected to local environments different from the rest of the trans molecules D-F and H-L: molecules A, B have a distinctly different orientation, and are attached (via their alkyl chains) in a different manner to the rest of the island, while molecule G is likely affected by the proximity of molecules B and C that produces a local potential dissimilar to that seen by the remaining trans molecules in the island (Figure 5.7a). A somewhat smaller perturbation at 1.9 eV is evident in the spectrum of molecule E (Figure 5.7b), which is only affected by the proximity of dissimilar molecule A.

While the DOS spectra of trans and cis conformers are qualitatively similar, we find that the spatial behavior of the *trans*-LUMOs is very different from that of

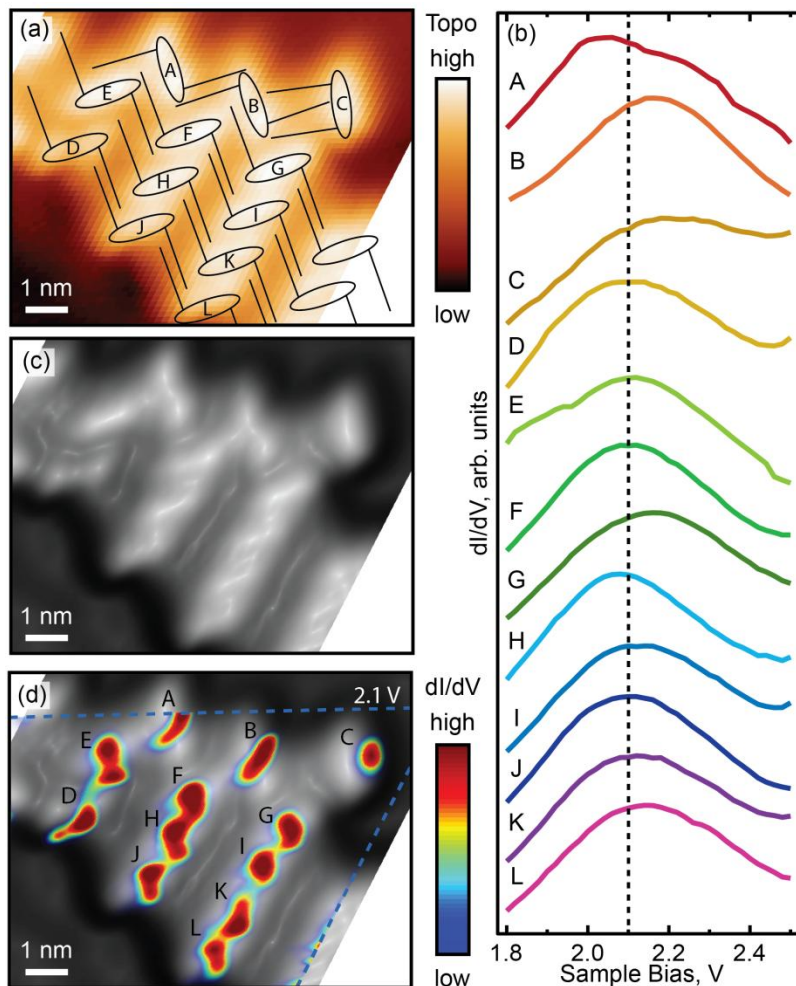


**Figure 5.7.** LUMO molecular orbital of the DDQT crystal of the type formed in the intermediate molecular coverage regime. (a) STM image [set point 100 mV, 5 pA] of part of the crystal with overlaid DDQT models of backbone (ellipse) with attached alkyl chains (lines). Shown are three regular rows of *trans*-DDQT comprising the crystal and three additional DDQT molecules attached to a crystal with perpendicular backbones (two *trans* and one *cis* conformer). (b) dI/dV spectroscopy scans [set point 1.0 V, 1.0 pA] of the LUMO orbitals taken on top of every backbone indicated with A-L in (a). Dashed line at 2.1 V is the most common LUMO peak energy in this crystal, but deviations from 2.1 V in both directions are observed. (c) STM image from (a) processed to “sharpen” the topographic features. (d) LUMO DOS map at 2.1 V superimposed on enhanced topography showing LUMO localization. The DOS maps are superimposed on the enhanced topography from (c), with areas of low DOS [Au(111) background] rendered transparent in order to reveal registry with the topography.

*cis*-LUMOs. LUMO states for *cis* conformers are generally localized slightly off-center from the DDQT backbones, on the opposite side from the ligands (Figure 5.6d and S2d, as well as the map of molecule C in Figure 5.7d). In contrast, each *trans*-LUMO state spanned a stripe-like area transecting the corresponding DDQT backbone, appearing on both sides of the backbone (Figure 5.7d), comparable to the LUMO patterns found for unsubstituted terthiophene on Au(111).<sup>22</sup> Furthermore, LUMO maps of different *trans* molecules showed substantial variations in their shapes, despite apparent similarities in spectra (compare, for example, molecules D, J, and K in Figure 5.7d). This observation may be explained by the fact that these molecules were interfaced with slightly different local atomic Au(111) structures, as shown in Figure 5.4d.

DOS maps of DDQT islands observed at higher coverages (Figure 5.4) offer another opportunity to test the impact of the atomic structure of the molecule-Au interface on the molecular DOS. As shown in Figure 5.4d, these molecules have very similar adsorption configurations relative to the Au(111) atomic lattice, suggesting that their DOS maps should look very similar. This is indeed the case, as shown in Figure 5.8. Specifically, unlike molecules in Figure 5.7d, molecules A-E in Figure 5.8a all show similarly shaped spatial distributions of their LUMO DOS (Figure 5.8d-g, see Figure C5 for a complete set of DOS maps). Similar trends are observed for other DDQT molecules self-assembled into similar 2D islands (Figure C6). Surprisingly, despite the similarities in their adsorption configurations and LUMO spatial maps, different molecules show varied LUMO energies, as can be seen in Figure 5.8b and S6b. A statistical survey of all studied molecules shows wide variations in LUMO state energies with the mean LUMO

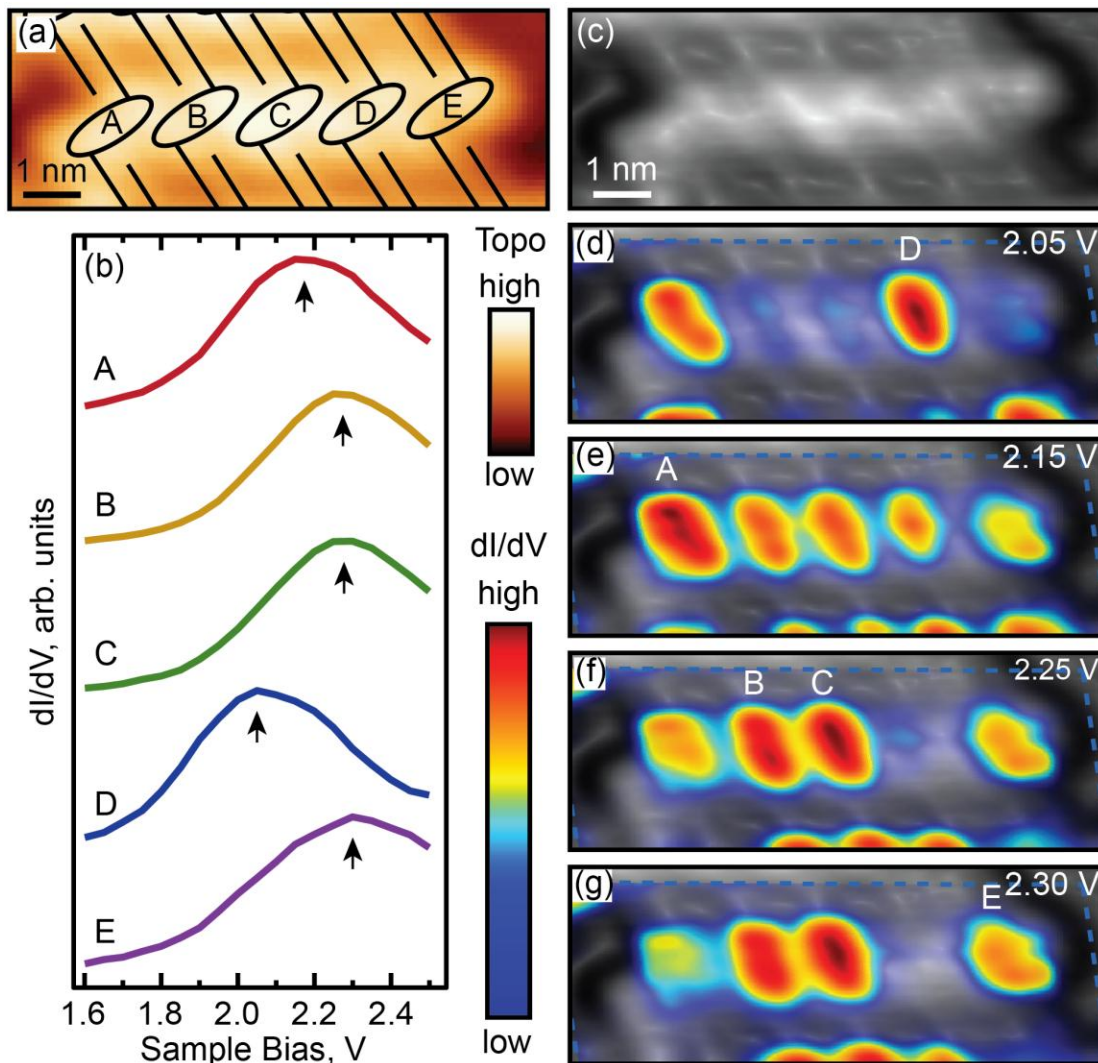


**Figure 5.8.** LUMO of a DDQT crystal of the type formed in the high molecular coverage regime. (a) STM image [set point 200 mV, 5 pA] of part of the crystal with overlaid DDQT models of backbone (ellipse) with attached alkyl chains (lines). Regular chain of the crystal consisting of five DDQT molecules is shown. (b)  $dI/dV$  spectroscopy scans [set point 1.8 V, 2.0 pA] of the LUMO orbitals taken on top of every backbone indicated with A-E in (a). (c) STM image from (a) processed to “sharpen” the topographic features. (d)-(g) LUMO DOS maps for voltages corresponding to specific LUMO peaks in (b). The DOS maps are superimposed on the enhanced topography from (c), with areas of low DOS [Au(111) background] rendered transparent in order to reveal registry with the topography.

energies for all conformations within the typical standard deviations of ~80 meV for each conformer (Figure C3). Several possible mechanisms are likely to be responsible for these variations. An important factor affecting molecular DOS is the spatially-modulated surface reactivity originating from the herringbone  $22 \times \sqrt{3}$  reconstruction of the Au(111) surface, as shown in recent density-functional calculations,<sup>44</sup> as well as STS studies of DDQT molecules in the dilute regime.<sup>41</sup> The surface reconstruction leads to variations in the coordination of the surface gold atoms, which, in turn, affects the local reactivity on the atomic scale. Indeed, as mentioned earlier, preferential adsorption of oligothiophene molecules in the fcc areas observed in Figure 5.2b, 5.4c, and 5.5a may be attributed to the higher surface reactivity of the fcc areas versus hcp. One can expect the spatially varied coordination of the surface Au atoms to have an effect on the Au-S interaction, which is likely to affect the energies of molecular orbitals, as was shown in a recent STS study.<sup>41</sup> However, the spatially varied surface reactivity alone does not explain the observed orbital energy variations, as can be seen, for example, from Figure 5.8d-g and C6c-j, where the variations in the LUMO peak energies are not monotonic across the island, which is located within a fcc region of Au(111). This suggests that subtle variations in molecular conformations resulting from slight variations in local environment, and indistinguishable in STM images, may be responsible for the variations in the LUMO peak energies. Conformational effects may also affect the nature of the Au-DDQT interface, leading to conformation-specific structural relaxations and hybridization of DDQT orbitals with the Au(111) states, both of which can result in conformation-dependent orbital shifts.<sup>45</sup> Similar conformational effects must be responsible, in part, for the differences in the orbital energies of cis and trans conformers.

## 5.5. Conclusions

Our results show that a significant degree of structural as well as electronic diversity can be expected even in a relatively simple system composed of short substituted oligothiophenes adsorbed on a metal surface. Diverse self-assembly regimes of DDQT molecules on the Au(111) surface result from competition between the different types of molecule-metal and molecule- molecule interactions, including the surface-thiophene atomic-level interactions and van der Waals interactions involving the alkyl ligands, thiophene backbones, and the Au surface. We find that the molecular conformations and registry with the Au(111) surface are dramatically different for different self-assembly modes suggesting that different “crystal” phases may exist in oligothiophene thin films used in electronic applications. While the coexistence of several self-assembly regimes and the resulting conformational diversity observed in our work suggests the existence of local variations in the molecular electronic structure, we observed that even with molecules of identical apparent adsorption configurations (as observed in STM images), significant electronic differences are found. These electronic differences between molecules of identical apparent adsorption conformations may be attributed to local atomic-scale variations of the surface reactivity, varied molecule-surface atomic interfaces, slightly different environments originating from the neighboring molecules, and subtle conformational variations unobservable by STM.

## 5.6. Bridge to Chapter VI

In the next chapter we will extend our studies of alkyl-substituted oligothiophenes to the molecules with longer oligothiophene backbones. Longer oligothiophenes have lower electronic energies, so more electronic states can be accessed and mapped with



STS technique. For each oligothiophene conformer, by mapping the electronic density of states in real space, we will identify a progression of particle-in-a-box-like states corresponding to the LUMO, LUMO+1 and LUMO+2 orbitals. These molecules also have a higher degree of conformational polymorphism, which allows one to investigate how greater conformational disorder affects interaction between the molecules, self-assembly in higher density regime and electronic structure of alkyl-substituted oligothiophenes. We show that different possible molecular conformations result in very similar molecular electronic structures. By using density functional theory calculations, we show that the lack of variation in electronic structures among the different oligothiophene conformers implies that the effect of the Au-oligothiophene interaction is nearly identical for all studied torsional conformations.

# CHAPTER VI

## OLIGOTHIOPHENE WIRES: IMPACT OF TORSIONAL CONFORMATION ON THE ELECTRONIC STRUCTURE

This chapter by Dmitry A. Kislitsyn, Benjamin N. Taber, Christian F. Gervasi, Lei Zhang, Stefan C. B. Mannsfeld, Jim S. Prell, Alejandro L. Briseno, and George V. Nazin has been previously published under the same title in *Phys. Chem. Chem. Phys.* **18**, 4842–4849 (2016). Copyright © 2016 Royal Society of Chemistry.

### 6.1. Introduction

Charge transport in polymer- and oligomer-based semiconductor materials depends strongly on the structural ordering of the constituent molecules. Variations in molecular conformations influence the electronic structures of polymers and oligomers, and thus impact their charge-transport properties. In this study, we used Scanning Tunneling Microscopy and Spectroscopy (STM/STS) to investigate the electronic structures of different alkyl-substituted oligothiophenes displaying varied torsional conformations on the Au(111) surface. STM imaging showed that on Au(111) oligothiophenes self-assemble into chain-like structures, binding to each other via interdigitated alkyl ligands. The molecules adopted distinct planar conformations with alkyl ligands forming cis- or trans- mutual orientations. For each molecule, by using STS mapping, we identify a progression of particle-in-a-box-like states corresponding to the LUMO, LUMO+1 and LUMO+2 orbitals. Analysis of STS data revealed very similar unoccupied molecular orbital energies for different possible molecular conformations. By

using density functional theory calculations, we show that the lack of variation in molecular orbital energies among the different oligothiophene conformers implies that the effect of the Au-oligothiophene interaction on molecular orbital energies is nearly identical for all studied torsional conformations. Our results suggest that cis-trans torsional disorder may not be a significant source of electronic disorder and charge carrier trapping in organic semiconductor devices based on oligothiophenes.

## 6.2. Background

Solution-processable thiophene-based polymers and oligomers represent an important class of organic semiconductor materials<sup>1,2</sup> with potential applications in field-effect transistors,<sup>3-5</sup> light-emitting diodes,<sup>6,7</sup> photodetectors<sup>8</sup> and photovoltaic devices.<sup>9-11</sup> The electronic structures of polymers and oligomers, and consequently their charge transport properties, are determined to a significant degree by the conformations of their  $\pi$ -conjugated backbones.<sup>12-14</sup> Molecular conformations not only govern the extent of electronic conjugation, but are also interdependent with molecular packing,<sup>15,16</sup> which controls intermolecular charge transport in polymer- and oligomer-based thin films.<sup>17</sup> While bulk molecular packing is of central importance in defining the electronic transport characteristics,<sup>18</sup> the latter are also often strongly affected by the properties of molecular interfaces with other materials used in electronic devices, where molecular structures can be quite different from those of the bulk.<sup>19,20</sup> Examples of such interfaces include the molecule-dielectric interfaces, found in field-induced conduction channels in transistors,<sup>21-23</sup> and molecule-electrode interfaces.<sup>24-26</sup> Furthermore, the thin film morphology can be strongly impacted by the structure of the molecular layer at the interface.<sup>27</sup> The nature of the interface has a profound impact on the molecular

morphology and self-organization, which are defined by the competition between the intermolecular and molecule-surface interactions. For this reason, molecular structures at interfaces with solids and other molecular layers have been a subject of numerous studies, with techniques based on scanning tunneling microscopy (STM) being particularly powerful in the absence of long-range order due to their ability to resolve local molecular structures. Many STM studies have focused on molecular self-assembly in the regime of weak molecule-surface interactions simulating molecule-dielectric interfaces, with molecules often deposited on highly-oriented pyrolytic graphite surfaces.<sup>28-34</sup> The resulting structures are typically dominated by the intermolecular interactions between the ligands, attached to thiophene backbones in order to enhance solubility and facilitate processing.

Several STM studies have addressed the regime of stronger molecule-surface interactions with molecules deposited on metal surfaces simulating molecule-electrode interfaces.<sup>30, 35-42</sup> A common observation of these studies was the existence of conformational polymorphisms of both polythiophenes<sup>40, 41</sup> and oligothiophenes,<sup>36-39</sup> with the overall degree of disorder being higher than that found for more weakly interacting surfaces.<sup>30, 40</sup> Understanding the degree of electronic disorder associated with such conformational polymorphisms is important in view of the potentially significant impact of molecular conformation on the electronic structure. Theoretical and optical spectroscopic investigations of organic donor-acceptor molecules incorporating thiophene donors revealed that unoccupied frontier electronic levels were largely unaffected by cis-trans conformational isomerization, finding variations in LUMO energies due to rotational disorder of less than 90 meV.<sup>43, 44</sup> STM offers the capability to

probe the impact of conformational polymorphism on molecular electronic structure directly via scanning tunneling spectroscopy (STS), which has been used to investigate oligothiophene electronic structures on both strongly and weakly interacting surfaces.<sup>29, 30, 45-49</sup> However, the role of conformational effects in defining the molecular electronic structure has so far only been investigated in very short oligothiophenes (incorporating only four thiophene rings), where few electronic states are accessible to STS due to their relatively high energies.<sup>50, 51</sup>

Here we report a conformation-resolved STM/STS study of alkyl-substituted oligothiophenes adsorbed on the Au(111) surface. To obtain a more complete physical picture of the oligothiophene properties on Au(111), we investigated two types of oligothiophenes with similar structures: molecules incorporating eight thiophene rings and four alkyl ligands (we will refer to these molecules as 8T in the following), as well as molecules incorporating seven thiophene rings and three alkyl ligands (7T in the following). Both types of molecules are sufficiently long to be considered as finite-length models for probing conformational effects in application-relevant alkyl-substituted thiophene-based polymers and oligomers. The Au(111) surface serves as a model of Au metal electrodes often used in proof-of-principle organic semiconductor devices. We obtained STS maps of oligothiophene molecules to identify the nature of molecular orbitals, and found that all molecules displayed particle-in-a-box-like progressions of electronic states. Further, we found that different oligothiophene conformations, despite considerable structural differences, result in nearly indistinguishable molecular electronic structures. We use density functional theory (DFT) calculations to show that the electronic structures of oligothiophenes of different torsional conformations (in the gas

phase) are quite similar. The lack of conformational sensitivity in our experimental electronic structure data thus suggests that the Au-oligothiophene interaction is relatively insensitive to the specific molecular torsional conformation.

### **6.3. Experimental details**

STM and STS measurements were performed at ~20 K using a home-built ultra-high vacuum (UHV) cryogenic (closed-cycle cryostat-based) STM system incorporating a STM scanner from RHK Technology.<sup>52</sup> Atomically clean Au(111) on mica was prepared in UHV by multiple cycles of Ne-ion bombardment followed by ~300°C anneals. 8T and 7T molecules were prepared by Briseno et al.<sup>53</sup> The composition was verified with nanoelectrospray ionization mass spectrometry (Figure D1). Sub-monolayers of oligothiophene molecules were deposited on the Au surface via in situ sublimation with the sample held at room temperature and vacuum pressure not exceeding  $10^{-10}$  Torr. STS spectra were measured in constant-height mode using the lock-in technique, with a modulation frequency of 570 Hz and a bias modulation of 50 mV. This allowed for the direct measurement of the local differential conductance ( $dI/dV$ ) of the sample, which serves as a measure to the local density of electronic states.<sup>54</sup> DFT computations were performed with Gaussian 09<sup>55</sup> using B3LYP/6-31G\*,<sup>56, 57</sup> and analyzed with Multiwfn.<sup>58</sup>

### **6.4. Results and discussion**

#### **Molecular adsorption configurations from STM imaging**

After deposition on the Au(111) surface, STM imaging revealed that 8T and 7T molecules self-assembled into chain-like aggregates comprised of varying numbers of

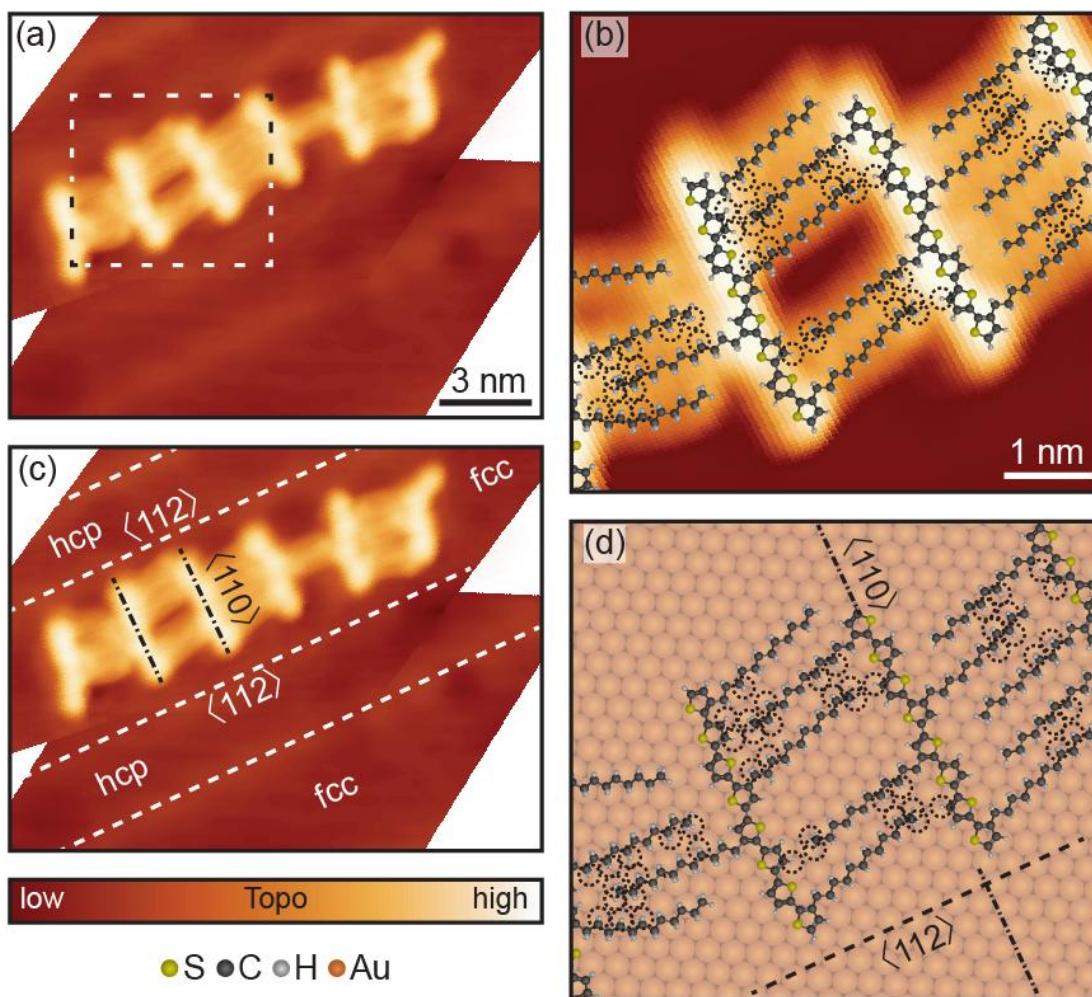


**Fig. 6.1.** Adsorption of 8T molecules on Au(111). (a) STM image [set point 100 mV, 5 pA] of an aggregate of oligothiophene molecules absorbed on the Au(111) surface. (b) Close-up STM topography of the region confined by the dotted rectangle in (a). Atomic models of 8T molecules are overlaid on the STM image. The atomic models show that molecules are attached to each other via alkyl substituents. The thiophene rings comprising the DDQT backbones are nearly flat on the Au(111) surface, as determined by STM topographies. (c) STM image from (a) with indicated molecular orientations and Au(111) crystallographic directions and highlighted surface-reconstruction ridges. The oligothiophene backbones of 8T molecules are aligned along the  $\langle 110 \rangle$  directions of the Au(111) surface, perpendicular to the straight sections of surface-reconstruction ridges which run parallel to the  $\langle 112 \rangle$  directions. (d) Model of 8T molecules from (b) matched to the Au(111) surface lattice. Au(111) crystallographic directions are indicated. Dashed circles indicate the van der Waals radii of the hydrogen atoms.

molecules (Figures 6.1a, D2a and D3a). High-resolution STM images show that the molecules bind to each other with their alkyl ligands, forming interdigitating patterns (Figures 6.1b and D2b). Adsorption of oligothiophenes was highly correlated with the structural features of the Au(111) surface associated with the Au(111)  $22 \times \sqrt{3}$  surface reconstruction, which results in the formation of regions with fcc (face-centered cubic) and hcp (hexagonal close-packed) surface structures separated by reconstruction “ridges” visible in STM images (dashed lines in Figures 6.1c, D2c and D3b). The molecular aggregates primarily formed in the fcc regions of the Au(111) surface, and were almost entirely absent from the hcp regions (Figures 6.1c, D2c and D3b), consistent with results for shorter oligo- thiophenes.<sup>45, 50</sup> This preferential adsorption has been attributed to different reactivities of the fcc and hcp regions, a result of varied coordination of the surface Au atoms in the two regions.<sup>50</sup> STM images of 8T and 7T backbones also showed molecular profiles of  $\sim 2$  Å with typical variations of  $< 0.1$  Å, consistent with flat molecular backbones.<sup>49</sup>

The molecular aggregates showed reproducible registry with the Au(111) surface lattice, as can be observed by comparing molecular orientations with the ridge-like surface reconstruction features (Figure 6.1c for 8T, D2c and D3b for 7T). In particular, in the straight sections of fcc regions, where the Au crystal structure is more regular, the oligothiophene backbones were preferentially oriented along the  $\langle 110 \rangle$  directions of Au(111), orthogonal to the growth-directions of molecular aggregates corresponding approximately to the  $\langle 112 \rangle$  directions (Figures 6.1c, D2c and D3b). This backbone orientation is analogous to that observed for shorter four-thiophene oligomers (4T in the following) on Au(111),<sup>50</sup> which is a direct consequence of the similarities in



intermolecular and molecule-surface interactions for both systems. In particular, the preferred orientations of 4T molecules along the  $\langle 110 \rangle$  directions have been attributed to the charge-transfer interaction involving S atoms of the thiophene units comprising 4T molecules and the Au surface. For individual thiophene units, this interaction results in preferential adsorption on Au top sites,<sup>59</sup> with a local energy minimum of 40 meV.<sup>60</sup> The tendency of 4T oligothiophenes to align along the  $\langle 110 \rangle$  directions on Au(111) has been explained by the fact that this orientation leads to the best matching of all four S-atoms of 4T to the top sites of the Au(111) surface lattice.<sup>50</sup> In accordance with this picture, locations of S-atoms in 8T and 7T molecules show similar patterns (Figure 6.1d and D2d), even though some deviations from perfect top-site placement are evident. The existence of these deviations is not unexpected, since the longer molecular structures of 7T and 8T molecules are more difficult to match to the Au(111) lattice. For example, while in 4T molecules the distance between the S-atoms of the outer thiophene rings (1.19 nm) was closely matched to four Au atoms along the  $\langle 110 \rangle$  direction (1.15 nm), for 8T molecules the distance between the S-atoms of the outer thiophene rings (~2.8 nm) is a poorer match to Au(111) surface lattice sites, with the best match corresponding to ten lattice constants (2.89 nm). The lack of commensurability between the molecular structures and the Au(111) surface may also be the reason for the commonly observed deviations from linearity of 7T and 8T backbones, in contrast to 4T molecules, which appeared straight in all STM images.<sup>50</sup>

Another important factor that likely impacted the shapes of 7T and 8T backbones is the intermolecular interactions originating from the alkyl ligands. These include both alkyl-alkyl interactions as well as interactions involving terminal methyl groups of alkyl

ligands and thiophene units of neighboring molecules. For example, the strength of the alkyl-alkyl interaction can be expected to be substantial given that for a pair of dodecane molecules the interaction energy is estimated to be 0.4-0.5 eV.<sup>61</sup> This interaction tends to affect individual molecules differently due to the widely varied inter-digitation patterns of alkyl substituents connecting neighboring molecules (Figures 6.1b and D2b), and may contribute to the observed deviations from linearity for the oligothiophene backbones. Indeed, this argument is supported by the fact that despite the variations in the oligothiophene backbone shapes, the patterns formed by alkyl chains show highly reproducible angles, especially when close alkyl-alkyl contacts are formed (Figures 6.1b and D2b). The observed orientations of tightly packed alkyl ligands on the Au(111) lattice form angles of  $\sim 12^\circ$  with respect to the  $\langle 110 \rangle$  direction (Figures 6.1d and D2d). This ligand orientation is intermediate between those of the gas-phase molecules (ligand nearly orthogonal to the backbones), and alkanes self-assembled on Au(111), which typically align themselves approximately along the  $\langle 110 \rangle$  directions<sup>62</sup> (with theoretical calculations giving an angle of  $\sim 7^\circ$ ).<sup>63</sup> This observation suggests that orientations of the alkyl ligands are also affected by the local bonding orientation and placement of the oligothiophene backbones.

The specific interdigitating structures formed by alkyl ligands of neighboring molecules depend on the particular torsional conformations adopted by the corresponding thiophene backbones. Oligothiophene aggregates studied in our work contained a variety of molecules adopting different torsional conformations (corresponding to the different possible mutual orientations of thiophene units along the oligothiophene backbone, as can be seen in Figures 6.1b and D2b), which is one of the reasons for varied intermolecular

binding interactions. In addition to controlling the structure of oligothiophene aggregates, torsional conformations can be expected to control the electronic structures of the corresponding molecules, since changing the mutual orientation of individual thiophene units can affect the energies of molecular orbitals. From the point of view of electronic applications based on oligothiophene materials, it is then important to understand the extent of electronic structure variations caused by the existence of different torsional conformers, as well as the physical driving forces responsible for the diversity of torsional conformations in oligothiophene thin films.

The observed tendency of 8T molecules to form relatively ordered aggregates suggests that after deposition, these molecules have sufficient energy (at room temperature) to be able to freely migrate on the surface on the Au(111) surface. Moreover, the well-ordered assembly of interconnecting alkyl ligands suggests that molecular torsional transformations readily occur in these conditions. This is illustrated, for example, by the fact that alkyl ligands unattached to neighbouring molecules were almost never observed in STM imaging, with one particular manifestation of this being the fact that molecules located at the ends of the oligothiophene aggregates typically assumed a conformation with all alkyl ligands facing the rest of the aggregate, whenever possible (a rare exception to this is the left molecule in Figure D2a, where one of the ligands is facing away from the molecular aggregate due to interference from a ligand of a neighbouring molecule).

### **Scanning Tunneling Spectroscopy**

We investigated the effect of length and conformation on oligothiophene electronic structure by using Scanning Tunneling Spectroscopy (STS) to measure the

local electronic structure of 8T and 7T molecules adsorbed on the Au(111) surface. Specifically, these measurements were carried out by recording the differential conductance (derivative of the tunneling current,  $dI/dV$ ), which is representative of the local electronic density of states (DOS). By recording the differential conductance as a function of the applied bias voltage (which serves as the energy scale), we obtain energy-dependent DOS spectra (see Experimental Methods for further details).<sup>54</sup> In total, 55 straight oligothiophene molecules were studied using this approach (see Figure D4), and STS maps were obtained for 31 molecules, as described below.

Among the different possible conformations of 8T molecules, we focus on three representative conformations: CCC (orientation of ligands corresponding to a cis-cis-cis combination, Figure 6.2a), TTT (trans-trans-trans ligand orientations, Figure 6.3a), and CTT (cis-trans-trans ligand orientations, Figure 6.4a). While we are unable to discern the orientations of thiophenes lacking alkyl chains, it is likely that, since the oligothiophene backbones are straight, neighboring thiophenes are preferentially oriented  $\sim 180^\circ$  relative to each other, as oligothiophene backbones containing neighboring thiophenes oriented  $\sim 0^\circ$  relative to each other have a tendency to bend due to the steric hindrance between neighboring thiophenes.<sup>30</sup> By recording progressions of STS spectra along the oligothiophene backbones (corresponding spatial paths shown in Figures 6.2b, 3b and 4b) we obtain DOS maps showing the spatial landscape of molecular electronic states (Figures 6.2c, 6.3c and 6.4c). Here we focus on the unoccupied states because the occupied molecular orbitals were not clearly distinguishable in the DOS spectra due to the structured background originating from the d-bands of the Au(111) surface. All three DOS patterns (Figures 6.2c, 6.3c and 6.4c) show a very high degree of similarity. Each

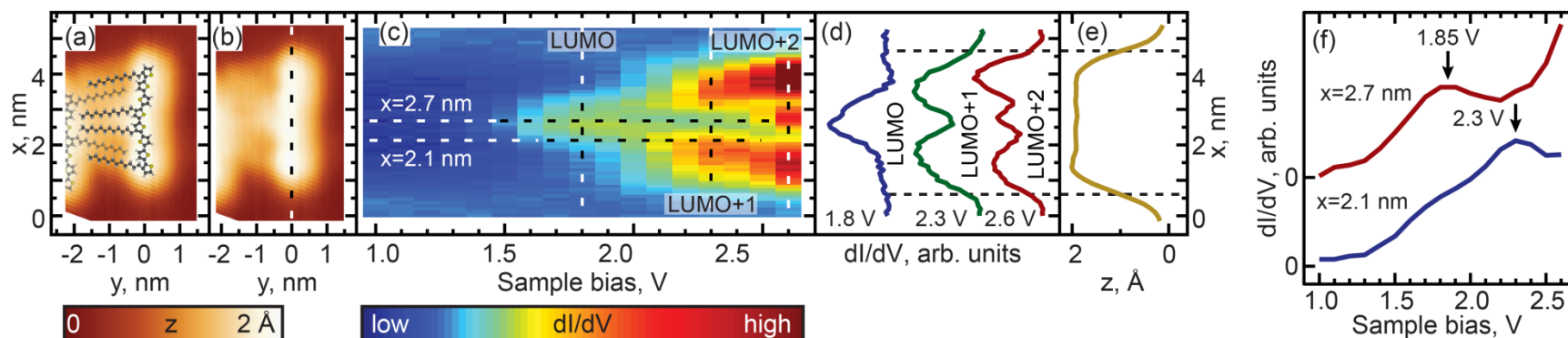


**Fig. 6.2.** Spatial (STS) DOS mapping across for a CCC conformer of 8T molecules. (a) STM image with an overlaid atomic model of the CCC-8T molecule. (b) STM image from (a) showing the path of mapping (dashed line). (c) DOS as a function of the bias voltage and position  $x$  along the path shown in (b). (d) LUMO, LUMO+1 and LUMO+2 DOS along the path shown in (b), obtained at voltages corresponding to the vertical dashed lines in (c). These voltages were chosen to maximize the contributions of the corresponding individual orbitals. Curves are shifted and normalized for clarity. (e) Backbone profile ( $z$  height vs.  $x$  coordinate) along the dashed line from (b). (f) Individual STS spectra from (c) measured at  $x=2.1$  and  $2.7$  nm as indicated by horizontal lines in (c). Spectra are shifted for clarity. The LUMO state manifests itself as a peak at  $1.85$  V in the spectrum measured at  $x=2.7$  nm, while LUMO+1 is observed as a peak at  $2.3$  V in the spectrum measured at  $x=2.1$  nm. Only a shoulder of the LUMO+2 states is observed at  $2.6$  V ( $x=2.7$  nm).

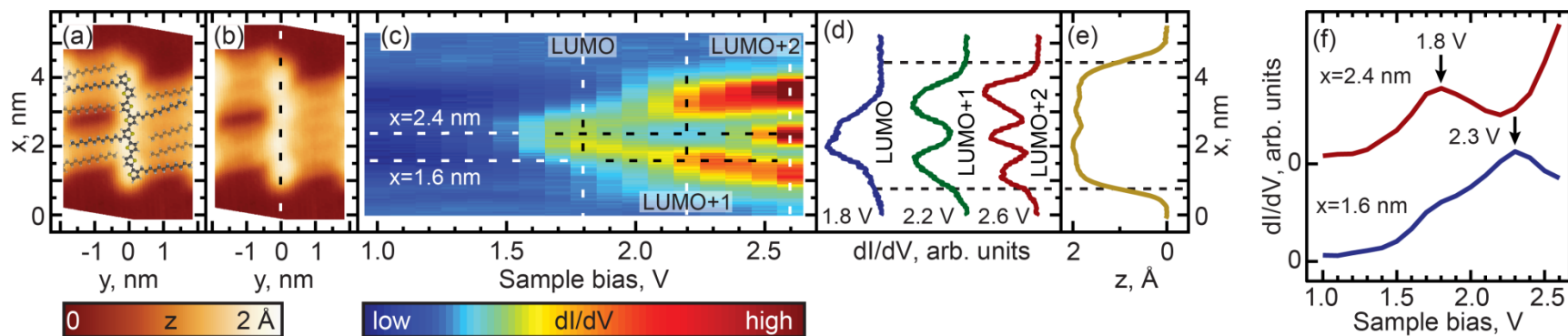


**Fig. 6.3.** Same as Figure 6.2 for a TTT conformer of 8T molecules. The molecule is situated in the center of the molecular aggregate, with alkyl chains on both sides (see Figure D1d).

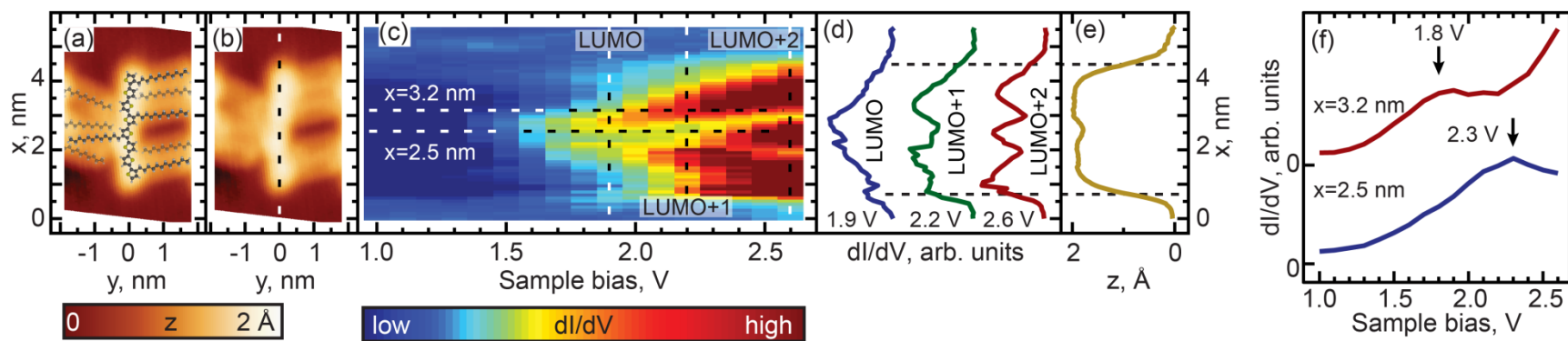


**Fig. 6.4.** Same as Figure 6.2 for a CTT conformer of 8T molecules.

map contains features attributable to a progression of three orbitals—LUMO, LUMO+1 and LUMO+2—showing the characteristic particle-in-a-box spatial distributions: the LUMO+1 and LUMO+2 orbitals show one and two spatial nodes respectively, while the LUMOs are relatively featureless along the molecular backbones (Figures 6.2d, 6.3d and 6.4d). The assignment of LUMO, LUMO+1 and LUMO+2 orbitals in Figures 6.2, 6.3 and 6.4 is supported by DFT calculations carried out for 8T molecules in gas phase (Figures 6.5, 6.6 and 6.7). Indeed, for CCC, TTT and CTT conformations DOS patterns similar to those of Figures 6.2c, 6.3c and 6.4c are found in calculations (Figures 6.5a, 6.6a and 6.7a). For each molecular conformation, the patterns are formed by three states, LUMO, LUMO+1 and LUMO+2 with particle-in-a-box-like spatial structures (Figures 6.5b, 6.6b and 6.7b) similar to those in Figures 6.2d, 6.3d and 6.4d. The particle-in-a-box-nature of these states is evident from the corresponding calculated wavefunctions showing the characteristic nodal patterns (Figures 6.5c, 6.6c and 6.7c).

The LUMO+1 and LUMO+2 orbitals appear more delocalized relative to the LUMO orbitals (compare DOS profiles in Figures 6.2d, 6.3d and 6.4d to topography profiles in Figures 6.2e, 6.3e and 6.4e), which is a consequence of several factors. First, due to the longer spatial wavelength of the lowest-energy particle-in-a-box state, the probability density of this state changes on a longer scale and therefore is suppressed over a longer spatial range at the ends of the oligothiophene backbone. In addition, higher-energy states are generally more spatially extended due to the lower effective tunneling barrier. Finally, the fact that the tunneling current (identical for all measured spectra) is composed of contributions from each unoccupied state means that the LUMO contribution is further suppressed via topographic effects when the tip is positioned near

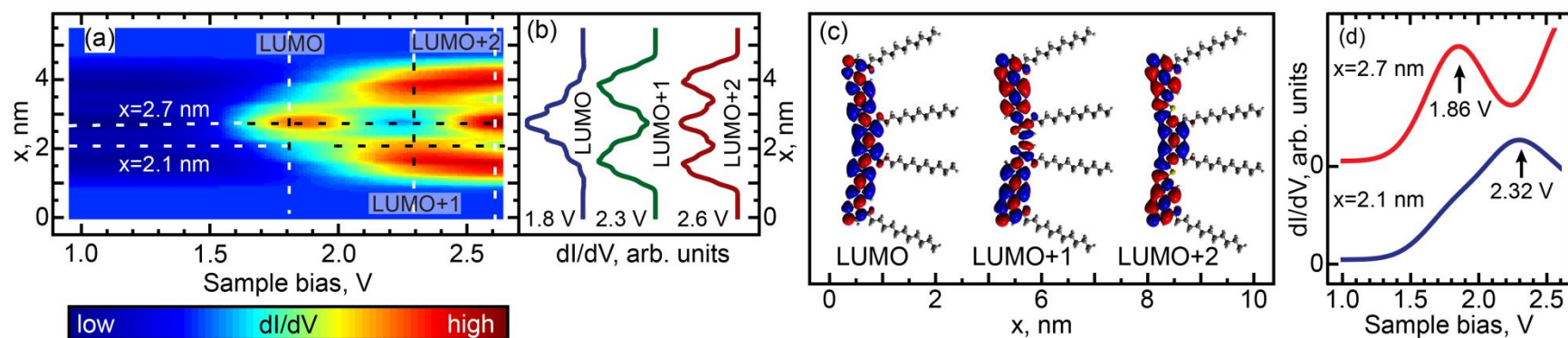


**Fig. 6.5.** Calculated electronic DOS for a CCC conformer of 8T molecules. (a) DOS (compare to Figure 6.2c) as a function of the bias voltage and position  $x$  along the path similar to that shown in Figure 6.2b. (b) LUMO, LUMO+1 and LUMO+2 DOS (compare to Figure 6.2d) along the same path as in (a), obtained at voltages corresponding to the vertical dashed lines in (a). These voltages were chosen to maximize the contributions of the corresponding individual orbitals. Curves are shifted and normalized for clarity. (c) Three-dimensional representations of DOS for LUMO, LUMO+1 and LUMO+2 showing nodal patterns (along the molecular backbone) characteristic of the particle-in-a-box nature of these states (no nodes for LUMO, one node for LUMO+1 and two nodes for LUMO+2). (d) Individual DOS spectra from (a) measured at spatial locations indicated by horizontal lines in (a). Spectra are shifted for clarity. The LUMO state manifests itself as a peak at 1.86 V (top curve), while LUMO+1 is observed as a peak at 2.32 V (bottom curve). Electronic structure calculations were performed with density functional theory (DFT) calculations using B3LYP/6-31G\*.



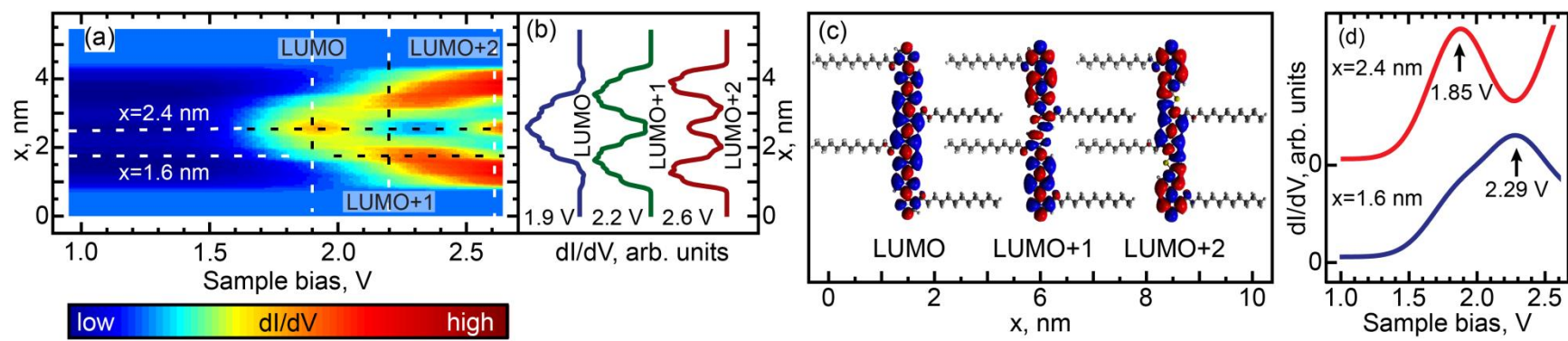


**Fig. 6.6.** Same as Figure 6.5 for a TTT conformer of 8T molecules.

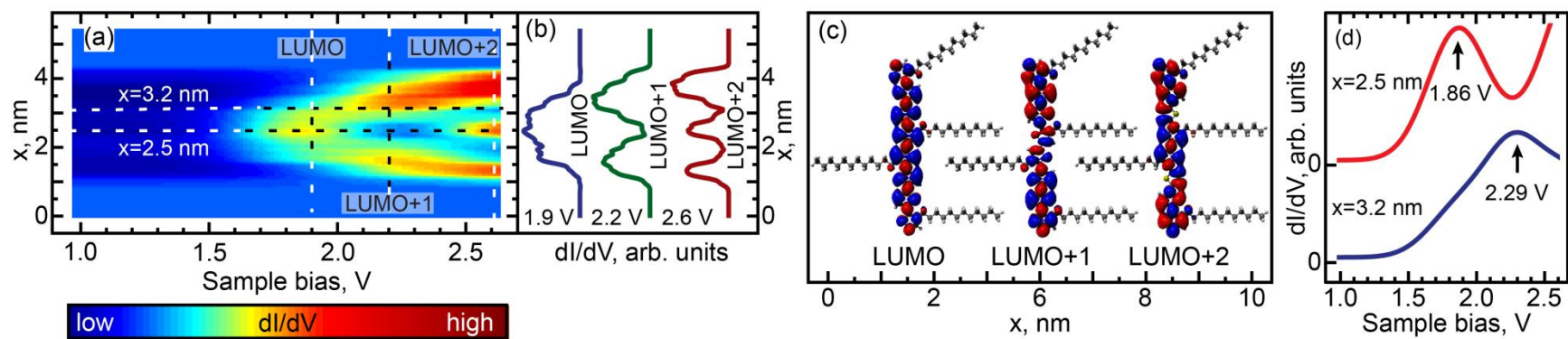


**Fig. 6.7.** Same as Figure 6.6 for a CTT conformer of 8T molecules.

the ends of the oligothiophene backbone, where higher-energy states have larger contributions to the tunneling current (the feedback loop was opened at a bias of 2.6 V for all STS maps. The tip height was therefore determined by contributions from the first three unoccupied molecular orbitals). A similar relationship between the localization scales of the LUMO, LUMO+1 and LUMO+2 orbitals is reproduced in our theoretical calculations (Figures 6.5b, 6.6b and 6.7b).

While the unoccupied molecular orbital energies are the same within experimental error for all conformations, there are asymmetries observed in DOS intensity across the molecular backbones (Figures 6.2d, 6.3d and 6.4d). Since DFT calculations for the CCC and TTT conformers do not exhibit asymmetry in DOS intensity (Figures 6.5b and 6.6b), it is likely that the observed asymmetric experimental DOS intensity (Figures 6.2d and 6.3d) is due to factors other than conformational variation for these conformers. This is unsurprising as all neighboring thiophenes in the CCC and TTT backbones adopt mutual cis- and trans-configurations, respectively. However, this is not the case for the CCT conformer, and indeed DFT results show uneven LUMO, LUMO+1 and LUMO+2 intensity across the molecular backbone (Figure 6.7b), suggesting that torsional conformation variations can lead to variations in DOS intensity.

Despite the completely different torsional conformations and variations in DOS intensity in the excited unoccupied molecular orbitals of the molecules in Figures 6.2, 6.3 and 6.4, their orbital energies are essentially the same (1.8V for LUMO and 2.3 V for LUMO+1, as determined from Figures 6.2f, 6.3f, and 6.4f) within the experimental error (~50 mV). These observations are mirrored by the calculated state energies (obtained from Figures 6.5d, 6.6d and 6.7d), which are very similar for all torsional conformations,

as summarized in Figure 6.8. Because our calculations were carried out for molecules in the gas phase, the similarity of the experimentally determined and calculated orbital energies suggests that the oligothiophene interaction with the Au(111) surface is relatively insensitive to the molecular conformation, with any differences between conformers being less than 50 mV. To further test this conclusion, we studied 7T molecules with analogous conformations to those of 8T (Figures D5, D6 and D7). Because of their different structure and reduced symmetry, the interaction of 7T molecules with Au(111) may be different from that of 8T molecules, which could potentially lead to a different magnitude of electronic structure variations for different 7T conformers. Similarly to 8T molecules, we identify three representative conformations: CC (orientation of ligands corresponding to a cis-cis combination, Figure D5a), TT (trans-trans ligand orientations, Figure D6a), and CT (cis-trans ligand orientations following an unsubstituted section of the backbone, Figure D7a). Analogously to the case of 8T molecules, DOS maps of different conformers of 7T oligothiophenes (Figures D5c, D6c and D7c) show patterns attributable to progressions of three particle-in-a-box-like orbitals, LUMO, LUMO+1 and LUMO+2, consistent with theoretical calculations (Figures D8, D9 and D10). As with the 8T molecules, all studied conformers of the 7T molecules showed, within the 50 mV experimental error, nearly the same orbital energies (1.9 V for LUMO and 2.5 V for LUMO+1), which are close to the theoretically predicted values summarized in Figure 6.8.

Another example of the lack of sensitivity of the oligothiophene electronic structure to molecular conformation is provided by our recent work on 4T molecules, where similar orbital energies were found for both cis and trans conformations, and the

variation in molecular orbital energies were found to be attributable to the local variations in the Au(111) surface reactivity caused by the  $22 \times \sqrt{3}$  surface reconstruction.<sup>50</sup> In the present study, similar orbital energy variations with standard deviations of 40-60 mV (depending on the molecular structure and conformation), comparable to the experimental error (~50 mV) were found. Thus, because the oligothiophene unoccupied molecular orbital energies were found to be insensitive to the torsional conformation of molecules with a wide range of structures, it is likely that conformational differences in the oligothiophene interaction with the Au(111) surface are less than 50 meV.

## 6.5. Conclusions

Our results, obtained using STS spectroscopy, demonstrate that different torsional conformers of oligothiophene molecules with different lengths and (alkyl) substitutional patterns show molecular orbital energies nearly independent of the molecular conformations. While these results are consistent with theoretical simulations for oligothiophenes in the gas phase, the experimental demonstration of similar unoccupied molecular orbital energies (within 50 meV) across multiple planar molecular conformation, as demonstrated in our work, suggests that the oligothiophene interaction with the Au(111) surface on molecular energy levels in general is relatively insensitive to the molecular conformation. This is an important result for applications utilizing charge transport through thin films based on longer substituted oligothiophenes and polythiophenes, where significant local variations in conformational structure are often found.<sup>30, 32, 40, 41</sup> While decreasing bulk crystallinity, indicating an increase in conformational disorder, in poly- and oligo-thiophene films is associated with an increase in trap density,<sup>64</sup> our results demonstrate that oligothiophene conformational disorder

does not lead to a corresponding diversity in planar molecular electronic structure, implying that previously observed bulk electronic disorder is due to intermolecular effects not investigated in this work. The insensitivity of the oligothiophene molecular electronic structure to torsional conformation presented here may mean a low degree of electronic disorder, and consequently, lower probability of charge carrier trapping within molecular backbones in poly- and oligo-thiophene materials. Indeed, molecular orbital energy variations found in our STS measurements are comparable to the energetic disorder (20-40 meV) characteristic of high-mobility ( $\sim 0.1 \text{ cm}^2/\text{Vs}$ ) polythiophene samples.<sup>65</sup>

## **6.6. Bridge to Chapter VII**

In the next chapter we will extend our STM/STS study of alkyl-substituted oligothiophenes to the molecules featuring conformations with bent backbones. We will fully utilize STM-UO potential in this final study by using two-dimensional (2-D) STS spatial mapping, that will help to visualize in real space particle-in-a-box-like oligothiophene molecular orbitals for backbones deviating from straight shape to different degree. It will be shown that different planar conformers with significant geometrical distortions of oligothiophene backbones possess similar electronic structures, strengthening the claim that oligothiophene materials have a negligible conformation-induced electronic disorder when deposited on a metal surface.

# CHAPTER VII

## REAL-SPACE VISUALIZATION OF CONFORMATION- INDEPENDENT OLIGOTHIOPHENE ELECTRONIC STRUCTURE

This chapter by Benjamin N. Taber, Dmitry A. Kislitsyn, Christian F. Gervasi, Jon M. Mills, Ariel E. Rosenfield, Lei Zhang, Stefan C. B. Mannsfeld, James S. Prell, Alejandro L. Briseno, and George V. Nazin has been previously published under the same title in *The Journal of Chemical Physics* **144**, 194703 (2016). Copyright © 2016 AIP Publishing LLC.

### 7.1. Introduction

We present scanning tunneling microscopy and spectroscopy (STM/STS) investigations of the electronic structures of different alkyl-substituted oligothiophenes on the Au(111) surface. STM imaging showed that on Au(111), oligothiophenes adopted distinct straight and bent conformations. By combining STS maps with STM images, we visualize, in real space, particle-in-a-box-like oligothiophene molecular orbitals. We demonstrate that different planar conformers with significant geometrical distortions of oligothiophene backbones surprisingly exhibit very similar electronic structures, indicating a low degree of conformation-induced electronic disorder. The agreement of these results with gas-phase DFT calculations implies that the oligothiophene interaction with the Au(111) surface is generally insensitive to molecular conformation.

## 7.2. Background

Alkyl-substituted, solution processable oligo- and polythiophenes are an important category of semiconductor materials,<sup>1-3</sup> with such applications as photovoltaic devices,<sup>4-6</sup> field-effect transistors,<sup>7-10</sup> and light-emitting diodes.<sup>11, 12</sup> The conformation of the  $\pi$ -conjugated backbone determines, to a considerable degree, the electronic structure of oligomers and polymers, and therefore can have an impact on their charge transport properties. Molecular conformation of substituted oligo- and polythiophenes is intertwined with molecular packing,<sup>13, 14</sup> which largely governs intermolecular charge transport in thin films based on oligomers and polymers.<sup>15, 16</sup> While bulk molecular packing is important in determining charge transport,<sup>17</sup> electronic transport is also strongly affected by the properties of interfaces between disparate materials, which can be structurally different from the bulk.

A powerful approach for investigating interfacial molecular structure is afforded by scanning tunneling microscopy (STM), with a large body of STM-based work available for molecular self-assembly in the regime of weak molecule-surface interactions, with molecules typically adsorbed on such surfaces as highly-oriented pyrolytic graphite.<sup>18-24</sup> In this weak substrate-interaction regime, molecular packing structures are generally defined by intermolecular interactions between the alkyl substituents. STM studies of stronger molecule-substrate interaction regimes often employed metal surfaces, representing molecule-electrode interfaces,<sup>20, 25-33</sup> and reported significant conformational polymorphism in polythiophenes<sup>26-28</sup> and oligothiophenes,<sup>29-32</sup> especially in contrast to thiophene-containing molecules on weakly interacting surfaces such as graphite.<sup>26</sup>

STM also enables investigations of the effect of molecular conformational disorder on electronic structure by using scanning tunneling spectroscopy (STS), which has been used to study oligothiophene electronic structure on a variety of surfaces.<sup>19, 20, 34-38</sup> In particular, STS studies of unsubstituted linear and cyclic oligothiophenes showed that, to a first approximation, electronic states in both types of oligothiophenes can be described as particle-in-a-box (PIAB) states subjected to appropriate boundary conditions.<sup>35</sup> Recently, by using STS, our group showed that the electronic structures of linear alkyl-substituted oligothiophenes of varied lengths displayed PIAB-character, and were not affected by variations in their torsional conformations.<sup>39</sup> The nature of electronic states in oligothiophenes subjected to other types of conformational distortions such as bending deformations, however, has so far not been established experimentally.

Here we report a STM/STS study of the electronic structures of alkyl-substituted oligothiophenes adsorbed in different conformations on the Au(111) surface. Substituted oligothiophenes with eight and seven thiophene subunits, hereafter referred to as 8T and 7T, respectively, are sufficiently long to be treated as finite-length models of polythiophenes. We deposited sub-monolayer coverages of these molecules on a Au(111) substrate, which serves as a model electrode surface. We visualize molecular orbitals by combining electronic density of states (DOS) maps with STM topographies, revealing progressions of PIAB-like molecular states. Surprisingly, these molecular electronic states are similar across different conformations, including highly bent, distorted molecules. Density functional theory (DFT) gas-phase electronic structure calculations closely correlate to the experimentally-observed molecular orbitals, which suggests that the Au-oligothiophene interaction is largely insensitive to planar molecular conformation.



### 7.3. Experimental details

STM and STS measurements were conducted at ~22 Kelvin, with a home-built cryogenic (closed-cycle cryostat-based) ultra-high vacuum (UHV) STM system featuring a Pan-style scanner from RHK Technology.<sup>40</sup> To prepare atomically flat Au(111) substrates in situ, gold films on mica were repeatedly subjected to a cycle consisting of Ne-ion bombardment and subsequent ~300° C anneals. 8T and 7T molecules were prepared by Briseno and coworkers,<sup>41</sup> nanoelectrospray ionization (nano-ESI) mass spectrometry [solution in THF, ESI voltage 1.4 kV] was used to confirm molecular structure (See Fig. D1 in the Supporting Information in Appendix D). Sub-monolayer concentrations of oligothiophene molecules were deposited on the Au surface at room temperature via in situ sublimation, with the vacuum pressure no higher than 10<sup>-10</sup> Torr. STS measurements were conducted using the lock-in technique (modulation frequency 570 Hz), which gives differential conductance (dI/dV) proportional to the local density of states (LDOS).<sup>42</sup>

Electronic structure calculations were performed by density functional theory (DFT) electronic structure calculations with Gaussian 09<sup>43</sup> using B3LYP/6-31G\*,<sup>44, 45</sup> and analyzed with Multiwfn.<sup>46</sup> In order to create theoretical density of states (DOS) maps similar to the experimental DOS maps, we created a cube file of the relevant molecular orbital in Gaussian09, squared the cube file using MultiWfn, and plotted the now squared cube in Matlab after applying a spatial blurring filter. For single-point experimental LDOS spectra, we assigned a full-width half-maximum of 500 meV in MultiWfn to the LDOS of the indicated spatial locations [MultiWfn option 3.12.4].

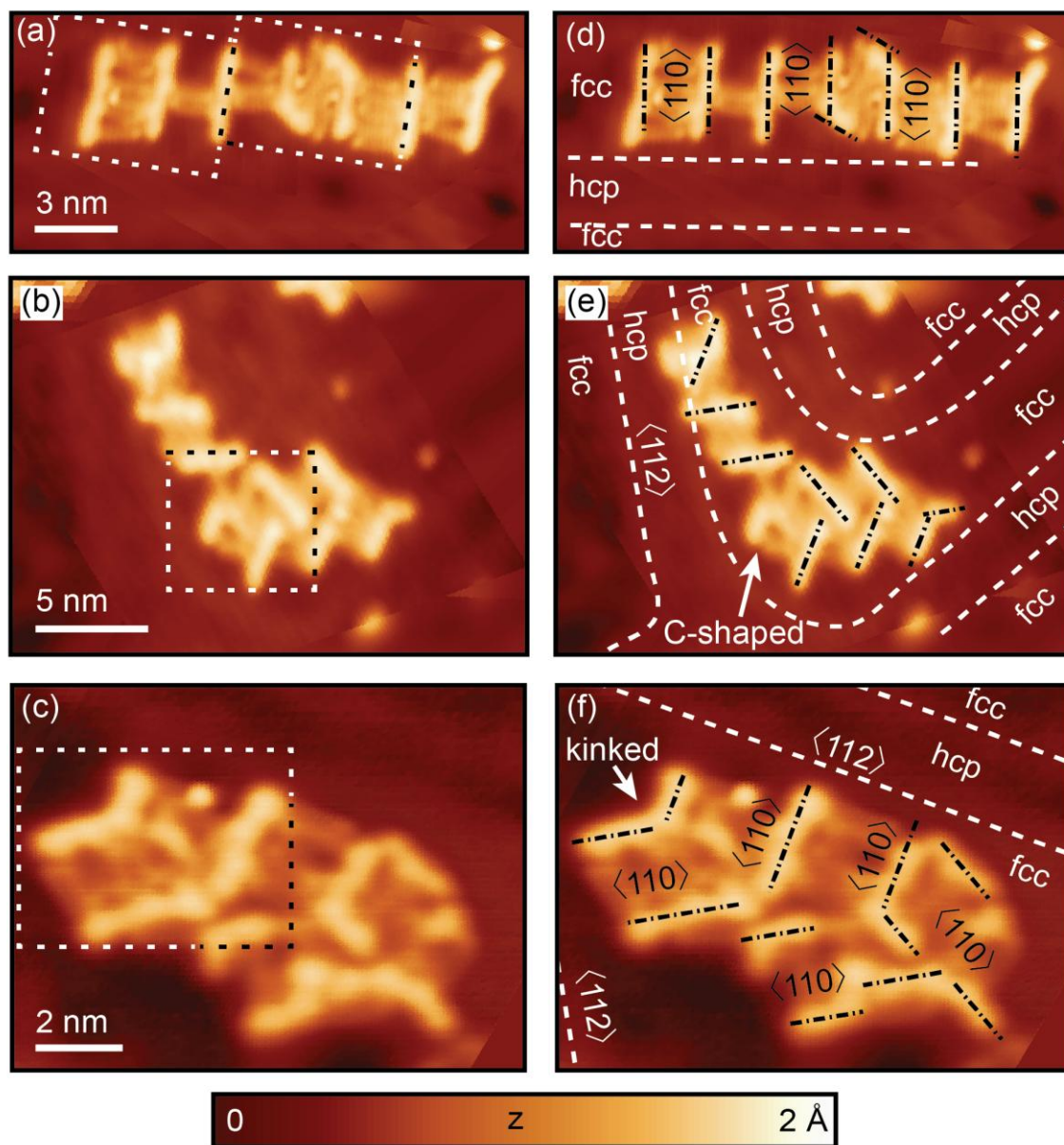


**Fig. 7.1.** Adsorption of oligothiophene molecules on Au(111). (a-c) STM images [set point 100 mV, 5 pA] of aggregates of oligothiophene molecules absorbed on the Au(111) surface. (d-f) STM images from (a-c) with indicated molecular orientations, Au(111) crystallographic directions, and highlighted surface-reconstruction ridges (white dashed lines). The oligothiophene backbones are aligned along the  $\langle 110 \rangle$  directions of the Au(111) surface, perpendicular to the straight sections of surface-reconstruction ridges, which run parallel to the  $\langle 112 \rangle$  directions. Dashed boxes in (a-c) correspond to STM images in Fig. 7.2.

## 7.4. Results and discussion

### Molecular adsorption arrangements.

STM imaging of 8T and 7T, following room-temperature sublimation on to the Au(111) surface, showed that the molecules self-assembled into aggregates of varying size (Fig. 7.1, see also Figs. 7.2a-d for the internal structures of molecular aggregates). The arrangement of molecules in such aggregates varied considerably, from linear chain-like structures (Fig. 7.1a) to “curved” chain-like structures (Fig. 7.1b) to two-dimensional islands (Fig. 7.1c). Oligothiophene adsorption corresponded to structural features of the Au(111)  $22 \times \sqrt{3}$  surface reconstruction, which produces alternating regions of face-centered cubic (fcc) and hexagonal close-packed (hcp) lattice structures separated by reconstruction “ridges” visible in STM images (dashed lines in Figs. 7.1d-f). Molecular aggregates formed primarily in the fcc regions of the Au(111) surface and were essentially nonexistent in the hcp regions (Figs. 7.1d-f), in agreement with observations for shorter oligothiophenes.<sup>34, 47, 48</sup> The oligothiophene preference for fcc adsorption is likely caused by the varied surface-Au atom coordination in the two regions, which results in differing reactivities.<sup>47</sup> The oligothiophene backbones within the molecular aggregates exhibited reproducible registry with the Au(111) lattice, as seen by comparing lattice directions (deduced from the ridge-like surface reconstruction features) with molecular backbone orientations in Figs. 7.1d-f. In straight fcc regions, indicative of a more regular Au surface crystal structure, the oligothiophene backbones are usually straight and generally oriented along the  $\langle 110 \rangle$  directions, perpendicular to the  $\langle 112 \rangle$  directions of the Au(111) surface reconstruction ridges (Figs. 7.1d-f).

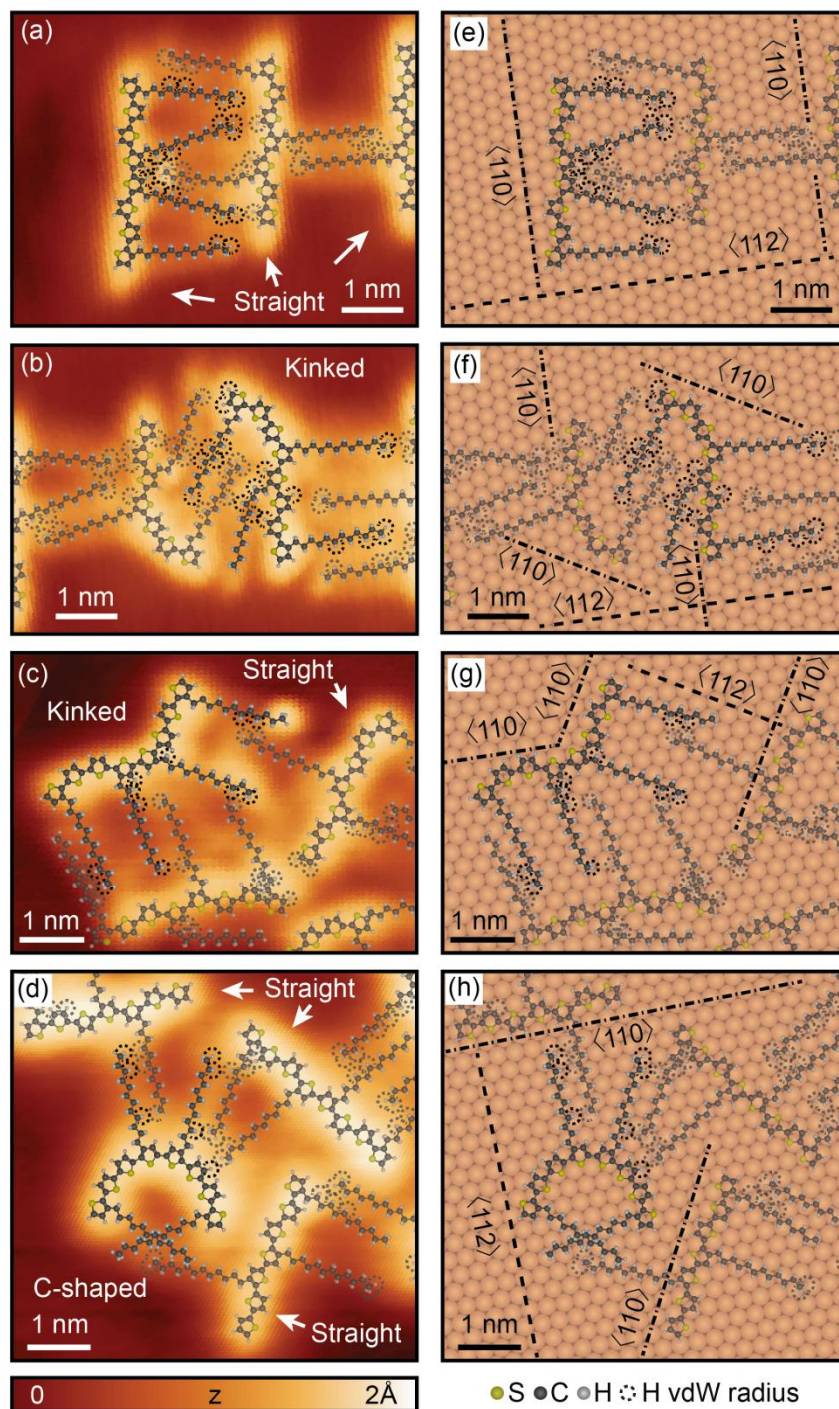


**Fig. 7.2.** Model of 8T molecules from Fig. 7.1 matched to the Au(111) surface lattice. (a-d) STM images [set point 100 mV, 5 pA] of sub-areas from Figs. 7.1a-c. (e-h) Models of oligothiophene molecules from (a-d) overlaid on the Au(111) lattice. Crystallographic directions are indicated. Dashed circles indicate the van der Waals radii of the hydrogen atoms.

High-resolution STM images show that along with relatively straight molecular conformations (Fig. 7.2a), “kinked” (Figs. 7.2b,c) and “C-shaped” (Fig. 7.2d) conformations also exist on the Au(111) surface. For all imaged oligothiophene molecules (Figs. 7.2a-d), alkyl ligands typically formed interdigitating patterns, suggesting that intermolecular interactions originating from the alkyl ligands play an important role in oligothiophene self-assembly, in accordance with previous studies.<sup>48-51</sup> The importance of ligand-ligand interactions is corroborated by theoretical modeling of the interaction energy for a pair of dodecane molecules, which gives values of 0.4-0.5 eV.<sup>52</sup> Figs. 7.2a-d further suggest that the self-assembly is also influenced by the interactions of thiophene sub-units and terminal methyl groups of alkyl ligands.

It is unlikely, however, that intermolecular interactions alone are responsible for the preferential orientations of oligothiophene backbones along the  $\langle 110 \rangle$  directions of Au(111). This follows from the lack of clear registry between the ligand orientation and the crystallographic directions of Au(111) [Figs. 7.2e-h], as well as varied backbone-ligand orientations, which were observed even for molecules corresponding to same conformational class (“straight” vs. “kinked” and “C-shaped” in Figs. 7.2e-h). The lack of directionality in ligand orientations is in contrast with STM-based experimental results<sup>53</sup> and theoretical calculations<sup>54</sup> for alkanes self-assembled on Au(111), where the molecules are found to align themselves approximately along the  $\langle 110 \rangle$  directions. These observations suggest that a mechanism other than intermolecular interaction is responsible for the observed preferential orientations of oligothiophene backbones.

An explanation for the preferential orientations of oligothiophene backbones along the  $\langle 110 \rangle$  directions of Au(111) is offered by recent studies of shorter four-

thiophene oligomers (4T in the following) on Au(111),<sup>47</sup> where intermolecular and molecule-surface interactions were similar to those for 8T and 7T molecules, and similar oligothiophene backbone orientations were observed. For 4T molecules, the preferred orientations along the  $\langle 110 \rangle$  directions were ascribed to the direction-sensitive charge-transfer interaction between S atoms of the thiophene subunits and the Au surface. In the case of single thiophene molecules, this charge-transfer interaction results in the S atoms preferentially adsorbing on Au top sites,<sup>55</sup> and having a local energy minimum of 40 meV.<sup>56</sup> By orienting along the  $\langle 110 \rangle$  directions, 4T backbones achieve the best matching of all four S-atoms to the Au(111) top-sites.<sup>47</sup> Straight 8T and 7T backbones exhibit a similar relationship (Figs. 7.2e-h), although there are some deviations from ideal Au top-site arrangements. These deviations are expected, as matching to the Au(111) lattice is more difficult for the longer 8T and 7T backbones. For 8T, the distance between the outer-most S atoms ( $\sim 2.8$  nm) most closely correlates to the distance between ten Au atoms in the  $\langle 110 \rangle$  direction (2.88 nm), while 4T better matches the Au(111) lattice, with the distance between the outer-most S atoms (1.19 nm) being comparable to the distance between four Au atoms in the  $\langle 110 \rangle$  direction (1.15 nm). Thus, while 4T backbones appeared straight in all STM images,<sup>47</sup> the discrepancy between the molecular structure and the Au(111) surface may have contributed to the observed non-linearity of 8T and 7T backbones in Fig. 7.2. Indeed, molecular models for “kinked” oligothiophene conformations (Figs. 7.2f-g) show that 8T and 7T backbones are effectively composed of segments, each roughly oriented along a different  $\langle 110 \rangle$  direction. The “C-shaped” conformation (Fig. 7.2f), while being less common, also allows placement of the majority

of its S atoms in the vicinity of the Au top sites (Fig. 7.2h), in accordance with the Au-S based molecule-surface interaction model.

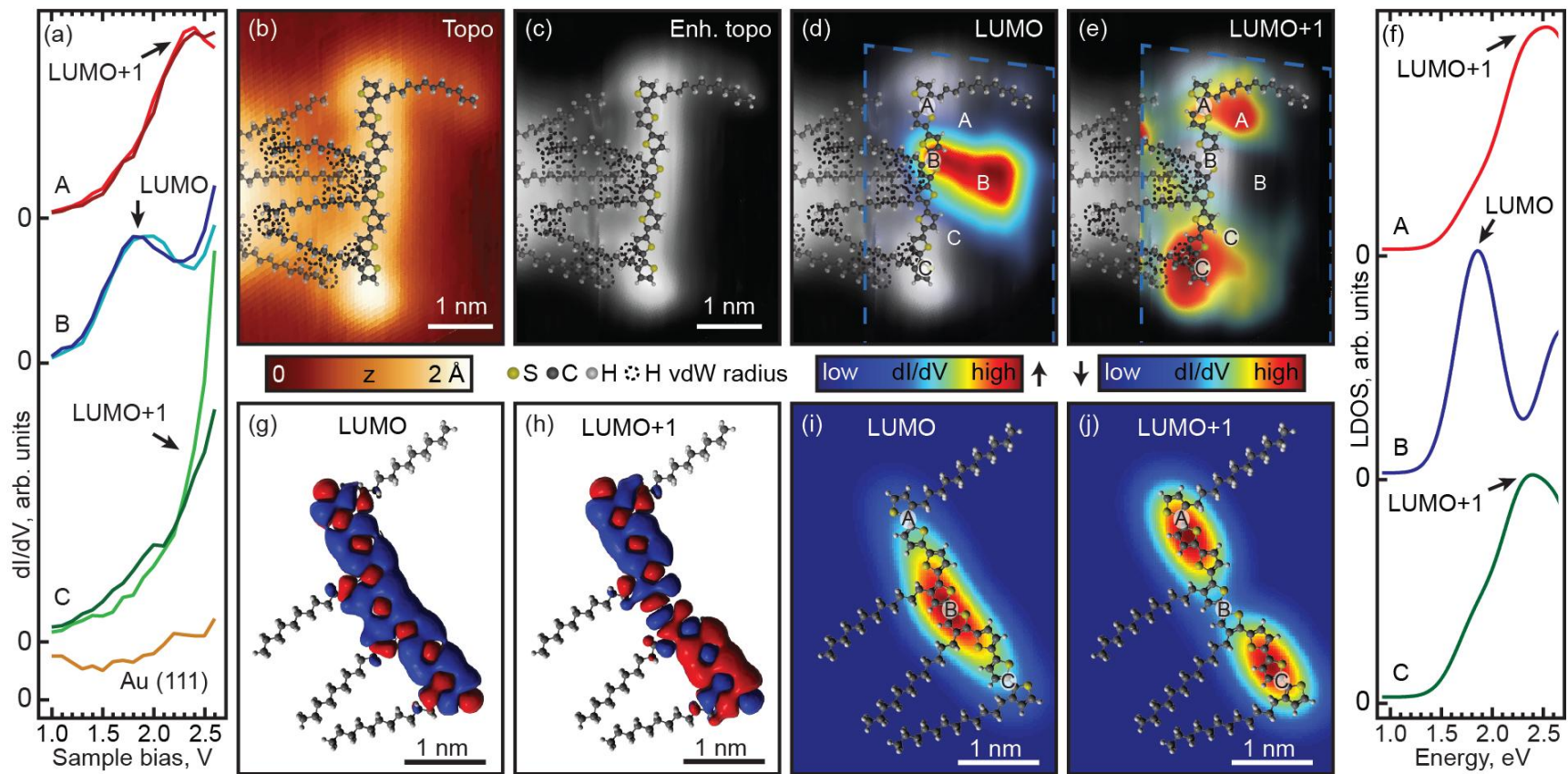
### **Scanning tunneling spectroscopy.**

In order to investigate the effect of length and conformation on oligothiophene molecular electronic structure, we used scanning tunneling spectroscopy (STS) to probe the electronic orbitals of 8T and 7T molecules. In our STS measurements, we recorded the differential conductance ( $dI/dV$ ) as a function of voltage under open feedback-loop conditions, giving a representation of the local energy-dependent DOS (see Experimental Methods for details).<sup>42</sup> Here we focus on the unoccupied molecular orbitals, as the occupied states were not clearly distinguishable from the structured background resulting from the Au(111) surface d-bands.

We investigated the spatial behavior of oligothiophene orbitals by recording two-dimensional spatial maps of the local DOS at selected bias voltages. An example of such

---

**Fig. 7.3.** Molecular orbitals for a straight 8T conformer. (a) DOS spectra measured on the straight 8T molecule in the locations indicated in (d-e) and DOS spectrum of the gold substrate. (b) STM image of the molecule. (c) STM image from (b) processed to “sharpen” the topographic features. (d) DOS for the LUMO orbital overlaid on image from (c). Mapped area is confined within the dashed lines. Areas with low DOS intensity (near-background) were rendered transparent to show registry with topography. (e) Same as (d) for the LUMO+1 orbital. (f) Individual DOS spectra calculated at spatial locations A, B, and C in (i) and (j). Spectra are shifted for clarity. (g-h) Theoretically calculated wavefunctions of LUMO and LUMO+1 showing the particle-in-a-box nature of these states (no nodes for LUMO, one node for LUMO+1). (i-j) Theoretically calculated DOS maps of LUMO and LUMO+1, exhibiting similar behavior to (d) and (e), respectively. For details of theoretical calculations see text.





a measurement for a “straight” 8T conformer is shown in Fig. 7.3. DOS spectra measured at different locations on the oligothiophene backbone show two main peaks, attributable to LUMO and LUMO+1 (Fig. 7.3a). DOS maps recorded at voltages corresponding to the LUMO peaks (Fig. 7.3d) show DOS concentrated in the centers of the 8T backbones, whereas in maps corresponding to LUMO+1 (Figs. 7.3e) the DOS intensities are more delocalized along the molecular backbones, with suppressed intensity in the centers of the backbones. This spatial behavior is indicative of the PIAB character of the LUMO and LUMO+1 states, which is more clearly seen in theoretically calculated unoccupied orbitals. Indeed, wavefunctions of unoccupied orbitals calculated using density functional theory (see Methods for details) can be described as standing waves with the number of nodes determined by the orbital energy, similar to the PIAB states. In the energy range corresponding to Figs. 7.3a, d and e, the theoretical DOS contains two states, which correspond to the LUMO and LUMO+1 orbitals (Fig. 7.3f). In accordance with the PIAB picture, the theoretically calculated LUMO (ground PIAB state) does not change sign along the molecular backbone (Fig. 7.3g), while LUMO+1 (first excited PIAB state) has different polarities at the opposite ends of the molecule (Fig. 7.3h). The spatial DOS distributions for the theoretically calculated LUMO and LUMO+1 wavefunctions (Figs. 7.3i-j) closely reproduce the experimental DOS maps (Figs. 7.3d-e), with the simulated LUMO DOS being relatively featureless along the molecular backbones (Fig. 7.3i), and the LUMO +1 DOS showing a spatial node (Fig. 7.3j).

In both the experimental and theoretical DOS maps, the LUMO appears more localized than the LUMO+1 (compare Figs. 7.3d and e, as well as Figs. 7.3i and j). This behavior can be attributed to the following factors. First, higher-energy states typically

appear more spatially extended due to the lower effective tunneling barrier at higher bias voltage. Second, the probability density of the lowest PIAB state changes over a longer spatial scale, and is therefore relatively suppressed at the ends of the oligothiophene backbone. Finally, because of the fact that all unoccupied states from the (substrate) Fermi level to the energy corresponding to the STM bias voltage contribute to the tunneling current (in this case including both the LUMO and LUMO+1), the LUMO is additionally suppressed via topographic effects near the ends of the molecular backbone due to the relatively greater contribution of the LUMO+1 state to the tunneling current. This “topographic” source of spatial modulation is responsible for the difference between the spatial extents of experimental and theoretical LUMO DOS (Figs. 7.3d and i, respectively). Even though this effect of “topographic” modulation can be well-reproduced in modeling, we do not incorporate it in Figs. 7.3i-j in order to show the intrinsic DOS distributions of LUMO and LUMO+1.

DOS measurements for “kinked” 8T molecules (Fig. 7.4) and even more strongly deformed “C-shaped” 8T molecules (Fig. 7.5) show behavior very similar to that described above for the “straight” 8T conformers. In particular, DOS spectra for both “kinked” and “C-shaped” 8T conformers show the presence of LUMO and LUMO+1 states (Figs. 7.4a and 5a), with spatial distributions showing the DOS concentrated in the center of the molecules for the LUMO (Figs. 7.4d and 5d), and at the ends of the molecule for the LUMO+1 (Figs. 7.4e and 5e). Mirroring the experimental results, theoretically calculated electronic orbitals for “kinked” and “C-shaped” conformers (Figs. 7.4f-g and 5f-g) are analogous to those obtained for “straight” conformers (Figs. 7.3f-g), and produce spatial DOS patterns (Figs. 7.4i and 5i for LUMOs, and Figs. 7.4j and 5j for

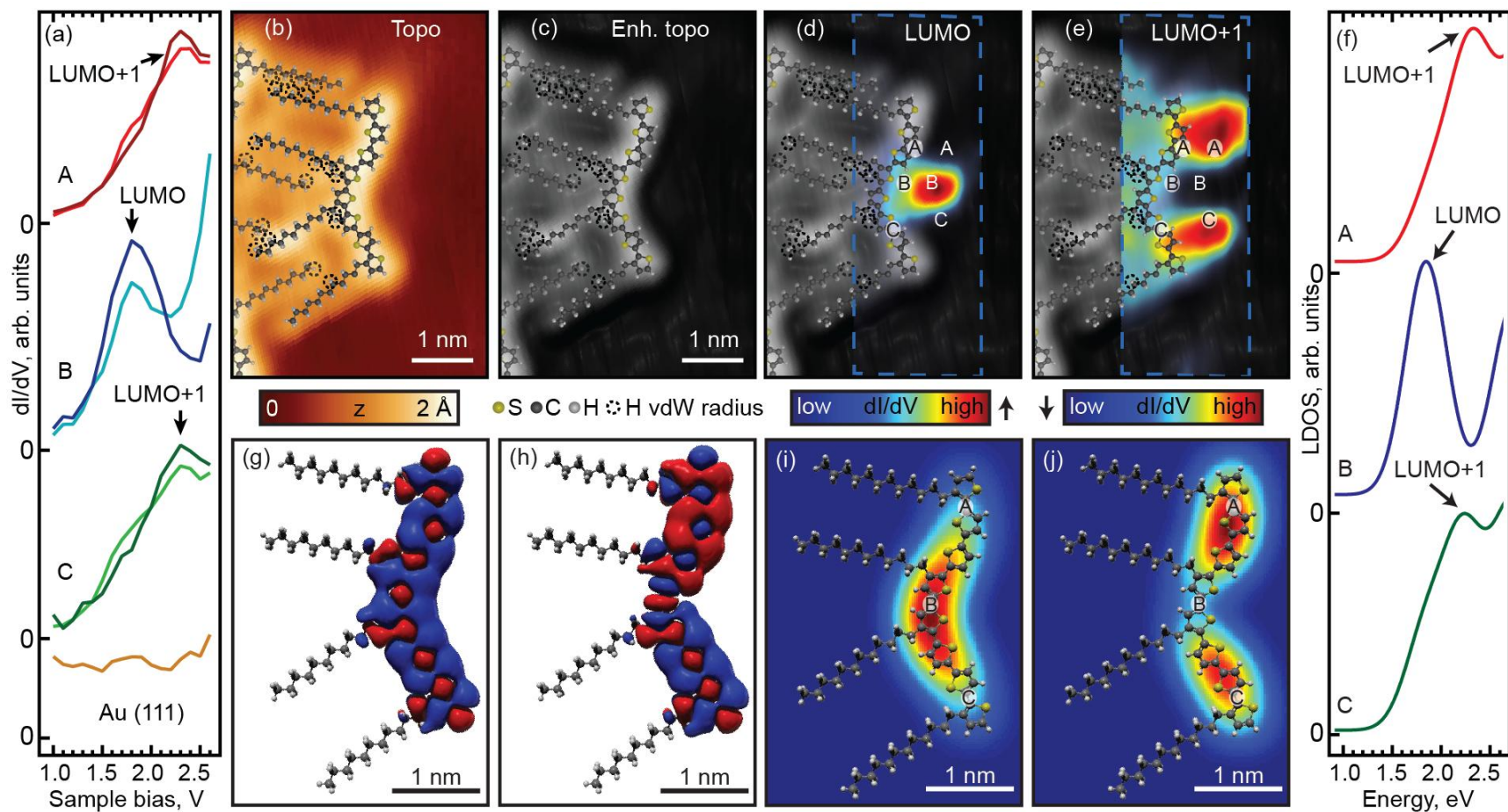


**Fig. 7.4.** Molecular orbitals for a kinked 8T conformer. Data arrangement and markings are identical to those used in Fig. 7.3.

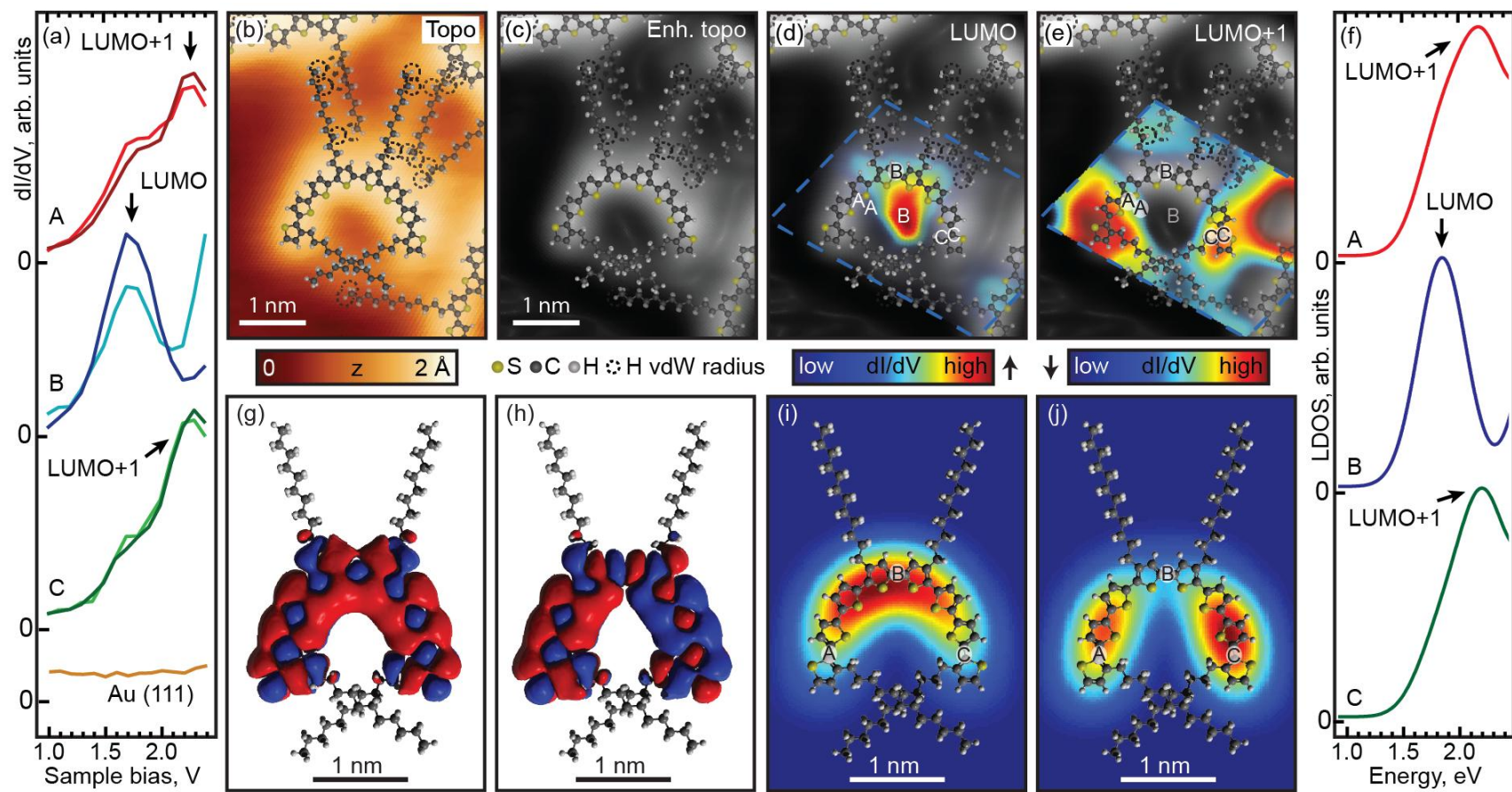


**Fig. 7.5.** Molecular orbitals for a curved 8T conformer. Data arrangement and markings are identical to those used in Fig. 7.3.

LUMO+1 states) similar to those found in Figs. 7.3i-j. Thus, the states in “kinked” and “C-shaped” 8T molecules can still be described as having PIAB character, despite the deviations from linearity of these molecular backbones.

To further study the effect of oligothiophene conformation on molecular electronic structure, we investigated alkyl-substituted 7T molecules, with structures similar to 8T molecules described above (See Figs. E1, E2, and E3 in the Supporting Information in Appendix D). Similarly to 8T molecules, we identified three representative conformations: “straight” (Fig. E1), “kinked” (Fig. E2), and “L-shaped” (Fig. E3, analogue of the 8T “C-shaped” conformation). Because of their different structure and reduced symmetry, the interaction of 7T molecules with Au(111) may be different from that of 8T molecules, which could potentially lead to a different magnitude of electronic structure variations for different 7T conformers. As was the case with 8T molecules, DOS mapping of the different 7T conformers (Figs. E1d-e, E2d-e, and E3d-e) showed very similar spatial patterns, attributable to the first two PIAB orbitals. The measured LUMO and LUMO+1 DOS distributions for 7T were also consistent with theoretical calculations (Figs. E1i-j, E2i-j, and E3i-j).

Surprisingly, despite the completely different conformations of “straight”, “kinked”, and “C-shaped” 8T and 7T conformers, their LUMO energies, summarized in Fig. 7.6, are essentially the same within the experimental error (~50 mV). Fig. 7.6 also shows the theoretically calculated LUMO energies (for the same 8T and 7T conformers), which are in close agreement with the experimental data. The similarity between the experimentally observed and calculated orbital energies implies that, since the DFT

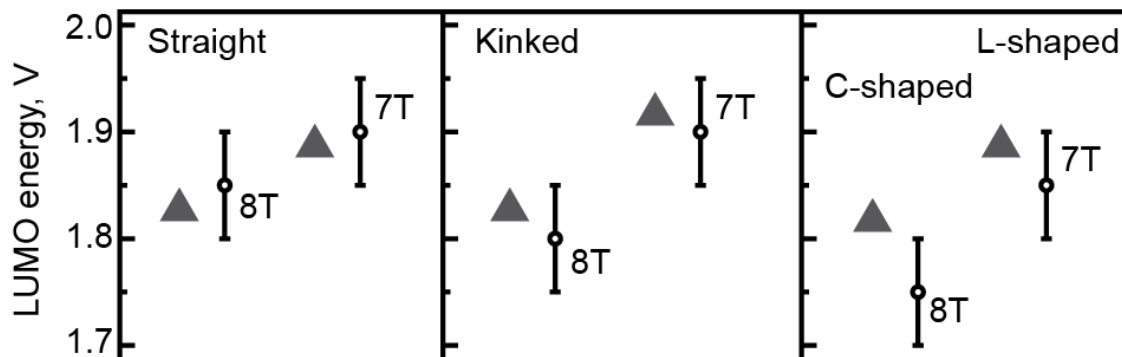


**Fig. 7.6.** LUMO energies for all measured and calculated 8T and 7T conformations. The data were obtained from Figs. 7.3f, 4f, 5f and Figs. E1f, E2f, E3f in the Supporting Information in Appendix D. Gray triangles are theoretical LUMO energies, and black circles are measured LUMO energies (experimental error  $\sim 50$  mV).

calculations were carried out in the gas phase, the oligothiophene interaction with the Au(111) surface is insensitive to molecular conformation.

Another illustration of the insensitivity of oligothiophene molecular electronic structure to molecular conformation has been reported in our recent, related work on 8T and 7T, where similar orbital energies were found for different torsional conformations of linear 8T and 7T molecules.<sup>39</sup> The observation that oligothiophene molecular electronic structure is insensitive to a wide range of bending and torsional conformations for oligothiophenes of different structures suggests that, in the general case, the oligothiophene interaction with the Au(111) surface is to a large extent insensitive to variations in molecular conformation.

## 7.5. Conclusions

By using spatially-resolved DOS mapping, we have demonstrated that different bending conformations of oligothiophenes adsorbed in a variety of planar configurations exhibit very similar electronic structures. These results are consistent with DFT gas-phase

calculations, indicating that the oligothiophene interaction with the Au(111) surface is insensitive to molecular conformation. Because similar results were reported recently for varied in-plane torsional conformations of oligothiophenes,<sup>39</sup> we can expect that the molecular electronic structures of different oligothiophene conformers may, in general, be largely insensitive to the molecular conformation as long as the thiophene units of the constituent molecules remain in-plane with each other. The experimental demonstration of this insensitivity is a significant result, since considerable local variations in conformational structure often exist in thin films (used in applications involving charge transport) based on substituted oligo- and polythiophenes.<sup>20, 22, 26-28</sup> The established insensitivity to conformational structure suggests that electronic disorder (and, consequently, charge carrier trapping) in oligo- and polythiophene materials with in-plane conformational disorder may not be significant. Indeed, the molecular orbital energy variations found in our experiments ( $\sim 50$  mV) are comparable to the energetic disorder of  $\sim 20$ - $40$  meV typically found in high-mobility ( $\sim 0.1$  cm<sup>2</sup>/Vs) polythiophene samples.<sup>1</sup> Experimental quantification of the impact of out-of-plane distortions on the molecular electronic structure, however, has not been carried out, and deserves further experimental study.

## **7.6. Bridge to Chapter VIII**

In the next series of chapters we will see application of STM-UO to even more challenging system for STM investigation on single particle level – colloidal quantum dots deposited from solution using in-vacuum pulse valve. In addition to demanding requirements for use of low tunneling currents and longer acquisition time due to low stability under excitation with tunneling electrons, this system presents challenges

associated with mobile ligands present on the surface of quantum dots as well as complex 3-D shape (in contrast to planar molecules). Unique characteristics of STM-UO allowed to overcome these difficulties and achieve unprecedented level of detail in characterization of electronic structures of colloidal quantum dots on molecular scale.



# CHAPTER VIII

## SPATIAL MAPPING OF SUB-BANDGAP STATES INDUCED BY LOCAL NON-STOICHIOMETRY IN INDIVIDUAL LEAD-SULFIDE NANOCRYSTALS

This chapter by Dmitry A. Kislitsyn, Christian F. Gervasi, Thomas Allen, Peter K. B. Palomaki, Jason D. Hackley, Ryuichiro Maruyama, and George V. Nazin has been previously published under the same title in *J. Phys. Chem. Lett.* **5**, 3701–3707 (2014).  
Copyright © 2014 American Chemical Society.

### 8.1. Introduction

The properties of photovoltaic devices based on colloidal nanocrystals are strongly affected by localized sub-bandgap states associated with surface imperfections. To understand the nature of such surface states, a correlation between their properties and the atomic-scale structure of chemical imperfections responsible for their appearance must be established. In this chapter, Scanning Tunneling Spectroscopy is used to visualize the manifold of electronic states in annealed ligand-free lead sulfide nanocrystals supported on the Au(111) surface. Delocalized quantum-confined states and localized sub-bandgap states are identified, for the first time, via spatial mapping. Maps of the sub-bandgap states show localization on non-stoichiometric adatoms self-assembled on the nanocrystal surfaces. The present model study sheds light onto the mechanisms of surface state formation that, in a modified form, may be relevant to the

more general case of ligand-passivated nanocrystals, where under-coordinated surface atoms exist due to the steric hindrance between passivating ligands attached to the nanocrystal surface.

## **8.2. Background**

Recently, thin films composed of lead chalcogenide colloidal semiconducting nanocrystals (NCs) have emerged as a promising class of photovoltaic materials that allow great flexibility in controlling their properties by means of tailored synthesis, processing and film deposition.<sup>1,2</sup> Further, quantum confinement effects in NCs can be exploited to control their photoexcitation dynamics in order to achieve multiplication of photo-generated carriers<sup>3-7</sup> and/or hot-electron extraction,<sup>8</sup> which may enable solar cells with efficiencies in excess of the Shockley–Queisser limit.<sup>9</sup> While substantial progress has been made towards improving the efficiency of NC-based photovoltaic devices, with recent reports of efficiencies above 8%,<sup>10,11</sup> the microscopic picture of the fundamental physical processes of photo-generation and charge transport in NC films remains incomplete. One of the important outstanding questions is the impact of the NC surface chemistry on the electronic properties of NCs. Imperfections in surface passivation or stoichiometry are thought to cause sub-bandgap states, which can have a significant impact on electron–hole recombination.<sup>12</sup> While evidence for such surface states was found in recent photoluminescence studies of as-synthesized lead chalcogenide NCs,<sup>13,14</sup> fabrication of functional photovoltaic devices may introduce further surface imperfections as it often involves a sequence of synthetic and processing steps including surface ligand exchange<sup>15,16</sup> and (in some studies) thermal annealing<sup>17,18</sup> that can both affect the nanocrystal surface chemistry. Indeed, sub-bandgap states have been identified

in processed NC films using a variety of techniques, including photoluminescence;<sup>14</sup> a combination of current-based deep level transient spectroscopy, thermal admittance and Fourier transform photocurrent spectroscopies;<sup>19</sup> Scanning Tunneling Spectroscopy (STS);<sup>20</sup> and photocurrent measurements in NC-based field-effect transistor devices.<sup>21</sup> Despite the insights provided by such studies, they do not provide direct information about the local chemical and spatial structures of surface states. This information is critically important for addressing the remaining uncertainties regarding the nature of such surface states, especially given the diversity of atomic sites present on NC surfaces arising from variations in ligand coverage and the presence of different crystallographic facets.

### **8.3. Experimental details**

Experiments were carried out in a home-built ultra-high vacuum (UHV) cryogenic STM system incorporating a STM scanner from RHK Technology.<sup>22</sup> An Au(111)/mica substrate was prepared *in situ* by using multiple sputter/anneal cycles. Thiol-terminated PbS NCs (synthesis of PbS NCs is described in the Supporting Information in Appendix F) were deposited on the Au(111) substrate in the load-lock section of the vacuum system using an in-vacuum solenoid pulse valve. The deposition parameters were chosen so as to obtain sub-monolayer NC coverage. The Au(111) substrate with deposited PbS NCs was then annealed overnight in ultra-high vacuum at progressively higher temperatures, with the final temperature of  $\sim 170^{\circ}\text{C}$ . This annealing temperature was chosen to achieve removal of residual unstable species remaining after the initial annealing steps. Figure F1 shows representative STM images of several NCs on a Au(111) surface. STM images were processed using the WSxM Software.<sup>23</sup>

All imaging and spectroscopic measurements were carried out at a temperature of 15 K using electrochemically etched silver tips. All STS spectra were recorded using the lock-in technique at ~600 Hz, and bias modulations varying from 10 mV (individual spectra, and one-dimensional spatial scans) to 50 mV (two-dimensional DOS maps).

#### **8.4. Results and discussion**

This chapter includes the first report of the spatial mapping of sub-bandgap states in individual PbS NCs using a combination of Scanning Tunneling Microscopy (STM) and Scanning Tunneling Spectroscopy (STS). PbS NCs deposited on Au(111) surfaces were annealed in ultra-high vacuum at 170 °C to remove surface ligands (see Experimental Details). Ligand-free NCs were targeted because they are unaffected by the uncertainties associated with different possible ligand shell configurations, and therefore serve as a useful model amenable to theoretical simulations.<sup>24-26</sup> (+ ref 37) NCs in devices are also often stripped of ligands to increase inter-particle electronic coupling\*.<sup>27</sup> In total, we studied 16 individual PbS NCs. The NCs were annealed at progressively higher temperatures until well-defined and reproducible NC topographies consistent with complete removal of ligands were obtained (Figure F1). The apparent heights of thus prepared NCs are typically 1-2 nm, while their lateral dimensions are 2-5 nm with width/height ratios being typically 2:1 to 3:1, which suggests that the NC shapes change significantly upon annealing. Importantly, annealed ligand-free NCs display topographic features, such as crystal facet steps and edges, showing visible angles consistent with different crystallographic directions (Figure F1).

STS spectra of individual NCs were obtained by measuring the differential tunneling conductance  $dI/dV$  as a function of the applied bias voltage (see Experimental

Details).<sup>28</sup> The recorded  $dI/dV$  signal serves as a measure of the local density of states (DOS). STS spectra of annealed NCs show progressions of occupied and unoccupied states separated by apparent band gaps of different magnitudes (Figure 8.1). All spectra in Figure 8.1 show similar progressions of states  $H_1$  (highest occupied state),  $E_{1,1}$  (lowest unoccupied state),  $E_{1,2}$  and  $E_2$  (both unoccupied states), with individual state energies varying for different NCs. The overall structure of the STS spectra shown in Figure 8.1 is consistent with the energy-dependent DOS curves calculated for ligand-free lead-chalcogenide NCs,<sup>24-26</sup> where DOS was found to be dominated by quantum-confined electronic states derived from the conduction and valence bands. These calculations show that the lowest-energy quantum-confined electronic states in stoichiometric ligand-free lead-chalcogenide NCs exhibit roughly s- and p- symmetries (the envelope component of the wavefunction), modulated on the atomic scale by their corresponding Bloch wavefunctions.<sup>24</sup> However, as we show below, the nature of states  $E_{1,1}$  and  $E_{1,2}$  in Figure 8.1 is different.

A common feature of all spectra in Figure 8.1 is that states  $E_{1,1}$  and  $E_{1,2}$  are separated by  $\sim 0.2$  V in all cases. Identifying the nature of states  $E_{1,1}$  and  $E_{1,2}$  is important because the lowest-lying unoccupied states are primarily responsible for the photophysical and electron transport properties of NC-based materials.<sup>21</sup> We note that overtones  $E_{1,2}$  are unlikely to be caused by vibrational excitation of NCs<sup>29</sup> due to their relatively large energetic spacing, inconsistent with the vibrational energy scale of PbS.<sup>30</sup> This energetic spacing also appears too large to be explained by electronic splitting (caused by the NC anisotropy) of the different L-valleys in the Brillouin zone.<sup>31</sup> Similar spectral features observed in STS studies of electrochemically-grown PbS NCs were

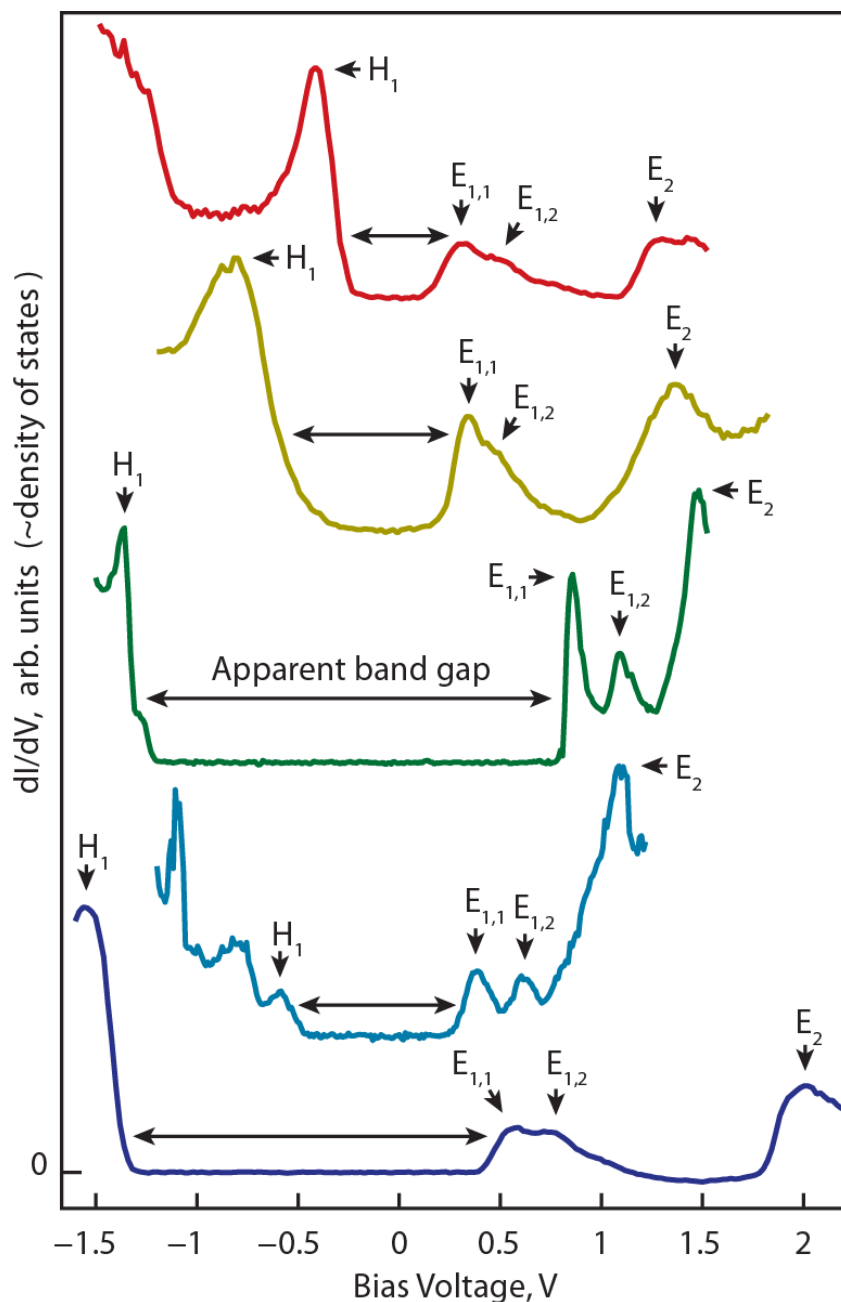


**Figure 8.1.** Representative  $dI/dV$  spectra for five PbS NCs (set point voltages and currents range from 1.2 V to 2.5 V, and 10 pA to 30 pA for the spectra shown). The bias voltage effectively serves as the energy scale (see, however, discussion associated with Figure F2 for a more complete description of the relationship between the bias voltage and energy). Occupied and unoccupied states are indicated by arrows and marked with an 'H' and 'E' for electrons and holes respectively. The apparent band gaps for each of the NCs are marked with double sided arrows.

attributed to particle-in-a-box-like states.<sup>32</sup> According to this interpretation, state  $E_{1,1}$  should correspond to the ground state, state  $E_2$  should correspond to the excited state varying along the Z-direction, and  $E_{1,2}$  is attributable to excited states varying in the XY plane. Spatial mapping of NC DOS shows that the nature of  $E_{1,n}$  states in the present case is more complex, as described below.

To understand the nature of the  $E_{1,n}$  bands, we have carried out DOS mapping for several NCs. Representative data for one such NC (referred to as  $NC_1$  in the following) are presented below. STM topography of  $NC_1$  shows a series of steps angled at  $120^\circ$  degrees with respect to each other (Figure 8.2a,b). This observation suggests that these directions correspond to the  $\langle 110 \rangle$  crystallographic directions, while the top surface of  $NC_1$  should correspond to the (111) crystallographic orientation, based on the stability of these facets established in TEM studies of restructuring of PbS NCs under similar temperatures in vacuum.<sup>33,34</sup> A cross-section of the topography for  $NC_1$  (Figure 8.2c) shows that the top facet, oriented at  $\sim 10^\circ$  with respect to the Au(111) surface, is relatively flat with corrugation at the angstrom-scale, consistent with complete removal of ligands.

A STS spectrum measured on top of  $NC_1$  (Figure 8.2d) shows an electronic DOS with a  $\sim 0.8$  eV bandgap formed by states  $E_{1,1}$  and  $H_1$ . Additional states  $E_2$  (1.3 eV) and  $H_2$  (-1.4 eV) are found at higher voltages. The lowest unoccupied state  $E_{1,1}$  shows a side-peak ( $E_{1,2}$ ), which is observed in most annealed NCs (Figure 8.1). STS spectra measured at different locations on  $NC_1$  show considerable variation in state energies and character. To visualize these variations, we recorded a spatial “cross-section” of the electronic DOS along a linear path across  $NC_1$  (Figure 8.3a). The resulting DOS cross-section (Figure 8.3b) shows quasi-periodic oscillations in intensity for the electronic DOS of states  $E_{1,n}$ .

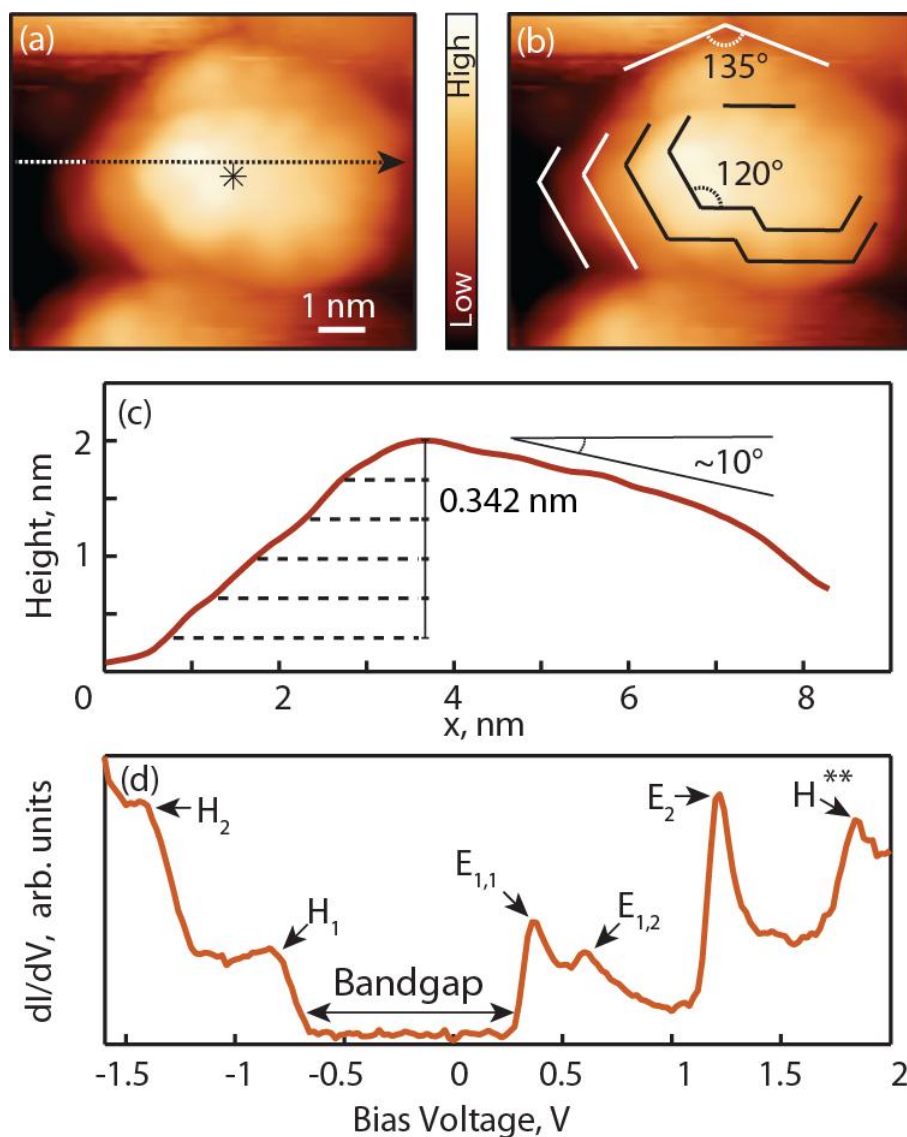


**Figure 8.2.** STM/STS characterization of a representative nanocrystal NC<sub>1</sub>. (a) STM topography image of NC<sub>1</sub> [set point 1.0 V, 1.0 pA]. (b) Topographical features attributable to step edges oriented along specific crystallographic directions. The majority of features indicate 120° angles, which suggests that the top facet of NC<sub>1</sub> corresponds to a {111} plane. (c) A cross-section of the topography [path indicated by the arrow in (a)] showing that the top facet of NC<sub>1</sub> is at a small angle with respect to the Au(111) surface. Individual steps are marked with dashed lines, with the step height (0.342 nm) corresponding to the distance between the sulfur {111} planes. (d) A representative STS spectrum [set point 2.0 V, 15 pA] measured at the location marked by the star in (a). Prominent occupied and unoccupied states are marked with an 'H' and 'E' respectively.



The spatial variations of all states  $E_{1,n}$  (Figure 8.3b) are nearly identical suggesting similar origins for the main peak and its sidebands. The spatial modulation of states  $E_{1,n}$  occurs with an average period of  $\sim 0.9$  nm, a large number as compared to the typical inter-atomic distances along the PbS(111) surface, which means that this modulation is not caused by the elemental contrast between Pb and S lattice sites that could be expected on a defect-free PbS surface.<sup>37</sup> In accordance with this assessment, the highest occupied state  $H_1$ , which is expected to be comprised of sulfur 3p atomic orbitals,<sup>26</sup> is not visibly modulated. The only identifiable variation of the  $H_1$  state is a minor change in  $H_1$  energy (from -0.8 V to -0.7 V and back to -0.8 V) as the scan progresses along the path in Figure 8.3a from  $P_1$  to  $P_5$ .

The trajectory of the  $H_1$  energy variation roughly follows the NC topography (high topographic locations correspond to the lower (in absolute value of applied voltage) onsets of resonant tunneling through  $H_1$ ), which is explained by the variation of the voltage drop inside the NC.<sup>38</sup> A smaller variation in the tunneling onset energy is found for the unoccupied states, which is attributable to the different work-functions of the tip and sample, as explained further in the Supporting Information in Appendix F. Insight into the nature of states  $E_{1,n}$  can be gained from a detailed analysis of their spatial behavior, as discussed in the following.

To characterize the spatial behavior of the  $NC_1$  electronic structure, we recorded STS spectra on a two-dimensional grid of (32 by 32) points covering the spatial range shown by the yellow rectangle in Figure 8.4a. In the overall bias voltage range sampled in these spectra, several spatial DOS patterns associated with distinct electronic states shown in Figure 8.3 are identified (Figure 8.4). These patterns show that the distributions

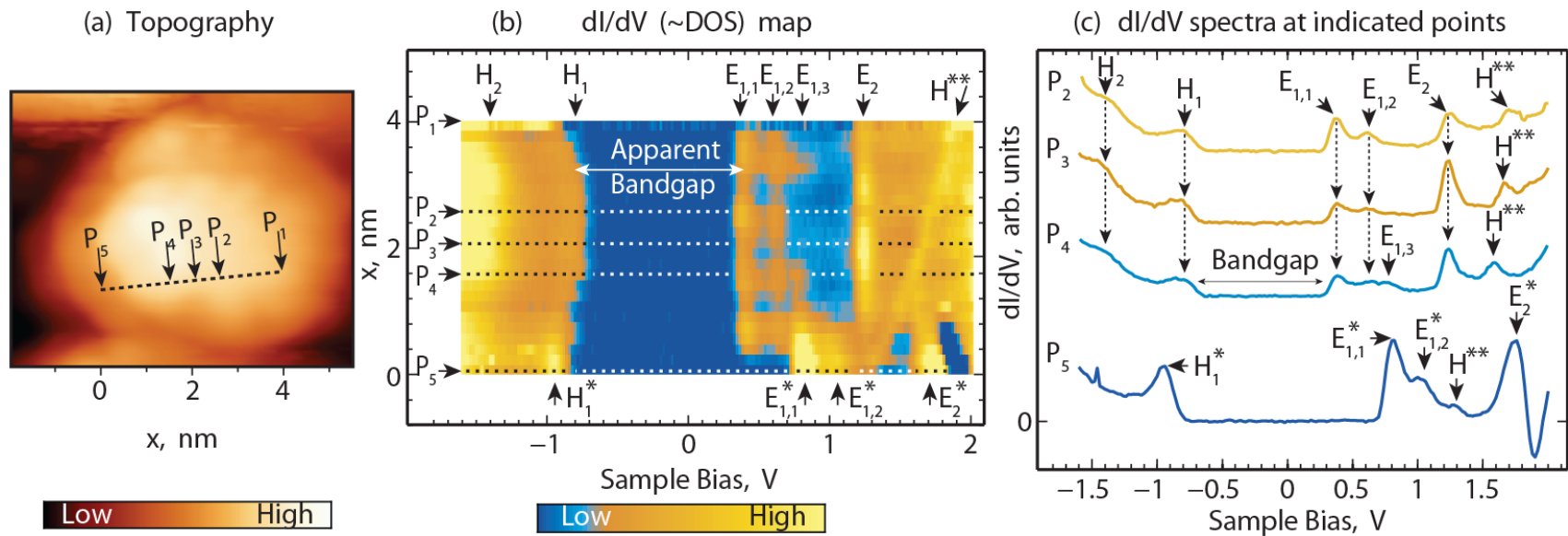
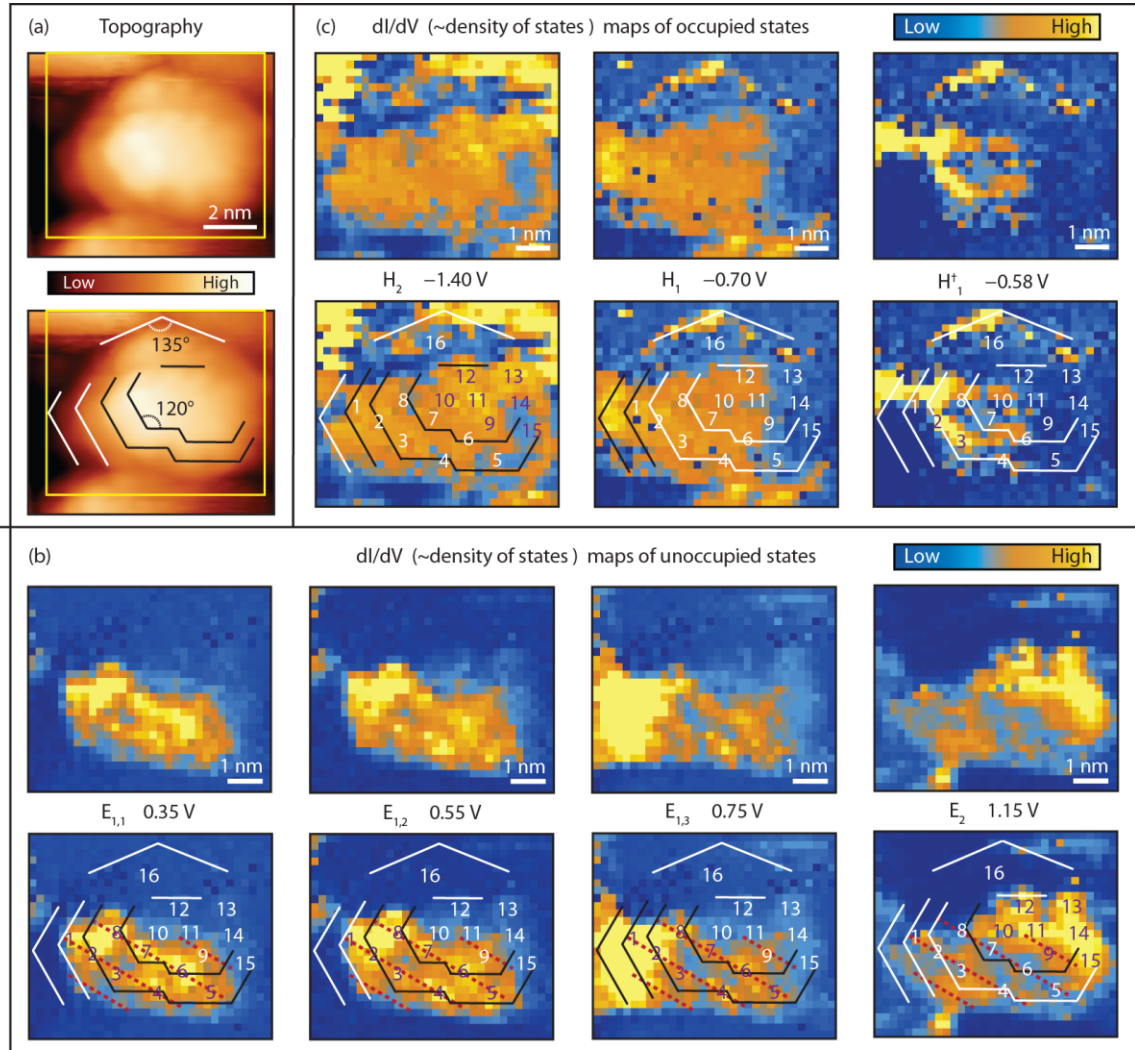


**Figure 8.3.** Spatial DOS (STS) mapping across nanocrystal NC<sub>1</sub>. (a) Topographic image [set point 1.0 V, 1 pA] showing the path of mapping (points P<sub>1</sub> through P<sub>5</sub>). (b) Density of states [set point 2.0 V, 10 pA] as a function of bias voltage and position  $x$  along the path shown in (a). (c) Individual STS spectra from (b) measured at points P<sub>2</sub> through P<sub>5</sub>. Occupied and unoccupied states are marked 'H' and 'E' respectively in both (b) and (c). Spectral feature H<sup>\*\*</sup> corresponds to “reverse” tunneling<sup>35,36</sup> through a localized occupied state outside of the mapping path.

of individual electronic states across  $NC_1$  are highly inhomogeneous. States  $E_{1,n}$  are primarily concentrated in the left and bottom parts of  $NC_1$  (locations 1-9 in Figure 8.4b, 0.35 V) in the vicinity of the steps observed in the STM topography (Figure 8.4a). The DOS intensity corresponding to these states forms stripe-like features running through locations 1-9 in Figure 8.4b. These four stripes correspond to the four DOS peaks observed along the x-coordinate for the  $E_{1,1}$  states in Figure 8.3b. All states  $E_{1,n}$  have very similar two-dimensional spatial distributions of their DOS, as can be seen in Figure 8.4b, consistent with the one-dimensional scan of Figure 8.3b. Figure 8.4b shows that the “stripes” are localized in the vicinity of the  $NC_1$  step edges (highlighted in the bottom maps of Figure 8.4b). In contrast, unoccupied state  $E_2$  is delocalized throughout  $NC_1$ , and

---

**Figure 8.4.** (a) Topographic images of  $NC_1$  [set point 1.0 V, 1 pA]. Bottom image is marked to indicate step edges with  $120^\circ$  angles oriented along  $\langle 110 \rangle$  directions, the same set of marks is used in the bottom images of (b) and (c) for reference. (b) DOS maps for unoccupied states of  $NC_1$  [set point 2.0 V, 15 pA] measured at the indicated bias voltages. Parallel dashed red lines indicate the apparent orientation of stripe-like features associated with states  $E_{1,n}$ . (c) DOS maps for occupied states of  $NC_1$  [set point 2.0 V, 15 pA] measured at the indicated bias voltages. High intensity signals in the top left and top right of the  $H_2$  map in (c) are attributed to spectral features of nearby NCs. The spatial extent of maps in (b) and (c) corresponds to the yellow rectangle shown in (a). Numbered markers in the bottom images of (b) and (c) [identical for both sets of maps] indicate locations of high DOS intensity for states  $E_{1,n}$  (1-9) and  $E_2$  (10-15). Location 16 marks a region with a localized higher energy state [  $\sim 1.9$  V, map not shown], likely corresponding to a smaller NC (with a different crystallographic orientation) that is in the process of merging with  $NC_1$ .



is primarily concentrated in the upper right part of NC<sub>1</sub> (locations 10-15 in Figure 8.4b, 1.15 V) where no clear topographic steps exist.

Similar distinction between localized states at the onset of tunneling and delocalized states at higher voltages is found for occupied states: the highest energy state  $H_1^\dagger$  appearing at -0.58 V (Figure 8.4c), is localized (analogously to states  $E_{1,n}$ ) near the step edges, while states  $H_1$  (-0.7 V) and  $H_2$  (-1.4 V) show relatively uniform distributions. The latter are, in fact, even more homogenous than they appear: their apparent DOS in locations 13-15 is suppressed due to the effect of variable voltage drop across the NC described in the discussion of Figure 8.3b.

Theoretical calculations show that unoccupied states in PbS are formed predominantly by Pb-derived atomic 6p orbitals, whereas occupied states are formed predominantly by S-derived atomic 3p orbitals.<sup>26</sup> According to these predictions, the DOS of states  $E_{1,n}$  and  $E_2$ , for unpassivated NCs, is carried by surface Pb-atoms, while the DOS of states  $H_1^\dagger$ ,  $H_1$  and  $H_2$  is carried by surface S-atoms. The S- and Pb-character of occupied and unoccupied states correspondingly holds true even in the presence of under-coordinated Pb- or S-atoms, which form localized states split-off from the conduction- and valence-bands.<sup>39</sup> Because Pb- and S-atoms located at step edges lack nearest neighbors, they are in under-coordinated environments compared to other surface atoms, and therefore may form sub-band gap states.<sup>40</sup> Localization of states  $E_{1,n}$  and  $H_1^\dagger$  near the step edges, where atomic coordination is disrupted, suggests that these states correspond to sub-bandgap trap states, while the spatially delocalized states  $E_2$ ,  $H_1$  and  $H_2$  are identified as quantum-confined states derived from the conduction ( $E_2$ ) and valence ( $H_1$  and  $H_2$ ) bands. Consistent with the identification of states  $E_{1,n}$  and  $H_1^\dagger$  as states primarily

localized on Pb- or S-atoms respectively, DOS maps for these states (Figure 8.3b,c) show complementary intensities in most of locations 1-15. The differences in the spatial distributions of states  $H_1^\dagger$  and  $E_{1,n}$  are attributable to the different spatial distributions of the under-coordinated Pb- and S-atoms, which is likely a result of the different quantities of Pb versus S atoms, as can be expected based on the fact that as-synthesized PbS NCs typically have Pb-rich surfaces.<sup>41,42</sup> Our spectroscopic data corroborates this expectation: the splitting of non-stoichiometric trap states from the main quantum-confined states has been predicted to be larger for NCs with greater non-stoichiometry,<sup>39</sup> and can thus be used as a measure of the degree of local non-stoichiometry. Specifically, on the energy scale, state  $H_1^\dagger$  appears only 0.12 eV higher than the onset of band  $H_1$  in Figures 8.3b,c, which is comparable with calculations for states localized at S-atoms within step edges on the stoichiometric PbS(100) surface.<sup>40</sup> In contrast, the energy difference  $E_2 - E_{1,1}$  is relatively large: ~0.8 eV. The same trends are observed in the spectra of most other NCs (Figure 8.1) suggesting that the number of under-coordinated Pb atoms is indeed higher than that of under-coordinated S-atoms in the studied NCs. These trends, and their consistency with the theoretical predictions<sup>39</sup> further reinforce our assignment of states  $E_{1,n}$  and  $H_1^\dagger$  as defect states.

Additional support for assignment of states  $E_{1,n}$  as trap states is provided by the analysis of their energies in other studied NCs. Inspection of STS spectra of such NCs (Figure 8.1) shows that energy splitting  $E_2 - E_{1,1}$  varies among different NCs, but does not show a correlation with their apparent bandgaps  $E_{1,1} - H_1$  (Figure F3). This is contrary to what would be expected if all states  $H_1$ ,  $E_{1,1}$  and  $E_2$  had quantum-confined nature – in this case, according to STS results obtained on PbS NCs with similar aspect ratios,<sup>32</sup> state  $E_2$

would be attributable to a higher-order particle-in-a-box-like state quantized in the Z-direction, which would mean that both energy differences  $E_2 - E_{1,1}$  and  $E_{1,1} - H_1$  would scale with the NC thicknesses, resulting in a linear correlation between them. Since it has been established above that states  $H_1$  and  $E_2$  are delocalized and are of quantum-confined nature, state  $E_{1,1}$  must be of different origin.

The origin of states  $E_{1,n}$  may be alternatively explained by using the physical picture developed in several recent STS studies of ordered chain-like atomic structures,<sup>43-45</sup> where the linear-combination-of-atomic-orbitals (LCAO) model was applied to describe the observed extended electronic states formed through coupling of orbitals associated with individual adatoms. According to this physical picture, in the present case  $E_{1,n}$  bands may correspond to LCAO-like states formed through coupling of the orbitals associated with individual under-coordinated Pb atoms, with individual  $E_{1,n}$  states roughly corresponding to different linear combinations of such orbitals. The model explains the presence of multiple states in STS spectra, as well as the similarity of their spatial DOS maps. The latter may only be different in their (spatial) nodal structures, which could not be resolved in our measurements.

While the precise atomic structure of the NC surface could not be determined from the collected STS data, the obtained maps of  $E_{1,n}$  states suggest that the NC surface is reconstructed analogously to the reconstructions of the PbS(111) surfaces predicted by recent density functional theory calculations.<sup>46</sup> This study concluded that PbS(111) surfaces tend to undergo an extensive reconstruction beyond surface bond-length modifications obtained in theoretical calculations of small metal-chalcogenide NCs.<sup>24</sup> Specifically, PbS(111) surface was found to reconstruct by forming *sub-monolayer*

stripe-like patterns of Pb adatoms that reduce the electrostatic energy of the PbS(111) surface.\*\* Indeed, our  $E_{1,n}$  maps show stripes oriented at  $\sim 30^\circ$  with respect to the step edges. Since the latter are aligned along the  $\langle 110 \rangle$  crystallographic directions, the  $E_{1,n}$  stripes are likely aligned with one of the  $\langle 211 \rangle$  directions, consistent with self-assembly of surface Pb atoms in patterns defined by surface crystallographic directions, as would be expected on a reconstructed surface. Existence of well-defined patterns of non-stoichiometric Pb adatoms is also consistent with the observation of the well-defined progressions of STS features corresponding to  $E_{1,n}$  states. Such STS features can be expected to be smeared out into featureless bands for less ordered NC surfaces, as was found for NCs annealed at lower temperatures (data not shown).

## 8.5. Conclusions

Presented results suggest that self-assembly of non-stoichiometric adatoms on PbS NC surfaces may result in formation of extended LCAO-like sub-bandgap states, which have important implications for the more general case of imperfectly passivated ligand-covered NCs. Even when the density of dangling bonds per NC is small, the tendency of under-coordinated adatoms to co-localize near structural imperfections, as observed in our work, may lead to stronger electronic coupling of dangling bonds resulting in larger modifications of the sub-bandgap electronic structure than that expected for isolated dangling bonds. The atomic-scale spatial structure of these sub-bandgap states should have a strong impact on the photophysical properties of such NCs, and will be a subject of our future studies. Finally, STS-based real-space mapping of electronic DOS demonstrated in this chapter has the potential to provide insights into the nature of a variety of defects and impurities occurring on NC surfaces.



## 8.6. Bridge to Chapter IX

In the next chapter we will further explore PbS NC electronic states using STS two-dimensional spatial mapping and will discover atomic-scale patterns that allow us to identify the possible atomic morphologies of surface reconstructions in the studied NCs. We will find that reconstruction of polar {111} surfaces in individual PbS NCs results in the formation of sub-bandgap electronic states. Several possible modes of surface reconstruction leading to varied occupied/unoccupied sub-bandgap states will be proposed. We will also identify, for the first time, strongly localized defect-related “edge-states” states arising from extreme local non-stoichiometry. These states are found deep in the main NC band gap, oftentimes nearly closing the gap between occupied and unoccupied states.

# CHAPTER IX

## DIVERSITY OF SUB-BANDGAP STATES IN LEAD-SULFIDE NANOCRYSTALS: REAL-SPACE SPECTROSCOPY AND MAPPING AT THE ATOMIC-SCALE

This chapter by Christian F. Gervasi, Dmitry A. Kislitsyn, Thomas L. Allen, Jason D. Hackley, Ryuichiro Maruyama, and George V. Nazin has been previously published under the same title in *Nanoscale* **7**, 19732–19742 (2015). Copyright © 2015 Royal Society of Chemistry.

### 9.1. Introduction

Colloidal semiconductor nanocrystals have emerged as a promising class of technological materials with optoelectronic properties controllable through quantum-confinement effects. Despite recent successes in this field, an important factor that remains difficult to control is the impact of the nanocrystal surface structure on the photophysics and electron transport in nanocrystal-based materials. In particular, the presence of surface defects and irregularities can result in the formation of localized sub-bandgap states that can dramatically affect the dynamics of charge carriers and electronic excitations. Here we use Scanning Tunneling Spectroscopy (STS) to investigate, in real space, sub-bandgap states in individual ligand-free PbS nanocrystals. In the majority of studied PbS nanocrystals, spatial mapping of electronic density of states with STS shows

atomic-scale variations attributable to the presence of surface reconstructions. STS spectra show that the presence of surface reconstructions results in formation of surface-bound sub-bandgap electronic states. The nature of the surface reconstruction varies depending on the surface stoichiometry, with lead-rich surfaces producing unoccupied sub-bandgap states, and sulfur-rich areas producing occupied sub-bandgap states. Highly off-stoichiometric areas produce both occupied and unoccupied states showing dramatically reduced bandgaps. Different reconstruction patterns associated with specific crystallographic directions are also found for different nanocrystals. This study provides insight into the mechanisms of sub-bandgap state formation that, in a modified form, are likely to be applicable to ligand-passivated nanocrystal surfaces, where steric hindrance between ligands can result in under-coordination of surface atoms.

## **9.2. Background**

Tunable thin-film structures formed from lead-chalcogenide (PbX, where X=S, Se or Te) nanocrystals (NCs) are a promising class of semiconducting materials with a combination of unique functionalities that makes them highly attractive for a new generation of optoelectronic applications.<sup>1-4</sup> Some of these functionalities are made possible by the ultra-small size of NCs, with such examples as greatly increased efficiencies for exciton-multiplication,<sup>5-10</sup> and enhanced extraction of unrelaxed hot charge-carriers.<sup>11</sup> Another important functionality of NCs is the tunability of their properties via synthetic means, which allows one to systematically control the electronic bandgap by tuning the NC size. Additional means of control, to improve the injection and extraction of charge carriers in PbX NC thin films, have been implemented through post-synthesis techniques<sup>12</sup> involving ligand exchange.<sup>13-15</sup> Thus processed PbSe NC thin

films show significantly reduced inter-particle spacings and dramatically increased conductivities.<sup>16-18</sup> Less commonly, thermal annealing of the NC films is used,<sup>15, 16, 19, 20</sup> which can result in extensive rearrangements of ligand shells as well as (at higher temperatures) sintering<sup>21</sup> and even fusion<sup>22, 23</sup> of NCs. These processing steps, necessary for achieving optimal charge transport properties in NC films, simultaneously present significant challenges because they tend to radically alter the surface chemistry of NCs, with the potential to create surface imperfections that can result in the appearance of sub-bandgap trap states, which, in turn, have a strong impact on charge-carrier dynamics, recombination, and extraction from NC films.<sup>24-26</sup>

Indeed, recent breakthroughs in increasing the efficiency of PbX NC-based photovoltaic devices were made possible, to a great extent, by developments in surface passivation techniques that enabled a significant reduction in the density of surface trap states,<sup>27, 28</sup> with some of the reported efficiencies exceeding ~8%.<sup>29, 30</sup> Some of the promising approaches have employed passivation with 3-mercaptopropionic acid,<sup>31</sup> atomic passivation with halogen ions and SCN<sup>-</sup>,<sup>25, 32</sup> and inorganic ligands,<sup>33</sup> metal halide and chalcogenide salts,<sup>18, 34</sup> amorphous alumina,<sup>18</sup> and alkylselenide ligands.<sup>35</sup> Conceptually, complete elimination of trap states requires consideration of the “passivating effect” of individual surface ligands, and careful balancing of the number of ligands with the NC core stoichiometry, a difficult task in practice. In particular, theoretical calculations show that in the limiting case of ligand-free stoichiometric NCs, midgap states do not exist,<sup>36, 37</sup> but in non-stoichiometric Pb-rich (Pb-poor) NCs sub-bandgap states are found near the conduction (valence) bands.<sup>36, 38</sup> A similar picture holds for ligand-passivated NCs: attachment of ligands effectively changes NC stoichiometry,

such that an appropriate number of ligands can effectively compensate for the non-stoichiometry of the NC core, and eliminate the sub-bandgap states.<sup>38</sup> The importance of NC stoichiometry in defining the NC electronic structure is corroborated by recent experimental studies where the trap state densities were found to be sensitive to controlled variations in NC stoichiometry achieved either through post-synthesis ligand exchange,<sup>35</sup> direct thermal deposition,<sup>39</sup> solution-based colloidal atomic layer deposition,<sup>40</sup> and successive ionic layer adsorption and reaction (SILAR).<sup>41</sup>

Optimization of the “effective” NC stoichiometry is complicated by the varied chemistry of facets associated with different crystallographic directions (typically {111}, {100} and, to a lesser extent, {110})<sup>42</sup>.<sup>35</sup> A stark manifestation of this variability is the fact that unlike stable {110} and {100} surfaces,<sup>43, 44</sup> (unpassivated) polar {111} surfaces are unstable and are predicted to undergo reconstruction resulting in formation of an ordered sub-monolayer of Pb atoms.<sup>45</sup> Evidence for surface reconstruction is provided by Rutherford backscattering experiments on PbSe thin films, where a sub-monolayer (~40%) of Pb atoms, consistent with surface reconstruction, was found.<sup>46</sup> Additional evidence was provided by TEM imaging of PbSe NC {111} facets showing ribbon-like Pb structures attributed to surface reconstruction.<sup>45</sup>

While considerable advances in controlling the properties of PbX NC films have been made, and several theoretical studies showing the importance of surface trap states are available,<sup>25, 38, 47</sup> the role of surface trap states in the physical picture of charge-carrier photo-generation and dynamics remains to be fully addressed. Experimental studies of surface trap states have been carried out using a variety of techniques. Photoluminescence studies showed the existence of trap states in as-synthesized ligand-

passivated PbX NCs,<sup>48, 49</sup> even before NC film formation. Photoluminescence measurements of ligand-exchanged PbX NC films demonstrated the presence of trap states<sup>31, 50</sup> that could be manipulated with NC size and surface treatment.<sup>31, 49</sup> Trap states in ligand-exchanged PbX NCs were also found in studies utilizing deep-level transient and Fourier-transform photocurrent spectroscopies,<sup>51</sup> and in spectroscopic measurements of photocurrent in PbS field-effect transistor devices.<sup>52</sup> Even though these studies have provided rich insights into the spectroscopic properties of surface trap states, they lacked the spatial resolution to visualize the relationship between the local structure of NC surfaces and properties of such states. The capability to probe this relationship is critically important for the development of a microscopic picture of surface trap states because of the wide diversity of local atomic-scale surface structures associated with variations in ligand-shell morphologies, the presence of different crystallographic facets, NC shape variations, and the effect of surface reconstruction.

A direct spectroscopic approach for real-space investigations of surface states in individual NCs is afforded by a combination of Scanning Tunneling Microscopy (STM) and Scanning Tunneling Spectroscopy (STS), which have been used to probe the electronic states in ligand-exchanged PbS NC films.<sup>53, 54</sup> Realization of this technique in a high-stability cryogenic STM system<sup>55</sup> enables detailed atomic-scale mapping of electronic states in individual NCs. STS-based mapping of the local density of states (DOS) was recently used to study the spatial localization and spectral properties of sub-bandgap states in NCs arising due to local off-stoichiometry.<sup>56</sup> Here we apply this experimental approach to obtain *atomic-scale* DOS maps of individual ligand-free PbS NCs. Ligand-free NCs represent a well-defined model PbX system, unaffected by the

uncontrolled variances of the ligand shell morphology, which makes this system more open to theoretical simulations.<sup>44, 57, 58</sup> STS maps show that the majority of studied NC surfaces underwent reconstruction accompanied by formation of ordered atomic patterns commensurate with the crystallographic structures of the NC surfaces. While these results are in accordance with density-functional theory calculations of polar PbS surfaces, where similar modes of surface reconstruction were predicted,<sup>45</sup> the current manuscript reports, for the first time, results demonstrating the connection between the atomic-scale NC surface morphology and atomic-scale variations in the electronic DOS. Importantly, we find that NC surface reconstruction results in formation of surface-bound sub-bandgap electronic states, with spectral and spatial properties sensitive to the local stoichiometry of NC surfaces. In addition, we find that highly off-stoichiometric NC regions show qualitatively different defect states with energies deep inside the NC bandgaps. By employing results of calculations for off-stoichiometric PbX NCs,<sup>38</sup> we infer the presence of off-stoichiometric areas from local DOS spectra, and use DOS maps to analyze the local spatial variations in stoichiometry.

### **9.3. Experimental details**

A Au(111) substrate surface was prepared, under ultra-high vacuum conditions ( $\sim 10^{-11}$  Torr), by several cycles of sputtering/annealing, using Ne gas, and annealed at  $\sim 400^\circ\text{C}$ . Pentanethiol-terminated PbS NCs were synthesized as described previously,<sup>1</sup> suspended in pentane, and deposited onto the Au(111) surface using a solenoid pulse-valve. During deposition, the Au(111) substrate was held inside the load-lock section of the vacuum system, with the pressure not exceeding  $10^{-6}$  Torr during deposition. Several successive bursts of the solenoid valve were used to obtain a sub-monolayer of PbS NCs

on the Au(111) surface. The Au(111) substrate with deposited NCs was annealed in ultra-high vacuum conditions at increasingly higher temperatures until well-defined reproducible STM imaging of individual NCs was achieved, with a final annealing temperature of  $\sim 170^\circ\text{C}$ .

Experiments were conducted using a home-built ultra-high-vacuum STM incorporating a Pan-type scanner provided by RHK Technology.<sup>2</sup> All STS spectra were recorded using a lock-in amplifier operating at a modulation frequency of  $\sim 600$  Hz, and bias voltage modulation varying from  $\sim 10$  mV (for individual spectra and one-dimensional spatial DOS maps) to  $\sim 50$  mV (for two-dimensional DOS maps). All STM images and STS spectra were obtained at a temperature of  $\sim 15$  K with electrochemically etched Ag tips. STM images were processed using WSxM Software.

## **9.4. Results and discussion**

### **Sample preparation**

PbS NCs with pentane-thiol ligand shells were deposited on Au(111) surfaces and annealed at progressively higher temperatures until ligands were removed. The removal of ligands was monitored with STM imaging, which, at the initial stages of annealing, typically showed fuzzy patterns consistent with dynamic reorientation of ligands present on the NC surface (Figures 9.1a-c). At the final stages of annealing, the majority of NCs showed reproducible topographic patterns suggesting the absence of ligand reorientation (Figures 9.1d-f). In addition, STM images of fully-annealed NCs showed disc-like width-to-height aspect ratios of 2:1 to 3:1 suggesting that significant reconstruction of the overall shapes of NCs occurred during the annealing process. The disc-like shapes of annealed NCs are consistent with similar shapes of PbS and PbSe NCs grown by



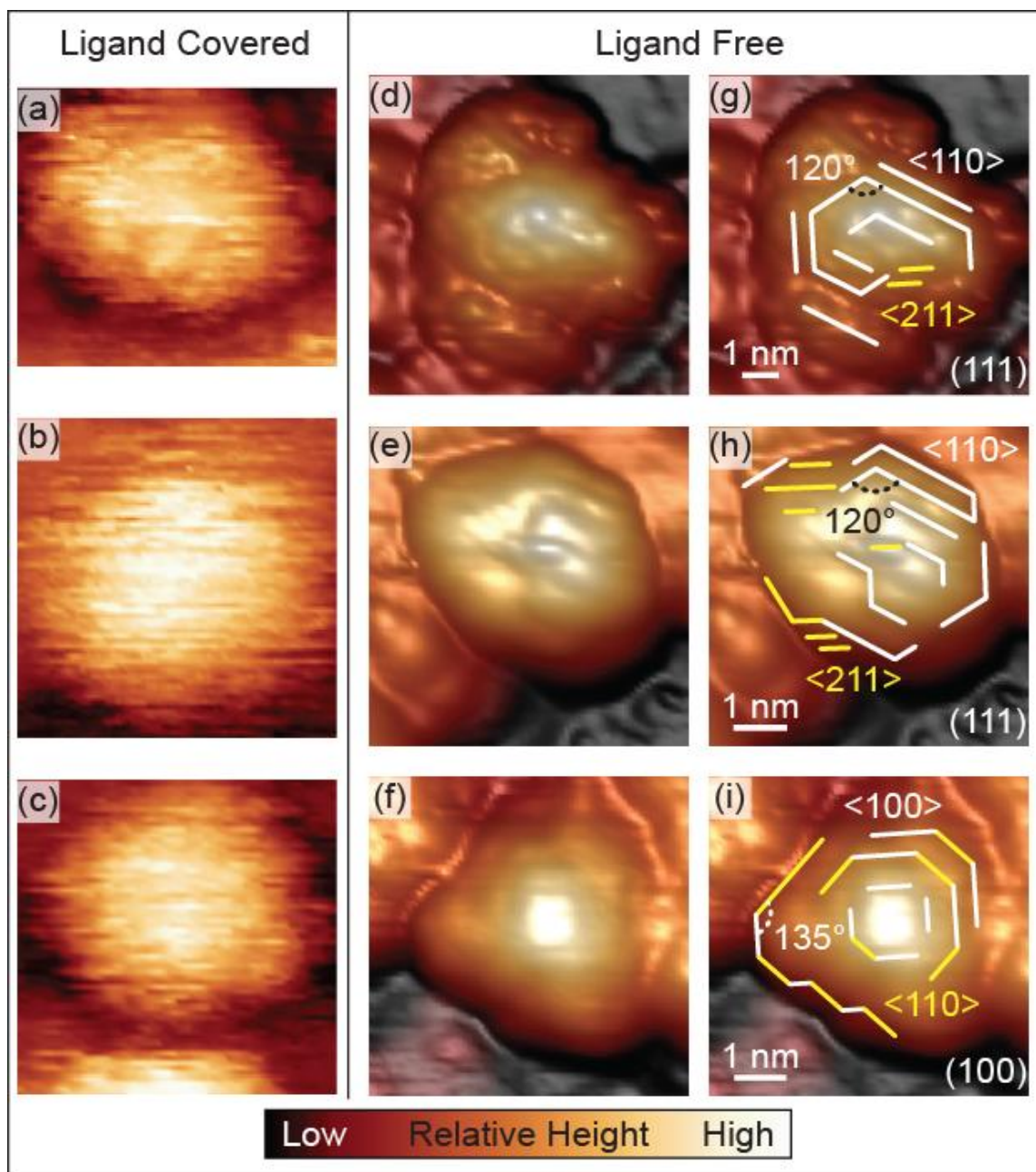


**Fig. 9.1.** STM topographies of ligand-covered (a)-(c) and ligand-free (d)-(f) PbS NCs. Figures (g)-(i) highlight topographical features observed in (d)-(f). The crystallographic directions and NC boundaries are identified with the aid of STS DOS mapping. All STM topographies measured with set-point 2.0 V bias, 1-2 pA tunneling current.

electrodeposition on Au(111).<sup>59, 60</sup> The predominance of disc-like shapes in a polar material like PbS, is attributable to the reduced electrostatic NC energy (due to screening by the gold surface) enabled by this geometry. Importantly, images of fully-annealed NCs often showed surface features aligned at specific angles attributable to well-defined crystallographic directions in PbS NCs (Figures 9.1g-i). The majority of fully-annealed NCs showed topographic features (e.g. NC boundaries and topographic steps) oriented along three main spatial directions (specific to each NC) forming 120 degree angles with respect to each other (Figures 9.1g and h), even though other orientations have also been observed (Figure 9.1i). The existence of such directional order suggests that the top-most NC surfaces (in most cases) roughly correspond to {111} crystallographic surfaces, consistent with results of TEM studies of PbS NCs terminated with Au clusters,<sup>61</sup> where the polar nature of the {111} facets was reported to lead to preferential formation of Au/PbS{111} interfaces. Results described in the following summarize our studies of 10 fully-annealed individual PbS NCs.

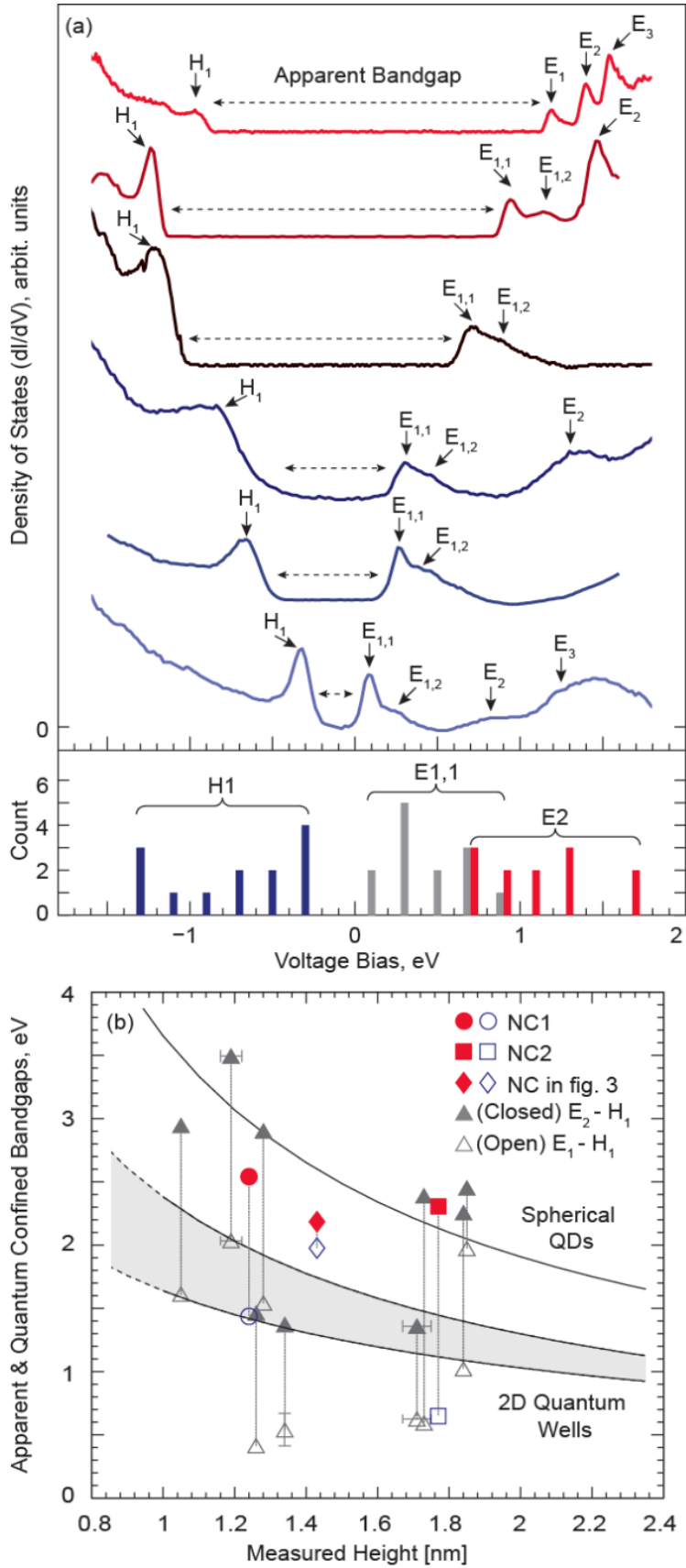
### **DOS-spectroscopy of NCs**

Energy-dependent DOS spectra (STS spectra) of individual PbS NCs were recorded by measuring the differential tunneling conductance,  $dI/dV$ , as a function of the bias voltage (see Methods for details of the measurements).<sup>62</sup> DOS spectra for all fully-annealed NCs show progressions of peaks associated with occupied (negative bias) and unoccupied (positive bias) electronic states (Figure 9.2a). Indeed, while Figure 9.2a shows considerable variations in the apparent band gaps ( $E_{1,1} - H_1$  energy difference) for different NCs, the DOS spectra, overall, appear quite similar and reminiscent of those calculated for stoichiometric ligand-free PbX NCs,<sup>44, 57, 58</sup> where the electronic states can

be described as quantum-confined particle-in-a-box (PIAB) states originating from the conduction and valence bands. The lowest-energy PIAB states are predicted to show s- and p- overall orbital symmetries, with their atomic-scale behavior determined by the corresponding Bloch wavefunctions.<sup>57</sup> A similar picture of PIAB-like electronic states has been used to describe STS spectra for a variety of NCs composed of different semiconductor materials.<sup>63</sup> Then, taking into account the disk-like aspect ratio of studied NCs, the unoccupied states in Figure 9.2a could be assigned in the following way: the doublet of closely spaced peaks  $E_{1,1}$  and  $E_{1,2}$ , may be attributed to electronic states quantized in the XY plane (with  $E_{1,1}$  being the ground state), whereas the  $E_2$  state may be attributed to a single-node state quantized in the Z-direction.<sup>59</sup> By using the PIAB-like picture of electronic states in Figure 9.2a, the variations in the apparent bandgap ( $E_{1,1} - H_1$  energy difference) could then be explained by variations in NC dimensions, which would modulate the energies of the PIAB states via quantum-size effects.<sup>64</sup>

---

**Fig. 9.2.** (a) DOS spectra for six representative PbS NCs (individual spectra shifted for clarity). Occupied (unoccupied) states denoted by  $H_n$  ( $E_n$ ) respectively. All  $dI/dV$  curves measured with set-point 1.6-2.6 V bias, 15-30 pA tunneling current. Histogram (bottom) of energetic locations and distributions for discernible states  $E_{1,1}$ ,  $E_2$ , and  $H_1$  for 13 NCs, bin size 0.2 eV (b) Bandgaps vs. height for measured NCs overlaid on data for two limiting cases: spherical NCs and 2D PbS quantum wells. Open symbols correspond to the  $E_{1,1} - H_1$  energy differences, whereas closed symbols correspond to values obtained from PIAB orbitals differences of many measured DOS spectra in Figure 9.2a are considerably lower than those (as determined from DOS mapping). The curve for spherical PbS NCs, and gray shaded region corresponding to 2D PbS quantum wells, were obtained from Moreels et al.<sup>65</sup> and Lee et al.,<sup>66</sup> respectively.



The PIAB-like picture of electronic states in Figure 9.2a is challenged, however, by the fact that the spacing between peaks  $E_{1,1}$  and  $E_{1,2}$  does not change appreciably from one NC to another, being consistently in the range of  $\sim 0.2$  eV despite significant variations in the NC lateral sizes. Further, the apparent bandgaps ( $E_{1,1} - H_1$ ) energy expected based on the physical dimensions of the corresponding NCs. Indeed, many of the apparent bandgaps are lower than what would be expected for two-dimensional PbS films of thicknesses matching the observed NC heights (Figure 9.2b),<sup>67</sup> which is the absolute minimum expected for NCs with large spatial dimensions in the XY plane. On the other hand, energy differences calculated from  $E_2 - H_1$  (and in some cases  $E_2 - H_2$ ) tend to fall in the range expected for bandgaps of disc-like PbS NCs (Figure 9.2b). Together, these observations suggest that  $E_{1,1}$  states in Figure 9.2a do not have PIAB-like character, and may potentially be associated with sub-bandgap states. Theoretical calculations predict that sub-bandgap states are often more strongly localized than PIAB-like states derived from the conduction and valence bands,<sup>38, 47</sup> which suggests that to establish the nature of electronic states observed in Figure 9.2a, it would be useful to obtain information regarding their spatial behavior. To this end, we carried out spatial mapping of DOS spectra for several NCs, as described below.

### **Surface-Reconstruction observed in DOS maps: Results**

We first present DOS maps for NCs that showed DOS delocalized over the NC surfaces. For example, Figure 9.3 shows a “cross-sectional” DOS mapping for a NC without apparent spectral or spatial features attributable to sub-bandgap states. Indeed, the apparent bandgap of this NC falls within the range expected for disc-like NCs (Figure 9.2a, diamond-shaped data-point), unlike the majority of studied NCs. The DOS map

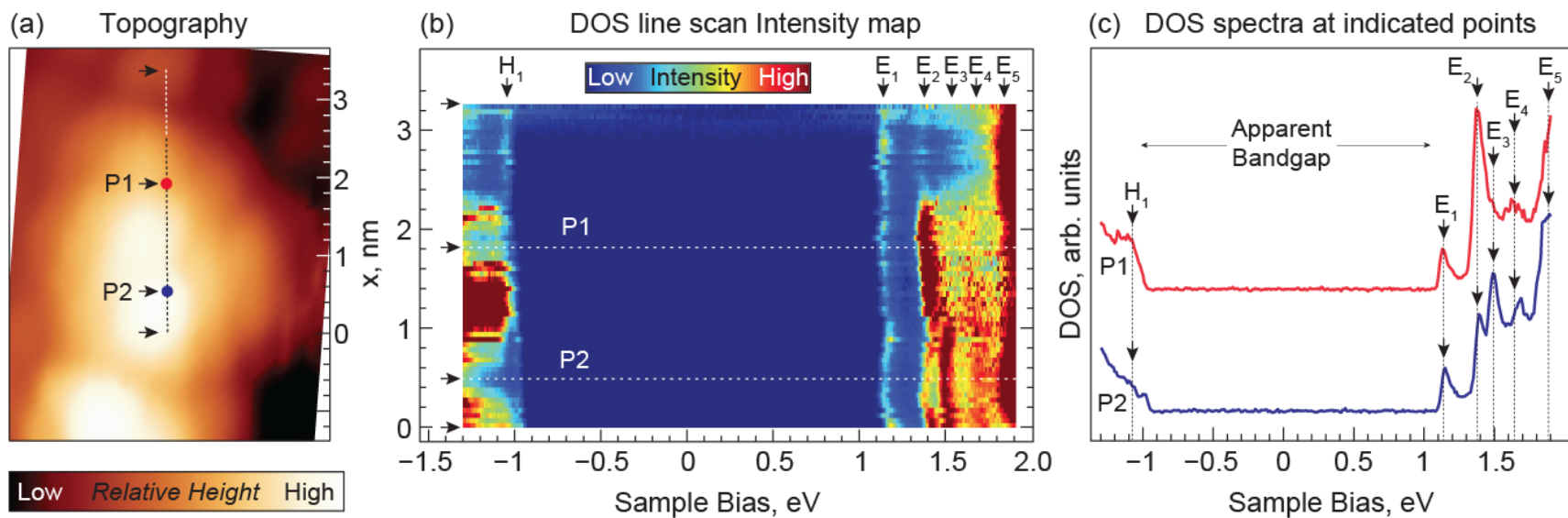


**Fig. 9.3.** (a) STM topographic image of a PbS NC. (b) DOS "cross-section" mapping along the path of the dotted line in (a). (c) Individual DOS spectra measured at locations marked in (a). STS measurements in (b) and (c) were taken with a set-point of 1.9 V bias and 30 pA tunneling current. Variations in the energies of electronic states across the NC roughly follow the NC topography, which is a result of the location-specific variation of the bias voltage drop inside the NC.<sup>56</sup>

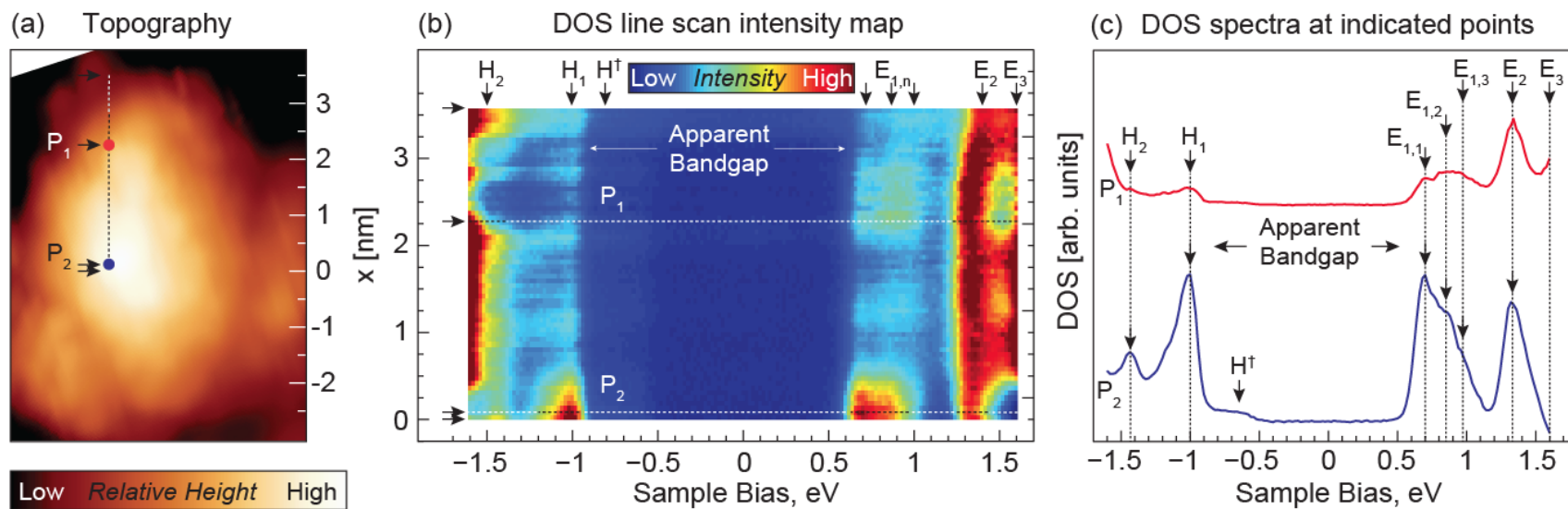


**Fig. 9.4.** (a) STM topographic image of NC1. (b) DOS mapping of NC1 along the path of the dotted line in (a). (c) Individual DOS spectra for locations marked in (a). STS measurements in (b) and (c) were taken with set-point 1.6 V bias, 30 pA tunneling current.

(Figure 9.3b) is composed of a progression of DOS spectra measured across the NC, as shown in Figure 9.3a. In Figure 9.3b, occupied state  $H_1$  and all unoccupied states  $E_n$  are visible throughout the scan (even though they also show some variations in their intensities), which suggests that they may correspond to delocalized PIAB-like states.

While delocalized states analogous to those of Figure 9.3b were observed for many other NCs, their maps were often different from that of Figure 9.3b in that they showed quasi-periodic spatial modulations of their DOS intensities. An example of a “cross-sectional” DOS map for one such NC (referred to as NC1 in the following) is shown in Figure 9.4. The DOS spectra measured at different locations on the NC1 surface show a similar grouping of occupied and unoccupied states with intensities modulated depending on the measurement location (Figures 9.4b and c). In particular, distinct modulations are observed for states  $H_1$ ,  $E_{1,1}$  and  $E_{1,2}$  (Figure 9.4b). These modulations occur on a spatial scale far exceeding the unit cell of PbS (0.59 nm), suggesting that they are not a product of elemental contrast originating from the PbS lattice. The magnitudes of  $E_{1,1} - H_1$  and  $E_2 - H_1$  bandgaps for NC1 (Figure 9.2a, open and closed circle data-points) suggest the presence of sub-bandgap states.

To further investigate the spatial behavior of electronic states in NC1, we recorded DOS spectra across a two-dimensional grid of points covering (roughly) the spatial extent of NC1. 2D-spatial maps of electronic states are obtained from this DOS dataset by taking values of the DOS at select bias voltages. Such 2D-maps for the most prominent occupied and unoccupied states are shown in Figure 9.5 and in supplementary Figures G1 and G2. The 2D-spatial maps in Figure 9.5 show that individual states in NC1 have very different characters, except in the  $E_{1,n}$  states (Figures 9.5c, and G1c-e), as well

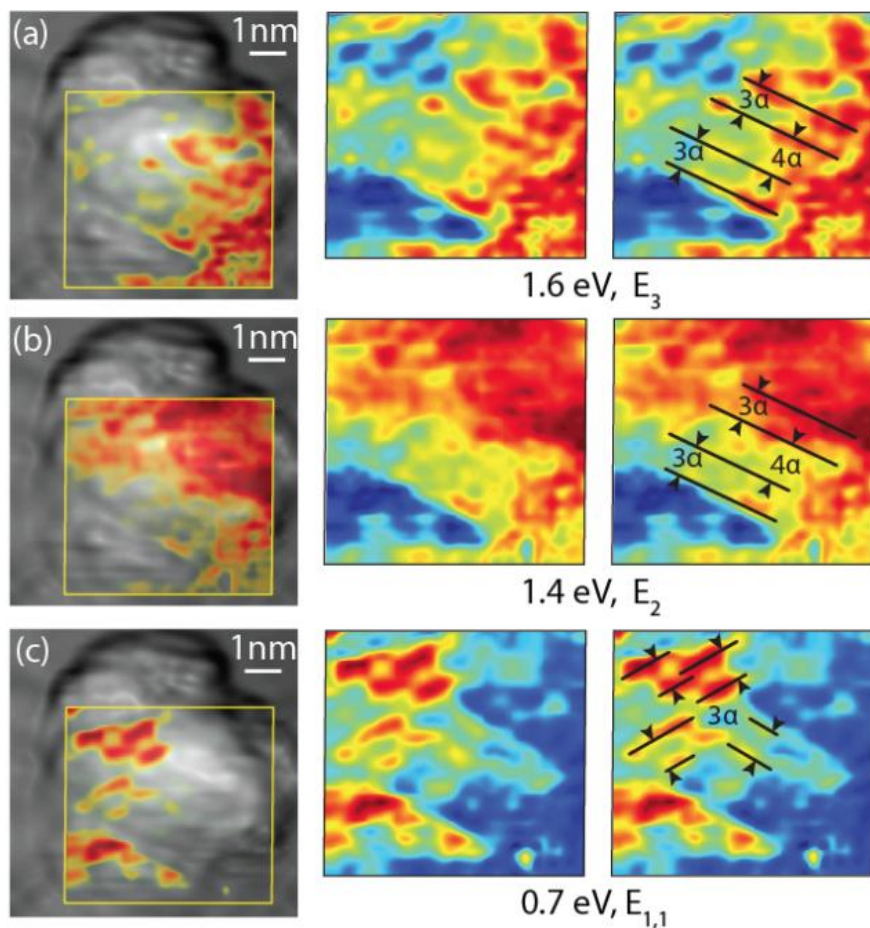


as states  $H_1$  and  $H^\dagger$  (Figures 9.5d,e; G2a,b), which exhibit similar features and spatial localizations respectively. All 2D DOS maps in Figure 9.5 show highly inhomogeneous spatial distributions with stripe-like “hot spots” oriented parallel to the  $\langle 110 \rangle$  crystallographic features observed in the STM topography of NC1 (Figure 9.1g). For example, the DOS map of state  $E_3$  (Figure 9.5a) shows two pairs of parallel bright “stripes” (marked by solid black lines in Figure 9.5a). The “stripes” in each pair are separated by distances equal to 0.726 nm, which is a close fit to the distance between atomic rows located in two different  $\{211\}$  planes. In the following this distance is defined as  $3\alpha$ , where  $\alpha$  is the distance between two neighboring  $\{211\}$  planes, as shown in the model in Figures 9.6a and b. The two pairs of bright stripes in Figure 9.5a are separated by a distance of 0.968 nm =  $4\alpha$ , which corresponds to the geometry shown in the model in Figure 9.6b, where, in contrast to the model in Figure 9.6a, one of the atomic rows is located in a different (lower)  $\{111\}$  atomic plane. This geometry is consistent with the topography of NC1 (Figure 9.1d), which shows atomic steps separating the regions with the two pairs of DOS stripes seen in Figure 9.5a. The DOS map of state  $E_2$  (Figure 9.5b) shows somewhat

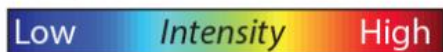
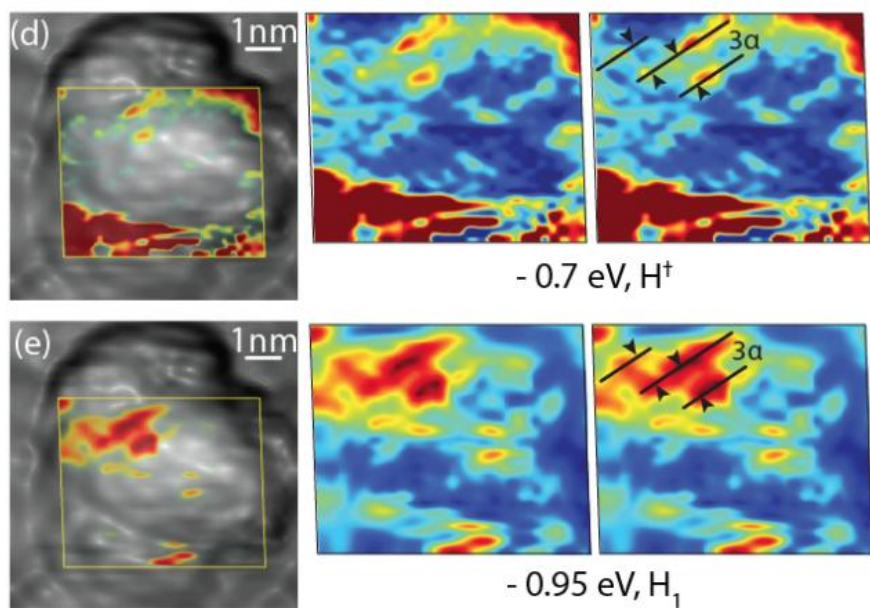
---

**Fig. 9.5.** 2D DOS maps of unoccupied (a-c) and occupied (d, e) states for NC1. DOS state representations show (from left to right) combination topography/DOS map overlay (yellow outline indicates area of DOS mapping), DOS map only, and DOS map with black lines showing DOS features that are in registry with NC1 crystallographic features from Figure 9.1g. Parameter  $\alpha$  is distance between two neighboring  $\{211\}$  planes, as shown in the model in Figures 9.6a and b. STS measurements taken with set-point 1.6 V bias, 30 pA tunneling current. STM topography image measured with set-point 2.0 V bias, 2 pA tunneling current.

DOS maps of unoccupied states



DOS maps of occupied states



less-developed structural order, but features aligned along the same set of black lines are visible.

In contrast, DOS maps of  $E_{1,n}$  states (Figures 9.5c, and G1c-e) show a different set of bright DOS “stripes” (marked with black lines), which are however, separated by the same distance of  $0.726 \text{ nm} = 3a$  as found in Figure 9.5a. In addition, all of the DOS “stripes” in Figures 9.5c, and G1c-e are either parallel to, or are oriented at exactly  $60^\circ$  with respect to the DOS “stripes” from Figure 9.5a, which is consistent with the mutual orientation of two different sets of  $\{211\}$  planes, as shown in the model in Figure 9.6a. This, together with the spacing of DOS “stripes” in maps of  $E_{1,n}$  states, suggests that the latter have a similar relationship with the PbS crystallographic structure as features found in the maps of states  $E_3$  and  $E_2$ . Stripe-like features similar to those found in maps of  $E_{1,n}$  states, are also observed for states  $H^\dagger$  and  $H_1$ , (black lines in Figures 9.5d and e). The DOS map of state  $H_2$  (Figure G2c) shows somewhat less-developed order, with several features orthogonal to the bright  $\{211\}$  plane features observed throughout (especially in Figures 9.5a,b) suggesting that they lie in  $\{110\}$  planes of NC1. This assignment is supported by the fact that these features are separated by distances of  $\sim 0.838 \text{ nm} = 4\beta$ , where  $\beta$  is a distance between two neighboring  $\{110\}$  planes (see Figures 9.6c and d).

The spatial order observed in the DOS maps of NC1 allows us to draw several conclusions. First, the fact that the orientations of bright DOS features in Figures 9.5, G1 and G2 are in registry with the crystallographic directions and lattice spacings expected for a (111) surface, supports the conclusion (originally based on features observed in STM imaging – Figure 9.1g) that one of the  $\{111\}$  crystallographic planes of NC1 is parallel to the Au(111) surface. By associating the DOS features with specific

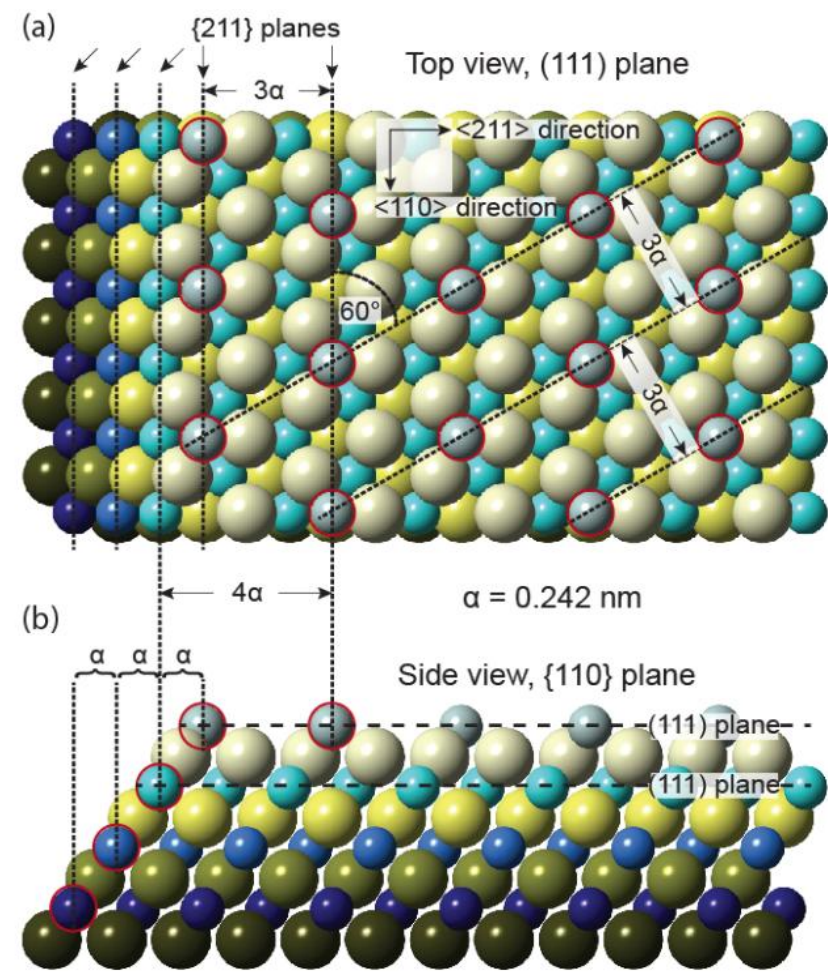
crystallographic directions, we are also able to identify orientations of topographic features in Figure 9.1g as corresponding to different  $\langle 110 \rangle$  directions. Further, the consistency of the spacing observed for these bright DOS features in all maps of Figure 9.5, G1 and G2 with the crystal structure of PbS suggests that these features are indeed associated with an atomic geometry analogous to that seen in the model of reconstructed PbS  $\{111\}$  surfaces displayed in Figure 9.6, even though the actual morphology of NC1 is more complex.

### Surface-Reconstruction: Discussion

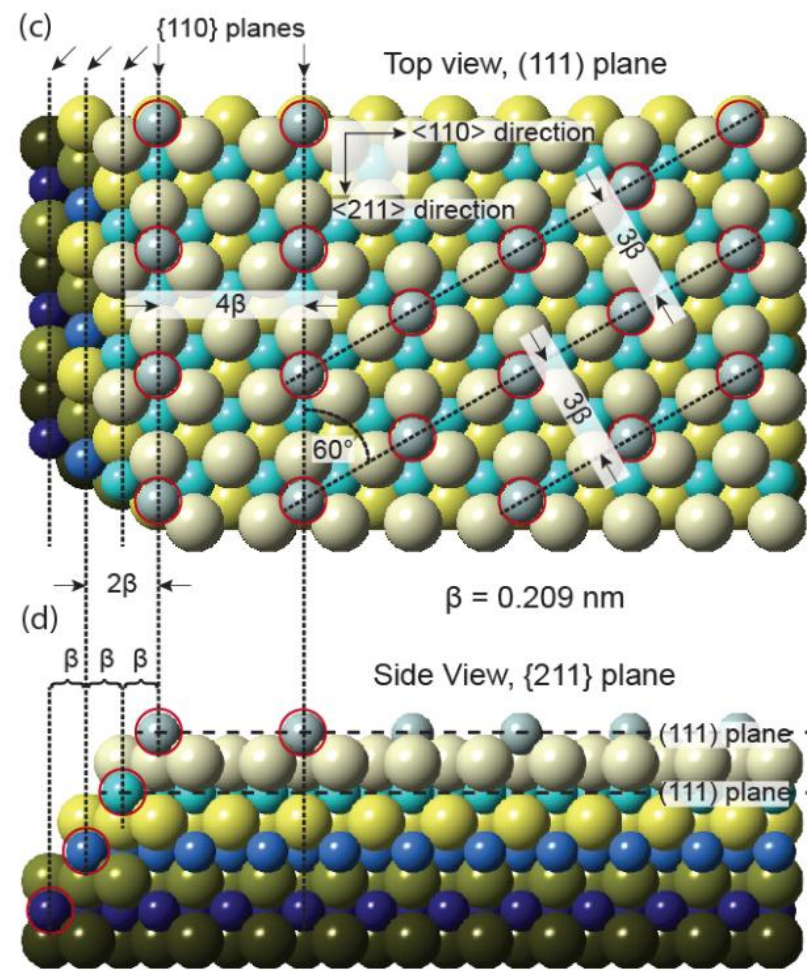
The distances between the stripe-like features in Figures 9.5, G1 and G2 are larger than the minimal inter-atomic distances expected for the identified crystallographic directions. As the idealized model in Figure 9.6 illustrates, this may result from a geometry where rows of atoms are missing on the PbS surface. Such surface morphology is consistent with the predicted reconstruction of the PbS(111) surface.<sup>45</sup> Indeed, the polar nature of PbS dictates that termination of a NC with a  $\{111\}$  facet composed of only one element is electrostatically unfavorable. Instead, reconstruction of the PbS(111) surface is predicted, where, in the ideal case, a  $\{111\}$  facet is stabilized by an additional ordered

---

**Fig. 9.6.** Model representations of relevant PbS fcc crystallographic facets with idealized reconstruction features. (a, c) (111)-plane views showing rows of Pb adatoms oriented along  $\langle 110 \rangle$  and  $\langle 211 \rangle$  directions respectively, with indicated inter-atomic-row distances in integer multiples of distances  $\alpha$  and  $\beta$  respectively. (b, d) (110)-, and (211)-plane side-views of same structures as in (a) and (c) showing vertical atomic steps responsible for appearance of varied distances between the bright DOS “stripes” in Figure 9.5 and Figure 9.8.



● Pb 1<sup>st</sup> layer ● Pb 2<sup>nd</sup> layer ● Pb 3<sup>rd</sup> layer ● Pb 4<sup>th</sup> layer



● S 1<sup>st</sup> layer ● S 2<sup>nd</sup> layer ● S 3<sup>rd</sup> layer ● S 4<sup>th</sup> layer

half-monolayer composed of the complementary element.<sup>45</sup> While different configurations of the additional half-monolayer are possible, one of the configurations that is predicted to give the lowest overall energy has a structure with atoms missing in every alternate  $\{211\}$  plane, as shown in the model in Figure 9.6a. This structure results in rows of atoms oriented and spaced in a manner identical to the arrangement of bright rows in the DOS maps of NC1, which strongly suggests that the observed NC1 DOS features are caused by surface reconstruction.

To establish the composition of the reconstructed layer as well as the nature of electronic states in Figures 9.5, G1 and G2, we compare these results to theoretical predictions. Electronic structure calculations for unpassivated PbS NCs of different shapes show that in PbS, unoccupied states are primarily formed from atomic 6p-orbitals of lead, while occupied states are primarily formed from atomic 3p-orbitals of sulfur.<sup>44</sup> This distinction is maintained regardless of the NC shape and stoichiometry,<sup>38</sup> which is important for the case of NC1, since the model surface reconstruction shown in Figure 9.6a results in surface adatoms in non-stoichiometric environments. We thus expect that states  $E_{1,n}$ ,  $E_2$  and  $E_3$  must be carried predominantly by surface Pb-atoms, whereas states  $H^\dagger$ ,  $H_1$  and  $H_2$  must be carried predominantly by surface S-atoms. Moreover, non-stoichiometric Pb-atoms (or S-atoms), are predicted to form localized sub-bandgap states split-off from the conduction-band (or valence-band for S-atoms).<sup>38</sup> This prediction implies that since  $E_{1,n}$  states are the lowest-energy unoccupied states, they must be associated with non-stoichiometric Pb-adatoms. The strong localization of  $E_{1,n}$  “hot spots” along the specific crystallographic lines associated with reconstruction features further reinforces this assignment.

In contrast, the high degree of delocalization of states  $E_2$  and  $E_3$  identifies them as quantum-confined PIAB states with spatial distributions modulated by the presence of the periodic surface structures formed from Pb-adatoms. Analogously, the spatial localization of states  $H^\dagger$  and  $H_1$  suggests that they correspond to surface states produced by reconstruction, whereas state  $H_2$  should correspond to a PIAB state. These assignments of the origins of the different NC1 states are supported by the fact that the NC1 bandgap calculated as  $E_2 - H_2$  is in the correct range for a disk-like NC (determined from Figure 9.2b), unlike the apparent bandgap  $E_{1,1} - H_1$ , which is at the extreme low end of values corresponding to a 2D PbS thin film.

Identification of states  $E_{1,n}$  as states carried by reconstructed Pb-adatoms allows us to address the existence of multiple peaks in the  $E_{1,n}$  band, an observation that was common for most studied PbS NCs. Indeed, most of the DOS spectra measured on PbS NCs showed at least two  $E_{1,n}$  states, separated in all spectra by roughly 200 mV (Figure 9.2a). This energetic separation is much larger than the typical vibrational energy scale of PbS,<sup>68</sup> which rules out current-induced vibrational excitation of NCs<sup>69</sup> as a potential cause for the appearance of multiple  $E_{1,n}$  peaks. Instead, the existence of  $E_{1,n}$  bands may be rationalized by considering adatom-adatom electronic coupling that has been shown to lead to formation of “bonding” and “anti-bonding” electronic states.<sup>47</sup> This interaction mechanism suggests a scenario analogous to that described in a number of recent STS studies of atomic structures similar to that exhibited in the model in Figure 9.6a, where ordered rows of atoms adsorbed on surfaces with well-defined crystallographic order were investigated.<sup>70-72</sup> In these studies, formation of extended electronic states was qualitatively described using the linear-combination-of-atomic-orbitals (LCAO) model.

By using this model,  $E_{1,n}$  bands may be similarly attributed to LCAO-like electronic states formed from orbitals of under-coordinated Pb adatoms, such that individual  $E_{1,n}$  states should correspond to distinctly different linear combinations of atomic orbitals. This physical picture not only explains the presence of multiple  $E_{1,n}$  states, but also the close similarities in their 2D DOS maps (Figures 9.5c, G1c-e): because these states are formed from the same atomic orbitals, their linear combinations should only differ in their mutual phases, and should produce the same spatial distributions.

### **NCs with Edge-Defects**

While the delocalized  $E_{1,n}$  states caused by surface-reconstruction were found in almost all of the studied NCs, a *qualitatively different* type of sub-bandgap state attributable (as will be shown in the following) to surface defects was also observed in several NCs. DOS spectra showing these defect states for a representative NC (this NC is referred to as NC2 in the following) are shown in Figure 9.7. Unlike  $E_{1,n}$  states, these defects exhibited a substantial DOS on the occupied side of the STS spectra (states  $H^\dagger$ ,  $H_{1,1}$  and  $H_{1,2}$  in Figure 9.7), while defect-related DOS features appearing on the unoccupied side were often less pronounced (state  $E^\dagger$  in Figure 9.7) or absent (see Figure G5 for additional NCs showing similar defect-related states). In contrast to  $E_{1,n}$  states, the defect states were tightly localized, as can be seen, for example, from the dramatic differences in DOS spectra measured in neighboring points P1 and P3 in Figure 9.7.

To visualize the entire spatial extents of these defect-states, we carried out 2D DOS mapping using the experimental approach described above for NC1. Maps of unoccupied states for NC2 (Figures 9.8a-c and G3) show a progression of  $E_{1,n}$  and  $E_2$  states analogous to that of NC1 (Figure 9.5), as well as state  $E^\dagger$  (Figure 9.8c). For NC2,



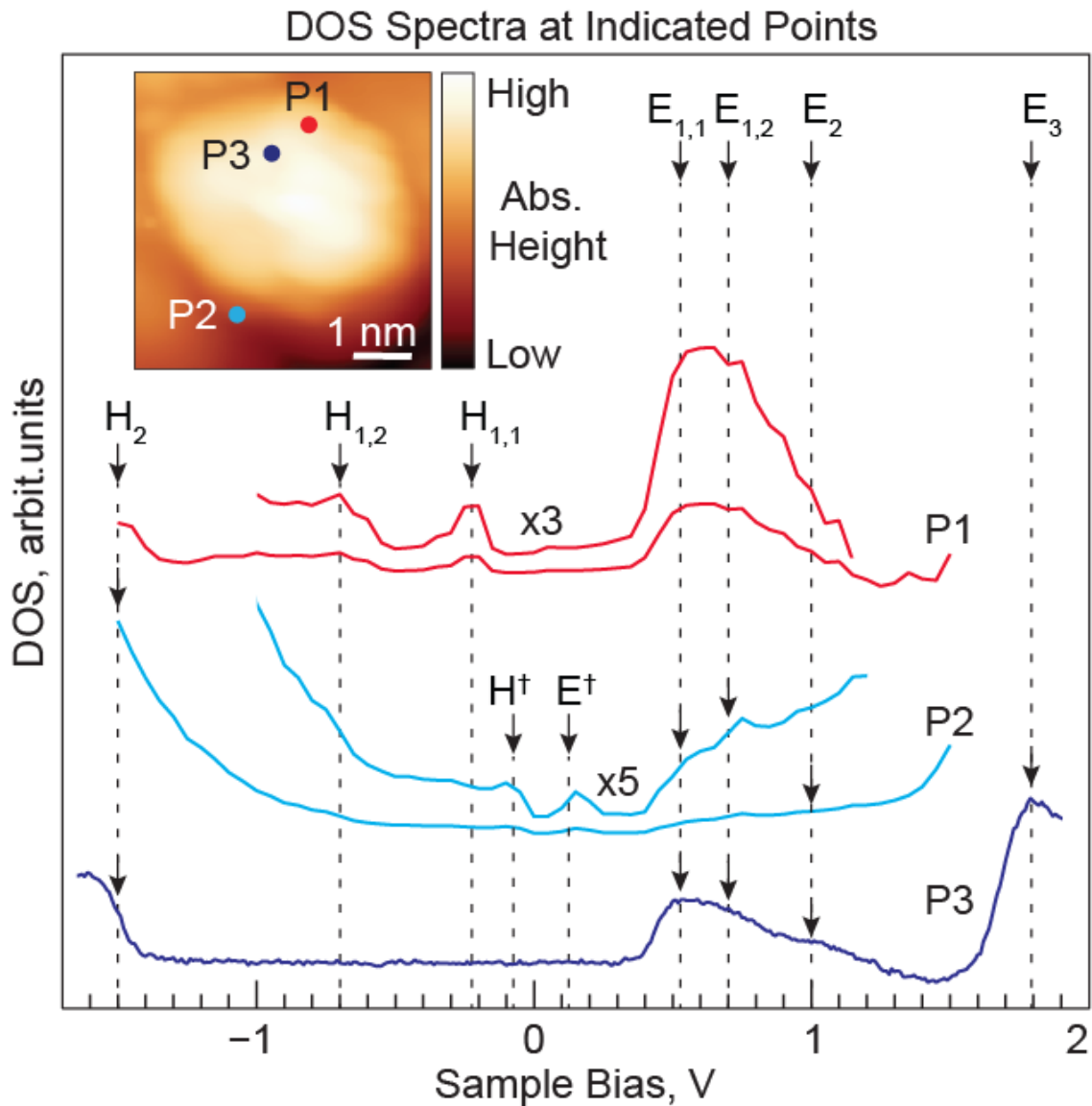


**Fig. 9.7.** DOS spectra for NC2 measured at locations P1-3 shown in the inset STM topography. Sections of spectra P1 and P2 containing relevant states have been magnified by designated amount for clarity. STS measurements were taken with set-points of 1.5-2.2 V bias, 10-20 pA tunneling current. STM topography image measured with set-point 2.0 V bias, 1 pA tunneling current.

however, the high-intensity DOS “stripes” of states  $E_{1,n}$  and  $E_2$  are oriented at an angle of  $30^\circ$  with respect to the NC2 edges, and exhibit spacings of  $0.42 \text{ nm} = 2\beta$  and  $0.63 \text{ nm} = 3\beta$  suggesting that these “stripes” are associated with a *different type* of surface reconstruction with atomic self-assembly along  $\langle 211 \rangle$  directions, as shown by the atomic model in Figures 9.6c and d.

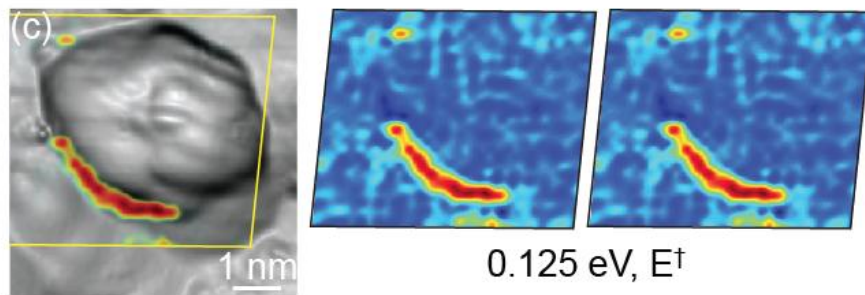
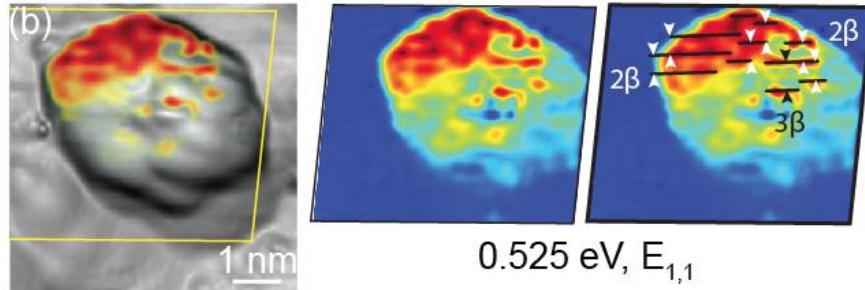
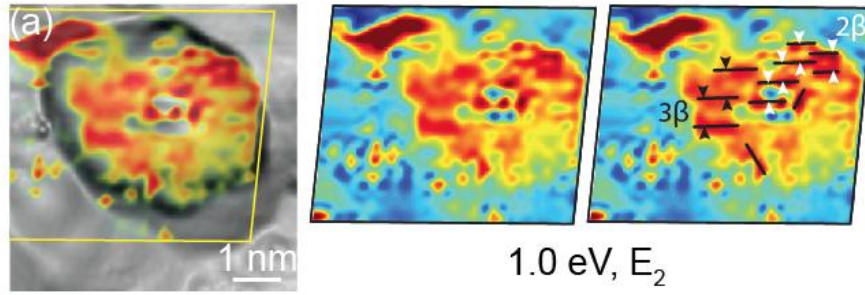
DOS maps of occupied states  $H_{1,n}$  and  $H_2$  (Figures 9.8d,e and G4b-d) show a progression analogous to that of  $E_{1,n}$  and  $E_2$ , except that DOS “stripes” in maps of  $H_{1,n}$  show reconstruction along a  $\langle 110 \rangle$  crystallographic direction. In addition, the nature of this reconstruction pattern is different from that of  $E_{1,n}$  states: comparison of  $H_{1,n}$  and  $E_{1,n}$  maps for NC2 shows that these states are anti-correlated in intensity on the atomic scale (Figure G6), which suggests that  $H_{1,n}$  and  $E_{1,n}$  patterns are formed by atoms corresponding to different elements. As with NC1,  $E_{1,n}$  states in NC2 should be primarily carried by Pb-atoms, which means that  $H_{1,n}$  states should be carried by S-atoms. This conclusion is further strengthened by the results of theoretical calculations, which, in the absence of strong non-stoichiometry, predict that occupied states should be formed mainly from 3-p orbitals of sulfur atoms.<sup>38</sup>

A spatial distribution that is dramatically different from previously considered reconstruction-induced states are found for the lowest-energy unoccupied state  $E^\dagger$

---

**Fig. 9.8.** Same as Figure 9.5 for NC2. Parameters  $\alpha$  and  $\beta$  are the distances between two neighboring  $\{211\}$  and  $\{110\}$  planes respectively, as shown in the model in Figures 9.6. STM topography image measured with set-point 2.0 V bias, 1 pA tunneling current. STS maps measured with set-point 1.5 V bias, 20 pA tunneling current.

DOS maps of unoccupied states



DOS maps of occupied states

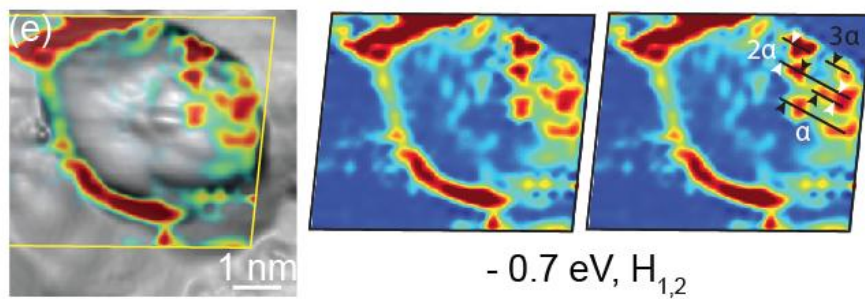
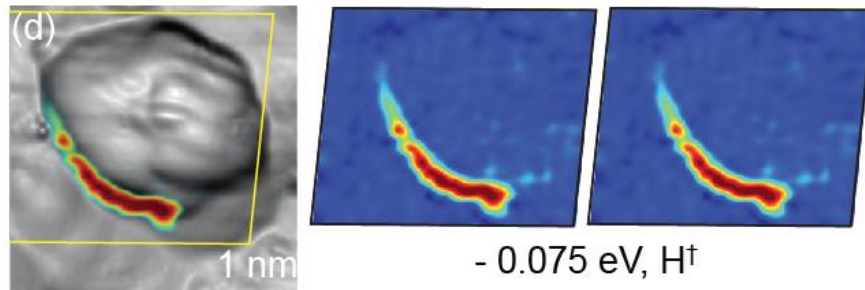


(Figure 9.8c) and highest occupied state  $H^\dagger$  (Figure 9.8d), which are both strongly localized near the bottom-left boundary of NC2. States localized near the same part of the NC2 boundary, almost identically to the localization patterns of  $E^\dagger$  and  $H^\dagger$ , are also identifiable in all maps for the remaining occupied states (Figure 9.8d,e and G4a-d). The very small apparent bandgap ( $E^\dagger - H^\dagger$ ) associated with these “boundary states”, together with the high degree of their spatial localization, suggests their defect-related origin. The spectral characteristics of these states are analogous to those obtained in model DFT simulations of highly off-stoichiometric PbS NCs.<sup>38</sup> As discussed earlier, in these calculations, excess of Pb (S) atoms leads to the appearance of split-off states below (above) the PIAB-like conduction (valence) band states. In highly off-stoichiometric conditions, the energies of split-off states become sufficiently low (high) for them to appear on the occupied (unoccupied) side of DOS spectra. Thus, because with the exception of state  $E^\dagger$ , no other unoccupied “boundary states” are observed (Figures 9.8a,b), and, in contrast, “boundary states” are observed in maps of all occupied states, we associate the “boundary states” with sulfur-rich areas of NC2.

This assignment is consistent with the presence of extra sulfur atoms in the areas of states  $H_{1,n}$ , (top-right area of NC2 in Figures 9.8e and G4b,c), which are also localized near the NC2 boundaries: the near-boundary localization of states  $E^\dagger$ ,  $H^\dagger$  and  $H_{1,n}$  suggests that they could have been formed in a similar fashion, possibly due to migration of some of the Pb atoms to the Au(111) surface during annealing. Indeed, migration of Pb atoms to the Au substrate appears necessary to explain the existence of sulfur-rich areas, since as-synthesized PbS NCs are known to have Pb-rich surfaces.<sup>65, 73</sup>

## 9.5. Conclusions

Our results show that reconstruction of polar PbS surfaces can produce a wide variety of sub-bandgap states with spatial structures and energies sensitive to the local stoichiometry. Both unoccupied and occupied trap states can be created in Pb-rich and S-rich areas, correspondingly. Wide bands of trap states crossing over the Fermi level can also exist in areas with sufficient local off-stoichiometry. The fact that the  $E_{1,n}$  states were observed in the majority of fully annealed NC DOS suggests that most of these NCs underwent surface reconstruction. Indeed, one can expect this behavior to be common for ligand-free NCs, since their surfaces are likely to terminate with (111) facets, which are prone to reconstruction due to their polar nature.<sup>45</sup> This is consistent with DFT calculations, which show that unreconstructed (111) facets, are, in fact, unstable, and stability is only obtained for non-polar reconstructed facets.<sup>45</sup> In contrast, other facets corresponding to main crystallographic directions (100) and (110) are stable in their unreconstructed forms.<sup>45</sup>

The presented results are directly applicable to thermally-processed NC solids, where loss of ligands is likely. Similar structure-dependent effects in the local DOS can also be expected for under-stoichiometric surfaces of ligand-passivated PbX NCs, where ligand self-assembly at the PbX-ligand interface may proceed with formation of surface-bound sub-bandgap states, as also suggested by calculations for CdSe NCs.<sup>74,75</sup> The STS-based characterization approach demonstrated in the present manuscript is applicable to NCs passivated with atomic-ligands,<sup>32</sup> where similar questions of surface adatom self-assembly and resulting electronic structure need to be addressed.

## 9.6. Bridge to Chapter X

While colloidal nanocrystals studied in this Chapter had to have their ligand shell removed in order to make them accessible to STM, it is possible to investigate colloidal nanocrystals with passivation intact as will be shown on the system of colloidal hydrogenated silicon nanocrystals (SiNCs). Hydrogen passivation models the shortest possible ligand and allows to achieve the most complete saturation of dangling bonds of nanocrystal's surface. We will use Scanning Tunneling Spectroscopy (STS) to study the impact of surface defects on the electronic structures of SiNCs and visualize, for the first time, the spatial structure of individual electronic states in SiNCs, which is essential for unequivocal identification of their nature (delocalized quantum-confined vs. localized defect-related). By using this analysis, we will identify, for the first time, the localized defect-related states, which, according to our theoretical calculations, likely correspond to Si–O–Si bridged oxygen or Si-OH surface defects.

## CHAPTER X

# MAPPING OF DEFECTS IN INDIVIDUAL SILICON NANOCRYSTALS USING REAL-SPACE SPECTROSCOPY

This chapter by Dmitry A. Kislitsyn, Vancho Kocevski, Jon M. Mills, Sheng-Kuei Chiu, Christian F. Gervasi, Benjamin N. Taber, Ariel E. Rosenfield, Olle Eriksson, Ján Ruzs, Andrea M. Goforth, and George V. Nazin has been previously published under the same title in *J. Phys. Chem. Lett.* **7**, 1047–1054 (2016). Copyright © 2016 American Chemical Society.

### 10.1. Introduction

The photophysical properties of silicon semiconductor nanocrystals (SiNCs) are extremely sensitive to the presence of surface chemical defects, many of which are easily produced by oxidation in ambient conditions. The diversity of chemical structures of such defects, and the lack of tools capable of probing individual defects continue to impede understanding of the roles of these defects in SiNC photophysics. In this letter, we use scanning tunneling spectroscopy to study the impact of surface defects on the electronic structures of hydrogen-passivated SiNCs supported on the Au(111) surface. Spatial maps of the local electronic density of states (LDOS) produced by our measurements allowed us to identify locally-enhanced defect-induced states as well as quantum-confined states delocalized throughout the SiNC volume. We use theoretical calculations to show that the LDOS spectra associated with the observed defects are attributable to Si–O–Si bridged oxygen or Si–OH surface defects.

## 10.2. Background

Silicon semiconductor nanocrystals (NCs) have recently emerged as a promising alternative to metal chalcogenide-based quantum dots (QDs) in a wide range of photophysical applications including light-emitting devices<sup>1,2</sup> and photovoltaics,<sup>3-6</sup> as well as in biomedical imaging and tracking.<sup>7,8</sup> Among the advantages of SiNCs are the lower toxicity of silicon and the potential for a more robust covalent passivation of SiNC surfaces.<sup>9,10</sup> For sufficiently small SiNCs, the indirect electronic bandgap of silicon, responsible for the inefficient coupling to light in larger NCs, becomes ill-defined,<sup>11-13</sup> which leads to a dramatic brightening of radiative transitions,<sup>14-17</sup> and thus enables optical and optoelectronic applications of SiNCs. Further, multiple exciton generation in ultra-small SiNCs has been considered as a potential route for increasing the efficiency of photovoltaic devices.<sup>18-20</sup> While beneficial for applications, the ultra-small size of SiNCs makes them extremely susceptible to the chemical structure of the NC surface. In particular, the tendency of SiNC surfaces to oxidize,<sup>21,22</sup> resulting in pronounced changes in optical properties, has been a major challenge not only for applications based on SiNCs, but also for the basic understanding of SiNC photophysics. The presence of oxidative defects on the SiNCs surface has been shown to produce red-shifted photoluminescence (PL), with photon energies being considerably less sensitive to the SiNC size than predicted for emission from quantum-confined states.<sup>23-28</sup> The exact origin of this emission remains poorly understood, which is due, in part, to the diversity of chemical defects resulting from surface oxidation of silicon,<sup>29,30</sup> and the lack of experimental techniques capable of directly identifying the chemical structures of defects responsible for the red-shifted PL. Theoretical studies suggest that Si–O–Si bridged



oxygen,<sup>31-33</sup> as well as sufficient coverage of Si–OH surface groups may result in red-shifted PL.<sup>13, 34</sup> Indeed, it would be natural to expect these defects to play a role in PL of SiNCs, since both defects appear prominently in Fourier transform infrared spectroscopy (FTIR) of porous hydrogen-passivated SiNCs within minutes of exposure to ambient air.<sup>23</sup> Alternatively, a red shift consistent with the experimental data may be attributed to emission from individual defects associated with surface silicon-oxygen double (Si=O) bonds,<sup>23, 31-33, 35-37</sup> which have not, however, been observed in FTIR spectra of emissive SiNCs. Finally, completely oxidized SiNCs have also been shown to possess delocalized electronic states with calculated energies consistent with the experimentally observed PL.<sup>38</sup> The plurality of theoretical models explaining the origin of red-shifted emission highlights the need for experimental studies that could directly identify the chemical nature and electronic structures of individual defects in individual SiNCs. This capability is offered by scanning tunneling spectroscopy (STS),<sup>39</sup> which has been used to study quantum confinement effects in individual SiNCs,<sup>40</sup> as well as localization of individual sub-bandgap states in PbS nanocrystals.<sup>41, 42</sup>

### 10.3. Experimental details

Experiments were carried out in a home-built ultra-high vacuum (UHV) cryogenic STM system.<sup>43</sup> A Au(111)/mica substrate was prepared in situ using multiple neon sputter/anneal cycles. Hydrogen-passivated SiNCs were fabricated via thermal disproportionation in a polymeric sol–gel hydrosilicate precursor, and subsequently liberated from the resulting oxide host matrix via a wet chemical etch (i.e., with HF/EtOH/H<sub>2</sub>O) using a protocol described previously<sup>44</sup> (for further details see Supporting Information in Appendix H). The SiNCs were suspended in pentane, and

deposited onto the Au(111) surface in high-vacuum conditions using a solenoid pulse-valve. The deposition parameters were chosen so as to obtain monolayer NC coverage. The Au(111) substrate with deposited SiNCs was then degassed overnight in UHV at ~50 °C to remove any residual pentane from the sample surface. All STM topographies and STS measurements were obtained at a temperature of ~20 K using silver tips prepared by electrochemical etching and subsequent sputtering in UHV. All STS spectra were recorded using the lock-in technique at 570 Hz and a bias modulations varying from 10 (individual spectra and 1-D spatial scans) to 50 mV (2-D LDOS maps). 2D LDOS mapping requires tip-sample spatial registry throughout the mapping process (typically, several hours). This capability is enabled by the unique spatial stability (better than ~0.2 Å/hour) of our STM system.<sup>43</sup>

Theoretical calculations were performed using DFT, as implemented in the pseudo-potential package SIESTA,<sup>45,46</sup> employing local density approximation (LDA) exchange and Ceperlay-Alder parameterization of the potential, as described previously.<sup>33</sup> Numerical atomic orbitals were used as a basis set: “single zeta with polarization” orbitals for Si and O, and “double zeta” for H. Further details of the basis sets for different elements are given in Ref. 12. For hydrogenated SiNCs smaller than 4 nm in diameter, the described approach provides a good approximation of electronic bandgaps.<sup>12</sup>

To simulate the experimental data, LDOS was calculated as probability density sum  $LDOS(x, y, z, V) = \sum_j |\Psi_j(x, y, z)|^2 \delta(eV - E_j)$  of individual Kohn-Sham orbitals  $\Psi_j(x, y, z)$  obtained from DFT. To account for finite spatial and spectral resolution of the experimental data, the contributions of individual orbitals to the total LDOS were

Gaussian-broadened by 50 meV in energy, and by 0.2 nm in space. To more closely reproduce experimental conditions where the integral of each  $dI/dV$  spectrum is equal to the setpoint current, calculated LDOS spectra for each specific spatial location were normalized such as to yield integrals  $I(x, y, z)$  equal to the setpoint value  $I_{sp}$ :

$$I_{sp} = I(x, y, z) = \int_0^{V_B} LDOS(x, y, z, V) dV$$

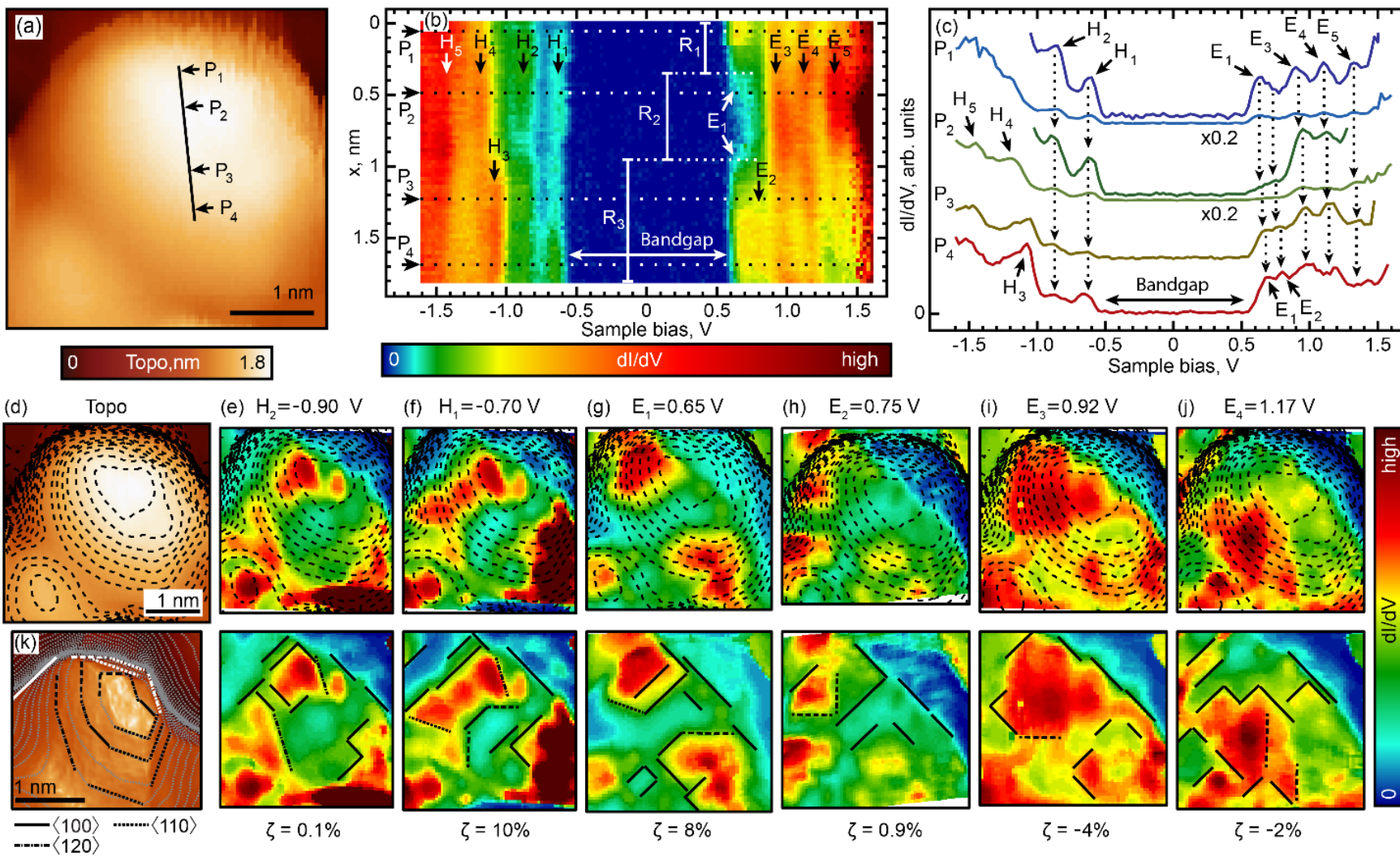
Here  $I(x, y, z)$  represents the calculated tunneling current in each spatial location, and  $V_B$  is the setpoint bias voltage (noted in the corresponding figure captions).

#### 10.4. Results and discussion

This chapter includes the first report of the studies of defect-induced electronic states on the surfaces of individual hydrogen-terminated SiNCs using spatially-resolved STS mapping. Hydrogen-terminated SiNCs were spray-deposited onto a Au(111) substrate in vacuum and studied using an ultra-high vacuum (UHV) cryogenic scanning tunneling microscope (STM) system<sup>43</sup> (see Methods for further experimental details). In STM images, SiNCs deposited on Au(111) surfaces appeared as protrusions with typical dimensions in the 2-4 nm range (Figures 10.1a and 10.3a). Using STS we recorded energy-dependent local density of states (LDOS) spectra of individual SiNCs by measuring the differential tunneling conductance ( $dI/dV$ ) as a function of the applied bias voltage (see Methods for details of the measurements). We focus our attention on the electronic states in the vicinity of the bandgap, since these are the states that are primarily responsible for the photophysical and electron transport properties of individual NCs and NC-based materials. In the following, we summarize our STS studies of 27 individual SiNCs.

Individual LDOS spectra measured on different SiNCs showed similar progressions of electronic states, comparable to the theoretically predicted progressions of states for hydrogen-passivated SiNCs with similar diameters (Figure H1). All SiNCs studied could be roughly divided into two classes: nominally “defect-free” SiNCs, which showed electronic states delocalized over the whole NC surface, and nominally “defect-containing” SiNCs exhibiting electronic states with LDOS strongly enhanced at specific

**Figure 10.1.** Spatial mapping of LDOS for NC<sub>1</sub>. (a) STM topographic image. (b) LDOS (measured as  $dI/dV$ ) as a function of the bias voltage and position  $x$  along the path shown in (a). R<sub>1</sub>-R<sub>3</sub> indicate regions with specific patterns of LDOS spectra. In (b), the individual unoccupied and occupied LDOS spectra were normalized separately, for clarity. (c) Individual LDOS spectra from (b) measured at points P<sub>1</sub> through P<sub>4</sub>. Spectra are offset for clarity. Identical spectra for P<sub>1</sub> and P<sub>2</sub> scaled by  $\times 0.2$  are also shown. Occupied and unoccupied states are marked “H” and “E” respectively in both (b) and (c). Individual LDOS peaks are observed at slightly different voltages across the NC due to the finite location-dependent voltage drop inside the NC. (d) Topography from (a) overlaid with its contour plot. Contours correspond to vertical separation of 0.68 Å (half of one Si(100) atomic step). (e-j) 2D LDOS maps for voltages corresponding to the peaks indicated in (c). Upper row shows the LDOS maps overlaid with contour lines from (d). Lower row of LDOS maps shows Si(100) lattice directions identified in the spatial LDOS intensity distributions. Solid lines are  $\langle 100 \rangle$  and  $\langle 010 \rangle$  directions (perpendicular to each other), dashed lines are  $\langle 110 \rangle$  and  $\langle \bar{1}10 \rangle$ , dotted lines are  $\langle 210 \rangle$  and  $\langle \bar{1}20 \rangle$ , dash-dotted lines are  $\langle 120 \rangle$  and  $\langle \bar{2}10 \rangle$ . [Assignment of the primary directions  $\langle 100 \rangle$  and  $\langle 010 \rangle$  is made using the predominant orientation of linear features in the LDOS patterns.] Measure of localization  $\zeta$  is calculated for every 2D map, as explained in the main text. (k) Calculated representation of NC<sub>1</sub> shape (see Supporting Information in Appendix H for details) with its contour plot overlaid. Black and white lines on top of the contours correspond to Si(100) directions.



locations. LDOS spectra of each “defect-free” SiNC contained a nearly identical set of electronic peaks  $H_n$  (occupied states) and  $E_n$  (unoccupied states) across the whole NC surface, as shown in Figures H2 and 10.1a-c for one representative SiNC ( $NC_1$  in the following). The relative intensities of electronic peaks  $H_n$  and  $E_n$  depend on the specific spatial location, as visualized in Figure 10.1b, which shows an array of LDOS spectra recorded along the line shown in Figure 10.1a.

Intriguingly, the LDOS spectra (and intensities of electronic peaks) are nearly identical within specific regions on the  $NC_1$  surface (regions  $R_1$ - $R_3$  in Figure 10.1b, representative LDOS spectra for each region are shown in Figure 10.1c), and change on the angstrom scale at the boundaries between the regions, a behavior that was also observed for other “defect-free” SiNCs (data not shown). To further explore the nature of peaks  $H_n$  and  $E_n$ , we recorded two-dimensional (2D) spatial LDOS maps showing the distribution of each electronic state across the  $NC_1$  surface (Figures 10.1e-j). To ensure that we could identify all of the (possibly localized) electronic states in SiNCs, we recorded LDOS spectra on a two-dimensional grid of points covering the spatial range corresponding to Figure 10.1d. The 2D maps in Figures 10.1e-j were then generated by taking subsections of this LDOS dataset corresponding to specific energies (voltages). Thus obtained 2D LDOS maps show that the main states of  $NC_1$  are completely delocalized (showing non-zero LDOS) on the observable part of the  $NC_1$  surface, even though 2D-regions of varied intensities (similar to 1D-regions  $R_1$ - $R_3$  in Figure 10.1b) are present. Strikingly, the boundaries of these regions are aligned along specific directions attributable to a  $\{100\}$  crystallographic facet (bottom Figures 10.1e-j, see caption for details), an observation that was common for the majority of SiNCs studied (in addition

to SiNCs showing crystallographic directions attributable to {100} facets, SiNCs showing directions consistent with {111} facets were also observed).

A crystallographic origin of directional order in the 2D LDOS maps is further supported by our analysis of the STM images of the corresponding SiNCs. In this analysis, we attempted to de-convolute the effects of STM tip-shape and finite tip-NC distance ( $\sim 0.8$  nm), which both lead to broadening and rounding of the apparent NC shapes observed in the STM images (see Figure H3 for details). Thus deconvoluted images show sharply-defined facets (see Figure 10.1k for NC<sub>1</sub>) with directions identical to those found in the LDOS maps (these directions are also present in as-recorded STM images – see Figure 10.1d), which strongly suggests that the observed directional order in both 2D maps and recalculated STM images originates from the crystallographic structures of the SiNCs.

The correlation with the crystallographic directions and the delocalized nature of electronic states in “defect-free” SiNCs together suggest that these states correspond to quantum-confined states delocalized throughout the bulk of NC<sub>1</sub> rather than defect states (the latter, in contrast, can be expected to show LDOS enhanced at the defect locations). To test this hypothesis, we carried out density-functional theory (DFT) calculations (see Methods for details) for a set of model NCs of different sizes. For the simulations, we chose approximately spherical NC shapes (Figure 10.2a), as expected for SiNCs with sizes below  $\sim 6$  nm.<sup>47, 48</sup>

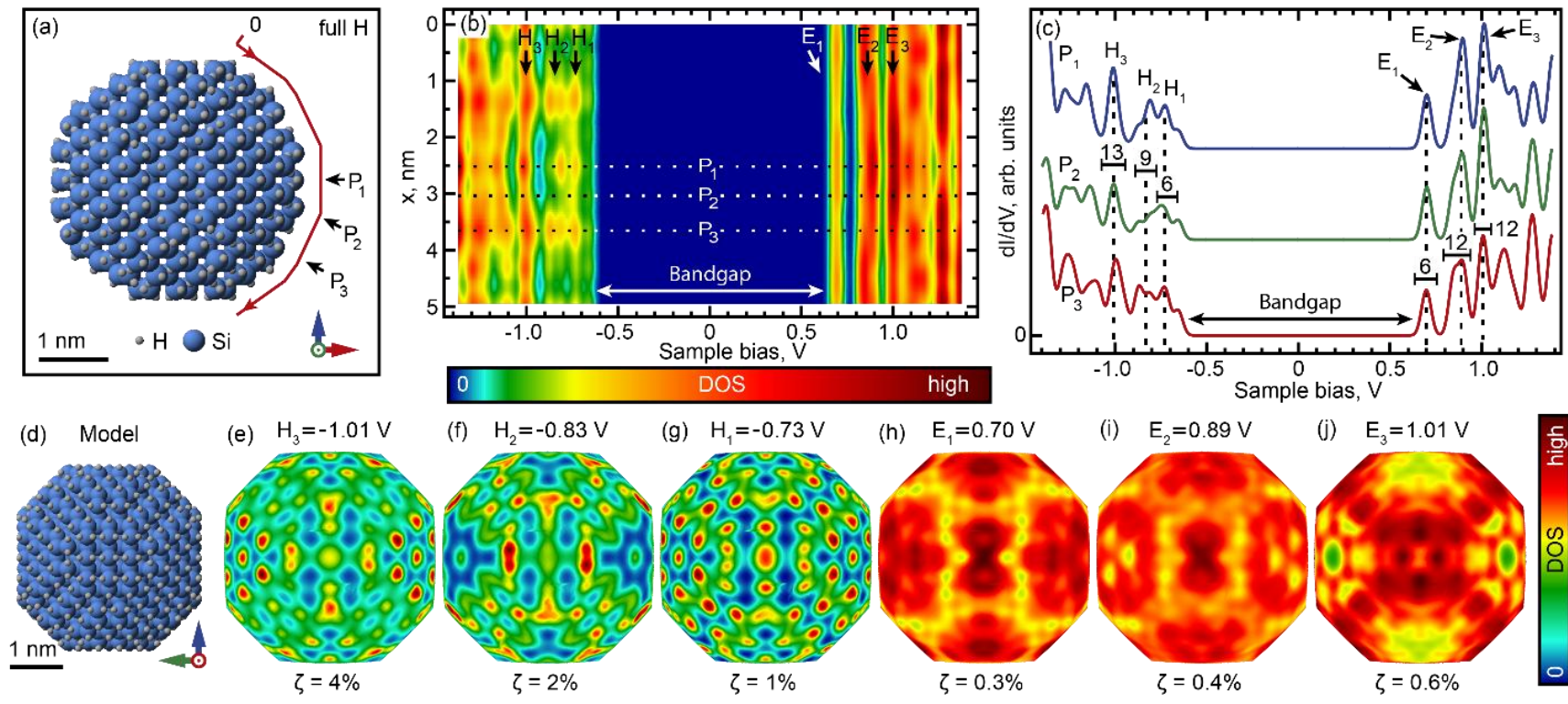
In agreement with the measured 2D LDOS maps, our calculations for defect-free SiNCs (see Figure 10.2 for a SiNC with a size of  $\sim 3.5$  nm, similar to that of NC<sub>1</sub>) reproduce the progressions of electronic peaks  $H_n$  and  $E_n$  observed in LDOS of studied

SiNCs. We note that each peak in Figures 10.2b-c is comprised of several closely-spaced distinct electronic states formed from states associated with different electronic valleys in the Brillouin zone of bulk Si.<sup>49</sup> These states are not completely resolved in our measurements, even though their presence is suggested by the fine structure of LDOS spectra (Figures H2c,d). Finer spectral structure could not be observed due to the intrinsic broadening of STS spectra associated with coupling of tunneling electrons to vibrational excitations,<sup>50</sup> which exceeds the inter-valley splitting for simulated SiNCs (~50 meV).

Significantly, our calculations reproduce the existence of distinct surface regions with specific LDOS spectra (Figures 10.2b-c), and the presence of directional order in the spatial LDOS distributions (Figures 10.2e-j), even though the precise spatial patterns for experimental and theoretical 2D maps are not identical. The differences in the two datasets are attributable to the fact that the precise shape of NC<sub>1</sub>, which has a profound

**Figure 10.2.** Theoretical LDOS for a model near-spherical (diameter ~3.5 nm) SiNC (with composition H<sub>412</sub>Si<sub>1087</sub>). (a) NC geometry. (b) Calculated 1D LDOS map as a function of the bias voltage and position  $x$  along the path shown in (a). (c) Individual LDOS spectra from (b) measured at points P<sub>1</sub> through P<sub>3</sub>. Spectra are offset for clarity. The number of discrete states in each peak is indicated. (d) NC geometry rotated by 90° around the vertical axis and exposing facets mapped in (b) as well as in (e-j). (e-j) 2D maps of LDOS for selected states near the electronic bandgap. LDOS intensities were calculated on a 3D surface equidistantly offset from the NC surface by 3 Å, similarly to the path shown in (a). In order to more closely reproduce experimental conditions, all spectra were normalized to give the same total current at 1.35 V (see Methods for details). Measure of localization  $\zeta$  is calculated for every 2D map, as explained in the main text.





impact on the electronic LDOS spatial distribution, is not known (since a large part of the NC<sub>1</sub> surface is not observable in STM imaging) and thus could not be modeled directly. The close similarity between the theoretical and experimental results in Figures 10.1 and 10.2 reinforces the interpretation of states in Figure 10.1 as those of quantum-confined nature, and delocalized in the interior of the NC, analogously to the calculated three-dimensional LDOS distributions shown in Figures H4 and H5.

In addition to “defect-free” SiNCs with delocalized electronic states, we have also observed SiNCs (6 out of 27 SiNCs studied in our experiments) showing localized areas with strongly enhanced LDOS. An example of this behavior is shown in Figures 10.3 and H6 for a representative SiNC (NC<sub>2</sub> in the following). For example, a one-dimensional LDOS map (Figure 10.3b) of NC<sub>2</sub> shows peaks E<sub>2</sub> and H<sub>2</sub> delocalized over the entire spatial range of the scan, while peaks H<sub>1</sub><sup>\*</sup> and H<sub>1</sub><sup>\*\*</sup> (corresponding to a smaller bandgap) are primarily concentrated in regions R<sub>1</sub> and R<sub>3</sub>, respectively. Closer inspection reveals peaks E<sub>1</sub> and H<sub>1</sub> with lower intensities everywhere along the mapping path (Figure 10.3c). The 2D LDOS maps of these electronic states (Figures 10.3e-j) give a more complete picture: states E<sub>n</sub> and H<sub>n</sub> of NC<sub>2</sub> appear over the entire observable part of NC<sub>2</sub>, showing 2D-regions of varied intensities. Similarly to the directional order in 2D LDOS maps of NC<sub>1</sub>, the boundaries of some of these regions are aligned along the main crystallographic directions of NC<sub>2</sub> (bottom Figures 10.3e-j). Importantly, spatial distributions of several LDOS features appear very different from those of NC<sub>1</sub>. In particular, pronounced spatially-confined maxima H<sub>1</sub><sup>\*</sup>, H<sub>1</sub><sup>\*\*</sup> and H<sub>2</sub><sup>\*</sup> are observed in Figures 10.3e and f, with the spatial LDOS concentration in the corresponding maps being significantly higher than that in the other maps for NC<sub>1</sub> and NC<sub>2</sub>. To analyze this

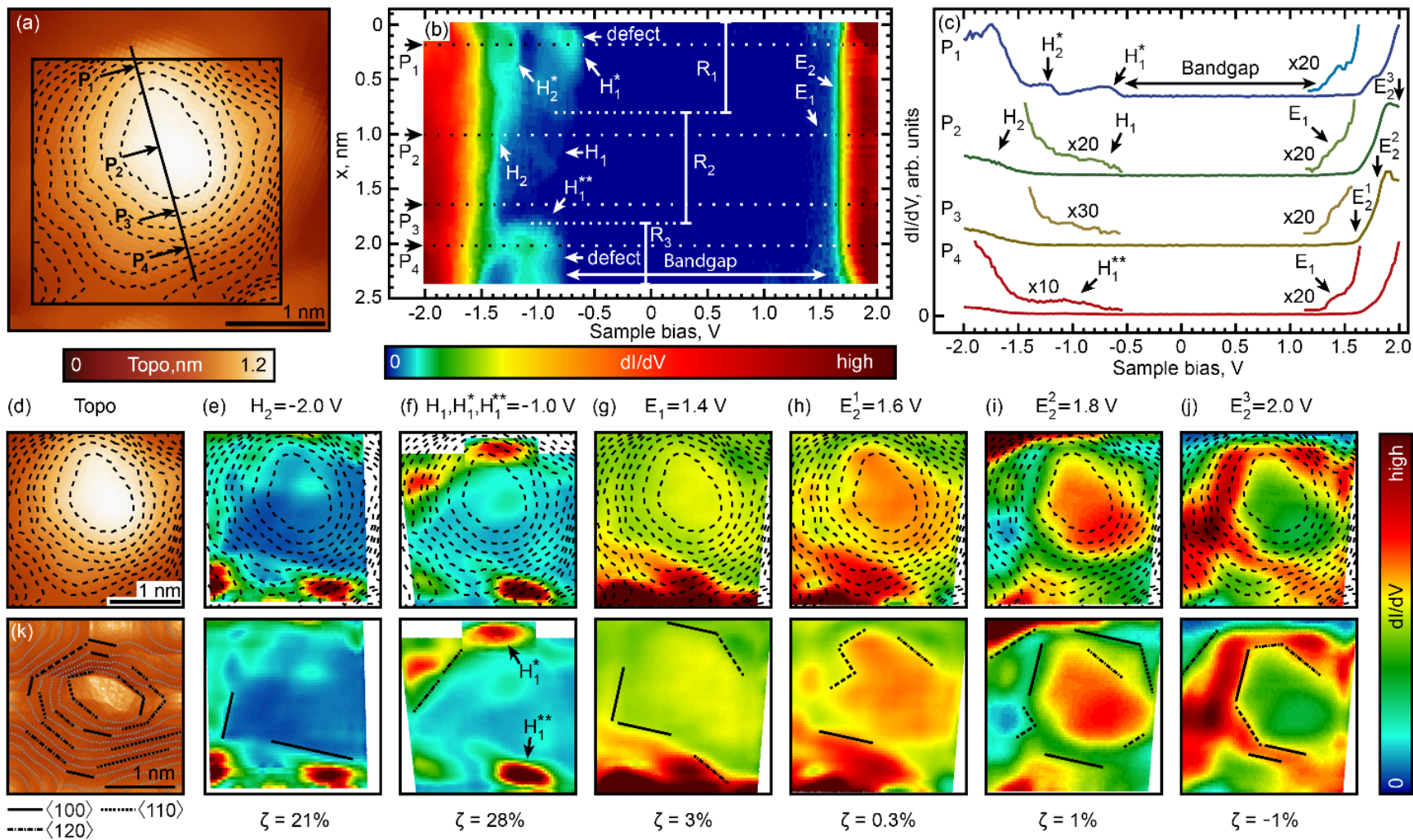


**Figure 10.3.** Spatial mapping of LDOS for  $NC_2$ . Data arrangement and markings are the same as in Figure 10.1. In (b), the individual unoccupied and occupied LDOS spectra were normalized separately, for clarity. Peak  $E_2$  is measured at three voltages  $E_2^n$ .

localization quantitatively, we implemented a comparison of average and median values for a particular LDOS map, which is sensitive to the presence of sharp intense peaks in DOS maps. We constructed a measure of localization of the form:  $\zeta = \frac{\overline{DOS} - \widetilde{DOS}}{\overline{DOS} + \widetilde{DOS}} \times 100\%$  (where  $\overline{DOS}$  and  $\widetilde{DOS}$  are the average and median values, respectively), which for more spatially-concentrated peaks  $H_1^*$ ,  $H_1^{**}$  and  $H_2^*$  gives values  $\zeta \geq 20\%$  (bottom Figures 10.3e and f), while the rest of the maps shows  $|\zeta| \leq 10\%$  (as listed in the respective figures), which we consider to be representative of “delocalized” states. The spatial concentration of peaks  $H_1^*$ ,  $H_1^{**}$  and  $H_2^*$  suggests that they may correspond to defect-related states (because  $H_1^*$  and  $H_1^{**}$  are spatially well-separated, they likely correspond to two different defects).

To investigate the nature of observed locally-enhanced peaks  $H_1^*$  and  $H_1^{**}$ , we carried out DFT calculations of the electronic structures of SiNCs containing individual chemical defects.<sup>33</sup> Because a substantial fraction (~22%) of studied SiNCs showed defects of the type shown in Figure 10.3, these are likely to be of the same chemical nature, and must be very common for the hydrogen-passivated SiNCs used in our study. Surface oxidation is particularly common for such SiNCs, and is known to produce a variety of oxygen-containing bonds on the SiNC surfaces often leading to formation of intra-gap states.<sup>23, 31, 35</sup> We thus restrict our consideration to elementary defects caused by oxidation, which include three main classes: Si–O–Si bridged oxygen, Si–OH groups, and Si=O bonds. For SiNCs studied in our experiments, the most likely candidate is the Si–O–Si bridged oxygen defect, which is the only type of defect identifiable in the FTIR spectra of as-synthesized hydrogen-passivated SiNCs used in our study.<sup>44, 51</sup> Another possible candidate are the Si–OH surface groups, which have been identified in FTIR

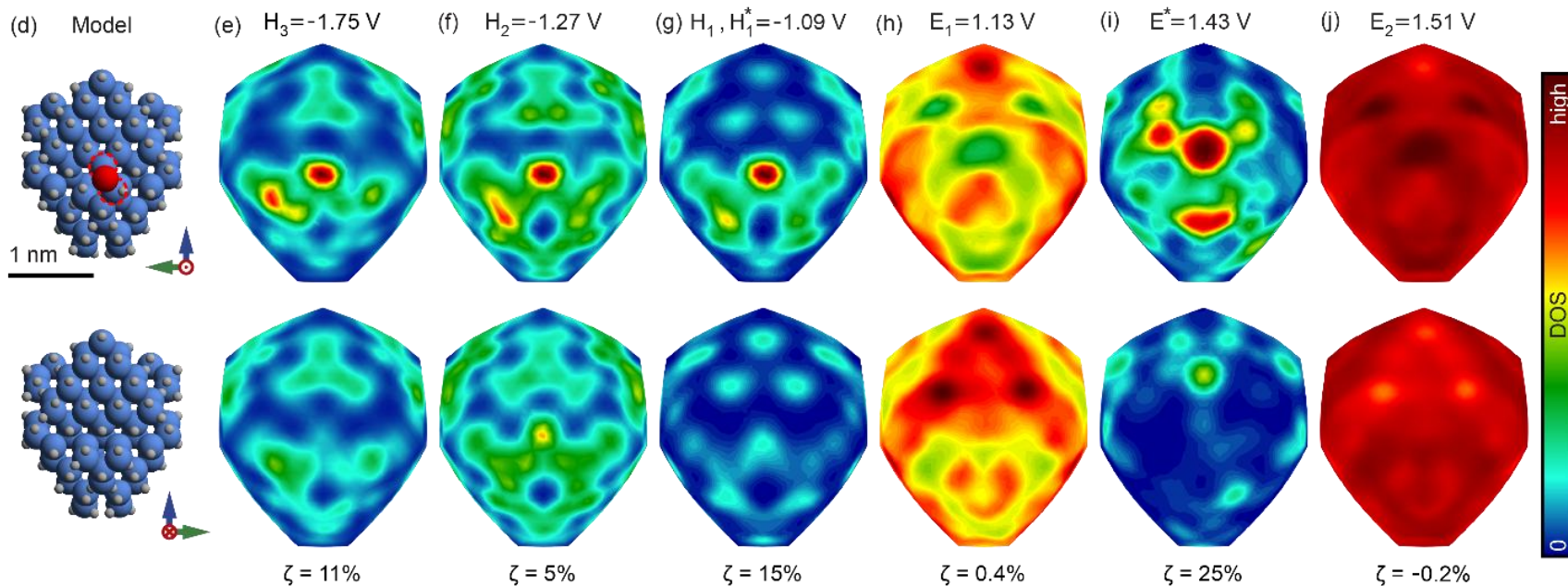
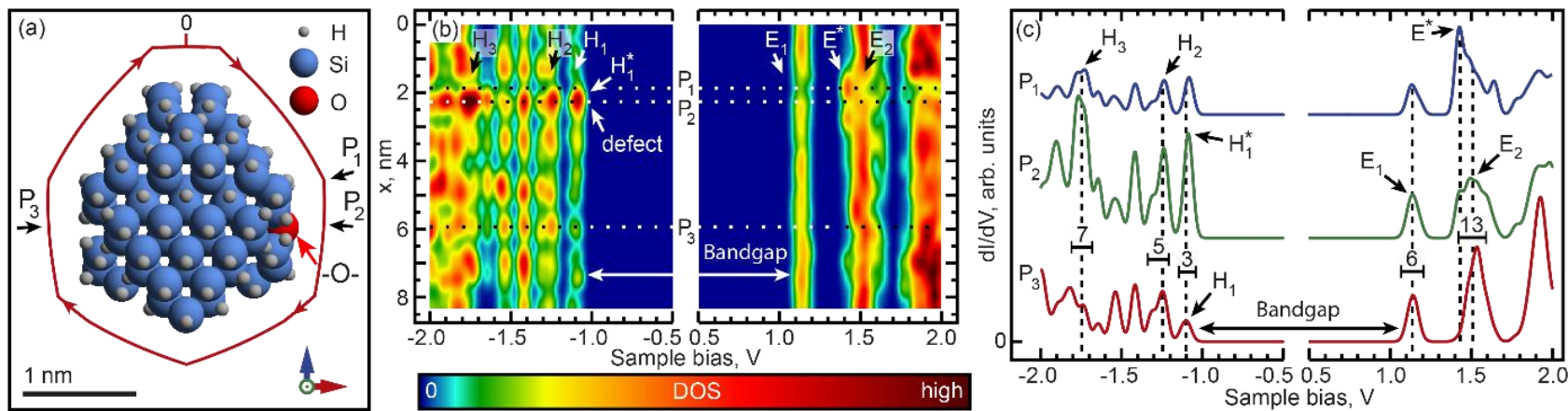
spectra of SiNCs synthesized using a similar technique.<sup>30</sup> However, the presence of these defects in our SiNCs may be somewhat less likely due to their instability under vacuum conditions.<sup>52</sup> Surface Si = O defects have been implicated as a possible source of the red-shifted defect-induced PL,<sup>23,31,35</sup> and have been observed on the SiNC surfaces under vacuum conditions.<sup>52</sup>

Theoretical simulations of one-dimensional LDOS maps for the Si = O defect on the surface of a model SiNC with a size of ~2 nm, similar to that of NC<sub>2</sub>, show two peaks enhanced at the defect location: the highest-occupied peak  $H_1^*$  and the lowest-unoccupied peak  $E_1^*$  (Figure H7b, see also Figures H7g and h). Comparison of a one-dimensional LDOS map of this NC (Figure H7b) to those of its defect-free variant (Figure H8b), shows that the bandgap of the defective NC is reduced at the defect location by ~300 meV. However, the energy differences between the delocalized peaks  $H_1$  and  $E_1$  are nearly identical for both NCs, suggesting that the defect-induced peaks  $H_1^*$  and  $E_1^*$  effectively correspond to trap states within the defect-free bandgap. In contrast, bandgaps obtained from theoretical LDOS of both Si–O–Si and Si–OH defects (Figures 10.4b and H9b, respectively) are quite similar to that of the defect-free SiNC (Figure H8b), consistent with previous theoretical results.<sup>23,31,33,35</sup> The impact of these defects is primarily in the redistribution of the SiNC LDOS, resulting in enhanced LDOS at the location of the corresponding defect (compare peaks  $H_1$  with maxima  $H_1^*$  in Figures 10.4e-g and H9e-g to Figure H8e-g). The varied impacts of the different types of defects on the SiNC LDOS are directly related to the specific spatial distributions of the corresponding electronic states (Figures H10-15). Indeed, in the case of the Si = O defect, the bandgap-forming states  $H_1^*$  and  $E_1^*$  are tightly localized (in three dimensions) within

the immediate vicinity of the defect (Figure H11), while the bandgap-forming states for the Si–O–Si and Si–OH defects are delocalized within the NC interiors, with only a small fraction of the total DOS found in the defect vicinity (Figures H12-15), reminiscent of the LDOS distributions for the defect-free NC (Figures H16-17).

Analysis of the specific spatial LDOS distributions expected for the different oxidative defects discussed above (Figures 10.4, H7 and H9) allows us to shed light into the nature of the defect-induced states shown in Figure 10.3. In particular, the presence of the locally-enhanced peak  $E_1^*$  in the theoretical LDOS is incompatible with the experimental LDOS for the lowest unoccupied state  $E_1$  of  $\text{NC}_2$  (Figure 10.3g), where only a small local maximum, instead of a strongly locally-enhanced peak is observed at the defect location corresponding to peak  $H_1^{**}$  in Figure 10.3f and no maximum is found at the location of peak  $H_1^*$  in Figure 10.3f. The same conclusion is suggested by the fact that in Figure 10.3g, the localization parameter  $\zeta$  is dramatically smaller than those found for Figure H7h or Figure 10.3f (3% versus 32% and 28%, respectively). The absence of strong local DOS maxima in Figure 10.3g thus suggests that the Si = O defects are

**Figure 10.4.** Theoretical LDOS for a model near-spherical (diameter ~2 nm) SiNC with a bridged oxygen (Si–O–Si) impurity, and composition  $\text{H}_{114}\text{Si}_{175}\text{O}$ . Data arrangement and markings are the same as in Figure 10.2. In (c),  $P_1$  corresponds to the maximum of orbital  $E^*$  LDOS,  $P_2$  corresponds to the defect location, and  $P_3$  is positioned on the opposite side of NC with respect to  $P_2$ . The top and bottom rows in (d-j) show two opposite sides of the NC, respectively. To more closely reproduce experimental conditions, all spectra were normalized to give the same total current at 1.7 V.



unlikely to be responsible for the locally-enhanced states observed in Figure 10.3. In contrast, we find that for the Si–O–Si and Si–OH defects, the agreement between the experimental and theoretical DOS is significantly better: the redistributions of the SiNC LDOS, resulting in enhanced occupied LDOS at the location of the corresponding defect (peaks  $H_1$  with local maxima  $H_1^*$  in Figures 10.4 and H9), are analogous to that found in the experimental LDOS for NC<sub>2</sub> (peak  $H_1$  with maxima  $H_1^*$  and  $H_1^{**}$  in Figure 10.3). Further, in both experimental and theoretical data, the highest occupied states are not completely localized at the defect locations, but persist over the whole NC surface (compare, for example, Figures 10.3f to 10.4g and 10.9g). The unoccupied states in the theoretical LDOS remain relatively uniform across the NC surface, which is also consistent with the unoccupied states in the experimental LDOS of NC<sub>2</sub> (compare, for example, Figures 10.3g-j to 10.4h,j and H9h,i). The unoccupied states in the theoretical LDOS are not significantly modified as compared to a completely hydrogen-passivated SiNC (Figure H8, H16 and H17), except for some band splitting in  $E_2$  (Figures 10.4b and H9b), which is more noticeable for Si–O–Si, a consequence of a stronger geometric perturbation resulting from this type of defect.<sup>31</sup> In addition, in the case of Si–O–Si, this splitting produces an orbital  $E^*$  concentrated around the defect (Figure 10.4i). This orbital, however, is not resolved in the experimental LDOS, which is likely due to the electron-vibrational band broadening effect discussed above. Significantly, the trends found for the localization parameter  $\zeta$  in Figures 10.4 and H9 are similar to those found in Figure 10.3 (we note that we do not expect the theoretical and experimental values of  $\zeta$  to be in precise quantitative agreement since the corresponding NC structures and surfaces used for calculation of  $\zeta$  are different). The close qualitative similarities between the



theoretical and experimental LDOS suggest that the defects of the type corresponding to peaks  $H_1^*$  and  $H_1^{**}$  in Figure 10.3b may be associated with either Si–OH or Si–O–Si defects (the latter is more likely, as mentioned earlier).

Defects of the type found for  $NC_2$  were observed only on SiNCs with relatively small diameters (less than  $\sim 2.5$  nm). In contrast, nominally “defect-free” SiNCs (with electronic states delocalized) similarly to those found for  $NC_1$  were typically larger. The lack of clearly identifiable defects on larger SiNCs does not mean that these SiNCs were entirely defect-free: our calculations show that the impact of elementary defects on the spatial LDOS patterns of such SiNCs is minimal and nearly nonexistent (for states close to the electronic bandgap) for sufficiently large SiNCs (Figure H18), which suggests that the LDOS in Figure 10.1 may be spatially modulated by defects, even though the presence of such defects could not be unequivocally established from our measurements.

## 10.5. Conclusions

Spatial mapping of the LDOS of individual SiNCs and theoretical calculations reported in this chapter show that oxidative defects spatially modulate the LDOS on SiNC surfaces producing LDOS patterns of varied degrees of inhomogeneity that depend on the NC size. For sufficiently small SiNCs, locally-enhanced LDOS attributable to either Si–OH or Si–O–Si defects are observed in LDOS mapping and reproduced in theoretical calculations. In contrast, spatial LDOS distributions (and, consequently, the photophysical properties) of larger SiNCs are relatively insensitive to the presence of such defects. The present work was carried out using an ultra-stable closed-cycle cryogenic STM system,<sup>43</sup> which uniquely enables detailed STS mapping of statistically-significant quantities of individual NCs. We anticipate that further STS studies of NCs

using our approach will contribute to building a more complete picture of the diverse types of defect states, in particular dangling bond defects, which are known to significantly affect the photophysical processes in SiNCs.<sup>53, 54</sup>

## **10.6. Bridge to Chapter XI**

In the next chapter we will broaden our study of individual point defects on the surface of SiNC by including defects caused by dehydrogenation of SiNC's passivation shell. We will experimentally study, for the first time, the process of DB-creation in individual SiNCs, and the impact of DBs on the SiNC electronic structure. DBs are created by injecting electrons into individual SiNCs, which results in gradual dehydrogenation of SiNC surfaces. We will monitor the changes in surface structure by using STS, which shows that dehydrogenation leads to shrinking of the electronic bandgap, and eventually produces midgap electronic states corresponding to DB effects. We will further find that DBs can exist in different charge states. These findings provide a first direct visualization of possible scenarios for defect generation in SiNC-based optical and opto-electronic applications, where photo-generated charge carriers with sufficient energies could induce creation of DB defects.

# CHAPTER XI

## VISUALIZATION AND SPECTROSCOPY OF DEFECTS INDUCED BY DEHYDROGENATION IN INDIVIDUAL SILICON NANOCRYSTALS

This chapter by Dmitry A. Kislitsyn, Jon M. Mills, Vancho Kocevski, Sheng-Kuei Chiu, William J. I. DeBenedetti, Christian F. Gervasi, Benjamin N. Taber, Ariel E. Rosenfield, Olle Eriksson, Ján Ruzs, Andrea M. Goforth, and George V. Nazin has been previously published under the same title in *The Journal of Chemical Physics* **144**, 241102 (2016). Copyright © 2016 AIP Publishing LLC.

### 11.1. Introduction

We present results of a scanning tunneling spectroscopy (STS) study of the impact of dehydrogenation on the electronic structures of hydrogen-passivated silicon nanocrystals (SiNCs) supported on the Au(111) surface. Gradual dehydrogenation is achieved by injecting high-energy electrons into individual SiNCs, which results, initially, in reduction of the electronic bandgap, and eventually produces midgap electronic states. We use theoretical calculations to show that the STS spectra of midgap states are consistent with the presence of silicon dangling bonds, which are found in different charge states. Our calculations also suggest that the observed initial reduction of the electronic bandgap is attributable to the SiNC surface reconstruction induced by conversion of surface dihydrides to monohydrides due to hydrogen desorption. Our

results thus provide the first visualization of the SiNC electronic structure evolution induced by dehydrogenation, and provide direct evidence for the existence of diverse dangling bond states on the SiNC surfaces.

## 11.2. Background

Silicon nanocrystals (SiNCs) have recently attracted a great deal of attention as a promising photophysical material with applications in photovoltaics,<sup>1-4</sup> light-emitting devices,<sup>5, 6</sup> and biological tagging.<sup>7, 8</sup> SiNCs offer the advantages of low toxicity and robust surface passivation involving, for example, formation of covalent Si-C bonds.<sup>9, 10</sup> Importantly, the optical properties of SiNCs are strongly dependent on their dimensions, with a dramatic brightening of radiative transitions observed for sufficiently small SiNCs,<sup>11-14</sup> a consequence of changes in the electronic structure leading to the relaxation of the momentum conservation rules known to suppress radiative transitions in bulk silicon.<sup>15-17</sup> While the ultra-small size of SiNCs is essential for optical applications, the resulting large surface to volume ratio means that SiNCs are very susceptible to their chemical environment and the presence of defects on their surfaces.

A wide variety of approaches for controlling the SiNC surface chemistry have been developed, including passivation with organic molecules<sup>18-20</sup> as well as oxidation.<sup>21-23</sup> One of the most common defects found at SiNC surfaces, regardless of the surface passivation technique, is the silicon dangling bond (DB). For example, DBs exist at Si-SiO<sub>2</sub> interfaces<sup>24, 25</sup> and at the surfaces of alkyl-passivated SiNCs.<sup>26</sup> DBs can also be produced by mild oxidation of hydrogenated SiNCs,<sup>27</sup> and by exposure to ultra-violet radiation.<sup>28, 29</sup> DBs are known to act as non-radiative recombination centers leading to de-excitation of electronically excited states.<sup>30</sup> In contrast, charged DBs have been found to

serve as radiative recombination centers in SiNCs with sufficiently large gap energies.<sup>31</sup> Further, depending on their charge and local stress, DBs at the surface of oxidized SiNCs were predicted to be capable of inducing intermittency in the SiNC photoluminescence.<sup>32</sup> However, the varied impact of the different DB charge states on the SiNC photophysics, especially in the context of the different possible surface passivations, remains to be fully addressed.

While the DB-induced electronic states in SiNCs have received a great deal of attention,<sup>33,34</sup> conventional experimental techniques are often limited to ensemble-level measurements, where the variations in DBs structures and local environments are averaged out.<sup>32</sup> A promising approach for addressing individual defects on SiNC surfaces is scanning tunneling microscopy (STM), which has proven to be uniquely suited for studies of individual DBs on silicon single-crystal surfaces.<sup>35-38</sup> Further, STM enables scanning tunneling spectroscopy (STS),<sup>39</sup> a technique that has been used to visualize the electronic structures of individual DBs,<sup>36</sup> as well as complex structures composed of many DBs.<sup>38,40-42</sup> However, until now, no STM/STS results describing DBs on SiNC surfaces have been reported, even though STS has been used to study quantum-confined,<sup>43</sup> as well as defect-induced,<sup>44</sup> electronic states in individual SiNCs.

### **11.3. Experimental details**

Using previously published protocols,<sup>44</sup> experiments were performed in a home-built ultra-high vacuum (UHV) cryogenic (closed-cycle cryostat-based) STM system.<sup>45</sup> A Au(111)/mica substrate was prepared in situ using multiple neon sputter/anneal cycles. Hydrogen-passivated SiNCs were fabricated using a protocol described previously.<sup>46</sup> The SiNCs were suspended in pentane, and using a solenoid pulse-valve were deposited onto

the Au(111) surface in high-vacuum conditions, parameters were chosen so as to obtain monolayer NC coverage. The SiNC covered Au(111) substrate was subsequently annealed overnight in UHV at  $\sim 50$  °C to remove any residual pentane from the sample surface. All STM topographies and STS measurements were obtained at a temperature of  $\sim 20$  K using silver tips prepared by electrochemical etching and subsequent sputtering in UHV. All STS spectra were recorded using the lock-in technique at 570 Hz and bias modulations varying from 10 (individual spectra and 1-D spatial scans) to 50 mV (2-D DOS maps). Thermal drift has to be carefully monitored during the STS measurements in order to maintain tip-sample spatial registry. Typical lateral drift values during the reported STS measurements were  $<0.2$  Å for single-point spectra,  $\sim 1.7$  Å for 1-D STS maps, and  $\sim 2.7$  Å for 2-D maps (the numbers are different due to the different acquisition times used for each type of measurement). While displacements during single-point STS were negligible, locations of individual data points in STS maps were drift-corrected by using an appropriate constant drift rate for each measurement (as determined from STM imaging). To ensure constant drift rates, the piezo creep associated with spatial repositioning was minimized by allowing the STM piezos to equilibrate for more than  $\sim 15$  hours, after which the drift rates were found to be nearly constant within the time frame required for acquisition of a STS map.<sup>45</sup> Theoretical calculations were performed using DFT, as implemented in the pseudo-potential package SIESTA,<sup>47, 48</sup> employing local density approximation (LDA) exchange, as described previously,<sup>49</sup> which, for hydrogenated SiNCs smaller than 4 nm in diameter, provides a good approximation of electronic bandgaps.<sup>16</sup>

#### 11.4. Results and discussion

In this chapter we describe spatially-resolved STS mapping of charged and neutral DB defects created by current-induced dehydrogenation of individual hydrogen-terminated SiNCs. SiNCs were sprayed onto a Au(111) substrate held in high-vacuum conditions, and studied using an ultra-high vacuum (UHV) cryogenic scanning tunneling microscope (STM).<sup>45</sup> The deposited SiNCs formed a near-monolayer film on Au(111), with individual SiNCs appearing as protrusions with lateral dimensions of 2 to 4 nm, as shown in Fig. 11.1(a). To characterize the electronic structures of individual SiNCs, we recorded the differential tunneling conductance ( $dI/dV$ ) as a function of the applied bias voltage and location. Thus produced  $dI/dV$  (STS) spectra are interpreted as energy-dependent local density of states (LDOS) spectra with the bias voltage giving the energy scale. Thirty individual SiNCs were studied in this fashion, as detailed in the following for one representative SiNC [Fig. 11.1(b)].

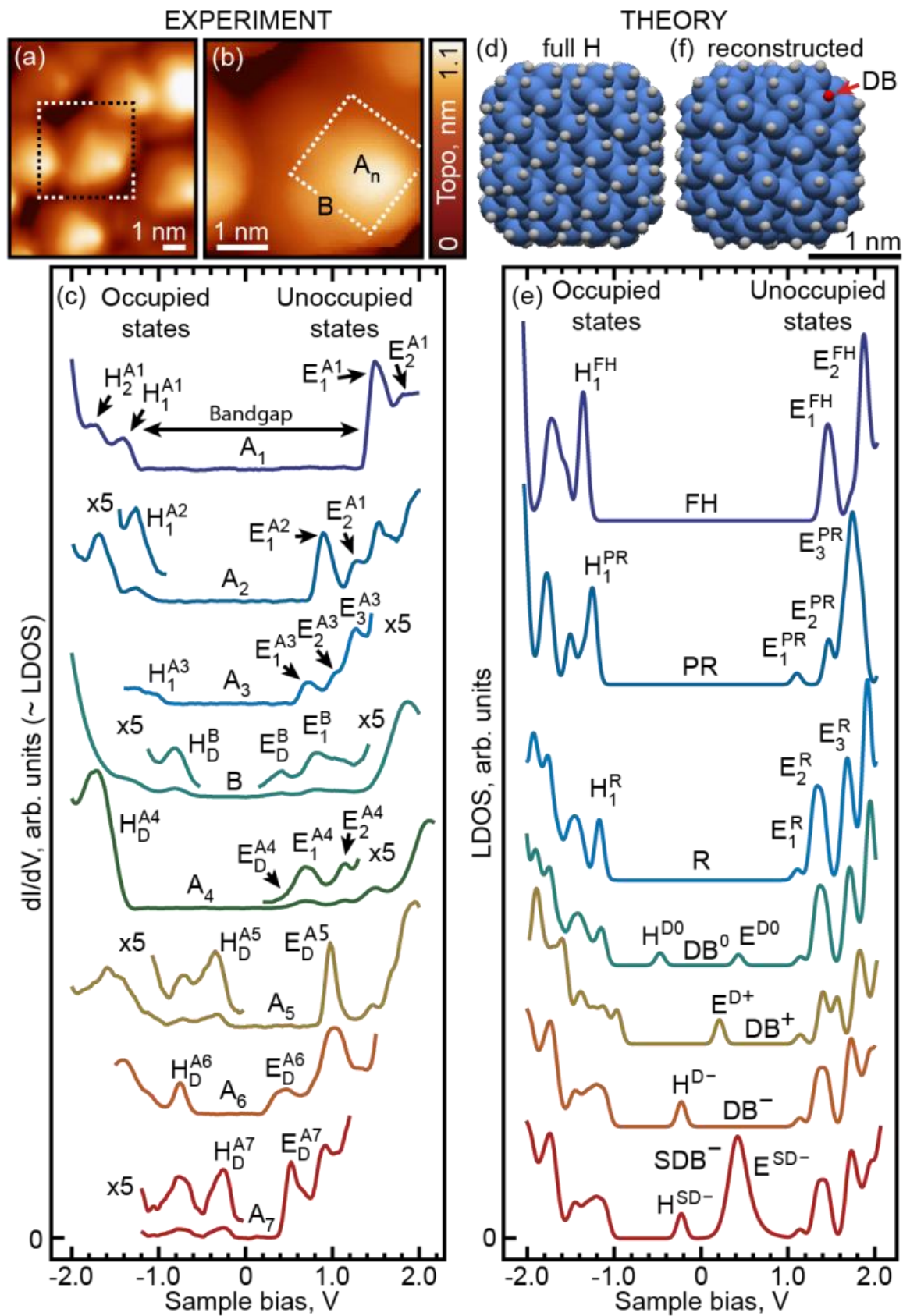
STM-induced dehydrogenation of single-crystal silicon surfaces has been studied in detail in the past two decades, with significant insights achieved into the physical mechanisms of hydrogen desorption<sup>50</sup> and the electronic structures of dehydrogenated areas.<sup>51, 52</sup> Generally, elevated bias voltages are required, with the exact magnitude of the bias voltage and tunneling current strongly affecting the mode of desorption, which can involve either direct electronic or multiple-vibrational excitation of the Si-H bond via tunneling electrons.<sup>53</sup> This process is thus referred to as electron-stimulated desorption (ESD).<sup>54</sup> Depending on the chosen parameters of the voltage pulse, hydrogen desorption can either occur one atom at a time, or involve several atoms.<sup>55</sup> In our experiments, in order to induce desorption of hydrogen, we applied voltages in the range of  $\sim 2.5 - 3$  V,

chosen to be sufficiently low to prevent extensive changes to the SiNC surfaces. For single-crystal silicon surfaces, the desorption of hydrogen at such bias voltages was previously attributed to multiple vibrational excitation via electrons tunneling through the  $\sigma^*$  (Si-H) unoccupied orbital.<sup>50, 53, 56</sup>

---

**FIG. 11.1.** STM/STS characterization and theoretical modeling of SiNCs. (a) Topography of an area showing several SiNCs. (b) Enlarged topography corresponding to the dashed square in (a). (c) STS spectra measured at locations A and B marked in (b). Curves A<sub>1</sub> through A<sub>7</sub> show transformations of the LDOS spectra in location A with successive application of bias voltage pulses (see text for details). States marked 'H' and 'E' correspond to occupied and unoccupied states, respectively, except for features caused by “reverse” tunneling, as described in the text. Spectra are offset for clarity. (d) Model of fully hydrogen-passivated SiNC (composition H<sub>172</sub>Si<sub>239</sub>). (e) Theoretical LDOS spectra averaged over the entire NC surface. Spectra FH and R correspond to the fully hydrogen-passivated SiNC in (d), and to the completely reconstructed SiNC in (f), respectively. Spectrum PR corresponds to a partially reconstructed version of SiNC from (d), with 33% of dihydrides converted to monohydride dimers. DB<sup>0</sup>, DB<sup>+</sup>, and DB<sup>-</sup> are spectra of the completely reconstructed model with an additional DB and charges 0, +*e*, and - *e*, correspondingly. Spectrum SDB<sup>-</sup> illustrates the effect of “bipolar” tunneling on STS of electronic states with LDOS described by curve DB<sup>-</sup>. Spectra were Gaussian-broadened by 100 mV, with onsets corresponding to the discrete energy levels obtained from DFT calculations. All spectra were modeled assuming a finite bias voltage drop inside the SiNC (see text). (f) Model of a monohydride-passivated SiNC (composition H<sub>100</sub>Si<sub>239</sub>) with 2×1:H surface reconstruction, and silicon core identical to that of (d). Location of the DB is also indicated. For further details of the measurements including spatial drift estimates, see Supporting Information in Appendix I.





Before ESD was induced by STM, LDOS spectra measured at different locations of “pristine” SiNCs showed progressions of electronic states with electronic bandgaps closely matching those predicted by theoretical calculations.<sup>44</sup> For example, in the case of the chosen representative SiNC from Fig. 11.1(b), the apparent bandgap of ~2.5 eV was found, formed by an occupied state  $H_1^{A1}$  and an unoccupied state  $E_1^{A1}$  in curve A<sub>1</sub> of Fig. 11.1(c) [we define the bandgap as the voltage difference between the onsets of conduction]. This bandgap value is expected to be larger than the real bandgap due to the finite bias voltage drop inside the NC: in a biased tunnel junction involving a NC, a finite voltage drop occurs across the NC volume shifting the energy of all electronic states by  $\alpha eV_B$  (where  $V_B$  is the bias voltage, and  $\alpha < 1$  is a function of the NC dimensions and dielectric susceptibility). This means that the voltage corresponding to the onset of tunneling for a state with energy  $E_S$  (this energy is measured with respect to the Fermi level of the sample, and can be positive or negative) can be then calculated as  $E_S/(1 - \alpha)$ .<sup>57, 58</sup> Here, we roughly estimate  $\alpha$  to be ~0.2 (as explained further in the Supporting Information in Appendix I, Fig. I1-I2), which gives a real bandgap of  $2.5 \text{ eV} \times 0.8 = 2 \text{ eV}$ . This value is consistent with that obtained from density functional theory calculations,<sup>49</sup> as illustrated by the LDOS spectrum FH in Fig. 11.1(e),<sup>16</sup> calculated (taking into account the finite value of  $\alpha$ ) for a model hydrogen-passivated SiNC shown in Fig. 11.1(d). (The diameter of this SiNC is ~2.2 nm, which matches that extracted from Fig. 11.1(b) after correcting for the tip convolution effects, as explained in Ref. 44.) Our calculations show that each one of the LDOS peaks is comprised of several quantum-confined electronic states formed from Bloch states associated with different electronic valleys in the Brillouin zone of bulk silicon.<sup>16, 17, 44</sup> Due to their close energy spacing,

these states are not completely resolved in our LDOS spectra, where electronic peaks are significantly broadened (typical peak width of ~200 mV) by coupling of tunneling electrons to vibrational excitations.<sup>59</sup>

For each “pristine” SiNC, after recording LDOS spectra at several representative locations, we attempted to induce ESD by applying higher bias voltages (2.5 - 3 V), and quantified the results at each step by detailed mapping of LDOS in order to establish the presence of DBs. For the SiNC from Fig. 11.1(b), application of higher bias voltages resulted in formation of new peaks  $H_n^{A2}$  and  $E_n^{A2}$  [curve A<sub>2</sub> of Fig. 11.1(c)], and a notable reduction in the apparent bandgap. Importantly, peaks  $H_n^{A2}$  and  $E_n^{A2}$  are delocalized over the entire SiNC surface (Fig. I3) suggesting that they do not correspond to localized defects. This behaviour can be explained by reconstruction of the SiNC surface induced by the hydrogen desorption. Specifically, while a significant portion of Si surface atoms in the as-synthesized SiNCs are passivated with dihydride groups (Fig. I4), hydrogen desorption from neighbouring SiH<sub>2</sub> can lead to their dimerization analogous to the 2×1:H reconstruction observed on the Si(100) surfaces [see Fig. 11.1(f) for a model of a fully reconstructed monohydride-only SiNC with the same Si core as in Fig. 11.1(e)]. The DBs at the neighbouring Si atoms form  $\pi$ -electronic bonds producing delocalized states with an electronic bandgap reduced by an amount dependent on the extent of surface reconstruction, as shown by curves PR and R in Fig. 11.1(e) for the partially- and fully reconstructed models of the SiNC. Indeed, curve A<sub>2</sub> of Fig. 11.1(c) likely corresponds to a partially reconstructed SiNC because further ESD pulses on this SiNC resulted in additional reduction of the bandgap [curve A<sub>3</sub> of Fig. 11.1(c)], with electronic peaks  $H_n^{A3}$  and  $E_n^{A3}$  delocalized across the SiNC surface (Fig. 11.2).

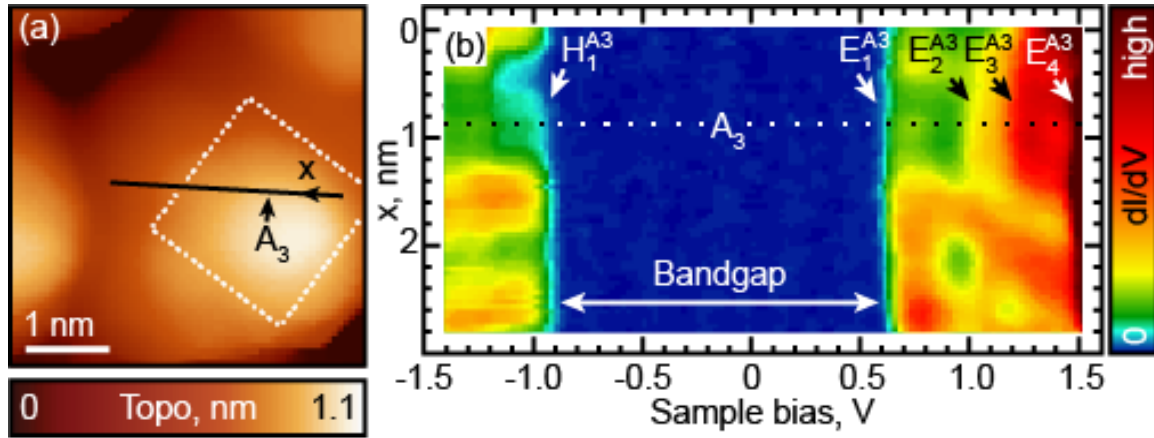


**FIG. 11.2.** Spatial mapping of LDOS for the SiNC from Fig. 11.1(b) after (partial) dehydrogenation, but before DBs were generated. (a) Topography of the SiNC. (b) LDOS as a function of the bias voltage and position  $x$  along the path (solid line) shown in (a).

With additional ESD pulses, however, spatially localized midgap LDOS features, attributable to defects, appear on the SiNC surface, with three representative examples demonstrated by curves B,  $A_4$  and  $A_5$  in Fig. 11.1(c). Specifically, curves B and  $A_5$  show pairs of midgap peaks ( $H_D^B$  and  $E_D^B$ , as well as  $H_D^{A5}$  and  $E_D^{A5}$ , respectively), while curve  $A_4$  shows only one midgap peak  $E_D^{A4}$ . Intriguingly, we found that inter-conversion between the different defect types was possible. In particular, defects B and  $A_4$  in Fig 1(c) could be spontaneously converted to defects of type  $A_5$  under typical tunneling conditions (bias voltage  $\sim 2$  V). For example, curve  $A_5$  was recorded at the same location as  $A_4$  immediately after a positive bias voltage of 2.4 V was applied. Further transformation could be induced by applying voltages of  $\sim -1.5$  V with the resulting LDOS spectrum corresponding to curve  $A_6$ , which is very similar to that of defect B measured earlier at location B [Fig. 11.1(b), and curve B in Fig. 11.1(c)]. Finally, the local spectrum at location A was converted from  $A_6$  to  $A_7$  [Fig. 11.1(c)] showing a shape qualitatively

similar to that of  $A_5$  (the origin of peak shifts in curve  $A_7$  versus  $A_5$  is explained in the following).

The spectral characteristics of the observed midgap states, as well as the possibility for their inter-conversion, can be explained in the most straightforward manner by attributing these midgap states to DB defects, as discussed further below. Some of the described peaks, however, are produced by different tunneling processes rather than distinctly different electronic states, as can be seen from the dramatically different spatial behaviours of these peaks. For example, for curve  $A_7$  in Fig. 11.1(c), peak  $E_D^{A7}$  shows substantial onset voltage variations across the NC, while peak  $H_D^{A7}$  and other unoccupied states appear at nearly the same voltages in all locations, as illustrated in Fig. 11.3(b). This is despite the fact that peaks  $E_D^{A7}$  and  $H_D^{A7}$  are closely co-localized in the vicinity of location A [Fig. 11.1(b)], as shown by LDOS maps of Fig. 11.3(b) and Fig 3(d)-(e), and should therefore correspond to the same defect. The described asymmetry in onset voltage variations are analogous to those reported for the “bipolar” tunneling investigated previously for a variety of molecular systems.<sup>57, 58, 60</sup> Bipolar tunneling is a consequence of the fact that in a biased tunnel junction involving a NC, a finite voltage drop occurs across the NC volume, which, in addition to the “direct” type of tunneling described earlier [Fig. 11(a)] with the onset voltage of  $E_S/(1 - \alpha)$ , also leads to “reverse” tunneling [Fig. 11(b)] with the onset voltage of  $-E_S/\alpha$  (where  $E_S$  and  $\alpha$  were defined previously).<sup>57, 58</sup> Voltage onsets for both “direct” and “reverse” tunneling (at opposite bias polarities) vary with tip position on the NC surface due to the sensitivity of  $\alpha$  to the geometry of the junction,<sup>57</sup> as shown in Fig. 12. Nevertheless, because  $\alpha$  is typically small [ $\alpha \approx 0.2$  for peaks  $E_D^{A7}$  and  $H_D^{A7}$ ], expression  $E_S/(1 - \alpha)$  varies significantly less

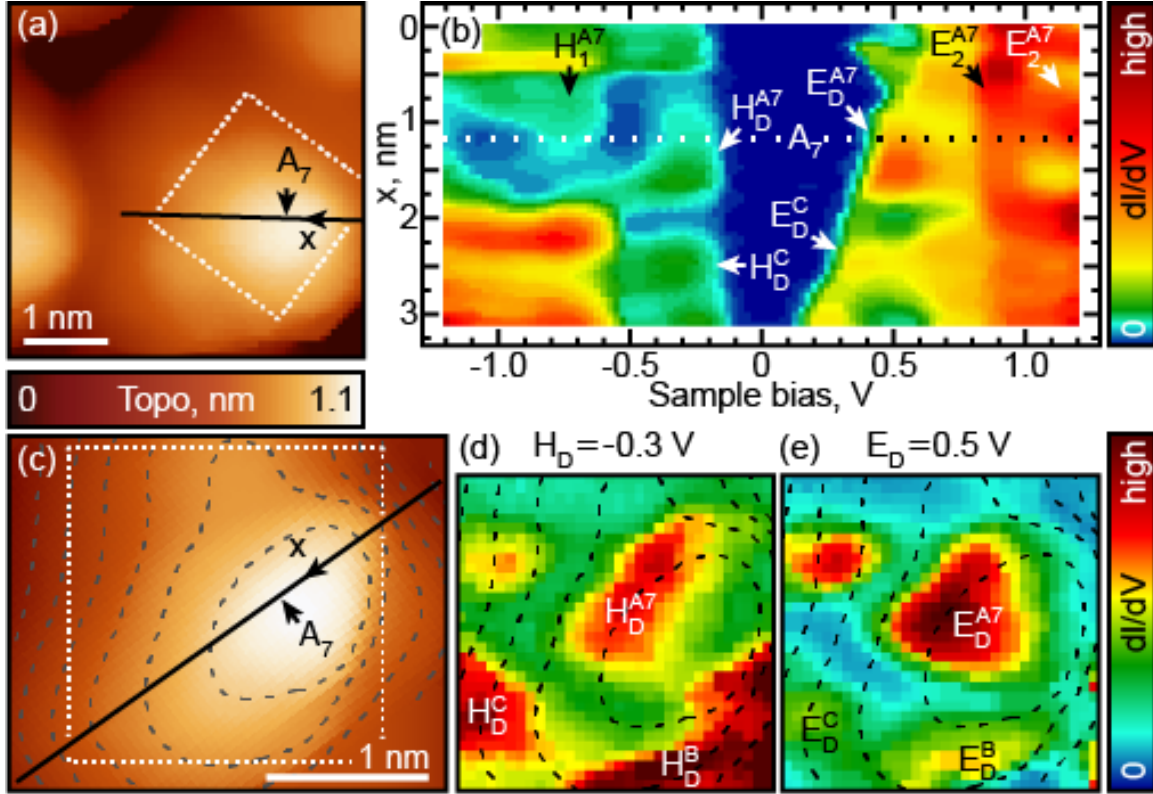


**FIG. 11.3.** Spatial mapping of LDOS for the SiNC from Fig. 11.1(b) after DBs were generated. (a,c) STM topographic images of the SiNC. (b) LDOS as a function of the bias voltage and position  $x$  along the path (solid line) shown in (a,c). (d,e) 2-D LDOS maps for voltages corresponding to  $H_D$ ,  $E_D$  LDOS peaks marked in (b). Mapping area corresponds to the dotted squares in (a,c). Dashed lines are topographic contours from (c).

than  $E_S/\alpha$ , which explains the differences in the onset voltage variations for peaks  $E_D^{A7}$  and  $H_D^{A7}$  in Fig. 11.3(b). In addition, the spectral lineshapes of the two types of bipolar peaks are affected by the asymmetry in the tip-NC and NC-substrate tunneling rates (the former is lower than the latter), which tends to produce notably more intense and sharper peaks at the onset of conduction for the “reverse” tunneling process.<sup>57, 61</sup> This is indeed observed for peak  $E_D^{A7}$ , which, together with its spatial voltage onset variations, suggests

that this peak corresponds to the “reverse” tunneling process, while peak  $H_D^{A7}$  corresponds to “direct” tunneling. The effect of “bipolar” tunneling on the dI/dV curves is illustrated by curve  $SDB^-$  in Fig. 11.1(e) [obtained from curve  $DB^-$  by assuming  $\alpha \approx 0.2$ , and a finite rate for tunneling between SiNC and substrate], where peaks  $E_D^{SD^-}$  and  $H_D^{SD^-}$  correspond to the “reverse” and “direct” tunneling processes, respectively, analogously to peaks  $E_D^{A7}$  and  $H_D^{A7}$  (we note that the overtone structures of peaks  $E_D^{A7}$  and  $H_D^{A7}$  were not included in the modelling).

Analysis similar to that presented above for peaks  $E_D^{A7}$  and  $H_D^{A7}$ , when applied to the rest of the spectra in Fig. 11.1(c), suggests that peaks  $E_D^B$ ,  $E_D^{A4}$ ,  $H_D^{A5}$ ,  $E_D^{A6}$  and  $H_D^{A7}$  are all produced by “direct” tunneling, while peaks  $H_D^B$ ,  $H_D^{A4}$ ,  $E_D^{A5}$ ,  $H_D^{A6}$  and  $E_D^{A7}$  should correspond to “reverse” tunneling. This assignment results in a clear distinction between curves B, A<sub>4</sub>, A<sub>6</sub> versus the curves A<sub>5</sub> and A<sub>7</sub>: while only unoccupied midgap states are distinguishable in curves B, A<sub>4</sub>, and A<sub>6</sub>, in curves A<sub>5</sub> and A<sub>7</sub>, only occupied midgap states are clearly observable. This assignment offers an explanation for the inter-conversion between the different types of spectra in Fig. 11.1(c). For example, the transitions from spectrum A<sub>4</sub> to spectrum A<sub>5</sub>, and spectrum A<sub>6</sub> to spectrum A<sub>7</sub> were induced with positive voltages (this corresponds to electrons being added to the SiNC), and resulted in disappearance of unoccupied midgap states  $E_D^{A4}$  and  $E_D^{A6}$ , as well as appearance of occupied midgap states  $H_D^{A5}$  and  $H_D^{A7}$ . Similar spectral transformations in individual atoms<sup>62</sup> and molecules<sup>63</sup> have been attributed to electron trapping. This suggests that individual electrons are likely being trapped in states  $E_D^{A4}$  and  $E_D^{A6}$ , which results in appearance of trap states  $H_D^{A5}$  and  $H_D^{A7}$ . On the other hand, transition from A<sub>5</sub> to A<sub>6</sub> occurred when negative voltage was applied, and the corresponding spectral changes may

be attributed to extraction of an electron from state  $H_D^{A5}$ , which is thereby converted to state  $E_D^{A6}$ , similarly to the de-trapping process described for molecules.<sup>63</sup>

The local charging of SiNC described above is consistent with the presence of DBs, which have been shown to exist in different charge states on silicon surfaces,<sup>36, 38, 64</sup> and is also consistent with the expectation that desorption of hydrogen atoms should lead to the creation of DBs. In addition, DBs appear deep in the silicon electronic bandgap, similarly to the states appearing near zero bias in Fig. 11.1(c). This similarity is illustrated by the theoretically calculated LDOS for DBs in different charge states on the surfaces of model SiNCs [curves  $DB^0$ ,  $DB^+$ , and  $DB^-$  in Fig. 11.1(e)]. For example, curve  $A_4$  only shows an unoccupied midgap state, consistent with curve  $DB^+$ , while curve  $A_5$  only shows an occupied state, consistent with curve  $DB^-$ . Assignment of spectra B,  $A_6$  and  $A_7$  is less certain because the “reverse” tunneling LDOS features seen in these curves may be obscuring “direct” tunneling features that would be expected for the neutral DB (curve  $DB^0$ ). The similarity of spectra  $A_5$  and  $A_7$ , however, suggests that  $A_7$  may also be associated with  $DB^-$ . Curves B and  $A_6$  are relatively similar, and given their distinct spectral shapes, may be attributed to a neutral state, even though they may also be variants of  $A_4$  ( $DB^+$  state) corresponding to slightly different local surface structures. We note that similar spectral features attributable to charged and neutral DBs were found in other studied SiNCs (Fig. I5).

## 11.5. Conclusions

This chapter shows that when sufficiently high-energy electrons are injected into SiNCs, dramatic changes in the SiNC electronic structures are observed: gradual shrinking of the SiNC electronic bandgap occurs initially, and is eventually followed by



the appearance of localized states deep in the electronic bandgap. We find that these midgap states can exist in different inter-convertible charge configurations. These observations are consistent with the hypothesis that high-energy electron injection can lead to dehydrogenation of the SiNC surfaces, resulting in surface reconstruction driven by conversion of surface dihydride species to monohydride groups, and creation of dangling bonds in different charge states. These findings provide a direct visualization of possible scenarios for defect generation in SiNC-based optical and opto-electronic applications, where photo-generated charge carriers with sufficient energies could induce creation of surface defects.

# CHAPTER XII

## CONCLUSIONS AND PROSPECTS

### 12.1. Conclusions

This dissertation presents a new STM instrument with a number of state-of-the-art, as well as new and unique, features and its application to the studies of a variety of different physical and chemical phenomena at the single-molecule (nanoparticle) level.

STS spatial mapping was used to study electronic states in SWCNTs deposited on the Au(111) surface and to identify locations of the quantum-confined states within the nanotube. Localization of the states was, for the first time, experimentally shown to result in a pronounced sequence of vibronic features, originating from the enhancement of the electron-vibrational coupling. The vibrational overtones were assigned as D-band Kekulé vibrations and K-point transverse out-of plane phonon modes, suggesting rippling distortion and dimerization of carbon atoms on the SWCNT surface.

STM/STS was used to study alkyl-substituted quaterthiophenes adsorbed onto the  $22 \times \sqrt{3}$  reconstructed Au(111) surface. Molecules were found to form dimers linked by their alkyl substituents and adopt cis-conformations, which is unlike the trans-conformation found in the bulk. The LUMO electronic state energy was found to be affected not by the conformation, but by to the local differences in the Au(111) surface reactivity. At higher concentrations (but less than half of a sub-monolayer) the molecules assume trans-conformation and self-assemble into two dimensional quazi-crystals. At higher than half-monolayer concentrations, the molecules show a different type of the trans-conformation and different adsorption configuration on the Au(111) surface.

Differences in local molecular environments cause variations in molecular distributions. Significant electronic structure differences are discovered between molecules of different conformations, as well as, unexpectedly, between the molecules of identical adsorption configurations. This study revealed that interfacial oligothiophene conformations and electronic structures significantly deviate from those derived from the band structures of bulk crystals. In addition, a remarkable electronic disorder exists even in a well-ordered quazi-crystal system composed of molecules featuring conformational diversity, adsorbed on a metal surface.

STM topographic and spectroscopic mapping was used to investigate the electronic structure of alkyl-substituted seven- and eight-thiophenes featuring different cis/trans conformations and backbone distortions onto the  $22 \times \sqrt{3}$  reconstructed Au(111) surface. Oligothiophenes on Au(111) were discovered to self-assemble into chain-like structures, binding to each other via interdigitated alkyl ligands. Distinct planar conformations of the molecules are revealed using alkyl ligand mutual orientations and backbone shapes. STS mapping showed a progression of particle-in-a-box-like states corresponding to the LUMO, LUMO+1 and LUMO+2 orbitals for each molecule. Unoccupied molecular orbitals of different molecular conformations with significant geometrical distortions have very similar energies. Density functional theory calculations showed that the absence of variations in the molecular orbital energies among the different conformers suggests that the interaction of Au atoms and oligothiophene units affects molecular orbital energies equally for all studied conformations. One can conclude that cis/trans torsional disorder is not a significant source of electronic disorder,

and therefore does not affect the charge carrier trapping in oligothiophene-based organic semiconductor films.

STS was used to study annealed ligand-free lead sulfide nanocrystals supported on the Au(111) surface, and to visualize the progression of occupied and unoccupied electronic states near the bandgap. STS spatial mapping helped to identify delocalized quantum-confined states and localized sub-bandgap states. Maps of the sub-bandgap states revealed the presence of surface reconstructions, such as non-stoichiometric adatoms self-assembled on the quantum dot surfaces. The formation of surface-bound sub-bandgap electronic states was associated with the presence of surface reconstructions. The surface stoichiometry was found to be responsible for the surface reconstruction type: lead-rich surfaces are associated with unoccupied sub-bandgap states, while sulfur-rich areas are associated with occupied sub-bandgap states. In addition, highly off-stoichiometric areas were found that produce both occupied and unoccupied states resulting in dramatically reduced bandgaps. The STM/STS study helped to create a model which sheds light onto the microscopic mechanisms of surface state formation. These findings will be applicable, in a modified form, to the more general case of ligand-passivated nanocrystals, where under-coordinated surface atoms can also be produced by the steric repulsion between passivating ligand molecules.

STS was used to study hydrogen-passivated silicon nanocrystals (SiNCs) supported on the Au(111) surface and to find the effects of surface chemical defects, produced by oxidation in ambient conditions, on the electronic structure of SiNCs. STS spatial maps revealed quasi-localized defect-induced states, as well as quantum-confined states delocalized throughout the SiNC volume. We supported the STM study with

theoretical calculations and found that the LDOS spectra associated with the observed defects are attributable to Si–O–Si bridged oxygen or Si–OH surface defects. These findings clarify the mechanisms responsible for early stages of SiNCs oxidation and the roles of these defects in SiNC photophysics.

STS was implemented to investigate the influence of dehydrogenation on the electronic structures of SiNCs supported on the Au(111) surface. Injection of high-energy tunneling electrons into individual SiNCs first results in gradual dehydrogenation and reduction of the electronic bandgap, and then produces electronic states deep in the bandgap. Theoretical calculations support the STS findings and help to attribute midgap states to silicon dangling bond defects, which can be neutral or acquire an elementary charge of either polarity. The calculations attribute the observed initial shrinking of the electronic bandgap to SiNC surface reconstruction caused by the conversion of surface dihydrides to monohydrides with hydrogen liberation. This study provided the first real-space visualization of changes in the SiNC electronic structure due to dehydrogenation. In addition, direct evidence for the existence of inter-converting charged dangling bonds on the SiNC surfaces was established.

The presented studies demonstrate how the unique capabilities of the STM-UO helped to obtain new knowledge that enhances the understanding of the properties of three classes of novel materials. The high spatial stability and extended operating time of the STM-UO opened new prospects in the research of carbon nanotubes, organic oligothiophenes and colloidal nanocrystals.

## 12.2. Prospects for future research

The STM-UO system was the first in the world to overcome both time and cost limits for cryogenic exploration of materials on the nanoscale. Further utilization of the STM-UO advantages will open even more exciting opportunities to investigate quantum properties and obtain deeper and complementary information by extending STM-UO instrumental techniques.

The first technique available for implementation is measuring the second derivative of the tunneling current, which requires extraordinary STM stability and noise cancelation ability. The second derivative spectra were shown to be equivalent to the inelastic electron scattering spectroscopy (IETS) and allow STM to measure molecular vibrations that provide the spectroscopic fingerprints to identify the local chemical composition.<sup>1,2</sup> STM-IETS technique can benefit tremendously from STM-UO's stability and the ability to run long-term experiments. Extending to STM-IETS spatial mapping, by analogy with STS spatial mapping, can potentially provide an unprecedented level of detail of the physical mechanisms involved on the sub-molecular scale, and reveal a plethora of new phenomena, which will greatly improve our understanding of quantum chemistry in general and the properties of specific materials. Preliminary experiments showed that STM-UO system is capable of measuring second and higher tunneling current derivatives, but hardware problems with the electronics were discovered, which resulted in the presence of artifacts in addition to real features in the spectra, thus preventing immediate wide use of the technique. However, these problems are not of a fundamental nature and can be overcome in the near future.

The second highly anticipated technique is based on combining electronic measurements of STM with capabilities of optical near-field scanning probe microscopy. The hardware of STM-UO system was conceived and designed with built-in extensibility to provide efficient optical access to the tunneling junction, as well as the capability to collect photons originating from the junction with very high efficiency. This can be achieved by incorporating a parabolic mirror inside of the STM scanner head, surrounding the tunneling junction, and providing record-high photon collection (35%).<sup>3</sup>

Injected tunneling electrons undergo a series of transitions in the sample, jumping to lower energy levels and eventually ending at the Fermi level of the metallic substrate. Some of the transitions go through radiative channels. As the energy of the electron injection is controlled by the tip-substrate bias voltage, emitted photons could thus provide spectroscopic information about the local electronic levels of the sample. This type of experiment is referred to as Scanning Tunneling Luminescence (STL). The task of collecting these photons is rather challenging in the case of UHV, cryogenic temperatures and STM geometry. It could be achieved by different methods: lens optics or a collection mirror either outside or inside of the vacuum chamber. A parabolic mirror inside of the STM will provide us with the highest photon collection efficiency, which leads to the best sensitivity. We expect significant improvements in the data acquisition rate and spectroscopic quality as compared to the existing instruments: for example, Chen et al. recently showed remarkable success even using less-effective photon collection by a lens mounted inside of the UHV chamber. They were able to reveal details about the vibronic coupling and broken degeneracy of the molecular orbitals and visualize intrinsic emission properties with submolecular resolution.<sup>4</sup>

We proposed two principal techniques for STL experiments. First is approaching the tip to a separately placed molecule. This will allow us to obtain intramolecular information about the molecule orbitals and vibrational properties.<sup>5,6</sup> Another experiment is studying spatially extended molecular complexes or closely situated molecules. This study will make it possible to investigate charge and energy transfer processes between molecules. This approach requires control of the relative alignment of the LUMO and HOMO states in order to conduct the experiment and interpret the results.

The disadvantage of these photon emission experiments is that high energy electrons inevitably disturb the environment and the molecule under investigation. For this reason, we plan to take advantage of the optical capabilities of the STM-UO and conduct less disturbing experiments. These experiments will also help to obtain a more universal picture less dependent on the conditions of a particular STM experiment (such as state and geometry of the end of the tip and the surface, position and orientation of the molecule, rehybridization of molecular orbitals due to the interaction with the substrate, etc.).

The first type of experiment requires special arrangements to create the most efficient conditions for the excitation of the plasmon resonances under the tip, which include usage of silver tips and substrates and special precautions to achieve atomically sharp tips and an atomically clean, well-defined surface. This single molecule absorption experiment is analogous to the usual optical absorption spectroscopy but with subdiffractional resolution. In this technique, inelastic electron tunneling between the tip and substrate excites local plasmon modes, which emit characteristic broad-band spectra (white-light).<sup>7-9</sup> Optical absorption transitions of an individual molecule or a part of the



molecule which is placed close enough to the tunneling junction are observed as dips in the broad-band spectra of emission caused by quenching at wavelengths corresponding to molecular absorption.<sup>10</sup> High spatial localizations of tip-induced plasmon modes allow one to achieve spatial resolution on the order of a few nanometers.

An analogy can be drawn between this type of experiment and the Enhancement of the Förster Resonance Energy Transfer in the vicinity of a metal nanoparticle.<sup>11</sup> The sharp STM tip plays the role of a nanoparticle, emission out of inelastic electron tunneling replaces the emission of a donor molecule and the molecule under study serves as an acceptor molecule. Experiments have shown that the resonance energy transfer is effectively enhanced by the presence of plasmon modes of metallic surface.<sup>12</sup> A significant increase (21 times) for the rate constant of energy transfer caused by the presence of silver particle has been reported.<sup>13</sup> That makes us believe that efficient energy transfer to the molecule will effectively quench the emitted light at the molecule's resonant wavelengths, providing us with a high sensitivity signal.

An alternative approach consists of the optical excitation of the near-field under the tip with the help of external laser beam. STM with optical spectroscopy will have a geometry that provides pathways for the incident and reflected beams, as well as equipment for precise focusing of these. This technique is known as Tip-Enhanced Near-Field Optical Microscopy (TENOM), and single molecule studies with 10 nm spatial resolution have been reported.<sup>14</sup> One type of experiment is near-field optical photoluminescence of the adsorbed molecule that is caused by optical transitions following optical excitation of a higher state. Unwanted signal of the incident wave scattered by the substrate can be eliminated using appropriate bandpass filters. Another

type of experiment is tip-enhanced Raman spectroscopy (TERS), which is a well established technique that achieves single-molecule sensitivity.<sup>15-17</sup> Our approach is to combine the STM study of electronic properties with the TENOM performed on the same molecule. These complementary measurements will provide us with new, insightful information on the correlation of electronic and vibrational properties of the molecules. The remarkable advantage of our STM-OS in comparison to existing studies is the ability to use pristine silver tips and substrates such as silver known to provide the best enhancement factor for the TENOM signal. The usage of silver is usually restricted because of the fast silver surface degradation due to formation of oxides and sulfides in ambient conditions.

In the following section, advantages of STM-UO combined with Optical Spectroscopy (STM-UO-OS) will be illustrated in application to the system of single-walled carbon nanotubes (SWCNTs) deposited on the surface in sub-monolayer amount. This is a model system that will benefit tremendously from the new instrument and highlights the strengths of STM-UO-OS approach for studies of physical properties of materials on the single-molecular level.

### **12.3. Combined Scanning Tunneling an Optical Probe Microscopy and Spectroscopy in application to SWCNT research**

#### **Background**

Single walled carbon nanotubes (SWCNTs) are of a great fundamental interest as a physical realization of the one-dimensional electronic system.<sup>18</sup> SWCNTs properties are very tunable because they strongly depend on the molecule's internal symmetry, and this dependence is essentially non-monotonic. In addition, their properties can be efficiently

altered by controlled chemical functionalization.<sup>19,20</sup> This makes SWCNTs promising for technical applications, such as development of the intramolecular field-effect transistors (FET).<sup>21,22</sup>

SWCNTs can be obtained by rolling up a narrow ribbon of graphene into the seamless cylinders. The position of the ribbon on the graphene 2D lattice is determined by the chiral vector which can be expressed by two integers (n,m). Each specific pristine SWCNT is unambiguously defined by the chiral vector, or, equivalently, by the chiral angle  $\theta$  and the nanotube diameter  $d$ . The bonding  $\pi$  and the anti-bonding  $\pi^*$  orbitals of graphene give rise to  $N$  branches of SWCNT's one-dimensional valence and conduction bands ( $N$  – number of the atoms in the nanotube unit cell). These bands can be used for the calculation of the electronic density of states (DOS) of the SWCNT. The maxima and minima in the 1-D band structure give rise to singularities, where the DOS goes to infinity (Van Hove singularities (vHS)). The described procedure is useful for identifying whether a SWCNT is semiconducting or metallic. This is determined by the density of states at the Fermi level and depends entirely on the (n,m) index for the pristine SWCNT. In the simple free-particle picture, optical transitions in SWCNTs occur predominantly between these vHSs, due to the high transition probability arising from the large DOS of initial and final state.<sup>23,18</sup>

This free-particle model is supported by STM studies which were shown to be capable of measuring the DOS revealing the vHSs,<sup>24,25</sup> and they also show quantitative agreement with the experiment after taking into account rehybridization of the  $\sigma$  and  $\pi$  states due to the curvature of the nanotube wall.<sup>26</sup> SWCNT became a subject of intense research using Scanning Tunneling Microscopy and Spectroscopy, which addresses

issues of inhomogeneity and imperfections of the SWCNTs placed in real environment. These include study of carbon-nanotube heterojunctions (change of chirality along the nanotube due to defects),<sup>27</sup> charge transfer between nanotubes and their substrates,<sup>28</sup> STM-induced reversible defect engineering,<sup>29</sup> radial collapse into a flattened tube while adsorbed on the surface<sup>30</sup> and properties of chemically functionalized SWCNTs.<sup>31–33</sup> STM-UO can contribute to understanding of these and related problems, and acquire improved and novel results, because of the unlimited time operation and stability of the STM-UO and advantages of complementing STM with optical spectroscopy studies as explained below.

1-D electronic band picture is usually sufficient for the description of the SWCNTs electronic and optical experiments, though, for the case of such a sensitive instrument as STM, a more detailed description may be needed to interpret high spatial resolution experiments. Recently it has been shown that details of the molecular  $\pi$  orbitals related to the different vHSs can be resolved by mapping the changes of the vHSs intensities along the SWCNT circumference.<sup>34</sup> It will be insightful to correlate orbital distribution details to the high-resolution optical excitation data. A similar study performed on one-dimensional chains of silver atoms allowed for the first time the visualization of the fundamental Fermi's golden rule.<sup>35</sup>

Contrary to the 3-D case, the free-particle description needs to be changed dramatically in the case of one-dimensional system in order to describe the optical properties. This is due to the enhanced role of Coulomb interactions between the charge carriers, which result in two opposite contributions to the energy level. One result of this is band gap renormalization (BGR) that has its origin in the repulsive electron-electron

interaction, which typically increases the energy of the free-particle band gap.<sup>36</sup> Another important effect is the formation of the excitonic states with energies well below the free-particle band gap. The exciton binding energy in SWCNTs is orders of magnitude larger than in 3-D semiconductors, where  $E_{\text{bind}}$  is only several meV and excitons are not stable at room temperature.<sup>37,38</sup> Most of the transition oscillator strength is transferred from the free-particle to the lowest exciton state. Hence excitons dominate the optical properties. The energy of the lowest optically allowed state responsible for photoluminescence is then given by equation  $E_{\text{PL}}=E_{\text{fp}}+E_{\text{BGR}}-E_{\text{bind}}$ , where  $E_{\text{fp}}$  is the free-particle band gap energy in the absence of charge carrier interactions. The band gap renormalization  $E_{\text{BGR}}$  is in the order of  $E_{\text{fp}}$  with hundreds of meV.<sup>39</sup> The exciton binding energy  $E_{\text{bind}}$  corresponds to the lowest optically active exciton ("bright" exciton). Theory also predicts excitonic states that do not interact with light due to selection rules ("dark" excitons).  $E_{\text{bind}}$  is also in the range of several hundreds of meV, but usually smaller than  $E_{\text{BGR}}$ .<sup>40,41</sup> The two shifts compensate to a large extent, so that  $E_{\text{PL}}$  is still close to  $E_{\text{fp}}$ .

While optical experiments allow one to find resonances associated with excitons ( $E_{\text{fp}} + E_{\text{BGR}} - E_{\text{bind}}$ ), Scanning Tunneling Microscopy measures distances between peaks in electronic density of states which give values of electron bands energies ( $E_{\text{fp}} + E_{\text{BGR}}$ ). The difference of these two quantities determines the exciton binding energies  $E_{\text{bind}}$ .<sup>42</sup> Experimental determination of this difference using STM and optical measurements, performed on the same isolated SWCNT, will contribute significantly to the fundamental understanding of SWCNT properties.

## **Scanning Tunneling Luminescence**

Literature search does not reveal any STL studies performed on SWCNTs at the moment. There are two studies of STM-induced luminescence in multi-wall carbon nanotubes (MWCNT).<sup>43,44</sup> These two works are lacking spatial resolution of emission signal. They also drew contradictory conclusions on the nature of the observed photon emission. The former work by Coratger et al. relates the photon emission to the defects or end effects on MWCNTs, while the later work by Uemura et al. brings forward arguments in favor of emission due to radiative transitions of electrons between the one-dimensional vHs in the density of states of MWCNTs. We plan to elucidate this issue and conduct a systematic study of the STL correlation with the local electronic structure, influence of endcaps, kinks, defects and dopant atoms, as well as dependence on the surface on which SWCNT is supported and its proximity to other nanotubes. This will help establish STL as one of the most detailed techniques for nanotube characterization.

## **Near-field optical spectroscopy**

After the discovery that SWCNTs' optical absorption and emission properties are dominated by excitons, numerous studies were conducted to understand their behavior and to find ways to control their properties. Excitons have a small size ( $\sim 1-2\text{nm}$ ) and short coherence length ( $\sim 10\text{nm}$ ), they are highly mobile (they visit  $\sim 10^4$  carbon atoms during their lifetimes) and are remarkably sensitive to chemical derivatization or defects.<sup>45-48</sup> As a consequence, their motion can be described as 1-D diffusion with a diffusion constant of about  $0.4\text{cm}^2/\text{s}$ .

While diffraction-limited optical studies successfully reveal optical characteristics of the whole SWCNTs or their large segments,<sup>49,50</sup> it is appealing to investigate them on

the smaller scale. Several near-field optical studies using tip-enhancement of signal with Scanning Probe Microscope and external laser excitation have been presented in the recent years. These studies revealed details of the local variations in the exciton behavior caused by defects, chemisorbed atoms or end effects. Tip-enhanced photoluminescence (PL) achieved spatial resolution of 15nm and presented two types of excitonic local behavior: exciton quenching near ends and defects<sup>51,52</sup> and exciton localization due to exciton energy variations.<sup>53</sup> The presented studies could not reveal what kind of SWCNTs' local features causes each type of the exciton behavior. STM will allow us to conduct systematic studies of the correlation between SWCNTs' defects and impurities, and the exciton phenomena.

Another study was performed with the help of UHV STM at the room temperature.<sup>54</sup> It is based on detecting the tunneling current change due to the optical absorption of the incident laser excitation by the molecule under the tip. Subnanometer spatial resolution was achieved and used to determine exciton penetration into the defect. However, the nature of obtained signal remains unclear: it definitely relates to the exciton population caused by the laser excitation but the interaction of excitons with the tunneling electron is a complex process and its influence on the tunneling probability is unclear and requires further investigation. The interaction of the charge carrier with the exciton is a question of particular interest in light of the recent discovery of the presence of trions in the PL spectra of p-doped CNTs<sup>55</sup> and pristine SWCNTs.<sup>56</sup> A trion is a coulomb-bound carrier complex of one electron and two holes or two electrons and one hole. The experiment for observation of trion peaks in the excitons emission spectra controlled by the applied bias of STM has been proposed and spectra were theoretically

calculated for the case of an isolated quantum dot under the STM tip.<sup>57</sup> Conformation of the triions' existence with the help of STM will be remarkable achievement in the research of 1-D systems, and will open new prospects for device applications.

STM-UO-OS can reproduce the aforementioned near-field optical experiments and significantly improve the depth and quality of results with the help of better spatial resolution, stability of adsorbed SWCNT, control of sample surface and combination with STS information. The proposed technique of using plasmonic resonance modes as a light source instead of the external laser excitation is believed to be a very promising approach for achieving this goal. For the case of nanotubes the theoretical foundation for this kind of experiments has been recently presented.<sup>58</sup>

Near-field photoluminescence has also been used to study energy transfer between closely situated aligned and crossed nanotubes.<sup>59</sup> Transfer efficiencies were explained by Forster-type electromagnetic near-field coupling. The presented study includes approximate indirect derivation of the distance between nanotubes from the optical data. This type of experiment will definitely benefit when complemented by the STM data about the local topography between SWCNTs. We also would like to perform studies of electron and energy transfer between nanotubes using scanning tunneling luminescence (by injecting the tunneling electron in one nanotube and obtaining the signal from the other) and using plasmon mode excitations induced by the inelastic electron tunneling as described before. With the careful control of the experimental conditions, we will be able to conduct various types of experiments that have fundamental and applied significance.



## **Tip-Enhanced Raman Spectroscopy**

Raman spectroscopy is a well-developed technique and is widely used for investigations of CNTs.<sup>60</sup> It is often used for the SWCNTs chirality assignment (though it usually requires data from other experiments to assign it unambiguously), for probing vibrational and electronic properties and also for investigating nanotube quality. The Raman-scattering signal of CNT is so large, that even single isolated tubes can be easily studied by far-field optical methods. However, near-field techniques, those based on the Scanning Probe technology, are required to overcome the diffractive limit. AFM was successfully used to simultaneously record AFM topography and Raman maps with the spatial resolution of about 25nm.<sup>61</sup> It is well understood that one needs to study SWCNTs' electronic properties simultaneously with their Raman spectra in order to completely characterize SWCNTs.<sup>62</sup> STM spectra obtained simultaneously on the same single SWCNT in unaltered experimental conditions will provide us with an indispensable tool for such characterization. There is a remarkable example on how complementary STM and TERS measurements benefit from each other.<sup>63</sup> In this work the spatial extent of the D-band signal in the vicinity of localized defects in graphene was determined by connecting the D-band intensity with the defect density measured by STM.

STM-UO-OS will show in more detail how SWCNT optical properties are influenced by various defects and chemical doping, as well as fluctuations in the local environment. Near-field Raman Spectroscopy has been proven to achieve high spatial resolution of 15 nm in imaging of localized defects in SWCNTs using the D-band

intensity.<sup>64</sup> New instrumentation will improve this result by several times with the help of UHV, cryogenic environment and improved junction stability.

The described application of STM-UO-OS to SWCNTs demonstrates how this powerful technique can tremendously benefit the field of study for one nanomaterial. Results of comparable breadth and impact are expected for other advanced materials that have bright technological futures in electronic and optoelectronic applications, such as organic semiconductors, quantum dots and nanowires.

## APPENDICES

### APPENDIX A

#### SUPPORTING INFORMATION TO CHAPTER III

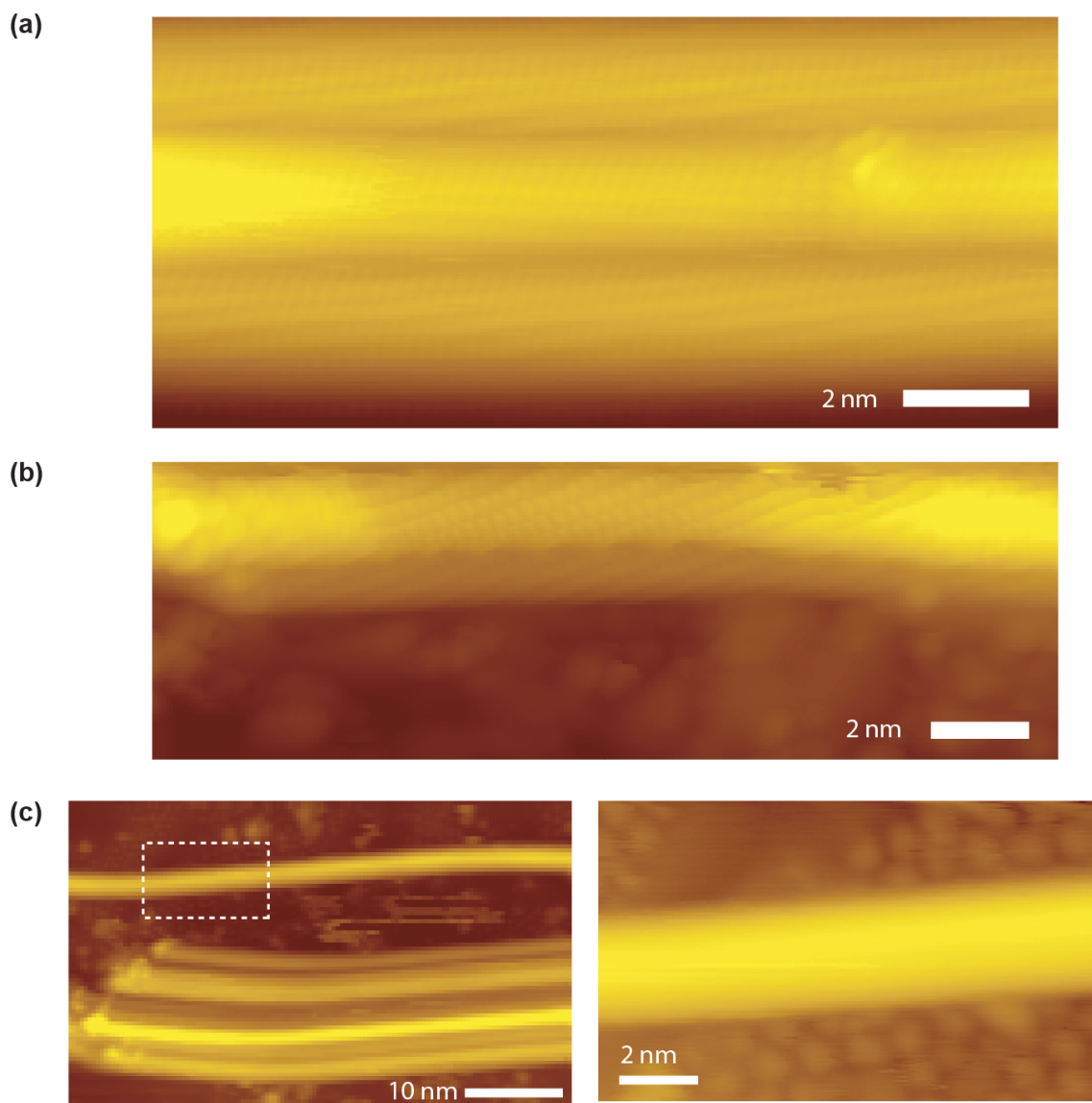


**Figure A1.** Representative STM images of several CNTs deposited on the Au(111) surface using the “dry contact transfer” method. Nanotubes constituted ~70% of the SWNT-containing powder obtained from Sigma-Aldrich, which explains the presence of small clusters around the nanotubes in the majority of the STM images.

**Figure A2.**

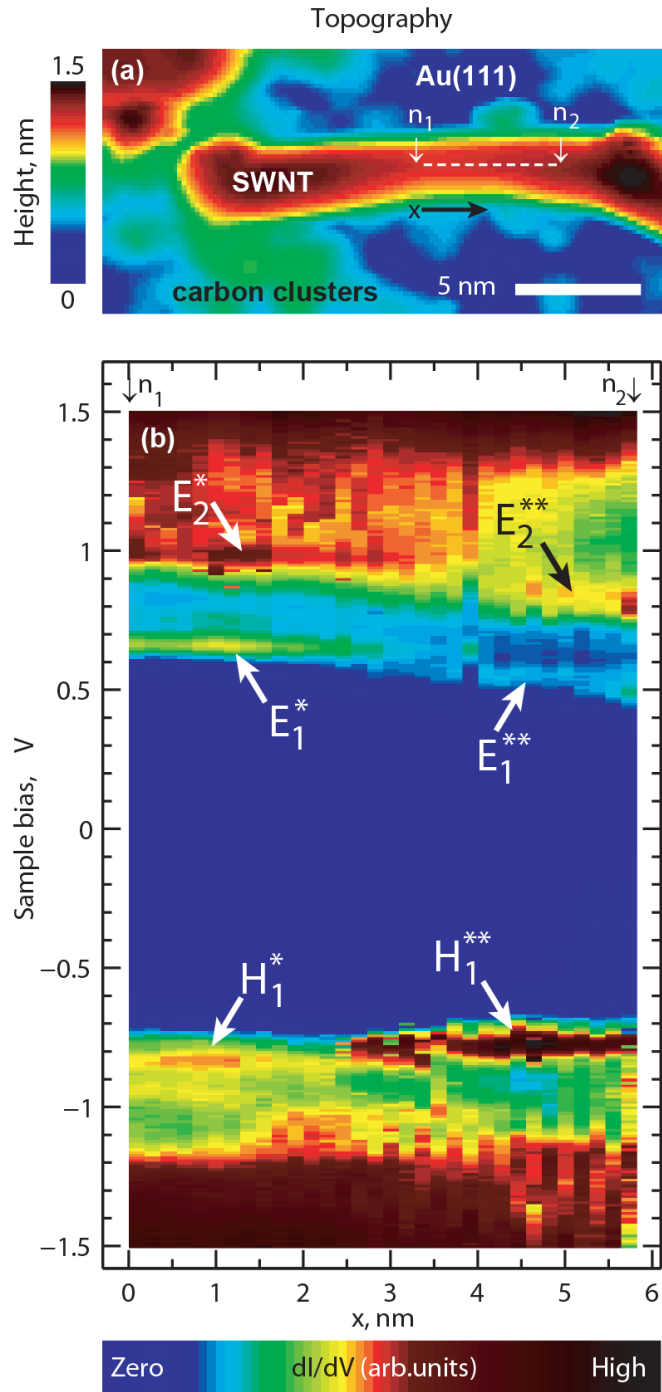
(a) STM topography of a SWNT, different from that of Figure 3.1b of the main text.

(b) STS signal as a function of the  $x$  coordinate [as shown in (a)] and sample bias voltage. (STS signal serves as a measure of the local density of electronic states.) The spatial range corresponds to the dashed line between points  $n_1$  and  $n_2$  in (a). Positive voltages correspond to unoccupied electronic states, while negative voltages correspond to occupied states. All data were measured along the nanotube centerline.

The spectra show Van Hove singularities, with the most visible states being  $H_1$ -type (derived from the valence band),  $E_1$ -type (derived from the conduction band), and  $E_2$ -type (derived from the band immediately above the conduction band).

Some bandgap variation is observed in the STS map shown in Figure

A2b, with levels  $E_n^*$  and  $H_1^*$  on the left side of the map, and levels  $E_n^{**}$  and  $H_1^{**}$  on the right side. The observed bandgap variation is likely a result of the non-uniform environment of the nanotube: the vicinity of point  $n_2$  shows a higher density of impurities located around the nanotube.



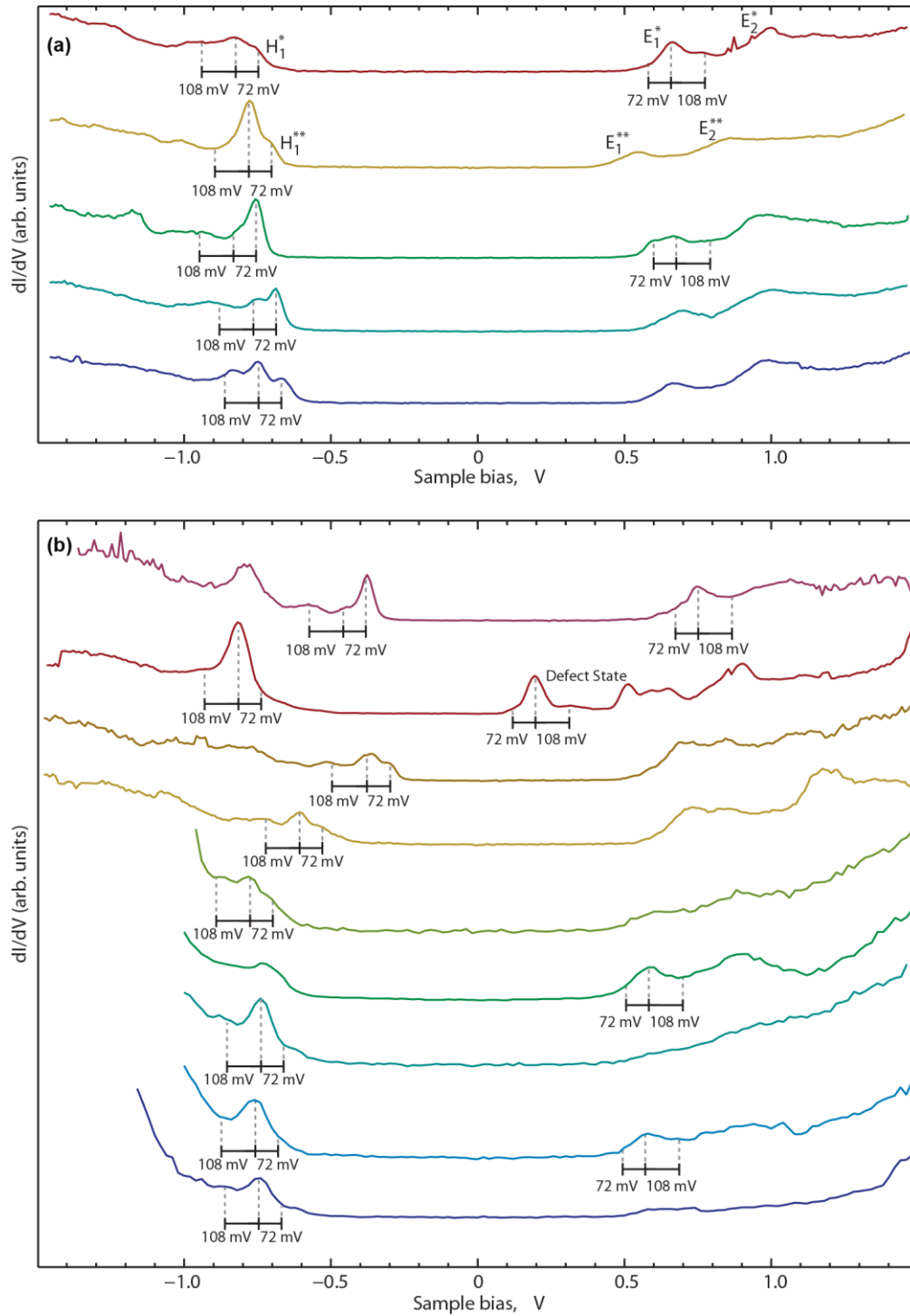


**Figure A3.** STS spectra showing fine spectral structures. (a) Spectra for the nanotube shown in Figure A2a, the bottom three spectra measured outside of the region contained between points  $n_1$  and  $n_2$ . (b) Additional spectra from localized states in other nanotubes.

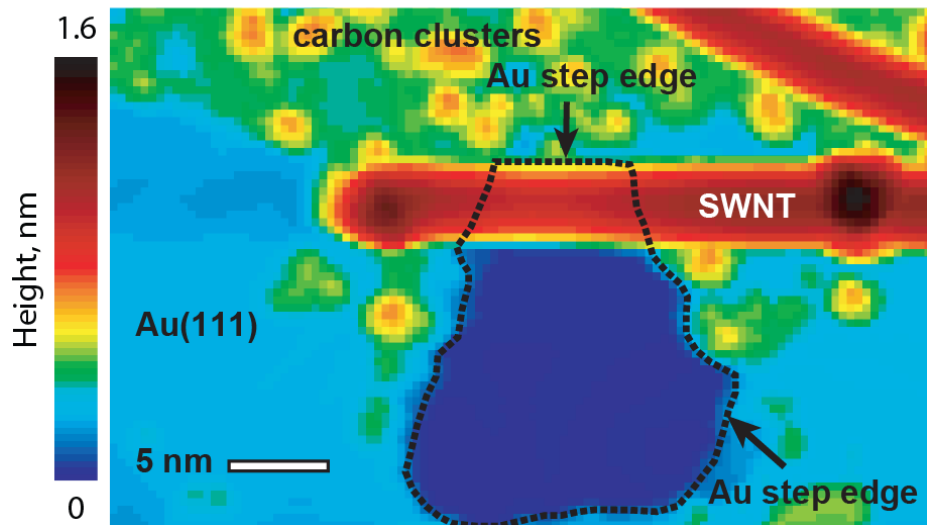


**Figure A4.** Zoomed-out view of the SWNT from Figure 3.1b showing the geometry of the Au trench straddled by the nanotube.

The band bending observed in points *L* and *R* in Figure 3.2 is explained by the charge transfer<sup>1</sup> between the nanotube and Au substrate caused by the mismatch in their effective work-functions.<sup>2</sup> As described in the main text, the SWCNT workfunction is 4.8 eV,<sup>1</sup> which is  $\sim 100$ meV higher than the effective workfunction of the Au substrate. This number is lower than the workfunction of the pristine Au(111) surface, 5.3 eV, apparently due to the direct proximity of a Au atomic step running along the SWCNT, shown in Figure A4. Indeed, as can be seen from Figure A4, the Au terrace shown in dark blue does not extend above the nanotube. On the other hand, Figure 1c clearly shows that the nanotube touches this Au terrace in point *L*, which is only possible if the top boundary of this terrace is runs roughly along the nanotube, as schematically shown in Figure A4. The Au step edge carries with it a workfunction-lowering charge redistribution caused by the Smoluchowski effect.<sup>1</sup>

Mismatch of workfunctions in the tip  $\phi_{tip}$  and substrate  $\phi_{Au}$ , together with the finite voltage drop  $\Delta V$  inside the SWNT, lead to a shift of electronic state  $E_1$  by  $e\Delta V = \alpha(eV_b + \Delta\phi)$ , where  $V_b$  is the applied bias voltage,  $\Delta\phi = \phi_{tip} - \phi_{Au}$ , and  $e$  is the electron charge. Parameter  $\alpha$  thus relates the average potential inside the nanotube to the external potentials applied across the tunneling gap. Therefore, states  $E_1$  (unoccupied) and  $H_1$  (occupied) are observed at voltages  $V_E$  and  $V_H$  that are defined by the following equations:

$$E_1 + \alpha\Delta\phi = (1 - \alpha) eV_E$$

$$H_1 + \alpha\Delta\phi = (1 - \alpha) eV_H$$

Where  $E_1$  and  $H_1$  are the true energies of states  $E_1$  and  $H_1$  with respect to the substrate Fermi level. Voltages  $V_E$  and  $V_H$  are determined directly from the STS spectra. Then we can eliminate unknown  $\Delta\phi$  so that:

$$E_1 - H_1 = (1 - \alpha)(eV_E - eV_H)$$

Quantities appearing on the right side of the equation depend on the relative lateral distance between the tip apex and the “centers of gravity” of the measured localized states  $E_1$  and  $H_1$ . Indeed, Figure 3.2 of the main text shows a noticeable “curving” of localized states  $E_{1,1}$ ,  $H_1^*$ ,  $H_1^{**}$ , and other states appearing at onsets of conduction. This is primarily a result of the variation of  $\alpha$  with distance  $\Delta x$  to the “center of gravity” of the corresponding state.

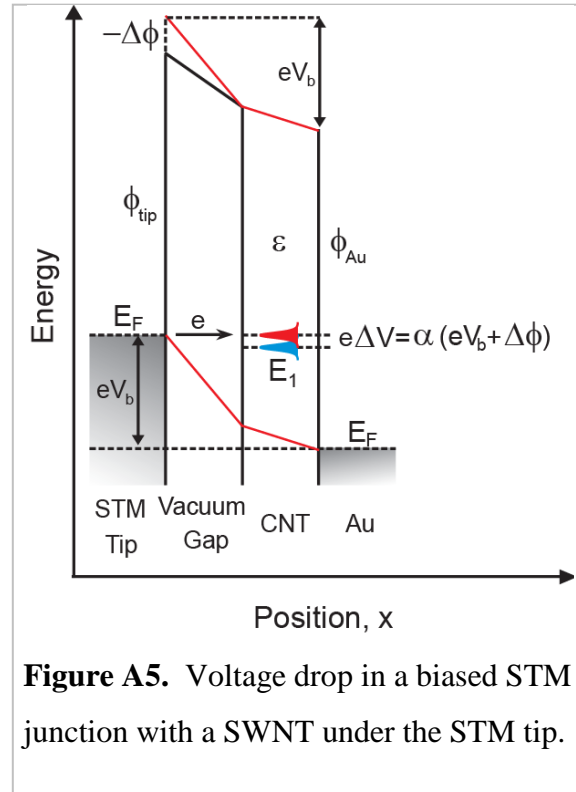


**Figure A5.** Voltage drop in a biased STM junction with a SWNT under the STM tip.

Then, when the tip is at a lateral distance  $\Delta x$  away from states  $E_1$  or  $H_1$ , we can write

$$E_1 - H_1 = (1 - \alpha_{\Delta x})(eV_{E,\Delta x} - eV_{H,\Delta x})$$

And when the tip is immediately above states  $E_1$  or  $H_1$ , we can write:

$$E_1 - H_1 = (1 - \alpha_0)(eV_{E,0} - eV_{H,0})$$

Then unknown difference  $E_1 - H_1$  is eliminated, so that:

$$\frac{1 - \alpha_0}{1 - \alpha_{\Delta x}} = \frac{V_{E,\Delta x} - V_{H,\Delta x}}{V_{E,0} - V_{H,0}} = \kappa = 1.045$$

Here, quantities  $V_{E,\Delta x}$  and  $V_{H,\Delta x}$ , as well as  $V_{E,0}$  and  $V_{H,0}$ , were extracted from Figure S6 using states  $E_{1,1}$  and  $H_1^*$ , and  $\Delta x = 3 \text{ nm}$  (offset from the “centers of gravity” of the corresponding states).

Quantity  $\gamma = \alpha_{\Delta x}/\alpha_0$  depends primarily on the shape of the tip, and can be measured independently by using spectra showing bipolar transport,<sup>3</sup> which was observed at a SWCNT defect located nearby (Figure A7). Bipolar transport through a given state

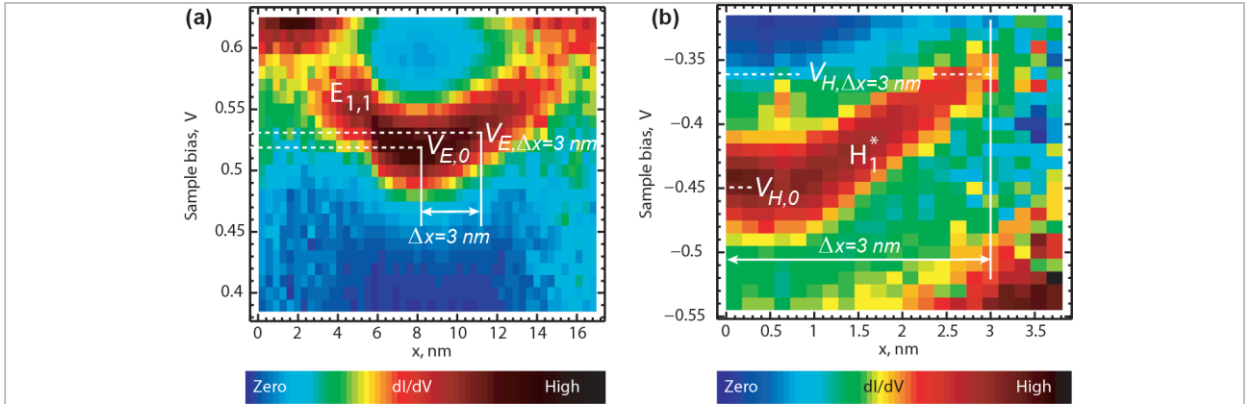


**Figure A6.** Spatial dependence of STS peaks corresponding to states  $E_{1,1}$  [shown in (a)] and  $H_1^*$  [shown in (b)] from Figure 3.2. The spatial coordinate  $x$  is identical to that used in Figure 3.2. The STS signal has been renormalized so as to give constant integral DOS within the ranges shown.



$E_d$  (in Figure A7 the state originates from a defect) can occur either at a positive voltage  $V_E^+$  or a negative voltage  $V_E^-$  described by the following formulae:

$$E_d + \alpha_d \Delta\phi = (1 - \alpha_d) eV_E^+$$

$$E_d + \alpha_d \Delta\phi = -\alpha_d eV_E^-$$

From these we have:

$$(1 - \alpha_d) V_E^+ = -\alpha_d V_E^-$$

Which gives for  $\alpha_d$ :

$$\alpha_d = \frac{V_E^+}{V_E^+ - V_E^-}$$

Here  $\alpha_d$  is a function that depends on coordinate  $x$ . In principle,

$\alpha_d$  may not be equal to  $\alpha$ , because the “center of gravity” of the defect state is not necessarily at the same height as that of states  $E_{1,1}$  and  $H_1^*$ . However, in the limit of a slowly changing tip profile, approximate equality

$$\frac{\alpha_{\Delta x}}{\alpha_0} \approx \frac{\alpha_{d,\Delta x}}{\alpha_{d,0}}$$

applies, which can be used for the evaluation of  $\gamma = \alpha_{\Delta x}/\alpha_0$ . From Figure S6 we determine  $V_E^+$  and  $V_E^-$ , at  $\Delta x = 0$  and  $\Delta x = 3 \text{ nm}$ , which give  $\gamma \approx 0.6 \pm 0.05$ . Then:

$$\alpha_0 = \frac{\kappa - 1}{\kappa - \gamma} \approx 0.10 \pm 0.01$$

is the quantity that determines the average potential inside the nanotube of Figure 3.2.

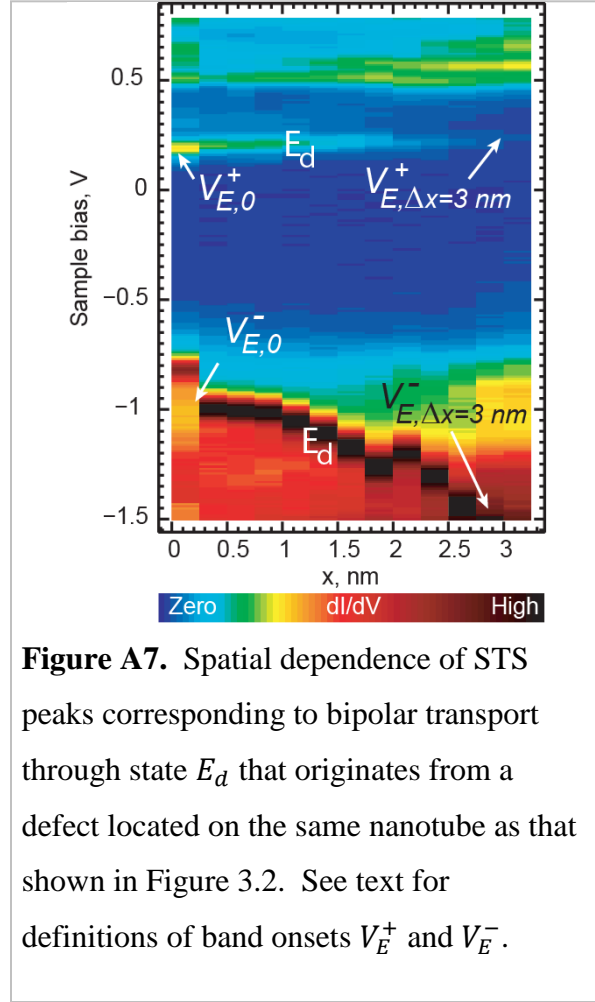


**Figure A7.** Spatial dependence of STS peaks corresponding to bipolar transport through state  $E_d$  that originates from a defect located on the same nanotube as that shown in Figure 3.2. See text for definitions of band onsets  $V_E^+$  and  $V_E^-$ .

## APPENDIX B

### SUPPORTING INFORMATION TO CHAPTER IV

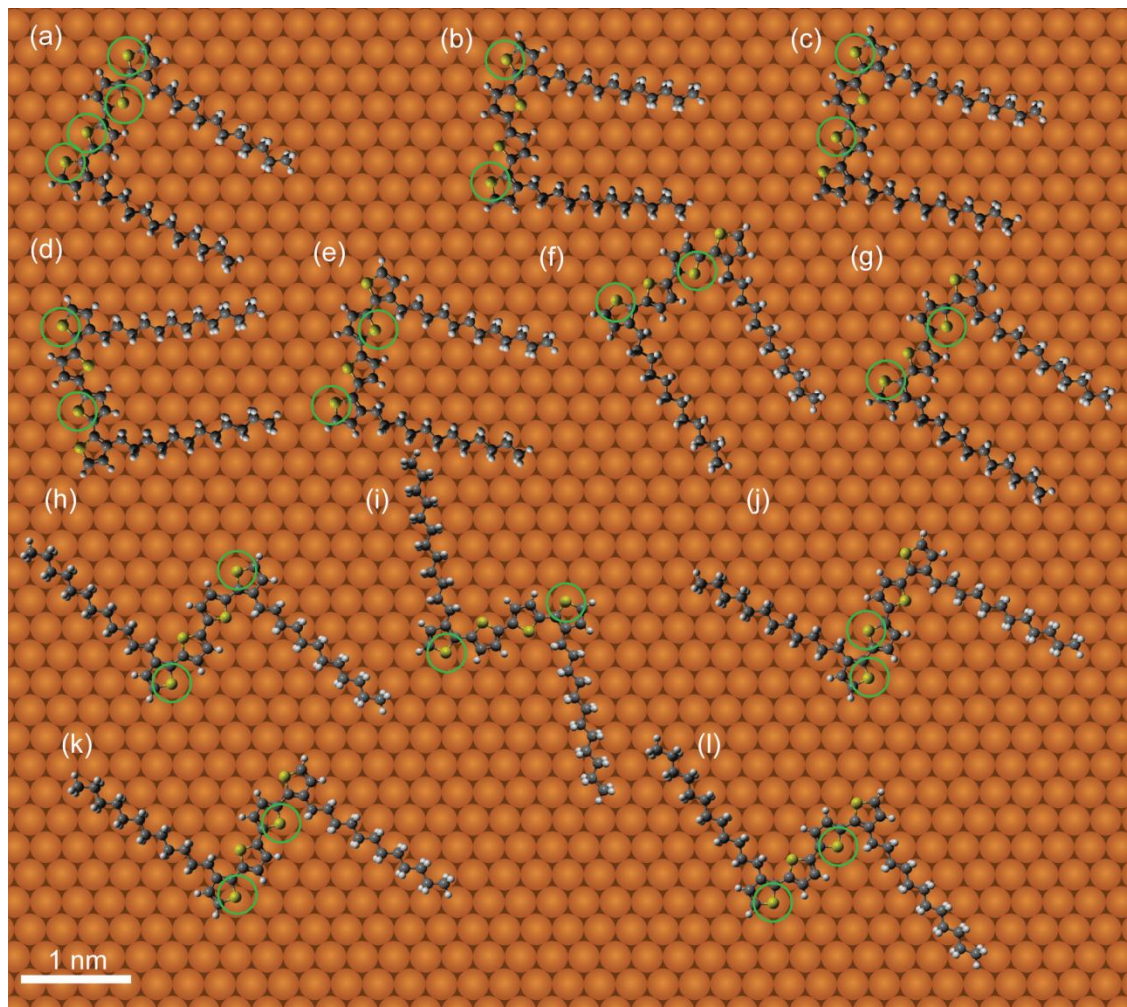


**Figure B1.** Possible adsorption configurations for DDQT conformers in the main text. S atoms at Au top-sites are highlighted by green circles. (a) *cis*-DDQT conformer with S atoms at Au top-sites as observed in Chapter IV along with other possible orientations with (b) both exterior S atoms at Au top-sites and (c)-(g) one exterior and one interior S atom at Au top-sites. (h) *trans*-DDQT conformer with exterior S atoms at Au top-sites as observed in Chapter IV along with other possible orientations with (i) both exterior S atoms at Au top-sites, (j) adjacent interior and exterior S atom in Au top-sites (this is the only possibility for *trans*-DDQT having neighboring S atoms located at Au top-sites), and (k) and (l) non-adjacent interior and exterior S atoms at Au top-sites.

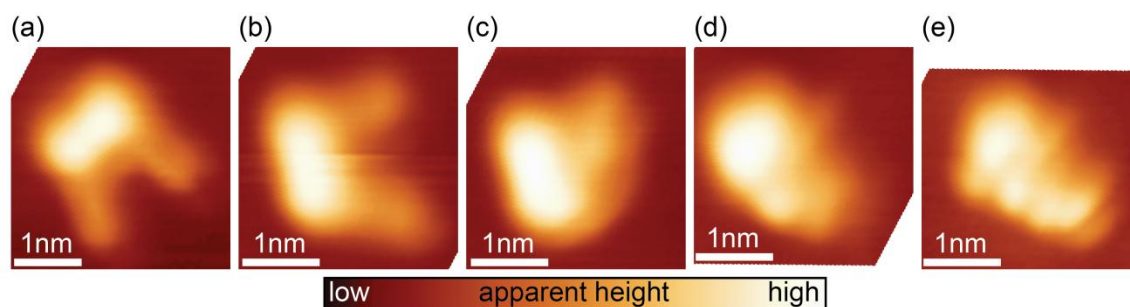


**Figure B2.** Manipulation of *cis*-DDQT monomer and alkyl side chains with STM tip. After the initial topography (a), the DDQT monomer rotated by 60° on the substrate (b). Subsequent STS measurements of this *cis*-conformer resulted in the alkyl chains folding over themselves (c) and the DDQT backbone (d)-(e). Topographies acquired at 1.0 V bias, 5.0 pA set point.

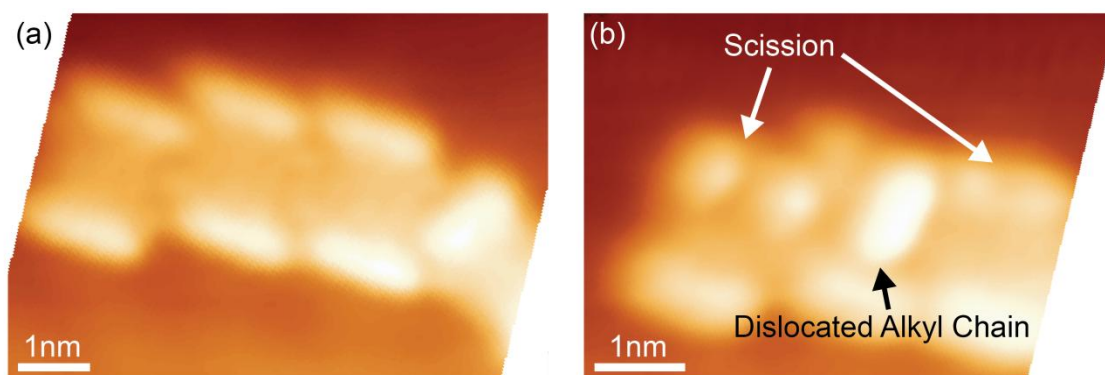


**Figure B3.** Examples of scission observed during STS at higher (~2.5-3.0 V) bias. Topographies (a) before STS, and (b) after. This susceptibility of DDQTs to scission limited the lifetime of individual DDQT *cis*-conformers and inhibited detailed study of unoccupied states beyond the LUMO. In addition to the scission of DDQT backbones, alkyl side chains could also dislocate from the stable dimer position (b). STM topographies were acquired at 100 mV bias, 5.0 pA set point.

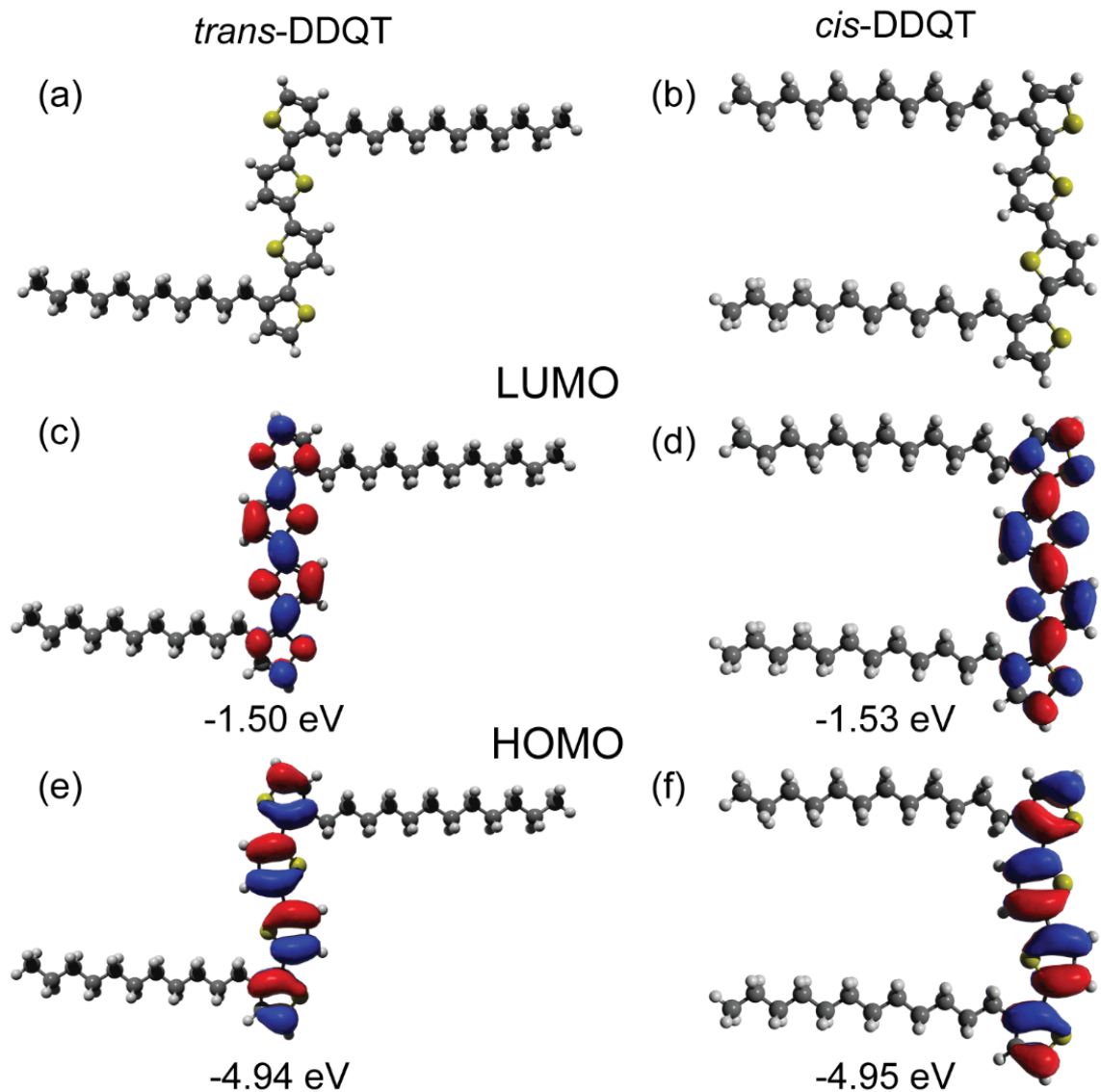


**Figure B4.** Density Functional Theory gas-phase electronic structure calculations of (a) *trans* DDQT and (b) *cis* DDQT. (c) and (d) LUMOs and their energies for *trans* and *cis* conformers, correspondingly. (e) and (f) HOMOs and their energies for *trans* and *cis* conformers, correspondingly. The dipole moment of the *trans* (*cis*) conformation is 0.06 Debye (2.32 Debye). Computations were performed with Gaussian09<sup>4</sup> using B3LYP/6-31G\* and visualized with Avogadro<sup>5</sup>.

Functional	DDQT Conformation	HOMO (eV)	LUMO (eV)	HOMO-LUMO Gap (eV)	Dipole Moment (Debye)
B3LYP	cis	-4.95	-1.53	3.41	2.32
	trans	-4.94	-1.50	3.45	0.06
PBE	cis	-4.37	-2.06	2.31	2.46
	trans	-4.36	-2.03	2.34	0.06
PW91	cis	-4.40	-2.10	2.30	2.45
	trans	-4.39	-2.07	2.33	0.06

**Table B1.** Frontier orbital energies and dipole moments from DFT calculations using the B3LYP<sup>6,7</sup> — a non-local (hybrid) functional — and PBE<sup>8</sup> and PW91<sup>9</sup> — semi-local exchange-correlation functionals. The calculated dipole moments of *cis*-DDQT (2.3-2.5 Debye) were significantly greater than that of *trans*-DDQT (0.06 Debye), leading to the enhanced interaction of the *cis*-conformer with image charges at the metal surface. In all three calculations, the *cis*-LUMO was found to be higher (by ~30 meV) than the *trans*-LUMO. All DFT computations used the 6-31G\* basis set.

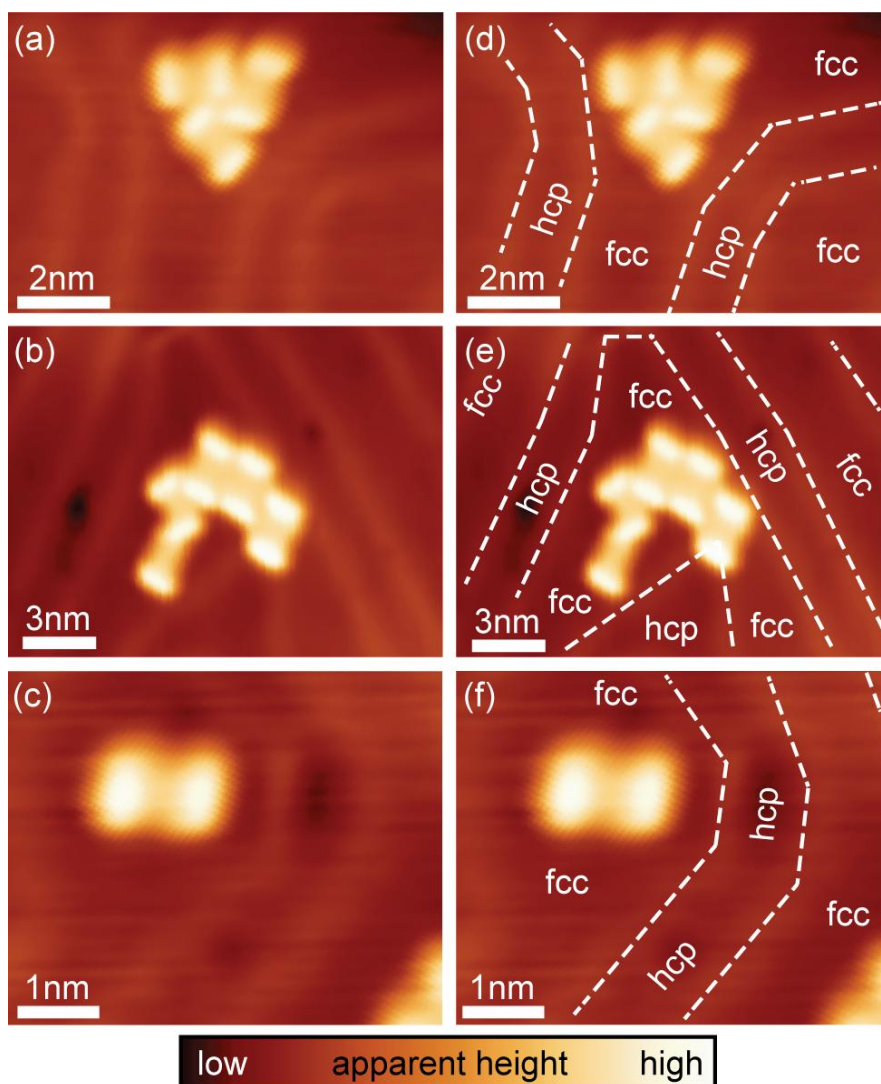


**Figure B5.** Registry of DDQT molecules with the underlying Au(111) surface as in Figure 4.2 of the main text, with surface reconstruction ridges highlighted by white dashed lines delineating face-centered-cubic (fcc) and hexagonal-close-packed (hcp) regions of the Au(111) surface (d)-(f). (a)-(c) STM images of DDQT molecules on Au(111) substrate. DDQT molecules primarily adsorbed in the fcc regions, with the quaterthiophene backbones aligned along one of three  $\langle 110 \rangle$  directions of the Au(111) surface, perpendicular to Au(111) surface reconstruction ridges aligned primarily along the  $\langle 112 \rangle$  directions, as shown in Figure 4.2 (main text). STM imaging was carried out at bias voltages 0.1-1.0 V and tunneling currents 1-5 pA.

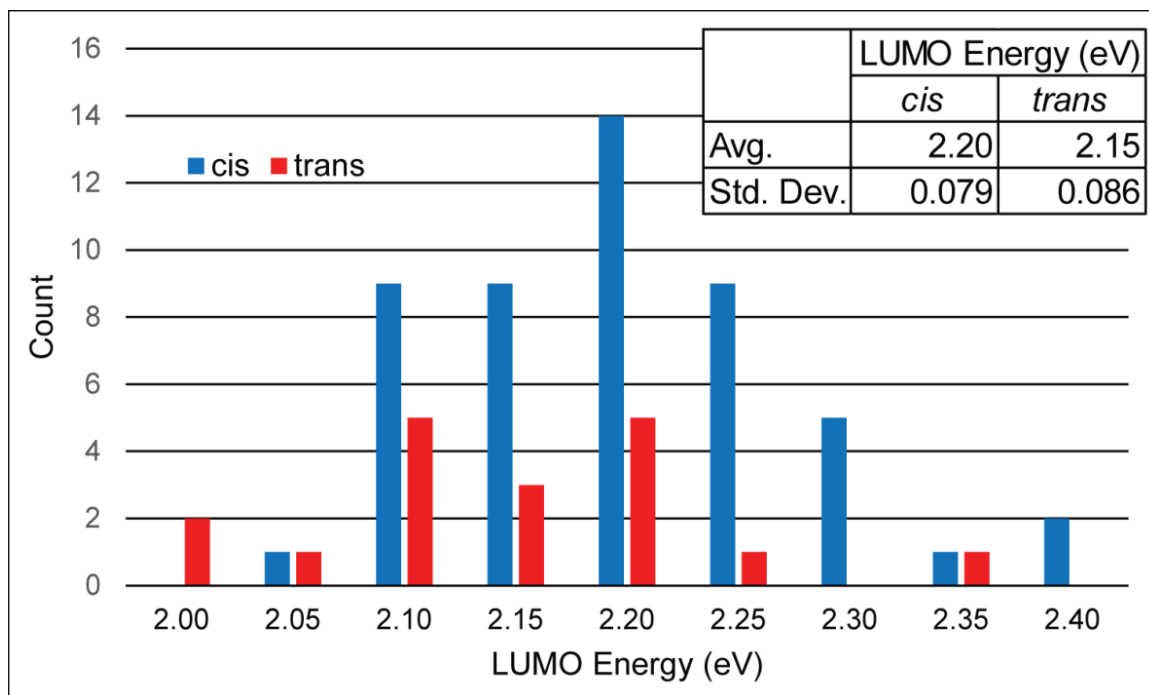


**Figure B6.** Distributions of LUMO energies for 50 *cis* and 18 *trans*-conformers, as measured by STS.

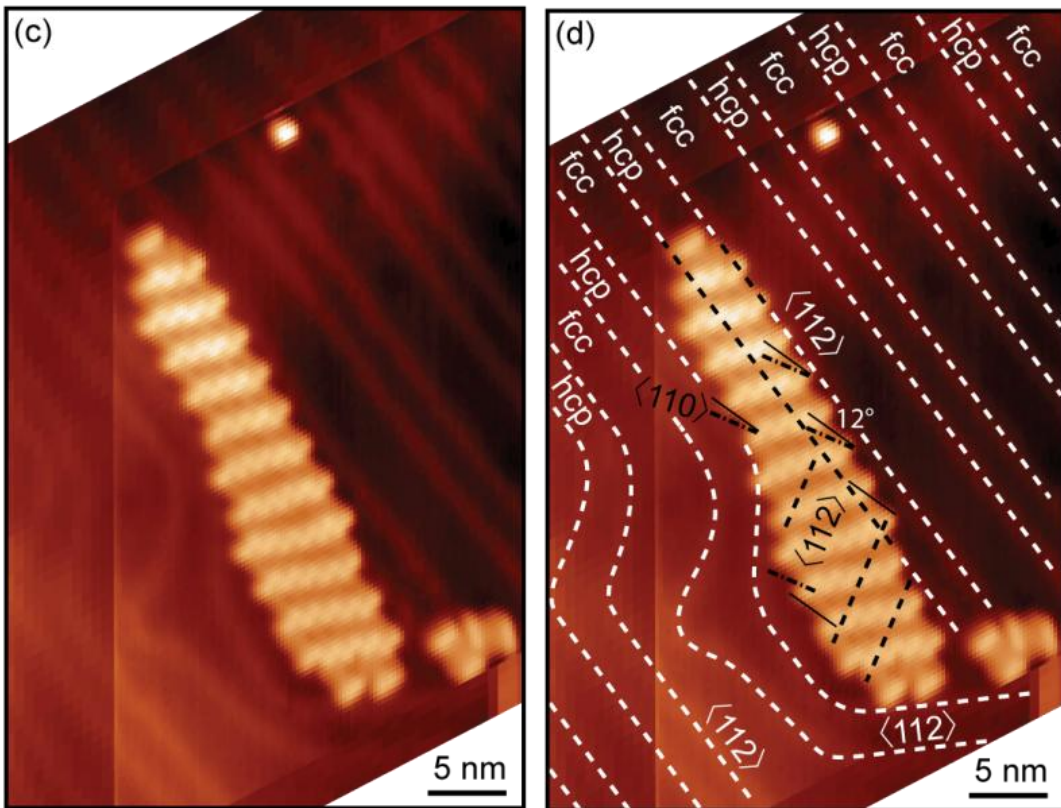
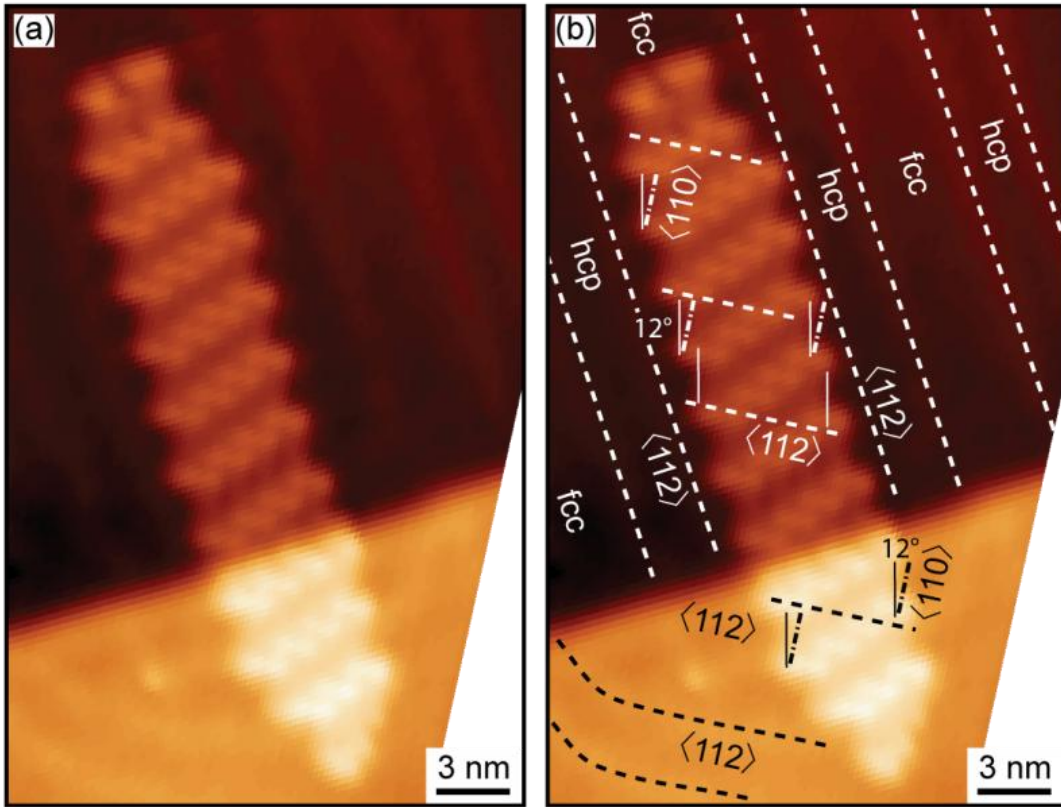
## APPENDIX C

### SUPPORTING INFORMATION TO CHAPTER V

---

**Figure C1.** DDQT crystals agnostic to Au(111) surface features. (a) STM image [set point 100 mV, 10 pA] of a crystal formed over a single-atom step. The crystal order on both sides of the step are identical, and the DDQT molecules on higher terrace are connected to the molecules below in a regular manner. Note that the hcp areas of the Au(111) reconstruction are avoided. (b) Image from (a) with marked molecular orientations and Au(111) crystallographic directions. Oligothiophene backbones are oriented along the  $\langle 112 \rangle$  directions and the alkyl ligands are positioned  $16^\circ$  from the  $\langle 110 \rangle$  direction, as evident from the edges of the crystal formation. (c) STM image [set point 100 mV, 5 pA] of a crystal formed over a Au(111) surface reconstruction ridge, resulting in occupation of the energetically unfavorable hcp region. The crystallographic order of the DDQT crystal and DDQT backbone orientation are not modified as compared to a regular case of crystal formed in fcc area. (d) Image from (c) with marked molecular orientations and Au(111) crystallographic directions. Oligothiophene backbones are oriented along the  $\langle 112 \rangle$  directions and the alkyl ligands are positioned  $16^\circ$  from the  $\langle 110 \rangle$  direction.





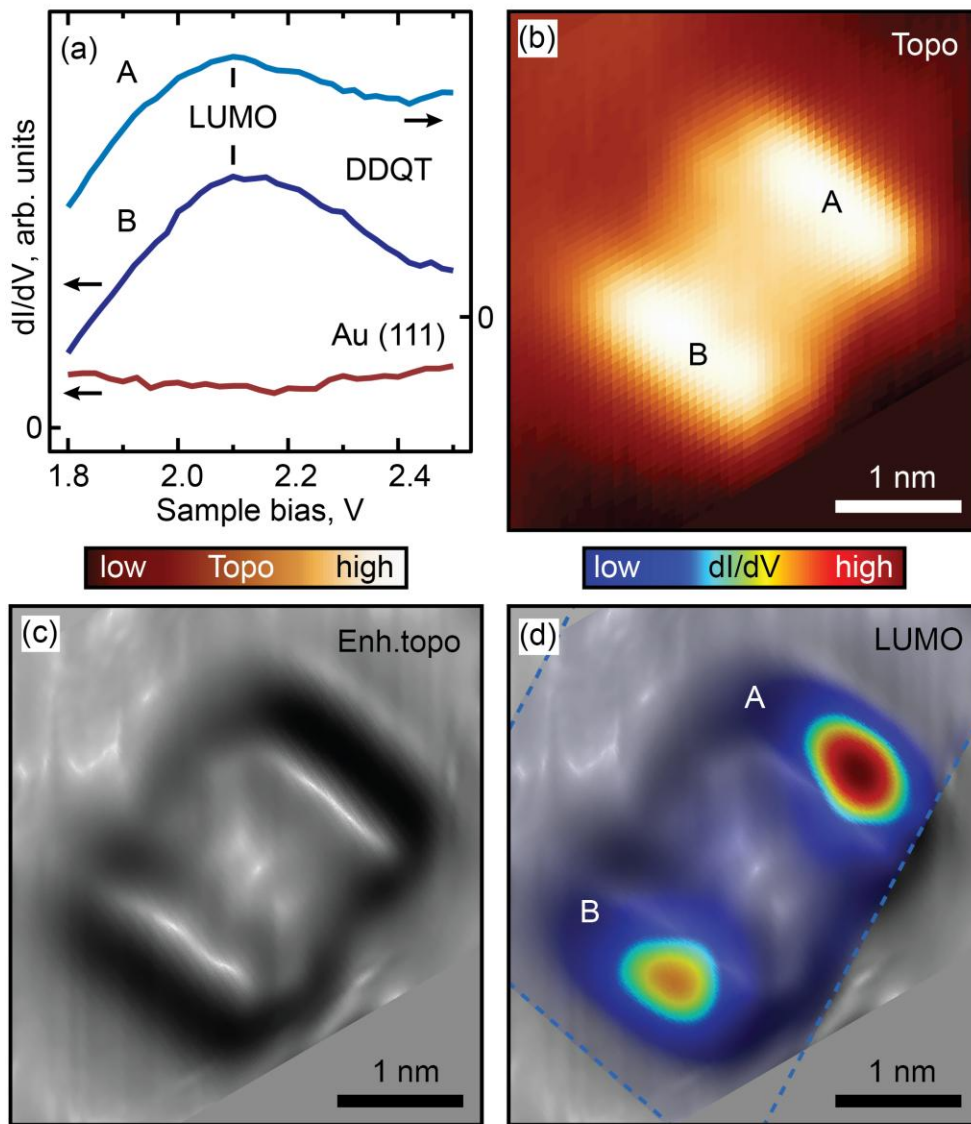


**Figure C2.** Spatial mapping of DDQT LUMO. (a) STS spectra measured on the quaterthiophene backbone of the molecules A and B indicated in (b) [curves DDQT], and STS spectrum of the gold substrate near the dimers [curve Au(111)]. Spectrum for molecule A is shifted for clarity as indicated by 0 of the signal on the right vertical axis. (b) STM image of a DDQT dimer. (c) STM image from (b) processed to “sharpen” the topographic features. (d) Density of states (DOS) for the LUMO orbital [2.1 V, see curve DDQT in (a)] overlaid on image from (c). Mapped area is confined within the dashed lines. Low DOS intensity (near-background) areas were rendered transparent to show registry with topography.

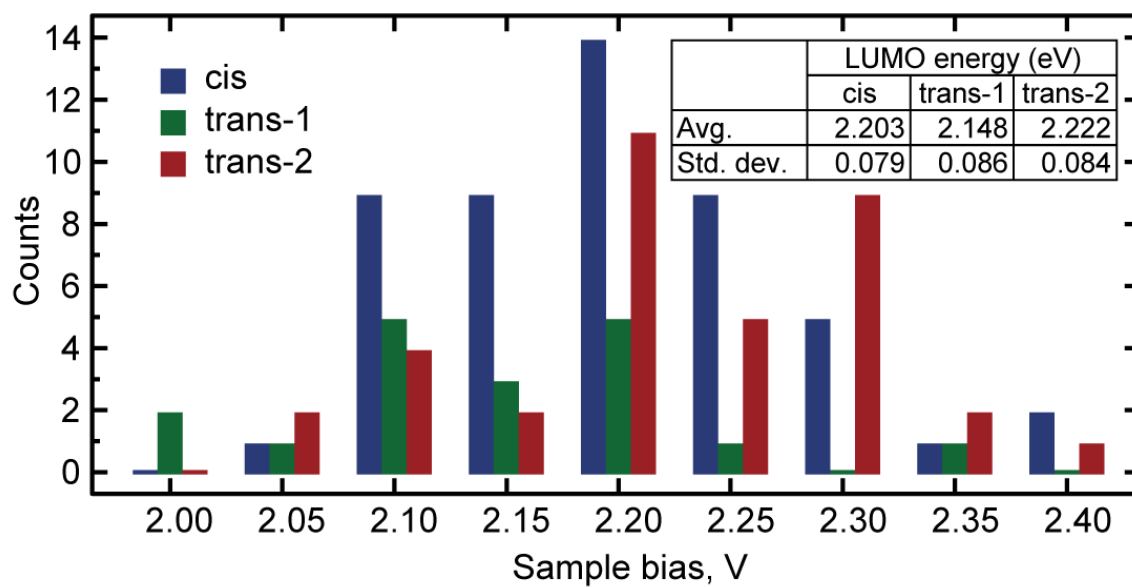


**Figure C3.** Distribution of LUMO orbital energies of DDQT backbones in cis and trans conformations. Trans-1 refers to trans conformers observed at low and intermediate coverage, and trans-2 refers to trans conformers observed in the high coverage regime.

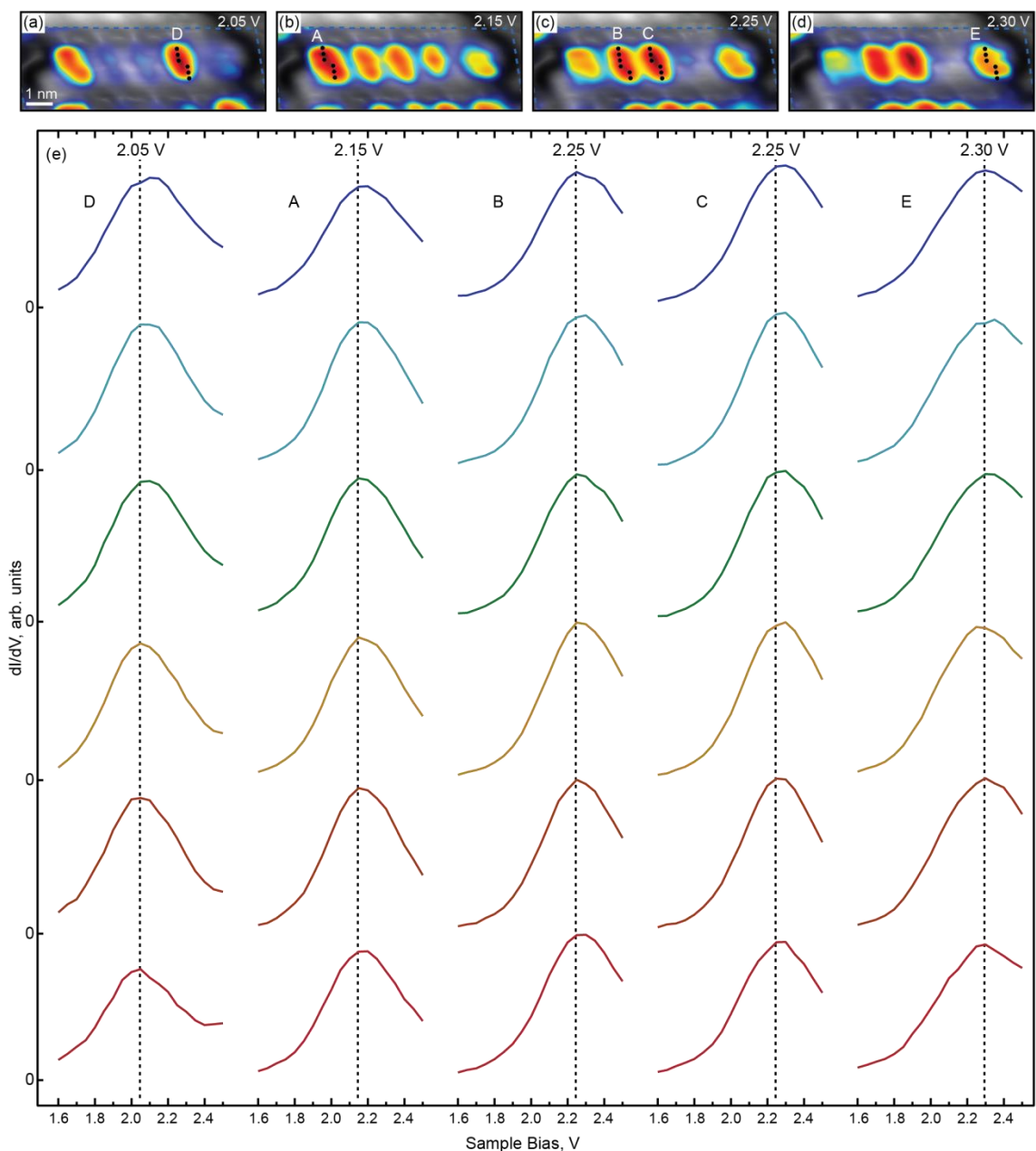


**Figure C4.** STS  $dI/dV$  scans of the DDQT crystal in Figure 5.8 of the main text, demonstrating that LUMO peak voltages were not sensitive to the precise location of the tip on the measured molecules. (a)-(d) Density of states maps obtained by overlaying spatially mapped STS  $dI/dV$  signal [set point 1.8 V, 2.0 pA, lock-in modulation 100 meV] on the enhanced topography to show LUMO orbital localization. Low  $dI/dV$  signal of the map (background) was rendered transparent in order to reveal alignment with the topography. (e)  $dI/dV$  spectroscopy scans [set point 1.8 V, 2.0 pA, lock-in modulation 100 meV] taken at indicated locations on top of backbones A-E in (a)-(d).

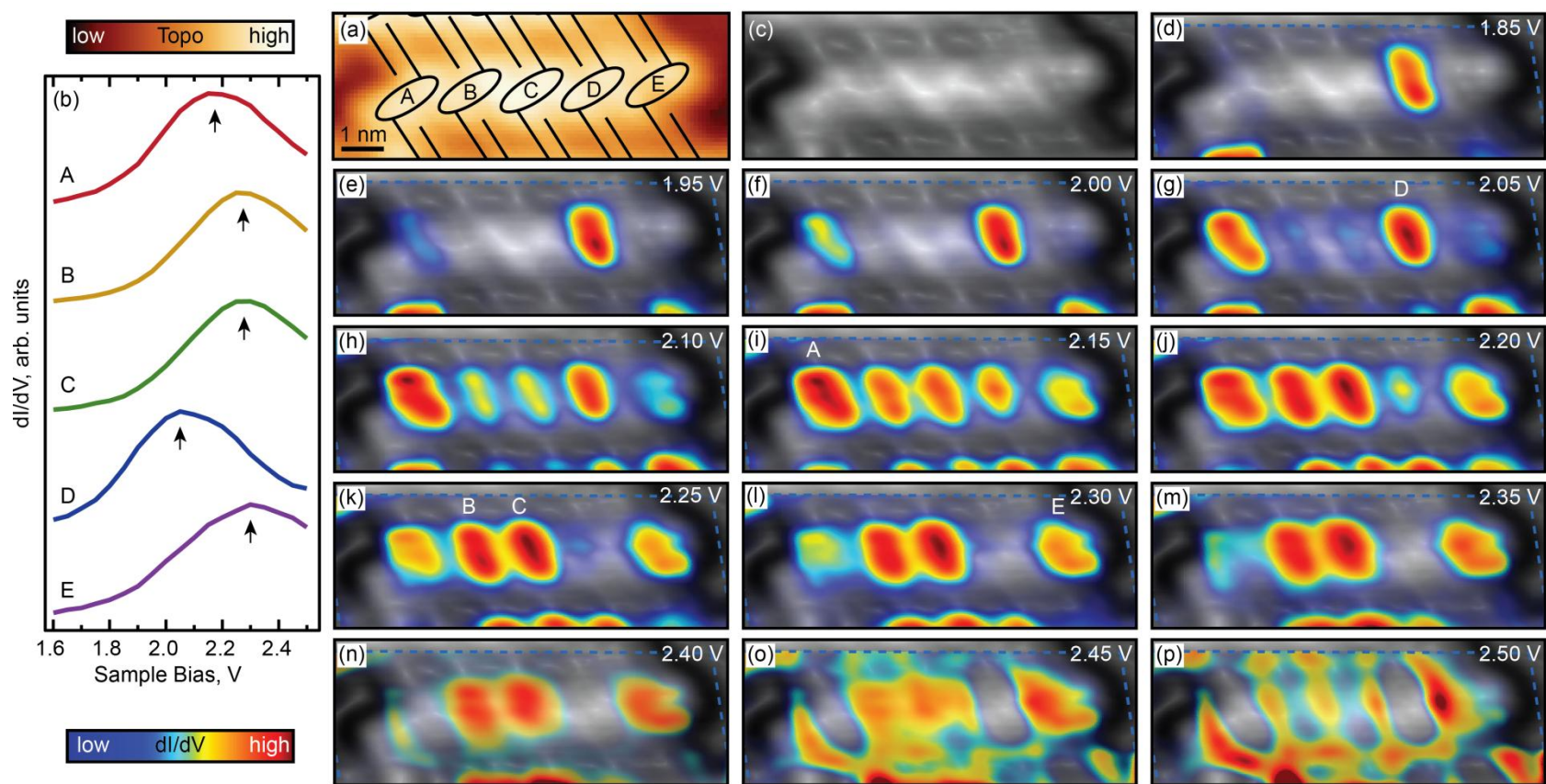


**Figure C5.** Expansion of the DOS maps shown in Figure 5.8 in the main text. (a) STM image [set point 200 mV, 5 pA] of part of the crystal with overlaid DDQT models of backbone (ellipse) with attached alkyl chains (lines). Regular chain of the crystal consisting of five DDQT molecules is shown. (b) dI/dV spectroscopy scans [set point 1.8 V, 2.0 pA, lock-in modulation 100 meV] taken on top of every backbone indicated with A-E in (a). (c) STM image from (a) processed to “sharpen” the topographic features. (d)- (p) DOS mapping from 1.85-2.50 V in 50 mV increments.

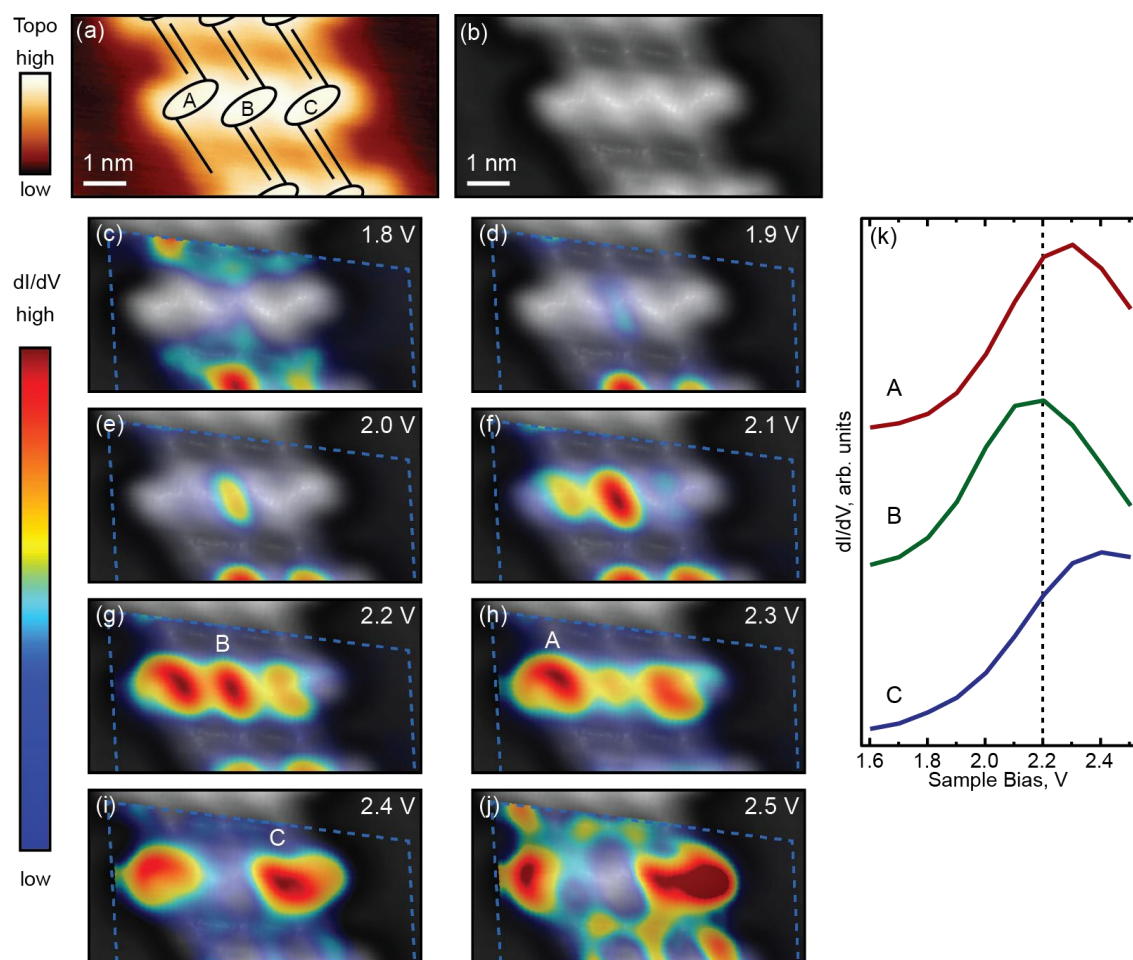


**Figure C6.** LUMO DOS maps of a DDQT crystal of the type formed in the high molecular coverage regime. (a) STM image [set point 200 mV, 5 pA] of part of the crystal with overlaid DDQT models of backbones (ellipses) with attached alkyl chains (lines). Regular chain of the crystal consisting of three DDQT molecules is shown. (b) STM image from (a) processed to “sharpen” the topographic features. (c)-(j) Density of states maps from 1.8-2.5 V in 100 mV increments obtained by overlaying spatially mapped STS dI/dV signal [set point 1.8 V, 2.0 pA, lock-in modulation 100 meV at 570 Hz] on the enhanced topography to show LUMO orbital localization. Low dI/dV signal of the map (background) was rendered transparent in order to reveal alignment with the topography. (k) dI/dV spectra [set point 1.8 V, 2.0 pA, lock-in modulation 100 meV at 570 Hz] taken on top of every backbone indicated with A-C in (a).

## APPENDIX D

### SUPPORTING INFORMATION TO CHAPTER VI

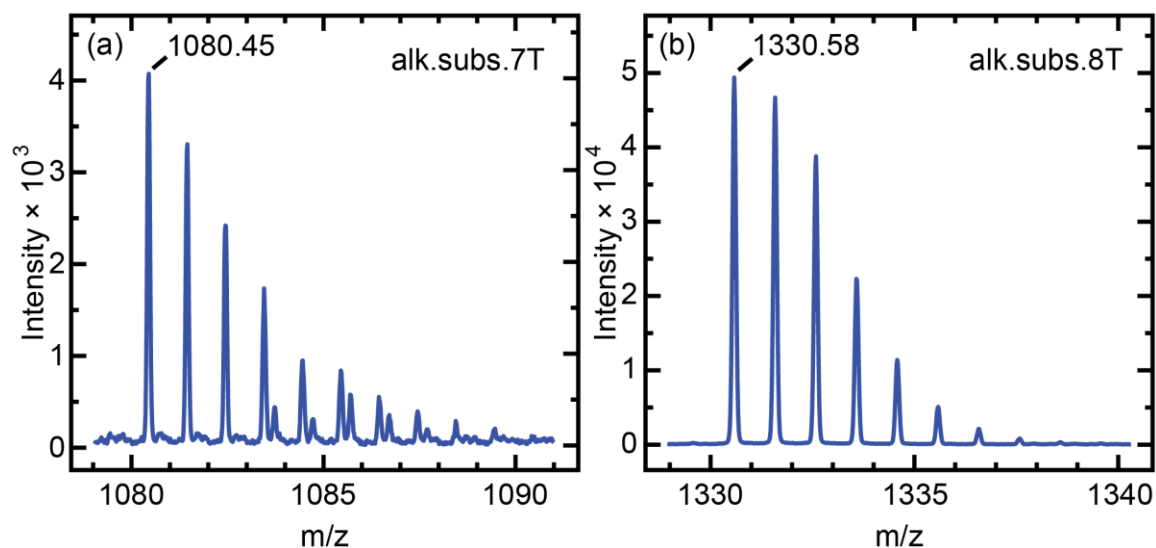


**Figure D1.** Sample characterization using nanoelectrospray ionization (nano-ESI) mass spectrometry [solution in THF, ESI voltage 1.4 kV]: (a) part of the spectra corresponding to alkyl-substituted 7T (calculated for  $C_{64}H_{88}S_7$  1080.49, found 1080.45), (b) part of the spectra corresponding to alkyl-substituted 8T (calculated for  $C_{80}H_{114}S_8$  1330.66, found 1330.58). The progression of peaks beyond the main m/z peak is the isotope series for each conformational isomer.

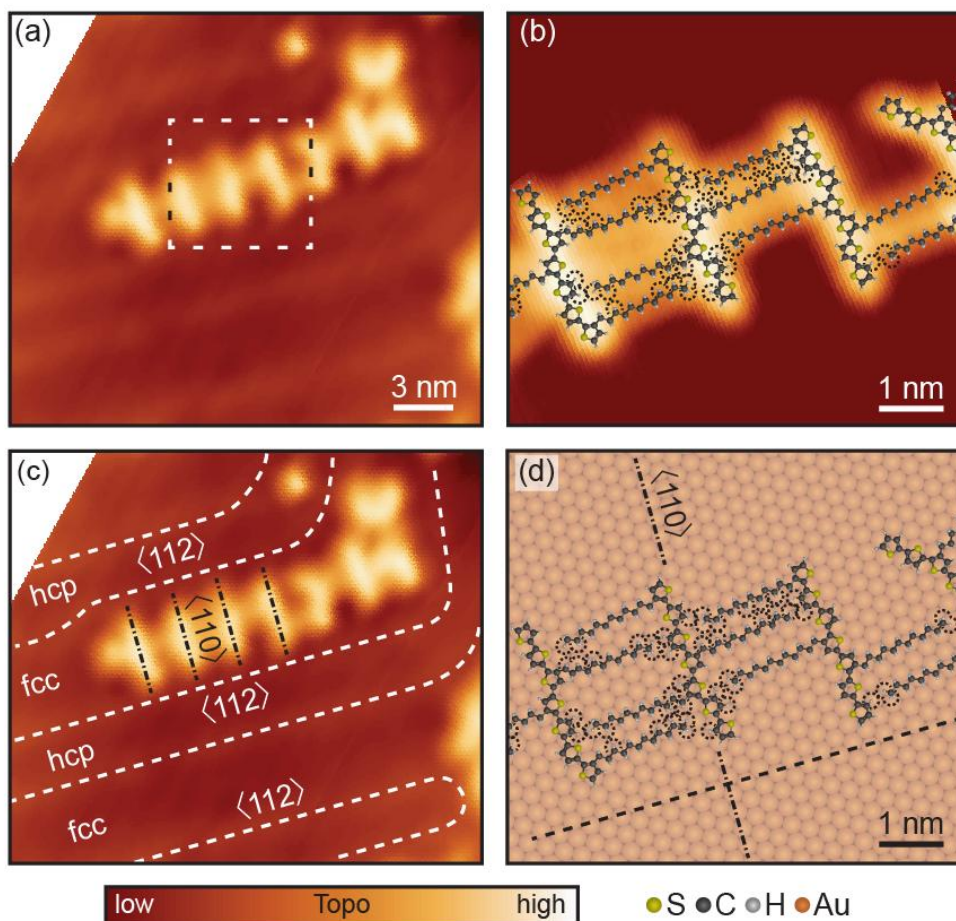


**Figure D2.** Adsorption of 7T molecules on Au(111). (a) STM image [set point 100 mV, 5 pA] of an aggregate of 7T molecules absorbed on the Au(111) surface. (b) Close-up STM topography of the region confined by the dotted rectangle in (a) with overlaid atomic models of 7T molecules showing that molecules attach to each other via alkyl substituents. The molecular models show that the thiophene rings comprising the DDQT backbones are nearly flat on the Au(111) surface, as determined from STM topography. (c) STM image from (a) with indicated molecular orientations and Au(111) crystallographic directions and highlighted surface reconstruction ridges. The oligothiophene backbones of 7T molecules are aligned along the  $\langle 110 \rangle$  directions of the Au(111) surface, perpendicular to the straight sections of surface-reconstruction ridges, which run parallel to the  $\langle 112 \rangle$  directions. (d) Model of 7T molecules from (b) matched to the Au(111) surface lattice. Au(111) crystallographic directions are indicated. 7T backbones are roughly aligned along the  $\langle 110 \rangle$  direction. Dashed circles indicate the van der Waals radii of the hydrogen atoms.



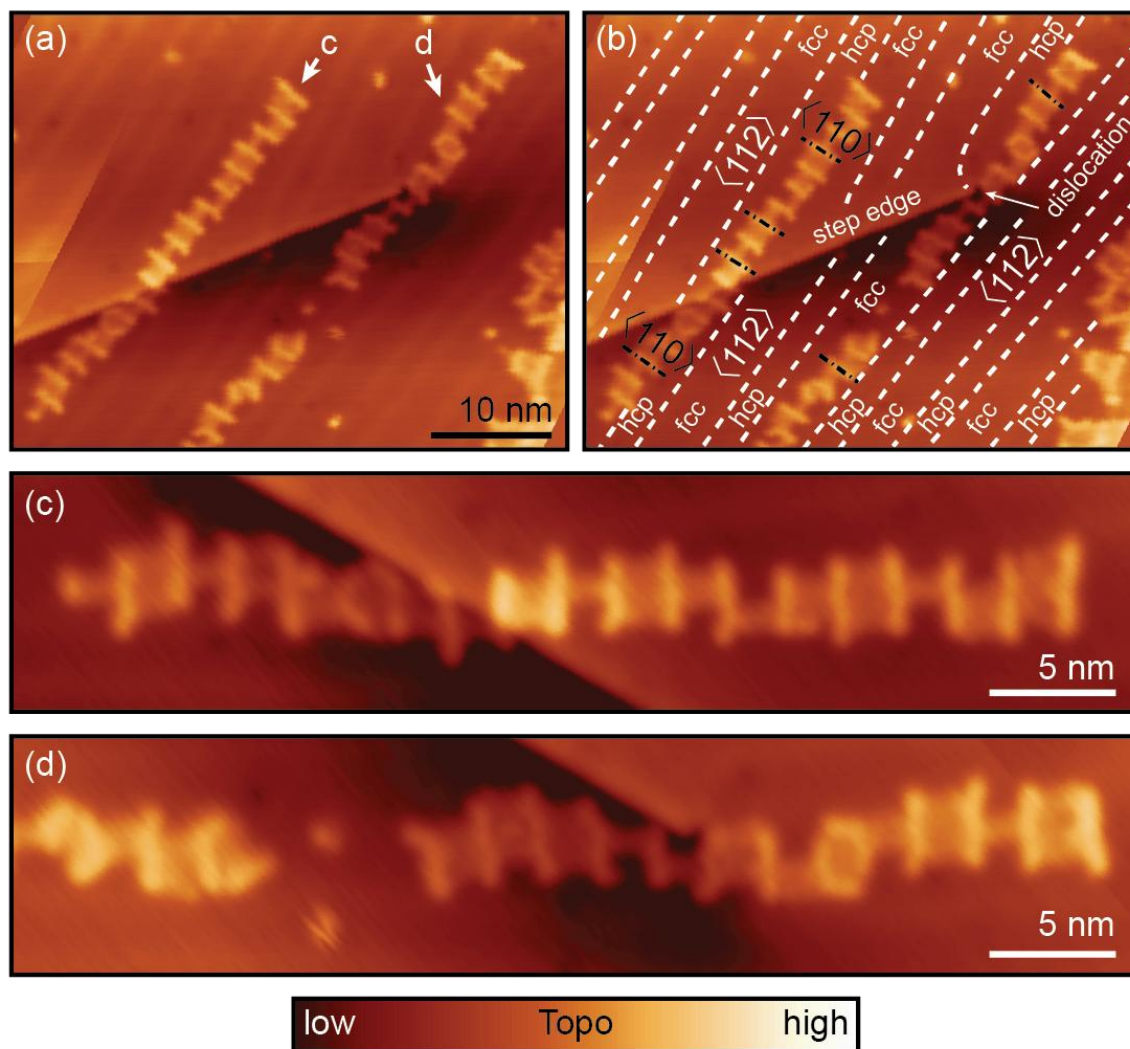


**Figure D3.** 7T molecular aggregates on Au(111). (a) STM image [set point 100 mV, 5 pA] of an aggregate of 7T molecules absorbed on the Au(111) surface. (b) STM image in (a) with indicated molecular orientations and Au(111) crystallographic directions and highlighted surface-reconstruction ridges. The oligothiophene backbones of 7T molecules are preferentially adsorbed in fcc regions of the Au(111) surface reconstruction and aligned along the  $\langle 110 \rangle$  directions of the Au(111) surface, perpendicular to the straight sections of surface reconstruction ridges, which run parallel to the  $\langle 112 \rangle$  directions. (c) and (d) close-up STM topographies of molecular chains indicated in (a) showing chains extending over a Au(111) step.

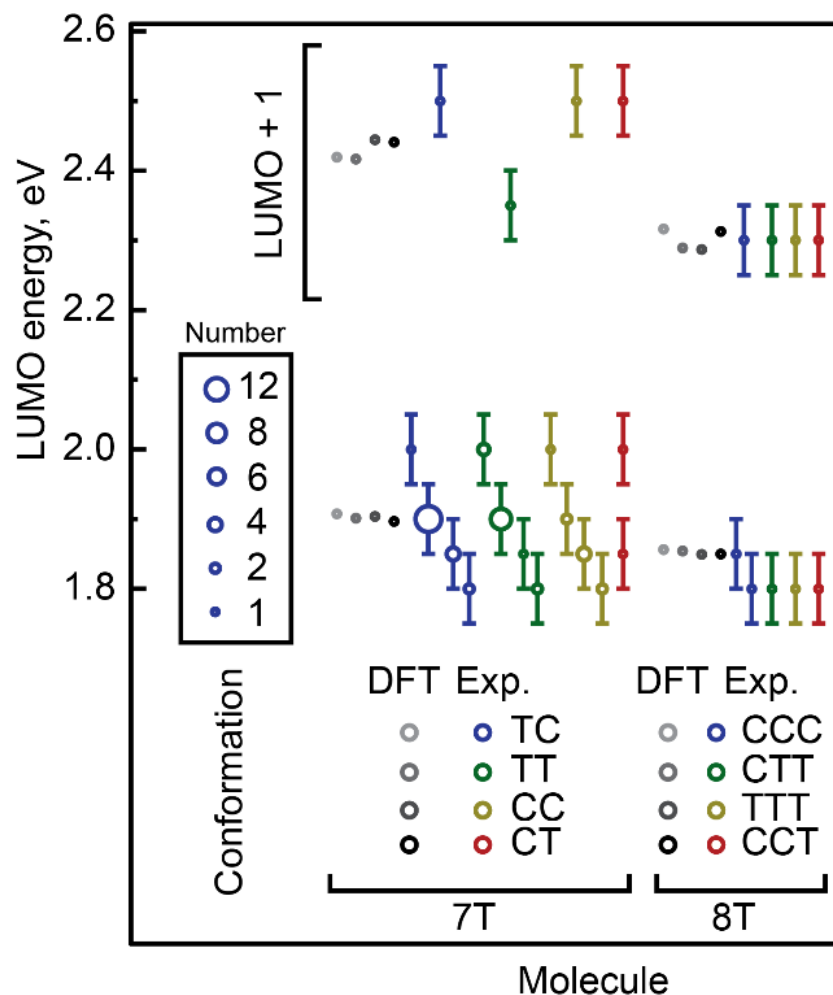


**Figure D4.** Distribution of LUMO and LUMO+1 energies of 7T and 8T acquired by STS. 5 8T molecules (2 CCC, 1 each of TTT, CCT and CTT) and 50 7T molecules (23 TC, 16 TT, 9 CC and 2 CT) were measured. Standard deviations for the 7T conformations are 0.031 eV (TC), 0.038 eV (TT), 0.051 eV (CC) and 0.117 eV (CT). DFT results are presented for comparison.

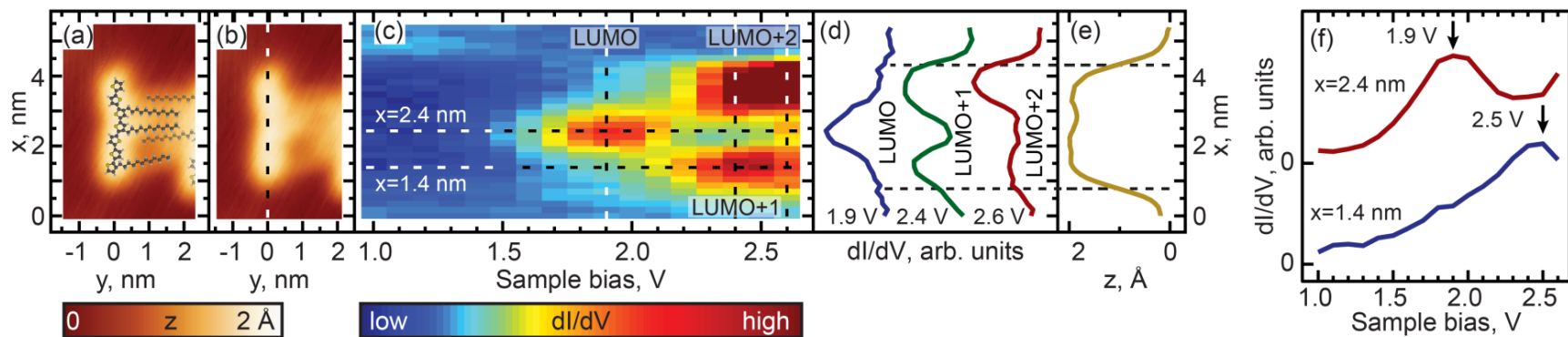


**Figure D5.** Same as Figure 6.3 for a CC conformer of 7T molecules. (a) STM image with an overlaid atomic model of the CCC-7T molecule. (b) STM image from (a) showing the path of mapping (dashed line). (c) DOS as a function of the bias voltage and position  $x$  along the path shown in (b). (d) LUMO, LUMO+1 and LUMO+2 DOS along the path shown in (b), obtained at voltages corresponding to the vertical dashed lines in (c). These voltages were chosen to maximize the contributions of the corresponding individual orbitals. Curves are shifted and normalized for clarity. (e) Backbone profile ( $z$  height vs.  $x$  coordinate) along the dashed line from (b). (f) Individual STS spectra from (c) measured at  $x=2.1$  and  $2.7$  nm as indicated by horizontal lines in (c). Spectra are shifted for clarity. The LUMO state manifests itself as a peak at  $1.85$  V in the spectrum measured at  $x=2.7$  nm, while LUMO+1 is observed as a peak at  $2.3$  V in the spectrum measured at  $x=2.1$  nm. Only a shoulder of the LUMO+2 state is observed.

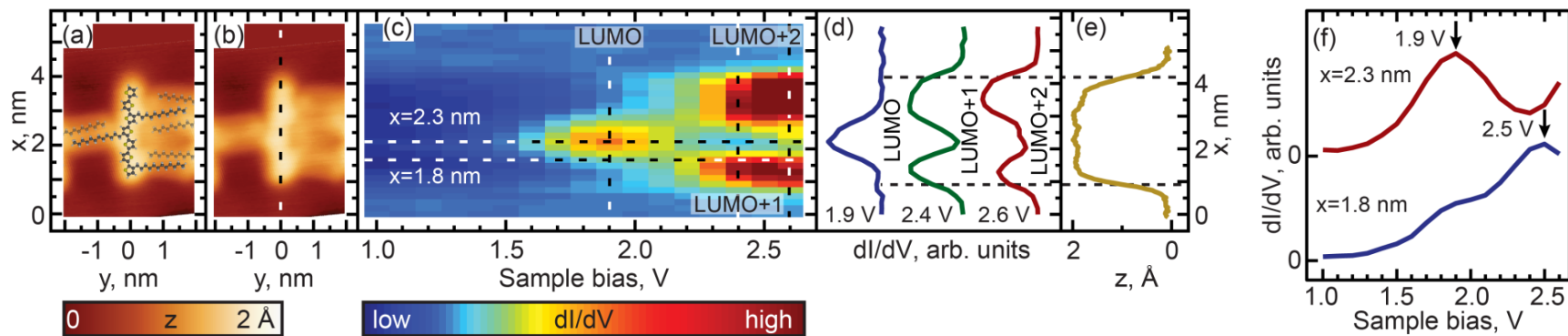


**Figure D6.** Same as Figure 6.3 for a TT conformer of 7T molecules.

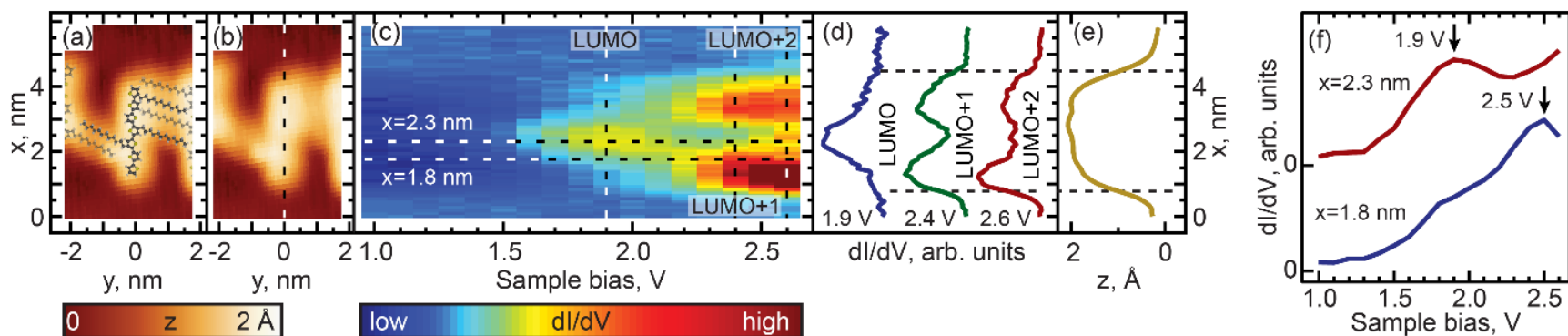


**Figure D7.** Same as Figure 6.3 for a TC conformer of 7T molecules.

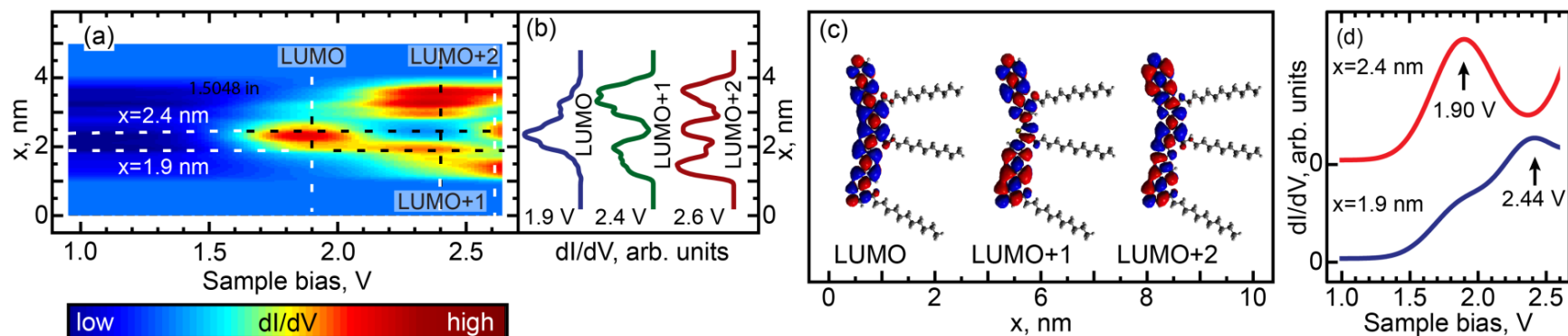


**Figure D8.** Calculated electronic DOS for a CC conformer of 7T molecules. (a) DOS (compare to Figure S3c) as a function of the bias voltage and position  $x$  along the path similar to that shown in Figure S3b. (b) LUMO, LUMO+1 and LUMO+2 DOS (compare to Figure S3d) along the same path as in (a), obtained at voltages corresponding to the vertical dashed lines in (a). These voltages were chosen to maximize the contributions of the corresponding individual orbitals. Curves are shifted and normalized for clarity. (c) Three-dimensional representations of DOS for LUMO, LUMO+1 and LUMO+2 showing the particle-in-a-box nature of these states. (d) Individual DOS spectra from (a) measured at spatial locations indicated by horizontal lines in (a). Spectra are shifted for clarity. The LUMO state manifests itself as a peak at 1.9 V (top curve), while LUMO+1 is observed as a peak at 2.3 V (bottom curve). Electronic structure calculations were performed with density functional theory (DFT) calculations using B3LYP/6-31G\*.

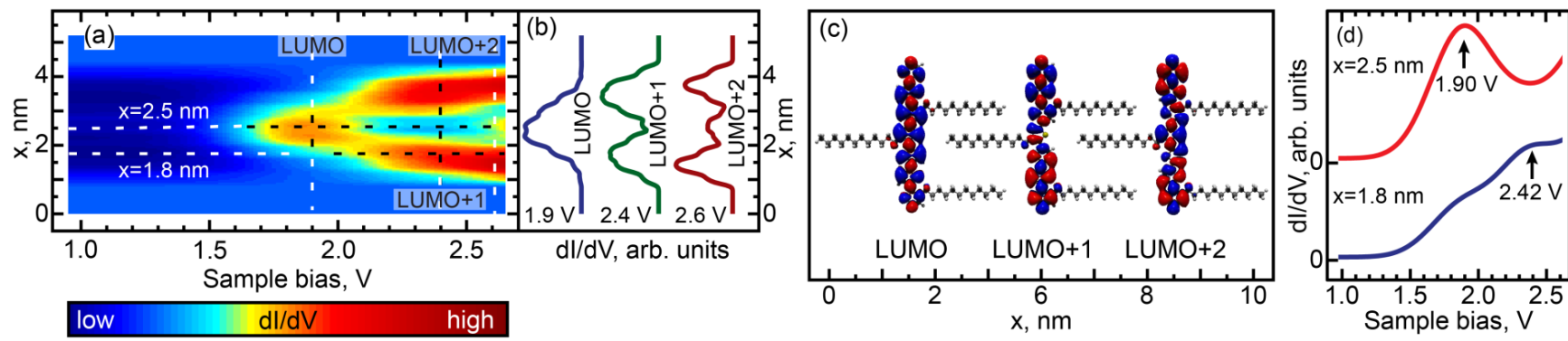


**Figure D9.** Same as Figure S8 for a TT conformer of 7T molecules.

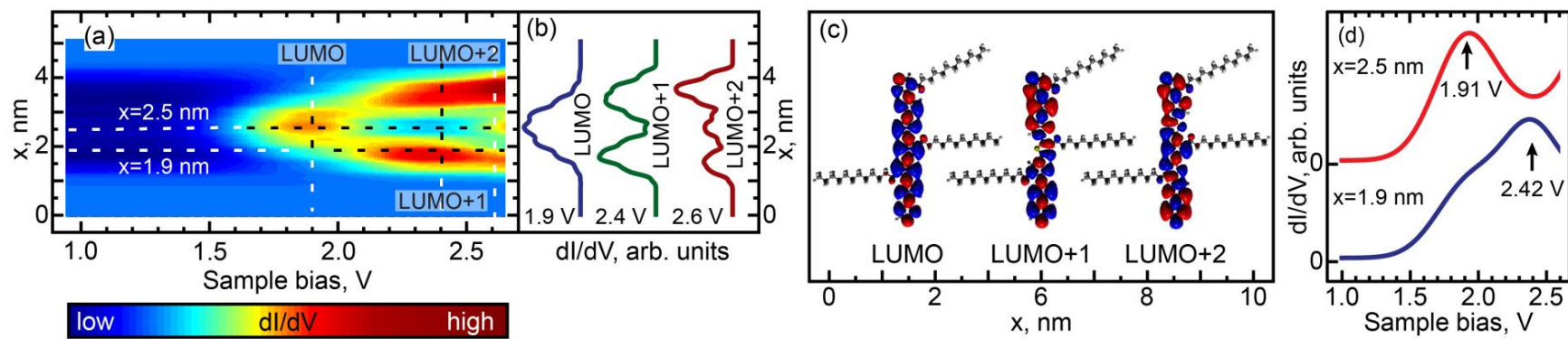


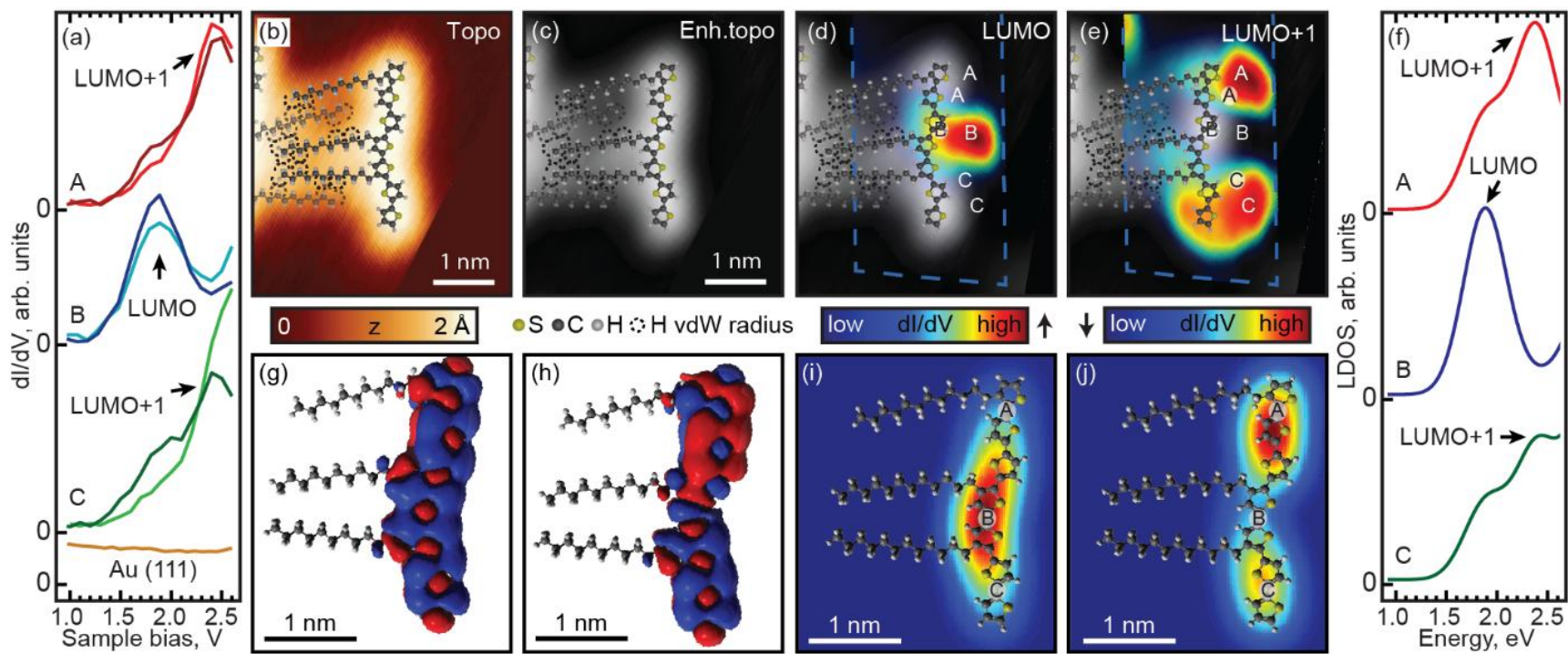
**Figure D10.** Same as Figure S8 for a TC conformer of 7T molecules.

## APPENDIX E

### SUPPORTING INFORMATION TO CHAPTER VII

---

**Figure E1.** Molecular orbitals for a straight 7T conformer. (a) DOS spectra measured on the straight 7T molecule in the locations indicated in (d-e) and DOS spectrum of the gold substrate. (b) STM image of the molecule. (c) STM image from (b) processed to “sharpen” the topographic features. (d) DOS for the LUMO orbital overlaid on image from (c). Mapped area is confined within the dashed lines. Areas with low DOS intensity (near-background) were rendered transparent to show registry with topography. (e) Same as (d) for the LUMO+1 orbital. (f) Individual DOS spectra calculated at spatial locations A, B, and C in (i) and (j). Spectra are shifted for clarity. (g-h) Theoretically calculated wavefunctions of LUMO and LUMO+1 showing the particle-in-a-box nature of these states (no nodes for LUMO, one node for LUMO+1). (i-j) Theoretically calculated DOS maps of LUMO and LUMO+1, exhibiting similar behavior to (d) and (e), respectively. For details of theoretical calculations, see Expanded Experimental Details above.





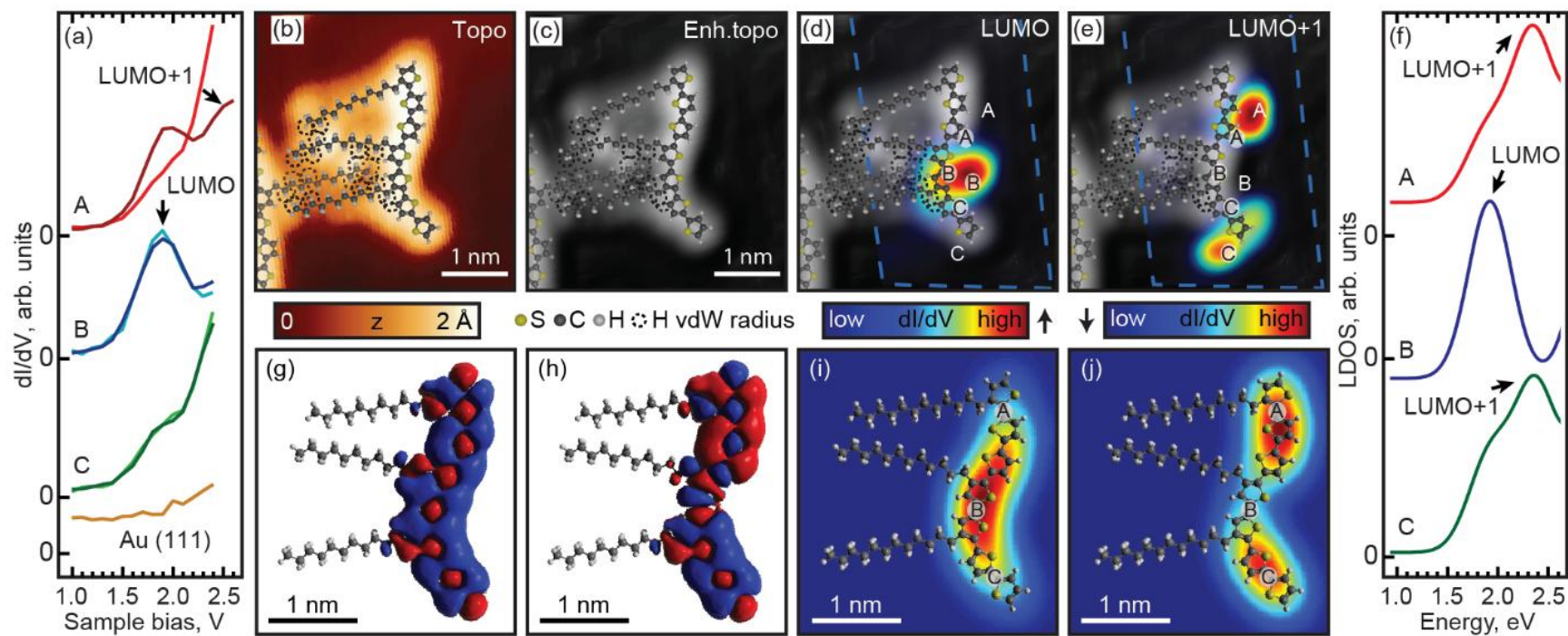


**Figure E2.** Molecular orbitals for a kinked 7T conformer. Data arrangement and makings are identical to those used in Figure E1.

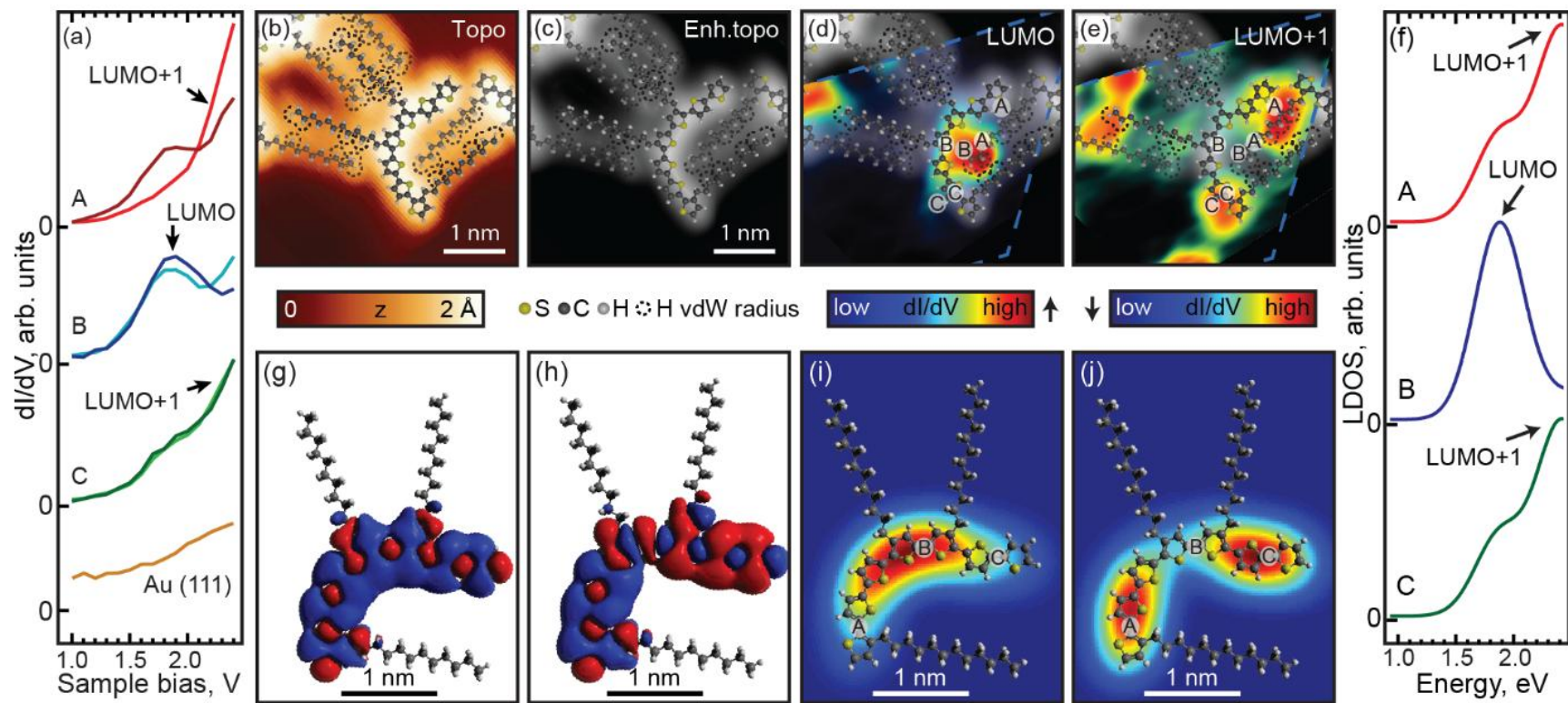


**Figure E3.** Molecular orbitals for an L-shaped 7T conformer. Data arrangement and makings are identical to those used in Figure E1.

## APPENDIX F

### SUPPORTING INFORMATION TO CHAPTER VIII

#### NC Crystallographic Orientation

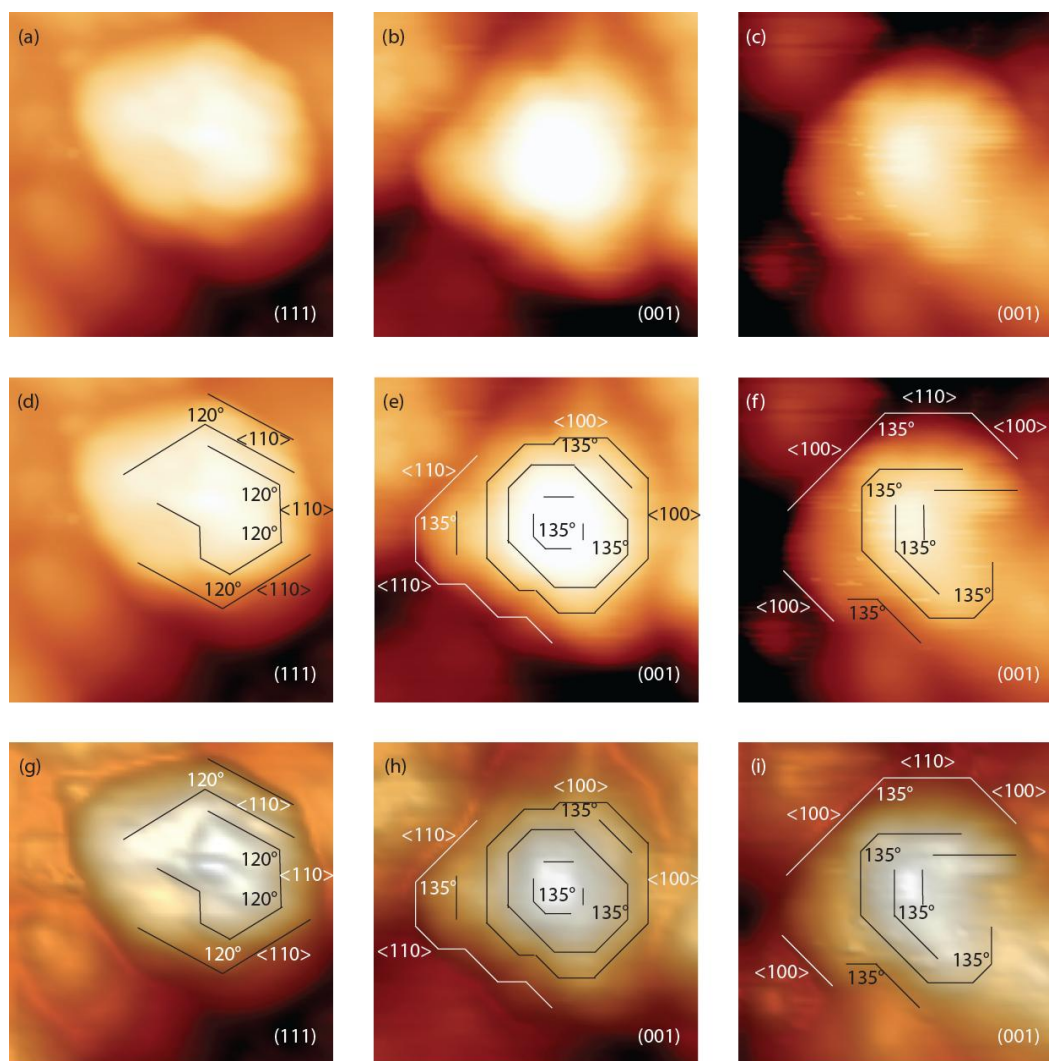


**Figure F1.** STM topographic images showing crystallographic features for three PbS NCs. (a), (b), (c) Topographies for three representative NCs. (d), (e), (f) NC topographies, [same as in (a), (b), and (c) respectively] with lines and relative angles indicating orientations of crystallographic features for each NC. The observed angles suggest that the top NC facets corresponds to crystal planes (111), (100), and (100) respectively. (g), (h), (i) Enhanced topographic images [for the same NCs] with same crystallographic markings as in (d), (e) and (f).

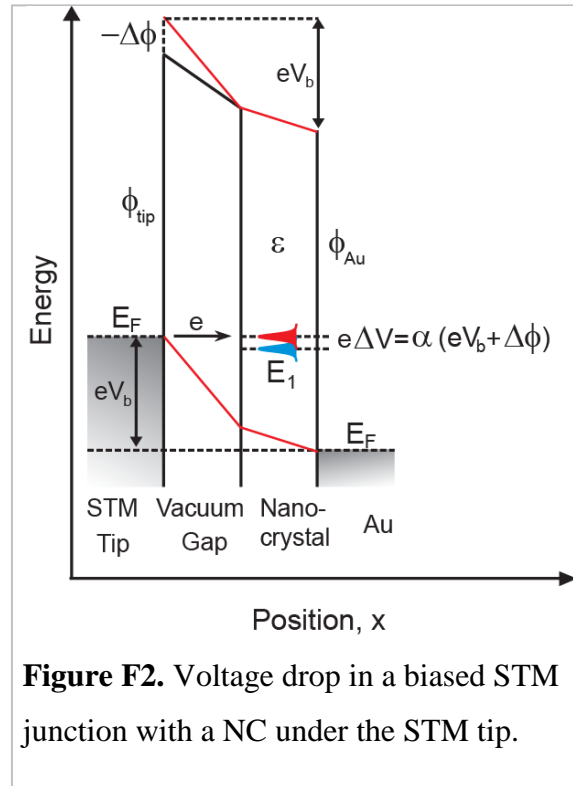
## NC Band Bending

Mismatch of workfunctions in the tip  $\phi_{tip}$  and substrate  $\phi_{Au}$ , together with the finite voltage drop  $\Delta V$  inside the NC, lead to a shift of electronic state  $E_1$  by  $e\Delta V = \alpha(eV_b + \Delta\phi)$ , where  $V_b$  is the applied bias voltage,  $\Delta\phi = \phi_{tip} - \phi_{Au}$ , and  $e$  is the electron charge. Parameter  $\alpha$  thus relates the average potential inside the nanocrystal to the external potentials applied across the tunneling gap. Therefore, states  $E_1$  (unoccupied) and  $H_1$  (occupied) are observed at voltages  $V_E$  and  $V_H$  that are defined by the following equations:<sup>3, 10</sup>

$$eV_E = \frac{E_1 + \alpha\Delta\phi}{1 - \alpha}$$

$$eV_H = \frac{H_1 + \alpha\Delta\phi}{1 - \alpha}$$

Where  $E_1$  and  $H_1$  are the true energies of states  $E_1$  and  $H_1$  with respect to the substrate Fermi level. Voltages  $V_E$  and  $V_H$  are determined directly from the STS spectra. Observations of “reverse” tunneling spectral features<sup>3, 11</sup> analogous to  $H^{**}$  lead to typical values of  $\alpha$  on the scale of a few percent.



The changes in voltages  $V_E$  and  $V_H$  observed in Figure 8.3b of the main text are caused by the fact that  $\alpha$  depends on the relative distance between the tip apex and the “centers of gravity” of states  $E_1$  and  $H_1$ . Factor  $\alpha$  is higher at the periphery of  $NC_1$ , as compared to the center of  $NC_1$ 's top facet because in the former case the tip is located

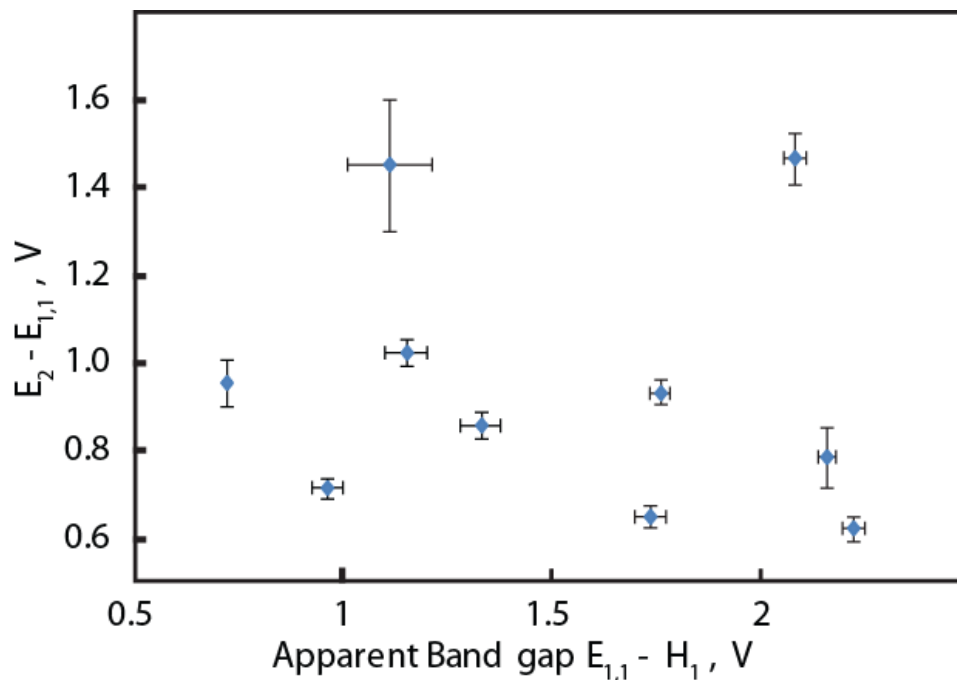


**Figure F3.** Plot of the energy difference between the  $E_2$  and  $E_{1,1}$  states vs. the energy difference between the  $E_{1,1}$  and  $H_1$  states for 10 measured NCs. During this experiment, many of the measured NCs did not exhibit clearly-defined  $H_1$  or  $E_2$  states, and thus were not included here.

closer to the Au surface, which results in a larger electric field inside the NC, leading to higher effective voltage drop inside the NC. Without the  $\Delta\phi$  term, this effect would lead to “curving” of  $V_E$  and  $V_H$  trajectories away from axis  $V = 0$  in Figure 8.3b, as observed for  $V_H$ . In the present case, however,  $\Delta\phi$  is nonzero and negative. This reinforces the “curving” trend observed for  $V_H$ , but counteracts the “curving” of  $V_E$ .

### **PbS nanocrystal synthesis**

Synthesis of PbS NCs was performed following a modified procedure from Hines and Scholes.<sup>12, 13</sup> Lead oxide (PbO, 99.0%), oleic acid (OA, technical grade 90%), 1-octadecene (ODE, technical grade 90%, pumped on at 80° C for 8 hours), toluene (99.8%, anhydrous), pentane (anhydrous), methanol (anhydrous), pentanethiol (98%),

and pentanedithiol (96%) were purchased from Sigma-Aldrich and used as received unless otherwise stated. Bis(trimethylsilyl)sulfide ((TMS)<sub>2</sub>S, synthesis grade) was purchased from Gelest.

All syntheses were conducted using standard Schlenk techniques. In a typical synthesis, 4 mL of ODE and 4 mL of OA were combined with 0.30 g of PbO (1.3 mmol). The mixture was heated, with stirring, to 100° C for 30 minutes, then heated to the injection temperature of 105° C for at least 30 minutes, all under vacuum. A sulfur precursor solution containing 0.167 mL (0.8 mmol) of (TMS)<sub>2</sub>S in 4 mL of ODE was prepared in a glovebox under nitrogen atmosphere. The sulfur precursor solution was quickly injected into the flask and held at 95° C for 1 minute, then cooled to room temperature in an ice bath. Removal of excess ligand and 1-octadecene was completed by repeated precipitation in acetone, centrifugation of the particles, and dispersion in small amounts of toluene. Finally, the NC dispersion was filtered through a 0.2 μm syringe filter to remove any insoluble material.

Prior to using PbS NCs in STS experiments, a ligand exchange was performed using a combination of pentanethiol and pentanedithiol in an effort to improve NC adhesion to the gold substrate and remove highly insulating OA ligands. In a typical ligand exchange procedure 0.3 mL of stock solution of PbS NC (15 mg/mL in toluene) was diluted with 5 mL of pentane in a centrifuge tube with an air-tight lid with septum. Several drops of pentanethiol stock solution (9:1 pentanethiol:pentanedithiol, total concentration 0.15 M in pentane) were added via syringe and then mixed. Pentanethiol capped PbS NCs were precipitated from pentane using methanol and centrifuged at 3500 rpm. Following removal of the supernatant, NCs were redispersed in

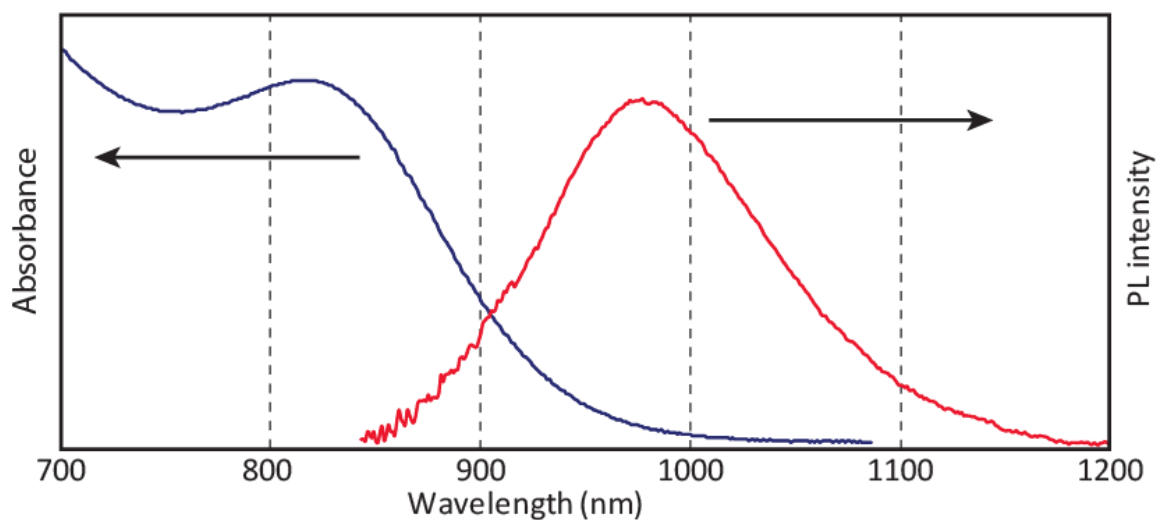


**Figure F4.** Absorbance and PL spectra of PbS NCs following thiol-ligand exchange. The emission peak at 977 nm (1.27 eV) corresponds to an approximate diameter of 3.2 nm PbS NC.

toluene. This cleaning procedure was repeated two times. Finally, PbS NCs were dispersed in anhydrous pentane to produce a 0.9 mg/mL stock solution. The suspension was centrifuged to remove aggregates, and the remaining dispersed NCs were transferred to a clean tube under  $N_2$  for use in STM experiments.

## APPENDIX G

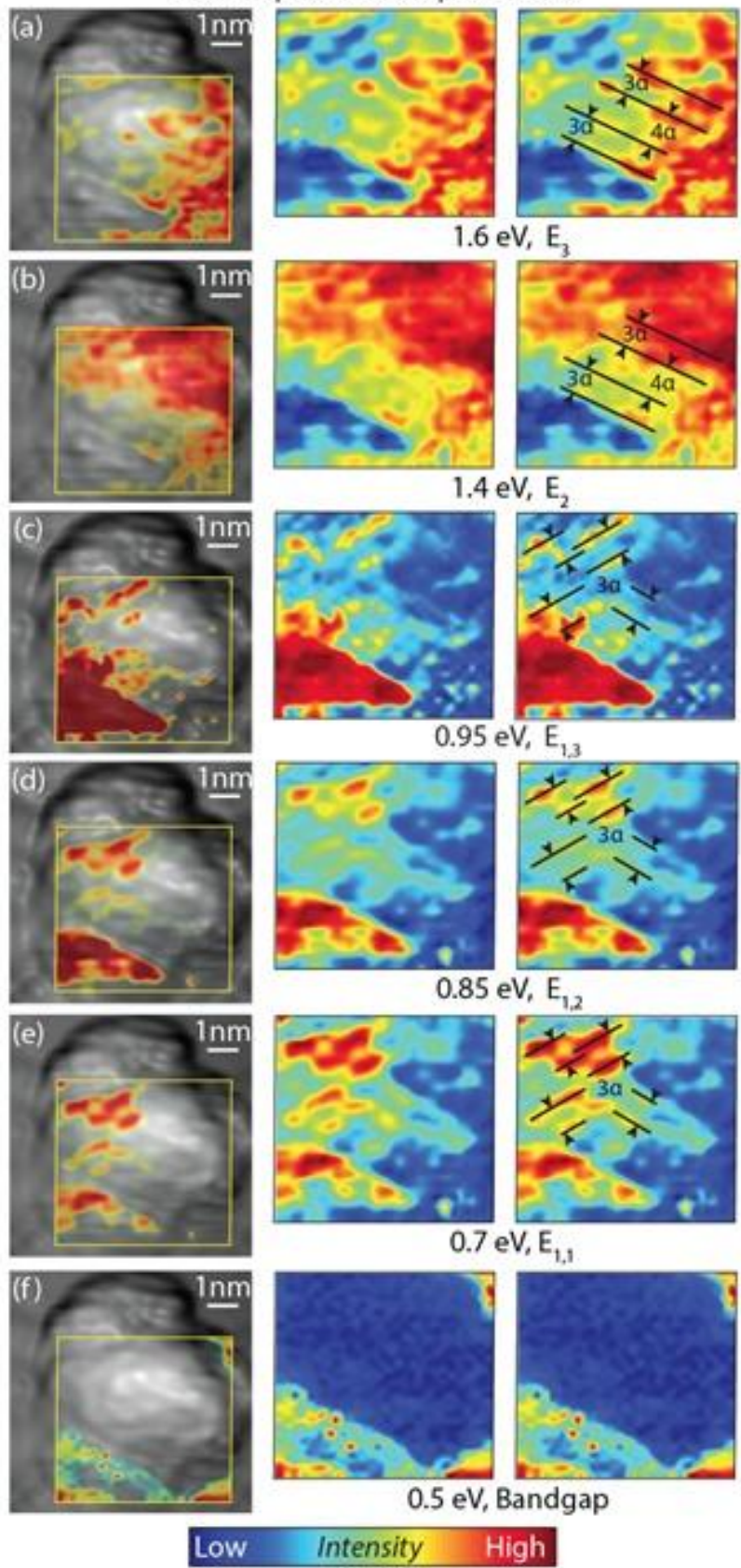
### SUPPORTING INFORMATION TO CHAPTER IX

---

**Figure G1.** Figure shows the prominent unoccupied states for NC1. Subfigures (a-f) include (from left to right) a combination of topography(grayscale), and DOS map(color) overlay (where the yellow outline encloses the area of DOS mapping), DOS map only, and DOS map with black lines showing DOS features that are in registry with NC1 crystallographic features from Figure 9.1g in the main text. Parameter  $\alpha$  is defined as the distance between two neighboring {211} planes, as shown in the model in Figures 9.6a and b in the main text. STS measurements taken with set-point 1.6 V bias, 30 pA tunnelling current. STM topography image measured with set-point 2.0 V bias, 2 pA tunneling current.



DOS maps of unoccupied states



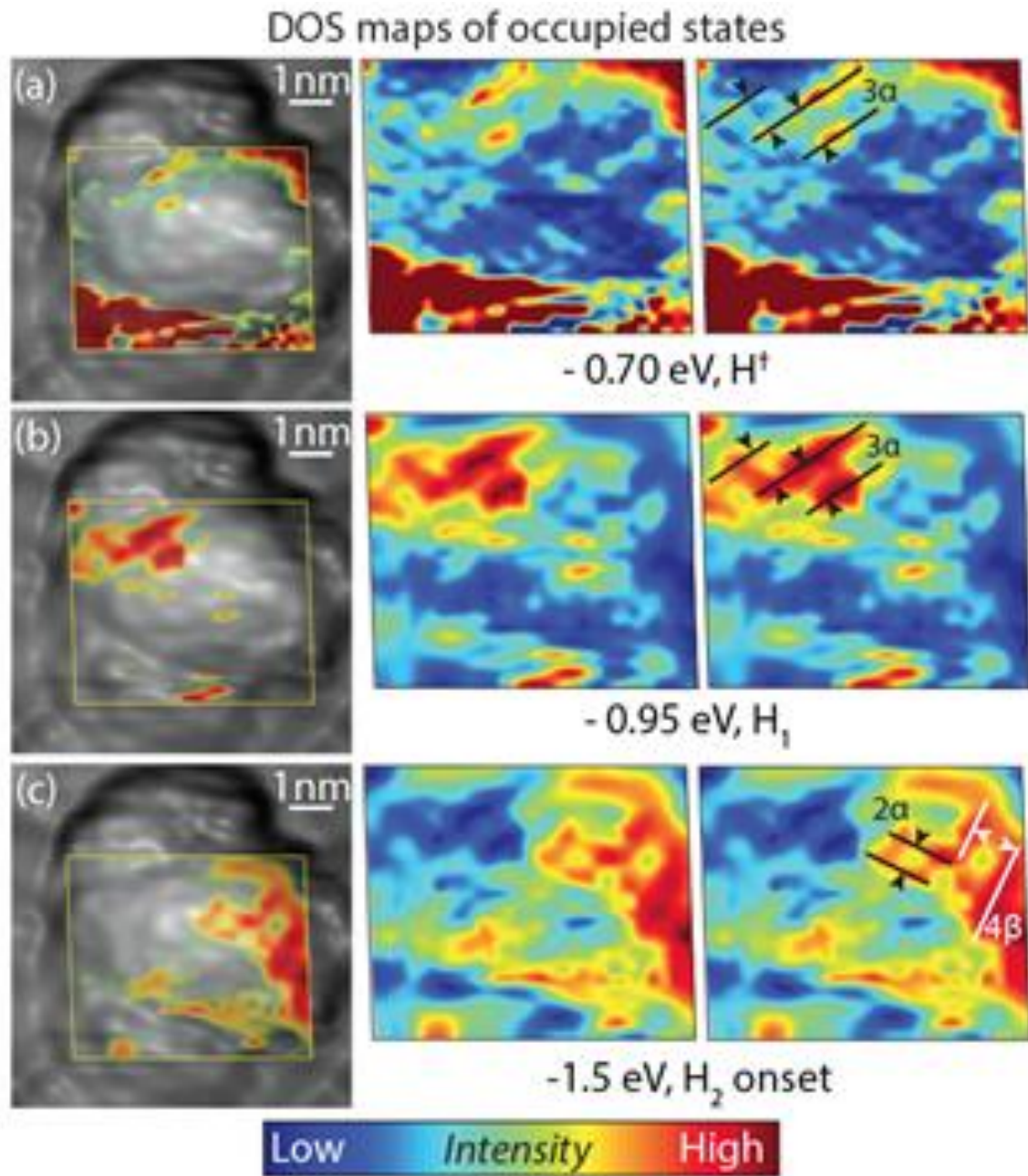


**Figure G2.** Figure shows the prominent occupied states for NC1. Same area and representation as Figure G1 for the occupied states of NC1. Parameter  $\beta$  is defined as the distance between two neighboring  $\{110\}$  planes, as shown in the model in Figures 9.6c and d in the main text. Set-points of STM topography image and STS maps same as in Figure G1.

### DOS maps of unoccupied states

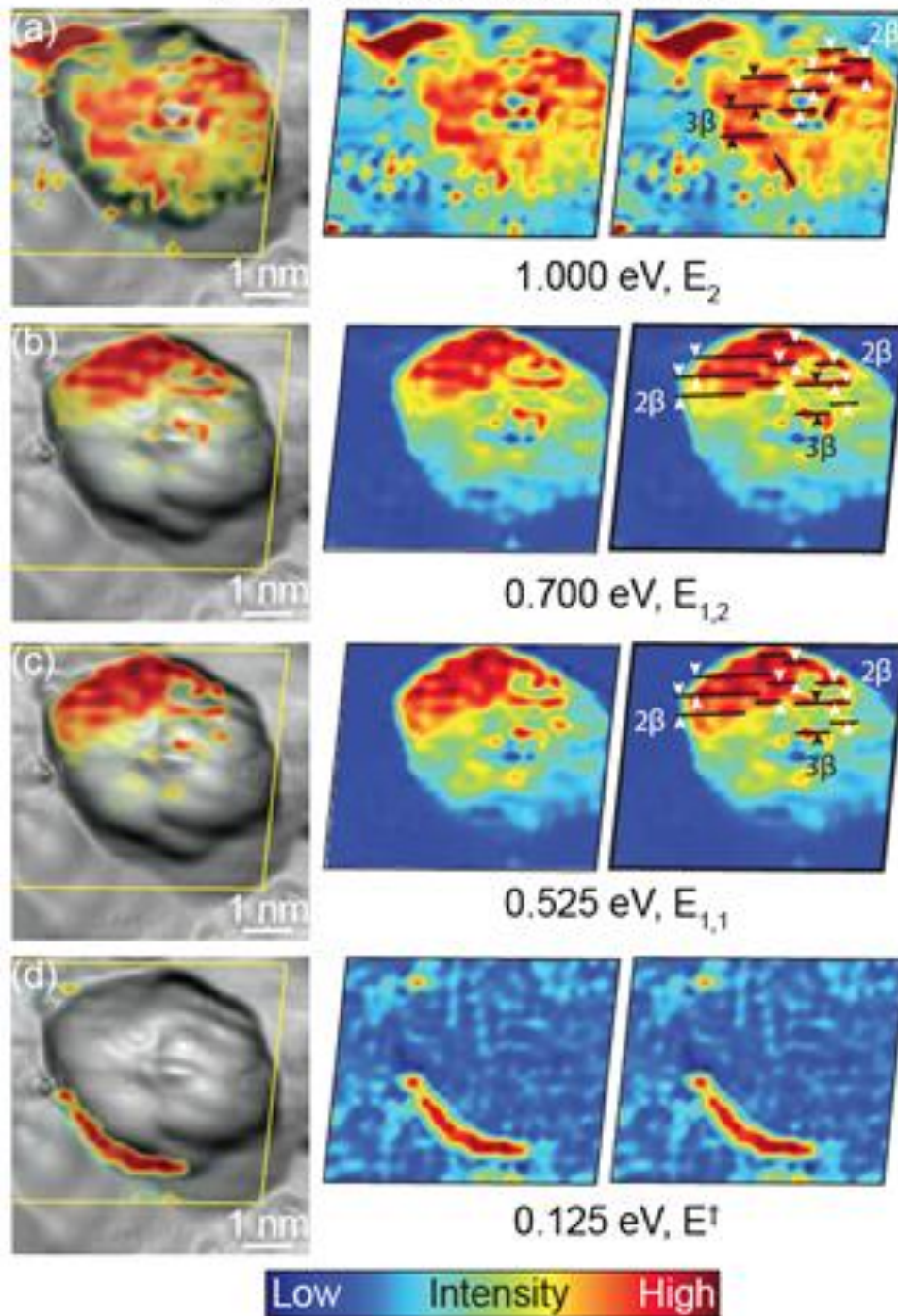


**Figure G3.** Figure shows the prominent unoccupied states of NC2. Same representation as in Figure G1 for NC1. Parameter  $\beta$  is defined as before for figure G2, and as shown in the model in Figures 9.6c and d in the main text. STM topography measured with set-point 2.0 V bias, 1 pA tunneling current. STS maps measured with set-point 1.5 V bias, 20 pA tunneling current.

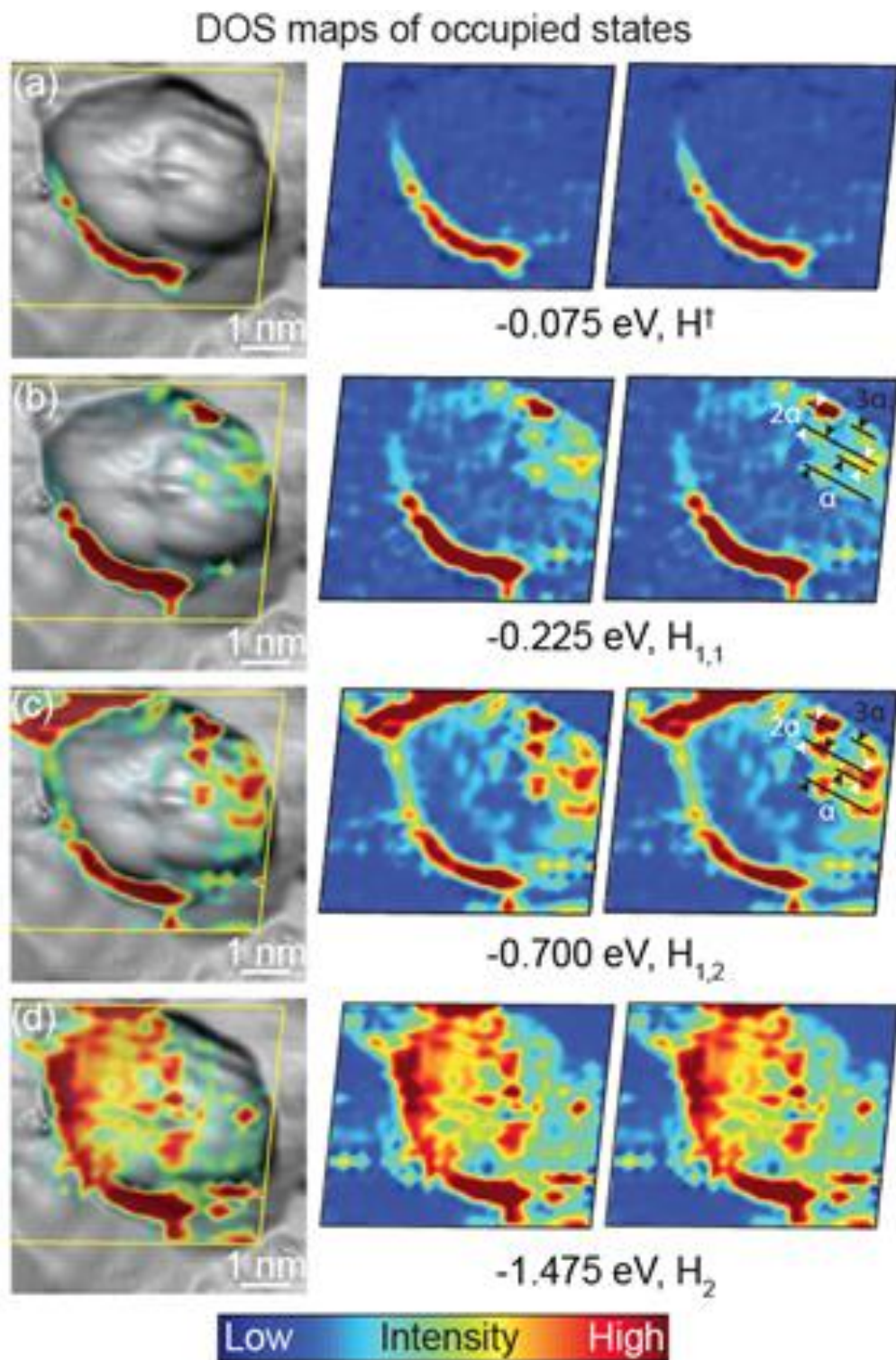
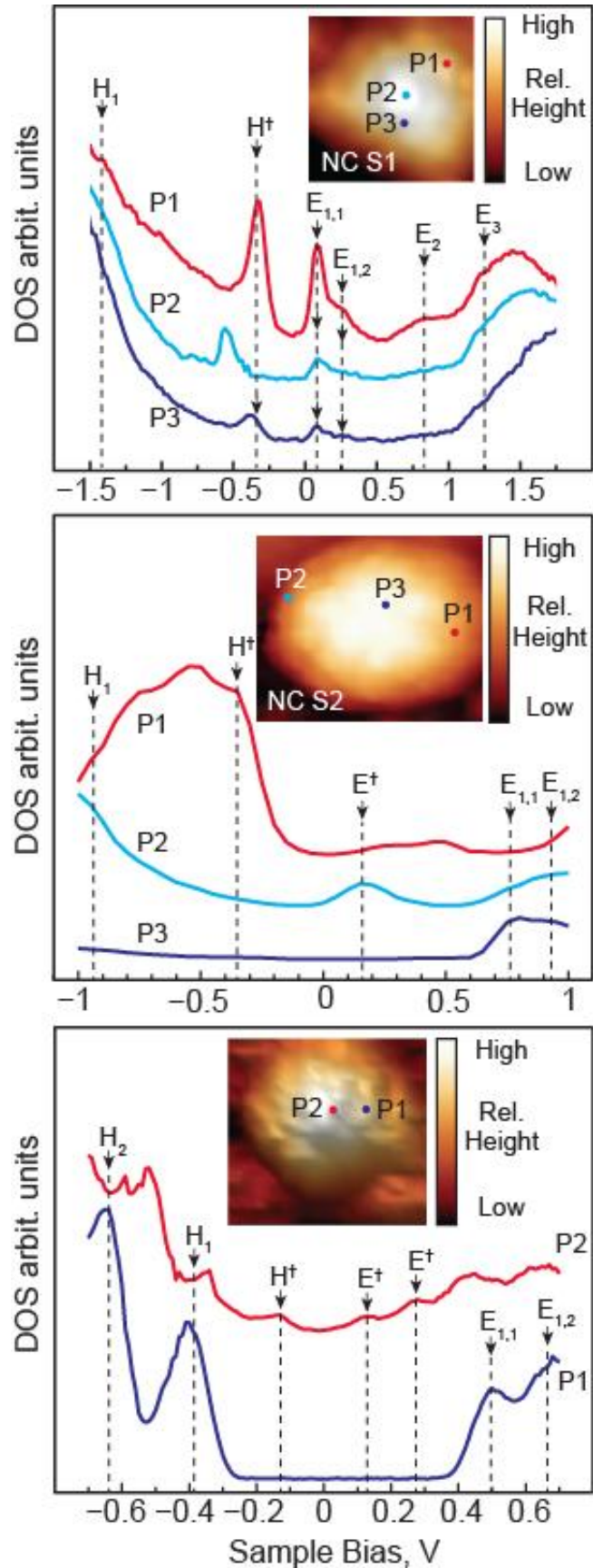


**Figure G4.** Figure shows the prominent occupied states of NC2. Same representation as in Figure G3 for NC2. Parameter  $\alpha$  is defined as the distance between two neighboring  $\{211\}$  planes, as shown in the model in Figures 9.6a and b in the main text. Set-points of STM topography image and STS maps same as in Figure G3.

**Figure G5.** (Right) Figure shows examples of PbS NCs displaying localized defect-related states in their DOS. Unoccupied  $E_{1,n}$  and occupied  $H_1$  states show marked intensity differences depending on location, and are associated with the reconstruction of polar PbS (111) surfaces or regions of marked non-stoichiometry in which excess S (Pb) atoms at the surface lead to sub-bandgap states broken off from the valence(conduction) bands. These observations are in keeping with and further support conclusions made with regard to the sub-bandgap states observed for NCs discussed in the main journal article.



Anti-correlation maps for  $H_{1,n}$  &  $E_{1,n}$  States of NC2

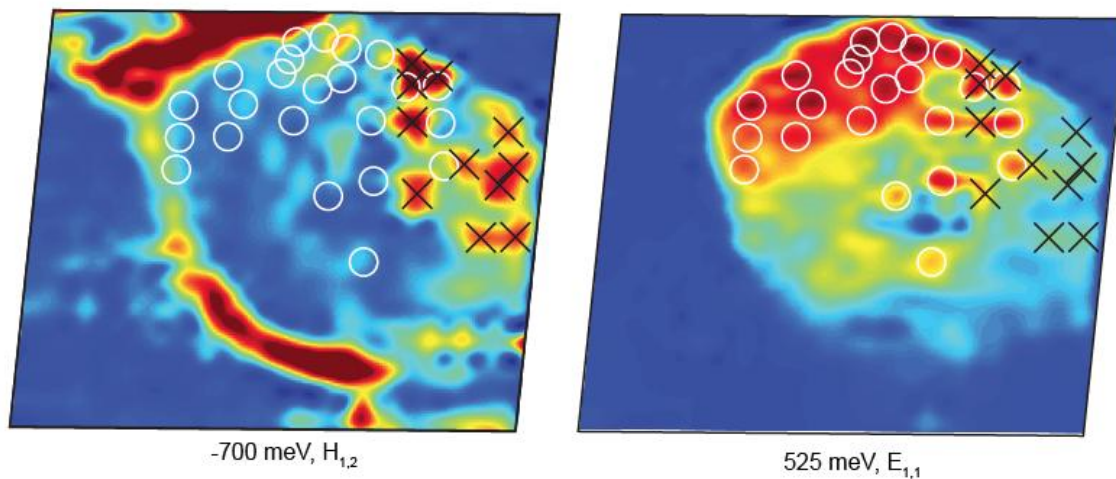
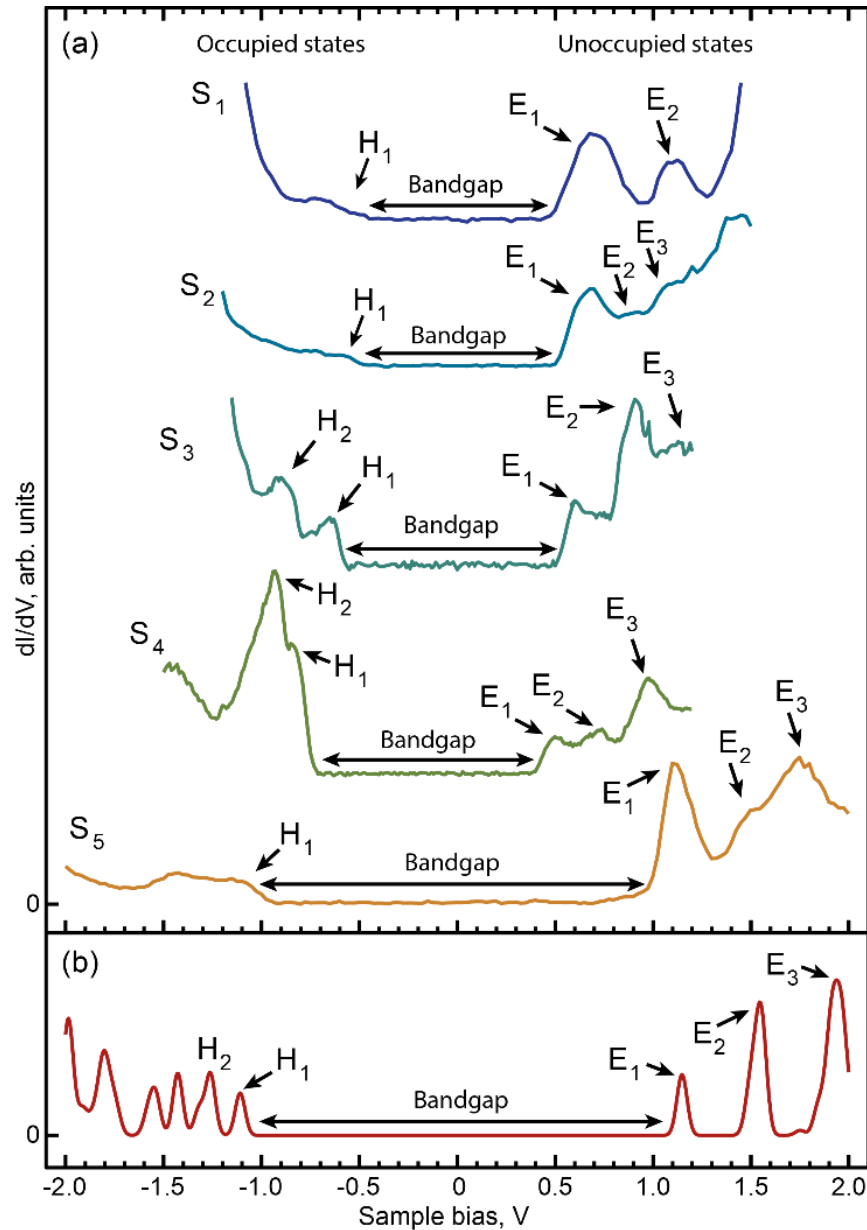


**Figure G6.** DOS maps for  $H_{1,n}$  and  $E_{1,n}$  states of NC2 showing anti-correlation in their spatial distributions. White circles (black x's) mark locations of local high intensity for states  $E_{1,n}$  ( $H_{1,n}$ )

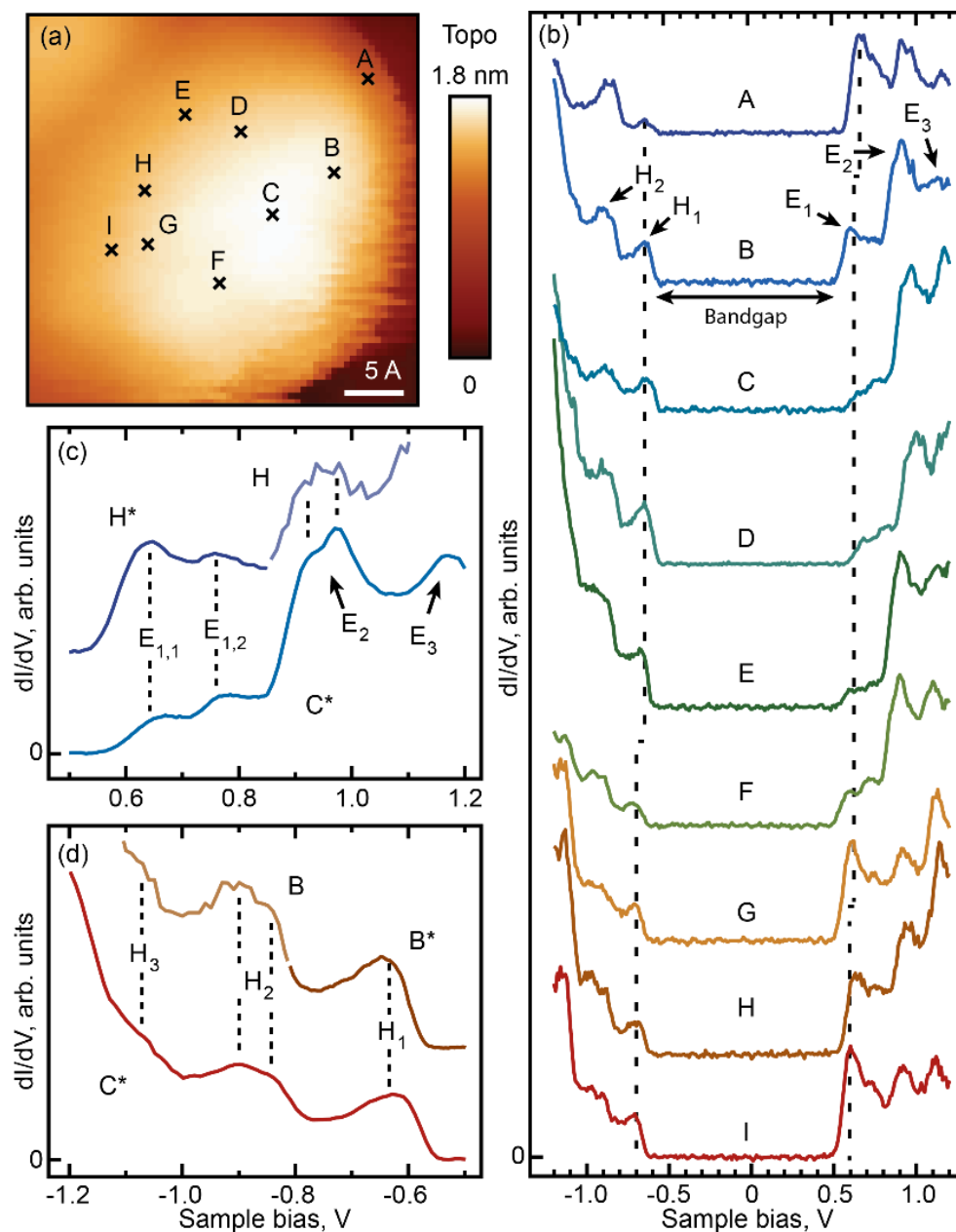
DOS intensity maps for the sub-bandgap states of NC2 (Figure G6), show that the locations of high intensity for states  $H_{1,n}$  in general correspond (on the atomic scale) to locations of low intensity for states  $E_{1,n}$ , and vice-versa suggesting that  $H_{1,n}$  and  $E_{1,n}$  patterns are carried by atoms corresponding to different elements. Theoretical calculations predict that  $H_{1,n}$  and  $E_{1,n}$  patterns result from non-stoichiometric surface S and Pb atoms respectively.<sup>14</sup>

## APPENDIX H

### SUPPORTING INFORMATION TO CHAPTER X

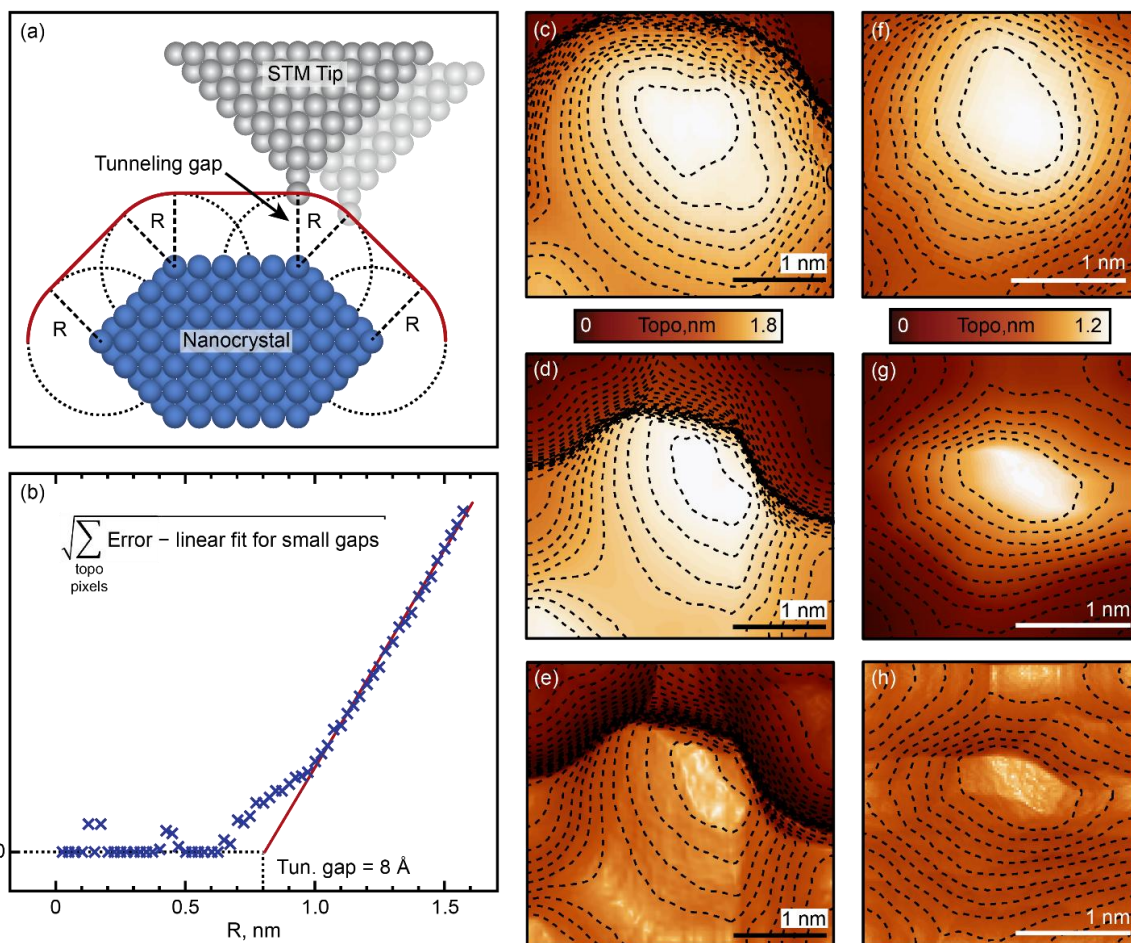


**Figure H1.** Scanning Tunneling Spectroscopy of SiNCs. (a) Representative DOS spectra for five different SiNCs (Set point voltages and currents range from 1.0 V to 1.5 V, and 5 pA to 10 pA for the spectra shown). (b) Calculated DOS for a model with size comparable to a NC featuring spectrum  $S_5$  from (a). Occupied and unoccupied states are indicated by arrows and marked with an 'H' and 'E' for holes and electrons respectively.



**Figure H2.** STM/STS characterization of NC<sub>1</sub>. (a) STM topography image of NC<sub>1</sub> [set point 1.2 V, 5.0 pA]. (b) STS spectra [set point 1.2 V, 10 pA] measured at the locations A-I marked in (a). Spectra are offset for clarity. Prominent occupied and unoccupied states are marked with an 'H' and 'E' respectively. Individual DOS peaks are observed at slightly different voltages across the NC due to the finite location-dependent voltage drop inside the NC. (c-d) Close-up of spectra from B, C and H locations showing finer structure (spectra marked “\*” were acquired with better signal-to-noise ratio by using longer acquisition times).

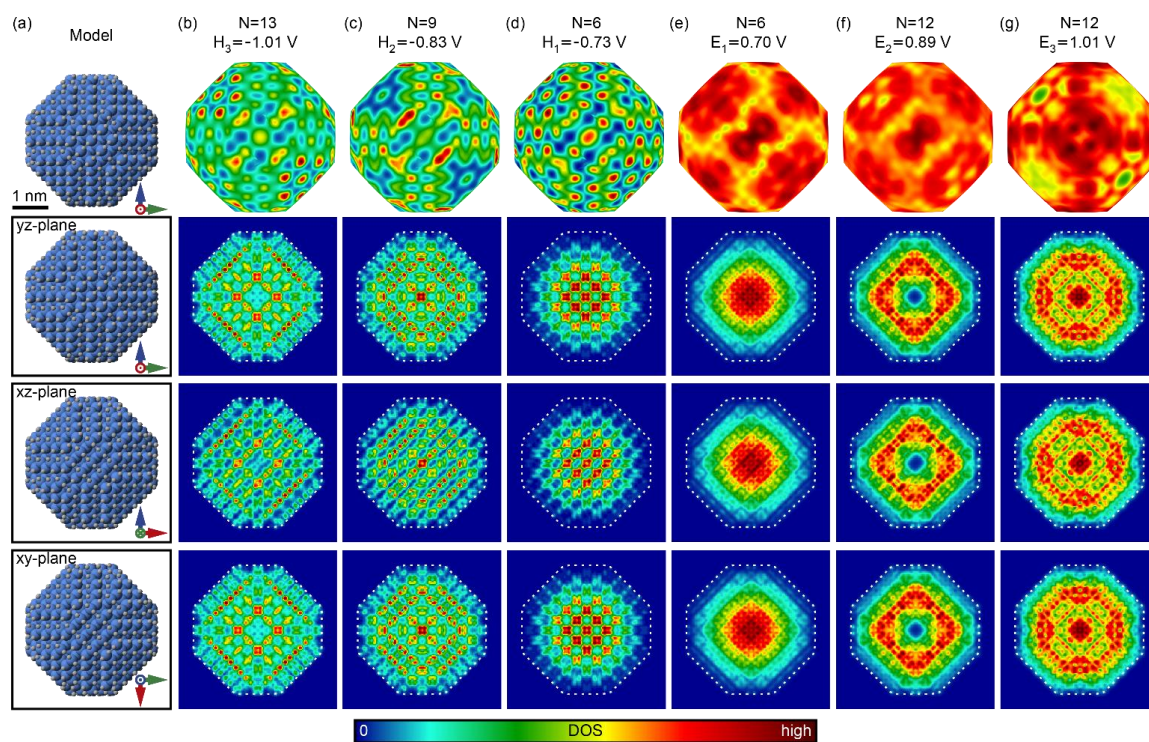




**Figure H3.** Reconstruction of the NC shape from STM topography. (a) Trajectory of a STM tip over a three-dimensional object when scanned in the “constant tunneling current” regime typically used for STM topography. Apparent object shape is enlarged and sharp features are rounded due to the finite tip-sample distance and the possibility to tunnel sideways. Additional broadening occurs, in a similar fashion, due to the finite dimensions of the tip apex. Both effects can be accounted for (in the first approximation) by assuming that the tunneling current only depends on the distance (defined in three dimensions) between the tip apex and object of interest. This is equivalent to assuming that the tip wavefunctions have an approximately s-orbital nature at the tip apex, a common approximation in theoretical calculations of STM images. If the tip-object separation  $R$  is known [see (a)], then a model of the actual object shape can be calculated by constructing a 3D surface that consists of points located at identical minimal distances  $R$  from the experimental topographical surface [see (a)].

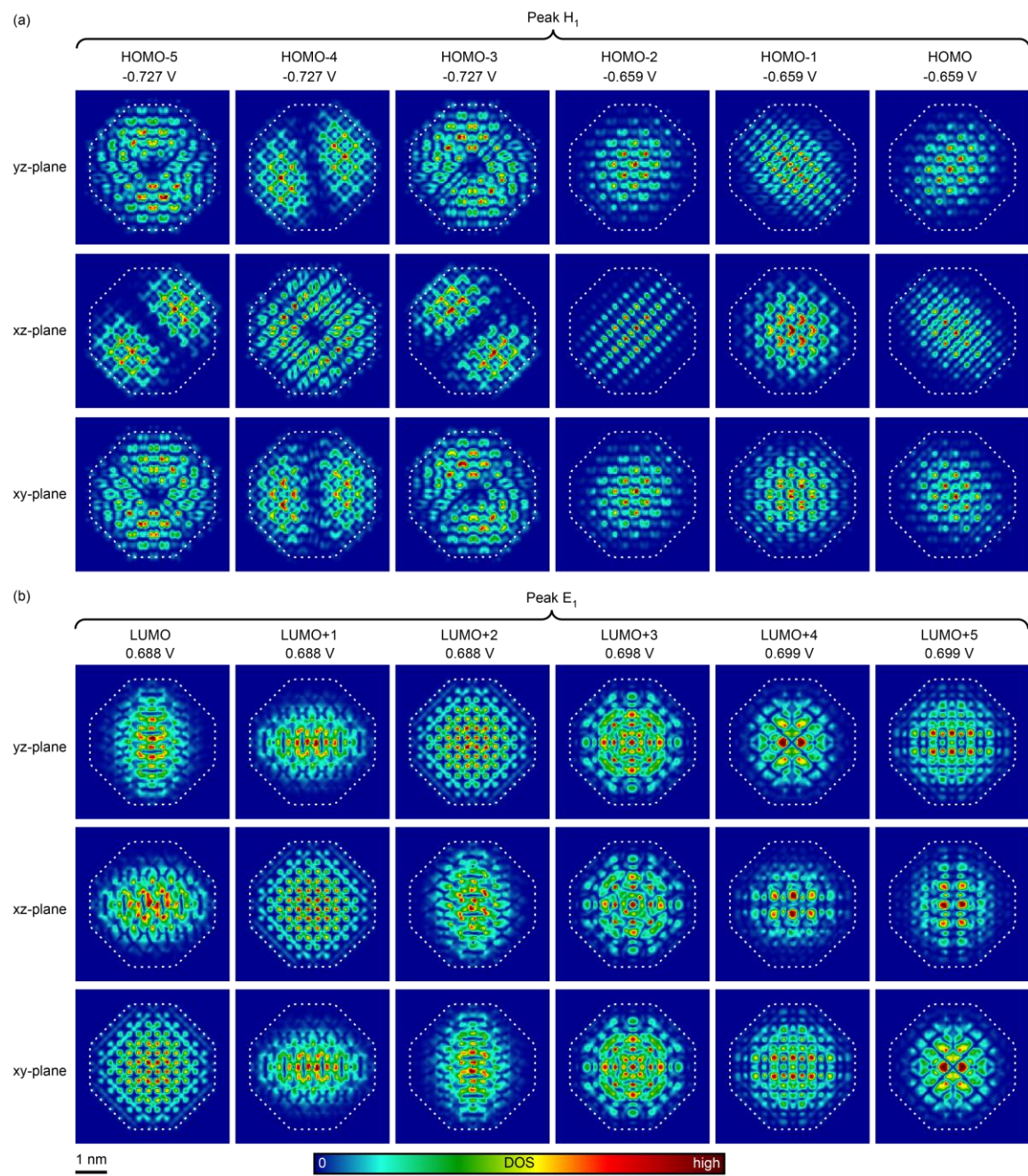
The calculation can also be reversed and a model of the STM topography can be recalculated from the calculated NC shape. The difference between the experimental STM topography and recalculated STM topography can be used as a measure of the accuracy of such a representation. The accuracy is affected by the noise in STM topography, and the value chosen as  $R$ . For example, if  $R$  is smaller than the characteristic dimensions of all features in the STM topography, the error is zero. If features with dimensions smaller than  $R$  are present in the STM topography, then they may not contribute to the model of real NC shape, and may be lost in the recalculated STM topography, thus adding to the error. This means that when  $R$  is smaller than the actual gap (usually on the scale of several angstroms), the error is mostly dominated by the topographic noise and atomic-scale features. However, once  $R$  exceeds the real tunneling gap (the latter defines the curvature of the features in STM topography), an additional component of the error, caused by the mismatch between the true and calculated NC shapes, becomes non-zero. It is easy to show that the dependence of this error component on  $R$  is quadratic. In order to find the best fit to the real effective gap, we calculated the described error using different values of  $R$ , and found that at small values of  $R$  (where noise dominates) the dependence is linear [see (b)]. By subtracting this component from the error and plotting its square root as a function of  $R$ , we found that at higher  $R$  the dependence is linear, in accordance with the geometric considerations. A linear fit to this function allows us to find the best approximation to true  $R$ , as shown in figure (b).

(c) Experimental STM topography of  $NC_1$  with its contour lines overlaid. (d) Calculated shape of the  $NC_1$  using  $R=0.8$  nm. Top facet of  $NC_1$  was found to be flat and almost horizontal. (e) Model of  $NC_1$  digitally processed to “sharpen” the features (pseudo-3D rendering). (f-h) Same as (c-e) for the  $NC_2$ .



**Figure H4.** Volume distribution of theoretical DOS for a model near-spherical (composition  $\text{H}_{412}\text{Si}_{1087}$ , diameter  $\sim 3.5$  nm) SiNC without impurities. (a) NC geometry. (b-g) DOS for the peaks from Figure 10.2c.  $N$  is the number of individual states comprising the peak. First row represents the normalized DOS maps on the surface (identical to Figure 10.2e-j). Second, third, and fourth rows show bulk unnormalized DOS distributions across the main coordinate planes going through the center of the SiNC. Each displayed DOS datapoint was averaged over a  $3.6 \text{ \AA}$ -long segment orthogonal to, and bisected by the corresponding plane.

**Figure H5.** Bulk cross-sections for individual orbitals of a model near-spherical (composition  $\text{H}_{412}\text{Si}_{1087}$ , diameter  $\sim 3.5$  nm) SiNC without impurities. Section planes and view angles are the same as in Figure H4. Each displayed DOS datapoint was averaged over a  $3.6 \text{ \AA}$ -long segment orthogonal to, and bisected by the corresponding plane. (a) Highest occupied molecular orbitals (HOMO). (b) Lowest unoccupied molecular orbitals (LUMO).



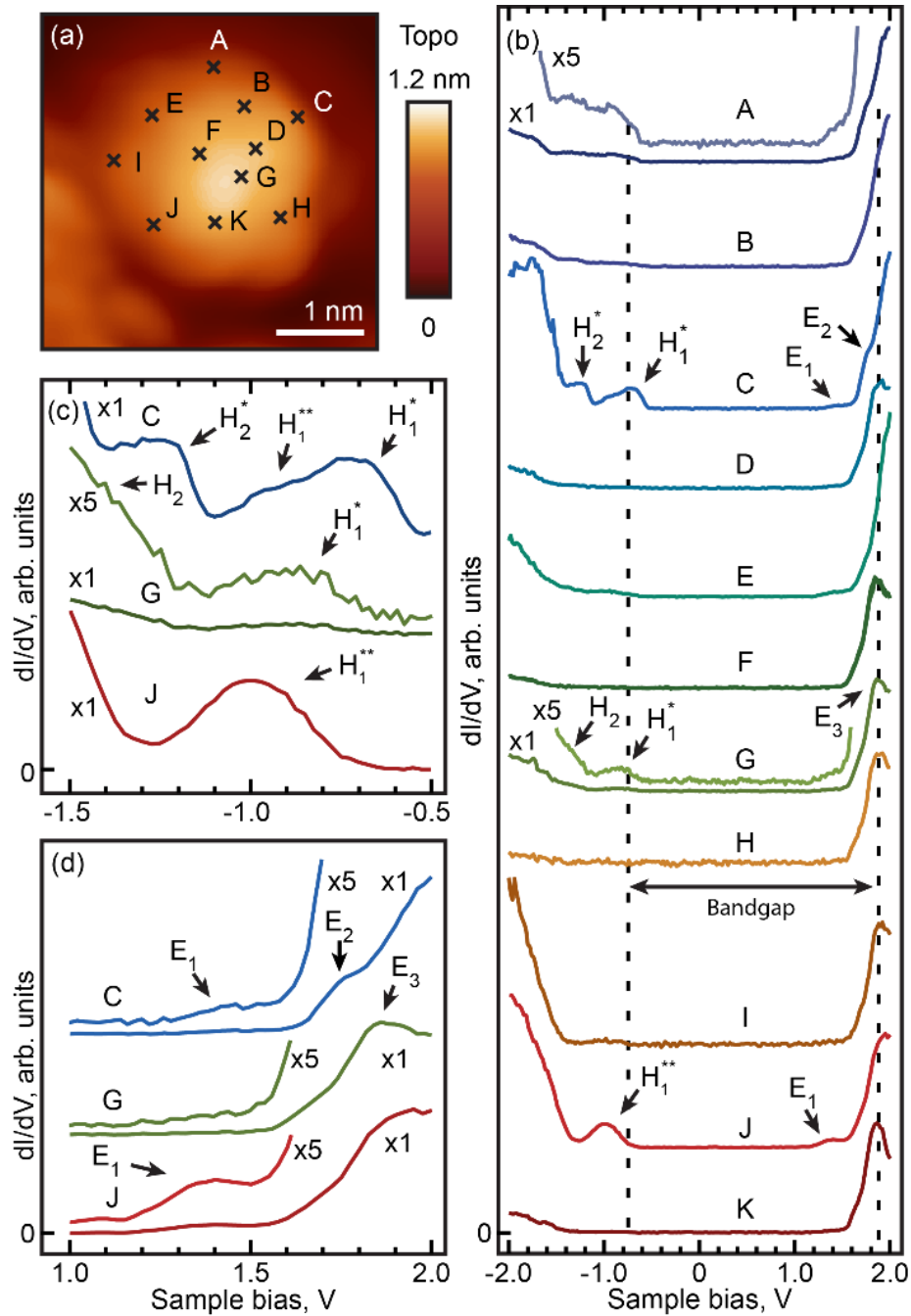
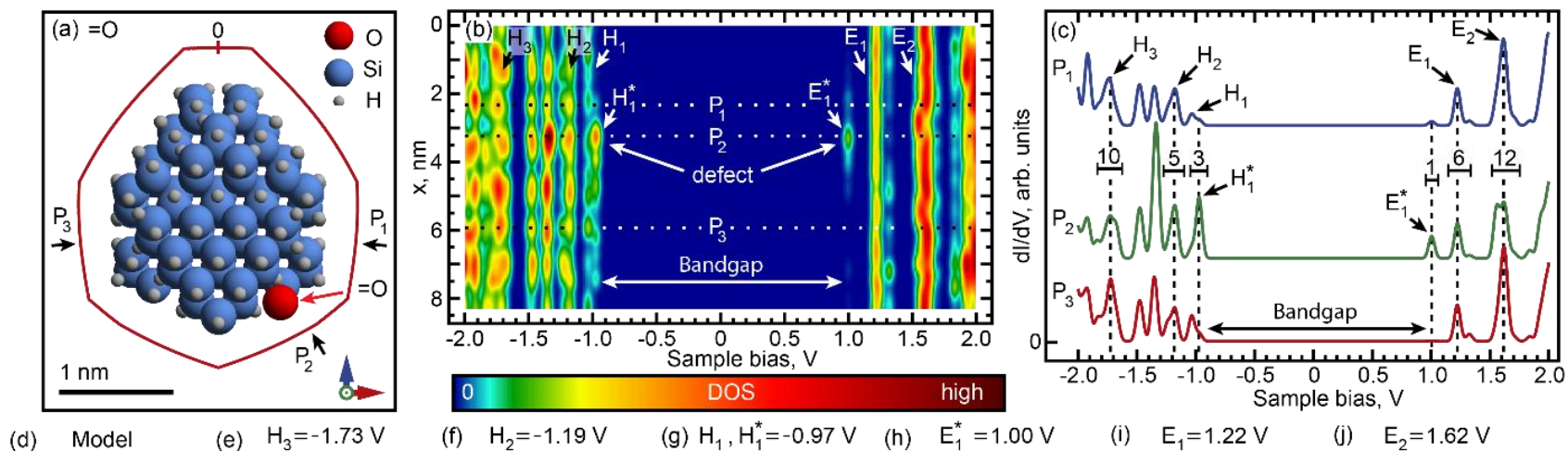


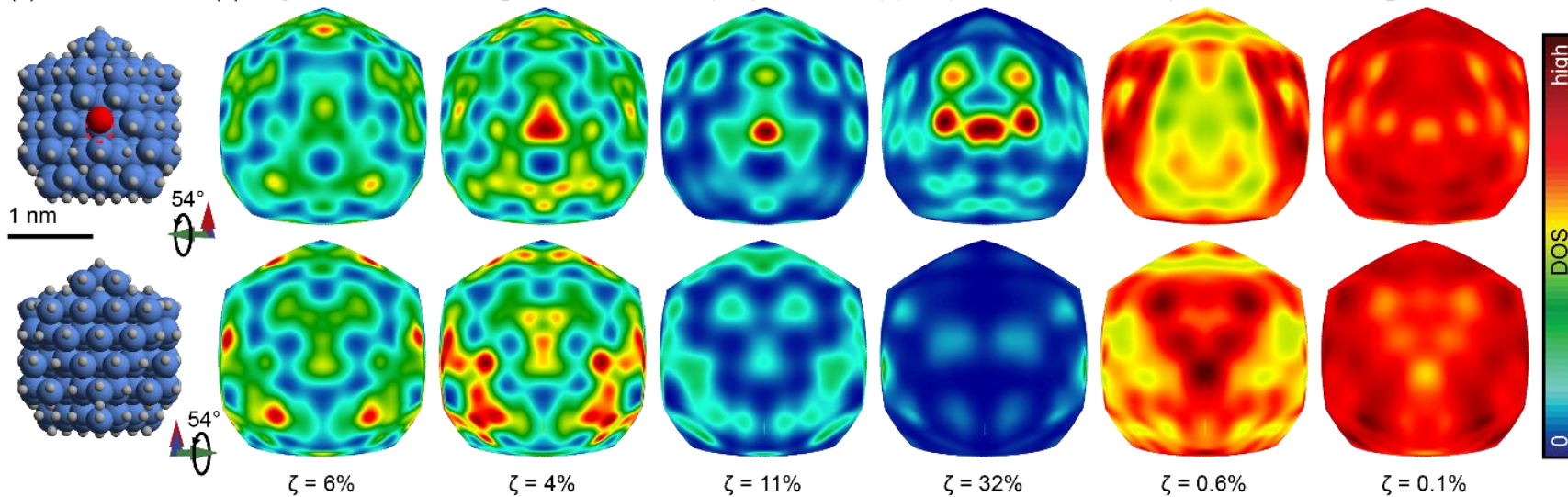
**Figure H6.** STM/STS characterization of NC<sub>2</sub>. (a) STM topography image of NC<sub>2</sub> [set point 2.2 V, 5.0 pA]. (b) DOS spectra [set point 2.0 V, 20 pA] measured at the locations A-I marked in (a). Spectra are offset for clarity. Prominent occupied and unoccupied states are marked with an 'H' and 'E' respectively. (c-d) Close-up of spectra from C, G and J locations.

---

**Figure H7.** Theoretical DOS for a model near-spherical (composition  $\text{H}_{114}\text{Si}_{175}\text{O}$ , diameter  $\sim 2$  nm) SiNC with a Si=O impurity. Data arrangement and markings are the same as in Figure 10.2. In (c),  $P_2$  corresponds to the defect location. Locations  $P_1$  and  $P_3$  correspond to locations  $P_2$  and  $P_3$  in Figures 10.4, H8 and H9. The top and bottom rows in (d-j) show opposite sides of the NC. To more closely reproduce experimental conditions, all spectra were normalized to give the same total current at 1.7 V.



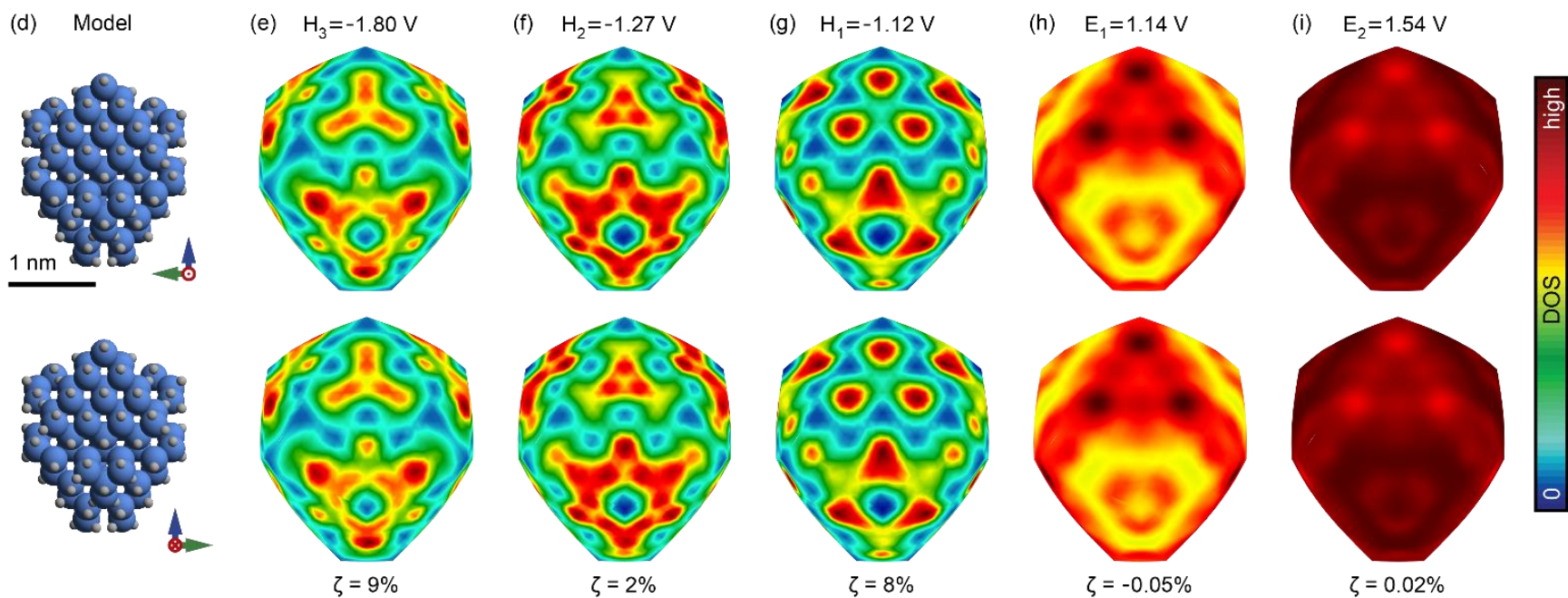
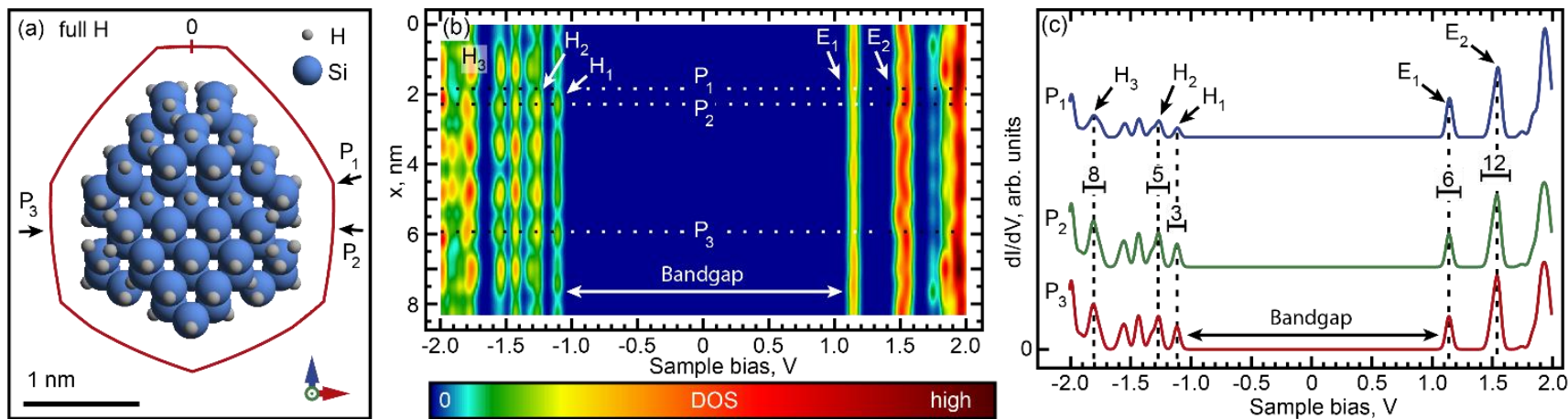
(d) Model (e)  $H_3 = -1.73$  V (f)  $H_2 = -1.19$  V (g)  $H_1, H_1^* = -0.97$  V (h)  $E_1^* = 1.00$  V (i)  $E_1 = 1.22$  V (j)  $E_2 = 1.62$  V



---

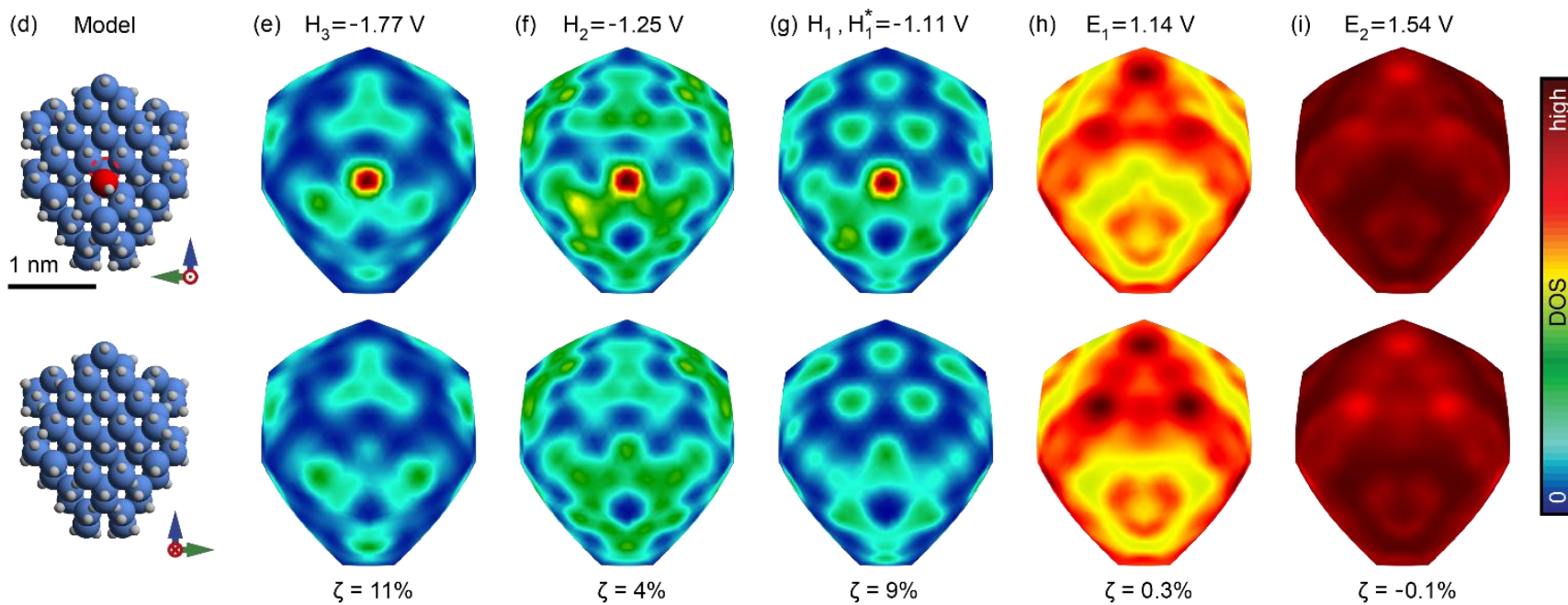
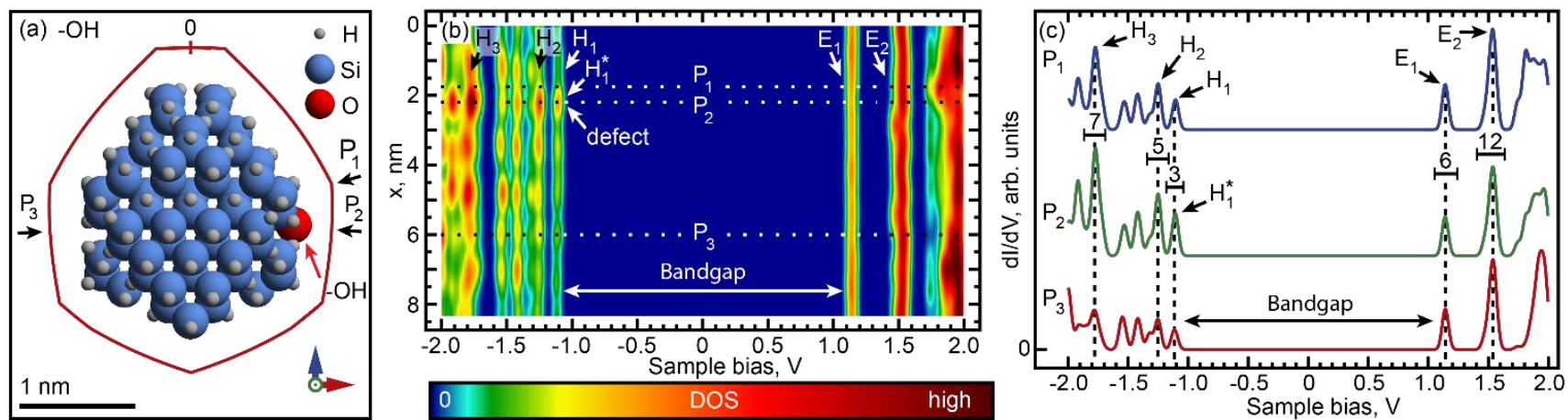
**Figure H8.** Theoretical DOS for a model near-spherical (composition  $\text{H}_{116}\text{Si}_{175}$ , diameter  $\sim 2$  nm) SiNC without impurities. Data arrangement and markings are the same as in Figure 10.2. In (c), locations  $P_1$ ,  $P_2$  and  $P_3$  are the same as in Figures 10.4 and H9. The top and bottom rows in (d-i) show opposite sides of the NC. To more closely reproduce experimental conditions, all spectra were normalized to give the same total current at 1.7 V.





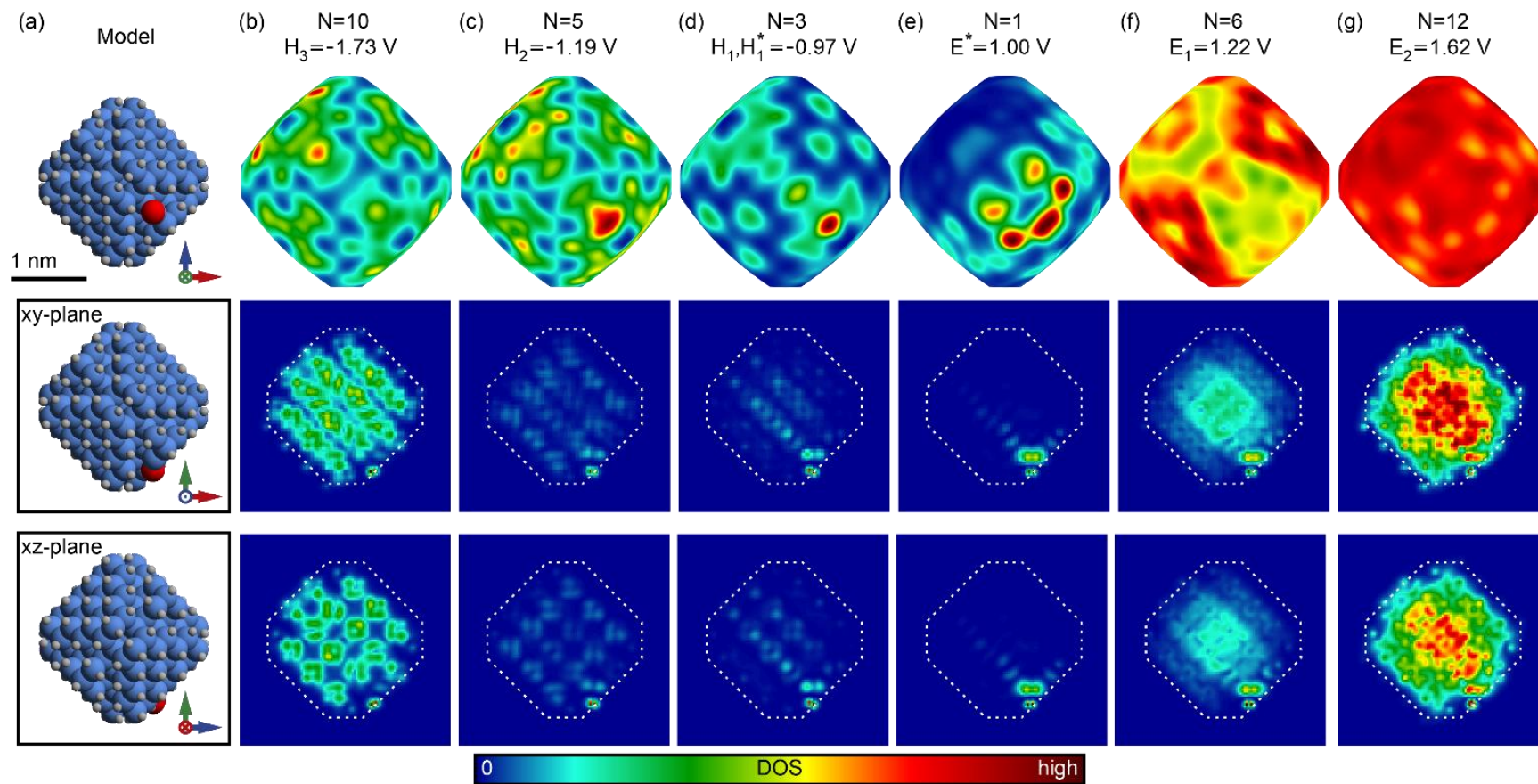
---

**Figure H9.** Theoretical DOS for a model near-spherical (composition  $\text{H}_{116}\text{Si}_{175}\text{O}$ , diameter  $\sim 2$  nm) SiNC with a Si–OH impurity. Data arrangement and markings are the same as in Figure 10.2. In (c),  $P_1$  is the same location as in Figure 10.4. Location  $P_2$  corresponds to the defect location. Location  $P_3$  is positioned on the opposite side of NC with respect to  $P_2$ . The top and bottom rows in (d-i) show opposite sides of the NC. To more closely reproduce experimental conditions, all spectra were normalized to give the same total current at 1.7 V.



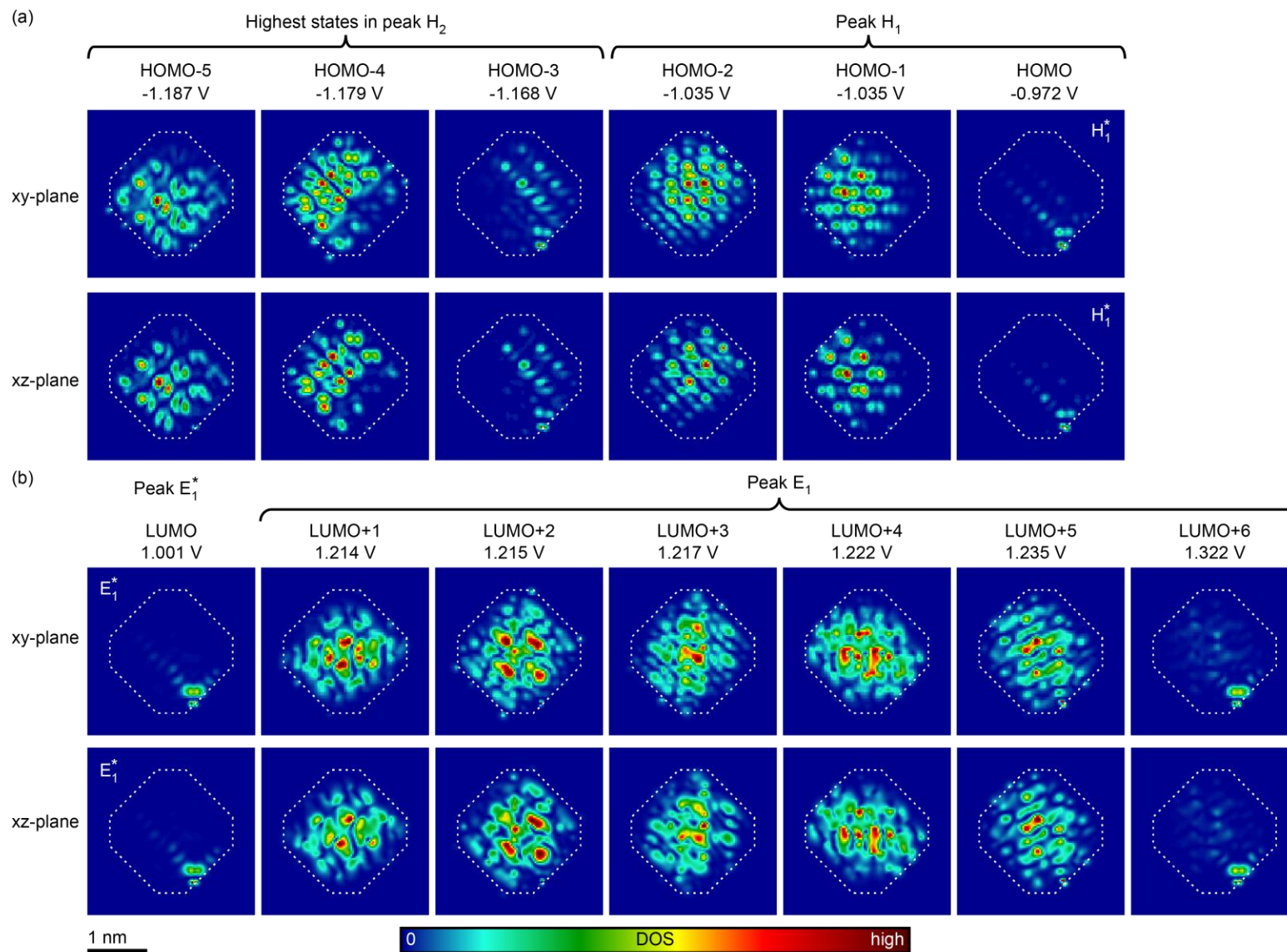
---

**Figure H10.** Volume distribution of theoretical DOS for a model near-spherical (composition  $\text{H}_{114}\text{Si}_{175}\text{O}$ , diameter  $\sim 2$  nm) SiNC with a Si=O impurity. (a) NC geometry. (b-g) DOS for the peaks from Figure H7c. N is the number of individual states comprising the peak. First row represents the normalized DOS maps on the surface (identical to Figure H7e-j). Second and third rows show bulk unnormalized DOS distributions across the main coordinate planes containing the oxygen atom. Each displayed DOS datapoint was averaged over a  $3.6 \text{ \AA}$ -long segment orthogonal to, and bisected by the corresponding plane.



---

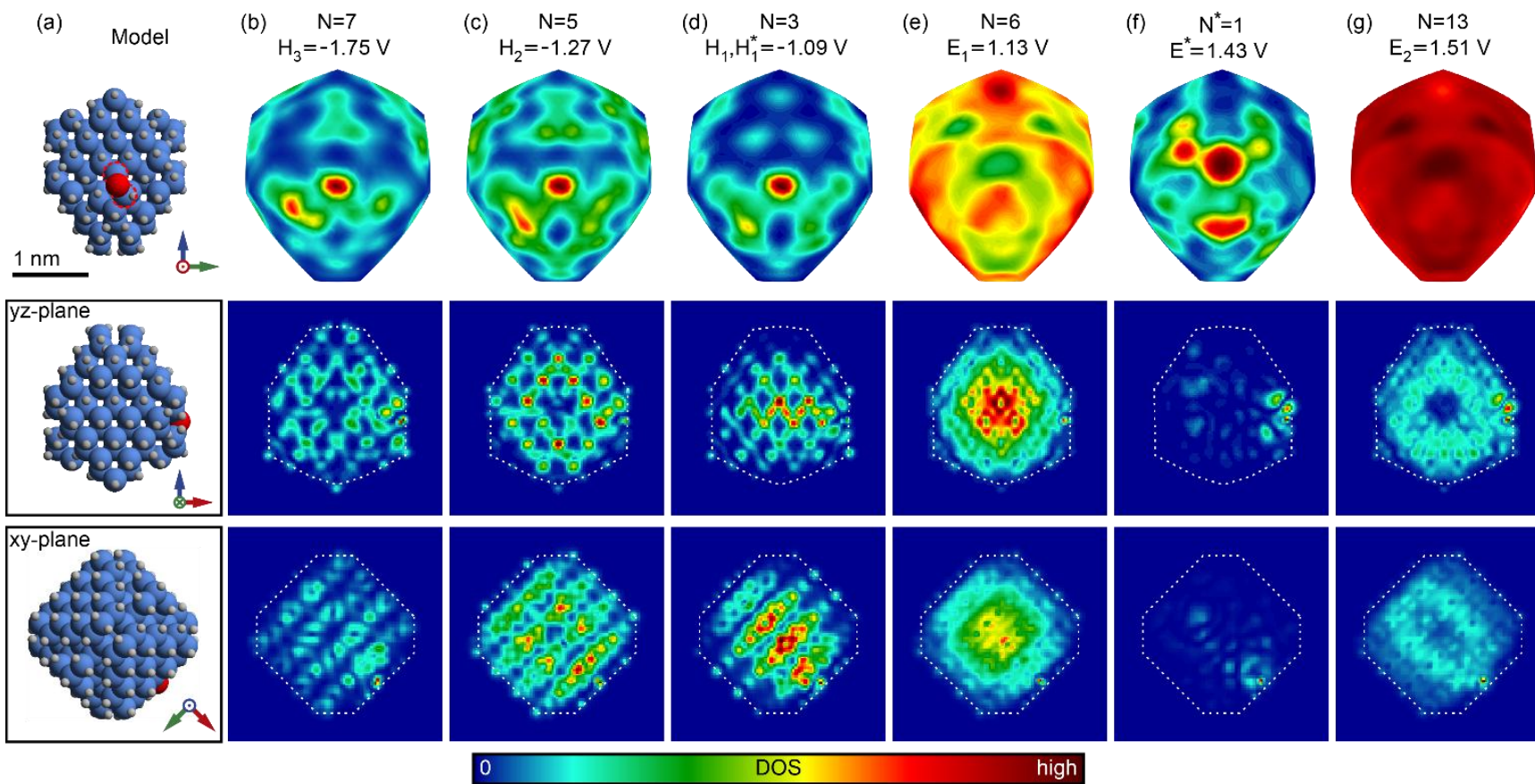
**Figure H11.** Bulk cross-sections for individual orbitals of a model near-spherical (composition  $\text{H}_{114}\text{Si}_{175}\text{O}$ , diameter  $\sim 2$  nm) SiNC with a Si=O impurity. Section planes and view angles are the same as in Figure H10. Each displayed DOS datapoint was averaged over a  $3.6 \text{ \AA}$ -long segment orthogonal to, and bisected by the corresponding plane. (a) Highest occupied molecular orbitals (HOMO). (b) Lowest unoccupied molecular orbitals (LUMO).



---

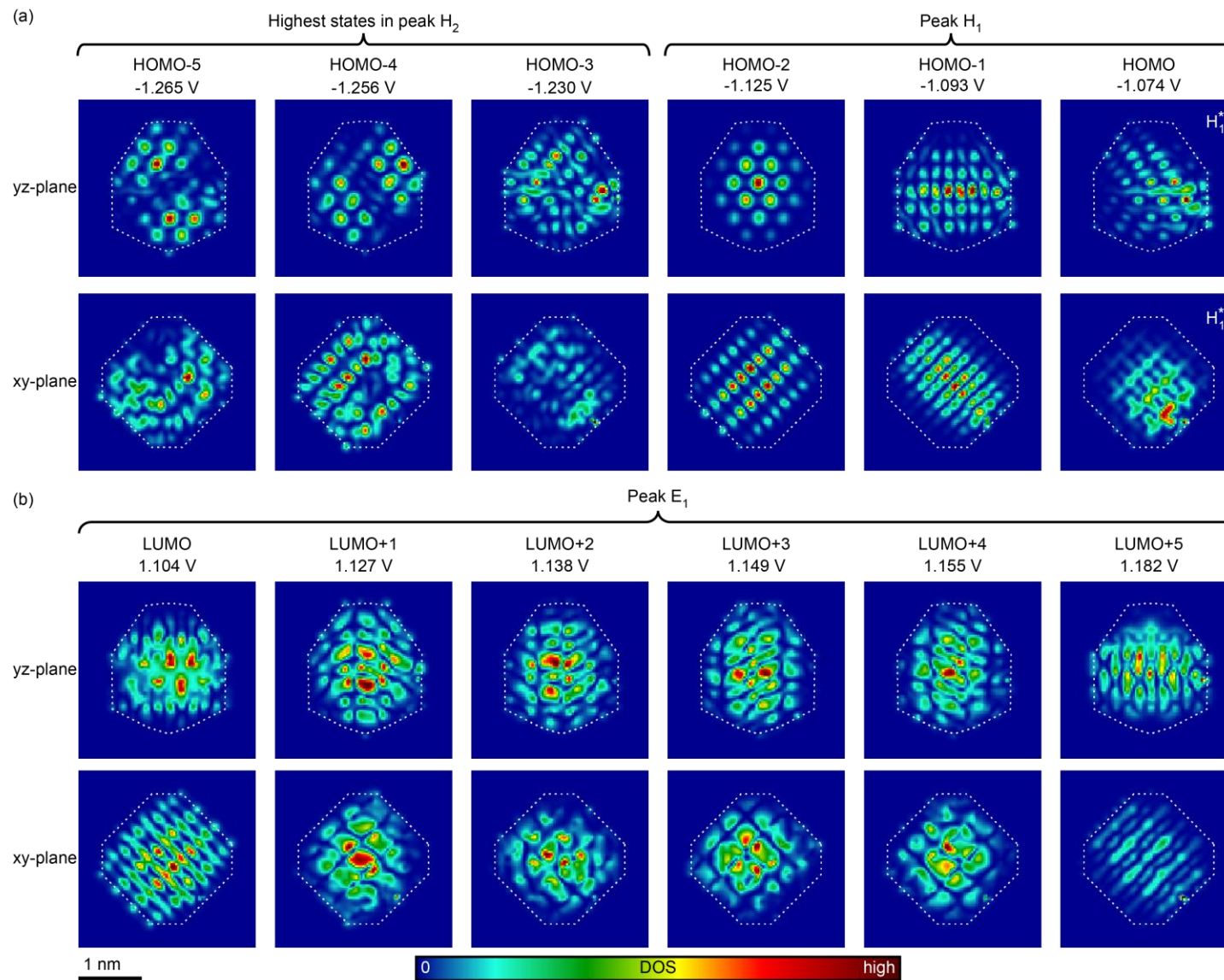
**Figure H12.** Volume distribution of theoretical DOS for a model near-spherical (composition  $\text{H}_{114}\text{Si}_{175}\text{O}$ , diameter  $\sim 2$  nm) SiNC with a Si–O–Si impurity. (a) NC geometry. (b-g) DOS for the peaks from Figure 10.4c. N is the number of individual states comprising the peak. First row represents the normalized DOS maps on the surface (identical to Figure 10.4e-j). Second and third rows show bulk unnormalized DOS distributions across the main coordinate planes containing the oxygen atom. Each displayed DOS datapoint was averaged over a  $3.6 \text{ \AA}$ -long segment orthogonal to, and bisected by the corresponding plane.





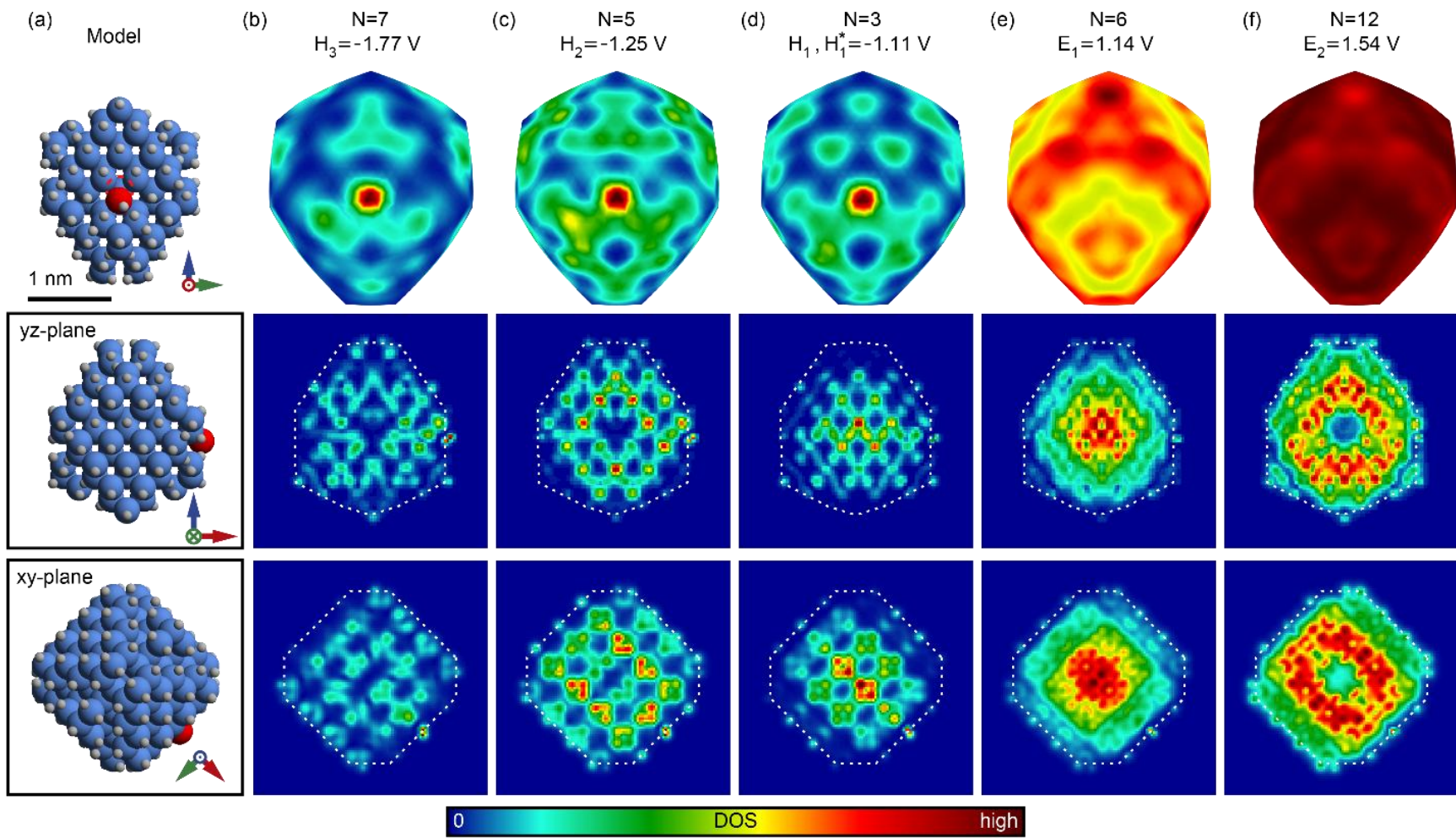
---

**Figure H13.** Bulk cross-sections for individual orbitals of a model near-spherical (composition  $\text{H}_{114}\text{Si}_{175}\text{O}$ , diameter  $\sim 2$  nm) SiNC with a Si–O–Si impurity. Section planes and view angles are the same as in Figure H12. Each displayed DOS datapoint was averaged over a  $3.6 \text{ \AA}$ -long segment orthogonal to, and bisected by the corresponding plane. (a) Highest occupied molecular orbitals (HOMO). (b) Lowest unoccupied molecular orbitals (LUMO).



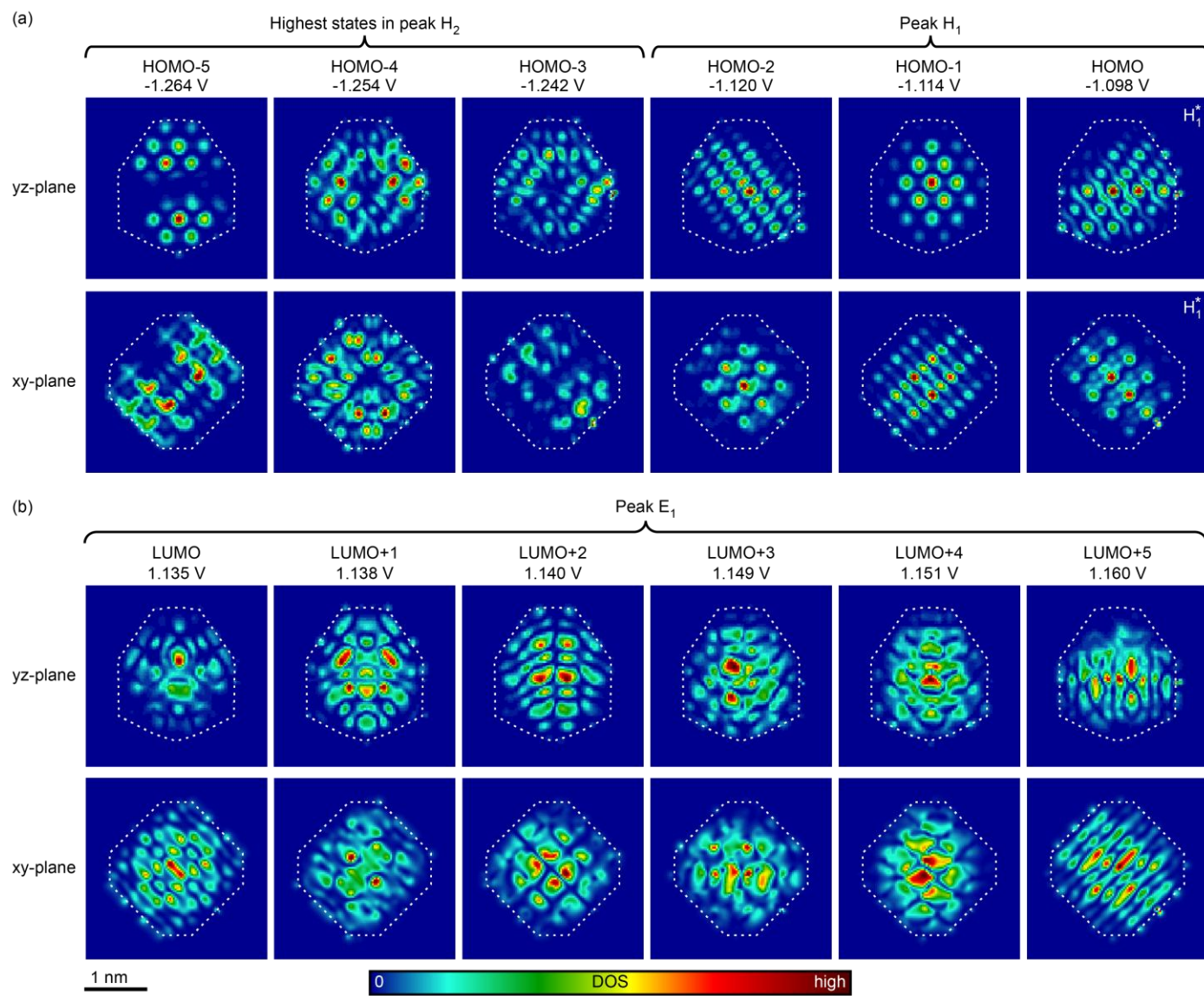
---

**Figure H14.** Volume distribution of theoretical DOS for a model near-spherical (composition  $\text{H}_{116}\text{Si}_{175}\text{O}$ , diameter  $\sim 2$  nm) SiNC with a Si–OH impurity. (a) NC geometry. (b-f) DOS for the peaks from Figure H9c. N is the number of individual states comprising the peak. First row represents the normalized DOS maps on the surface (identical to Figure H9e-i). Second and third rows show bulk unnormalized DOS distributions across the main coordinate planes containing the oxygen atom. Each displayed DOS datapoint was averaged over a  $3.6 \text{ \AA}$ -long segment orthogonal to, and bisected by the corresponding plane.



---

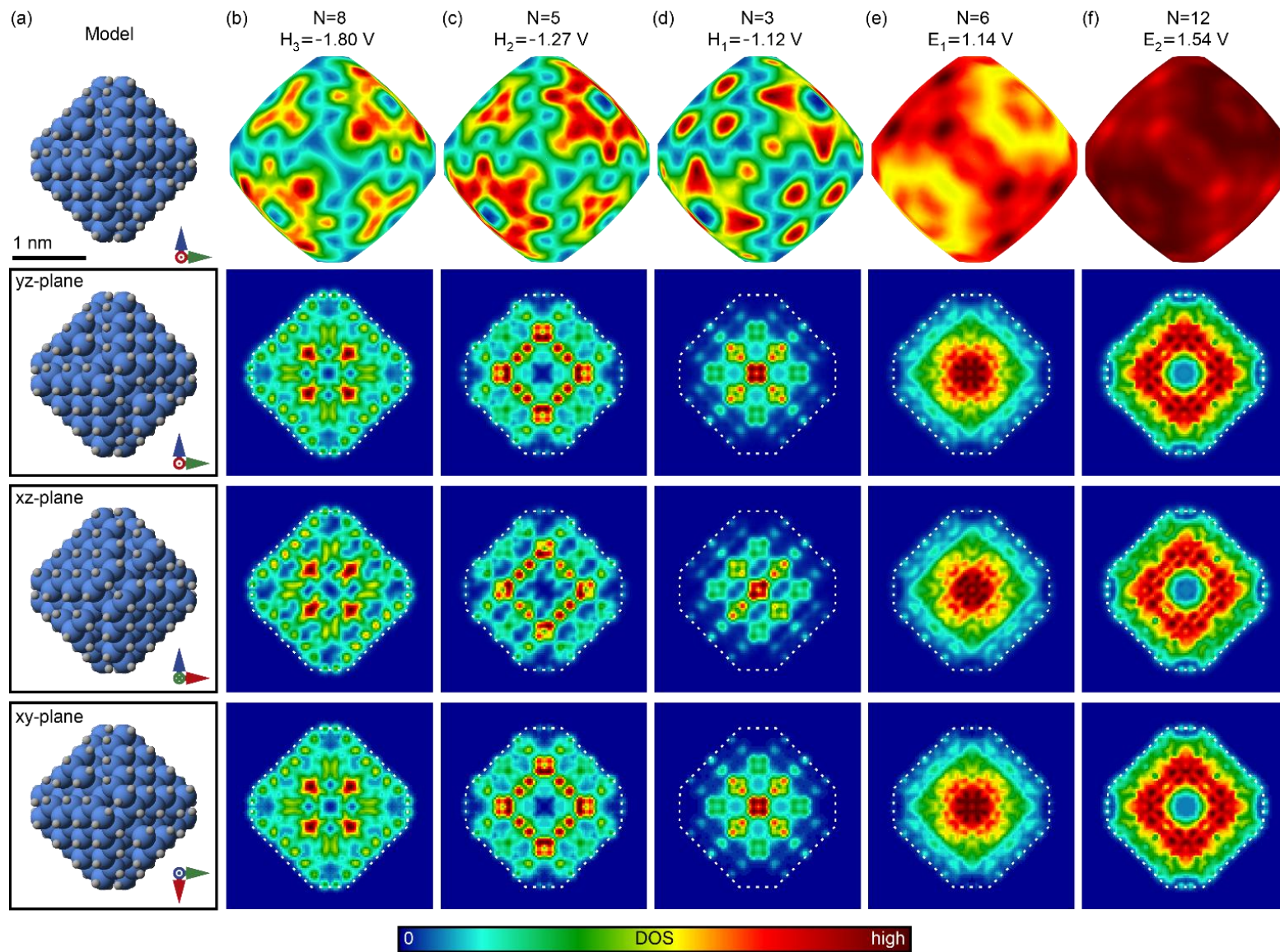
**Figure H15.** Bulk cross-sections for individual orbitals of a model near-spherical (composition  $\text{H}_{116}\text{Si}_{175}\text{O}$ , diameter  $\sim 2$  nm) SiNC with a Si–OH impurity. Section planes and view angles are the same as in Figure H14. Each displayed DOS datapoint was averaged over a  $3.6 \text{ \AA}$ -long segment orthogonal to, and bisected by the corresponding plane. (a) Highest occupied molecular orbitals (HOMO). (b) Lowest unoccupied molecular orbitals (LUMO).



---

**Figure H16.** Volume distribution of theoretical DOS for a model near-spherical (composition  $\text{H}_{116}\text{Si}_{175}$ , diameter  $\sim 2$  nm) SiNC without impurities. (a) NC geometry. (b-f) DOS for the peaks from Figure H8c. N is the number of individual states comprising the peak. First row represents the normalized DOS maps on the surface (identical to Figure H8e-i). Second and third rows show bulk unnormalized DOS distributions across the main coordinate planes containing the oxygen atom. Each displayed DOS datapoint was averaged over a  $3.6 \text{ \AA}$ -long segment orthogonal to, and bisected by the corresponding plane.





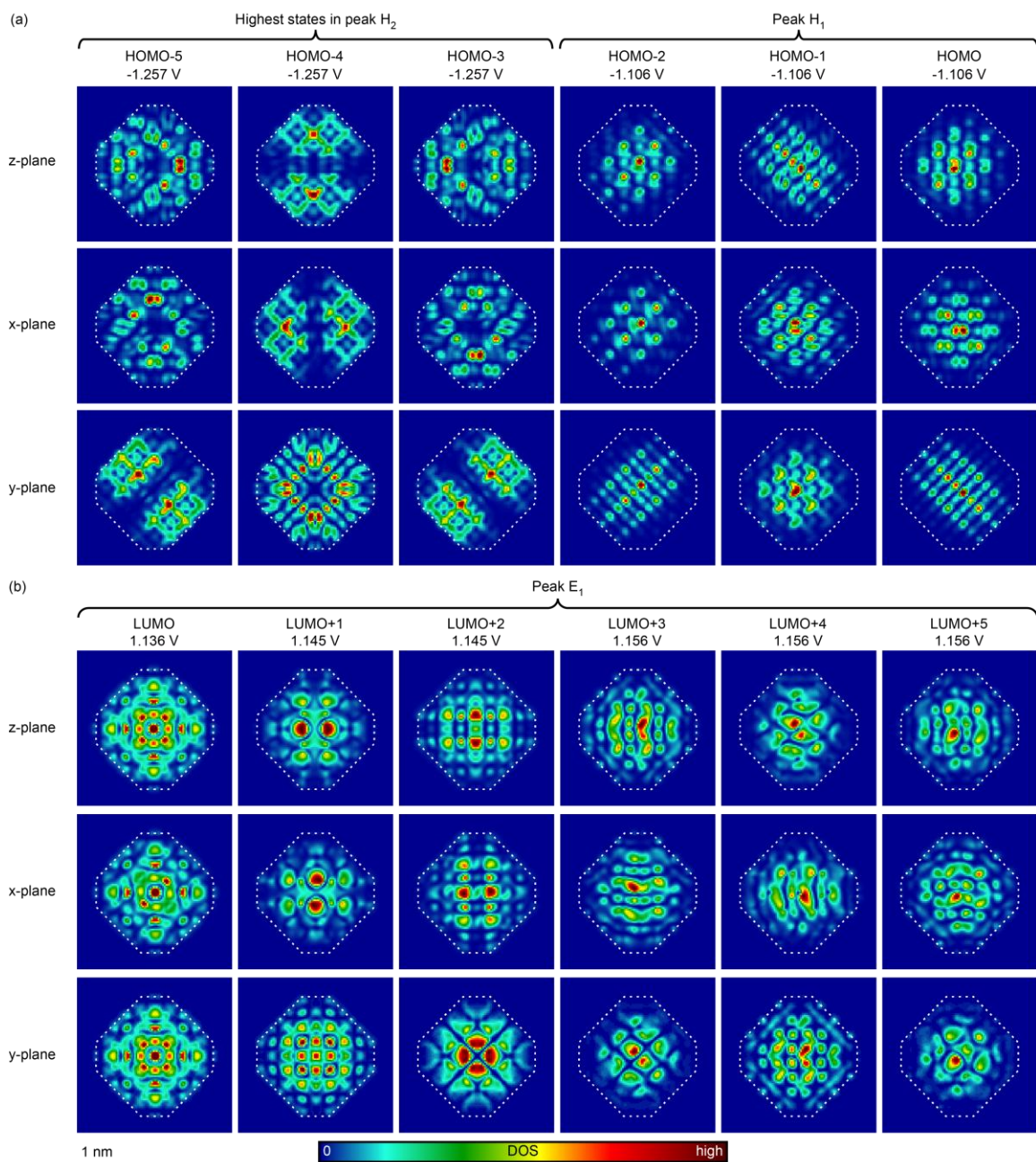


**Figure H17.** Bulk cross-sections for individual orbitals of a model near-spherical (composition  $H_{116}Si_{175}$ , diameter  $\sim 2$  nm) SiNC without impurities. Section planes and view angles are the same as in Figure H16. Each displayed DOS datapoint was averaged over a  $3.6 \text{ \AA}$ -long segment orthogonal to, and bisected by the corresponding plane. (a) Highest occupied molecular orbitals (HOMO). (b) Lowest unoccupied molecular orbitals (LUMO).

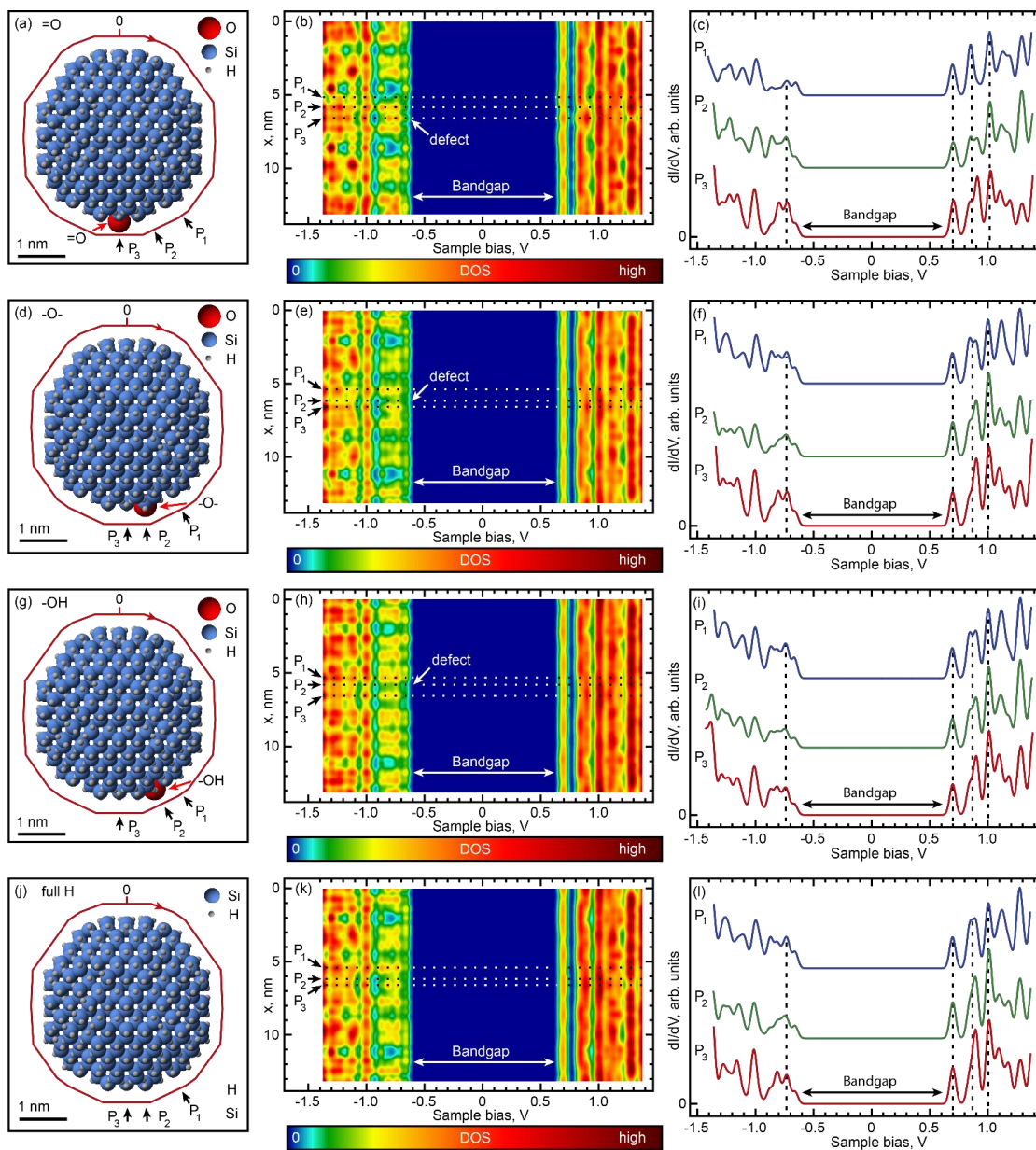


**Figure H18.** Comparison of theoretical DOS for model near-spherical (diameter  $\sim 3.5$  nm) SiNCs with and without impurities. (a) Geometry of a NC with a Si=O impurity and composition  $\text{H}_{410}\text{Si}_{1087}\text{O}$ . (b) Calculated 1D DOS map as a function of bias voltage and position  $x$  along the path shown in (a). (c) Individual DOS spectra from (b) measured at points P1 through P3. Spectra are offset for clarity. (d-f) Same as (a-c) for a NC with a Si-O-Si impurity and composition  $\text{H}_{410}\text{Si}_{1087}\text{O}$ . (g-i) Same as (a-c) for a NC with a Si-OH impurity and composition  $\text{H}_{412}\text{Si}_{1087}\text{O}$ . (j-l) Same as (a-c) for a NC without impurities, and composition  $\text{H}_{412}\text{Si}_{1087}$ . To more closely reproduce experimental conditions, all spectra were normalized to give the same total current at 1.35 V.

### Free-standing H-SiNCs synthesis

Free-standing H-SiNCs were synthesized following a modified literature procedure<sup>15</sup>. Trichlorosilane ( $\text{HSiCl}_3$ ,  $\leq 98\%$ ; Alfa Aesar), pentane (anhydrous  $\text{C}_5\text{H}_{12}$ , Sigma-Aldrich), aqueous hydrofluoric acid (HF, 48.0–51.0%, Fisher Scientific), aqueous hydrochloric acid (HCl, 12N, Fisher Scientific), and ethanol (anhydrous EtOH, ACS grade, Pharmco-Aaper) were purchased for syntheses and used without further purification.

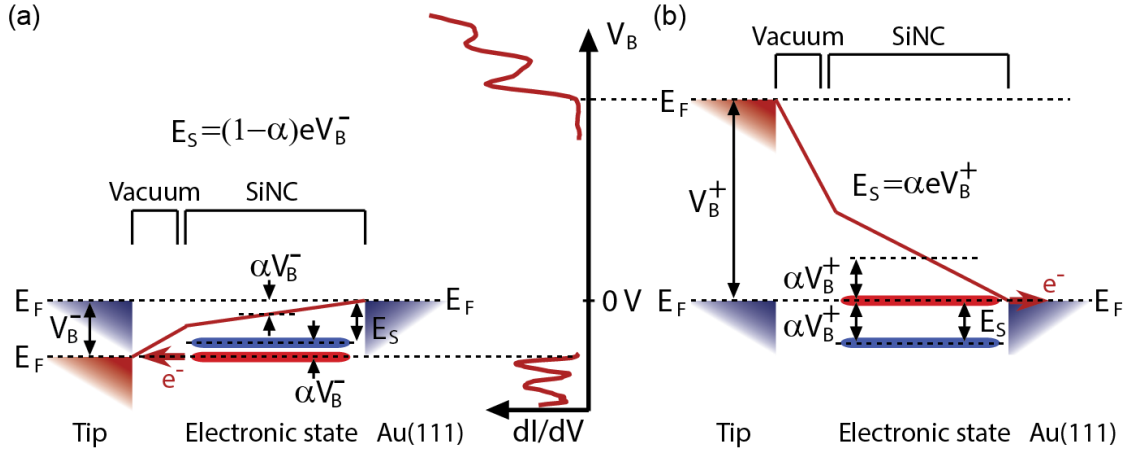
A Schlenk line was utilized to maintain an air-free environment during the sol-gel polycondensation with Ar flow as the inert gas. Other synthetic procedures, such as etching and solvent media switching, were done in air. For all aqueous solutions, electrophoretically pure water (nanopure water, 18  $\text{M}\Omega\cdot\text{cm}$  resistivity) was used for aqueous mixtures preparation.

In a typical reaction, 4.5 mL of  $\text{HSiCl}_3$  (45 mmol) was injected into a two-necked round-bottom flask, equipped with a small PTFE-coated magnetic stir bar. The flask with  $\text{HSiCl}_3(\text{l})$  was cooled in an ice bath for 10 minutes, then an aliquot (90 mmol) of nanopure water was quickly injected into the flask to accomplish hydrolysis and polycondensation of  $\text{HSiCl}_3$ . The mixture was cooled for another 3 minutes, then left under flowing Ar for 18h to purge  $\text{HCl}(\text{g})$  byproduct. The resulting sol-gel hydrosilicate polymer was subsequently dried in *vacuo* for 18 hrs. This solid precursor was placed in an alumina boat, and was annealed at 1100 °C under flowing  $\text{N}_2$  in a horizontal tube furnace (Lindberg Blue, Model TF55035A, Lindberg Scientific, Asheville, NC) for 10 hrs to produce nanocrystalline Si nanoparticles (NC Si NPs) embedded in  $\text{SiO}_x$  ( $x \leq 2$ ) matrix (NC Si NPs/ $\text{SiO}_x$ ). The annealed NC Si NPs/ $\text{SiO}_x$  powders (0.5 g) were ball-milled for 10

seconds in a tungsten carbide lined milling vial with two 1 cm tungsten carbide balls using a Spex 8000M mill mixer (SPEX SamplePrep, Metuchen, NJ). The milled NC Si NPs/SiO<sub>x</sub> powder was subsequently etched in a chemical etching solution of 1:1:1 (by volume) ethanol/water/HF<sub>(aq)</sub> for 1 hr to liberate hydride-terminated Si NPs (SiNCs), which were then partitioned into pentane by biphasic extraction (10 × 5 mL of pentane extractions).

## APPENDIX I

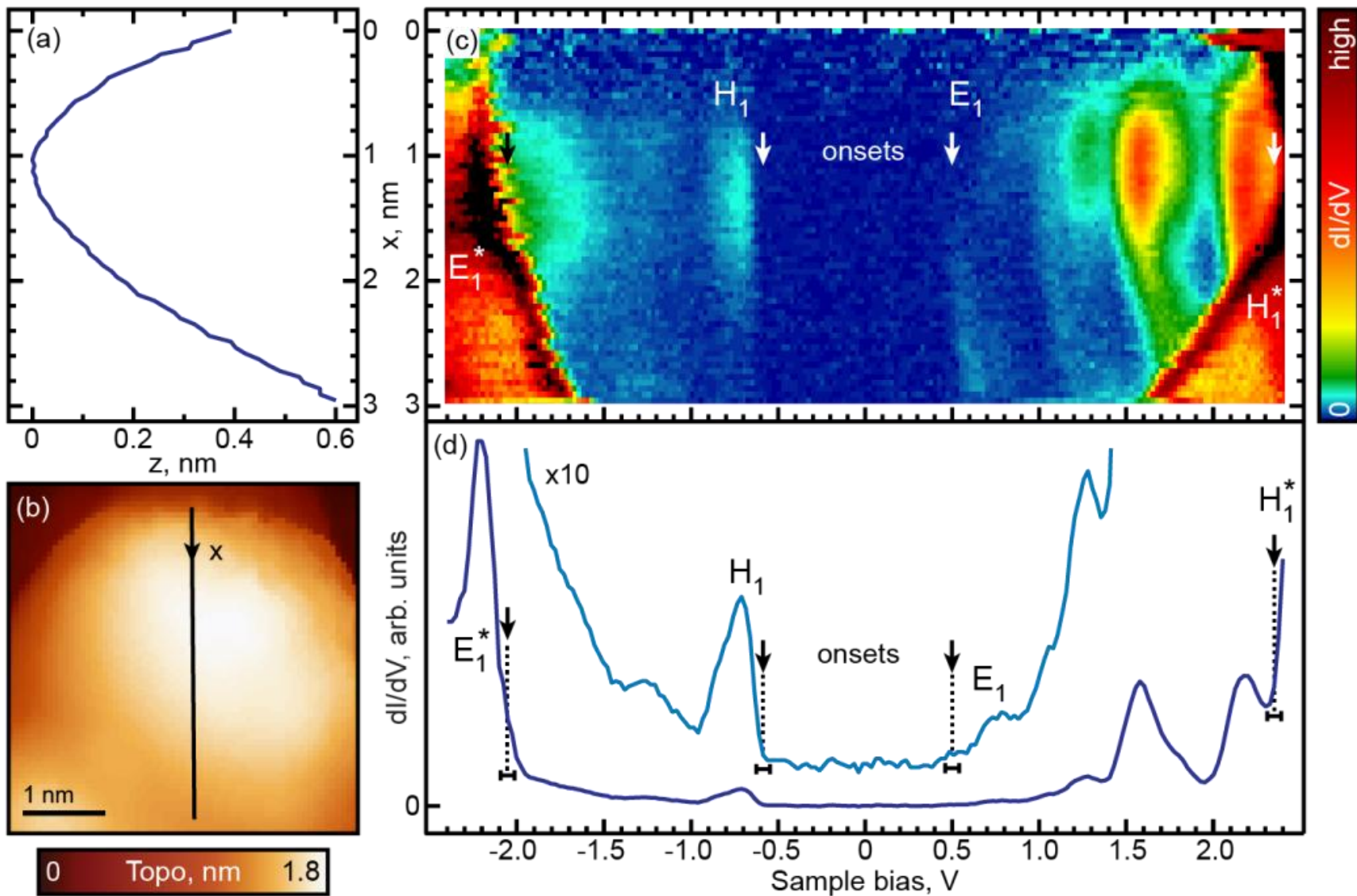
### SUPPORTING INFORMATION TO CHAPTER XI



**FIG. 11.** Impact of the finite bias voltage drop inside a SiNC on the STS spectra. (a) “Direct” tunnelling through an occupied electronic state with energy  $E_S$  below the Fermi level ( $E_F$ ) of the Au(111) substrate (corresponding states shown in blue). In a biased tunnel junction involving a SiNC (corresponding states shown in red), a finite voltage drop occurs across the SiNC volume changing the energy of all electronic states by  $\alpha eV_B$ , where  $V_B$  is the bias voltage, and  $\alpha < 1$  is a function of the SiNC dimensions and dielectric susceptibility. Tunnelling into the state thus occurs when the Fermi level of the tip is aligned with the electronic state, which happens when  $E_S = (1 - \alpha)eV_B$  (here, and everywhere in Fig. 11, we assume that all quantities are positive). The onset tunnelling voltage can thus be calculated as  $E_S/(1 - \alpha)$ .<sup>3, 11</sup> (b) “Reverse” tunneling through an occupied state. In contrast to “direct” tunnelling, “reverse” tunneling is initiated when the Fermi level of the Au(111) substrate is aligned with the electronic state, which happens at opposite polarity to that of (a), when  $E_S = \alpha eV_B$ . This gives the onset tunnelling voltage of  $E_S/\alpha$ .<sup>3, 11</sup>

---

**FIG. 12.** Spatial mapping of LDOS for a representative SiNC showing spectral peaks corresponding to “direct” and “reverse” tunneling. (a) STM topographic profile [ $z$  height vs.  $x$  coordinate along the path shown in (b)]. (b) STM topographic image. Solid line is a trajectory for 1D STS mapping in (c). (c)  $dI/dV$  as a function of the bias voltage and position  $x$  along the path shown in (a). (d) Individual LDOS spectrum from (c) measured in the center of the path. Peaks originating from occupied (unoccupied) states produced by “direct” tunneling are marked 'H' ('E'), while peaks originating from “reverse” tunneling are marked 'H\*' ('E\*'). Horizontal error bars indicate the uncertainty in identification of the peak onsets. At the center of the SiNC, the ratio of the onsets for peaks  $E_1$  and  $E_1^*$  gives  $\alpha = 0.18 \pm 0.02$ , and  $\alpha = 0.20 \pm 0.02$  for peaks  $H_1$  and  $H_1^*$ . (In the main text, we use  $\alpha = 0.2$  as a representative value for SiNCs, to estimate the energy-voltage relationships for STS features corresponding to “direct” and “reverse” tunneling.) Voltage onsets for both “direct” and “reverse” tunnelling (at opposite bias polarities) vary with tip position on the NC surface. This is particularly noticeable for “reverse” tunneling peaks  $E_1^*$  and  $H_1^*$ , while the onsets of “direct” tunneling peaks  $E_1$  and  $H_1$  are relatively insensitive to the position along the SiNC. These onset variations are explained by the sensitivity of  $\alpha$  to the geometry of the junction.<sup>3</sup> Indeed, both the tip position with respect to the SiNC, and the relative tip height  $z$ , which can both be expected to affect  $\alpha$ , vary considerably across the scan range shown in the topography profiles (a) and (b). The larger sensitivity of peaks  $E_1^*$  and  $H_1^*$  to spatial location is explained by the fact that the onsets for these are inversely proportional to  $\alpha$  (changes significantly), while the onsets for peaks  $E_1$  and  $H_1$  are inversely proportional to  $1 - \alpha$  (changes relatively insignificantly due to the small value of  $\alpha$ ).





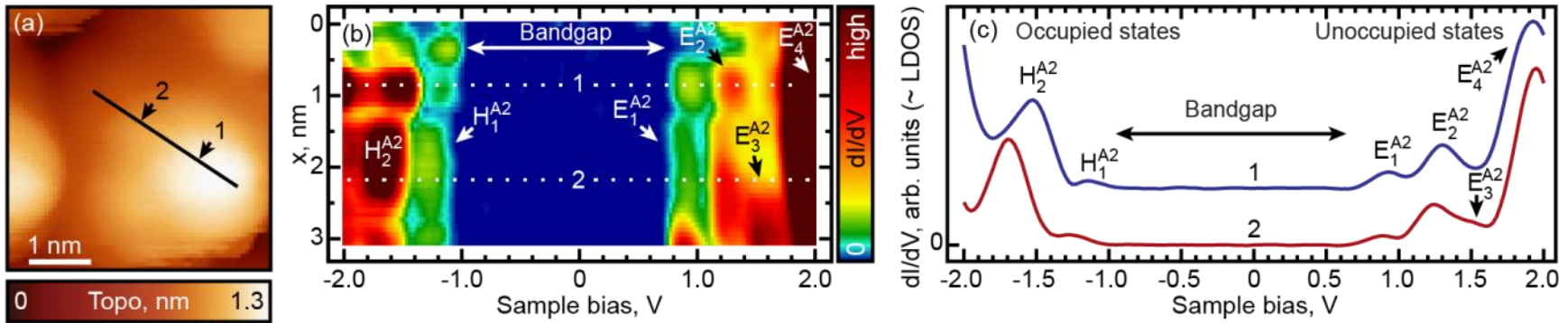


**FIG. I3.** Spatial mapping of LDOS for the SiNC from Fig. 11.1(b) after partial dehydrogenation, but before DBs were generated. (a) Topography of the SiNC. (b) LDOS as a function of the bias voltage and position  $x$  along the path (solid line) shown in (a). (c) Individual LDOS spectra from (b) measured at points 1 and 2. Spectra are offset for clarity. Occupied and unoccupied states are marked 'H' and 'E' respectively.

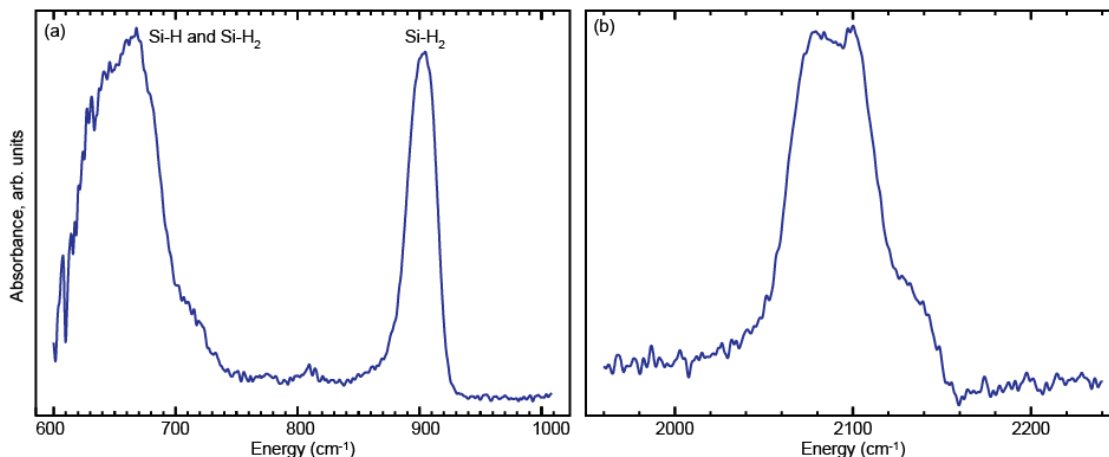


**FIG. 14.** FT-IR spectra of as-prepared hydrogen-terminated SiNCs dispersed in a hexane solution as described elsewhere.<sup>16</sup> (a) Low frequency region. Broad peak at 600-700  $\text{cm}^{-1}$  includes: 1) the Si-H bending modes and Si-H<sub>2</sub> rocking mode of Si(100),<sup>17</sup> 2) the Si-H bending mode of Si(111)-(1 $\times$ 1),<sup>18</sup> and 3) the Si-H bending modes and Si-H<sub>2</sub> wagging mode originating from step-edges of vicinal H/Si(111) surfaces.<sup>19</sup> The peak at 904  $\text{cm}^{-1}$ , on the other hand, has no contribution from Si-H: it contains the Si-H<sub>2</sub> scissoring bending mode,<sup>17, 20</sup> as well as the Si-H<sub>3</sub> degenerate deformation mode<sup>21</sup> (note that Si-H<sub>3</sub> population is expected to be significantly lower due to 2 times higher oxidation rate while exposed to the air during the measurement).<sup>22</sup> Intensity of both peaks are comparable, which suggests a significant presence of Si-H<sub>2</sub> on the {100}Times facets of measured SiNCs. For comparison, for the Si(100)-(3 $\times$ 1) surface, where  $\sim 1/3$  of the surface Si atoms are terminated with dihydrides (and the rest are terminated with monohydrides), the relative intensity of the  $\sim 900 \text{ cm}^{-1}$  region is an order of magnitude smaller than that of the  $\sim 600 \text{ cm}^{-1}$ .<sup>17</sup> (b) High-frequency spectral region associated with silicon-hydride stretching modes. While the peak at 2100  $\text{cm}^{-1}$  may be associated with both Si-H and Si-H<sub>2</sub>, the shoulder observed at 2120-2140  $\text{cm}^{-1}$  is indicative of Si-H<sub>2</sub>.<sup>17</sup>

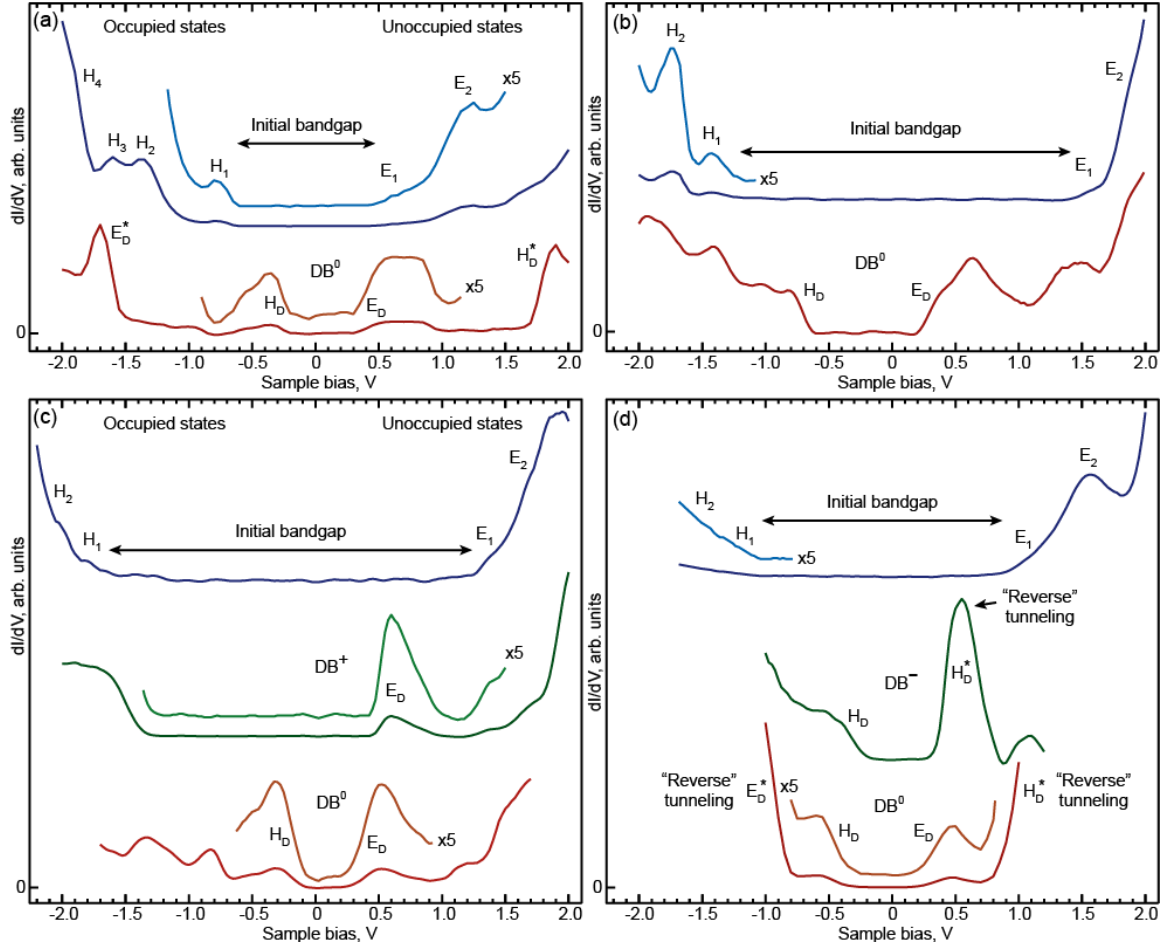


**FIG. 15.** STS characterization of additional SiNCs of different sizes. (a-d) STS spectra before (“pristine” state) and after application of ESD pulses causing reconstruction (narrowing of the bandgap) and the creation of localized DB states deep in the bandgap. The observed charge state of the DB is neutral ( $DB^0$ ) in (a, b), switching from positive ( $DB^+$ ) to neutral ( $DB^0$ ) in (c), and switching from negative ( $DB^-$ ) to neutral ( $DB^0$ ) in (d). Note that “reverse” tunneling features (marked with “\*”) are observed in (a) and (d) with different values of  $\alpha$ .

## REFERENCES CITED

### REFERENCES CITED FOR CHAPTER I

- (1) Binnig, G.; Rohrer, H.; Gerber, C.; Weibel, E. Tunneling through a Controllable Vacuum Gap. *Appl. Phys. Lett.* **1982**, *40* (2), 178–180.
- (2) Binnig, G.; Rohrer, H.; Gerber, C.; Weibel, E. Surface Studies by Scanning Tunneling Microscopy. *Phys. Rev. Lett.* **1982**, *49* (1), 57–61.
- (3) Binnig, G.; Rohrer, H. Scanning Tunneling Microscopy. *Helvetica Phys. Acta* **1982**, *55*, 726–735.
- (4) Bottomley, L. A. Scanning Probe Microscopy. *Anal. Chem.* **1998**, *70* (12), 425–476.
- (5) Wiesendanger, R. *Scanning Probe Microscopy: Analytical Methods*; Springer Science & Business Media, 1998.
- (6) Bhushan, B.; Marti, O. Scanning Probe Microscopy – Principle of Operation, Instrumentation, and Probes. In *Springer Handbook of Nanotechnology*; Bhushan, P. B., Ed.; Springer Berlin Heidelberg, 2010; pp 573–617.
- (7) Meyer, E.; Hug, H. J.; Bennewitz, R. *Scanning Probe Microscopy: The Lab on a Tip*; Springer Science & Business Media, 2003.
- (8) Chen, C. J. *Introduction to Scanning Tunneling Microscopy*, 2nd ed.; Oxford University Press, USA, 2007.
- (9) Pia, A. D.; Costantini, G. Scanning Tunneling Microscopy. In *Surface Science Techniques*; Bracco, G., Holst, B., Eds.; Springer Series in Surface Sciences; Springer Berlin Heidelberg, 2013; pp 565–597.
- (10) Ho, W. Single-Molecule Chemistry. *J. Chem. Phys.* **2002**, *117*, 11033.
- (11) Zandvliet, H. J. W.; Houselt, A. van. Scanning Tunneling Spectroscopy. *Annu. Rev. Anal. Chem.* **2009**, *2* (1), 37–55.

- (12) Temirov, R.; Soubatch, S.; Neucheva, O.; Lassise, A. C.; Tautz, F. S. A Novel Method Achieving Ultra-High Geometrical Resolution in Scanning Tunnelling Microscopy. *New J. Phys.* **2008**, *10* (5), 053012.
- (13) Gross, L. Recent Advances in Submolecular Resolution with Scanning Probe Microscopy. *Nat. Chem.* **2011**, *3* (4), 273–278.
- (14) Wagner, C.; Temirov, R. Tunnelling Junctions with Additional Degrees of Freedom: An Extended Toolbox of Scanning Probe Microscopy. *Prog. Surf. Sci.* **2015**, *90* (2), 194–222.
- (15) Chiang, C.; Xu, C.; Han, Z.; Ho, W. Real-Space Imaging of Molecular Structure and Chemical Bonding by Single-Molecule Inelastic Tunneling Probe. *Science* **2014**, *344* (6186), 885–888.
- (16) Betzig, E.; Trautman, J. K. Near-Field Optics: Microscopy, Spectroscopy, and Surface Modification Beyond the Diffraction Limit. *Science* **1992**, *257* (5067), 189–195.
- (17) Qiu, X. H.; Nazin, G. V.; Ho, W. Vibrationally Resolved Fluorescence Excited with Submolecular Precision. *Science* **2003**, *299* (5606), 542–546.
- (18) Čavar, E.; Blüm, M.-C.; Pivetta, M.; Patthey, F.; Chergui, M.; Schneider, W.-D. Fluorescence and Phosphorescence from Individual C<sub>60</sub> Molecules Excited by Local Electron Tunneling. *Phys. Rev. Lett.* **2005**, *95* (19), 196102.
- (19) Keizer, J. G.; Garleff, J. K.; Koenraad, P. M. Simple and Efficient Scanning Tunneling Luminescence Detection at Low-Temperature. *Rev. Sci. Instrum.* **2009**, *80* (12), 123704.
- (20) Kramar, J. A. Nanometre Resolution Metrology with the Molecular Measuring Machine. *Meas. Sci. Technol.* **2005**, *16* (11), 2121.
- (21) Sugimoto, Y.; Yurtsever, A.; Hirayama, N.; Abe, M.; Morita, S. Mechanical Gate Control for Atom-by-Atom Cluster Assembly with Scanning Probe Microscopy. *Nat. Commun.* **2014**, *5*, 4360.

- (22) Inami, E.; Hamada, I.; Ueda, K.; Abe, M.; Morita, S.; Sugimoto, Y. Room-Temperature-Concerted Switch Made of a Binary Atom Cluster. *Nat. Commun.* **2015**, *6*, 6231.
- (23) Mohn, F.; Gross, L.; Moll, N.; Meyer, G. Imaging the Charge Distribution within a Single Molecule. *Nat. Nanotechnol.* **2012**.
- (24) Yamazaki, S.; Maeda, K.; Sugimoto, Y.; Abe, M.; Zobač, V.; Pou, P.; Rodrigo, L.; Mutombo, P.; Pérez, R.; Jelínek, P.; et al. Interplay between Switching Driven by the Tunneling Current and Atomic Force of a Bistable Four-Atom Si Quantum Dot. *Nano Lett.* **2015**, *15* (7), 4356–4363.
- (25) Repp, J.; Meyer, G.; Stojković, S. M.; Gourdon, A.; Joachim, C. Molecules on Insulating Films: Scanning-Tunneling Microscopy Imaging of Individual Molecular Orbitals. *Phys. Rev. Lett.* **2005**, *94* (2), 026803.
- (26) Wu, S. W.; Ogawa, N.; Nazin, G. V.; Ho, W. Conductance Hysteresis and Switching in a Single-Molecule Junction. *J Phys Chem C* **2008**, *112* (14), 5241–5244.
- (27) Repp, J.; Liljeroth, P.; Meyer, G. Coherent Electron-Nuclear Coupling in Oligothiophene Molecular Wires. *Nat. Phys.* **2010**, *6* (12), 975–979.
- (28) Gross, L.; Moll, N.; Mohn, F.; Curioni, A.; Meyer, G.; Hanke, F.; Persson, M. High-Resolution Molecular Orbital Imaging Using a P-Wave STM Tip. *Phys. Rev. Lett.* **2011**, *107* (8), 086101.
- (29) Bellec, A.; Ample, F.; Riedel, D.; Dujardin, G.; Joachim, C. Imaging Molecular Orbitals by Scanning Tunneling Microscopy on a Passivated Semiconductor. *Nano Lett.* **2009**, *9* (1), 144–147.
- (30) Wiesendanger, R. *Scanning Probe Microscopy and Spectroscopy: Methods and Applications*, 1 edition.; Cambridge University Press: Cambridge England ; New York, 1994.
- (31) Stroscio, J. A.; Feenstra, R. M.; Newns, D. M.; Fein, A. P. Voltage-dependent Scanning Tunneling Microscopy Imaging of Semiconductor Surfaces. *J. Vac. Sci. Technol. A* **1988**, *6* (2), 499–507.

- (32) Li, J.; Schneider, W.-D.; Berndt, R. Local Density of States from Spectroscopic Scanning-Tunneling-Microscope Images: Ag(111). *Phys. Rev. B* **1997**, *56* (12), 7656–7659.
- (33) Ziegler, M.; Néel, N.; Sperl, A.; Kröger, J.; Berndt, R. Local Density of States from Constant-Current Tunneling Spectra. *Phys. Rev. B* **2009**, *80* (12), 125402.
- (34) Pradhan, N. A.; Liu, N.; Silien, C.; Ho, W. Atomic Scale Conductance Induced by Single Impurity Charging. *Phys. Rev. Lett.* **2005**, *94* (7), 076801.
- (35) Nazin, G. V.; Qiu, X. H.; Ho, W. Charging and Interaction of Individual Impurities in a Monolayer Organic Crystal. *Phys. Rev. Lett.* **2005**, *95* (16), 166103.
- (36) Chen, C.; Bobisch, C. A.; Ho, W. Visualization of Fermi's Golden Rule Through Imaging of Light Emission from Atomic Silver Chains. *Science* **2009**, *325* (5943), 981–985.
- (37) Reece, G.; Bulou, H.; Scheurer, F.; Speisser, V.; Carrière, B.; Mathevet, F.; Schull, G. Oligothiophene Nanorings as Electron Resonators for Whispering Gallery Modes. *Phys. Rev. Lett.* **2013**, *110* (5), 056802.
- (38) Nazin, G. V.; Qiu, X. H.; Ho, W. Visualization and Spectroscopy of a Metal-Molecule-Metal Bridge. *Science* **2003**, *302* (5642), 77–81.
- (39) Sagisaka, K.; Luce, A.; Fujita, D. Silicon Adatom Switching and Manipulation on Si(111)- $7 \times 7$ . *Nanotechnology* **2010**, *21* (4), 045707.
- (40) Wong, D.; Velasco Jr, J.; Ju, L.; Lee, J.; Kahn, S.; Tsai, H.-Z.; Germany, C.; Taniguchi, T.; Watanabe, K.; Zettl, A.; et al. Characterization and Manipulation of Individual Defects in Insulating Hexagonal Boron Nitride Using Scanning Tunneling Microscopy. *Nat. Nanotechnol.* **2015**, *10* (11), 949–953.
- (41) Baumeister, W.; Grütter, P.; Guckenberger, R.; Güntherodt, H.-J.; Hartmann, T.; Heinzlmann, H.; Knapp, H. F.; Mamin, H. J.; Meyer, E.; Pohl, D. W.; et al. *Scanning Tunneling Microscopy II: Further Applications and Related Scanning Techniques*, 2nd edition.; Wiesendanger, R., Güntherodt, H.-J., Eds.; Springer: Berlin ; New York, 1995.

- (42) Kuk, Y.; Silverman, P. J. Scanning Tunneling Microscope Instrumentation. *Rev. Sci. Instrum.* **1989**, *60* (2), 165–180.
- (43) Hallmark, V. M.; Chiang, S.; Rabolt, J. F.; Swalen, J. D.; Wilson, R. J. Observation of Atomic Corrugation on Au(111) by Scanning Tunneling Microscopy. *Phys. Rev. Lett.* **1987**, *59* (25), 2879–2882.
- (44) Tessmer, S. H.; Harlingen, D. J. V.; Lyding, J. W. Integrated Cryogenic Scanning Tunneling Microscopy and Sample Preparation System. *Rev. Sci. Instrum.* **1994**, *65* (9), 2855–2859.
- (45) Stipe, B. C.; Rezaei, M. A.; Ho, W. A Variable-Temperature Scanning Tunneling Microscope Capable of Single-Molecule Vibrational Spectroscopy. *Rev. Sci. Instrum.* **1999**, *70* (1), 137.
- (46) Pan, S. H.; Hudson, E. W.; Davis, J. C. <sup>3</sup>He Refrigerator Based Very Low Temperature Scanning Tunneling Microscope. *Rev. Sci. Instrum.* **1999**, *70* (2), 1459–1463.
- (47) Albrecht, P. M.; Lyding, J. W. Ultrahigh-Vacuum Scanning Tunneling Microscopy and Spectroscopy of Single-Walled Carbon Nanotubes on Hydrogen-Passivated Si(100) Surfaces. *Appl. Phys. Lett.* **2003**, *83* (24), 5029–5031.
- (48) Zhang, L.; Colella, N. S.; Liu, F.; Trahan, S.; Baral, J. K.; Winter, H. H.; Mannsfeld, S. C. B.; Briseno, A. L. Synthesis, Electronic Structure, Molecular Packing/Morphology Evolution, and Carrier Mobilities of Pure Oligo-/Poly(alkylthiophenes). *J. Am. Chem. Soc.* **2013**, *135* (2), 844–854.
- (49) Swart, I.; Liljeroth, P.; Vanmaekelbergh, D. Scanning Probe Microscopy and Spectroscopy of Colloidal Semiconductor Nanocrystals and Assembled Structures. *Chem. Rev.* **2016**.
- (50) Bernard, R.; Comtet, G.; Dujardin, G.; Huc, V.; Mayne, A. J. Imaging and Spectroscopy of Individual CdSe Nanocrystals on Atomically Resolved Surfaces. *Appl. Phys. Lett.* **2005**, *87* (5), 053114–053114–3.



## REFERENCES CITED FOR CHAPTER II

- (1) C. J. Chen, Introduction to Scanning Tunneling Microscopy, Oxford University Press New York (2008).
- (2) S. Behler, M. K. Rose, J. C. Dunphy, D. F. Ogletree, M. Salmeron and C. Chapelier Review of Scientific Instruments **68**, (1997).
- (3) B. C. Stipe, M. A. Rezaei and W. Ho Review of Scientific Instruments **70**, (1999).
- (4) E. T. Foley, N. L. Yoder, N. P. Guisinger and M. C. Hersam Review of Scientific Instruments **75**, (2004).
- (5) G. Meyer Review of Scientific Instruments **67**, (1996).
- (6) S. H. Pan, E. W. Hudson and J. C. Davis Review of Scientific Instruments **70**, (1999).
- (7) B. J. Albers, M. Liebmann, T. C. Schwendemann, M. Z. Baykara, M. Heyde, M. Salmeron, E. I. Altman and U. D. Schwarz Review of Scientific Instruments **79**, (2008).
- (8) S. Zhang Nature, doi:10.1038/nature.2013.13819, (2013).
- (9) CS202PF-X20B Cryostat from Advanced Research Systems, Inc., 7476 Industrial Park Way, Macungie, PA 18062, United States.
- (10) T. Tomaru, T. Suzuki, T. Haruyama, T. Shintomi, A. Yamamoto, T. Koyama and R. Li Cryogenics **44**, (2004).
- (11) Cryostat noise specifications are available from Advanced Research Systems, Inc., 7476 Industrial Park Way, Macungie, PA 18062, United States.
- (12) RHK Technology, Inc., 1050 East Maple Road, Troy, Michigan 48083, United States.
- (13) H. J. Hug, B. Stiefel, P. J. A. van Schendel, A. Moser, S. Martin and H. J. Guntherodt Review of Scientific Instruments **70**, (1999).
- (14) X. H. Qiu, G. V. Nazin and W. Ho Science **299**, (2003).

- (15) C. Chen, P. Chu, C. A. Bobisch, D. L. Mills and W. Ho Physical Review Letters **105**, (2010).
- (16) G. V. Nazin, X. H. Qiu and W. Ho Physical Review Letters **90**, (2003).
- (17) S. W. Wu, G. V. Nazin and W. Ho Phys. Rev. B **77**, (2008).
- (18) Shapal , Precision Ceramics, 86 Lower Tower Street, Birmingham B19 3PA, England.
- (19) P. M. Albrecht and J. W. Lyding Applied Physics Letters **83**, (2003).
- (20) Series 99 Pulse Valve, Parker Hannifin Corporation, 26 Clinton Drive, Unit 103, Hollis, NH 03049, United States.
- (21) Z. Q. Wei, S. Guo and S. A. Kandel J. Phys. Chem. B **110**, (2006).
- (22) J. V. Barth, H. Brune, G. Ertl and R. J. Behm Phys. Rev. B **42**, (1990).
- (23) B. C. Stipe, M. A. Rezaei and W. Ho Science **280**, (1998).

### REFERENCES CITED FOR CHAPTER III

- (1) Avouris, P.; Freitag, M.; Perebeinos, V. Carbon-nanotube photonics and optoelectronics. *Nat. Photonics* **2008**, 2 (6), 341-350.
- (2) Dresselhaus, M. S.; Dresselhaus, G.; Saito, R.; Jorio, A. Exciton photophysics of carbon nanotubes. *Annu. Rev. Phys. Chem.* **2007**, 58, 719-747.
- (3) Avouris, P.; Chen, Z. H.; Perebeinos, V. Carbon-based electronics. *Nat. Nanotechnol.* **2007**, 2 (10), 605-615.
- (4) Charlier, J. C.; Blase, X.; Roche, S. Electronic and transport properties of nanotubes. *Rev. Mod. Phys.* **2007**, 79 (2), 677-732.
- (5) Freitag, M.; Tsang, J. C.; Bol, A.; Avouris, P.; Yuan, D. N.; Liu, J. Scanning photovoltage microscopy of potential modulations in carbon nanotubes. *Appl. Phys. Lett.* **2007**, 91 (3), 031101.

- (6) Biercuk, M.; Ilani, S.; Marcus, C.; McEuen, P. Electrical Transport in Single-Wall Carbon Nanotubes. In *Carbon Nanotubes*, Jorio, A.; Dresselhaus, G.; Dresselhaus, M., Eds. Springer Berlin Heidelberg: 2008; Vol. 111, pp 455-493.
- (7) Stokes, P.; Khondaker, S. I. Evaluating Defects in Solution-Processed Carbon Nanotube Devices via Low-Temperature Transport Spectroscopy. *ACS Nano* **2010**, *4* (5), 2659-2666.
- (8) Gao, B.; Glattli, D. C.; Plaças, B.; Bachtold, A. Cotunneling and one-dimensional localization in individual disordered single-wall carbon nanotubes: Temperature dependence of the intrinsic resistance. *Phys. Rev. B* **2006**, *74* (8), 085410.
- (9) Bachtold, A.; Fuhrer, M. S.; Plyasunov, S.; Forero, M.; Anderson, E. H.; Zettl, A.; McEuen, P. L. Scanned Probe Microscopy of Electronic Transport in Carbon Nanotubes. *Phys. Rev. Lett.* **2000**, *84* (26), 6082-6085.
- (10) Wang, N. P.; Heinze, S.; Tersoff, J. Random-telegraph-signal noise and device variability in ballistic nanotube transistors. *Nano Lett.* **2007**, *7* (4), 910-913.
- (11) Liu, F.; Bao, M. Q.; Kim, H. J.; Wang, K. L.; Li, C.; Liu, X. L.; Zhou, C. W. Giant random telegraph signals in the carbon nanotubes as a single defect probe. *Appl. Phys. Lett.* **2005**, *86* (16), 163102.
- (12) Tans, S. J.; Dekker, C. Molecular transistors: Potential modulations along carbon nanotubes. *Nature* **2000**, *404* (6780), 834-835.
- (13) Purewal, M. S.; Hong, B. H.; Ravi, A.; Chandra, B.; Hone, J.; Kim, P. Scaling of Resistance and Electron Mean Free Path of Single-Walled Carbon Nanotubes. *Phys. Rev. Lett.* **2007**, *98* (18), 186808.
- (14) Matsuda, K.; Inoue, T.; Murakami, Y.; Maruyama, S.; Kanemitsu, Y. Exciton fine structure in a single carbon nanotube revealed through spectral diffusion. *Phys. Rev. B* **2008**, *77* (19), 193405.
- (15) Xue, Y. Q.; Ratner, M. A. Scaling analysis of electron transport through metal-semiconducting carbon nanotube interfaces: Evolution from the molecular limit to the bulk limit. *Phys. Rev. B* **2004**, *70* (20), 205416.

- (16) Albrecht, P. M.; Lyding, J. W. Ultrahigh-vacuum scanning tunneling microscopy and spectroscopy of single-walled carbon nanotubes on hydrogen-passivated Si(100) surfaces. *Appl. Phys. Lett.* **2003**, *83* (24), 5029-5031.
- (17) Clair, S.; Rabot, C.; Kim, Y.; Kawai, M. Adsorption mechanism of aligned single wall carbon nanotubes at well defined metal surfaces. *J. of Vac. Sci. Technol. B* **2007**, *25* (4), 1143-1146.
- (18) Chen, C. J. *Introduction to Scanning Tunneling Microscopy*. Second Edition ed.; Oxford University Press: New York, 2008.
- (19) Wildoer, J. W. G.; Venema, L. C.; Rinzler, A. G.; Smalley, R. E.; Dekker, C. Electronic structure of atomically resolved carbon nanotubes. *Nature* **1998**, *391* (6662), 59-62.
- (20) Odom, T. W.; Huang, J. L.; Kim, P.; Lieber, C. M. Atomic structure and electronic properties of single-walled carbon nanotubes. *Nature* **1998**, *391* (6662), 62-64.
- (21) Shin, H.-J.; Clair, S.; Kim, Y.; Kawai, M. Substrate-induced array of quantum dots in a single-walled carbon nanotube. *Nat. Nanotechnol.* **2009**, *4* (9), 567-570.
- (22) Clair, S.; Kim, Y.; Kawai, M. Energy level alignment of single-wall carbon nanotubes on metal surfaces. *Phys. Rev. B* **2011**, *83* (24), 245422.
- (23) Nazin, G. V.; Qiu, X. H.; Ho, W. Vibrational spectroscopy of individual doping centers in a monolayer organic crystal. *J. Chem. Phys.* **2005**, *122* (18), 181105.
- (24) Nazin, G. V.; Wu, S. W.; Ho, W. Tunneling rates in electron transport through double-barrier molecular junctions in a scanning tunneling microscope. *Proc. Natl. Acad. Sci. U. S. A.* **2005**, *102* (25), 8832-8837.
- (25) Qiu, X. H.; Nazin, G. V.; Ho, W. Vibronic states in single molecule electron transport. *Phys. Rev. Lett.* **2004**, *92* (20), 206102.
- (26) Wu, S. W.; Nazin, G. V.; Chen, X.; Qiu, X. H.; Ho, W. Control of relative tunneling rates in single molecule bipolar electron transport. *Phys. Rev. Lett.* **2004**, *93* (23), 236802.

- (27) Barbara, P. F.; Meyer, T. J.; Ratner, M. A. Contemporary issues in electron transfer research. *J. Phys. Chem.* **1996**, *100* (31), 13148-13168.
- (28) Park, H.; Park, J.; Lim, A. K. L.; Anderson, E. H.; Alivisatos, A. P.; McEuen, P. L. Nanomechanical oscillations in a single-C<sub>60</sub> transistor. *Nature* **2000**, *407* (6800), 57-60.
- (29) Lee, J.; Perdue, S. M.; Perez, A. R.; Apkarian, V. A. Vibronic Motion with Joint Angstrom-Femtosecond Resolution Observed through Fano Progressions Recorded within One Molecule. *ACS Nano* **2014**, *8* (1), 54-63.
- (30) Lee, J.; Perdue, S. M.; Perez, A. R.; El-Khoury, P. Z.; Honkala, K.; Apkarian, V. A. Orbiting Orbitals: Visualization of Vibronic Motion at a Conical Intersection. *J. Phys. Chem. A* **2013**, *117* (46), 11655-11664.
- (31) Harigaya, K.; Fujita, M. Dimerization Structures of Metallic and Semiconducting Fullerene Tubules. *Phys. Rev. B* **1993**, *47* (24), 16563-16569.
- (32) Matsuo, Y.; Tahara, K.; Nakamura, E. Theoretical studies on structures and aromaticity of finite-length armchair carbon nanotubes. *Org. Lett.* **2003**, *5* (18), 3181-3184.
- (33) Yumura, T.; Nozaki, D.; Bandow, S.; Yoshizawa, K.; Iijima, S. End-cap effects on vibrational structures of finite-length carbon nanotubes. *J. Am. Chem. Soc.* **2005**, *127* (33), 11769-11776.
- (34) Martín-Martínez, F. J.; Melchor, S.; Dobado, J. A. Clar-Kekulé Structuring in Armchair Carbon Nanotubes. *Org. Lett.* **2008**, *10* (10), 1991-1994.
- (35) Hiberty, P. C.; Shaik, S. The distortive tendencies of p electronic systems, their relationship to isoelectronic s bonded analogs, and observables: A description free of the classical paradoxes. *Phys. Chem. Chem. Phys.* **2004**, *6* (2), 224-231.
- (36) Kertesz, M.; Choi, C. H.; Yang, S. J. Conjugated polymers and aromaticity. *Chem. Rev.* **2005**, *105* (10), 3448-3481.

- (37) Zhou, Z. Y.; Steigerwald, M.; Hybertsen, M.; Brus, L.; Friesner, R. A. Electronic structure of tubular aromatic molecules derived from the metallic (5,5) armchair single wall carbon nanotube. *J. Am. Chem. Soc.* **2004**, *126* (11), 3597-3607.
- (38) Tretiak, S.; Kilina, S.; Piryatinski, A.; Saxena, A.; Martin, R. L.; Bishop, A. R. Excitons and Peierls distortion in conjugated carbon nanotubes. *Nano Lett.* **2007**, *7* (1), 86-92.
- (39) Dresselhaus, M. S.; Eklund, P. C. Phonons in carbon nanotubes. *Adv. Phys.* **2000**, *49* (6), 705-814.
- (40) LeRoy, B. J.; Lemay, S. G.; Kong, J.; Dekker, C. Electrical generation and absorption of phonons in carbon nanotubes. *Nature* **2004**, *432* (7015), 371-374.

#### REFERENCES CITED FOR CHAPTER IV

- (1) Braun, S.; Salaneck, W. R.; Fahlman, M., Energy-Level Alignment at Organic/Metal and Organic/Organic Interfaces. *Adv. Mater.* **2009**, *21* (14-15), 1450-1472.
- (2) Heimel, G.; Romaner, L.; Zojer, E.; Bredas, J.-L., The Interface Energetics of Self-Assembled Monolayers on Metals. *Acc. Chem. Res.* **2008**, *41* (6), 721-729.
- (3) Koch, N., Energy levels at interfaces between metals and conjugated organic molecules. *J. Phys.-Condens. Matter* **2008**, *20* (18), 184008.
- (4) Höfer, A.; Duncker, K.; Kiel, M.; Wedekind, S.; Widdra, W., Adsorption of  $\alpha$ -sexithiophene on Au(001): Molecule-induced partial lifting of the substrate reconstruction. *Phys. Rev. B* **2011**, *83* (7), 075414.
- (5) Dong, S.; Zhang, H.; Yang, L.; Bai, M.; Yao, Y.; Chen, H.; Gan, L.; Yang, T.; Jiang, H.; Hou, S.; Wan, L.; Guo, X., Solution-Crystallized Organic Semiconductors with High Carrier Mobility and Air Stability. *Adv. Mater.* **2012**, *24* (41), 5576-5580.
- (6) Sokolov, A. N.; Sumrak, J. C.; MacGillivray, L. R., Conformational polymorphism facilitates assignment of trans and cis-conformers of an alpha-

- substituted oligothiophene via IR spectroscopy. *Chem. Commun.* **2010**, 46 (1), 82-84.
- (7) Zhang, L.; Colella, N. S.; Cherniawski, B. P.; Mannsfeld, S. C. B.; Briseno, A. L., Oligothiophene Semiconductors: Synthesis, Characterization, and Applications for Organic Devices. *ACS Appl. Mater. Interfaces* **2014**, 6 (8), 5327-5343.
- (8) Barbarella, G.; Zambianchi, M.; Antolini, L.; Ostoja, P.; Maccagnani, P.; Bongini, A.; Marseglia, E. A.; Tedesco, E.; Gigli, G.; Cingolani, R., Solid-state conformation, molecular packing, and electrical and optical properties of processable beta-methylated sexithiophenes. *J. Am. Chem. Soc.* **1999**, 121 (38), 8920-8926.
- (9) Di Maria, F.; Fabiano, E.; Gentili, D.; Biasiucci, M.; Salzillo, T.; Bergamini, G.; Gazzano, M.; Zanelli, A.; Brillante, A.; Cavallini, M.; Della Sala, F.; Gigli, G.; Barbarella, G., Polymorphism in Crystalline Microfibers of Achiral Octithiophene: The Effect on Charge Transport, Supramolecular Chirality and Optical Properties. *Adv. Funct. Mater.* **2014**, 24 (31), 4943-4951.
- (10) Nishiyama, F.; Ogawa, K.; Tanaka, S.; Yokoyama, T., Direct Conformational Analysis of a 10 nm Long Oligothiophene Wire. *J. Phys. Chem. B* **2008**, 112 (17), 5272-5275.
- (11) Duncker, K.; Kiel, M.; Hofer, A.; Widdra, W., Commensurate surface structures and concerted cis-trans-isomerization within ordered monolayers of alpha-sexithiophene on Ag(001). *Phys. Rev. B* **2008**, 77 (15).
- (12) Förster, S.; Kohl, E.; Ivanov, M.; Gross, J.; Widdra, W.; Janke, W., Polymer adsorption on reconstructed Au(001): A statistical description of P3HT by scanning tunneling microscopy and coarse-grained Monte Carlo simulations. *J. Chem. Phys.* **2014**, 141 (16), 164701.
- (13) Yang, Z.-Y.; Zhang, H.-M.; Yan, C.-J.; Li, S.-S.; Yan, H.-J.; Song, W.-G.; Wan, L.-J., Scanning tunneling microscopy of the formation, transformation, and property of oligothiophene self-organizations on graphite and gold surfaces. *Proc. Natl. Acad. Sci. U. S. A.* **2007**, 104 (10), 3707-3712.

- (14) Mena-Osteritz, E.; Urdanpilleta, M.; El-Hosseiny, E.; Koslowski, B.; Ziemann, P.; Bauerle, P., STM study on the self-assembly of oligothiophene-based organic semiconductors. *Beilstein J. Nanotechnol.* **2011**, *2*, 802-808.
- (15) Hackley, J. D.; Kislitsyn, D. A.; Beaman, D. K.; Ulrich, S.; Nazin, G. V., High-Stability Cryogenic Scanning Tunneling Microscope Based on a Closed-Cycle Cryostat. *Review of Scientific Instruments* **2014**, *85* (10), 103704.
- (16) Zhang, L.; Colella, N. S.; Liu, F.; Trahan, S.; Baral, J. K.; Winter, H. H.; Mannsfeld, S. C. B.; Briseno, A. L., Synthesis, Electronic Structure, Molecular Packing/Morphology Evolution, and Carrier Mobilities of Pure Oligo-/Poly(alkylthiophenes). *J. Am. Chem. Soc.* **2012**, *135* (2), 844-854.
- (17) Chen, C. J., *Introduction to Scanning Tunneling Microscopy*. Second Edition ed.; Oxford University Press: New York, **2008**.
- (18) Antolini, L.; Horowitz, G.; Kouki, F.; Garnier, F., Polymorphism in oligothiophenes with an even number of thiophene subunits. *Adv. Mater.* **1998**, *10* (5), 382-385.
- (19) Goursot, A.; Mineva, T.; Kevorkyants, R.; Talbi, D., Interaction between n-Alkane Chains: Applicability of the Empirically Corrected Density Functional Theory for Van der Waals Complexes. *Journal of Chemical Theory and Computation* **2007**, *3*, 755-763.
- (20) Vujanovich, E. C.; Bloom, J. W. G.; Wheeler, S. E., Impact of Neighboring Chains on Torsional Defects in Oligothiophenes. *J. Phys. Chem. A* **2012**, *116* (11), 2997-3003.
- (21) Sandig, N.; Biscarini, F.; Zerbetto, F., Driving Force for the Adsorption of Sexithiophene on Gold. *J. Phys. Chem. C* **2008**, *112* (49), 19516-19520.
- (22) Zhou, J.; Yang, Y. X.; Liu, P.; Camillone, N., III; White, M. G., Electronic Structure of the Thiophene/Au(111) Interface Probed by Two-Photon Photoemission. *J. Phys. Chem. C* **2010**, *114* (32), 13670-13677.



- (23) Tonigold, K.; Gross, A., Adsorption of small aromatic molecules on the (111) surfaces of noble metals: A density functional theory study with semiempirical corrections for dispersion effects. *J. Chem. Phys.* **2010**, *132* (22).
- (24) Buimaga-Iarinca, L.; Morari, C., Adsorption of small aromatic molecules on gold: a DFT localized basis set study including van der Waals effects. *Theor. Chem. Acc.* **2014**, *133* (7).
- (25) Varene, E.; Bogner, L.; Meyer, S.; Pennec, Y.; Tegeder, P., Coverage-dependent adsorption geometry of octithiophene on Au(111). *Phys. Chem. Chem. Phys.* **2012**, *14* (2), 691-696.
- (26) Zhang, H. M.; Xie, Z. X.; Mao, B. W.; Xu, X., Self-Assembly of Normal Alkanes on the Au (111) Surfaces. *Chemistry-A European Journal* **2004**, *10* (6), 1415-1422.
- (27) Hanke, F.; Björk, J., Structure and local reactivity of the Au(111) surface reconstruction. *Phys. Rev. B* **2013**, *87* (23), 235422.
- (28) Koslowski, B.; Tschetschetkin, A.; Maurer, N.; Mena-Osteritz, E.; Bauerle, P.; Ziemann, P., Terthiophene on Au(111): A scanning tunneling microscopy and spectroscopy study. *Beilstein J. Nanotechnol.* **2011**, *2*, 561-568.
- (29) Callsen, M.; Atodiresei, N.; Caciuc, V.; Blügel, S., Semiempirical van der Waals interactions versus ab initio nonlocal correlation effects in the thiophene-Cu (111) system. *Phys. Rev. B* **2012**, *86* (8), 085439.
- (30) Zhao, J.; Feng, M.; Dougherty, D. B.; Sun, H.; Petek, H., Molecular Electronic Level Alignment at Weakly Coupled Organic Film/Metal Interfaces. *ACS Nano* **2014**, *8* (10), 10988-10997.

## REFERENCES CITED FOR CHAPTER V

- (1) Walzer, K.; Maennig, B.; Pfeiffer, M.; Leo, K. Highly Efficient Organic Devices Based on Electrically Doped Transport Layers. *Chem. Rev.* **2007**, *107* (4), 1233-1271.

- (2) Katz, H. E.; Huang, J. Thin-Film Organic Electronic Devices. *Annu. Rev. Mater. Res.* **2009**, *39* (1), 71-92.
- (3) Armstrong, N. R.; Wang, W. N.; Alloway, D. M.; Placencia, D.; Ratcliff, E.; Brumbach, M. Organic/Organic' Heterojunctions: Organic Light Emitting Diodes and Organic Photovoltaic Devices. *Macromol. Rapid Commun.* **2009**, *30* (9-10), 717-731.
- (4) Hains, A. W.; Liang, Z. Q.; Woodhouse, M. A.; Gregg, B. A. Molecular Semiconductors in Organic Photovoltaic Cells. *Chem. Rev.* **2010**, *110* (11), 6689-6735.
- (5) Shirota, Y.; Kageyama, H. Charge carrier transporting molecular materials and their applications in devices. *Chem. Rev.* **2007**, *107* (4), 953-1010.
- (6) Menard, E.; Meitl, M. A.; Sun, Y. G.; Park, J. U.; Shir, D. J. L.; Nam, Y. S.; Jeon, S.; Rogers, J. A. Micro- and nanopatterning techniques for organic electronic and optoelectronic systems. *Chem. Rev.* **2007**, *107* (4), 1117-1160.
- (7) Gao, Y. Surface analytical studies of interfaces in organic semiconductor devices. *Materials Science and Engineering: R: Reports* **2010**, *68* (3), 39-87.
- (8) Koch, N. Organic Electronic Devices and Their Functional Interfaces. *ChemPhysChem* **2007**, *8* (10), 1438-1455.
- (9) Braun, S.; Salaneck, W. R.; Fahlman, M. Energy-Level Alignment at Organic/Metal and Organic/Organic Interfaces. *Adv. Mater.* **2009**, *21* (14-15), 1450-1472.
- (10) Heimel, G.; Romaner, L.; Zojer, E.; Bredas, J.-L. The Interface Energetics of Self-Assembled Monolayers on Metals. *Acc. Chem. Res.* **2008**, *41* (6), 721-729.
- (11) Koch, N. Energy levels at interfaces between metals and conjugated organic molecules. *J. Phys.-Condens. Matter* **2008**, *20* (18), 184008.
- (12) Höfer, A.; Duncker, K.; Kiel, M.; Wedekind, S.; Widdra, W. Adsorption of  $\alpha$ -sexithiophene on Au(001): Molecule-induced partial lifting of the substrate reconstruction. *Phys. Rev. B* **2011**, *83* (7), 075414.

- (13) Dong, S.; Zhang, H.; Yang, L.; Bai, M.; Yao, Y.; Chen, H.; Gan, L.; Yang, T.; Jiang, H.; Hou, S.; Wan, L.; Guo, X. Solution-Crystallized Organic Semiconductors with High Carrier Mobility and Air Stability. *Adv. Mater.* **2012**, *24* (41), 5576-5580.
- (14) Fitzner, R.; Mena-Osteritz, E.; Mishra, A.; Schulz, G.; Reinold, E.; Weil, M.; Körner, C.; Ziehlke, H.; Elschner, C.; Leo, K.; Riede, M.; Pfeiffer, M.; Uhrich, C.; Bäuerle, P. Correlation of  $\pi$ -Conjugated Oligomer Structure with Film Morphology and Organic Solar Cell Performance. *J. Am. Chem. Soc.* **2012**, *134* (27), 11064-11067.
- (15) Zhang, L.; Liu, F.; Diao, Y.; Marsh, H. S.; Colella, N. S.; Jayaraman, A.; Russell, T. P.; Mannsfeld, S. C. B.; Brisenno, A. L. The Good Host: Formation of Discrete One-Dimensional Fullerene "Channels" in Well-Ordered Poly(2,5-bis(3-alkylthiophen-2-yl)thieno 3,2-b thiophene) Oligomers. *J. Am. Chem. Soc.* **2014**, *136* (52), 18120-18130.
- (16) Cnops, K.; Rand, B. P.; Cheyns, D.; Verreert, B.; Empl, M. A.; Heremans, P. 8.4% efficient fullerene-free organic solar cells exploiting long-range exciton energy transfer. *Nat. Commun.* **2014**, *5*.
- (17) Sokolov, A. N.; Sumrak, J. C.; MacGillivray, L. R. Conformational polymorphism facilitates assignment of trans and cis-conformers of an alpha-substituted oligothiophene via IR spectroscopy. *Chem. Commun.* **2010**, *46* (1), 82-84.
- (18) Zhang, L.; Colella, N. S.; Cherniawski, B. P.; Mannsfeld, S. C. B.; Brisenno, A. L. Oligothiophene Semiconductors: Synthesis, Characterization, and Applications for Organic Devices. *ACS Appl. Mater. Interfaces* **2014**, *6* (8), 5327-5343.
- (19) Barbarella, G.; Zambianchi, M.; Antolini, L.; Ostojica, P.; Maccagnani, P.; Bongini, A.; Marseglia, E. A.; Tedesco, E.; Gigli, G.; Cingolani, R. Solid-state conformation, molecular packing, and electrical and optical properties of processable beta-methylated sexithiophenes. *J. Am. Chem. Soc.* **1999**, *121* (38), 8920-8926.

- (20) Di Maria, F.; Fabiano, E.; Gentili, D.; Biasiucci, M.; Salzillo, T.; Bergamini, G.; Gazzano, M.; Zanelli, A.; Brillante, A.; Cavallini, M.; Della Sala, F.; Gigli, G.; Barbarella, G. Polymorphism in Crystalline Microfibers of Achiral Octithiophene: The Effect on Charge Transport, Supramolecular Chirality and Optical Properties. *Adv. Funct. Mater.* **2014**, *24* (31), 4943-4951.
- (21) Varene, E.; Martin, I.; Tegeder, P. Optically Induced Inter- and Intrafacial Electron Transfer Probed by Two-Photon Photoemission: Electronic States of Sexithiophene on Au(111). *J. Phys. Chem. Lett.* **2011**, *2* (3), 252-256.
- (22) Koslowski, B.; Tschetschetkin, A.; Maurer, N.; Mena-Osteritz, E.; Bauerle, P.; Ziemann, P. Terthiophene on Au(111): A scanning tunneling microscopy and spectroscopy study. *Beilstein J. Nanotechnol.* **2011**, *2*, 561-568.
- (23) Reece, G.; Bulou, H.; Scheurer, F.; Speisser, V.; Carrière, B.; Mathevet, F.; Schull, G. Oligothiophene Nanorings as Electron Resonators for Whispering Gallery Modes. *Phys. Rev. Lett.* **2013**, *110* (5), 056802.
- (24) Repp, J.; Liljeroth, P.; Meyer, G. Coherent electron-nuclear coupling in oligothiophene molecular wires. *Nat. Phys.* **2010**, *6* (12), 975-979.
- (25) Jäckel, F.; Perera, U. G. E.; Iancu, V.; Braun, K. F.; Koch, N.; Rabe, J. P.; Hla, S. W. Investigating Molecular Charge Transfer Complexes with a Low Temperature Scanning Tunneling Microscope. *Phys. Rev. Lett.* **2008**, *100* (12), 126102.
- (26) Varene, E.; Pennec, Y.; Tegeder, P. Assembly and electronic structure of octithiophene on Au(111). *Chem. Phys. Lett.* **2011**, *515* (1-3), 141-145.
- (27) Oeter, D.; Egelhaaf, H. J.; Ziegler, C.; Oelkrug, D.; Gopel, W. Electronic-Transitions in Alpha-Oligothiophene Thin-Films - Comparison of Ultraviolet-Visible Absorption-Spectroscopy and High-Resolution Electron-Energy-Loss Spectroscopy Investigations. *J. Chem. Phys.* **1994**, *101* (7), 6344-6352.
- (28) Hill, I. G.; Kahn, A.; Soos, Z. G.; Pascal, J. R. A. Charge-separation energy in films of  $\pi$ -conjugated organic molecules. *Chem. Phys. Lett.* **2000**, *327* (3-4), 181-188.

- (29) Varene, E.; Bogner, L.; Meyer, S.; Pennec, Y.; Tegeder, P. Coverage-dependent adsorption geometry of octithiophene on Au(111). *Phys. Chem. Chem. Phys.* **2012**, *14* (2), 691-696.
- (30) Yang, Z.-Y.; Zhang, H.-M.; Pan, G.-B.; Wan, L.-J. Effect of the Bridge Alkylene Chain on Adlayer Structure and Property of Functional Oligothiophenes Studied with Scanning Tunneling Microscopy and Spectroscopy. *ACS Nano* **2008**, *2* (4), 743-749.
- (31) Yang, Z.-Y.; Zhang, H.-M.; Yan, C.-J.; Li, S.-S.; Yan, H.-J.; Song, W.-G.; Wan, L.-J. Scanning tunneling microscopy of the formation, transformation, and property of oligothiophene self-organizations on graphite and gold surfaces. *Proc. Natl. Acad. Sci. U. S. A.* **2007**, *104* (10), 3707-3712.
- (32) Wang, L.; Tongol, B. J. V.; Yau, S.-L.; Otsubo, T.; Itaya, K. Substrate-Induced Varied Conformation and Molecular Assemblies: In Situ STM Observation of  $\beta$ -Substituted Oligothiophene Adlayers on Au(111). *Langmuir* **2010**, *26* (10), 7148-7152.
- (33) Mena-Osteritz, E.; Urdanpilleta, M.; El-Hosseiny, E.; Koslowski, B.; Ziemann, P.; Bauerle, P. STM study on the self-assembly of oligothiophene-based organic semiconductors. *Beilstein J. Nanotechnol.* **2011**, *2*, 802-808.
- (34) Linares, M.; Scifo, L.; Demadrille, R.; Brocorens, P.; Beljonne, D.; Lazzaroni, R.; Grevin, B. Two-Dimensional Self-Assemblies of Thiophene-Fluorenone Conjugated Oligomers on Graphite: A Joint STM and Molecular Modeling Study. *The Journal of Physical Chemistry C* **2008**, *112* (17), 6850-6859.
- (35) Bonini, M.; Zalewski, L.; Orgiu, E.; Breiner, T.; Dötz, F.; Kastler, M.; Samorì, P. H-Bonding Tuned Self-Assembly of Phenylene-Thiophene-Thiophene-Phenylene Derivatives at Surfaces: Structural and Electrical Studies. *The Journal of Physical Chemistry C* **2011**, *115* (19), 9753-9759.
- (36) Wang, X.-Y.; Jiang, W.; Chen, T.; Yan, H.-J.; Wang, Z.-H.; Wan, L.-J.; Wang, D. Molecular Evidence for the Intermolecular S-S Interaction in the Surface

- Molecular Packing Motifs of a Fused Thiophene Derivative. *Chemical Communications* **2013**, 49 (18), 1829-1831.
- (37) Nishiyama, F.; Ogawa, K.; Tanaka, S.; Yokoyama, T. Direct Conformational Analysis of a 10 nm Long Oligothiophene Wire. *J. Phys. Chem. B* **2008**, 112 (17), 5272-5275.
- (38) Duncker, K.; Kiel, M.; Hoefler, A.; Widdra, W. Commensurate surface structures and concerted cis-trans-isomerization within ordered monolayers of alpha-sexithiophene on Ag(001). *Phys. Rev. B* **2008**, 77 (15).
- (39) Yokoyama, T.; Kogure, Y.; Kawasaki, M.; Tanaka, S.; Aoshima, K. Scanning Tunneling Microscopy Imaging of Long Oligothiophene Wires Deposited on Au(111) Using Electrospray Ionization. *J. Phys. Chem. C* **2013**, 117 (36), 18484-18487.
- (40) Förster, S.; Kohl, E.; Ivanov, M.; Gross, J.; Widdra, W.; Janke, W. Polymer adsorption on reconstructed Au(001): A statistical description of P3HT by scanning tunneling microscopy and coarse-grained Monte Carlo simulations. *J. Chem. Phys.* **2014**, 141 (16), 164701.
- (41) Taber, B. N.; Kislitsyn, D. A.; Gervasi, C. F.; Mannsfeld, S. C. B.; Zhang, L.; Briseno, A. L.; Nazin, G. V. Adsorption-Induced Conformational Isomerization of Alkyl-Substituted Thiophene Oligomers on Au(111): Impact on the Interfacial Electronic Structure. *ACS Appl. Mater. Interfaces* **2015**.
- (42) Hackley, J. D.; Kislitsyn, D. A.; Beaman, D. K.; Ulrich, S.; Nazin, G. V. High-Stability Cryogenic Scanning Tunneling Microscope Based on a Closed-Cycle Cryostat. *Rev. Sci. Instrum.* **2014**, 85 (10), 103704.
- (43) Zhang, L.; Colella, N. S.; Liu, F.; Trahan, S.; Baral, J. K.; Winter, H. H.; Mannsfeld, S. C. B.; Briseno, A. L. Synthesis, Electronic Structure, Molecular Packing/Morphology Evolution, and Carrier Mobilities of Pure Oligo-/Poly(alkylthiophenes). *J. Am. Chem. Soc.* **2012**, 135 (2), 844-854.
- (44) Hanke, F.; Björk, J. Structure and local reactivity of the Au(111) surface reconstruction. *Phys. Rev. B* **2013**, 87 (23), 235422.

- (45) Callsen, M.; Atodiresei, N.; Caciuc, V.; Blügel, S. Semiempirical van der Waals interactions versus ab initio nonlocal correlation effects in the thiophene-Cu (111) system. *Phys. Rev. B* **2012**, *86* (8), 085439.
- (46) Lee, K.; Morikawa, Y.; Langreth, D. C. Adsorption of n-butane on Cu(100), Cu(111), Au(111), and Pt(111): Van der Waals density-functional study. *Phys. Rev. B* **2010**, *82* (15).
- (47) Sandig, N.; Biscarini, F.; Zerbetto, F. Driving Force for the Adsorption of Sexithiophene on Gold. *J. Phys. Chem. C* **2008**, *112* (49), 19516-19520.
- (48) Goursot, A.; Mineva, T.; Kevorkyants, R.; Talbi, D. Interaction between n-Alkane Chains: Applicability of the Empirically Corrected Density Functional Theory for Van der Waals Complexes. *Journal of Chemical Theory and Computation* **2007**, *3*, 755-763.
- (49) Zhao, J.; Feng, M.; Dougherty, D. B.; Sun, H.; Petek, H. Molecular Electronic Level Alignment at Weakly Coupled Organic Film/Metal Interfaces. *ACS Nano* **2014**, *8* (10), 10988-10997.
- (50) Zhang, H. M.; Xie, Z. X.; Mao, B. W.; Xu, X. Self-Assembly of Normal Alkanes on the Au (111) Surfaces. *Chemistry-A European Journal* **2004**, *10* (6), 1415-1422.
- (51) Yamada, R.; Uosaki, K. Two-dimensional crystals of alkanes formed on Au (111) surface in neat liquid: Structural investigation by scanning tunneling microscopy. *J. Phys. Chem. B* **2000**, *104* (25), 6021-6027.
- (52) Baxter, R. J.; Teobaldi, G.; Zerbetto, F. Modeling the adsorption of alkanes on an Au (111) surface. *Langmuir* **2003**, *19* (18), 7335-7340.
- (53) Zhou, J.; Yang, Y. X.; Liu, P.; Camillone, N., III; White, M. G. Electronic Structure of the Thiophene/Au(111) Interface Probed by Two-Photon Photoemission. *J. Phys. Chem. C* **2010**, *114* (32), 13670-13677.
- (54) Tonigold, K.; Gross, A. Adsorption of small aromatic molecules on the (111) surfaces of noble metals: A density functional theory study with semiempirical corrections for dispersion effects. *J. Chem. Phys.* **2010**, *132* (22).

- (55) Buimaga-Iarinca, L.; Morari, C. Adsorption of small aromatic molecules on gold: a DFT localized basis set study including van der Waals effects. *Theor. Chem. Acc.* **2014**, *133* (7).
- (56) Chen, C. J. *Introduction to Scanning Tunneling Microscopy*. Second Edition ed.; Oxford University Press: New York, 2008.
- (57) Facchetti, A.; Yoon, M. H.; Stern, C. L.; Hutchison, G. R.; Ratner, M. A.; Marks, T. J. Building blocks for N-type molecular and polymeric electronics. Perfluoroalkyl- versus alkyl-functionalized ligothiophenes (nTs; n=2-6). Systematic synthesis, spectroscopy, electrochemistry, and solid-state organization. *J. Am. Chem. Soc.* **2004**, *126* (41), 13480-13501.

#### REFERENCES CITED FOR CHAPTER VI

- (1) L. Zhang, N. S. Colella, B. P. Cherniawski, S. C. B. Mannsfeld and A. L. Briseno, *ACS Appl. Mater. Interfaces*, 2014, **6**, 5327-5343.
- (2) L. Xu, L. Yang and S. Lei, *Nanoscale*, 2012, **4**, 4399-4415.
- (3) I. McCulloch, M. Heeney, C. Bailey, K. Genevicius, I. MacDonald, M. Shkunov, D. Sparrowe, S. Tierney, R. Wagner, W. Zhang, M. L. Chabinyc, R. J. Kline, M. D. McGehee and M. F. Toney, *Nat. Mater.*, 2006, **5**, 328-333.
- (4) A. R. Murphy, J. M. J. Fréchet, P. Chang, J. Lee and V. Subramanian, *J. Am. Chem. Soc.*, 2004, **126**, 1596-1597.
- (5) C. Videlot-Ackermann, J. Ackermann, H. Brisset, K. Kawamura, N. Yoshimoto, P. Raynal, A. El Kassmi and F. Fages, *J. Am. Chem. Soc.*, 2005, **127**, 16346-16347.
- (6) M. Mazzeo, V. Vitale, F. Della Sala, M. Anni, G. Barbarella, L. Favaretto, G. Sotgiu, R. Cingolani and G. Gigli, *Adv. Mater.*, 2005, **17**, 34-39.
- (7) R. H. Friend, R. W. Gymer, A. B. Holmes, J. H. Burroughes, R. N. Marks, C. Taliani, D. D. C. Bradley, D. A. D. Santos, J. L. Bredas, M. Logdlund and W. R. Salaneck, *Nature*, 1999, **397**, 121-128.



- (8) L. Tong, C. Li, F. E. Chen, H. Bai, L. Zhao and G. Q. Shi, *Journal of Physical Chemistry C*, 2009, **113**, 7411-7415.
- (9) R. Fitzner, E. Mena-Osteritz, A. Mishra, G. Schulz, E. Reinold, M. Weil, C. Körner, H. Ziehlke, C. Elschner, K. Leo, M. Riede, M. Pfeiffer, C. Uhrich and P. Bäuerle, *J. Am. Chem. Soc.*, 2012, **134**, 11064-11067.
- (10) L. Zhang, F. Liu, Y. Diao, H. S. Marsh, N. S. Colella, A. Jayaraman, T. P. Russell, S. C. B. Mannsfeld and A. L. Briseno, *J. Am. Chem. Soc.*, 2014, **136**, 18120-18130.
- (11) K. Cnops, B. P. Rand, D. Cheyns, B. Verreert, M. A. Empl and P. Heremans, *Nat. Commun.*, 2014, **5**.
- (12) C. Schubert, J. T. Margraf, T. Clark and D. M. Guldi, *Chemical Society Reviews*, 2015, **44**, 988-998.
- (13) B. Q. Xu, X. L. Li, X. Y. Xiao, H. Sakaguchi and N. J. Tao, *Nano Letters*, 2005, **5**, 1491-1495.
- (14) B. Capozzi, E. J. Dell, T. C. Berkelbach, D. R. Reichman, L. Venkataraman and L. M. Campos, *Journal of the American Chemical Society*, 2014, **136**, 10486-10492.
- (15) N. Koch, *J. Phys.-Condens. Matter*, 2008, **20**, 184008.
- (16) A. Höfer, K. Duncker, M. Kiel, S. Wedekind and W. Widdra, *Phys. Rev. B*, 2011, **83**, 075414.
- (17) H. Sirringhaus, P. J. Brown, R. H. Friend, M. M. Nielsen, K. Bechgaard, B. M. W. Langeveld-Voss, A. J. H. Spiering, R. A. J. Janssen, E. W. Meijer, P. Herwig and D. M. de Leeuw, *Nature*, 1999, **401**, 685-688.
- (18) Y. Wu, P. Liu, B. S. Ong, T. Srikumar, N. Zhao, G. Botton and S. Zhu, *Appl. Phys. Lett.*, 2005, **86**, 142102.
- (19) S. Duhm, G. Heimel, I. Salzmann, H. Glowatzki, R. L. Johnson, A. Vollmer, J. P. Rabe and N. Koch, *Nat. Mater.*, 2008, **7**, 326-332.

- (20) R. Joseph Kline, M. D. McGehee and M. F. Toney, *Nat. Mater.*, 2006, **5**, 222-228.
- (21) A. Dodabalapur, L. Torsi and H. E. Katz, *Science*, 1995, **268**, 270-271.
- (22) J. Huang, J. Sun and H. E. Katz, *Adv. Mater.*, 2008, **20**, 2567-+.
- (23) S. Fabiano, C. Musumeci, Z. Chen, A. Scandurra, H. Wang, Y.-L. Loo, A. Facchetti and B. Pignataro, *Adv. Mater.*, 2012, **24**, 951-+.
- (24) G. R. Dholakia, M. Meyyappan, A. Facchetti and T. J. Marks, *Nano Lett.*, 2006, **6**, 2447-2455.
- (25) J. E. Lyon, A. J. Cascio, M. M. Beerbom, R. Schlaf, Y. Zhu and S. A. Jenekhe, *Appl. Phys. Lett.*, 2006, **88**, 222109.
- (26) H. Ishii, K. Sugiyama, E. Ito and K. Seki, *Adv. Mater.*, 1999, **11**, 605-+.
- (27) S. Wang, A. Kiersnowski, W. Pisula and K. Müllen, *J. Am. Chem. Soc.*, 2012, **134**, 4015-4018.
- (28) E. Mena-Osteritz, A. Meyer, B. M. W. Langeveld-Voss, R. A. J. Janssen, E. W. Meijer and P. Bäuerle, *Angewandte Chemie International Edition*, 2000, **39**, 2679-2684.
- (29) Z.-Y. Yang, H.-M. Zhang, G.-B. Pan and L.-J. Wan, *ACS Nano*, 2008, **2**, 743-749.
- (30) Z.-Y. Yang, H.-M. Zhang, C.-J. Yan, S.-S. Li, H.-J. Yan, W.-G. Song and L.-J. Wan, *Proc. Natl. Acad. Sci. U. S. A.*, 2007, **104**, 3707-3712.
- (31) E. Mena-Osteritz, M. Urdanpilleta, E. El-Hosseiny, B. Koslowski, P. Ziemann and P. Bauerle, *Beilstein J. Nanotechnol.*, 2011, **2**, 802-808.
- (32) X. J. Ma, Y. Guo, T. Wang and Z. H. Su, *J. Chem. Phys.*, 2013, **139**.
- (33) T. Jaroch, M. Knor, R. Nowakowski, M. Zagorska and A. Pron, *Phys. Chem. Chem. Phys.*, 2008, **10**, 6182-6189.
- (34) B. Grévin, P. Rannou, R. Payerne, A. Pron and J. P. Travers, *J. Chem. Phys.*, 2003, **118**, 7097-7102.

- (35) L. Wang, B. J. V. Tongol, S.-L. Yau, T. Otsubo and K. Itaya, *Langmuir*, 2010, **26**, 7148-7152.
- (36) F. Nishiyama, K. Ogawa, S. Tanaka and T. Yokoyama, *J. Phys. Chem. B*, 2008, **112**, 5272-5275.
- (37) K. Duncker, M. Kiel, A. Hoefler and W. Widdra, *Phys. Rev. B*, 2008, **77**.
- (38) T. Yokoyama, Y. Kogure, M. Kawasaki, S. Tanaka and K. Aoshima, *J. Phys. Chem. C*, 2013, **117**, 18484-18487.
- (39) B. J. V. Tongol, L. Wang, S.-L. Yau, T. Otsubo and K. Itaya, *Langmuir*, 2010, **26**, 982-989.
- (40) Y. F. Liu, K. Krug and Y. L. Lee, *Nanoscale*, 2013, **5**, 7936-7941.
- (41) S. Förster, E. Kohl, M. Ivanov, J. Gross, W. Widdra and W. Janke, *J. Chem. Phys.*, 2014, **141**, 164701.
- (42) D. Wang, L.-J. Wan and C.-L. Bai, *Materials Science and Engineering: R: Reports*, 2010, **70**, 169 - 187.
- (43) L. V. Brownell, K. A. Robins, Y. Jeong, Y. Lee and D. C. Lee, *Journal of Physical Chemistry C*, 2013, **117**, 25236-25247.
- (44) B. He, A. B. Pun, D. Zherebetsky, Y. Liu, F. Liu, L. M. Klivansky, A. M. McGough, B. A. Zhang, K. Lo, T. P. Russell and L. W. Wang, *Journal of the American Chemical Society*, 2014, **136**, 15093-15101.
- (45) B. Koslowski, A. Tschetschetkin, N. Maurer, E. Mena-Osteritz, P. Bauerle and P. Ziemann, *Beilstein J. Nanotechnol.*, 2011, **2**, 561-568.
- (46) G. Reecht, H. Bulou, F. Scheurer, V. Speisser, B. Carrière, F. Mathevet and G. Schull, *Phys. Rev. Lett.*, 2013, **110**, 056802.
- (47) J. Repp, P. Liljeroth and G. Meyer, *Nat. Phys.*, 2010, **6**, 975-979.
- (48) F. Jäckel, U. G. E. Perera, V. Iancu, K. F. Braun, N. Koch, J. P. Rabe and S. W. Hla, *Phys. Rev. Lett.*, 2008, **100**, 126102.
- (49) E. Varene, Y. Pennec and P. Tegeder, *Chem. Phys. Lett.*, 2011, **515**, 141-145.

- (50) B. N. Taber, D. A. Kislitsyn, C. F. Gervasi, S. C. B. Mannsfeld, L. Zhang, A. L. Briseno and G. V. Nazin, *ACS Appl. Mater. Interfaces*, 2015.
- (51) D. A. Kislitsyn, B. N. Taber, C. F. Gervasi, S. C. B. Mannsfeld, L. Zhang, A. L. Briseno and G. V. Nazin, *The Journal of Physical Chemistry C*, 2015.
- (52) J. D. Hackley, D. A. Kislitsyn, D. K. Beaman, S. Ulrich and G. V. Nazin, *Review of Scientific Instruments*, 2014, **85**, 103704.
- (53) L. Zhang, N. S. Colella, F. Liu, S. Trahan, J. K. Baral, H. H. Winter, S. C. B. Mannsfeld and A. L. Briseno, *Journal of the American Chemical Society*, 2012, **135**, 844-854.
- (54) C. J. Chen, *Introduction to Scanning Tunneling Microscopy*, Oxford University Press, New York, Second Edition edn., 2008.
- (55) M. J. Frisch, G. W. Trucks, H. B. Schlegel, G. E. Scuseria, M. A. Robb, J. R. Cheeseman, G. Scalmani, V. Barone, B. Mennucci, G. A. Petersson, H. Nakatsuji, M. Caricato, X. Li, H. P. Hratchian, A. F. Izmaylov, J. Bloino, G. Zheng, J. L. Sonnenberg, M. Hada, M. Ehara, K. Toyota, R. Fukuda, J. Hasegawa, M. Ishida, T. Nakajima, Y. Honda, O. Kitao, H. Nakai, T. Vreven, J. A. Montgomery Jr., J. E. Peralta, F. Ogliaro, M. J. Bearpark, J. Heyd, E. N. Brothers, K. N. Kudin, V. N. Staroverov, R. Kobayashi, J. Normand, K. Raghavachari, A. P. Rendell, J. C. Burant, S. S. Iyengar, J. Tomasi, M. Cossi, N. Rega, N. J. Millam, M. Klene, J. E. Knox, J. B. Cross, V. Bakken, C. Adamo, J. Jaramillo, R. Gomperts, R. E. Stratmann, O. Yazyev, A. J. Austin, R. Cammi, C. Pomelli, J. W. Ochterski, R. L. Martin, K. Morokuma, V. G. Zakrzewski, G. A. Voth, P. Salvador, J. J. Dannenberg, S. Dapprich, A. D. Daniels, Ö. Farkas, J. B. Foresman, J. V. Ortiz, J. Cioslowski and D. J. Fox, *Gaussian 09 Revision C.01*, Gaussian, Inc., Wallingford CT, 2009.
- (56) A. D. Becke, *The Journal of Chemical Physics*, 1993, **98**, 5648.
- (57) P. J. Stephens, F. J. Devlin, C. F. Chabalowski and M. J. Frisch, *The Journal of Physical Chemistry*, 1994, **98**, 11623-11627.
- (58) T. Lu and F. Chen, *Journal of Computational Chemistry*, 2012, **33**, 580-592.

- (59) J. Zhou, Y. X. Yang, P. Liu, N. Camillone, III and M. G. White, *J. Phys. Chem. C*, 2010, **114**, 13670-13677.
- (60) K. Tonigold and A. Gross, *J. Chem. Phys.*, 2010, **132**.
- (61) A. Goursot, T. Mineva, R. Kevorkyants and D. Talbi, *Journal of Chemical Theory and Computation*, 2007, **3**, 755-763.
- (62) H. M. Zhang, Z. X. Xie, B. W. Mao and X. Xu, *Chemistry-A European Journal*, 2004, **10**, 1415-1422.
- (63) R. J. Baxter, G. Teobaldi and F. Zerbetto, *Langmuir*, 2003, **19**, 7335-7340.
- (64) A. Salleo, T. W. Chen, A. R. Völkel, Y. Wu, P. Liu, B. S. Ong and R. A. Street, *Physical Review B*, 2004, **70**, 115311.
- (65) H. Sirringhaus, *Adv. Mater.*, 2005, **17**, 2411-2425.

#### REFERENCES CITED FOR CHAPTER VII

- (1) Sirringhaus, H. Device physics of Solution-processed organic field-effect transistors. *Adv. Mater.* **2005**, *17* (20), 2411-2425.
- (2) Zhang, L.; Colella, N. S.; Cherniawski, B. P.; Mannsfeld, S. C. B.; Briseno, A. L. Oligothiophene Semiconductors: Synthesis, Characterization, and Applications for Organic Devices. *ACS Appl. Mater. Interfaces* **2014**, *6* (8), 5327-5343.
- (3) Xu, L.; Yang, L.; Lei, S. Self-assembly of conjugated oligomers and polymers at the interface: structure and properties. *Nanoscale* **2012**, *4* (15), 4399-4415.
- (4) Fitzner, R.; Mena-Osteritz, E.; Mishra, A.; Schulz, G.; Reinold, E.; Weil, M.; Körner, C.; Ziehlke, H.; Elschner, C.; Leo, K.; Riede, M.; Pfeiffer, M.; Uhrich, C.; Bäuerle, P. Correlation of  $\pi$ -Conjugated Oligomer Structure with Film Morphology and Organic Solar Cell Performance. *J. Am. Chem. Soc.* **2012**, *134* (27), 11064-11067.
- (5) Zhang, L.; Liu, F.; Diao, Y.; Marsh, H. S.; Colella, N. S.; Jayaraman, A.; Russell, T. P.; Mannsfeld, S. C. B.; Briseno, A. L. The Good Host: Formation of Discrete One-Dimensional Fullerene "Channels" in Well-Ordered Poly(2,5-bis(3-

- alkylthiophen-2-yl)thieno 3,2-b thiophene) Oligomers. *J. Am. Chem. Soc.* **2014**, *136* (52), 18120-18130.
- (6) Cnops, K.; Rand, B. P.; Cheyns, D.; Verreert, B.; Empl, M. A.; Heremans, P. 8.4% efficient fullerene-free organic solar cells exploiting long-range exciton energy transfer. *Nat. Commun.* **2014**, *5*.
- (7) McCulloch, I.; Heeney, M.; Bailey, C.; Genevicius, K.; MacDonald, I.; Shkunov, M.; Sparrowe, D.; Tierney, S.; Wagner, R.; Zhang, W.; Chabinyc, M. L.; Kline, R. J.; McGehee, M. D.; Toney, M. F. Liquid-crystalline semiconducting polymers with high charge-carrier mobility. *Nat. Mater.* **2006**, *5* (4), 328-333.
- (8) Murphy, A. R.; Fréchet, J. M. J.; Chang, P.; Lee, J.; Subramanian, V. Organic Thin Film Transistors from a Soluble Oligothiophene Derivative Containing Thermally Removable Solubilizing Groups. *J. Am. Chem. Soc.* **2004**, *126* (6), 1596-1597.
- (9) Videlot-Ackermann, C.; Ackermann, J.; Brisset, H.; Kawamura, K.; Yoshimoto, N.; Raynal, P.; El Kassmi, A.; Fages, F.  $\alpha,\omega$ -Distyryl Oligothiophenes: High Mobility Semiconductors for Environmentally Stable Organic Thin Film Transistors. *J. Am. Chem. Soc.* **2005**, *127* (47), 16346-16347.
- (10) Allard, S.; Forster, M.; Souharce, B.; Thiem, H.; Scherf, U. Organic semiconductors for solution-processable field-effect transistors (OFETs). *Angewandte Chemie-International Edition* **2008**, *47* (22), 4070-4098.
- (11) Mazzeo, M.; Vitale, V.; Della Sala, F.; Anni, M.; Barbarella, G.; Favaretto, L.; Sotgiu, G.; Cingolani, R.; Gigli, G. Bright White Organic Light-Emitting Devices from a Single Active Molecular Material. *Adv. Mater.* **2005**, *17* (1), 34-39.
- (12) Friend, R. H.; Gymer, R. W.; Holmes, A. B.; Burroughes, J. H.; Marks, R. N.; Taliani, C.; Bradley, D. D. C.; Santos, D. A. D.; Bredas, J. L.; Logdlund, M.; Salaneck, W. R. Electroluminescence in conjugated polymers. *Nature* **1999**, *397* (6715), 121-128.
- (13) Koch, N. Energy levels at interfaces between metals and conjugated organic molecules. *J. Phys.-Condens. Matter* **2008**, *20* (18), 184008.

- (14) Höfer, A.; Duncker, K.; Kiel, M.; Wedekind, S.; Widdra, W. Adsorption of  $\alpha$ -sexithiophene on Au(001): Molecule-induced partial lifting of the substrate reconstruction. *Phys. Rev. B* **2011**, *83* (7), 075414.
- (15) Sirringhaus, H.; Brown, P. J.; Friend, R. H.; Nielsen, M. M.; Bechgaard, K.; Langeveld-Voss, B. M. W.; Spiering, A. J. H.; Janssen, R. A. J.; Meijer, E. W.; Herwig, P.; de Leeuw, D. M. Two-dimensional charge transport in self-organized, high-mobility conjugated polymers. *Nature* **1999**, *401* (6754), 685-688.
- (16) Dasgupta, N. P.; Lee, W.; Prinz, F. B. Atomic Layer Deposition of Lead Sulfide Thin Films for Quantum Confinement. *Chemistry of Materials* **2009**, *21* (17), 3973-3978.
- (17) Wu, Y.; Liu, P.; Ong, B. S.; Srikumar, T.; Zhao, N.; Botton, G.; Zhu, S. Controlled orientation of liquid-crystalline polythiophene semiconductors for high-performance organic thin-film transistors. *Appl. Phys. Lett.* **2005**, *86* (14), 142102.
- (18) Mena-Osteritz, E.; Meyer, A.; Langeveld-Voss, B. M. W.; Janssen, R. A. J.; Meijer, E. W.; Bäuerle, P. Two-Dimensional Crystals of Poly(3-Alkylthiophene)s: Direct Visualization of Polymer Folds in Submolecular Resolution. *Angewandte Chemie International Edition* **2000**, *39* (15), 2679-2684.
- (19) Yang, Z.-Y.; Zhang, H.-M.; Pan, G.-B.; Wan, L.-J. Effect of the Bridge Alkylene Chain on Adlayer Structure and Property of Functional Oligothiophenes Studied with Scanning Tunneling Microscopy and Spectroscopy. *ACS Nano* **2008**, *2* (4), 743-749.
- (20) Yang, Z.-Y.; Zhang, H.-M.; Yan, C.-J.; Li, S.-S.; Yan, H.-J.; Song, W.-G.; Wan, L.-J. Scanning tunneling microscopy of the formation, transformation, and property of oligothiophene self-organizations on graphite and gold surfaces. *Proc. Natl. Acad. Sci. U. S. A.* **2007**, *104* (10), 3707-3712.
- (21) Mena-Osteritz, E.; Urdanpilleta, M.; El-Hosseiny, E.; Koslowski, B.; Ziemann, P.; Bauerle, P. STM study on the self-assembly of oligothiophene-based organic semiconductors. *Beilstein J. Nanotechnol.* **2011**, *2*, 802-808.

- (22) Ma, X. J.; Guo, Y.; Wang, T.; Su, Z. H. Scanning tunneling microscopy investigation of self-assembled poly(3-hexylthiophene) monolayer. *J. Chem. Phys.* **2013**, *139* (1).
- (23) Jaroch, T.; Knor, M.; Nowakowski, R.; Zagorska, M.; Pron, A. Effect of molecular mass on supramolecular organisation of poly(4,4'-dioctyl-2,2':5',2'-terthiophene). *Phys. Chem. Chem. Phys.* **2008**, *10* (40), 6182-6189.
- (24) Grévin, B.; Rannou, P.; Payerne, R.; Pron, A.; Travers, J. P. Multi-scale scanning tunneling microscopy imaging of self-organized regioregular poly(3-hexylthiophene) films. *J. Chem. Phys.* **2003**, *118* (15), 7097-7102.
- (25) Wang, L.; Tongol, B. J. V.; Yau, S.-L.; Otsubo, T.; Itaya, K. Substrate-Induced Varied Conformation and Molecular Assemblies: In Situ STM Observation of  $\beta$ -Substituted Oligothiophene Adlayers on Au(111). *Langmuir* **2010**, *26* (10), 7148-7152.
- (26) Liu, Y. F.; Krug, K.; Lee, Y. L. Self-organization of two-dimensional poly(3-hexylthiophene) crystals on Au(111) surfaces. *Nanoscale* **2013**, *5* (17), 7936-7941.
- (27) Forster, S.; Widdra, W. Structure of single polythiophene molecules on Au(001) prepared by in situ UHV electrospray deposition. *J. Chem. Phys.* **2014**, *141* (5).
- (28) Förster, S.; Kohl, E.; Ivanov, M.; Gross, J.; Widdra, W.; Janke, W. Polymer adsorption on reconstructed Au(001): A statistical description of P3HT by scanning tunneling microscopy and coarse-grained Monte Carlo simulations. *J. Chem. Phys.* **2014**, *141* (16), 164701.
- (29) Nishiyama, F.; Ogawa, K.; Tanaka, S.; Yokoyama, T. Direct Conformational Analysis of a 10 nm Long Oligothiophene Wire. *J. Phys. Chem. B* **2008**, *112* (17), 5272-5275.
- (30) Duncker, K.; Kiel, M.; Hofer, A.; Widdra, W. Commensurate surface structures and concerted cis-trans-isomerization within ordered monolayers of alpha-sexithiophene on Ag(001). *Phys. Rev. B* **2008**, *77* (15).



- (31) Yokoyama, T.; Kogure, Y.; Kawasaki, M.; Tanaka, S.; Aoshima, K. Scanning Tunneling Microscopy Imaging of Long Oligothiophene Wires Deposited on Au(111) Using Electrospray Ionization. *J. Phys. Chem. C* **2013**, *117* (36), 18484-18487.
- (32) Tongol, B. J. V.; Wang, L.; Yau, S.-L.; Otsubo, T.; Itaya, K. Direct Observation of Conformational Changes of  $\beta$ -Substituted Duodecithiophene on a Au(111)-( $\sqrt{3} \times 22$ ) Substrate Using in Situ Electrochemical STM in 0.1 M HClO<sub>4</sub>. *Langmuir* **2010**, *26* (2), 982-989.
- (33) Murphy, C. J.; Shi, X. R.; Jewell, A. D.; McGuire, A. F.; Bellisario, D. O.; Baber, A. E.; Tierney, H. L.; Lewis, E. A.; Sholl, D. S.; Sykes, E. C. H. Impact of branching on the supramolecular assembly of thioethers on Au(111). *Journal of Chemical Physics* **2015**, *142* (10), 101915.
- (34) Koslowski, B.; Tschetschetkin, A.; Maurer, N.; Mena-Osteritz, E.; Bauerle, P.; Ziemann, P. Terthiophene on Au(111): A scanning tunneling microscopy and spectroscopy study. *Beilstein J. Nanotechnol.* **2011**, *2*, 561-568.
- (35) Reeht, G.; Bulou, H.; Scheurer, F.; Speisser, V.; Carrière, B.; Mathevet, F.; Schull, G. Oligothiophene Nanorings as Electron Resonators for Whispering Gallery Modes. *Phys. Rev. Lett.* **2013**, *110* (5), 056802.
- (36) Repp, J.; Liljeroth, P.; Meyer, G. Coherent electron-nuclear coupling in oligothiophene molecular wires. *Nat. Phys.* **2010**, *6* (12), 975-979.
- (37) Jäckel, F.; Perera, U. G. E.; Iancu, V.; Braun, K. F.; Koch, N.; Rabe, J. P.; Hla, S. W. Investigating Molecular Charge Transfer Complexes with a Low Temperature Scanning Tunneling Microscope. *Phys. Rev. Lett.* **2008**, *100* (12), 126102.
- (38) Varene, E.; Pennec, Y.; Tegeder, P. Assembly and electronic structure of octithiophene on Au(111). *Chem. Phys. Lett.* **2011**, *515* (1-3), 141-145.
- (39) Kislitsyn, D. A.; Taber, B.; Gervasi, C. F.; Zhang, L.; Mannsfeld, S. C. B.; Prell, J.; Briseno, A.; Nazin, G. Y. Oligothiophene Wires: Impact of Torsional Conformation on the Electronic Structure. *Physical Chemistry Chemical Physics* **2016**.

- (40) Hackley, J. D.; Kislitsyn, D. A.; Beaman, D. K.; Ulrich, S.; Nazin, G. V. High-Stability Cryogenic Scanning Tunneling Microscope Based on a Closed-Cycle Cryostat. *Review of Scientific Instruments* **2014**, *85* (10), 103704.
- (41) Zhang, L.; Colella, N. S.; Liu, F.; Trahan, S.; Baral, J. K.; Winter, H. H.; Mannsfeld, S. C. B.; Briseno, A. L. Synthesis, Electronic Structure, Molecular Packing/Morphology Evolution, and Carrier Mobilities of Pure Oligo-/Poly(alkylthiophenes). *Journal of the American Chemical Society* **2012**, *135* (2), 844-854.
- (42) Chen, C. J. *Introduction to Scanning Tunneling Microscopy*. Second Edition ed.; Oxford University Press: New York, 2008.
- (43) Talapin, D. V.; Murray, C. B. PbSe nanocrystal solids for n- and p-channel thin film field-effect transistors. *Science* **2005**, *310* (5745), 86-89.
- (44) Hetsch, F.; Zhao, N.; Kershaw, S. V.; Rogach, A. L. Quantum Dot Field Effect Transistors. *Materials Today* **2013**, *16* (9), 312-325.
- (45) Stephens, P. J.; Devlin, F. J.; Chabalowski, C. F.; Frisch, M. J. Ab Initio Calculation of Vibrational Absorption and Circular Dichroism Spectra Using Density Functional Force Fields. *The Journal of Physical Chemistry* **1994**, *98*, 11623-11627.
- (46) Lu, T.; Chen, F. Multiwfn: A Multifunctional Wavefunction Analyzer. *Journal of Computational Chemistry* **2012**, *33* (5), 580-592.
- (47) Taber, B. N.; Kislitsyn, D. A.; Gervasi, C. F.; Mannsfeld, S. C. B.; Zhang, L.; Briseno, A. L.; Nazin, G. V. Adsorption-Induced Conformational Isomerization of Alkyl-Substituted Thiophene Oligomers on Au(111): Impact on the Interfacial Electronic Structure. *Acs Applied Materials & Interfaces* **2015**, *7* (28), 15138-15142.
- (48) Kislitsyn, D. A.; Taber, B. N.; Gervasi, C. F.; Mannsfeld, S. C. B.; Zhang, L.; Briseno, A. L.; Nazin, G. V. Coverage-Dependent Self-Assembly Regimes of Alkyl-Substituted Thiophene Oligomers on Au(111): Scanning Tunneling Microscopy and Spectroscopy. *The Journal of Physical Chemistry C* **2015**.

- (49) Franceschetti, A. Structural and electronic properties of PbSe nanocrystals from first principles. *Physical Review B* **2008**, *78* (7), 075418.
- (50) Kimura, K.; Nakajima, K.; Fujii, Y.; Mannami, M. Observation of the Pbse(111) Surface Using High-Resolution Rutherford Backscattering Spectroscopy. *Surface Science* **1994**, *318* (3), 363-367.
- (51) Moreels, I.; Lambert, K.; Smeets, D.; De Muynck, D.; Nollet, T.; Martins, J. C.; Vanhaecke, F.; Vantomme, A.; Delerue, C.; Allan, G.; Hens, Z. Size-Dependent Optical Properties of Colloidal PbS Quantum Dots. *Acs Nano* **2009**, *3* (10), 3023-3030.
- (52) Luther, J. M.; Law, M.; Song, Q.; Perkins, C. L.; Beard, M. C.; Nozik, A. J. Structural, Optical and Electrical Properties of Self-Assembled Films of PbSe Nanocrystals Treated with 1,2-Ethanedithiol. *Acs Nano* **2008**, *2* (2), 271-280.
- (53) Zhang, H. M.; Xie, Z. X.; Mao, B. W.; Xu, X. Self-Assembly of Normal Alkanes on the Au (111) Surfaces. *Chemistry-A European Journal* **2004**, *10* (6), 1415-1422.
- (54) Baxter, R. J.; Teobaldi, G.; Zerbetto, F. Modeling the adsorption of alkanes on an Au (111) surface. *Langmuir* **2003**, *19* (18), 7335-7340.
- (55) Zhou, J.; Yang, Y. X.; Liu, P.; Camillone, N., III; White, M. G. Electronic Structure of the Thiophene/Au(111) Interface Probed by Two-Photon Photoemission. *J. Phys. Chem. C* **2010**, *114* (32), 13670-13677.
- (56) Tonigold, K.; Gross, A. Adsorption of small aromatic molecules on the (111) surfaces of noble metals: A density functional theory study with semiempirical corrections for dispersion effects. *J. Chem. Phys.* **2010**, *132* (22).

## REFERENCES CITED FOR CHAPTER VIII

- (1) Kershaw, S. V.; Susha, A. S.; Rogach, A. L. Narrow Bandgap Colloidal Metal Chalcogenide Quantum Dots: Synthetic Methods, Heterostructures, Assemblies, Electronic and Infrared Optical Properties. *Chem. Soc. Rev.* **2013**, *42* (7), 3033-3087.

- (2) Tang, J. A.; Sargent, E. H. Infrared Colloidal Quantum Dots for Photovoltaics: Fundamentals and Recent Progress. *Adv. Mater.* **2011**, *23* (1), 12-29.
- (3) Nozik, A. J. Spectroscopy and Hot Electron Relaxation Dynamics in Semiconductor Quantum Wells and Quantum Dots. *Annu. Rev. Phys. Chem.* **2001**, *52*, 193-231.
- (4) Nozik, A. J. Quantum Dot Solar Cells. *Physica E* **2002**, *14* (1-2), 115-120.
- (5) Beard, M. C.; Ellingson, R. J. Multiple Exciton Generation in Semiconductor Nanocrystals: Toward Efficient Solar Energy Conversion. *Laser Photon. Rev.* **2008**, *2* (5), 377-399.
- (6) Beard, M. C.; Midgett, A. G.; Hanna, M. C.; Luther, J. M.; Hughes, B. K.; Nozik, A. J. Comparing Multiple Exciton Generation in Quantum Dots To Impact Ionization in Bulk Semiconductors: Implications for Enhancement of Solar Energy Conversion. *Nano Lett.* **2010**, *10* (8), 3019-3027.
- (7) Sandeep, C. S. S.; Cate, S. t.; Schins, J. M.; Savenije, T. J.; Liu, Y.; Law, M.; Kinge, S.; Houtepen, A. J.; Siebbeles, L. D. A. High Charge-Carrier Mobility Enables Exploitation of Carrier Multiplication in Quantum-Dot Films. *Nat. Commun.* **2013**, *4*, 2360.
- (8) Tisdale, W. A.; Williams, K. J.; Timp, B. A.; Norris, D. J.; Aydil, E. S.; Zhu, X. Y. Hot-Electron Transfer from Semiconductor Nanocrystals. *Science* **2010**, *328* (5985), 1543-1547.
- (9) Shockley, W.; Queisser, H. J. Detailed Balance Limit of Efficiency of P-N Junction Solar Cells. *J. Appl. Phys.* **1961**, *32* (3), 510-519.
- (10) Chuang, C.-H. M.; Brown, P. R.; Bulović, V.; Bawendi, M. G. Improved Performance and Stability in Quantum Dot Solar Cells through Band Alignment Engineering. *Nat. Mater.* **2014**, *13* (8), 796-801.
- (11) Ning, Z. J.; Voznyy, O.; Pan, J.; Hoogland, S.; Adinolfi, V.; Xu, J. X.; Li, M.; Kirmani, A. R.; Sun, J. P.; Minor, J.; Kemp, K. W.; Dong, H. P.; Rollny, L.; Labelle, A.; Carey, G.; Sutherland, B.; Hill, I.; Amassian, A.; Liu, H.; Tang, J.;

- Bakr, O. M.; Sargent, E. H. Air-Stable N-Type Colloidal Quantum Dot Solids. *Nat. Mater.* **2014**, *13* (8), 822-828.
- (12) Ip, A. H.; Thon, S. M.; Hoogland, S.; Voznyy, O.; Zhitomirsky, D.; Debnath, R.; Levina, L.; Rollny, L. R.; Carey, G. H.; Fischer, A.; Kemp, K. W.; Kramer, I. J.; Ning, Z.; Labelle, A. J.; Chou, K. W.; Amassian, A.; Sargent, E. H. Hybrid passivated colloidal quantum dot solids. *Nat. Nanotechnol.* **2012**, *7* (9), 577-582.
- (13) Fernee, M. J.; Thomsen, E.; Jensen, P.; Rubinsztein-Dunlop, H. Highly Efficient Luminescence from a Hybrid State Found in Strongly Quantum Confined PbS Nanocrystals. *Nanotechnology* **2006**, *17* (4), 956-962.
- (14) Gao, J.; Johnson, J. C. Charge Trapping in Bright and Dark States of Coupled PbS Quantum Dot Films. *ACS Nano* **2012**, *6* (4), 3292-3303.
- (15) Tang, J.; Kemp, K. W.; Hoogland, S.; Jeong, K. S.; Liu, H.; Levina, L.; Furukawa, M.; Wang, X.; Debnath, R.; Cha, D.; Chou, K. W.; Fischer, A.; Amassian, A.; Asbury, J. B.; Sargent, E. H. Colloidal-quantum-dot photovoltaics using atomic-ligand passivation. *Nat. Mater.* **2011**, *10* (10), 765-771.
- (16) Hughes, B. K.; Ruddy, D. A.; Blackburn, J. L.; Smith, D. K.; Bergren, M. R.; Nozik, A. J.; Johnson, J. C.; Beard, M. C. Control of PbSe Quantum Dot Surface Chemistry and Photophysics Using an Alkylselenide Ligand. *ACS Nano* **2012**, *6* (6), 5498-5506.
- (17) Kovalenko, M. V.; Scheele, M.; Talapin, D. V. Colloidal Nanocrystals with Molecular Metal Chalcogenide Surface Ligands. *Science* **2009**, *324* (5933), 1417-1420.
- (18) Luther, J. M.; Law, M.; Song, Q.; Perkins, C. L.; Beard, M. C.; Nozik, A. J. Structural, Optical and Electrical Properties of Self-Assembled Films of PbSe Nanocrystals Treated with 1,2-Ethanedithiol. *ACS Nano* **2008**, *2* (2), 271-280.
- (19) Bozyigit, D.; Volk, S.; Yarema, O.; Wood, V. Quantification of Deep Traps in Nanocrystal Solids, Their Electronic Properties, and Their Influence on Device Behavior. *Nano Lett.* **2013**, *13* (11), 5284-5288.

- (20) Diaconescu, B.; Padilha, L. A.; Nagpal, P.; Swartzentruber, B. S.; Klimov, V. I. Measurement of Electronic States of PbS Nanocrystal Quantum Dots Using Scanning Tunneling Spectroscopy: The Role of Parity Selection Rules in Optical Absorption. *Phys. Rev. Lett.* **2013**, *110* (12), 127406.
- (21) Nagpal, P.; Klimov, V. I. Role of mid-gap states in charge transport and photoconductivity in semiconductor nanocrystal films. *Nat. Commun.* **2011**, *2*, 486.
- (22) Hackley, J. D.; Kislitsyn, D. A.; Beaman, D. K.; Ulrich, S.; Nazin, G. V. High-Stability Cryogenic Scanning Tunneling Microscope Based on a Closed-Cycle Cryostat. *Rev. Sci. Instrum.* **2014**, *85* (10), 103704.
- (23) Horcas, I.; Fernández, R.; Gómez-Rodríguez, J. M.; Colchero, J.; Gómez-Herrero, J.; Baro, A. M. WSXM: A Software for Scanning Probe Microscopy and a Tool for Nanotechnology. *Rev. Sci. Instrum.* **2007**, *78* (1), 2432410.
- (24) Kilina, S. V.; Craig, C. F.; Kilin, D. S.; Prezhdo, O. V. Ab Initio Time-Domain Study of Phonon-Assisted Relaxation of Charge Carriers in a PbSe Quantum Dot. *J. Phys. Chem. C* **2007**, *111* (12), 4871-4878.
- (25) Kilina, S. V.; Kilin, D. S.; Prezhdo, O. V. Breaking the Phonon Bottleneck in PbSe and CdSe Quantum Dots: Time-Domain Density Functional Theory of Charge Carrier Relaxation. *ACS Nano* **2008**, *3* (1), 93-99.
- (26) Kaushik, A. P.; Lukose, B.; Clancy, P. The Role of Shape on Electronic Structure and Charge Transport in Faceted PbSe Nanocrystals. *ACS Nano* **2014**, *8* (3), 2302-2317.
- (27) Hetsch, F.; Zhao, N.; Kershaw, S. V.; Rogach, A. L. Quantum Dot Field Effect Transistors. *Mater. Today* **2013**, *16* (9), 312-325.
- (28) Chen, C. J. *Introduction to Scanning Tunneling Microscopy*. Second Edition ed.; Oxford University Press New York, U.S.A., 2008.
- (29) Sun, Z. X.; Swart, I.; Delerue, C.; Vanmaekelbergh, D.; Liljeroth, P. Orbital and Charge-Resolved Polaron States in CdSe Dots and Rods Probed by Scanning Tunneling Spectroscopy. *Phys. Rev. Lett.* **2009**, *102* (19), 196401.

- (30) Krauss, T. D.; Wise, F. W.; Tanner, D. B. Observation of Coupled Vibrational Modes of a Semiconductor Nanocrystal. *Phys. Rev. Lett.* **1996**, *76* (8), 1376-1379.
- (31) Overgaag, K.; Vanmaekelbergh, D.; Liljeroth, P.; Mahieu, G.; Grandidier, B.; Delerue, C.; Allan, G. Electron-Phonon Coupling and Intervalley Splitting Determine the Linewidth of Single-Electron Transport through PbSe Nanocrystals. *J. Chem. Phys.* **2009**, *131* (22), 224510.
- (32) Hens, Z.; Vanmaekelbergh, D.; Stoffels, E.; van Kempen, H. Effects of Crystal Shape on the Energy Levels of Zero-Dimensional PbS Quantum Dots. *Phys. Rev. Lett.* **2002**, *88* (23), 236803.
- (33) van Huis, M. A.; Kunneman, L. T.; Overgaag, K.; Xu, Q.; Pandraud, G.; Zandbergen, H. W.; Vanmaekelbergh, D. Low-Temperature Nanocrystal Unification through Rotations and Relaxations Probed by in Situ Transmission Electron Microscopy. *Nano Lett.* **2008**, *8* (11), 3959-3963.
- (34) Baik, S. J.; Kim, K.; Lim, K. S.; Jung, S.; Park, Y.-C.; Han, D. G.; Lim, S.; Yoo, S.; Jeong, S. Low-Temperature Annealing for Highly Conductive Lead Chalcogenide Quantum Dot Solids. *J. Phys. Chem. C* **2011**, *115* (3), 607-612.
- (35) Nazin, G. V.; Wu, S. W.; Ho, W. Tunneling Rates in Electron Transport through Double-Barrier Molecular Junctions in a Scanning Tunneling Microscope. *Proc. Natl. Acad. Sci. U. S. A.* **2005**, *102* (25), 8832-8837.
- (36) Nazin, G. V.; Qiu, X. H.; Ho, W. Vibrational Spectroscopy of Individual Doping Centers in a Monolayer Organic Crystal. *J. Chem. Phys.* **2005**, *122* (18), 181105.
- (37) Eggleston, C. M.; Hochella, M. F. Scanning Tunneling Microscopy of Sulfide Surfaces. *Geochim. Cosmochim. Acta* **1990**, *54* (5), 1511-1517.
- (38) Nguyen, T. H.; Habinshuti, J.; Justo, Y.; Gomes, R.; Mahieu, G.; Godey, S.; Nys, J. P.; Carrillo, S.; Hens, Z.; Robbe, O.; Turrell, S.; Grandidier, B. Charge Carrier Identification in Tunneling Spectroscopy of Core-Shell Nanocrystals. *Phys. Rev. B* **2011**, *84* (19), 195133.

- (39) Kim, D.; Kim, D.-H.; Lee, J.-H.; Grossman, J. C. Impact of Stoichiometry on the Electronic Structure of PbS Quantum Dots. *Phys. Rev. Lett.* **2013**, *110* (19), 196802.
- (40) Becker, U.; Rosso, K. M. Step Edges on Galena (100): Probing the Basis for Defect Driven Surface Reactivity at the Atomic Scale. *Am. Mineral.* **2001**, *86* (7-8), 862-870.
- (41) Moreels, I.; Lambert, K.; Smeets, D.; De Muynck, D.; Nollet, T.; Martins, J. C.; Vanhaecke, F.; Vantomme, A.; Delerue, C.; Allan, G.; Hens, Z. Size-Dependent Optical Properties of Colloidal PbS Quantum Dots. *ACS Nano* **2009**, *3* (10), 3023-3030.
- (42) Moreels, I.; Justo, Y.; De Geyter, B.; Haustraete, K.; Martins, J. C.; Hens, Z. Size-Tunable, Bright, and Stable PbS Quantum Dots: A Surface Chemistry Study. *ACS Nano* **2011**, *5* (3), 2004-2012.
- (43) Nilius, N.; Wallis, T. M.; Ho, W. Development of One-Dimensional Band Structure in Artificial Gold Chains. *Science* **2002**, *297* (5588), 1853-1856.
- (44) Fölsch, S.; Hyldgaard, P.; Koch, R.; Ploog, K. H. Quantum Confinement in Monatomic Cu Chains on Cu(111). *Phys. Rev. Lett.* **2004**, *92* (5), 056803.
- (45) Fölsch, S.; Yang, J.; Nacci, C.; Kanisawa, K. Atom-By-Atom Quantum State Control in Adatom Chains on a Semiconductor. *Phys. Rev. Lett.* **2009**, *103* (9), 096104.
- (46) Fang, C.; van Huis, M. A.; Vanmaekelbergh, D.; Zandbergen, H. W. Energetics of Polar and Nonpolar Facets of PbSe Nanocrystals from Theory and Experiment. *ACS Nano* **2009**, *4* (1), 211-218.

## REFERENCES CITED FOR CHAPTER IX

- (1) S. A. McDonald, G. Konstantatos, S. G. Zhang, P. W. Cyr, E. J. D. Klem, L. Levina and E. H. Sargent, *Nat. Mater.*, 2005, **4**, 138-U114.
- (2) J. Tang, H. Liu, D. Zhitomirsky, S. Hoogland, X. H. Wang, M. Furukawa, L. Levina and E. H. Sargent, *Nano Lett.*, 2012, **12**, 4889-4894.



- (3) E. J. D. Klem, D. D. MacNeil, P. W. Cyr, L. Levina and E. H. Sargent, *Appl. Phys. Lett.*, 2007, **90**, 183113.
- (4) L. Sun, J. J. Choi, D. Stachnik, A. C. Bartnik, B.-R. Hyun, G. G. Malliaras, T. Hanrath and F. W. Wise, *Nat. Nanotechnol.*, 2012, **7**, 369-373.
- (5) A. J. Nozik, *Annu. Rev. Phys. Chem.*, 2001, **52**, 193-231.
- (6) A. J. Nozik, *Phys. E (Amsterdam, Neth.)*, 2002, **14**, 115-120.
- (7) M. C. Beard and R. J. Ellingson, *Laser Photonics Rev.*, 2008, **2**, 377-399.
- (8) M. C. Beard, A. G. Midgett, M. C. Hanna, J. M. Luther, B. K. Hughes and A. J. Nozik, *Nano Lett.*, 2010, **10**, 3019-3027.
- (9) C. S. S. Sandeep, S. t. Cate, J. M. Schins, T. J. Savenije, Y. Liu, M. Law, S. Kinge, A. J. Houtepen and L. D. A. Siebbeles, *Nat. Commun.*, 2013, **4**, 2360.
- (10) J. B. Sambur, T. Novet and B. A. Parkinson, *Science*, 2010, **330**, 63-66.
- (11) W. A. Tisdale, K. J. Williams, B. A. Timp, D. J. Norris, E. S. Aydil and X. Y. Zhu, *Science*, 2010, **328**, 1543-1547.
- (12) M. V. Kovalenko, L. Manna, A. Cabot, Z. Hens, D. V. Talapin, C. R. Kagan, V. I. Klimov, A. L. Rogach, P. Reiss, D. J. Milliron, P. Guyot-Sionnest, G. Konstantatos, W. J. Parak, T. Hyeon, B. A. Korgel, C. B. Murray and W. Heiss, *Acs Nano*, 2015, **9**, 1012-1057.
- (13) Y. Liu, M. Gibbs, J. Puthussery, S. Gaik, R. Ihly, H. W. Hillhouse and M. Law, *Nano Lett.*, 2010, **10**, 1960-1969.
- (14) J. M. Luther, M. Law, Q. Song, C. L. Perkins, M. C. Beard and A. J. Nozik, *Acs Nano*, 2008, **2**, 271-280.
- (15) M. V. Kovalenko, M. Scheele and D. V. Talapin, *Science*, 2009, **324**, 1417-1420.
- (16) D. V. Talapin and C. B. Murray, *Science*, 2005, **310**, 86-89.
- (17) E. Talgorn, Y. Gao, M. Aerts, L. T. Kunneman, J. M. Schins, T. J. Savenije, M. A. van Huis, H. S. J. van der Zant, A. J. Houtepen and L. D. A. Siebbeles, *Nat. Nanotechnol.*, 2011, **6**, 733-739.

- (18) Y. Liu, J. Tolentino, M. Gibbs, R. Ihly, C. L. Perkins, Y. Liu, N. Crawford, J. C. Hemminger and M. Law, *Nano Lett.*, 2013, **13**, 1578-1587.
- (19) F. Hetsch, N. Zhao, S. V. Kershaw and A. L. Rogach, *Mater. Today*, 2013, **16**, 312-325.
- (20) B. Ding, Y. Wang, P.-S. Huang, D. H. Waldeck and J.-K. Lee, *J. Phys. Chem. C*, 2014, **118**, 14749-14758.
- (21) S. J. Baik, K. Kim, K. S. Lim, S. Jung, Y.-C. Park, D. G. Han, S. Lim, S. Yoo and S. Jeong, *J. Phys. Chem. C*, 2011, **115**, 607-612.
- (22) M. A. van Huis, L. T. Kunneman, K. Overgaag, Q. Xu, G. Pandraud, H. W. Zandbergen and D. Vanmaekelbergh, *Nano Lett.*, 2008, **8**, 3959-3963.
- (23) G. S. Shanker, A. Swarnkar, A. Chatterjee, S. Chakraborty, M. Phukan, N. Parveen, K. Biswas and A. Nag, *Nanoscale*, 2015, **7**, 9204-9214.
- (24) D. V. Talapin, J.-S. Lee, M. V. Kovalenko and E. V. Shevchenko, *Chem. Rev.*, 2010, **110**, 389-458.
- (25) A. H. Ip, S. M. Thon, S. Hoogland, O. Voznyy, D. Zhitomirsky, R. Debnath, L. Levina, L. R. Rollny, G. H. Carey, A. Fischer, K. W. Kemp, I. J. Kramer, Z. J. Ning, A. J. Labelle, K. W. Chou, A. Amassian and E. H. Sargent, *Nat. Nanotechnol.*, 2012, **7**, 577-582.
- (26) D. Zhitomirsky, I. J. Kramer, A. J. Labelle, A. Fischer, R. Debnath, J. Pan, O. M. Bakr and E. H. Sargent, *Nano Lett.*, 2012, **12**, 1007-1012.
- (27) G. H. Carey, I. J. Kramer, P. Kanjanaboos, G. Moreno-Bautista, O. Voznyy, L. Rollny, J. A. Tang, S. Hoogland and E. H. Sargent, *Acs Nano*, 2014, **8**, 11763-11769.
- (28) S. M. Thon, A. H. Ip, O. Voznyy, L. Levina, K. W. Kemp, G. H. Carey, S. Masala and E. H. Sargent, *ACS Nano*, 2013, **7**, 7680-7688.
- (29) C.-H. M. Chuang, P. R. Brown, V. Bulović and M. G. Bawendi, *Nat. Mater.*, 2014, **13**, 796-801.

- (30) Z. J. Ning, O. Voznyy, J. Pan, S. Hoogland, V. Adinolfi, J. X. Xu, M. Li, A. R. Kirmani, J. P. Sun, J. Minor, K. W. Kemp, H. P. Dong, L. Rollny, A. Labelle, G. Carey, B. Sutherland, I. Hill, A. Amassian, H. Liu, J. Tang, O. M. Bakr and E. H. Sargent, *Nat. Mater.*, 2014, **13**, 822-828.
- (31) K. S. Jeong, J. Tang, H. Liu, J. Kim, A. W. Schaefer, K. Kemp, L. Levina, X. H. Wang, S. Hoogland, R. Debnath, L. Brzozowski, E. H. Sargent and J. B. Asbury, *ACS Nano*, 2012, **6**, 89-99.
- (32) J. Tang, K. W. Kemp, S. Hoogland, K. S. Jeong, H. Liu, L. Levina, M. Furukawa, X. H. Wang, R. Debnath, D. K. Cha, K. W. Chou, A. Fischer, A. Amassian, J. B. Asbury and E. H. Sargent, *Nat. Mater.*, 2011, **10**, 765-771.
- (33) D. N. Dirin, S. Dreyfuss, M. I. Bodnarchuk, G. Nedelcu, P. Papagiorgis, G. Itskos and M. V. Kovalenko, *J. Am. Chem. Soc.*, 2014, **136**, 6550-6553.
- (34) R. W. Crisp, D. M. Kroupa, A. R. Marshall, E. M. Miller, J. B. Zhang, M. C. Beard and J. M. Luther, *Sci. Rep.*, 2015, **5**.
- (35) B. K. Hughes, D. A. Ruddy, J. L. Blackburn, D. K. Smith, M. R. Bergren, A. J. Nozik, J. C. Johnson and M. C. Beard, *Acs Nano*, 2012, **6**, 5498-5506.
- (36) Y. Gai, H. Peng and J. Li, *J. Phys. Chem. C*, 2009, **113**, 21506-21511.
- (37) A. Franceschetti, *Phys. Rev. B*, 2008, **78**, 075418.
- (38) D. Kim, D.-H. Kim, J.-H. Lee and J. C. Grossman, *Phys. Rev. Lett.*, 2013, **110**, 196802.
- (39) S. J. Oh, N. E. Berry, J.-H. Choi, E. A. Gaulding, T. Paik, S.-H. Hong, C. B. Murray and C. R. Kagan, *ACS Nano*, 2013, **7**, 2413-2421.
- (40) S. J. Oh, N. E. Berry, J.-H. Choi, E. A. Gaulding, H. Lin, T. Paik, B. T. Diroll, S. Muramoto, C. B. Murray and C. R. Kagan, *Nano Lett.*, 2014, **14**, 1559-1566.
- (41) H. Wang, I. Barceló, T. Lana-Villarreal, R. Gómez, M. Bonn and E. Cánovas, *Nano Lett.*, 2014, **14**, 5780-5786.
- (42) H. Choi, J.-H. Ko, Y.-H. Kim and S. Jeong, *J. Am. Chem. Soc.*, 2013, **135**, 5278-5281.

- (43) C. R. Bealing, W. J. Baumgardner, J. J. Choi, T. Hanrath and R. G. Hennig, *ACS Nano*, 2012, **6**, 2118-2127.
- (44) A. P. Kaushik, B. Lukose and P. Clancy, *Acs Nano*, 2014, **8**, 2302-2317.
- (45) C. Fang, M. A. van Huis, D. Vanmaekelbergh and H. W. Zandbergen, *Acs Nano*, 2009, **4**, 211-218.
- (46) K. Kimura, K. Nakajima, Y. Fujii and M. Mannami, *Surf. Sci.*, 1994, **318**, 363-367.
- (47) O. Voznyy, S. M. Thon, A. H. Ip and E. H. Sargent, *J. Phys. Chem. Lett.*, 2013, **4**, 987-992.
- (48) M. J. Fernee, E. Thomsen, P. Jensen and H. Rubinsztein-Dunlop, *Nanotechnology*, 2006, **17**, 956-962.
- (49) J. Gao and J. C. Johnson, *Acs Nano*, 2012, **6**, 3292-3303.
- (50) C. A. Nelson and X. Y. Zhu, *J. Am. Chem. Soc.*, 2012, **134**, 7592-7595.
- (51) D. Bozyigit, S. Volk, O. Yarema and V. Wood, *Nano Lett.*, 2013, **13**, 5284-5288.
- (52) P. Nagpal and V. I. Klimov, *Nat. Commun.*, 2011, **2**, 486.
- (53) B. Diaconescu, L. A. Padilha, P. Nagpal, B. S. Swartzentruber and V. I. Klimov, *Phys. Rev. Lett.*, 2013, **110**, 127406.
- (54) Y. Zhang, D. Zherebetsky, N. D. Bronstein, S. Barja, L. Lichtenstein, D. Schuppisser, L.-W. Wang, A. P. Alivisatos and M. Salmeron, *Nano Lett.*, 2015, **15**, 3249-3253.
- (55) J. D. Hackley, D. A. Kislitsyn, D. K. Beaman, S. Ulrich and G. V. Nazin, *Rev. Sci. Instrum.*, 2014, **85**, 103704.
- (56) D. A. Kislitsyn, C. F. Gervasi, T. Allen, P. K. B. Palomaki, J. D. Hackley, R. Maruyama and G. V. Nazin, *J. Phys. Chem. Lett.*, 2014, **5**, 3701-3707.
- (57) S. V. Kilina, C. F. Craig, D. S. Kilin and O. V. Prezhdo, *J. Phys. Chem. C*, 2007, **111**, 4871-4878.
- (58) S. V. Kilina, D. S. Kilin and O. V. Prezhdo, *ACS Nano*, 2008, **3**, 93-99.

- (59) Z. Hens, D. Vanmaekelbergh, E. Stoffels and H. van Kempen, *Phys. Rev. Lett.*, 2002, **88**, 236803.
- (60) Z. Hens, E. S. Kooij, G. Allan, B. Grandidier and D. Vanmaekelbergh, *Nanotechnology*, 2005, **16**, 339-343.
- (61) J. Yang, H. I. Elim, Q. Zhang, J. Y. Lee and W. Ji, *J. Am. Chem. Soc.*, 2006, **128**, 11921-11926.
- (62) C. J. Chen, *Introduction to Scanning Tunneling Microscopy*, Oxford University Press, New York, Second Edition edn., 2008.
- (63) U. Banin, Y. W. Cao, D. Katz and O. Millo, *Nature*, 1999, **400**, 542-544.
- (64) L. Jdira, P. Liljeroth, E. Stoffels, D. Vanmaekelbergh and S. Speller, *Phys. Rev. B*, 2006, **73**.
- (65) I. Moreels, K. Lambert, D. Smeets, D. De Muynck, T. Nollet, J. C. Martins, F. Vanhaecke, A. Vantomme, C. Delerue, G. Allan and Z. Hens, *Acs Nano*, 2009, **3**, 3023-3030.
- (66) W. Lee, N. P. Dasgupta, H. J. Jung, J. R. Lee, R. Sinclair and F. B. Prinz, *Nanotechnology*, 2010, **21**.
- (67) N. P. Dasgupta, W. Lee and F. B. Prinz, *Chem. Mater.*, 2009, **21**, 3973-3978.
- (68) T. D. Krauss, F. W. Wise and D. B. Tanner, *Phys. Rev. Lett.*, 1996, **76**, 1376-1379.
- (69) Z. X. Sun, I. Swart, C. Delerue, D. Vanmaekelbergh and P. Liljeroth, *Phys. Rev. Lett.*, 2009, **102**, 196401.
- (70) N. Nilius, T. M. Wallis and W. Ho, *Science*, 2002, **297**, 1853-1856.
- (71) S. Fölsch, P. Hyldgaard, R. Koch and K. H. Ploog, *Phys. Rev. Lett.*, 2004, **92**, 056803.
- (72) S. Fölsch, J. Yang, C. Nacci and K. Kanisawa, *Phys. Rev. Lett.*, 2009, **103**, 096104.

- (73) I. Moreels, Y. Justo, B. De Geyter, K. Haustraete, J. C. Martins and Z. Hens, *Acs Nano*, 2011, **5**, 2004-2012.
- (74) S. Kilina, S. Ivanov and S. Tretiak, *J. Am. Chem. Soc.*, 2009, **131**, 7717-7726.
- (75) J. T. Margraf, A. Ruland, V. Sgobba, D. M. Guldi and T. Clark, *Langmuir*, 2013, **29**, 15450-15456.
- (76) I. Horcas, R. Fernández, J. M. Gómez-Rodríguez, J. Colchero, J. Gómez-Herrero and A. M. Baro, *Rev. Sci. Instrum.*, 2007, **78**, 2432410.

#### REFERENCES CITED FOR CHAPTER X

- (1) Xin, Y.; Nishio, K.; Saitow, K. White-blue electroluminescence from a Si quantum dot hybrid light-emitting diode. *Applied Physics Letters* **2015**, *106* (20), 201102-201102.
- (2) Hirschman, K. D.; Tsybeskov, L.; Dutttagupta, S. P.; Fauchet, P. M. Silicon-based visible light-emitting devices integrated into microelectronic circuits. *Nature* **1996**, *384* (6607), 338-341.
- (3) Govoni, M.; Marri, I.; Ossicini, S. Carrier multiplication between interacting nanocrystals for fostering silicon-based photovoltaics. *Nature Photonics* **2012**, *6* (10), 672-679.
- (4) Eun-Chel Cho, S. P., Xiaojing Hao, Dengyuan Song, Gavin Conibeer, Sang-Cheol Park, Martin A. Green. Silicon quantum dot/crystalline silicon solar cells. *Nanotechnology* **2008**, *19* (24), 245201-245201.
- (5) Baxter, J. B.; Aydil, E. S. Nanowire-based dye-sensitized solar cells. *Applied Physics Letters* **2005**, *86* (5).
- (6) Plass, R.; Pelet, S.; Krueger, J.; Gratzel, M.; Bach, U. Quantum dot sensitization of organic-inorganic hybrid solar cells. *Journal of Physical Chemistry B* **2002**, *106* (31), 7578-7580.

- (7) Gao, X. H.; Cui, Y. Y.; Levenson, R. M.; Chung, L. W. K.; Nie, S. M. In vivo cancer targeting and imaging with semiconductor quantum dots. *Nat. Biotechnol.* **2004**, *22* (8), 969-976.
- (8) Park, J.-H.; Gu, L.; von Maltzahn, G.; Ruoslahti, E.; Bhatia, S. N.; Sailor, M. J. Biodegradable luminescent porous silicon nanoparticles for in vivo applications. *Nat. Mater.* **2009**, *8* (4), 331-336.
- (9) Buriak, J. M. Organometallic chemistry on silicon surfaces: formation of functional monolayers bound through Si-C bonds. *Chem. Commun.* **1999**, (12), 1051-1060.
- (10) Aldana, J.; Wang, Y. A.; Peng, X. G. Photochemical instability of CdSe nanocrystals coated by hydrophilic thiols. *J. Am. Chem. Soc.* **2001**, *123* (36), 8844-8850.
- (11) Trani, F.; Cantele, G.; Ninno, D.; Iadonisi, G. Tight-binding calculation of the optical absorption cross section of spherical and ellipsoidal silicon nanocrystals. *Physical Review B* **2005**, *72* (7).
- (12) Kocevski, V.; Eriksson, O.; Ruzs, J. Transition between direct and indirect band gap in silicon nanocrystals. *Physical Review B* **2013**, *87* (24), 245401-245401.
- (13) Hapala, P.; Kůsová, K.; Pelant, I.; Jelínek, P. Theoretical analysis of electronic band structure of 2- to 3-nm Si nanocrystals. *Physical Review B* **2013**, *87* (19), 195420-195420.
- (14) Wilson, W. L.; Szajowski, P. F.; Brus, L. E. Quantum Confinement in Size-Selected, Surface-Oxidized Silicon Nanocrystals. *Science* **1993**, *262* (5137), 1242-1244.
- (15) Pavesi, L.; Dal Negro, L.; Mazzoleni, C.; Franzo, G.; Priolo, F. Optical gain in silicon nanocrystals. *Nature* **2000**, *408* (6811), 440-444.
- (16) Anthony, R.; Kortshagen, U. Photoluminescence quantum yields of amorphous and crystalline silicon nanoparticles. *Physical Review B* **2009**, *80* (11).

- (17) Timmerman, D.; Valenta, J.; Dohnalova, K.; de Boer, W. D. A. M.; Gregorkiewicz, T. Step-like enhancement of luminescence quantum yield of silicon nanocrystals. *Nature Nanotechnology* **2011**, *6* (11), 710-713.
- (18) Beard, M. C.; Knutsen, K. P.; Yu, P.; Luther, J. M.; Song, Q.; Metzger, W. K.; Ellingson, R. J.; Nozik, A. J. Multiple exciton generation in colloidal silicon nanocrystals. *Nano Lett.* **2007**, *7* (8), 2506-2512.
- (19) Fischer, S. A.; Madrid, A. B.; Isborn, C. M.; Prezhdo, O. V. Multiple Exciton Generation in Small Si Clusters: A High-Level, Ab Initio Study. *J. Phys. Chem. Lett.* **2010**, *1* (1), 232-237.
- (20) Jaeger, H. M.; Hyeon-Deuk, K.; Prezhdo, O. V. Exciton Multiplication from First Principles. *Acc. Chem. Res.* **2013**, *46* (6), 1280-1289.
- (21) Pi, X. D.; Mangolini, L.; Campbell, S. A.; Kortshagen, U. Room-temperature atmospheric oxidation of Si nanocrystals after HF etching. *Phys. Rev. B* **2007**, *75* (8).
- (22) Kanemitsu, Y.; Okamoto, S.; Otake, M.; Oda, S. Photoluminescence mechanism in surface-oxidized silicon nanocrystals. *Phys. Rev. B* **1997**, *55* (12), R7375-R7378.
- (23) Wolkin, M. V.; Jorne, J.; Fauchet, P. M.; Allan, G.; Delerue, C. Electronic States and Luminescence in Porous Silicon Quantum Dots: The Role of Oxygen. *Physical Review Letters* **1999**, *82* (1), 197-200.
- (24) van Buuren, T.; Dinh, L. N.; Chase, L. L.; Siekhaus, W. J.; Terminello, L. J. Changes in the electronic properties of Si nanocrystals as a function of particle size. *Phys. Rev. Lett.* **1998**, *80* (17), 3803-3806.
- (25) Hessel, C. M.; Henderson, E. J.; Kelly, J. A.; Cavell, R. G.; Sham, T.-K.; Veinot, J. G. C. Origin of luminescence from silicon nanocrystals: a near edge X-ray absorption fine structure (NEXAFS) and X-ray excited optical luminescence (XEOL) study of oxide-embedded and free-standing systems. *Journal of Physical Chemistry C* **2008**, *112* (37), 14247-14254.



- (26) Godefroo, S.; Hayne, M.; Jivanescu, M.; Stesmans, A.; Zacharias, M.; Lebedev, O. I.; Van Tendeloo, G.; Moshchalkov, V. V. Classification and control of the origin of photoluminescence from Si nanocrystals. *Nature nanotechnology* **2008**, *3* (3), 174-8.
- (27) de Boer, W. D. A. M.; Timmerman, D.; Dohnalova, K.; Yassievich, I. N.; Zhang, H.; Buma, W. J.; Gregorkiewicz, T. Red spectral shift and enhanced quantum efficiency in phonon-free photoluminescence from silicon nanocrystals. *Nature Nanotechnology* **2010**, *5* (12), 878-884.
- (28) Liu, S.-M. Luminescent silicon nanoparticles formed in solution. *Journal of Nanoscience and Nanotechnology* **2008**, *8* (3), 1110-1125.
- (29) Godefroo, S.; Hayne, M.; Jivanescu, M.; Stesmans, A.; Zacharias, M.; Lebedev, O. I.; Van Tendeloo, G.; Moshchalkov, V. V. Classification and control of the origin of photoluminescence from Si nanocrystals. *Nat. Nanotechnol.* **2008**, *3* (3), 174-178.
- (30) Dasog, M.; Yang, Z.; Regli, S.; Atkins, T. M.; Faramus, A.; Singh, M. P.; Muthuswamy, E.; Kauzlarich, S. M.; Tilley, R. D.; Veinot, J. G. C. Chemical Insight into the Origin of Red and Blue Photoluminescence Arising from Freestanding Silicon Nanocrystals. *ACS Nano* **2013**, *7* (3), 2676-2685.
- (31) Puzder, A.; Williamson, A. J.; Grossman, J. C.; Galli, G. Surface control of optical properties in silicon nanoclusters. *J. Chem. Phys.* **2002**, *117* (14), 6721-6729.
- (32) Luppi, M.; Ossicini, S. Ab initio study on oxidized silicon clusters and silicon nanocrystals embedded in SiO<sub>2</sub>: Beyond the quantum confinement effect. *Phys. Rev. B* **2005**, *71* (3).
- (33) Kocevski, V.; Eriksson, O.; Ruzs, J. Size dependence of the stability, electronic structure, and optical properties of silicon nanocrystals with various surface impurities. *Physical Review B* **2015**, *91* (12), 125402-125402.
- (34) Ramos, L. E.; Furthmuller, J.; Bechstedt, F. Effect of backbond oxidation on silicon nanocrystallites. *Phys. Rev. B* **2004**, *70* (3).

- (35) Vasiliev, I.; Chelikowsky, J. R.; Martin, R. M. Surface oxidation effects on the optical properties of silicon nanocrystals. *Phys. Rev. B* **2002**, *65* (12).
- (36) Puzder, A.; Williamson, A. J.; Grossman, J. C.; Galli, G. Computational studies of the optical emission of silicon nanocrystals. *J. Am. Chem. Soc.* **2003**, *125* (9), 2786-2791.
- (37) Pennycook, T. J.; Hadjisavvas, G.; Idrobo, J. C.; Kelires, P. C.; Pantelides, S. T. Optical gaps of free and embedded Si nanoclusters: Density functional theory calculations. *Phys. Rev. B* **2010**, *82* (12).
- (38) Zhou, Z. Y.; Brus, L.; Friesner, R. Electronic structure and luminescence of 1.1- and 1.4-nm silicon nanocrystals: Oxide shell versus hydrogen passivation. *Nano Letters* **2003**, *3* (2), 163-167.
- (39) Chen, C. J. *Introduction to Scanning Tunneling Microscopy*. Second Edition ed.; Oxford University Press: New York, 2008.
- (40) Wolf, O.; Dasog, M.; Yang, Z.; Balberg, I.; Veinot, J. G. C.; Millo, O. Doping and Quantum Confinement Effects in Single Si Nanocrystals Observed by Scanning Tunneling Spectroscopy. *Nano Lett.* **2013**, *13* (6), 2516-2521.
- (41) Kislitsyn, D. A.; Gervasi, C. F.; Allen, T.; Palomaki, P. K. B.; Hackley, J. D.; Maruyama, R.; Nazin, G. V. Spatial Mapping of Sub-Bandgap States Induced by Local Nonstoichiometry in Individual Lead Sulfide Nanocrystals. *J. Phys. Chem. Lett.* **2014**, *5* (21), 3701-3707.
- (42) Gervasi, C. F.; Kislitsyn, D. A.; Allen, T. L.; Hackley, J. D.; Maruyama, R.; Nazin, G. V. Diversity of sub-bandgap states in lead-sulfide nanocrystals: real-space spectroscopy and mapping at the atomic-scale. *Nanoscale* **2015**, *7* (46), 19732-19742.
- (43) Hackley, J. D.; Kislitsyn, D. A.; Beaman, D. K.; Ulrich, S.; Nazin, G. V. High-Stability Cryogenic Scanning Tunneling Microscope Based on a Closed-Cycle Cryostat. *Rev. Sci. Instrum.* **2014**, *85* (10), 103704.
- (44) Chiu, S.-K.; Manhat, B. A.; DeBenedetti, W. J. I.; Brown, A. L.; Fichter, K.; Vu, T.; Eastman, M.; Jiao, J.; Goforth, A. M. Aqueous red-emitting silicon

- nanoparticles for cellular imaging: Consequences of protecting against surface passivation by hydroxide and water for stable red emission. *J. Mater. Res.* **2013**, *28* (2), 216-230.
- (45) Ordejon, P.; Artacho, E.; Soler, J. M. Self-consistent order-N density-functional calculations for very large systems. *Phys. Rev. B* **1996**, *53* (16), 10441-10444.
- (46) Soler, J. M.; Artacho, E.; Gale, J. D.; Garcia, A.; Junquera, J.; Ordejon, P.; Sanchez-Portal, D. The SIESTA method for ab initio order-N materials simulation. *J. Phys.-Condens. Matter* **2002**, *14* (11), 2745-2779.
- (47) Hadjisavvas, G.; Remediakis, I. N.; Kelires, P. C. Shape and faceting of Si nanocrystals embedded in a-SiO<sub>2</sub>: A Monte Carlo study. *Physical Review B* **2006**, *74* (16), 165419-165419.
- (48) Wang, Y. Q.; Smirani, R.; Ross, G. G. Nanotwinning in Silicon Nanocrystals Produced by Ion Implantation. *Nano Letters* **2004**, *4* (10), 2041-2045.
- (49) Hapala, P.; Kusova, K.; Pelant, I.; Jelinek, P. Theoretical analysis of electronic band structure of 2- to 3-nm Si nanocrystals. *Phys. Rev. B* **2013**, *87* (19).
- (50) Zhang, J.; Fu, Y.; Lakowicz, J. R. Enhanced Förster Resonance Energy Transfer (FRET) on a Single Metal Particle. *J. Phys. Chem. C* **2006**, *111* (1), 50-56.
- (51) Hessel, C. M.; Henderson, E. J.; Veinot, J. G. C. Hydrogen silsesquioxane: A molecular precursor for nanocrystalline Si-SiO<sub>2</sub> composites and freestanding hydride-surface-terminated silicon nanoparticles. *Chem. Mater.* **2006**, *18* (26), 6139-6146.
- (52) Weeks, S. L.; Chaukulkar, R. P.; Stradins, P.; Agarwal, S. Photoluminescence behavior of plasma synthesized Si nanocrystals oxidized at low temperature in pure O<sub>2</sub> and H<sub>2</sub>O. *Journal of Vacuum Science & Technology A* **2014**, *32* (5), 050604.
- (53) Brawand, N. P.; Voros, M.; Galli, G. Surface dangling bonds are a cause of B-type blinking in Si nanoparticles. *Nanoscale* **2015**, *7* (8), 3737-3744.

- (54) Miller, J. B.; Dandu, N.; Velizhanin, K. A.; Anthony, R. J.; Kortshagen, U. R.; Kroll, D. M.; Kilina, S.; Hobbie, E. K. Enhanced Luminescent Stability through Particle Interactions in Silicon Nanocrystal Aggregates. *ACS Nano* **2015**, *9* (10), 9772-9782.

## REFERENCES CITED FOR CHAPTER XI

- (1) M. Govoni, I. Marri and S. Ossicini *Nat. Photonics* **6**, (2012).
- (2) E. C. Cho, S. Park, X. Hao, D. Song, G. Conibeer, S. C. Park and M. A. Green *Nanotechnology* **19**, (2008).
- (3) J. B. Baxter and E. S. Aydil *Appl. Phys. Lett.* **86**, (2005).
- (4) R. Plass, S. Pelet, J. Krueger, M. Gratzel and U. Bach *J. Phys. Chem. B* **106**, (2002).
- (5) Y. Xin, K. Nishio and K. Saitow *Appl. Phys. Lett.* **106**, (2015).
- (6) K. D. Hirschman, L. Tsybeskov, S. P. Duttagupta and P. M. Fauchet *Nature* **384**, (1996).
- (7) X. H. Gao, Y. Y. Cui, R. M. Levenson, L. W. K. Chung and S. M. Nie *Nat. Biotechnol.* **22**, (2004).
- (8) J.-H. Park, L. Gu, G. von Maltzahn, E. Ruoslahti, S. N. Bhatia and M. J. Sailor *Nat. Mater.* **8**, (2009).
- (9) J. M. Buriak *Chem. Commun.*, (1999).
- (10) J. Aldana, Y. A. Wang and X. G. Peng *J. Am. Chem. Soc.* **123**, (2001).
- (11) W. L. Wilson, P. F. Szajowski and L. E. Brus *Science* **262**, (1993).
- (12) L. Pavesi, L. Dal Negro, C. Mazzoleni, G. Franzo and F. Priolo *Nature* **408**, (2000).
- (13) R. Anthony and U. Kortshagen *Phys. Rev. B* **80**, (2009).
- (14) D. Timmerman, J. Valenta, K. Dohnalova, W. D. A. M. de Boer and T. Gregorkiewicz *Nat Nanotechnol* **6**, (2011).

- (15) F. Trani, G. Cantele, D. Ninno and G. Iadonisi *Phys. Rev. B* **72**, (2005).
- (16) V. Kocevski, O. Eriksson and J. Rusz *Phys. Rev. B* **87**, (2013).
- (17) P. Hapala, K. Kůsová, I. Pelant and P. Jelínek *Phys. Rev. B* **87**, (2013).
- (18) W. J. I. DeBenedetti, S. K. Chiu, C. M. Radlinger, R. J. Ellison, B. A. Manhat, J. Z. Zhang, J. Y. Shi and A. M. Goforth *J. Phys. Chem. C* **119**, (2015).
- (19) B. Gelloz, H. Sano, R. Boukherroub, D. D. M. Wayner, D. J. Lockwood and N. Koshida *Appl. Phys. Lett.* **83**, (2003).
- (20) L. M. Wheeler, N. R. Neale, T. Chen and U. R. Kortshagen *Nat Commun* **4**, (2013).
- (21) J. D. Holmes, K. J. Ziegler, R. C. Doty, L. E. Pell, K. P. Johnston and B. A. Korgel *J. Am. Chem. Soc.* **123**, (2001).
- (22) D. S. English, L. E. Pell, Z. H. Yu, P. F. Barbara and B. A. Korgel *Nano Lett.* **2**, (2002).
- (23) Y. Ding, M. Sugaya, Q. Liu, S. Zhou and T. Nozaki *Nano Energy* **10**, (2014).
- (24) K. Keunen, A. Stesmans and V. V. Afanas'ev *Phys. Rev. B* **84**, (2011).
- (25) Y. Li, P. Liang, Z. Hu, S. Guo, Q. You, J. Sun, N. Xu and J. Wu *Appl. Surf. Sci.* **300**, (2014).
- (26) F. A. Reboredo and G. Galli *J. Phys. Chem. B* **109**, (2005).
- (27) R. N. Pereira, D. J. Rowe, R. J. Anthony and U. Kortshagen *Phys. Rev. B* **83**, (2011).
- (28) Y. Saito and A. Yoshida *Philos Mag B* **66**, (1992).
- (29) J. J. Wu and U. Kortshagen *RSC Advances*, (2015).
- (30) H. Li, Z. Wu and M. T. Lusk *J. Phys. Chem. C* **118**, (2014).
- (31) M. Lannoo, C. Delerue and G. Allan *J. Lumin.* **57**, (1993).
- (32) N. P. Brawand, M. Voros and G. Galli *Nanoscale* **7**, (2015).
- (33) C.-Y. Liu, Z. C. Holman and U. R. Kortshagen *Nano Lett.* **9**, (2009).

- (34) J. B. Miller, N. Dandu, K. A. Velizhanin, R. J. Anthony, U. R. Kortshagen, D. M. Kroll, S. Kilina and E. K. Hobbie ACS Nano **9**, (2015).
- (35) R. J. Hamers J. Vac. Sci. Technol., B: Microelectron. Nanometer Struct. **6**, (1988).
- (36) H. Labidi, M. Taucer, M. Rashidi, M. Koleini, L. Livadaru, J. Pitters, M. Cloutier, M. Salomons and R. A. Wolkow New J. Phys. **17**, (2015).
- (37) P. G. Piva, G. A. DiLabio, L. Livadaru and R. A. Wolkow Phys. Rev. B **90**, (2014).
- (38) S. R. Schofield, P. Studer, C. F. Hirjibehedin, N. J. Curson, G. Aeppli and D. R. Bowler Nat Commun **4**, (2013).
- (39) C. J. Chen, *Introduction to Scanning Tunneling Microscopy* (Oxford University Press, New York, 2008).
- (40) M. B. Haider, J. L. Pitters, G. A. DiLabio, L. Livadaru, J. Y. Mutus and R. A. Wolkow Phys. Rev. Lett. **102**, (2009).
- (41) J. L. Pitters, L. Livadaru, M. B. Haider and R. A. Wolkow J Chem Phys **134**, (2011).
- (42) M. Englund, R. Zuzak, S. Godlewski, M. Kolmer, T. Frederiksen, A. García-Lekue, D. Sánchez-Portal and M. Szymonski Sci. Rep. **5**, (2015).
- (43) O. Wolf, M. Dasog, Z. Yang, I. Balberg, J. G. C. Veinot and O. Millo Nano Lett. **13**, (2013).
- (44) D. A. Kislitsyn, V. Kocevski, J. M. Mills, S.-K. Chiu, C. F. Gervasi, B. N. Taber, A. E. Rosenfield, O. Eriksson, J. Ruzs, A. M. Goforth and G. V. Nazin The Journal of Physical Chemistry Letters **7**, (2016).
- (45) J. D. Hackley, D. A. Kislitsyn, D. K. Beaman, S. Ulrich and G. V. Nazin Rev. Sci. Instrum. **85**, (2014).
- (46) S.-K. Chiu, B. A. Manhat, W. J. I. DeBenedetti, A. L. Brown, K. Fichter, T. Vu, M. Eastman, J. Jiao and A. M. Goforth J. Mater. Res. **28**, (2013).

- (47) P. Ordejon, E. Artacho and J. M. Soler Phys. Rev. B **53**, (1996).
- (48) M. S. José, A. Emilio, D. G. Julian, G. Alberto, J. Javier, O. Pablo and S.-P. Daniel J. Phys.: Condens. Matter **14**, (2002).
- (49) V. Kocevski, O. Eriksson and J. Ruzs Phys. Rev. B **91**, (2015).
- (50) L. Soukiassian, A. J. Mayne, M. Carbone and G. Dujardin Phys. Rev. B **68**, (2003).
- (51) Bellec, D. Riedel, G. Dujardin, O. Boudrioua, L. Chaput, L. Stauffer and P. Sonnet Phys. Rev. B **80**, (2009).
- (52) W. Ye, K. Min, P. Peña Martin, A. A. Rockett, N. R. Aluru and J. W. Lyding Surf. Sci. **609**, (2013).
- (53) T. C. Shen, C. Wang, G. C. Abeln, J. R. Tucker, J. W. Lyding, P. Avouris and R. E. Walkup Science **268**, (1995).
- (54) R. S. Becker, G. S. Higashi, Y. J. Chabal and A. J. Becker Phys. Rev. Lett. **65**, (1990).
- (55) Bellec, D. Riedel, G. Dujardin, N. Rompotis and L. N. Kantorovich Phys. Rev. B **78**, (2008).
- (56) P. Avouris, R. E. Walkup, A. R. Rossi, H. C. Akpati, P. Nordlander, T. C. Shen, G. C. Abeln and J. W. Lyding Surf. Sci. **363**, (1996).
- (57) G. V. Nazin, S. W. Wu and W. Ho Proc. Natl. Acad. Sci. U. S. A. **102**, (2005).
- (58) G. V. Nazin, X. H. Qiu and W. Ho J. Chem. Phys. **122**, (2005).
- (59) Z. Sun, I. Swart, C. Delerue, D. Vanmaekelbergh and P. Liljeroth Phys. Rev. Lett. **102**, (2009).
- (60) N. A. Pradhan, N. Liu, C. Silien and W. Ho Nano Lett. **5**, (2005).
- (61) S. W. Wu, G. V. Nazin, X. Chen, X. H. Qiu and W. Ho Phys. Rev. Lett. **93**, (2004).
- (62) Bellec, L. Chaput, G. Dujardin, D. Riedel, L. Stauffer and P. Sonnet Phys. Rev. B **88**, (2013).

- (63) S. W. Wu, N. Ogawa, G. V. Nazin and W. Ho *J. Phys. Chem. C* **112**, (2008).
- (64) G. W. Brown, H. Grube, M. E. Hawley, S. R. Schofield, N. J. Curson, M. Y. Simmons and R. G. Clark *J. Appl. Phys.* **92**, (2002).

## REFERENCES CITED FOR CHAPTER XII

- (1) Ho, W. Single-Molecule Chemistry. *J. Chem. Phys.* **2002**, *117*, 11033.
- (2) Zandvliet, H. J. W.; Houselt, A. van. Scanning Tunneling Spectroscopy. *Annu. Rev. Anal. Chem.* **2009**, *2* (1), 37–55.
- (3) Nazin, G. *Single Molecule Studies with a Scanning Tunneling Microscope*; Thesis: University of California, Irvine, 2007.
- (4) Chen, C.; Chu, P.; Bobisch, C. A.; Mills, D. L.; Ho, W. Viewing the Interior of a Single Molecule: Vibronically Resolved Photon Imaging at Submolecular Resolution. *Phys. Rev. Lett.* **2010**, *105* (21), 217402.
- (5) Qiu, X. H.; Nazin, G. V.; Ho, W. Vibrationally Resolved Fluorescence Excited with Submolecular Precision. *Science* **2003**, *299* (5606), 542–546.
- (6) Čavar, E.; Blüm, M.-C.; Pivetta, M.; Patthey, F.; Chergui, M.; Schneider, W.-D. Fluorescence and Phosphorescence from Individual C<sub>60</sub> Molecules Excited by Local Electron Tunneling. *Phys. Rev. Lett.* **2005**, *95* (19), 196102.
- (7) Lambe, J.; McCarthy, S. L. Light Emission from Inelastic Electron Tunneling. *Phys. Rev. Lett.* **1976**, *37* (14), 923–925.
- (8) Berndt, R.; Gimzewski, J. K.; Johansson, P. Inelastic Tunneling Excitation of Tip-Induced Plasmon Modes on Noble-Metal Surfaces. *Phys. Rev. Lett.* **1991**, *67* (27), 3796–3799.
- (9) Nazin, G. V.; Qiu, X. H.; Ho, W. Atomic Engineering of Photon Emission with a Scanning Tunneling Microscope. *Phys. Rev. Lett.* **2003**, *90* (21), 216110.
- (10) Romero, M. J.; van de Lagemaat, J.; Mora-Sero, I.; Rumbles, G.; Al-Jassim, M. M. Imaging of Resonant Quenching of Surface Plasmons by Quantum Dots. *Nano Lett* **2006**, *6* (12), 2833–2837.



- (11) Zhang, J.; Fu, Y.; Chowdhury, M. H.; Lakowicz, J. R. Enhanced Förster Resonance Energy Transfer on Single Metal Particle. 2. Dependence on Donor–Acceptor Separation Distance, Particle Size, and Distance from Metal Surface. *J Phys Chem C* **2007**, *111* (32), 11784–11792.
- (12) Lakowicz, J. R.; Ray, K.; Chowdhury, M.; Szymanski, H.; Fu, Y.; Zhang, J.; Nowaczyk, K. Plasmon-Controlled Fluorescence: A New Paradigm in Fluorescence Spectroscopy. *The Analyst* **2008**, *133* (10), 1308–1346.
- (13) Zhang, J.; Fu, Y.; Lakowicz, J. R. Enhanced Förster Resonance Energy Transfer (FRET) on a Single Metal Particle. *J Phys Chem C* **2006**, *111* (1), 50–56.
- (14) Hartschuh, A. Tip-Enhanced Near-Field Optical Microscopy. *Angew. Chem. Int. Ed.* **2008**, *47* (43), 8178–8191.
- (15) Neacsu, C. C.; Dreyer, J.; Behr, N.; Raschke, M. B. Scanning-Probe Raman Spectroscopy with Single-Molecule Sensitivity. *Phys. Rev. B* **2006**, *73* (19), 193406.
- (16) Zhang, W.; Yeo, B. S.; Schmid, T.; Zenobi, R. Single Molecule Tip-Enhanced Raman Spectroscopy with Silver Tips. *J Phys Chem C* **2007**, *111* (4), 1733–1738.
- (17) Steidtner, J.; Pettinger, B. Tip-Enhanced Raman Spectroscopy and Microscopy on Single Dye Molecules with 15 Nm Resolution. *Phys. Rev. Lett.* **2008**, *100* (23), 236101.
- (18) Reich, S.; Thomsen, C.; Maultzsch, J. *Carbon Nanotubes: Basic Concepts and Physical Properties*, 1st ed.; Wiley-VCH, 2004.
- (19) Kelly, K. F.; Chiang, I. W.; Mickelson, E. T.; Hauge, R. H.; Margrave, J. L.; Wang, X.; Scuseria, G. E.; Radloff, C.; Halas, N. J. Insight into the Mechanism of Sidewall Functionalization of Single-Walled Nanotubes: An STM Study. *Chem. Phys. Lett.* **1999**, *313* (3-4), 445–450.
- (20) Burghard, M. Electronic and Vibrational Properties of Chemically Modified Single-Wall Carbon Nanotubes. *Surf. Sci. Rep.* **2005**, *58* (1-4), 1–109.

- (21) Tans, S. J.; Verschueren, A. R. M.; Dekker, C. Room-Temperature Transistor Based on a Single Carbon Nanotube. *Nature* **1998**, *393* (6680), 49–52.
- (22) Jorio, A.; Dresselhaus, G.; Dresselhaus, M. S. *Carbon Nanotubes: Advanced Topics in the Synthesis, Structure, Properties and Applications*, 1st ed.; Springer, 2008.
- (23) Saito, R.; Dresselhaus, M. S.; Dresselhaus, G. *Physical Properties of Carbon Nanotubes*; World Scientific Publishing Company, 1998.
- (24) Wilder, J. W. G.; Venema, L. C.; Rinzler, A. G.; Smalley, R. E.; Dekker, C. Electronic Structure of Atomically Resolved Carbon Nanotubes. *Nature* **1998**, *391* (6662), 59–62.
- (25) Odom, T. W.; Huang, J.-L.; Kim, P.; Lieber, C. M. Atomic Structure and Electronic Properties of Single-Walled Carbon Nanotubes. *Nature* **1998**, *391* (6662), 62–64.
- (26) Avramov, P. V.; Kudin, K. N.; Scuseria, G. E. Single Wall Carbon Nanotubes Density of States: Comparison of Experiment and Theory. *Chem. Phys. Lett.* **2003**, *370* (5-6), 597–601.
- (27) Ruppalt, L. B.; Lyding, J. W. Metal-Induced Gap States at a Carbon-Nanotube Intramolecular Heterojunction Observed by Scanning Tunneling Microscopy. *Small* **2007**, *3* (2), 280–284.
- (28) Ruppalt, L. B.; Lyding, J. W. Charge Transfer between Semiconducting Carbon Nanotubes and Their Doped GaAs(110) and InAs(110) Substrates Detected by Scanning Tunnelling Spectroscopy. *Nanotechnology* **2007**, *18*, 215202.
- (29) Berthe, M.; Yoshida, S.; Ebine, Y.; Kanazawa, K.; Okada, A.; Taninaka, A.; Takeuchi, O.; Fukui, N.; Shinohara, H.; Suzuki, S.; et al. Reversible Defect Engineering of Single-Walled Carbon Nanotubes Using Scanning Tunneling Microscopy. *Nano Lett* **2007**, *7* (12), 3623–3627.
- (30) Giusca, C. E.; Tison, Y.; Silva, S. R. P. Atomic and Electronic Structure in Collapsed Carbon Nanotubes Evidenced by Scanning Tunneling Microscopy. *Phys. Rev. B* **2007**, *76* (3), 035429.

- (31) Nemes-Incze, P.; Kónya, Z.; Kiricsi, I.; Pekker, A.; Horváth, Z. E.; Kamarás, K.; Biró, L. P. Mapping of Functionalized Regions on Carbon Nanotubes by Scanning Tunneling Microscopy. *J Phys Chem C* **2011**, *115* (8), 3229–3235.
- (32) Zheng, B.; Hermet, P.; Henrard, L. Scanning Tunneling Microscopy Simulations of Nitrogen- and Boron-Doped Graphene and Single-Walled Carbon Nanotubes. *ACS Nano* **2010**, *4* (7), 4165–4173.
- (33) Bonifazi, D.; Nacci, C.; Marega, R.; Campidelli, S.; Ceballos, G.; Modesti, S.; Meneghetti, M.; Prato, M. Microscopic and Spectroscopic Characterization of Paintbrush-like Single-Walled Carbon Nanotubes. *Nano Lett* **2006**, *6* (7), 1408–1414.
- (34) Lin, H.; Lagoute, J.; Repain, V.; Chacon, C.; Girard, Y.; Ducastelle, F.; Amara, H.; Loiseau, A.; Hermet, P.; Henrard, L.; et al. Imaging the Symmetry Breaking of Molecular Orbitals in Single-Wall Carbon Nanotubes. *Phys. Rev. B* **2010**, *81* (23), 235412.
- (35) Chen, C.; Bobisch, C. A.; Ho, W. Visualization of Fermi's Golden Rule Through Imaging of Light Emission from Atomic Silver Chains. *Science* **2009**, *325* (5943), 981–985.
- (36) Walsh, A. G.; Nickolas Vamivakas, A.; Yin, Y.; Cronin, S. B.; Selim Ünlü, M.; Goldberg, B. B.; Swan, A. K. Scaling of Exciton Binding Energy with External Dielectric Function in Carbon Nanotubes. *Phys. E Low-Dimens. Syst. Nanostructures* **2008**, *40* (7), 2375–2379.
- (37) Ando, T. Excitons in Carbon Nanotubes. *J. Phys. Soc. Jpn.* **1997**, *66*, 1066–1073.
- (38) Wang, F.; Dukovic, G.; Brus, L. E.; Heinz, T. F. The Optical Resonances in Carbon Nanotubes Arise from Excitons. *Science* **2005**, *308* (5723), 838–841.
- (39) Kane, C. L.; Mele, E. J. Electron Interactions and Scaling Relations for Optical Excitations in Carbon Nanotubes. *Phys. Rev. Lett.* **2004**, *93* (19), 197402.
- (40) Perebeinos, V.; Tersoff, J.; Avouris, P. Scaling of Excitons in Carbon Nanotubes. *Phys. Rev. Lett.* **2004**, *92* (25), 257402.

- (41) Capaz, R. B.; Spataru, C. D.; Ismail-Beigi, S.; Louie, S. G. Diameter and Chirality Dependence of Exciton Properties in Carbon Nanotubes. *Phys. Rev. B* **2006**, *74* (12), 121401.
- (42) Lin, H.; Lagoute, J.; Repain, V.; Chacon, C.; Girard, Y.; Lauret, J.-S.; Ducastelle, F.; Loiseau, A.; Rousset, S. Many-Body Effects in Electronic Bandgaps of Carbon Nanotubes Measured by Scanning Tunnelling Spectroscopy. *Nat Mater* **2010**, *9* (3), 235–238.
- (43) Coratger, R.; Salvetat, J.-P.; Carladous, A.; Ajustron, F.; Beauvillain, J.; Bonard, J.-M.; Forró, L. STM Induced Luminescence in Carbon Nanotubes. *Eur. Phys. J. Appl. Phys.* **2001**, *15*, 177–180.
- (44) Uemura, T.; Yamaguchi, S.; Akai-Kasaya, M.; Saito, A.; Aono, M.; Kuwahara, Y. Tunneling-Current-Induced Light Emission from Individual Carbon Nanotubes. *Surf. Sci.* **2006**, *600* (3), L15–L19.
- (45) Cognet, L.; Tsyboulski, D. A.; Rocha, J.-D. R.; Doyle, C. D.; Tour, J. M.; Weisman, R. B. Stepwise Quenching of Exciton Fluorescence in Carbon Nanotubes by Single-Molecule Reactions. *Science* **2007**, *316* (5830), 1465–1468.
- (46) Luer, L.; Hoseinkhani, S.; Polli, D.; Crochet, J.; Hertel, T.; Lanzani, G. Size and Mobility of Excitons in (6, 5)Carbon Nanotubes. *Nat Phys* **2009**, *5* (1), 54–58.
- (47) Miyauchi, Y.; Hirori, H.; Matsuda, K.; Kanemitsu, Y. Radiative Lifetimes and Coherence Lengths of One-Dimensional Excitons in Single-Walled Carbon Nanotubes. *Phys. Rev. B* **2009**, *80* (8), 081410.
- (48) Ma, Y.-Z.; Graham, M. W.; Fleming, G. R.; Green, A. A.; Hersam, M. C. Ultrafast Exciton Dephasing in Semiconducting Single-Walled Carbon Nanotubes. *Phys. Rev. Lett.* **2008**, *101* (21), 217402.
- (49) Fagan, J. A.; Simpson, J. R.; Bauer, B. J.; De Paoli Lacerda, S. H.; Becker, M. L.; Chun, J.; Migler, K. B.; Hight Walker, A. R.; Hobbie, E. K. Length-Dependent Optical Effects in Single-Wall Carbon Nanotubes. *J Am Chem Soc* **2007**, *129* (34), 10607–10612.

- (50) Joh, D. Y.; Herman, L. H.; Ju, S.-Y.; Kinder, J.; Segal, M. A.; Johnson, J. N.; Chan, G. K. L.; Park, J. On-Chip Rayleigh Imaging and Spectroscopy of Carbon Nanotubes. *Nano Lett* **2010**, *11* (1), 1–7.
- (51) Georgi, C.; Böhmler, M.; Qian, H.; Novotny, L.; Hartschuh, A. Probing Exciton Propagation and Quenching in Carbon Nanotubes with Near-field Optical Microscopy. *Phys. Status Solidi B* **2009**, *246* (11-12), 2683–2688.
- (52) Hartschuh, A.; Qian, H.; Meixner, A. J.; Anderson, N.; Novotny, L. Nanoscale Optical Imaging of Excitons in Single-Walled Carbon Nanotubes. *Nano Lett* **2005**, *5* (11), 2310–2313.
- (53) Georgi, C.; Green, A. A.; Hersam, M. C.; Hartschuh, A. Probing Exciton Localization in Single-Walled Carbon Nanotubes Using High-Resolution Near-Field Microscopy. *ACS Nano* **2010**, *4* (10), 5914–5920.
- (54) Scott, G.; Ashtekar, S.; Lyding, J.; Gruebele, M. Direct Imaging of Room Temperature Optical Absorption with Subnanometer Spatial Resolution. *Nano Lett* **2010**, *10* (12), 4897–4900.
- (55) Matsunaga, R.; Matsuda, K.; Kanemitsu, Y. Observation of Charged Excitons in Hole-Doped Carbon Nanotubes Using Photoluminescence and Absorption Spectroscopy. *Phys. Rev. Lett.* **2011**, *106* (3), 037404.
- (56) Santos, S. M.; Yuma, B.; Berciaud, S.; Shaver, J.; Gallart, M.; Gilliot, P.; Cognet, L.; Lounis, B. All-Optical Trion Generation in Single-Walled Carbon Nanotubes. *Phys. Rev. Lett.* **2011**, *107* (18), 187401.
- (57) Kuo, D. M.-T.; Chang, Y.-C. Theory of Electron Tunneling through a Scanning Tunneling Microscopy-Tip/quantum Dot Junction. *J. Vac. Sci. Technol. B Microelectron. Nanometer Struct.* **2008**, *26*, 1483.
- (58) Waxenegger, J.; Trügler, A.; Hohenester, U. Mapping Excitons in Semiconducting Carbon Nanotubes with Plasmonic Nanoparticles. *Phys. Rev. B* **2011**, *83* (24), 245446.

- (59) Qian, H.; Georgi, C.; Anderson, N.; Green, A. A.; Hersam, M. C.; Novotny, L.; Hartschuh, A. Exciton Energy Transfer in Pairs of Single-Walled Carbon Nanotubes. *Nano Lett* **2008**, 8 (5), 1363–1367.
- (60) Dresselhaus, M. S.; Dresselhaus, G.; Saito, R.; Jorio, A. Raman Spectroscopy of Carbon Nanotubes. *Phys. Rep.* **2005**, 409 (2), 47–99.
- (61) Hartschuh, A.; Sánchez, E. J.; Xie, X. S.; Novotny, L. High-Resolution Near-Field Raman Microscopy of Single-Walled Carbon Nanotubes. *Phys. Rev. Lett.* **2003**, 90 (9), 095503.
- (62) Hartschuh, A.; Pedrosa, H. N.; Novotny, L.; Krauss, T. D. Simultaneous Fluorescence and Raman Scattering from Single Carbon Nanotubes. *Science* **2003**, 301 (5638), 1354–1356.
- (63) Lucchese, M. M.; Stavale, F.; Ferreira, E. H. M.; Vilani, C.; Moutinho, M. V. O.; Capaz, R. B.; Achete, C. A.; Jorio, A. Quantifying Ion-Induced Defects and Raman Relaxation Length in Graphene. *Carbon* **2010**, 48 (5), 1592–1597.
- (64) Georgi, C.; Hartschuh, A. Tip-Enhanced Raman Spectroscopic Imaging of Localized Defects in Carbon Nanotubes. *Appl. Phys. Lett.* **2010**, 97, 143117.

## REFERENCES CITED FOR APPENDICES

- (1) Clair, S.; Kim, Y.; Kawai, M. Energy level alignment of single-wall carbon nanotubes on metal surfaces. *Phys. Rev. B* **2011**, 83 (24), 245422.
- (2) Shin, H.-J.; Clair, S.; Kim, Y.; Kawai, M. Substrate-induced array of quantum dots in a single-walled carbon nanotube. *Nat. Nanotechnol.* **2009**, 4 (9), 567-570.
- (3) Nazin, G. V.; Wu, S. W.; Ho, W. Tunneling rates in electron transport through double-barrier molecular junctions in a scanning tunneling microscope. *Proc. Natl. Acad. Sci. U. S. A.* **2005**, 102 (25), 8832-8837.
- (4) Frisch, M.; Trucks, G. W.; Schlegel, H. B.; Scuseria, G. E.; Robb, M. A.; Cheeseman, J. R.; Scalmani, G.; Barone, V.; Mennucci, B.; Petersson, G. Gaussian 09, Revision A. 02, Gaussian, Inc., Wallingford, CT **2009**, 200.

- (5) Hanwell, M. D.; Curtis, D. E.; Lonie, D. C.; Vandermeersch, T.; Zurek, E.; Hutchison, G. R. Avogadro: an advanced semantic chemical editor, visualization, and analysis platform. *Journal of Cheminformatics* **2012**, *4*.
- (6) Becke, A. D. Density-Functional Thermochemistry. III. The Role of Exact Exchange. *Journal of Chemical Physics* **1993**, *98* (7), 5648-5652.
- (7) Stephens, P. J.; Devlin, F. J.; Chabalowski, C. F.; Frisch, M. J. Ab-Initio Calculation of Vibrational Absorption and Circular-Dichroism Spectra Using Density-Functional Force-Fields. *Journal of Physical Chemistry* **1994**, *98* (45), 11623-11627.
- (8) Perdew, J. P.; Burke, K.; Ernzerhof, M. Generalized gradient approximation made simple. *Physical Review Letters* **1996**, *77* (18), 3865-3868.
- (9) Perdew, J. P.; Wang, Y. Accurate and Simple Analytic Representation of the Electron-Gas Correlation-Energy. *Physical Review B* **1992**, *45* (23), 13244-13249.
- (10) Wu, S. W.; Nazin, G. V.; Chen, X.; Qiu, X. H.; Ho, W. Control of relative tunneling rates in single molecule bipolar electron transport. *Phys. Rev. Lett.* **2004**, *93* (23), 236802.
- (11) Nazin, G. V.; Qiu, X. H.; Ho, W. Vibrational spectroscopy of individual doping centers in a monolayer organic crystal. *J. Chem. Phys.* **2005**, *122* (18), 181105.
- (12) Hines, M. A.; Scholes, G. D. Colloidal PbS nanocrystals with size-tunable near-infrared emission: Observation of post-synthesis self-narrowing of the particle size distribution. *Advanced Materials* **2003**, *15* (21), 1844-1849.
- (13) Moreels, I.; Lambert, K.; Smeets, D.; De Muynck, D.; Nollet, T.; Martins, J. C.; Vanhaecke, F.; Vantomme, A.; Delerue, C.; Allan, G.; Hens, Z. Size-Dependent Optical Properties of Colloidal PbS Quantum Dots. *ACS Nano* **2009**, *3* (10), 3023-3030.
- (14) Kim, D.; Kim, D.-H.; Lee, J.-H.; Grossman, J. C. Impact of Stoichiometry on the Electronic Structure of PbS Quantum Dots. *Physical Review Letters* **2013**, *110* (19), 196802.

- (15) Henderson, E. J.; Kelly, J. A.; Veinot, J. G. C. Influence of  $\text{HSiO}_{1.5}$  Sol-Gel Polymer Structure and Composition on the Size and Luminescent Properties of Silicon Nanocrystals. *Chemistry of Materials* **2009**, *21* (22), 5426-5434.
- (16) DeBenedetti, W. J. I.; Chiu, S. K.; Radlinger, C. M.; Ellison, R. J.; Manhat, B. A.; Zhang, J. Z.; Shi, J. Y.; Goforth, A. M. Conversion from Red to Blue Photoluminescence in Alcohol Dispersions of Alkyl-Capped Silicon Nanoparticles: Insight into the Origins of Visible Photoluminescence in Colloidal Nanocrystalline Silicon. *J. Phys. Chem. C* **2015**, *119* (17), 9595-9608.
- (17) Weldon, M. K.; Queeney, K. T.; Gurevich, A. B.; Stefanov, B. B.; Chabal, Y. J.; Raghavachari, K. Si-H bending modes as a probe of local chemical structure: Thermal and chemical routes to decomposition of  $\text{H}_2\text{O}$  on Si(100)-(2 $\times$ 1). *J. Chem. Phys.* **2000**, *113* (6), 2440.
- (18) Ferguson, G. A.; Raghavachari, K.; Michalak, D. J.; Chabal, Y. Adsorbate-Surface Phonon Interactions in Deuterium-Passivated Si(111)-(1  $\times$  1). *J. Phys. Chem. C* **2008**, *112* (4), 1034-1039.
- (19) Caudano, Y.; Thiry, P. A.; Chabal, Y. J. Investigation of the bending vibrations of vicinal H/Si(1 1 1) surfaces by infrared spectroscopy. *Surf. Sci.* **2002**, *502-503*, 91-95.
- (20) Dumas, P.; Chabal, Y. J. Electron energy loss spectroscopy of H-terminated Si(111) and Si(100) prepared by chemical etching. *J. Vac. Sci. Technol., A* **1992**, *10* (4), 2160-2165.
- (21) Holm, J.; Roberts, J. T. Surface Chemistry of Aerosolized Silicon Nanoparticles: Evolution and Desorption of Hydrogen from 6-nm Diameter Particles. *J. Am. Chem. Soc.* **2007**, *129* (9), 2496-2503.
- (22) Zhang, X.; Garfunkel, E.; Chabal, Y. J.; Christman, S. B.; Chaban, E. E. Stability of HF-etched Si(100) surfaces in oxygen ambient. *Appl. Phys. Lett.* **2001**, *79* (24), 4051-4051.